

Copyright is owned by the Author of the thesis. Permission is given for a copy to be downloaded by an individual for the purpose of research and private study only. The thesis may not be reproduced elsewhere without the permission of the Author.



VOLCANIC
RISK SOLUTIONS



**Understanding magmatic processes and their
timescales beneath the Tongariro Volcanic Centre
through microanalytical investigations of
the tephra record**

A thesis presented in partial fulfilment of the requirements for
the degree of

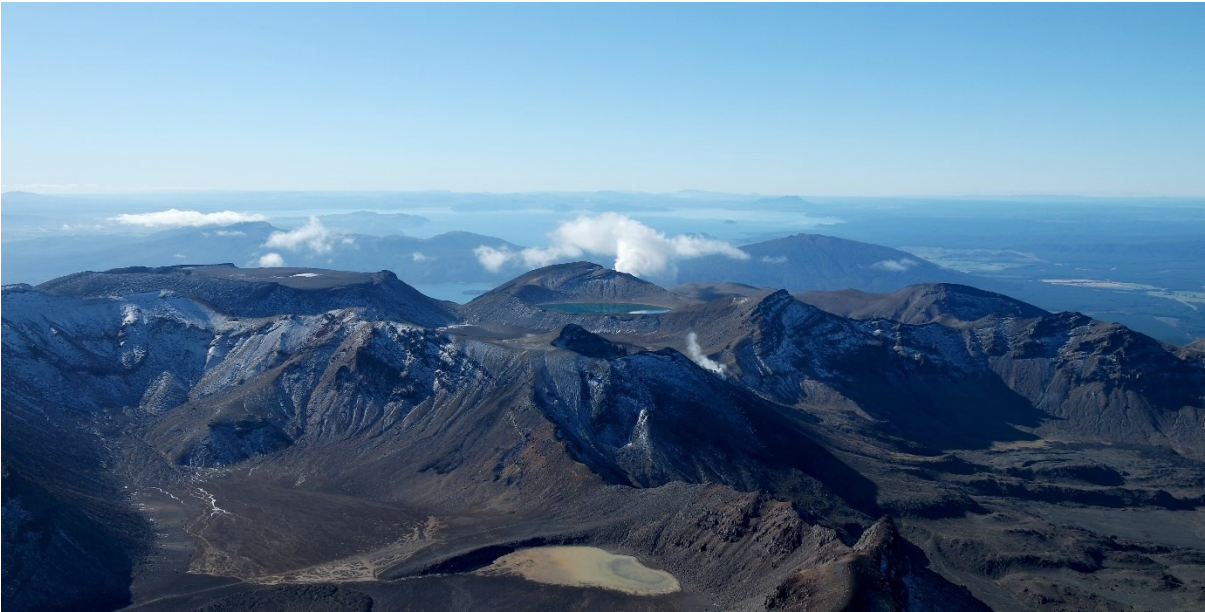
**Doctor of Philosophy
in
Earth Sciences**

at Massey University (Manawatū campus),
Palmerston North, New Zealand

Charline Lormand

2020





“Climb the mountain not to plant your flag, but to embrace the challenge, enjoy the air and behold the view. Climb it so you can see the world, not so the world can see you.”

David McCullough Jr.

Abstract

The Tongariro Volcanic Centre (TgVC) is a complex volcanic system located at the southern end of the Taupo Volcanic Zone in New Zealand, and has produced historical explosive eruptions of different eruptive styles. Its three ski fields and its iconic Tongariro Alpine Crossing attract more than 130,000 visitors annually. The last eruption occurred in 2012 on the northern flank of Tongariro, at the Te Maari vent. Due to the lack of precursory activity, this eruption could have turned into a tragedy if it had happened during day time. Previous studies have focused on the TgVC phenocrysts, which do not provide insights into shallow magmatic processes, essential to mitigate the resulting volcanic hazards. To understand magma ascent processes and their associated timescales, the textures and compositions of the micrometre-sized crystal cargo (i.e. microlites and micro-phenocrysts) carried during explosive eruptions are investigated, along with their conditions of crystallisation [i.e. P-T-X(H₂O)], which are constrained using hygrothermobarometry and MELTS modelling. Glass shards from five tephra formations spanning from *c.* 12 ka BP to 1996 AD, associated with explosive eruptions ranging from Strombolian to Plinian in style, are studied here. High resolution images and chemical maps of the tephra and the crystals are acquired using scanning electron microscopy (SEM) and secondary ion mass spectrometry. The variety of disequilibrium textures and compositions found in the micro-phenocrysts (< 100 μm) indicates multiple events of magma mixing, magma recharge, pressure fluctuations, and suggests an antecrystic origin. Crystal size distribution (CSD) of 60,000 microlites (< 30 μm) of plagioclase and pyroxene are generated from back-scattered-electron (BSE) images using a semi-automatic method developed here to undertake this study, employing the Weka Trainable Segmentation plugin to ImageJ. Combined with a well-constrained growth rate, crystallisation times are derived and indicate that microlites crystallised 2 to 4 days before the eruption, regardless of the eruption style. Microlite crystallisation occurred between mid-crustal depths and the surface (average of *c.* 4 km), at unusually high temperature for arc magmas of intermediate composition (average of 1076 °C), and at low water contents (average of 0.4 wt%). Considering the inferred depths and the crystallisation times of 2 to 4 days, ascent rates of only up to 9 cm s⁻¹ prior to shallow water exsolution are calculated. Vent exit velocities are not exceeding 27 m s⁻¹ after complete water exsolution, too slow to feed explosive eruptions characterised by supersonic exit velocities. This

research proposes a new conceptual model for the magmatic plumbing system beneath TgVC, where the microlitic crystal cargos result from multiple intrusions of aphyric melts through dykes, which most of the time stall and evolve at depth as deep as the mid-crust. Eventually, a magma injection percolates through previous intrusions and entrains crystals of differing textures and histories. Dykes feeding volcanism funnel into a narrow cylinder towards the surface, allowing acceleration and triggering explosive eruptions. Therefore, the conduit geometry at TgVC is a key controlling factor on the explosivity, with narrower conduits resulting in more explosive eruptions, suggesting that volatile-poor magmas can still trigger explosive eruptions. This study supports that vertical foliation of the igneous upper crust is consistent with dyking and thus may be more common than typically acknowledged.

Acknowledgments

Many people have participated to the accomplishment of my PhD thesis, whether they directly contributed to this research by assisting me in the field, in the lab, or with manuscript editing, or by any means of support over the past three years.

First of all, I would like to thank my chief-supervisor Georg Zellmer for giving me the opportunity to undertake this research, for sharing his knowledge, his guidance, his contagious enthusiasm about volcanic crystals, and for supporting me to share my research. I am grateful to have received the constructive advice and expertise from my co-supervisor Geoff Kilgour (GNS Science, Wairakei, New Zealand), who I am also thankful for welcoming and introducing me to the monitoring team during my visits to GNS Science at Taupo. I am thankful to my co-supervisors Károly Németh and Alan Palmer for assisting me in the field, and for their knowledge about volcanism and tephra stratigraphy. Thank you to Hisayoshi Yurimoto and Naoya Sakamoto (Hokkaido University, Japan) for welcoming me to the Isotope Imaging Laboratory (IIL) at Hokkaido University, Japan, and for their invaluable help and expertise with the SEM and SIMS analyses. Many thanks to Kate Arentsen for facilitating my travels to the field, to Japan and to conferences, and for her help with the administration of my doctoral studies. My special thanks are extended to the staff and students of the Volcanic Risk Solutions for their support and for welcoming me as a member of VRS, and especially Gabor Kereszturi and Stuart Mead for their outstanding academic advice and fruitful discussions.

This research was financed by the Ministry of Business, Innovation, and Employment through a Catalyst Global Strategic Partnership project “Mitigating volcanic hazards through advanced technologies”. I feel fortunate to have benefitted from this funding and the ensuing partnership. Thank you to the Department of Conservation/Te Papa Atawhai for allowing access and permit to the Tongariro National Park. I am also thankful for the support of Massey University – especially the School of Agriculture and Environment –, the Geological Society of New Zealand and Project Tongariro through awards and funding to share my research at international conferences.

Thank you to Anja Moebis, Niki Minards, John Irons (Massey University, New Zealand), Yoshiyuki Iizuka (Academica Sinica, Taiwan), Isabelle Chambefort (GNS Science, New Zealand), Takeshi Kuritani and Akiko Matsumoto (Hokkaido University, Japan) for their assistance with sample preparation and data acquisition. Thank you to all the IIL members and especially Abe Koutaro, Minami Kuroda, Ryosuke Fujita and Nozomi Matsuda for facilitating my stay in Japan, for introducing me to the beautiful Japanese culture, and for their help with anything related to the SIMS and EPMA analyses.

I am forever grateful to Timothy Druitt (Laboratoire Magmas et Volcans, France), and my MSc. supervisors Andrew Harris, (Laboratoire Magmas et Volcans, France) and

Tom Shea (University of Hawai‘i at Mānoa, USA) for encouraging me to pursue research in the field of volcanology at Massey University in Aotearoa/New Zealand.

A special thanks to May Sas (University of Auckland, New Zealand) for cheering me up all along this PhD journey. Thank you for being such a great “PhD wife”, and for enhancing my trips to Japan. I love you Matcha!

This life achievement would have never been possible without the moral support of my New-Zealand-based friends and PhD fellows, who became my Palmy family and who made my stay in New Zealand memorable. Through the parties, the potlucks, the hikes, the sports, the road trips, and so much more, their company was invaluable in keeping up my every day’s motivation and was something to look forward after a long day/week/month at the office. This includes Eric, Layla, Patry, Braden, Santiago, Ivan, Cecilia, Angela, Gabor, Jessica, Juan-Camilo, Kelly, Natalie, Omar, Dimitrios, Boglarka, Daniel, Cindy, Aniek, Flo, Sebastian, Camila, Rupsa, Istvan, Raimundo, Ari, Danny, Kevin, Andrea, Marija and many more wonderful people. I am also thankful to the encouragement of my life-long friends, especially Gabrielle, Maud, Léa, Mathieu, Manon, Yoann, Vincent, Alice and Alexis. Thank you all for your unconditional friendship.

Endless thanks to the incredible and loving human being I have met here in New Zealand, Taylor, who always believed in me during this journey. Thank you for supporting me through my ups and downs with your patience, sense of humour, advice, excitement, and, most importantly, love.

Last, but not least, there is not enough words to say how thankful I am to my family and especially my parents, Véronique and Frédéric, for their support throughout my PhD study. I will be forever grateful for encouraging me to follow my dreams, even from the other side of the world.

Table of Contents

Chapter 1. Introduction	1
1.1. Research introduction and motivations	2
1.2. Objectives	5
1.3. Thesis outline	8
Chapter 2. Geological background of the Tongariro Volcanic Centre	13
2.1. Eruptive styles of explosive eruptions.....	14
2.2. Tectonic and Geological Setting of the Taupo Volcanic Zone	19
2.3. Eruptive History of the Tongariro Volcanic Centre	24
2.3.1. Tongariro.....	27
2.3.2. Ngauruhoe	29
2.3.3. Ruapehu	33
Chapter 3. Methodologies of characterising crystals and magmas.....	39
3.1. Crystals in volcanic rocks.....	40
3.2. Crystal Size Distributions.....	48
3.3. Growth rate.....	54
3.4. Thermodynamics in magmas.....	57
3.4.1. Thermobarometry.....	59
3.4.2. Hygrometry	64
3.4.3. MELTS modelling	66
3.5. Sample selection, preparation, and analysis	68
3.5.1. Sample selection.....	68
3.5.2. Sample preparation.....	72
3.5.3. Analytical techniques used for this study.....	72
Chapter 4. Semi-automatic segmentation of crystals in BSE images for Crystal Size Distributions purposes.....	77
4.1. Introduction	80
4.2. Materials and Methods	81
4.2.1. Image acquisition and cleaning (Steps 1-2)	82
4.2.2. Image segmentation (Steps 3-5).....	85
4.2.3. Generation (Steps 6-8)	86
4.2.4. Manual Segmentation versus Trainable Weka Segmentation: a comparison	90
4.3. Results	92

4.4. Discussion and implications.....	99
Chapter 5. Textures of the crystal cargos.....	103
5.1. Introduction.....	108
5.1.1. Magmatic processes.....	108
5.1.2. Crystal textures.....	109
5.1.3. Crystal sizes and origins.....	111
5.2. Geological setting.....	113
5.3. Analytical methods.....	114
5.3.1. Tephra selection and sample preparation.....	114
5.3.2. Mineral and glass major element analysis and equilibrium.....	115
5.3.3. Tephra imaging.....	116
5.3.3.1. Scanning Electron Microscopy (SEM).....	116
5.3.3.2. Secondary Ion Mass Spectroscopy (SIMS).....	118
5.3.4. Crystal texture classification.....	118
5.4. Results.....	120
5.4.1. Major element chemistry.....	120
5.4.2. Plagioclase textures and zonations.....	130
5.4.2.1. Resorption and overgrowth.....	130
5.4.2.2. Oscillatory zoning.....	130
5.4.2.3. Single compositional jump.....	130
5.4.2.4. Featureless crystals.....	131
5.4.2.5. Sieve texture.....	133
5.4.2.6. Fractured crystals and overgrowth.....	133
5.4.2.7. Strontium zonation.....	133
5.4.3. Pyroxene textures and zonations.....	135
5.4.3.1. Resorption and overgrowth.....	135
5.4.3.2. Calcium-rich rims.....	135
5.4.3.3. Magnesian core and calcic rim.....	135
5.4.3.4. Fractured crystals and overgrowth.....	138
5.4.3.5. Aluminum zonation.....	138
5.5. Discussion.....	140
5.5.1. A diversity of magmatic processes.....	140
5.5.2. Magma recharge and mixing.....	140
5.5.3. Recycling of crystals.....	141
5.5.4. (Over)growth in aphyric magmas.....	142

5.5.5. Rapid decompression events	143
5.5.6. Rapid cooling-induced crystallisation.....	144
5.5.7. Dyking of magma.....	145
5.5.8. Entrainment of crystals into aphyric to sparsely phyrlic ascending melts ...	146
5.6. Conclusions	150
Chapter 6. Crystal Size Distributions and magma ascent rates.....	153
6.1. Introduction	155
6.2. Geological background and sample selection	157
6.3. Methods	162
6.3.1. Tephra sampling and image acquisition.....	162
6.3.2. Crystal Size Distributions (CSDs)	163
6.3.3. Compositional characterisation using Electron Probe Micro-Analysis (EPMA).....	165
6.3.4. Hygrothermobarometry.....	165
6.3.5. MELTS modelling	166
6.4. Results	167
6.4.1. Petrography	167
6.4.2. Texture and CSDs	167
6.4.3. Combining hygrothermobarometry and MELTS modelling to constrain magmatic P-T-X(H ₂ O) conditions	172
6.5. Discussion	178
6.5.1. Petrography and CSD shape	178
6.5.2. Microlite population growth time and plagioclase crystal growth rate.....	180
6.5.3. Unusually high temperature and quasi-anhydrous andesite magmas	185
6.5.4. Influence of regional tectonic setting and conduit geometry	187
6.5.5. Correlating geophysical signals and timescales.....	190
6.6. Conclusions	191
Chapter 7. Discussion: Dynamics and Geometry of Arc Magmatic Systems	193
7.1. Geochemical constraints on magmatic processes and plumbing system architectures.....	194
7.1.1. Common architectural models of magmatic reservoirs	194
7.1.1.1. Single stratified magma chamber.....	196
7.1.1.2. Independent magmatic chambers.....	202
7.1.1.3. The “crystal mush” model.....	206
7.1.2. Mafic, intermediate and felsic magmatic systems	210

7.1.2.1. Mafic systems	210
7.1.2.2. Intermediate systems.....	217
7.1.2.3. Felsic systems	225
7.1.3. Reflection on the existing conceptual models.....	231
7.2. A new architectural model beneath the Tongariro Volcanic Centre	236
7.2.1. Magma mixing	239
7.2.2. Crystal uptake from a crystal mush.....	239
7.2.3. Cooling-induced microlite crystallisation	240
7.2.4. Pulsatile regime of ascent	241
7.2.5. Ascent through dykes.....	242
7.3. Implications of new results and hazard assessment	244
7.3.1. Implications.....	244
7.3.2. Monitoring and hazard assessment	247
Chapter 8. Conclusions and outlook	249
8.1. Summary of results and implications	250
8.2. Future directions of research	256
8.3. Concluding remark.....	262
References	263
Appendix A: Supplementary Data	317
Appendix B: Supplementary Figures	335
Appendix C: Supplementary Tables	352
Appendix D: Statements of Contribution.....	450

List of Figures

- Figure 2.1. Figure 28.2 of Clarke *et al.* (2015) inspired by the initial classification of explosive eruptive styles of Walker *et al.*, (1973). It represents (vertical axis) the percentage of clasts < 1 mm in diameter at the intersection with the isopach equals to 10% of the maximum thickness of the deposit (F%) versus (horizontal axis) the area of dispersal (D) of the pyroclasts/deposits. This classification includes the initial classification of Walker *et al.*, (1973) and the Vulcanian classification based on the study of Wright (1980)..... 15
- Figure 2.2. (Figure in the next page) (A) Map of the current tectonic setting in New Zealand illustrating by the subduction of the Pacific Plate beneath the Australian Plate (source: GNS Science). The location of the Tongariro Volcanic Centre is indicated by the yellow arrow. (B) Map of the locations of the recently active volcanoes (Tongariro, Ngauruhoe and Ruapehu), volcanic vents (Te Maari, Red Crater, Tama Lakes and Saddle Cone), the inactive/extinct volcanoes (Kakaramaea, Pihanga, Pukeonake, Hauhungatahi and Ohakune Craters), the ski fields (Whakapapa, Tukino and Turoa), and the lakes (Rotoaira and Taupo) at TgVC. This is a shaded relief map derived from the 8-m-Digital-Elevation-Model (source: LINZ data). The colour gradient corresponds to the elevation variation. Georeference system: NZGD2000/New Zealand Transverse Mercator 2000.22
- Figure 2.3. Modified Figure 8.1.6 of Moebis (2010) illustrating the frequency of eruptions of the Tongariro Volcanic Centre for the last 26,000 years.....26
- Figure 2.4. Figure 2 of Auer *et al.* (2015) illustrating the single or multiple sources of each tephra emitted during the climactic eruptive period of the *c.* 10 ka Pahoka-Mangamate Formation. The vents are located along a large fissure between Ruapehu and Tongariro volcanoes.....29
- Figure 2.5. (A) Modified Figure 3 of Hobden *et al.* (2002) illustrating the discharge rates and the eruptive deposits of the most recent eruptions of Ngauruhoe. (B) Modified Figures 10a and 10b of Shane *et al.* (2017) illustrating the MgO and ⁸⁷Sr-⁸⁶Sr variations of compositions and isotopic signatures of the Ngauruhoe magmas over time. 31
- Figure 2.6. (A) Vulcanian to sub-Plinian eruption of Mt. Ruapehu in September 1995 observed from Whakapapa Village. Photo credits: Tim Whittaker. (B) Figure 4 of Christenson (2000) of an aerial photograph of the crater area of Mt. Ruapehu in January 1996 in which a lava spine and active fumaroles (A, B, C and D) were identified.36
- Figure 3.1. Modified figure 2.2 of Sen (2014) representing a microscopic schematic view of a volcanic rock composed of crystals (phenocrysts, glommerocrysts, microphenocrysts, microlites and a xenolith), vesicles and melt. The reaction rim around the xenolith is due to the disequilibrium between the crystals and the hosting melt.41

- Figure 3.2. Figure 2.11 from Sen (2014) illustrating the relationship between the undercooling ΔT ($T_{\text{liquidus}} - T_{\text{current}}$) and the nucleation and growth rates of crystals. Quenching (large degree of undercooling = rapid cooling rate) triggers the formation of glass and many small crystals. Small degree of undercooling (slow cooling rate) produces a few nuclei for coarse crystals. 43
- Figure 3.3. Shapes of crystal size distributions found in natural and experimental samples. (A) Figure 3 of Fornaciai *et al.* (2009) representing a linear CSD of plagioclase from a scoria of the 2002-2003 eruption of Stromboli, Aeolian Islands, Italy. (B) Figure 2 of Brugger & Hammer (2010) demonstrating curved-upwards CSD of plagioclase formed during decompression experiments of hydrous rhyodacite magma at different decompression rates. Downturn at smallest size interpreted as intersection artefact. 50
- Figure 3.4. Figure 4d of Morgan & Jerram (2006) illustrating the level of fit (R^2) versus the number of crystal slices considered. Note that at least 300 crystals are required to obtain confident results for intermediate and acicular shapes. 53
- Figure 3.5. The Rhodes diagram presents tests of orthopyroxene- and clinopyroxene-melt equilibrium (Rhodes *et al.*, 1979). It is based on 785 experimental data for orthopyroxene (opx) which yield $K_D(\text{Fe-Mg})^{\text{opx-liq}} = 0.29 \pm 0.06$, and based on 1245 experimental observations for clinopyroxene (cpx) which yield $K_D(\text{Fe-Mg})^{\text{cpx-liq}} = 0.28 \pm 0.08$. The blue area is the window where the putative pyroxene-melt should plot if in equilibrium. 60
- Figure 3.6. Sample location map of the tephra selected for this study. This is a shaded relief map derived from the 8-m-Digital-Elevation-Model (source: LINZ data). The colour gradient corresponds to the elevation variation. Georeference system: NZGD2000/New Zealand Transverse Mercator 2000. 70
- Figure 4.1. (Figure in the next page) Automation protocol to derive robust crystal size distributions using the Trainable Weka Segmentation (TWS) plugin of ImageJ. (1) BSE images of the samples are obtained using a scanning electron microscope. (2) Adobe Photoshop is used for image processing to make the background of the image homogeneous (i.e., black) and to remove noise (i.e., dust, scratch) using a despeckle filter. (3) The interface of the TWS plugin, where the cleaned image is loaded for input of sets of training pixels (STP's) of each class by the user. (4) Result of the TWS using the input STP's. Red, green, purple, and yellow are, respectively, background, groundmass (i.e., volcanic glass), plagioclase, and pyroxene microlites. (5) The segmented image is the post-segmentation image processed manually using Adobe Photoshop to separate clusters and to homogenise crystals. (6) Measurements of crystals (e.g., length and width) are obtained using the Analyze Particles tool in ImageJ. (7) Lengths and widths are implemented into CSDSlice (Morgan and Jerram, 2006) to obtain the five best matching crystal shapes (i.e., aspect ratios) for the studied crystal population. The one with the best level of fit is chosen and integrated into CSDCorrections (Higgins, 2000). (8) The CSD plot is obtained with CSDCorrections by using length, the best-fit shape factors and the area of the sample. I) Interpretations from CSD slope and intercept are made. 88

Figure 4.2. Example of pyroxene microlites of Mangamate – Te Rato classified using both manual and TWS segmentations, and the associated terms related to the performance evaluation of the automatic classifier. TN, TP, FN, and FP, respectively, stand for true negative, true positive, false negative, and false positive..... 92

Figure 4.3. (Figure in the next page) Examples of BSE images, binary images, and the best-fit shape curves of the plagioclase populations obtained from *CSDSlice* (Morgan & Jerram, 2006). a: BSE image of the Mangatawai glass shard captured using a JEOL NEOSCOPE 6000plus desktop-SEM, and its associated binary image and best-fit crystal habits. The bright white areas are due to residual gold coating in the vesicles. b: BSE image of the Mangamate – Te Rato glass shard, captured using a high resolution JEOL JSM-7000F FE-SEM, and its associated binary image and best-fit crystal habits. c: BSE image of a lava flow from the 1886 Tarawera eruption, captured using the FEI Quanta 200 Environmental SEM, and its associated binary image and best-fit crystal habits curve..... 93

Figure 4.4. (Figure in the next page) Binary images of the pyroxene population for a selected part of the Mangatawai glass shard (see (1a) in the upper left corner) with the associated CSD curves resulting from both manual and TWS segmentations. The manual CSD curve results from the manual segmentation of the image acquired with a high-resolution SEM (HR-SEM; JEOL JSM-7000F FE-SEM). The automatic CSD curves result from the segmentation using TWS of (1) the image acquired with the HR-SEM (i.e., Auto - HR SEM) and (2) the image acquired using the desktop SEM (i.e., Auto – Desktop SEM; JEOL NEOSCOPE 6000plus). The R^2 values are the level of fit for crystal habits of the pyroxene population extracted from *CSDslice* (Morgan and Jerram, 2006). STP stands for set (A) CSD curves resulting from manual segmentation and automatic segmentation with three STP by the user. (B) CSD curves resulting from manual segmentation and automatic segmentation with ten input STP by the user. The edges of the shard are less visible as in the segmented image (1a) as a new STP was added to classify them as the background. (C) CSD curves resulting from manual segmentation and automatic segmentation with ten STP and after post-segmentation image processing (P-S image processing; see step 5 from Figure 4.1). (D) CSD curves resulting from manual segmentation and automatic segmentation with ten STP and after post-segmentation image processing and setting a particle size range of $> 1\mu\text{m}^2$ 96

Figure 5.1. Typical back-scattered electron images of the tephra from the Tongariro Volcanic Centre of this study: Mangamate, Mangatawai, Tufa Trig, Ngauruhoe 1972-1975 and Ruapehu 1995-1996. The Mangamate image was captured using the FE-SEM JEOL JSM-7000F of the Isotope Imaging Laboratory at Hokkaido University, Japan. Mangatawai and Tufa Trig images were captured using the Environmental-SEM (FEI Quanta 200) of Massey University in Palmerston North, New Zealand. Ngauruhoe and Ruapehu images were captured using the JEOL NEOSCOPE 6000plus desktop SEM of GNS Science Wairakei Research Centre in Taupo, New Zealand. Ox, plg, px, mph, ph and gl stand for oxide, plagioclase, pyroxene, micro-phenocryst, phenocryst and glass, respectively..... 117

Figure 5.2. Comparison of glass and mineral major elements: (a) TAS diagram (Le Bas *et al.*, 1986), (b) histogram of anorthite contents of plagioclase microlites and (c)

discriminating chart for pyroxenes (Morimoto, 1989). Data for plagioclases and pyroxenes involve microlites and micro-phenocrysts only, except the field for Mangamate (data of Auer et al. 2015). All plotted compositions are recalculated to 100% anhydrous..... 123

Figure 5.3. (Figure in the next page) Rhodes diagram to assess the equilibrium of the rims of plagioclase microlites from TgVC tephros using the anorthite content $[An\# = 100 \times Ca / (Ca + Na + K)]$ of the plagioclase and melt compositions. Each horizontal bar is a range in glass An hosting a single mineral grain. The blue and grey fields in a-c represent the H₂O-saturated and dry experiments from basaltic to rhyolitic melts used in Figure 3a of Waters and Lange (2015), excluding the anhydrous felsic melts from the synthetic experiments of Brugger *et al.* (2003). According to previous studies (Arpa *et al.*, 2017; Deering *et al.*, 2011a; Kilgour *et al.*, 2009; Kilgour *et al.*, 2013), TgVC magmas are water-poor magmas, which is confirmed by the prevalence of plagioclase-liquid pairs in equilibrium. Note that disequilibrium is not uncommon, especially for the Mangatawai and Tufa Trig tephros. 124

Figure 5.4. (Figure in the next page) Rhodes diagram to assess the equilibrium of the rims of orthopyroxene microlites from TgVC tephros using the Mg# $[Mg\# = 100 \times Mg / (Mg + Fe^{2+})]$ of the orthopyroxene and glass compositions. Each horizontal bar is a range in glass Mg# hosting a single mineral grain. Orthopyroxene-liquid and clinopyroxene-liquid equilibria were assessed using the Fe-Mg exchange coefficients determined by Putirka (2008) i.e. $Kd(Fe-Mg)^{opx-liq} = 0.29 \pm 0.06$. Note that disequilibrium is not uncommon, especially for the Mangatawai and Tufa Trig tephros. 126

Figure 5.5. (Figure in the next page) Rhodes diagram to assess the equilibrium of the rims of clinopyroxene microlites from TgVC tephros using the Mg# $[Mg\# = 100 \times Mg / (Mg + Fe^{2+})]$ of the clinopyroxene and glass compositions.. Each horizontal bar is a range in glass Mg# hosting a single mineral grain. Clinopyroxene-liquid equilibria were assessed using the Fe-Mg exchange coefficients determined by Putirka (2008) i.e. $Kd(Fe-Mg)^{cpx-liq} = 0.28 \pm 0.08$. Note that disequilibrium is not uncommon, especially for the Mangatawai and Tufa Trig tephros. 128

Figure 5.6. Four of the seven main observed textures with descriptions and sketches of potential processes explaining the texture in plagioclase phenocrysts, but especially in plagioclase microlites and micro-phenocrysts, of the Tongariro Volcanic Centre andesitic tephros: (a) resorption and overgrowth textures and (b) oscillatory zoning, indicating multiple events of magma mixing and recharge; (c) single compositional jump that develops after resorption and rapid decompression events; (d) featureless crystals due to late-stage crystallisation. The black scale at the bottom left corner of each SCAPS image is 10 μ m in size. Ca, Si, Sr, Na, and BSE respectively stand for calcium, silica, strontium, sodium, and back-scattered electron images. 132

Figure 5.7. Three of the seven main observed textures with descriptions and sketches of potential processes explaining the texture in plagioclase microlites, micro-phenocrysts and phenocrysts of the Tongariro Volcanic Centre andesitic tephros: (a) sieve textures resulting from rapid decompression; (b) fracture (and overgrowth)

triggered by entrainment of crystals from a crystal-mush-like environment; (c) strontium zonation (Sr) associated with a negative correlation with An suggesting recycling of old crystals. Ca, Si, Sr, Na, BSE and An stand, respectively, for calcium, silica, strontium, sodium, back-scattered electron and anorthite content. 134

Figure 5.8. Three of the five main observed textures with descriptions and sketches of potential processes explaining the texture in pyroxene microlites, micro-phenocrysts and phenocrysts of the Tongariro Volcanic Centre andesitic tephra: (a) resorption and overgrowth textures indicating multiple events of magma mixing; (b) Ca-rich rims and (c) magnesian-core and calcic-rim demonstrating a shift of mineral phase (i.e. orthopyroxene to clinopyroxene) resulting from rapid decompression. Fe, Ca and BSE respectively stand for iron, calcium and back-scattered electron images. The white scale at the bottom left corner of each map is 10 μm in length. 137

Figure 5.9. Two of the five main observed textures with descriptions and sketches of potential processes explaining the texture in pyroxene microlites, micro-phenocrysts and phenocrysts of the Tongariro Volcanic Centre andesitic tephra: (a) fracture (and overgrowth) triggered by entrainment of crystals from a crystal-mush-like environment; (b) aluminium zonation with sharp and fuzzy zonation boundaries suggesting rapid growth kinetics rather than diffusion-controlled zonation. Mg, F, Ca, Al and BSE respectively stand for magnesium, fracture, calcium, aluminum and back-scattered electron images. The white scale at the bottom left corner of each map is 10 μm in length..... 139

Figure 5.10. Conceptual model of the magma plumbing system feeding the explosive eruptions of the Tongariro Volcanic Centre. Considering the crustal extension of the TgVC at a rate of $c. 7 \pm 1.2$ mm/yr since 20 ka (Gómez-Vasconcelos *et al.*, 2017), we infer a vertical geometry, where magma ascends via dykes. The windows (a-h) are representative of processes occurring within the dykes and places randomly into the figure as examples. The various textures observed in microlites, micro-phenocrysts, and phenocrysts of the crystal cargos from TgVC intermediate magmas result from a variety of magmatic processes: (a) magma mixing, (b-c) pressure and temperature fluctuations, (d) high undercooling, and (e) shallow degassing-induced crystallization. Batches of aphyric magmas enter the upper crust through previously intruded semi-solidified dykes (g-h), which occasionally reach the surface, resulting in a wide variety of eruption styles. The phreatic eruption of Upper Te Maari and the heating cycles of Mt. Ruapehu's Crater Lake may be related to failed eruptions triggered by magma injections..... 149

Figure 6.1. Fe-maps of some orthopyroxene microlites obtained using the FE-SEM JEOL JSM-7000F at the Isotope Imaging Laboratory of Hokkaido University in Sapporo, Japan. Note the resorbed cores and the complex zonations in iron (arrows) where RC and F stand for resorbed core and fracture, respectively. The scale of 10 μm is represented by a white bar at the left bottom corner of each image. 163

Figure 6.2. Pyroxene crystal size distributions (logarithm of the population density versus the size in μm) of various historical tephra from the Tongariro Volcanic Centre, New Zealand. The grey field represents the full range covered by the CSD plots. CSD parameters such as the number of crystals, the best fit shape factors for the studied

crystal population and their associated coefficient of determination obtained with *CSDslice* (Morgan & Jerram, 2006), and the crystal content from *CSDCorrections* (Higgins, 2000) are reported in Table 6.2..... 169

Figure 6.3. Plagioclase crystal size distributions (logarithm of the population density versus the size in μm) of various historical tephra from the Tongariro Volcanic Centre, New Zealand. The grey field represents the full range covered by the CSD plots. CSD parameters such as the number of crystals, the best fit shape factors for the studied crystal population and their associated coefficient of determination obtained with *CSDslice* (Morgan & Jerram, 2006), and the crystal content from *CSDCorrections* (Higgins, 2000) are reported in Table 6.2. 170

Figure 6.4. Pyroxene and plagioclase CSD slopes (left y-axis), and residence time (right y-axis) derived from the slope and a well-constrained growth rate. Plagioclase CSD slopes are indicated by yellow diamonds, orthopyroxene CSD slopes by light blue diamonds. Residence time calculated from the pyroxene slopes and an orthopyroxene growth rate determined for Mangatawai 407-17 (Zellmer *et al.*, 2016c; Zellmer *et al.*, 2018), are represented by magenta triangles. As orthopyroxene and plagioclase were crystallising concomitantly, a plagioclase growth rate range is derived ($1.65 \times 10^{-11} \text{ m s}^{-1}$ to $6.43 \times 10^{-11} \text{ m s}^{-1}$). Mm, TR, Oh, Wha, Ng, Rua respectively stand for Mangamate, Te Rato, Ohinepango, Wharepu, Ngauruhoe and Ruapehu..... 172

Figure 6.5. P-T-X(H_2O) plots retrieved from hygrometry (Putirka, 2008; Waters & Lange, 2015) and *MELTS* modelling (Asimow & Ghiorso, 1998; Ghiorso & Sack, 1995) for the TgVC deposits studied. Parameters for *MELTS* were fixed at 0, 0.5, 1, 1.5 and 2 wt.% for the water contents and from 0.1 to 800 MPa at 25 MPa intervals for pressures. Grey plots in (c) and (d) are copies of plots in (a) and (b). Note that *MELTS* data points (plots c and d) indicate the average (in color) and their range (i.e. not uncertainties)..... 175

Figure 6.6. Crystal size distributions of the pyroxene microlite population. Slopes used to derive microlite crystallisation times (reported in Table 6.4) were calculated from this size section (10-30 μm). See text for discussion. The grey field represents the full range covered by the CSD plots. 182

Figure 6.7. Crystal size distributions of the plagioclase microlite population. Slopes used to derive microlite crystallisation times (reported in Table 6.4) were calculated from this size section (10-30 μm). See text for discussion. The grey field represents the full range covered by the CSD plots. 183

Figure 6.8. Conceptual model of the shallow magma plumbing system beneath the TgVC. Temperatures, pressures and water contents are based on the results obtained with *MELTS*. (1) Hot (*c.* 1076 °C) andesitic/dacitic magmas ascending with microphenocrysts displaying complex oscillatory zonings. Nuclei sites for microlites of orthopyroxene and plagioclase at an average of 4 km depth and with water contents of *c.* 1 wt. %. (2) Microlite nucleation and growth due to cooling. (3) Microlites keep on nucleating and growing while degassing at *c.* 1 km yields to bubble nucleation and volume expansion and thus faster ascent rates, but not fast enough to feed the most explosive eruptions. (4) A change in geometry of the conduit cross-section

- (from dyke to cylinder) is thus required to accelerate these magmas to up to 400 m s^{-1} upon exit. 190
- Figure 7.1. Figure 16 of Fichaut *et al.* (1989) representing the magma chamber(s) beneath Mt. Pelée. 1, 2 and 3 are symbols for various dioritic and gabbroic cumulates. ... 198
- Figure 7.2. Figure 9 of Nairn *et al.* (2004) representing the conceptual model of the stratified plumbing system beneath Tarawera volcano (A) before and (B) during the c. 1315 AD Kaharoa eruption. The 8 km linear vent zone involved during the eruption suggests vertical magma rise. T1, T2 and T3 are three magma layers of distinct crystallinities, and compositions. The white arrows in (A) represent the uprising siliceous melt expelled from the fractional crystallisation of the deeper mafic magma.....200
- Figure 7.3. Figure 14 of Carrasco-Núñez *et al.* (2012) illustrating a cross section of Los Humeros volcano at the onset of the c. 0.1 Ma BP Zaragoza eruption, which was fed by two main magma reservoirs of distinct chemistry and petrology suggesting separate evolutions. D, RD, BA, B, A, TA, FMQ, NNO and xtal stand for dacite, rhyodacite, basaltic andesite, basalt, andesite, trachyandesite, fayalite-magnetite-quartz, nickel-nickel-oxide and crystal, respectively.....204
- Figure 7.4. Figure 1 of Cashman *et al.* (2017) illustrating the common view of magmatic system with crystal mush based on previous works. (A) Upper crustal magmatic system mostly composed of a large crystal mush and smaller melt silicic melt pods which result from the frequent replenishment of mafic magma inspired from the study of Hildreth (2004). (B) Schematic representation of a trans-crustal magmatic systems with interconnected magma batches resulting from the destabilisation of melt lenses (Christopher *et al.*, 2015). (C) The effect of the particle volume fraction on the change of rheology from magma (orange) to mush (grey). The blue and red curves are calculated using different rheological models (red curve based on the model of Costa *et al.*, 2009a; blue curve based on the model of Marsh, 1981). The insert represents the changes in mush strength as a function of the particle volume fraction where the green dashed curve is based on the experimental data using the Westerly granite and the purple-dashed curve is based on experimental data using Delegate aplite (Rosenberg & Handy, 2005).....209
- Figure 7.5. Paroxysmal activity of Stromboli volcano in July 2019 generating a pyroclastic flow after the crater collapse. Photo credits: Sailactive I Segelreisen & Yachtcharter.211
- Figure 7.6. Figure 9 of Bragagni *et al.*, (2014) illustrating a conceptual model of the feeding system beneath Stromboli volcano during normal Strombolian and effusive activity (a) and during paroxysm events (b).213
- Figure 7.7. Figure 7 of Ubide & Kamber (2018) representing the magmatic plumbing system beneath Mt. Etna composed of multilevel interconnected magma chambers interpreted by the study of Ubide & Kamber (2018) and references therein. A main storage region is at c. 10 km depth at the interface between the crystalline basement and the shallower sedimentary sequence. The blue bars represent the magma storage depths inferred from geophysical data. Detected high-VP body (HVP) and the

shallow low-Vp zone (LVZ) are used to interpret the magma ascent rates. The magmatic system consists of the accumulation of intruding repeated batches of new mafic magmas, which mix with the resident crystal mush. Injections of mafic intrusions either feed progressively the main central conduit or may feed eccentric eruptions (yellow dashed line)..... 216

Figure 7.8. Figure 13 of Nakada *et al.* (2019) illustrating the cumulative volume of dome growth formation over time for different eruptions. 221

Figure 7.9. Figure 1 of Johnston *et al.* (2000) representing schematic cross sections and photographs from the 1945 activity at Mt. Ruapehu. P is a reference of Pyramid peak. 225

Figure 7.10. Figure 5.6 of Sas (submitted) illustrating a conceptual model of the magmatic system of Okataina Volcanic Centre, New Zealand, that is largely intruded by mafic underplating intrusions, which differentiate by assimilating mid-crustal components. The intrusions transfer heat and volatile to the overlying silicic crystal mush, forming rhyolitic melt pods which eventually feed explosive eruptions and domes..... 230

Figure 7.11. (Figure in the next page) Common magmatic plumbing systems beneath arc volcanoes. Mafic magmatic systems are composed of a single or multiple interconnected reservoir(s) which is/are frequently replenished by deep mafic intrusions, feeding mostly effusive (lava flows and Strombolian style) eruptions, and sometimes explosive eruptions (paroxysms). Flank eruptions are common and may be fed by rapidly ascending magma (e.g. Ubide & Kamber, 2018). Intermediate magmatic systems are composed of a single or multiple interconnected reservoir(s) which is/are frequently replenished by deep mafic intrusions which stall, evolve and form a crystal mush in the crust. Intermediate compositions are reached either due to convection between the silicic crystal mush and the replenished mafic intrusions (Reubi & Blundy, 2009), or due to fractional crystallisation (Tait *et al.*, 1989). The entire range of eruption styles can be associated with intermediate magmatic systems, from effusive eruptions (lavas and domes) to Plinian with formation of pyroclastic density currents and high eruptive column. Viscous lava flows and volatile-rich domes may be associated with transitions forth and back to explosive eruptions (Preece *et al.*, 2016). Felsic magmatic systems are fed by a large reservoir which consists of a crystal mush which has experienced crustal assimilation and fractional crystallisation. Melt pods form within this framework due to underplating of mafic intrusions causing heating and remobilisation of the crystal mush. Eventually, mafic intrusions trigger climatic eruptions of up to ultra-Plinian in style (e.g. Wilson, 2001) fed by crystal-bearing or crystal-free rhyolites, possibly mingled with more mafic magma(s)..... 232

Figure 7.12. Figure 6 of Tibaldi (2015) representing the the preferential geometry of the magma plumbing system in the lower crust governed by the local stress field. Strike-slip fault would enhance the formation of dyke, whereas reverse faults would preferentially develop sill and arrest dyke propagation, and a normal fault will likely develop sill at depth and dyke towards the surface where the dip is increasing.... 235

Figure 7.13. (Figure in the next page) The conceptual model of the shallow magma plumbing system beneath TgVC inferred from this study. The magmas that feed

explosive eruptions at TgVC are nearly phenocryst-free and are composed of micro-phenocrysts and large microlites with complex textures and zonations suggesting an antecrystic origin (Chapter 5). Microlites consist of plagioclases and pyroxenes that grew concomitantly due to cooling during magma ascent. Unusually high temperatures and low water contents at microlite crystallisation suggest that cooling drove microlite crystallisation (section 5.4.3). Microlite crystallisation time inferred from CSDs (section 5.4.2) are used with the depth constraint from MELTs modelling and thermobarometry calculations (section 5.4.3) to calculate magma ascent rates, which are too slow to feed explosive eruptions. Thus, a reduction of the conduit cross-section (from dyke to cylinder) is required to accelerate the magmas feeding explosive eruptions at TgVC (Vulcanian eruption with exit velocities of up to 400 m s^{-1}), consistent with the extensional tectonic setting of the region which is accommodated by dyke intrusions (Gómez-Vasconcelos et al., 2017).237

Figure 8.1. Ca (calcium) map of a large microlite of pyroxene from Mangatawai showing Ca-rich rims, cryptic in BSE image.257

Figure 8.2. Melt inclusion observed (yellow arrow) in a pyroxene microlite from Mangatawai 407-17.259

Figure 8.3. BSE images of two glass shards from (a) the 1995 Ruapehu (sub-Plinian) and (b) the 1996 Ruapehu (Strombolian) eruptions. Note the different morphology of the vesicles between the two eruptions.261

List of Tables

Table 3.1. (Table in the next page) Schematic representations of the common plagioclase crystals and textures observed in volcanic rocks, and their interpretations.....	46
Table 3.2. Descriptive table of the samples selected for this study. Mangamate (Mm) units were sampled and prepared during this study, and described by Donoghue <i>et al.</i> (1995). Mangatawai and Tufa Trig units were sampled, prepared and described by Moebis (2010). Ngauruhoe and Tufa Trig 19 units were sampled by GNS science, prepared and described during this study. Rua, Ng, TL, and SC stand for Ruapehu, Ngauruhoe, Tama Lakes and Saddle Cone, respectively. S, sP, V, pm, and P stand for Strombolian, sub-Plinian, Vulcanian, phreatomagmatic and Plinian, respectively.....	71
Table 4.1. Descriptive table of the samples used in this study and their segmentation characteristics: crystallinity, mineral assemblages, and the duration of segmentation, the number of crystals segmented and the best-fit crystal habit with level of fit for both manual and automatic (i.e., TWS) segmentations.....	84
Table 4.2. Results of the classifier performance for the Trainable Weka Segmentation (TWS) tested on two volcanic glass shards. The predictive positive value (PPV), the true positive rate (TPR) and the precision-recall F measure (F-score) are calculated using the ROCR package in RStudio for resulting binary images of plagioclase and pyroxene microlite populations.	98
Table 5.1. Summary table of number of images acquired using (1) the Cameca IMS-1270 SIMS instrument equipped with a Stacked CMOS-type Active Pixel Sensor (SCAPS) and (2) the FE-SEM; JEOL JSM-7000F at IIL, Hokkaido University, Japan. Crystals were classified into different categories based on their texture. N/A stands for non-applicable/no analysis.....	119
Table 5.2. (Table in the next page) Anorthite content (An) and Mg number (Mg#) of the plagioclases and the pyroxenes, respectively, for all tephra formations but Mangamate. The tephra member labels for Mangatawai (e.g. 407-14) and Tufa Trig (e.g. Tf8) correspond to the sample names used in Moebis <i>et al.</i> (2011) and Donoghue <i>et al.</i> (1997), respectively. N/A, n, E, P, A and D respectively stand for non-applicable/no analysis, number of analyses, enstatite, pigeonite, augite and diopside.....	121
Table 6.1. Descriptive table of the TgVC tephtras selected for this study. Plg, ens, pg, aug and ox stand for plagioclase, enstatite, pigeonite, augite and oxide, respectively.	161
Table 6.2. CSD parameters for TgVC pyroxene and plagioclase microlite populations, i.e. the number of crystals considered for CSD generation, the best fit shape factors and the associated coefficient of determination retrieved from <i>CSDslice</i> (Morgan & Jerram, 2006), and the crystal content (vol. %) calculated by <i>CSDCorrections</i> (Higgins, 2000).....	171

- Table 6.3. (Table in the next page) Temperature (T), pressure (P), and water content (H₂O) ranges of crystallisation obtained from hygrobarmetry and MELTS for the TgVC tephtras. The temperatures and pressures were calculated using the orthopyroxene-liquid thermobarometer of Putirka (2008), namely the Eq. 28a and Eq. 29a (SEE=39 °C and SEE=±210 MPa), and the clinopyroxene-liquid thermometer from Putirka (2008; Eq. 33) and the clinopyroxene-liquid barometer of Neave & Putirka (2017) for Ng72* (SEE=±45 °C and SEE=±140 MPa). The water content was determined by the plagioclase hygrometer (SEE=±0.35 wt. %; Waters & Lange, 2015). Guided by the hygrobarmetric results, *MELTS* modelling was performed (Asimow & Ghiorso, 1998; Ghiorso & Sack, 1995). The temperatures, pressures and water contents reported correspond to ranges for which *MELTS* successfully reproduce the minerals observed. The maximum ascent rates were calculated using the minimum residence time derived from the CSD slope and a well-constrained orthopyroxene growth rate (Zellmer et al., 2016c; Zellmer et al., 2018), and the maximum depth derived from hygrobarmetry and *MELTS* modelling. Mangatawai Formation: 407-14 to 407-59. Tf, Ng and Rua stand for Tufa Trig, Ngauruhoe and Ruapehu, respectively..... 176
- Table 6.4. Microlite population CSD slopes, crystallisation time and plagioclase growth rate for the TgVC tephtras. The slope was calculated from the average CSD slope between 10 and 30 µm. The microlite crystallisation time was calculated using the slope and a constrained orthopyroxene growth rate for Mangatawai (Zellmer *et al.*, 2016c; Zellmer *et al.*, 2018). 184

Glossary/Abbreviations

AD	Anno Domini
BP	Before Present
<i>c.</i>	<i>circa</i> , used for “around/about/approximately”
Cpx	Clinopyroxene
CSD	Crystal Size Distribution
e.g.	exempli grati, used for “for example”
(FE-)SEM	(Field Emission) Scanning Electron Microscope
i.e.	<i>id est</i> , used for “that is to say”
IIL	Isotope Imaging Laboratory
ka	Kiloanni
kyrs	Kiloyears
Opx	Orthopyroxene
Plg	Plagioclase
SIMS	Secondary Ion Mass Spectrometer
TAC	Tongariro Alpine Crossing
TgVC	Tongariro Volcanic Centre
TVZ	Taupo Volcanic Zone

Chapter 1. Introduction

Chapter content:

1.1. Research introduction and motivations	2
1.2. Objectives	5
1.3. Thesis outline	8

1.1. Research introduction and motivations

One of the most important aspects of current research is focused on assessing volcanic hazards and how to forecast volcanic eruptions. Notably, explosive eruptions may be less predictable and may impact larger areas than effusive activity (e.g. tephra deposition, fast-moving pyroclastic density currents), particularly in highly populated areas e.g. Napoli, Italy, near Vesuvius; Arequipa, Peru, near El Misti; Goma, Democratic Republic of Congo, near Lake Nyiragongo; Quito, Ecuador, near Cotopaxi and Guagua Pichincha; Catania, Sicily, near Mt. Etna; and Auckland, New Zealand, built on the Auckland Volcanic Field (e.g. Bonaccorso *et al.*, 2011; Favalli *et al.*, 2009; Kereszturi *et al.*, 2014; Marzocchi *et al.*, 2004; Pistolesi *et al.*, 2014; Sandri *et al.*, 2014).

Estimation of the time windows between geophysical unrest and the actual eruption have awakened the interest of volcanologists and stakeholders to provide insights into hazards mitigation and to establish reliable evacuation plans. Volcanoes are typically characterised by complex precursory patterns leading to challenging predictions of future eruptions. If patterns in the timing of eruptive processes for a volcanic edifice can be identified, mitigation may become easier through devising appropriate volcanic hazards maps and evacuation plans. In the literature, many geochemical approaches are used to infer eruptive processes and help forecast eruptions. Some of the most common methods used in petrology are:

1. Textural analyses of pyroclasts, crystals or bubbles are used for inferring eruptive processes such as nucleation, crystal growth and degassing (Donoghue *et al.*, 1997; Gardner *et al.*, 1998; Klug & Cashman, 1994; Shea *et al.*, 2010b).
2. Crystal textures (e.g. zonation) can also be used as geo-speedometer to monitor ascent rate (e.g., hornblende breakdown rims during decompression, Rutherford & Devine, 2003).

3. Crystal Size Distributions (CSDs) are commonly-used to reveal information about crystallisation dynamics, and, if the growth rate is constrained, residence time of crystals can be inferred from the slope of the CSD (Higgins & Roberge, 2007; Marsh, 1988; Muir *et al.*, 2011).
4. Modelling of diffusion has become a powerful tool to infer timing of crystallisation processes and characterization of the origin of crystals (e.g. Chakraborty, 2008; Costa *et al.*, 2003; Costa & Dungan, 2005; Costa *et al.*, 2008; Flaherty *et al.*, 2016; Kilgour *et al.*, 2014; Morgan *et al.*, 2004; Shea *et al.*, 2015).

The estimation of magmatic timescales and especially crystal residence time are combined with thermodynamic modelling of magmatic processes to recover critical parameters (e.g. temperature, pressure, water content, crystallinity) to comprehend the evolution of the magmatic system (e.g. Cooper & Kent, 2014; Masotta *et al.*, 2016; Pamukcu *et al.*, 2015; Stock *et al.*, 2016b; Venugopal *et al.*, 2016; Zellmer *et al.*, 2014b). Generally, petrologists and volcanologists have focussed on phenocryst crystals ($> 100 \mu\text{m}$) to infer processes and timescales. These time capsules, however, record mainly deep magmatic processes ($> 15 \text{ km}$) occurring up to hundreds of thousands of years before the actual eruption (e.g. Blundy & Annen, 2016; Menand *et al.*, 2015; Petrelli & Zellmer, in press). Shallow signals are covered by geophysical signals (e.g. seismicity, tomography, remote sensing) and gas chemistry surveys, hence providing short-term and syn-eruptive forecasting of an imminent eruption. However, they do not supply information about the internal magmatic processes at work during ascent through the upper crust. Therefore, there is a gap in the understanding of magmatic processes occurring between the lower-crustal and the shallow depths. Smaller crystals ($< 100 \mu\text{m}$), referred as micro-phenocrysts ($100\text{-}30 \mu\text{m}$) and microlites ($< 30 \mu\text{m}$), are interpreted to form due to decompression-induced degassing and cooling (Hammer *et al.*, 1999; Noguchi *et al.*,

2006; Sano & Toramaru, 2017; Szramek *et al.*, 2006; Szramek *et al.*, 2010). Consequently, they crystallise at shallower depths and may record shallow magmatic processes, which would provide significant indications in forecasting short-term timescales of magma ascent, essential for hazard mitigation and evacuation planning.

The Tongariro Volcanic Centre (TgVC) is situated in the southern part of the Taupo Volcanic Zone (TVZ) in the North Island of New Zealand and at the southern end of the 2800 km long Tonga-Kermadec arc-back-arc, resulting from the convergence of the Pacific and Australian tectonic plates (e.g. Stern *et al.*, 2006). It is composed of two historically active eruptive centres, namely Ruapehu and Tongariro, with several vent sites of which the Ngauruhoe volcanic cone is one. Ngauruhoe is one of the fastest growing cones over older vents at TgVC (Hobden *et al.*, 2002; Moebis, 2010). TgVC has exhibited several eruptive styles from Strombolian to Plinian style eruptions (Walker, 1973), some with phreatic-to-phreatomagmatic phases. Ruapehu volcano, notably, has been quite active over the Holocene with at least 66 eruptive periods, including 40 of them over the past 70 years (Smithsonian Institution's Global Volcanism Program, 2019). TgVC is located in the Tongariro National Park, which is the oldest national park of New Zealand as well as a dual United Nations Educational, Scientific, and Cultural Organization (UNESCO) World Heritage Area since 1993 for its remarkable landscapes and cultural richness (Cleere, 1995; Rössler, 2006). Both local and international visitors come every year to enjoy the outdoor activities available in the area. Three ski resorts (Whakapapa, Turoa and Tukino) on Mount Ruapehu are open from June to the end of October. The Tongariro Alpine Crossing (TAC) is the most famous day-hike of New Zealand. During the busiest season, between November and April, up to 1500 visitors are on the TAC daily (Jolly *et al.*, 2014b) and 130,000 visitors were reported for the full year of 2017 (DOC, 2017). Also, numerous rivers in the national park are used for river rafting.

However, all these activities expose visitors to the risk of eruptions and their consequences as eruption-fed and meteorologically triggered lahars and landslides. Indeed, the last eruption occurred in August 2012 within the Upper Te Maari Crater, on the northern slope of Mt. Tongariro. It began with a 770,000 m³ landslide (Procter *et al.*, 2014) and was followed by high-velocity and wide-spread pyroclastic density currents that reached the TAC walkway (Lube *et al.*, 2014). Ballistics were ejected as far as the Ketetahi Hut (ca. 400-500 m in distance), used by many hikers of the TAC (Breard *et al.*, 2014). Also, a farming community of 100 residents, who live on the northern slopes of the volcano, and their livestock are permanently at risk. It was fortunate that the last eruption occurred during the night when there were few people at the park. If such an eruption occurred during day time, many lives would be exposed to the associated volcanic hazards. Thus, there is a real need of identifying the shallow magmatic processes and timescales that have occurred during the past TgVC explosive eruptions.

By combining different petrological methods on a tephra record from TgVC, this study will provide a better understanding of the magmatic processes occurring during microlite crystallisation at the onset of explosive eruptions in this actively hazardous area.

1.2. Objectives

This research aims to visualise, characterise and estimate timescales of late-stage ascent processes down to submicron scale for different eruption styles of explosive eruptions (Strombolian, Vulcanian, sub-Plinian and Plinian). Unlike the phenocrysts, which record deep processes, the study of smaller crystals called microlites (< 30 µm) yield the characteristics of the latest pre-eruptive processes, at the onset of an explosive eruption. Indeed, as microlites crystallize in the conduit prior to the eruption, microlites record chemical information that can be used to harvest timescales of crystal growth and

ascent. Further high-resolution analysis of chemical zoning in micro-phenocrysts will allow detailed constraints to be made on their origin and growth histories. We focus our study on TgVC for several reasons: (i) it has exhibited frequent and intense eruptive activity in historical time; (ii) it has produced various styles of explosive eruption (Strombolian to Plinian) with variable influence of external water (ground, surface and hydrothermal); (iii) previous studies have only focussed on the information recorded by the phenocrystic crystal cargos revealing deep magmatic and ascent processes; and (iv) it is a very touristic area and requires reliable information to appropriately assess the hazards it poses. To this end, four main objectives were set:

1. Development of an automated method to characterise microlite crystal size distributions (CSD) from back-scattered electron (BSE) images.

Crystal size distribution (CSD) in volcanic rock may be used as a powerful tool to understand crystallisation dynamics because they provide information about nucleation, growth of crystals and ascent processes. The term CSD basically represents a line of the logarithm of the population density n plotted against the linear crystal size L (where $n=dN/dL$, where N is the cumulative number of crystals per unit) (Marsh, 1988). In general, CSDs are typically obtained from thin section photographs in which the crystals have been outlined manually using image processing software (e.g. Photoshop). Even though their acquisition can be simple and gives relevant information, this method implies time consuming computational work. Previous studies have developed automatic techniques to outline the crystals from chemical maps, where each major element (e.g. Fe, Mg, Si, Na, Ca, Al) has an assigned colour and thus each phase (i.e. different minerals and melt) will appear in different colour (e.g. Muir *et al.*, 2012). However, obtaining chemical maps is a time-consuming (*c.* 20-30 min for one image) and expensive acquisition when compared with BSE images acquisition. BSE images are obtained using

a scanning electron microscope (SEM) which allows the sample to scatter the electrons it receives; BSE brightness reflects the electron density per unit volume of the target and thus the denser the structure (e.g. heavy atoms with a high atomic number Z), the brighter the image. BSE images of high resolution can be acquired in less than one minute. The first objective of my PhD will be to develop an (semi-) automated method to characterize CSDs of microlite crystals from BSE images. Plagioclase and pyroxene are suitable target minerals as they are the main mineral phases in andesitic magmas (Sen, 2014). A comparison between the resulting CSDs of this new technique and CSDs of the more labour-intensive classic technique (explained further in the literature review) will then be completed to verify the reliability of the automation and the accuracy performance of the classifiers used.

2. Origin of microlites and micro-phenocrysts through high-resolution imaging.

Three hypotheses about the origin of the microlites and micro-phenocrysts of the TgVC tephras can be made; (1) crystals are grown from the melt during its ascent, through degassing and/or cooling (Cichy *et al.*, 2010; Noguchi *et al.*, 2006; Sano & Toramaru, 2017); (2) crystals are from one or several interconnected and small reservoirs that were active during the eruptions, involving mixing and mingling processes (Hobden *et al.*, 1999; Rowlands *et al.*, 2005); (3) crystals are derived from earlier intrusive rocks, and have been picked up by aphyric ascending melt at the onset of eruption. Imaging and elemental mapping of microlites and micro-phenocrysts at ultra-high resolution will provide detailed insights into the textural and chemical characteristics of these crystals, from which their origin and growth histories may be deduced. To distinguish between these hypotheses, mineral-melt equilibria and constraints on the intensive parameters (pressure, temperature and water content) during microlite crystallisation will be investigated.

3. Usage of the microlite CSDs to estimate the timescales of magma transfer through the volcanic conduit at the onset of explosive eruptions of TgVC.

The insights gained from the high-resolution imaging can be usefully employed in this third objective, providing key information on how to interpret the shape of crystal size distributions. Then, by coupling the relevant slopes of the CSD with a well-constrained growth rate of the crystals, we can estimate the growth time of microlite population. The timescales obtained will thus represent the duration of magma transfer through the volcanic conduit from the onset of degassing.

4. Identification of the P-T-X(H₂O) conditions during microlite crystallisation to understand the magmatic processes at work during magma ascent.

The residence time derived from the CSD will be combined with thermodynamic models to determine essential conditions namely the pressure, the temperature and the water content during microlite crystallisation. Using hygrometry and MELTS modelling, these parameters can be derived. Subsequently, the calculated times combined with the constrained pressures will provide magma ascent rates which will in turn unravel insights on forces driving ascent (e.g. volatiles) and how these may or may not differ in eruptions displaying a range of explosiveness.

Ultimately, the resulting insights from these objectives will be combined to propose a new conceptual model for the upper-crustal magmatic system underneath TgVC, which will be contrasted with the existing models globally.

1.3. Thesis outline

This thesis, which consists of eight chapters, can be subdivided into three main sections. The first three chapters involves an introduction to this research (Chapter 1), the geological background with a literature review of TVZ and specifically TgVC (Chapter

2), and the existing methodologies that characterise crystals in volcanic rocks (Chapter 3). Chapter 2 introduces the reader to the eruption styles associated with explosive eruptions, gives a brief review of the tectonic and geological setting of the TVZ and a detailed summary of the eruptive history at TgVC and specifically at Tongariro, Ngauruhoe and Ruapehu volcanoes. Chapter 3 reviews the textural and thermodynamic methods which will be used in this study to characterise the microlite and micro-phenocryst populations.

The core of this thesis is presented in Chapters 4, 5, and 6 which contain the a new textural method and the results of the qualitative and quantitative analysis of the crystal cargo of TgVC magmas. More specifically, Chapter 4 describes a new semi-automatic method developed during this research to outline crystals for CSD generation purposes. This technique was published in *Microscopy and Microanalysis* (Lormand *et al.*, 2018a). Qualitative analysis of the textures and zonations found in the microlite and micro-phenocrysts populations of pyroxene and plagioclase are presented in Chapter 5. This chapter will be submitted for publication under the title of “*Intermittent ascent of aphyric andesitic melts revealed by cryptic micro-antecryst textures*”. Chapter 6 consists of the quantitative and textural analyses of the microlites and their chemical compositions to constrain the microlite growth time, and the conditions P-T-X(H₂O) associated with their crystallisation. This chapter has been submitted and reviewed for publication in *Journal of Petrology*, was deemed acceptable pending revisions, and the revised script has been resubmitted under the title of “*Slow ascent of unusually hot intermediate magmas triggering Strombolian to sub-Plinian eruptions*”.

The final section of the thesis provides a discussion contrasting the existing conceptual models globally and the resulting model of this research in terms of architecture of the magmatic system at arc setting and confers the implications and

contributions of the investigation of microlite crystals to understand the upper-crustal processes beneath volcanoes (Chapter 7). The conclusion (Chapter 8) summarises the findings of this study in the context of the set research objectives and suggests directions for future research which would greatly contribute in our understanding of late-stage magmatic processes at the onset of eruptions.

Chapter 2. Geological background of the Tongariro Volcanic Centre

Chapter content:

2.1. Eruptive styles of explosive eruptions.....	14
2.2. Tectonic and Geological Setting of the Taupo Volcanic Zone	19
2.3. Eruptive History of the Tongariro Volcanic Centre	24
2.3.1. Tongariro	27
2.3.2. Ngauruhoe	29
2.3.3. Ruapehu	33

2.1. Eruptive styles of explosive eruptions

There are different ways to classify volcanoes (Sigurdsson *et al.*, 2015): by their shape (e.g. stratovolcano, caldera, pyroclastic cone, lava dome, fissure vents), by their origin (e.g. intraplate volcanism, hotspot activity, subduction) or by their eruption style (e.g. Strombolian, Vulcanian, Plinian). In fact, the morphology of a volcano is predominantly governed by its eruptive behaviour (Cembrano *et al.*, 2008; Sielfeld *et al.*, 2017), which can vary over time within a single volcanic edifice. Therefore, we consider volcanic classification by eruptive style to be the most useful descriptor of a volcano. Six main eruption styles can be described: Hawaiian/Icelandic, Strombolian, Vulcanian, sub-Plinian, Plinian and Ultra-Plinian. Walker (1973) proposed a classification for these eruption styles based on the fragmentation index and the area of dispersion of the deposits (Figure 2.1). The fragmentation index is determined by the percentage of pyroclasts finer than 1 mm sampled at the intersection of the isopach $0.1T_{\max}$, where T_{\max} is the maximum thickness of deposit in the axis of dispersal.

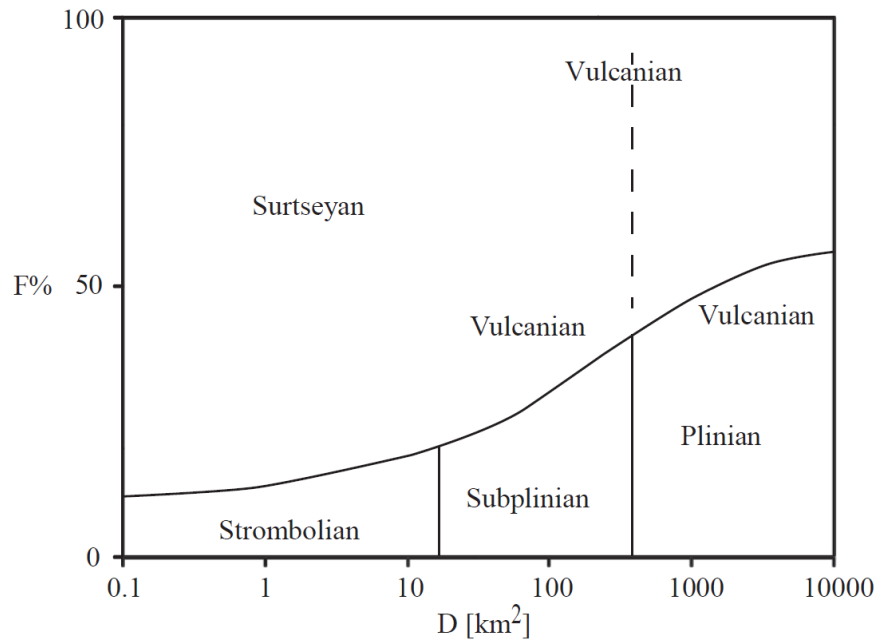


Figure 2.1. Figure 28.2 of Clarke *et al.* (2015) inspired by the initial classification of explosive eruptive styles of Walker *et al.*, (1973). It represents (vertical axis) the percentage of clasts < 1 mm in diameter at the intersection with the isopach equals to 10% of the maximum thickness of the deposit (F%) versus (horizontal axis) the area of dispersal (D) of the pyroclasts/deposits. This classification includes the initial classification of Walker *et al.*, (1973) and the Vulcanian classification based on the study of Wright (1980).

First, eruptions are classified into two main types: *effusive* and *explosive*. One important factor that divides effusive from explosive eruptions is the amount of water dissolved in the melt (Sigurdsson *et al.*, 2015). Effusive eruptions are fed by degassed magma and produce lavas. Effusive eruptions are usually associated with Hawaiian or Icelandic eruption styles. Hawaiian eruptions can either feed long-lived summit lava lake or produce sustained lava fountains feeding fluid, low-viscosity lava flows such as the typical activity of the shield volcano of Mauna Loa in Hawaii (Rowland *et al.*, 2005). The Icelandic eruption style displays similar activity but is initiated from regional fissures such as the last eruption of Bárðarbunga in Iceland, which produced the Holuhraun lava field in 2014-2015 (Ágústsdóttir *et al.*, 2016). Magmas of effusive eruptions are usually basaltic, with a low amount of silica (*c.* < 52% SiO₂), a high temperature (> 1000 °C) and

a low viscosity, although explosive basaltic eruptions are not unknown (e.g. Carrasco-Núñez *et al.*, 2012; Houghton *et al.*, 2004). However, more differentiated magmas can also produce effusive eruptions such as the andesitic lava flows produced by Ngauruhoe volcano in New Zealand (Hobden *et al.*, 2002), the dacitic lava flows produced by Santiaguito volcano in Guatemala (e.g. Harris *et al.*, 2002), the rhyolite lava flows emplaced on San Pietro Island, Sardinia in Italy (Cioni & Funedda, 2005) and the obsidian flows of Lipari Island, Aeolian Island, Italy (e.g. Gottsman & Dingwell, 2001). Effusive eruptions at intermediate and felsic systems also produce dome formation (Loughlin *et al.*, 1998) such as the dacitic domes of Mount St Helens, Washington, USA (e.g. Berlo *et al.*, 2007; Donnadieu & Merle, 1998), the andesitic lava domes of Soufrière Hills, Montserrat, British West Indies (e.g. Cole *et al.*, 1998), the dacitic lava dome of Sinabung, North Sumatra, Indonesia (Nakada *et al.*, 2019), the obsidian domes of Inyo, California, USA (Swanson *et al.*, 1989), and the rhyolitic dome of Cerro Pizarro, Mexico (Carrasco-Núñez & Riggs, 2008). Although some volcanoes are usually associated with effusive activity, paroxysmal events producing explosive eruptions are not uncommon (e.g. the 2002-2003 eruptions of Stromboli, Italy, Cigolini *et al.*, 2008; the 1924 eruption of Kilauea Volcano, Hawaii, Dvorak, 1992; and several paroxysmal eruptions of Fuego volcano, Guatemala, Naismith *et al.*, 2019).

Explosive eruptions, however, are fed by viscous volatile-rich andesitic to rhyolitic magmas and produce pyroclasts (e.g. volcanic ash, bombs, lapilli). There are five main explosive eruption styles: Strombolian, Vulcanian, sub-Plinian, Plinian and ultra-Plinian. Strombolian eruptions, named after Stromboli volcano, Aeolian Islands, Italy, are thought to be generated by bursting of gas slugs (e.g. Blackburn *et al.*, 1976; Jaupart & Vergnolle, 1988; Macdonald, 1972; Vergnolle & Brandeis, 1996). The formation of the gas slug has been a point of debate and two models to explain it are available in the literature: the first

of which – a collapsing foam model (Jaupart & Vergnolle, 1988) – assumes that the origin of the slug is the accumulation of small bubbles/foam on top of the magma reservoir before it collapses and results in a large amount of gas coalescence, which then ascends towards the surface. The second model – a rise-speed dependent model (Wilson, 1980) – assumes that bubbles of different sizes are ascending buoyantly in the conduit and larger bubbles, which travel faster and coalesce with slower and smaller bubbles to finally form a large gas slug.

Vulcanian eruptions, named after Vulcano volcano, Aeolian Islands, Italy, are still a topic of debate. In the Walker (1973) classification, Vulcanian eruptions have no proper delimitations since they can generate pyroclasts being as dispersed as those generated by sub-Plinian to Plinian eruptions, but they also should contain a larger amount of fine-grained pyroclasts and can have a wide range of fragmentation (Clarke *et al.*, 2015). Vulcanian eruptions result from the rapid decompression within a volcanic conduit containing highly pressurized and crystallised magma of intermediate composition (i.e. basaltic andesite, andesite or dacite; Clarke *et al.*, 2015). A mathematical model for Vulcanian eruptions was proposed by Turcotte *et al.* (1990), which assumes that they are triggered by the disruption of a conduit plug or dome due to the high pressure gradient of the underlying magma. Simultaneously, a decompression wave propagates downward into the saturated magma and triggers the exsolution of volatiles, and a gas-pyroclast mixture is ejected from the vent into the atmosphere at sonic to supersonic velocities ($c. 400 \text{ m s}^{-1}$, Self *et al.*, 1978). It can last for seconds to minutes if transition to subsonic regime occurs, and thus the jet evolves into a buoyant plume that may collapse gravitationally to form pyroclastic density currents (Clarke *et al.*, 2015). The magma plug that generates the Vulcanian eruption is usually the result of degassing and microlite crystallisation, which increases the pressure below the viscous plug. Vulcanian eruptions

are characterised by unsteady and impulsive behaviours which is also suggested by the variation of vesicularity, crystal textures and glass compositions in the juvenile material of individual events (Cassidy *et al.*, 2015).

Plinian eruptions were first described and named after Pliny the Younger to report on his uncle's death during the AD 79 eruption of Vesuvius in Italy. He compared the eruptive cloud with a pine tree with a high vertical trunk enlarging into several branches. Cioni *et al.* (2015) describe Plinian eruptions as a quasi-steady high-speed discharge into the atmosphere of a high-temperature multiphase mixture (e.g. gas, solid and liquid particles), which feeds a sustained buoyant vertical plume of tens of kilometres (up to 30 km). The eruptive column will eventually spread laterally to form an umbrella cloud when it reaches the tropopause. The basal part of the column may collapse to form pyroclastic density currents dispersed around the volcano. Plinian eruptions usually consist of a sustained phase, but they may also involve a complex succession of volcanic pulses of varying intensities and dynamics, and thus a sequence of different eruption styles may result (e.g. Vulcanian explosions to phreatomagmatic activity to effusive activity). Ultra-Plinian eruptions are similar to Plinian eruptions, but with higher mass flow rate, which is reflected in higher eruptive columns (up to 55 km high) and larger dispersal distances. This term was first used by Walker to describe the AD 186 Taupo eruption in New Zealand (Walker, 1980). The sub-Plinian eruptions, however, have lower magnitude and intensity than Plinian events. They are usually characterized by unsteady phases of short period oscillations (i.e. minutes to hours) that can be repeated several times over a long duration (i.e. days to weeks). Formation of unsteady short-lived eruptive columns is usually followed by the generation of small-volume pyroclastic density currents. The decrease of ejection velocity is likely to be the reason for unsteadiness of these sub-Plinian events (Cioni *et al.*, 2015).

Finally, variable amounts of external water (the “wet” component) will affect the eruption styles. Phreatomagmatic (also called hydrovolcanic) and phreatic eruptions are largely volatile-driven eruptions for which the magma supplies the heat and the water source is exogenous (i.e. external water e.g. ice, lake, groundwater): phreatomagmatic eruptions are characterised by direct interaction between magma and external water, whereas phreatic events involve heating of fluids by the magma, without magma erupting at the surface (Houghton *et al.*, 2015). The phreatomagmatic process is associated to the fuel-coolant interaction (Wohletz, 1983) and consists of the rapid conversion of the thermal energy of the magma into kinetic and mechanic energy at the magma-water interface. Surtseyan eruptions are a type of phreatomagmatic eruption that were first observed, described and named after the 1963-1968 formation of Surtsey Island in Iceland. These eruptions initially behave like submarine eruption until it reaches the surface to create an island (White, 1996). As soon the magma reaches the surface, the fragmentation is so strong that magma is converted into tephra and tephra jetting or cock’s tail plumes (e.g. tephra jet with an arching, multi-fingered form likened to the shape of a rooster’s tail) are observed. If there is no interaction with external water, the explosive eruptions are understood to be driven by the volatile content of the magma.

2.2. Tectonic and Geological Setting of the Taupo Volcanic Zone

The Taupo Volcanic Zone (TVZ) is a 300 km-long and up to 60 km-wide volcano-tectonic depression extending southward from White Island to Mt. Ruapehu (Stern *et al.*, 2006). It is located at the southernmost segment of the 2800-km-long Tonga-Kermadec arc-back-arc system (e.g. Ewart *et al.*, 1977). New Zealand is affected by an Alpine-style orogeny, part of the Wilson cycle, named after the Canadian geophysicist J. Tuzo Wilson. The Wilson cycle is initiated by the break-up of a continent and the opening of an ocean (i.e. the Tasman Sea in the case of New Zealand). From the early Miocene, the northern

and central North Island were strongly influenced by extensional stresses due to increase of the subduction angle and slab-rollback (Mortimer *et al.*, 2007). Since 16 Myrs, the subduction has jumped from Northland to the Colville ridge, before finally switching to the currently active Kermadec arc (Herzer, 1995; Mortimer *et al.*, 2010).

The current tectonic settings of the North Island of New Zealand consist of the westward and oblique subduction of an old and thickened oceanic crust, the Hikurangi Plateau (Figure 2.2b). The Hikurangi Plateau is located offshore on the East coast of the North Island, and the convergence exhibits a shallow angle of subduction (*c.* 20°) with a velocity of 38 mm/yr at the south and 47-55 mm/yr at the north (e.g. Ballance, 1976; Mortimer *et al.*, 2010; Reyners, 2013). The forearc is characterized by a clockwise rotation of 0.5-3.8 degree per Ma (constrained by GPS measurements) relative to the Australian plate and by extension created through the reverse faulting of the accretionary wedge between the Hikurangi Trough and the East coast of the North Island (Davey *et al.*, 1986; Wallace *et al.*, 2004). Also, the fore-arc located at the eastern margin of the Axial Ranges is affected by extensive shortening expressed as dextral strike-slip motion of several discrete blocks, active for at least 1 Ma (Barnes & Lépinay, 1997; Kelsey *et al.*, 1995). The combination of these processes has allowed an extensional regime beyond the fore-arc basin, resulting in the opening north-eastward of the Taupo Volcanic Zone at about 4 to 2 Ma ago, when the transition of volcanic activity from the Coromandel Volcanic Zone to the TVZ began (Gravley *et al.*, 2016; Stern, 1987; Wilson *et al.*, 1995). The boundary of the volcanic arc has changed over time. Indeed, the so-called “old TVZ” was active from 2 Ma to 0.34 Ma and the current “young TVZ” margin is located about 100 km from the old TVZ margin (Wilson *et al.*, 1995).

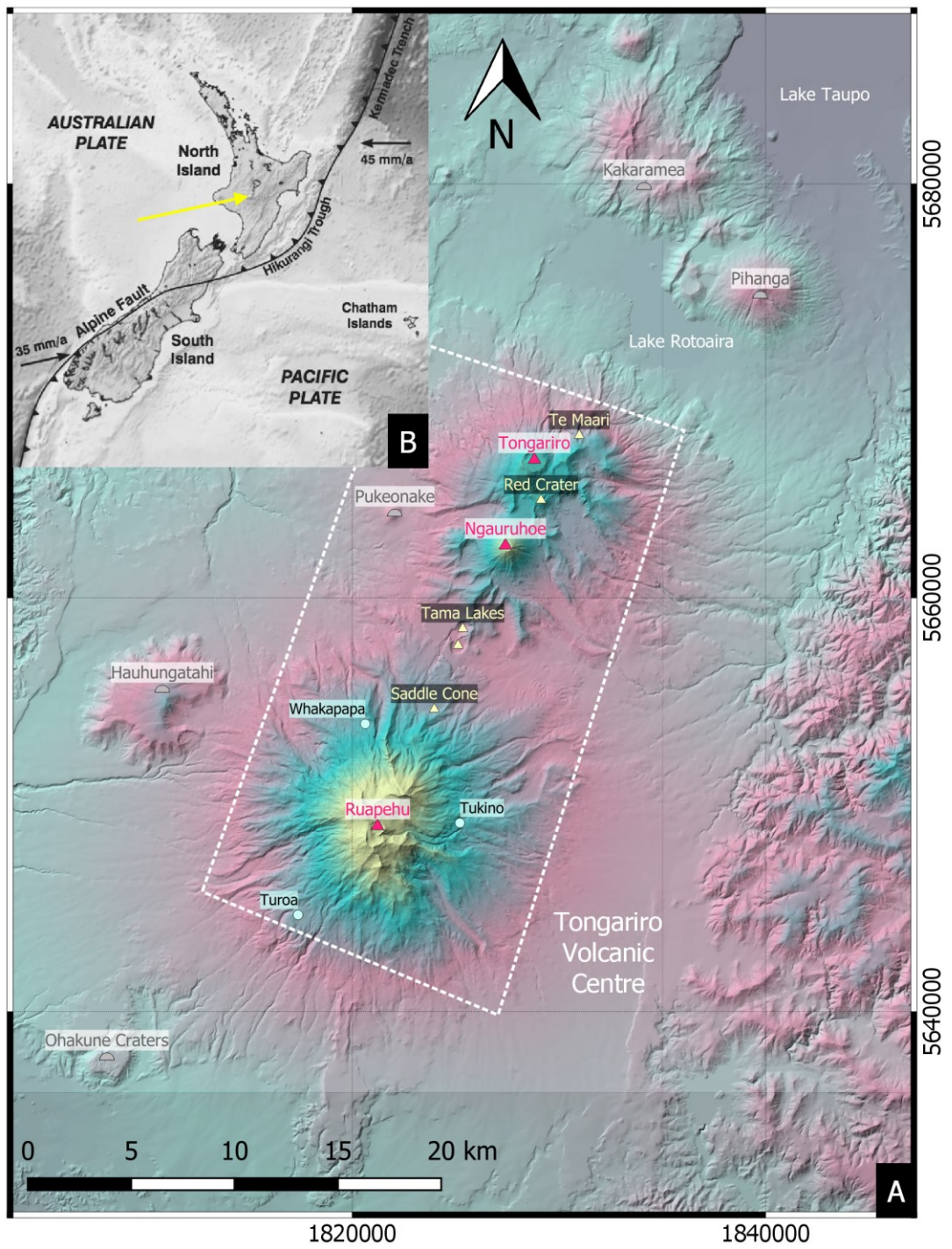
The TVZ lies above a graben, where subsidence of the basement rocks, mainly greywacke (i.e. metamorphosed sandstones and mudstones) and argillite of Mesozoic-

Late Paleozoic age (100-300 Ma) have subsided more than 3 km below sea level (e.g. Lillie, 1980). When the subducting slab enters the trench, metasomatism occurs and fluids from the slab are being released (Stern, 2002). These fluids may in turn induce partial melting of the overlying mantle wedge at the base of the continental crust (e.g. Bebout, 2012). Partial melting may be enhanced through extension related mantle decompression underneath TVZ. These partial melts thus provide a source of calc-alkaline magmas variably affected by crustal contamination they experience during ascent. Indeed, studies have shown that mafic magmas generated in the TVZ assimilate with the underlying greywacke basement while migrating through the crust (Cole, 1978; Graham *et al.*, 1995; Hobden *et al.*, 2002).

A few mafic magmas were erupted within the TVZ and are thought to reach the surface via dyke intrusion, such as the 1886 eruption of Tarawera volcano (Seebeck & Nicol, 2009). The volcanic activity of the TVZ started with andesitic eruptions and formations of the now eroded stratovolcanoes of Titiraupenga and Pureora, today located on the western margin of the central TVZ. The TVZ has erupted more than 10,000 km³ (sum of uncorrected volumes) of volcanic materials (95% of rhyolitic magma, e.g. ignimbrite, and 5% of less evolved magma, e.g. dacitic/andesitic tephra/lavas) from four main eruptive centres: Okataina, Maroa, Taupo, Rotorua and Tongariro (Graham, 2008). The TVZ encompasses isolated andesite volcanoes, e.g. Mt. Edgecumbe, Whale Island and White Island (Duncan, 1970), isolated rhyolite domes, e.g. Pohaturua, Mokauteure and Whakapapa (Leonard, 2003), and monogenetic volcanoes, e.g. Ohakune Volcanic Complex, Pukeonake and Punatekahi (Hackett, 1985; Kósik *et al.*, 2016). Rhyolitic volcanism is focussed in the centre of the TVZ near the Taupo and Rotorua calderas, while andesitic arc volcanism is predominant in the north and the south (Wilson *et al.*, 1995). The unusually intense and frequent volcanic activity of the TVZ is related to the

combination of an extensional regime with rates increasing from the SSW to the NNE of 6 to 15 mm/yr (e.g. Lamb *et al.*, 2017; Wallace *et al.*, 2004), and the high heat flux of *c.* 4300 MW, similar to that of Iceland and Yellowstone (Stern *et al.*, 2006). Nakagawa *et al.* (1998) defined two types of volcanism that have occurred within TVZ: (1) eruptive episodes induced by rifting periods such as the most recent 10 ka ago, which triggered a series of Plinian eruptions, i.e. the Mangamate Formation (Auer *et al.*, 2015); (2) volcanic activity driven by magmatic processes without involvement of major tectonic events. It is thought that there have been many rifting episodes triggering eruptions, but if a large rhyolitic eruption such as the Oruanui eruption (25.36 ± 0.16 cal. ka BP; Vandergoes *et al.*, 2013) from Lake Taupo would have been triggered, any evidence of rifting would have been buried near the source. Considering the variety of volcanic landforms and magma chemistries detailed above, the volcanoes of TVZ have exhibited a wide range of eruption styles.

Figure 2.2. (Figure in the next page) (A) Map of the current tectonic setting in New Zealand illustrating by the subduction of the Pacific Plate beneath the Australian Plate (source: GNS Science). The location of the Tongariro Volcanic Centre is indicated by the yellow arrow. (B) Map of the locations of the recently active volcanoes (Tongariro, Ngauruhoe and Ruapehu), volcanic vents (Te Maari, Red Crater, Tama Lakes and Saddle Cone), the inactive/extinct volcanoes (Kakaramea, Pihanga, Pukeonake, Hauhungatahi and Ohakune Craters), the ski fields (Whakapapa, Tukino and Turoa), and the lakes (Rotoaira and Taupo) at TgVC. This is a shaded relief map derived from the 8-m-Digital-Elevation-Model (source: LINZ data). The colour gradient corresponds to the elevation variation. Georeference system: NZGD2000/New Zealand Transverse Mercator 2000.



2.3. Eruptive History of the Tongariro Volcanic Centre

TgVC is currently the most frequently active volcanic centre of the TVZ. It is located at the southern end of the Tonga-Kermadec arc-back-arc system and within the NNE-oriented Tongariro graben, which has been subjected to extension at 7 ± 1.2 mm/yr over the last 20 ka (Gómez-Vasconcelos *et al.*, 2017). TgVC consists of large dacitic-andesitic volcanoes, i.e. Kakaramea-Tihia, Pihanga, Ruapehu and Tongariro (including the Ngauruhoe vent), the last two of which are currently active, and four smaller volcanic centres: Maungakatote, Pukeonake, Hauhungatahi and Ohakune (Figure 2.2; Kósik *et al.*, 2016; Shane, 2017). They have exhibited a wide variety of eruption styles from small phreatic and Strombolian to Plinian eruptions. The formation of lava domes, and potentially, eruptive fissure(s), also took place during the Mangamate eruptive sequence where several lineated vents were activated (Auer *et al.*, 2015). The frequency of eruptions for these volcanoes over the last 26 ka has been examined (Moebis, 2010); two main behaviours are apparent (Figure 2.3): (1) long-term quasi-continuous eruption frequency (i.e. Ruapehu and Rotoaira Lapilli Formation). (2) short-term, discontinuous and intense periods of volcanic activity (i.e. Mangamate, Ngauruhoe and Red Crater). However, Ruapehu has transitioned from behaviour 1 to 2 in the last 2000 years, during which the Tufa Trig Formation has been deposited. The tephrae erupted from TgVC have been deposited in the East due to dominant westerly winds. The desert road is the best location to observe the accumulation of these deposits, consisting of ash and lapilli fallout interbedded with debris flow and lahar deposits, and with rhyolitic tephrae from the Taupo and the Okataina Volcanic Centres (Donoghue *et al.*, 1995). The volcanoes exhibit typical compositions of arc lavas, although petrological and geochemical variations have been identified and interpreted to result from different degree of assimilation-fractionation-crystallisation and complex magma plumbing systems, including shallow crustal

assimilation of the underneath greywacke (Graham *et al.*, 1995; Moebis *et al.*, 2011; Price *et al.*, 2007; Price *et al.*, 2016).

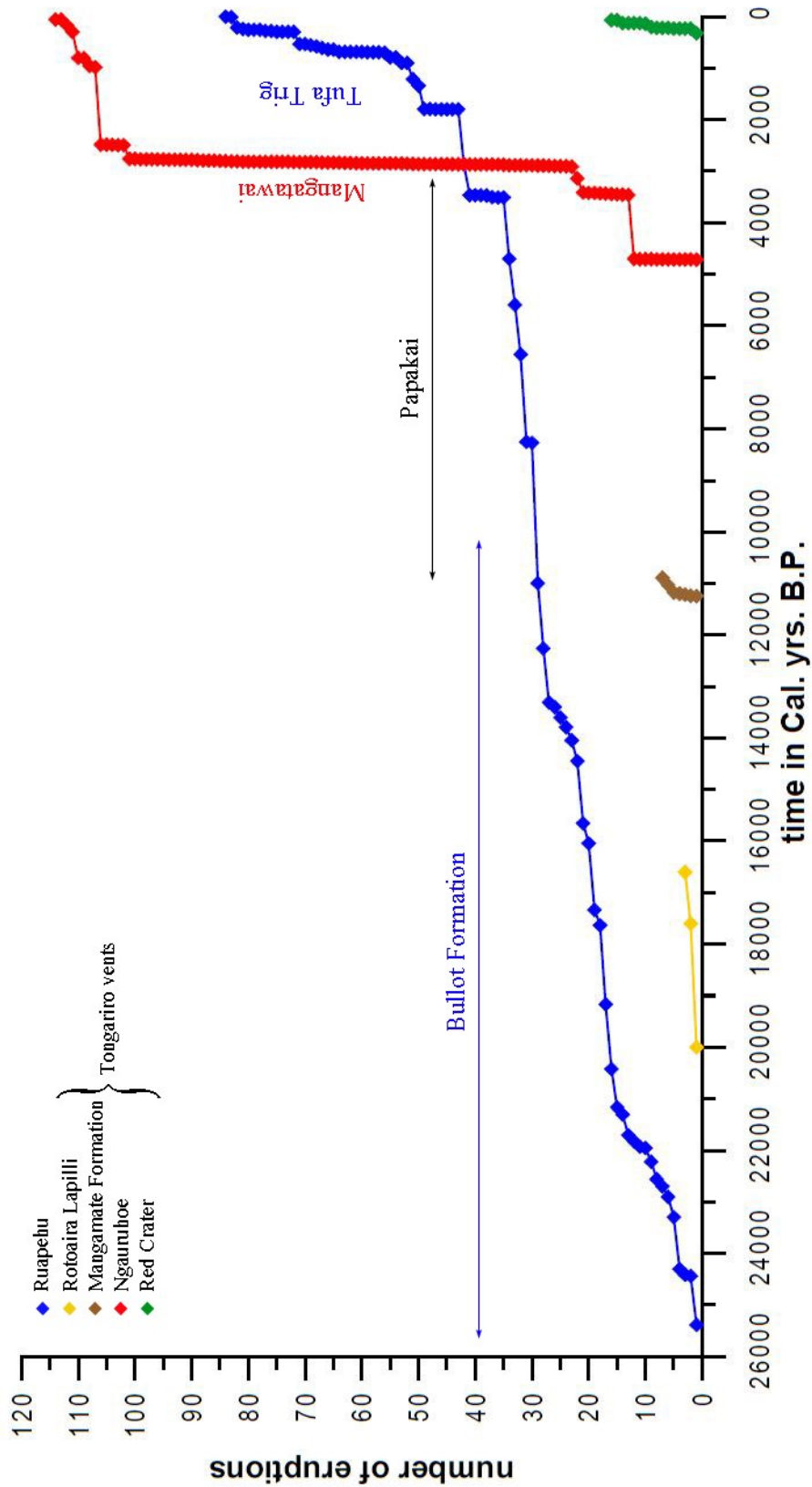


Figure 2.3. Modified Figure 8.1.6 of Moebis (2010) illustrating the frequency of eruptions of the Tongariro Volcanic Centre over the last 26,000 years.

2.3.1. Tongariro

Tongariro, also referred as the Absolute Warrior (Matua te Toa) in the Māori legends (Pardo *et al.*, 2015), is a complex andesitic volcano, which consists of the overlap of *c.* 17 composite cones ranging from 0.3 to 12 km³ in volume (Nicol *et al.*, 2017). Several periods of eruptive activity have allowed its formation, starting *c.* 300 ka ago and followed by periods of growth at 210-200 ka, 180-70 ka and from 25 ka to present (Hobden *et al.*, 1996). The last episode has produced the current complex system of cones (Rowlands *et al.*, 2005). Porphyritic andesite is the most common rock type on Tongariro, whereas basaltic andesite also occurs, and dacite is rare.

The Mangamate Formation, dated *c.* 11-to-12-ka BP, had an estimated total depositional duration of 200-400 years, and has produced six Plinian eruptions – Te Rato, Oturere, Waihohonu-Ohinepango, Wharepu and Poutu – and several minor pyroclastic eruptions (Nairn *et al.*, 1998). However, the most recent studies have associated the underlying tephra, Pahoka Tephra, to be part of the Mangamate Formation (i.e. Pahoka-Mangamate Formation referred as PM) due to the similar petrography, source and age (Auer *et al.*, 2015; Pardo *et al.*, 2012). At least 1000 km² of the pre-Mangamate forest was destroyed during this series of eruptions (Kohn & Topping, 1978). The PM stratigraphy is interbedded with two rhyolitic tephtras (i.e. Poronui and Karapiti tephtras) and two unnamed andesitic tephtras. Several vents located in a fissure system between and beyond Ruapehu and Tongariro were formed during the accumulation of PM tephtras, and it is not clear if some products were erupted from a single or several sources (Figure 2.4); for instance, there is stratigraphical evidence that the Poutu deposit was generated from Tama Lakes, proto-Ngauruhoe and Half Cone (Auer *et al.*, 2015). The resulting rocks were almost aphyric with an initially evolved dacitic composition before shifting towards basaltic andesite at the end of the eruptive sequence. The combination of very short

duration and large volume for this eruptive sequence has drawn the attention of volcanologists. Its origin has been related to a period of accelerated regional extension of the TVZ that occurred *c.* 10 ka ago (Nairn *et al.*, 1998).

Hitchcock & Cole (2007) have assessed the impacts that such an eruption (i.e. the youngest eruption of the sequence, Poutu) would have today: more than 3,000 people living in the Tokaanu-Turangi area, south of Lake Taupo (Census 2013 data) would be affected by > 20 cm thick ash/lapilli, which would eventually trigger roof collapses. Areas up to 100 km from the source would also be affected, with a smaller impact.

The Papakai Formation (11.1 - 3.7 cal. ka; Donoghue *et al.*, 1995), defined by Grange (1931) as part of the “Tongariro Shower” (the name previously used for Tongariro tephra older than Mangatawai), is a more complex sequence, which contains paleosols interbedded with tephra layers from different eruptions and sources. It is underlain by Poutu, the youngest tephra of the PM Formation and its top unit underlies the Mangatawai Formation. The Papakai tephra pile accumulated over a long period while many vents were active. Indeed, andesitic tephra from Tongariro, Ruapehu and Ngauruhoe, and three rhyolitic layers from the Taupo Volcanic Centre, were identified within Papakai (Moebis, 2010).

Ngauruhoe and Red Crater are the two most recent and active volcanic vents of the Tongariro volcanic complex (e.g., Cole, 1978). The latest eruptions of the Tongariro volcanic complex were the Vulcanian eruptions in 1973-1975 from Ngauruhoe, and a phreatic eruption in 2012 from Upper Te Maari Crater, as stated earlier.

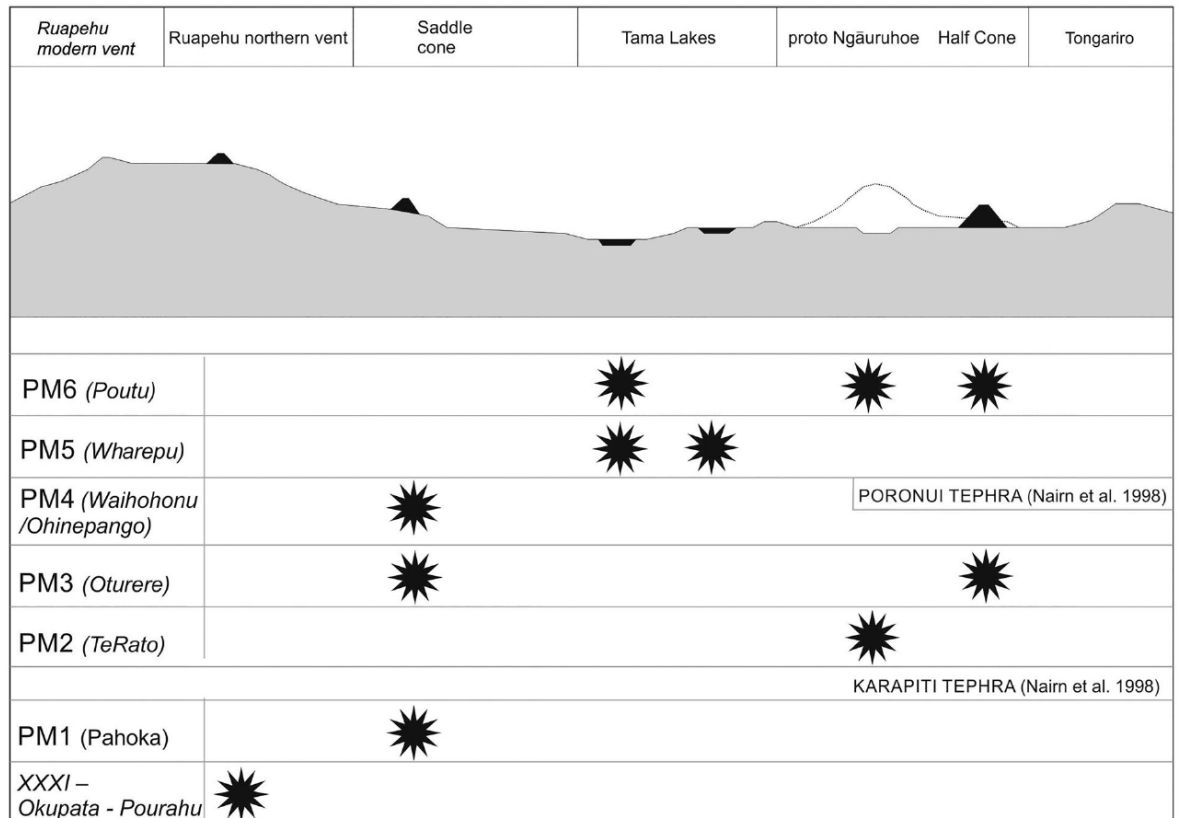


Figure 2.4. Figure 2 of Auer *et al.* (2015) illustrating the single or multiple sources of each tephra emitted during the climactic eruptive period of the *c.* 10 ka Pahoka-Mangamate Formation. The vents are located along a large fissure between Ruapehu and Tongariro volcanoes.

2.3.2. Ngauruhoe

Ngauruhoe, also referred as the Absolute Negotiator (Matua te Pononga) in the Māori legends (Pardo et al., 2015), is the youngest of the three main vents of the TgVC. The first climber who described the volcano was J. C. Bidwill in March 1839 and reported that: “*The crater was the most terrific abyss I ever looked into or imagined... It was not possible to see above 10 yards into it from the quantity of steam which it was continually discharging*” (Government of New Zealand, 1966). For a long time, it was thought that

the Mangatawai Formation, dated 3.4 – 2.8 ka BP from its abundance in beech leaves, was associated to the primary episode of growth of the cone (Fergusson & Rafter, 1959). However, a recent study of Moebis *et al.* (2011) has shown that discrete tephras as old as *c.* 7 ka within the Upper Papakai are Ngauruhoe-sourced and the oldest significant eruption appeared to occur *c.* 4.7 ka BP, likely to be related to an increase of the cone height (Moebis, 2010). Since 1830, Ngauruhoe has erupted every two to three years, although its last eruption was in 1977 (Hobden *et al.*, 2002).

Major historical eruptions occurred in 1870, 1949, 1954-1955 and 1972-1975, and have exhibited variations over short timescales in (1) eruptive style (e.g. effusive, Strombolian, Vulcanian and sub-Plinian), and in (2) both chemical and isotopic compositions (Figure 2.5; Hobden *et al.*, 1999; Hobden *et al.*, 2002). It has been proposed that this chemical variability was due to a complex plumbing system of partially interconnected conduits and small holding chambers feeding small batches of magma (< 0.1 km³) (Hobden *et al.*, 1999). The wide range in eruptive styles and the variability in composition of plagioclase cores from lavas, however, were interpreted by changes in conduit and magma ascent rate, which affects the degree of degassing and the syn-eruptive crystallisation of microlites (Coote & Shane, 2016).

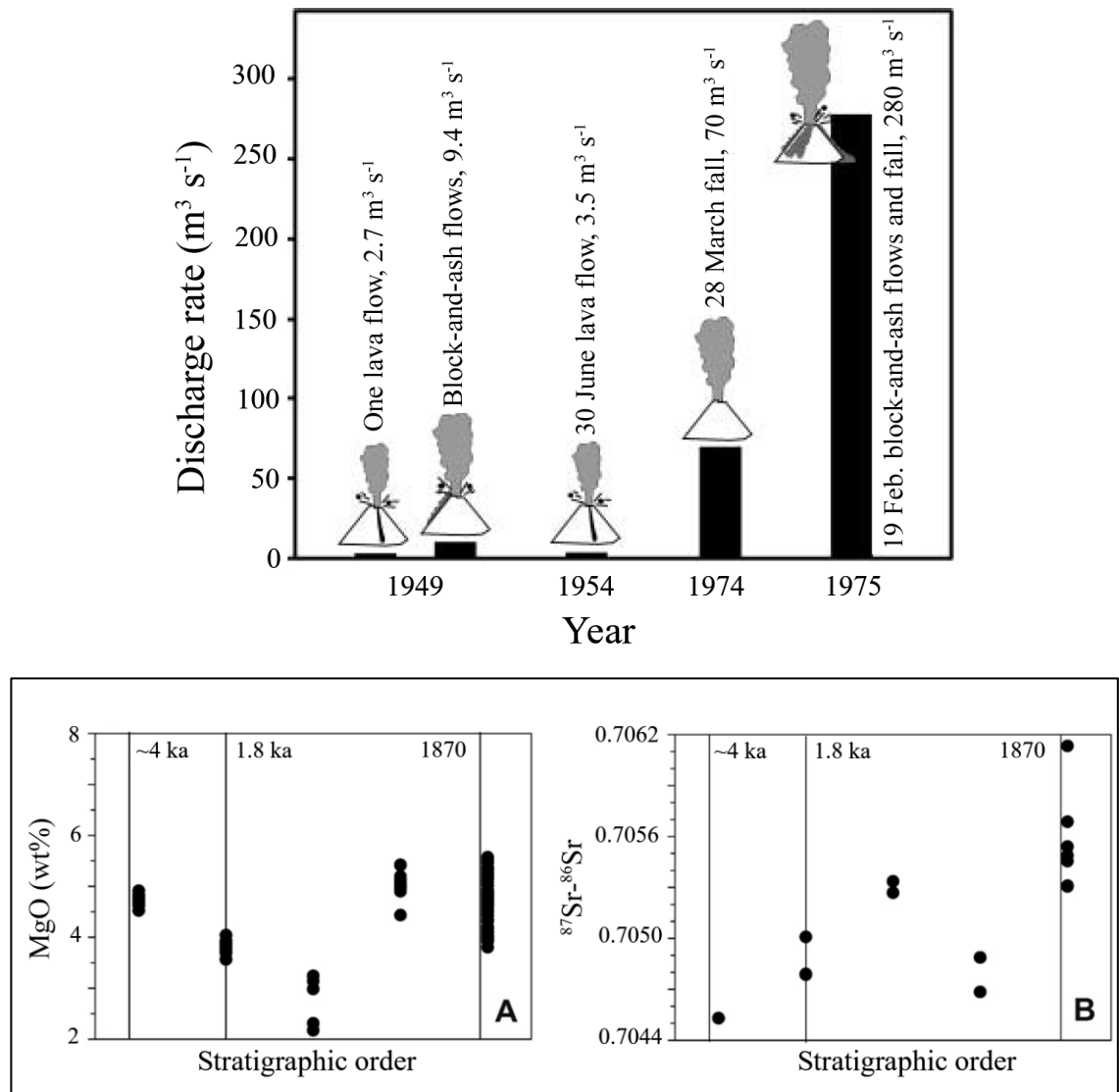


Figure 2.5. (A) Modified Figure 3 of Hobden *et al.* (2002) illustrating the discharge rates and the eruptive deposits of the most recent eruptions of Ngauruhoe. (B) Modified Figures 10a and 10b of Shane *et al.* (2017) illustrating the MgO and $^{87}\text{Sr}-^{86}\text{Sr}$ variations of compositions and isotopic signatures of the Ngauruhoe magmas over time.

At about 1 km from the current main vent, 42 tephra layers beneath the Taupo pumice (1.718 ± 0.005 cal. ka BP; Hogg *et al.* (2011)) were identified as sourced from Ngauruhoe, and a total of 60 lava flows and block-and-ash deposits have been attributed to Ngauruhoe (Hobden *et al.*, 2002; Moebis, 2010). Geochemically speaking, Ngauruhoe has produced calc-alkaline basaltic andesite to andesite magmas, typical of subduction-related magmatism (Coote & Shane, 2016). Lavas are porphyritic and consist of phenocrysts of plagioclase, subordinate clinopyroxene, orthopyroxene, Fe–Ti oxides, and rare olivine (Cole *et al.*, 1986).

The Mangatawai Formation was deposited during the most explosive and frequent eruptive period of Ngauruhoe. The climactic phase of pyroclastic activity occurred between 2.9-2.8 ka and has produced 37% of the total known volume of tephras from Ngauruhoe (Moebis, 2010). Mangatawai tephras were generated by Vulcanian to sub-Plinian eruptions, and tephras have accumulated above the Papakai Formation as a very distinctive series of pale-grey, red, purple to black layers containing a large amount of beech leaves (Hobden *et al.*, 2002 and therein; Moebis, 2010). This variety of colours was interpreted to be caused by a combination of various eruption styles, weathering, and different sources (Moebis *et al.*, 2007). Indeed, 20-40% of the tephras were geochemically associated to a Ruapehu source. Also, a combination of textural and sedimentological evidence (i.e. vesicular deposit, presence of accretionary lapilli, the highly fragmented texture of the ash particles and the fine grained feature of the layers) indicate a magma-water interaction during the eruptions. It is unclear if pyroclastic surges were generated or if tephras were deposited by rain-flushing of the eruptive column (Moebis *et al.*, 2007). Mangatawai tephras are crystal-poor, with a few phenocrysts of plagioclase, orthopyroxene and minor clinopyroxene and/or olivine, and well-formed

microlites of plagioclase and orthopyroxene, all set in very fine-grained or glassy matrix (Zellmer *et al.*, 2016c)

The latest eruptive period occurred in 1972 to 1975 and initiated with intermittent ash emission. A minor eruptive period associated with increased seismic activity occurred between July and October 1973. Ash samples analysed from this period have witnessed injection(s) of fresh andesitic magma(s) (Nairn *et al.*, 1976). The 1974-1975 eruptions were predominantly Vulcanian in style and ended with a sub-Plinian eruption on the 19th February 1975, which produced a 10-km-high-sustained eruptive column and pyroclastic density currents travelling 1-2 km from the vent, towards the current TAC track (Lube *et al.*, 2007; Nairn & Self, 1978).

2.3.3. Ruapehu

Ruapehu, also referred as the Absolute Wisdom (Matua te Mana) in the Māori legends (Pardo *et al.*, 2015), is the highest peak of the North Island (2797 m), is a stratovolcano that has been active over the past 200-250 ka (Conway *et al.*, 2016; Conway *et al.*, 2018; Gamble *et al.*, 2003). However, a proto-Ruapehu-sourced conglomerate containing pumice clasts with amphibole-bearing xenoliths was identified and dated at *c.* 340 ka BP (Tost *et al.*, 2016). The summit of Ruapehu consists of three vents, of which the currently active and southernmost is occupied by an acidic Crater Lake with lake temperature varying from 10 °C to 60 °C over the last 50 years (Hurst *et al.*, 1991). Lavas and pyroclasts produced by Mt. Ruapehu generally exhibit andesitic compositions (88%), with a few showing basaltic andesite composition (8%), but rare are dacitic compositions occur (4%; Price *et al.*, 2016). The Pleistocene and Holocene activity of Ruapehu has produced diverse styles of eruption and deposits; several well-described lava flows, ash falls, rare pyroclastic density current, frequent lahars and debris-avalanche deposits (e.g. Cronin *et al.*, 1999; Donoghue *et al.*, 1995; Gamble *et al.*, 2003; Graham & Hackett,

1987; Palmer & Neall, 1989; Pardo *et al.*, 2012; Topping, 1973). The most explosive eruptions of Ruapehu formed the Bullock Formation and occurred immediately before the Mangamate eruptive sequence. The Bullock Formation, recently described by Pardo *et al.* (2012), was dated between 25-11 cal. ka BP and is composed of at least 33 eruptions that were classified into six eruptive sequences. This period consisted of short-lived sub-Plinian to Plinian eruptions associated with sustained or unsteady eruptive columns regularly generating pyroclastic density currents.

More recently, Mount Ruapehu has also produced smaller eruptions primarily of Strombolian and phreatomagmatic natures (e.g. Cronin *et al.*, 2003; Gamble *et al.*, 1999; Kilgour *et al.*, 2014; Price *et al.*, 2012). The Tufa Trig Formation is composed of the last 2,000 years of activity of Ruapehu, encompasses at least 19 andesitic tephra and has contributed a small volume of tephra to the ring plane ($< 0.1 \text{ km}^3$; Donoghue & Neall, 1996). It was characterised by one phreatomagmatic Strombolian to rarely sub-Plinian eruption every century. However, in the past century, eruptions have occurred every 50 years. The eruptions themselves do not represent the main hazard, but lahars created by the outrush of water from the crater lake are some of the most dangerous volcano-related phenomena (Cronin *et al.*, 1999).

The last member of the Tufa Trig Formation (i.e. Tf19 in Donoghue *et al.*, 1997) corresponds to the 1995-1996 eruptions of Ruapehu, which began in November 1994 with heating cycles at the Crater Lake associated with phreatic activity until July 1995 (Christenson, 2000). In September 1995, phreatomagmatic eruptions generated lahars and high emissions of SO_2 . There was a shift from phreatomagmatic to sub-Plinian on the 11-14th of October 1995, producing several 10-12 km high ash plumes and generating multiple lahars, which emptied most of the water from Crater Lake (Figure 2.6; Christenson, 2000). This intense activity was accompanied with volcanic earthquakes and

tremors (Bryan & Sherburn, 1999). From February to June 1996, the lake was getting replenished and a lava spine emerged from the lake (Figure 2.6b). During that time, about 50 volcanic-tectonic earthquakes were reported. The activity increased again in mid-June with intermittent and pulsing ash eruptions, and ejections of blocks and bombs. This eruptive sequence provided a good opportunity for the government and stakeholders to manage small volcanic eruptions, but it also caused financial loss for ski operators, disrupted the air traffic, caused animal deaths due to ash ingestion and fluorosis poisoning, and generated lahars in the rivers (Cronin *et al.*, 1998; Cronin *et al.*, 2003; Johnston *et al.*, 2000).

Variability in whole rock and isotopic chemistry has been highlighted for Ruapehu, and studies of the petrography of the lavas and pyroclasts have identified several xenoliths (Gamble *et al.*, 1999; Price *et al.*, 2012; Tost *et al.*, 2016). The xenoliths are meta-sedimentary and meta-igneous, pyroxene-plagioclase granulitic rocks and have been attributed to local basement greywacke and underlying oceanic crust (Graham & Hackett, 1987). Geochemical and petrographic variations were associated with open-system processes. A complex plumbing system composed of several small individual magma storage bodies and dykes/sills from the upper mantle to the crust under the volcano is envisaged (Gamble *et al.*, 1999; Price *et al.*, 2005; Price *et al.*, 2007; Price *et al.*, 2012).

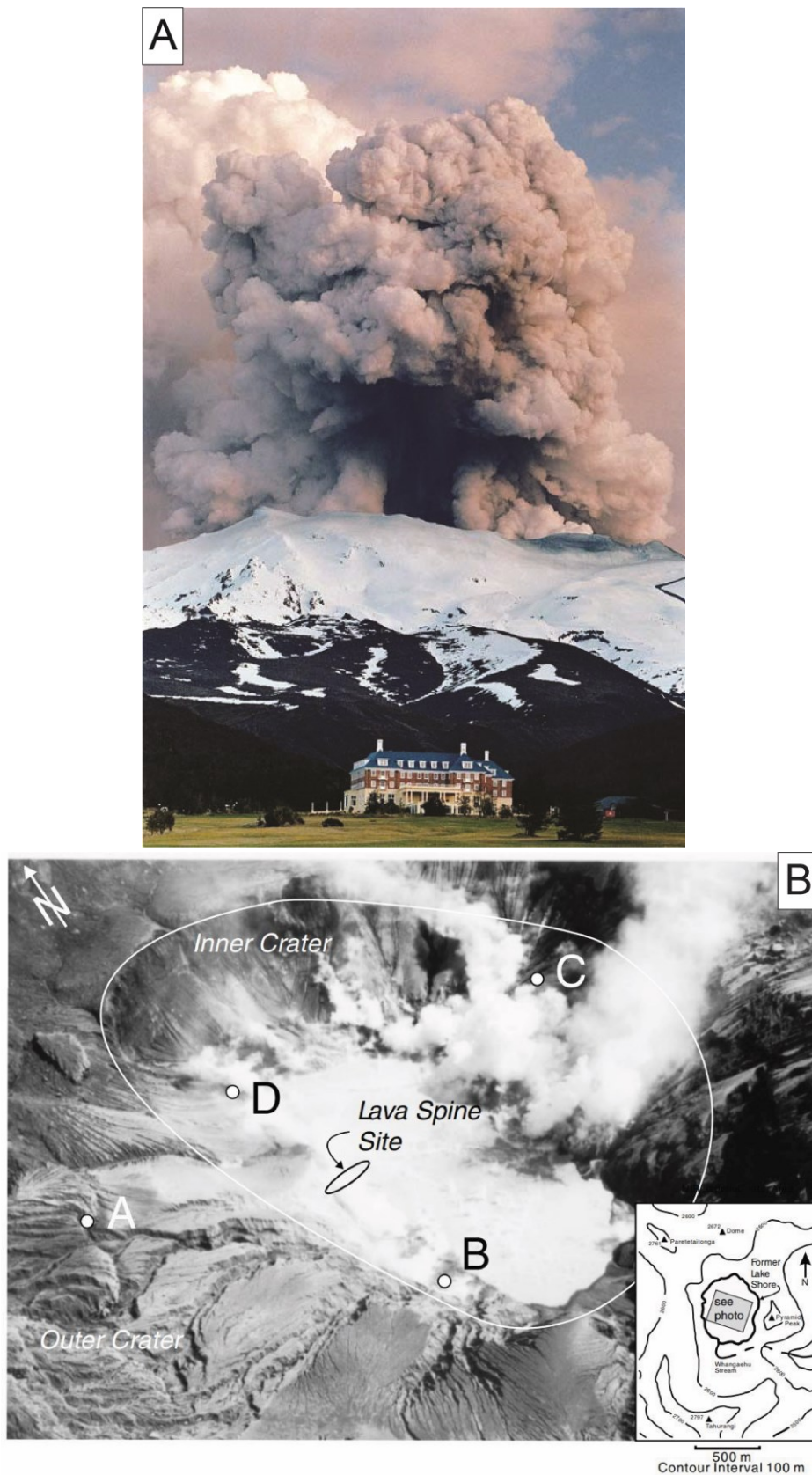


Figure 2.6. (A) Vulcanian to sub-Plinian eruption of Mt. Ruapehu in September 1995 observed from Whakapapa Village. Photo credits: Tim Whittaker. (B) Figure 4 of Christenson (2000) of an aerial photograph of the crater area of Mt. Ruapehu in January 1996 in which a lava spine and active fumaroles (A, B, C and D) were identified.

In summary, the TgVC has a complex history involving the formation of different stratovolcanoes (e.g. Ruapehu), compound of cones (e.g. Tongariro complex), isolated cones (e.g. Pukeonake), and hydrothermal active areas (e.g. Emerald Lake). Over the Holocene, the TgVC has produced a wide variety of eruption styles spanning from effusive (lava flows and lava domes) to explosive (i.e. Strombolian, Vulcanian, sub-Plinian, Plinian), and eventually involving magma-water interaction, which produced phreatic and phreatomagmatic eruptions (e.g. 1995 eruption of Ruapehu and the 2012 eruption of Te Maari). The crystal cargo and more specifically the phenocrysts of the tephra and lavas associated with the TgVC eruptions have provided insights into the magmatic system and the origin of the feeding magmas at depth (e.g. Auer *et al.*, 2015; Coote & Shane, 2016; Kilgour *et al.*, 2013; Price *et al.*, 2016; Shane, 2017; Shane *et al.*, 2017). However, magmatic and ascent processes occurring at upper crustal depths before an explosive eruption remain uncertain and are required to improve hazard mitigation and evacuations plans. Therefore, this study aims to refine the understanding of the shallow processes at TgVC using the microlite crystal cargos found in tephra from historical explosive eruptions.

Chapter 3. Methodologies of characterising crystals and magmas

Appendices for this chapter can be found in Appendices A and C.

Chapter content:

3.1. Crystals in volcanic rocks.....	40
3.2. Crystal Size Distributions.....	48
3.3. Growth rate.....	54
3.4. Thermodynamics in magmas.....	57
3.4.1. Thermobarometry.....	59
3.4.2. Hygrometry.....	64
3.4.3. MELTS modelling.....	66
3.5. Sample selection, preparation, and analysis.....	68
3.5.1. Sample selection.....	68
3.5.2. Sample preparation.....	72
3.5.3. Analytical techniques used for this study.....	72

3.1. Crystals in volcanic rocks

Volcanic explosive eruptions are fed by complex three-phase systems composed of silicate melt, crystals and bubbles. Magmas may be produced in a range of tectonomagmatic settings (e.g. subduction, mantle plume, oceanic/continental rift zone), before rising towards the surface. During their ascent from source to surface, the three phases start coexisting due to cooling and/or degassing; with the system no longer in equilibrium, minerals will start to form one after another, depending on their respective solidus temperature. Magma ascent triggers depressurization of the system, and exsolution of the gas phases previously dissolved in the magma (i.e. H₂O and CO₂; Voight *et al.* 1998). Several types of crystals can grow in magmas (Figure 3.1): Phenocrysts are thought to form first as their size clearly demonstrates that they had time to grow. Microphenocrysts and microlites are likely to form shortly before the eruption starts or after, within a cooling lava flow if the eruption is effusive (e.g. Cashman *et al.*, 1999). However, entrainment of earlier formed crystalline materials called xenoliths (e.g. Beier *et al.*, 2017; Erlund *et al.*, 2009) may also happen either during the ascent e.g. from the conduit walls, or from an accumulation zone such as crystal mushes in magma chambers (e.g. Marsh, 1998a; Nakamura, 1995; Pyle *et al.*, 1988). Phenocrysts can also occur in clusters called glomerocrysts. The mixing of two batches of magma will result in the coexistence of at least two crystal populations (e.g. Clynne, 1999; Snyder, 1997). Glomerocrysts can also form during resorption of phenocrysts that aggregate, or may be a sign of crystal entrainment from a crystal mush (e.g. Bennett *et al.*, 2019b; Renjith, 2014).

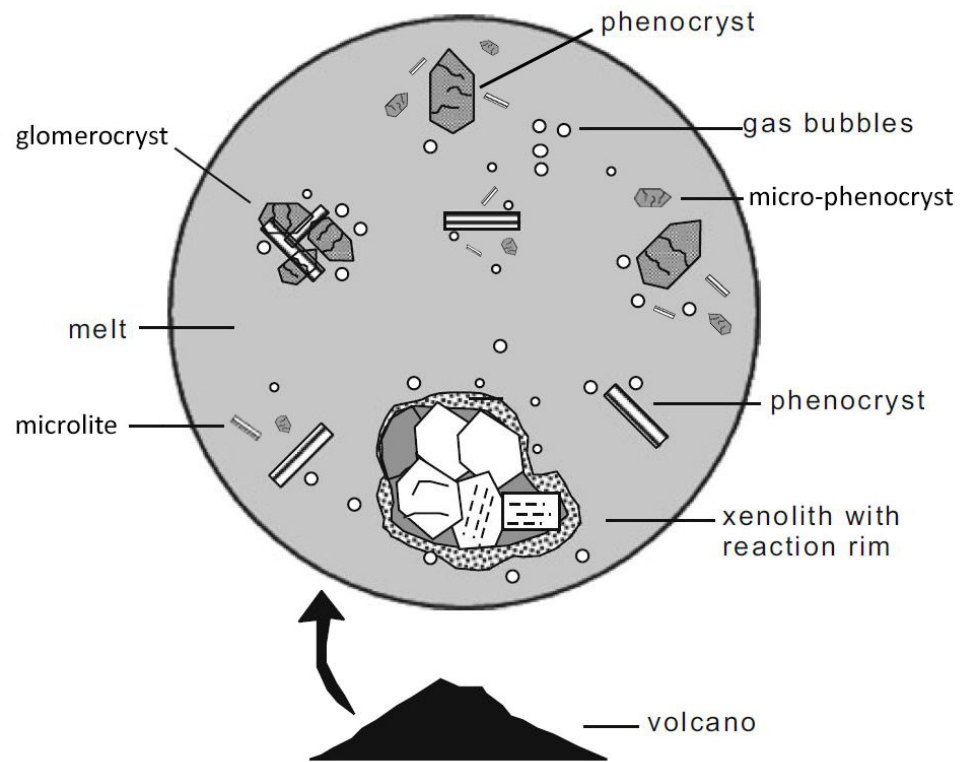


Figure 3.1. Modified figure 2.2 of Sen (2014) representing a microscopic schematic view of a volcanic rock composed of crystals (phenocrysts, glommerocrysts, micro-phenocrysts, microlites and a xenolith), vesicles and melt. The reaction rim around the xenolith is due to the disequilibrium between the crystals and the hosting melt.

Whether a nuclei will form a crystal or not depends on its radius and the free energy of activation for nucleation (Dowty, 1980). The critical nucleus theory is two-fold: the nuclei reaches or exceeds a critical size and will thus grow spontaneously as its growth will reduce the total free energy. If a nuclei is smaller than the critical nucleus, it will become unstable and dissolve. During its formation, a crystal will exchange chemical elements with the melt depending on crystal/melt equilibrium partition coefficients (K_d), defined by experimental petrology (e.g. Bouhifd & Jephcoat, 2011; Ford *et al.*, 1983; Nagasawa & Schnetzler, 1971; Norman *et al.*, 2005). For instance, a basaltic melt will start coexisting with olivine as soon as it cools through the liquidus, before coexisting with plagioclase, augite, oxides, etc. (Sen, 2014). However, the crystallisation sequence depends on magma composition and is also controlled by a process known as

undercooling. Undercooling is the rate at which the magma is cooled below its liquidus. It has a major controlling effect on chemistry, shape, and nucleation of crystals, and on crystal growth rate (e.g. Cashman & Marsh, 1988; Fenn, 1977; Gibb, 1974; Lofgren, 1980). Large undercooling can be considered as a high rate of energy removal from the system, allowing rapid removal of latent heat (Dowty, 1980). The volume of crystals that can be formed per unit of time depends on the removal of latent heat, thus many nuclei will form, but they will grow at a low rate and thus form small crystals (Figure 3.2). On the contrary, a lower degree of undercooling (e.g. during slow magma ascent) will lead to few nuclei that will form coarse crystals, if there is a long time for them to grow. Rapid melt ascent will lead to a large degree of undercooling and thus the formation of glass (i.e. quenching). A high rate of undercooling may change the order of appearance or even remove olivine from the crystallisation sequence (e.g. Corrigan, 1982; Shea & Hammer, 2013). Undercooling will also determine the morphology of a crystal. Indeed, crystals of olivine, pyroxene and plagioclase are generally euhedral, tabular and prismatic, respectively, at slow cooling rates, whereas they tend to be skeletal, fork-shaped or feathery at high cooling rates (Coish & Taylor, 1979; Frey & Lange, 2011; Sato, 1995; Sen, 2014; Shea & Hammer, 2013).

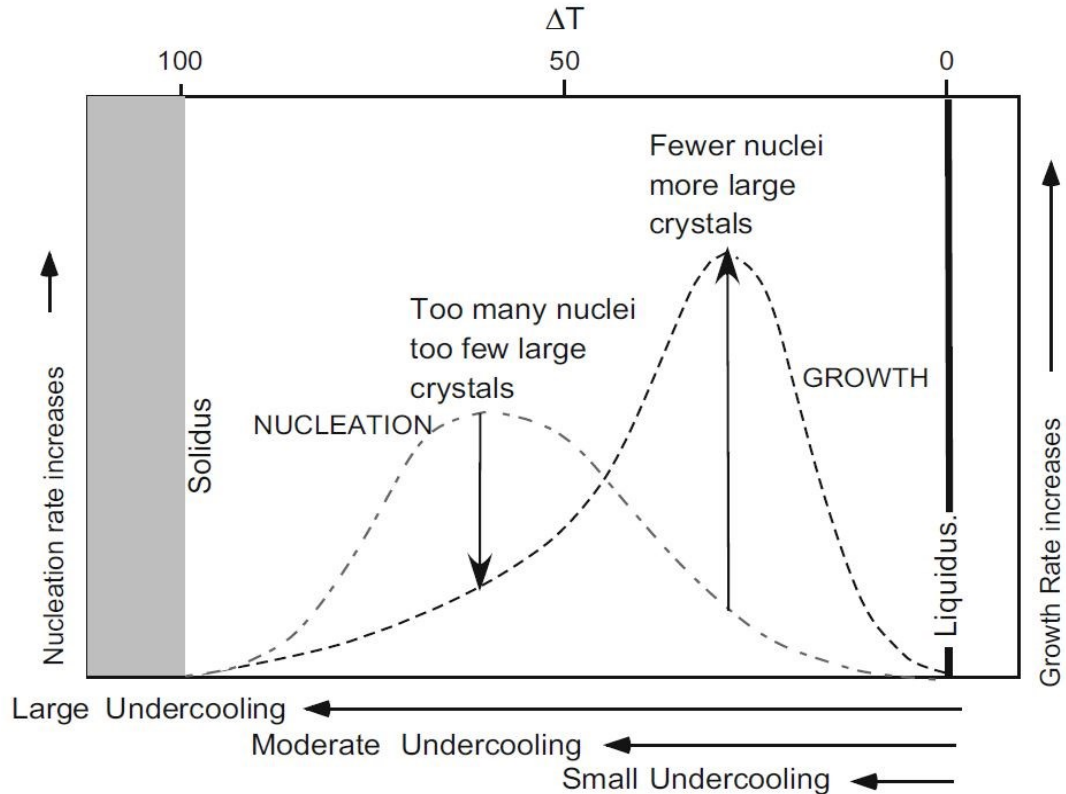


Figure 3.2. Figure 2.11 from Sen (2014) illustrating the relationship between the undercooling ΔT ($T_{\text{liquidus}} - T_{\text{current}}$) and the nucleation and growth rates of crystals. Quenching (large degree of undercooling = rapid cooling rate) triggers the formation of glass and many small crystals. Small degree of undercooling (slow cooling rate) produces a few nuclei for coarse crystals.

Microlite crystals are present in almost all products of volcanic eruptions from various eruptive styles and magma chemistries (Castro & Mercer, 2004; Geschwind & Rutherford, 1995; Pallister *et al.*, 1996; Polacci *et al.*, 2001; Taddeucci *et al.*, 2004). They have recently been studied to determine crystallisation time and growth rate, and also to understand pre- and syn-eruptive processes that occur in the magma at the onset of an eruption (e.g. Hammer *et al.*, 1999; Noguchi *et al.*, 2008; Piochi *et al.*, 2005). Just like phenocrysts and micro-phenocrysts, microlites record magma history from their formation until the eruption. Microlites are generally interpreted as the result of decompression-induced degassing (Couch *et al.*, 2003; Lipman & Banks, 1987; Pinkerton & Sparks, 1978; Swanson *et al.*, 1989), which results in an increase in the liquidus temperature (e.g. Anderson, 1984; Cashman & Blundy, 2000; Kuritani, 1999; Métrich *et*

al., 2001). Due to degassing at shallow depth, decompression-induced crystallisation of microlites is also associated with high degree of undercooling, which promotes nucleation rather than growth (e.g. Crabtree & Lange, 2011; Kirkpatrick, 1977). Degassing will alter physical properties such as the density and the viscosity of the magma, and can thus change the eruption dynamics (Sable *et al.*, 2009). However, when microlite growth is prevailing over microlite nucleation, microlites may have formed due to cooling-induced crystallisation (e.g. Sano & Toramaru, 2017). Cooling-induced crystallisation was interpreted for pumice clasts erupted during the April 1999 sub-Plinian eruption of Shishaldin volcano, in which radial textures from cores to rim indicate that the microlites formed after fragmentation while the clast was cooling down (Szramek *et al.*, 2010).

Crystals have been studied widely to retrieve information about the magmatic processes occurring at depth during crystallisation, and their timescales. During crystallisation, chemical gradients form within the crystal lattice and will remain as textures (Table 4.1). These gradients can be the result of growth or elemental diffusion, or the combination of both, in which case they may overlap and be complex to distinguish. Diffusion occurs at different rates depending on the diffusivity of a specific element and the temperature, and thus can mask growth-induced textures (e.g. Ague & Baxter, 2007; Konrad-Schmolke *et al.*, 2008; Kuritani, 1999; Zellmer *et al.*, 2016c). One method to distinguish between diffusion-induced and growth-induced patterns in crystals is to study multi-element diffusion in crystals (e.g. Costa & Dungan, 2005; Guo & Zhang, 2016; Shea *et al.*, 2015; Suzuki *et al.*, 2008). In magmas, diffusion can be driven by a change of pressure, temperature, or by chemical potential. In the crystal, vibrating atoms jump to adjacent vacant sites within the crystalline lattice during diffusion (e.g. Chakraborty, 2008; Sepiol *et al.*, 1998). Diffusion begins as soon as the nucleus starts to grow and results in equilibration of the chemical potential if the diffusion time is long enough.

Geospeedometry, a term introduced by Lasaga (1983), uses diffusion profiles to estimate crystal residence time at magmatic temperature (e.g. Costa *et al.*, 2003; Morgan *et al.*, 2004; Zellmer *et al.*, 2011). Forward modelling is the most common method to model diffusion in volcanic crystals (e.g. Ague & Baxter, 2007; Bradshaw & Kent, 2017; Cooper & Kent, 2014; Costa *et al.*, 2003; Druitt *et al.*, 2012; Morgan & Blake, 2006; Petrone *et al.*, 2015) and has been extensively used in crystals presenting normal or reverse zoning (e.g. Costa & Chakraborty, 2004; Hartley *et al.*, 2016; Kahl *et al.*, 2015). Many crystals exhibit textures that are growth-induced and have not been affected by equilibration due to diffusion (Bennett *et al.*, 2019a; Renjith, 2014; Shea *et al.*, 2015). These textures can be qualitatively studied using optical microscopy or high-resolution imaging instruments. Magmatic processes such as magma mixing, magma recharge, magma degassing and magma cooling are recorded during crystallisation and lead to multiple patterns and zonations (e.g. Bennett *et al.*, 2019b; Erdmann *et al.*, 2012; Holness *et al.*, 2005; Ohnenstetter & Brown, 1992; Pappalardo *et al.*, 2018; Piochi *et al.*, 2005; Pompilio *et al.*, 2017). Disequilibrium textures are common in phenocrysts and are usually a result of change of pressure or temperature, resulting from magma recharge or mixing (e.g. Agostini *et al.*, 2013; Browne *et al.*, 2006) or rapid decompression (e.g. Nelson & Montana, 1992). These textures consist of resorbed crystal cores, sometimes associated with a single or multiple overgrowing layers, and dissolution patterns such as sieve textures (e.g. spongy-, dusty-textured; Kawamoto, 1992), often found in plagioclase (Izbekov *et al.*, 2002; Jeffery *et al.*, 2013; Shane *et al.*, 2019; Table 3.1). Sieve textures can either be coarse or fine, depending on the degree of dissolution. Coarse-sieve textures are usually found in the core of large crystals whereas fine-sieve textures occur as a part of an outer layer between the core and the rim (Renjith, 2014). Oscillatory zoning is also a disequilibrium texture which is commonly found in phenocrysts that have witnessed a

dynamic environment with pressure and temperature fluctuations due to magma recharge or magma mixing (e.g. Haase *et al.*, 1980; Petrone *et al.*, 2016; Shore & Fowler, 1996), or change in the magma composition (e.g. Chen *et al.*, 2015), change in the growth rate (e.g. Halden & Hawthorne, 1993), or may be diffusion-induced (e.g. Grove *et al.*, 1984).

Some of these textures have been described for the phenocryst cargos of TgVC and have therefore provided key information about the mid-crustal depths processes within the magmatic system (Auer *et al.*, 2015; Kilgour *et al.*, 2013; Moebis *et al.*, 2011; Nakagawa *et al.*, 1998; Pardo *et al.*, 2012; Price *et al.*, 2007; Shane *et al.*, 2008a; Stewart, 2010). The presence of such textures in microlites and micro-phenocrysts would allow essential insights to be gained into shallow ascent processes, which may be linked to the resulting eruption style.

Table 3.1. (Table in the next page) Schematic representations of the common plagioclase crystals and textures observed in volcanic rocks, and their interpretations.

Texture	Description	Interpretation	Reference
 <p>~10⁻² m</p>	Resorbed core, mantled by a single or multiple overgrowing layers	Rapid decompression or magma recharge or magma mixing with a more primitive, hotter and/or volatile-rich magma	Agostini <i>et al.</i> (2013); Bennett <i>et al.</i> (2019); Browne <i>et al.</i> (2006); Nelson & Montana (1992); Ubide <i>et al.</i> (2019)
	Coarsely sieved, usually found in the core region, may be mantled by euhedral oscillatory zones	Rapid decompression or magma recharge or magma mixing with a more primitive, hotter and/or volatile-rich magma	Kawamoto (1992); Renjith (2014); Singer <i>et al.</i> (1993); Viccaro <i>et al.</i> (2010)
	Finely sieved, usually found as a continuous layer between the core and the rim	Rapid decompression or magma recharge or magma mixing with a more primitive, hotter and/or volatile-rich magma	Kawamoto (1992); Renjith (2014); Singer <i>et al.</i> (1993); Viccaro <i>et al.</i> (2010)
	Oscillatory zoned, sometimes mantling a resorbed core	Dynamic magma reservoir with magma recharge or magma mixing or change in the magma composition, change in the growth rate, or may be diffusion-induced	Chen <i>et al.</i> (2015); Grove <i>et al.</i> (1984); Haase <i>et al.</i> (1980); Halden & Hawthorne (1993); Petrone <i>et al.</i> (2016); Shore & Fowler (1996)
	Glomerocryst, sometimes composed of different minerals	Aggregates of resorbed crystals, entrained disaggregated mush	Bennett <i>et al.</i> (2019); Renjith (2014); Viccaro <i>et al.</i> (2010)
	Euhedral microlites	Decompression-induced or cooling-induced crystallisation	Armenti <i>et al.</i> (1994); Cashman <i>et al.</i> (1999); Castro <i>et al.</i> (2003); Couch <i>et al.</i> (2003); Geschwind and Rutherford (1995); Hammer <i>et al.</i> (1999); Jerram <i>et al.</i> (2018); Lipman & Banks (1987); Noguchi <i>et al.</i> (2006) Pinkerton & Sparks (1978); Swanson <i>et al.</i> (1989)
	Skeletal, hopper and fork-shaped textures, mainly found in microlites	High undercooling-induced crystallisation, rapid cooling	Coish & Taylor (1979); Frey & Lange (2011); Sato (1995); Sen (2014); Shea & Hammer (2013)

3.2. Crystal Size Distributions

The theory of Crystal Size Distributions (CSDs), initially developed for chemical engineering (Randolph & Larson, 1971), was first applied to geological systems by Marsh (1988) after observing a quasi-linear negative trend between the number of crystal per unit size and their representative sizes for many lavas. CSDs have become a useful tool to infer space- and time-integrated information about plumbing systems such as storage and mixing (Gutierrez & Parada, 2010; Magee *et al.*, 2010; Simakin & Bindeman, 2008), and detailed eruptive histories of magmas (Hammer *et al.*, 1999; Higgins, 1996b; Mangan, 1990). Kinetics extracted from CSDs can also provide identification of crystal nucleation and growth mechanisms, determination of magma cooling rates, and thus elucidate the timescales of these events (Higgins, 1996b). In addition, information about the petrological processes such as crystal accumulation and fractionation in the system can be derived. CSDs are a popular tool due to their low acquisition cost and the simplicity of the data collection process. CSDs consist of plotting the crystal size L (e.g. crystal length in mm) against the population density, which is expressed as $\log(n(L))$, where $n(L)$ is the number of crystals per unit length (L) per unit volume of magma (Marsh, 1988). The CSD slope can be used to constrain the linear growth rate and the time for crystal growth, whereas the intercept on the coordinate axis provides the instantaneous nucleation density of zero-sized nuclei. Considering critical nucleation theory, a nucleus needs to reach a specific size to be stable, i.e. to avoid shrinking and dissolution rather than growth (Dowty, 1980). Three types of CSD shapes can be identified: (1) an exponential distribution or a linear CSD (Figure 3.3a) infers a steady-state open system (Marsh, 1998a) associated with constant cooling and growth rates (e.g. Fornaciai *et al.*, 2009; Piochi *et al.*, 2005); linear CSDs were found for several eruptions of Stromboli volcano (Armienti *et al.*, 2007); (2) a power-law-type (e.g. Noguchi *et al.*, 2006;

Toramaru *et al.*, 2008), lognormal (Kile & Eberl, 2003) distribution or concave-up curved CSD (Figure 3.3b) has first been interpreted by Marsh (1988) as (i) change of growth rate, (ii) change of cooling rate, (iii) crystal accumulation and (iv) magma mixing. It has also been associated to changes in dissolved water during magma ascent (Armienti *et al.*, 1994); Higgins (2006) suggests that it is the result of coarsening – also called Ostwald ripening (Voorhees, 1992) – or mixing, whereas some have interpreted it as the consequence of crystallisation by decompression (Brugger & Hammer, 2010); It could also be due to variation in the growth rate or to the acceleration of nucleation and growth during magma ascent (Shea *et al.*, 2010a). Finally, Fornaciai *et al.* (2015) related this shape to a rapid change in undercooling due to a strong and sudden degassing. This distribution type has been described for several volcanic edifices such as Mount Etna (e.g. Armienti *et al.*, 1994), Kameni (Higgins, 1996b), Soufrière Hills (Higgins & Roberge, 2003), Eldfell (Higgins & Roberge, 2007), Tseax (Higgins, 2009), Mount Saint Helens (Muir *et al.*, 2012) and Merapi (Preece *et al.*, 2016) volcanoes. (3) A third shape has also been observed in a CSD as a downturn at smallest grain sizes (Figure 3.3b). It was first interpreted due to the low resolution of the image (e.g. Fornaciai *et al.*, 2009; Marsh, 1998a). After the quality of measurements has improved, the downturn was still observed in CSDs and was explained as an intersection artefact, because of the prismatic shape of some minerals e.g. pyroxene (Cashman & McConnell, 2005). Higgins (2006) interpreted this shape to result from a textural coarsening in which the smaller crystals are dissolved and larger ones have a growth rim whereas it has also been interpreted as an effect of quenching (Armienti *et al.*, 2007). Studies of explosive eruptions have generally focused on plagioclase as it is the most common mineral to form microlites, but a few have also included pyroxenes (e.g. Castro *et al.*, 2003; Szramek *et al.*, 2010; Toramaru *et al.*, 2008).

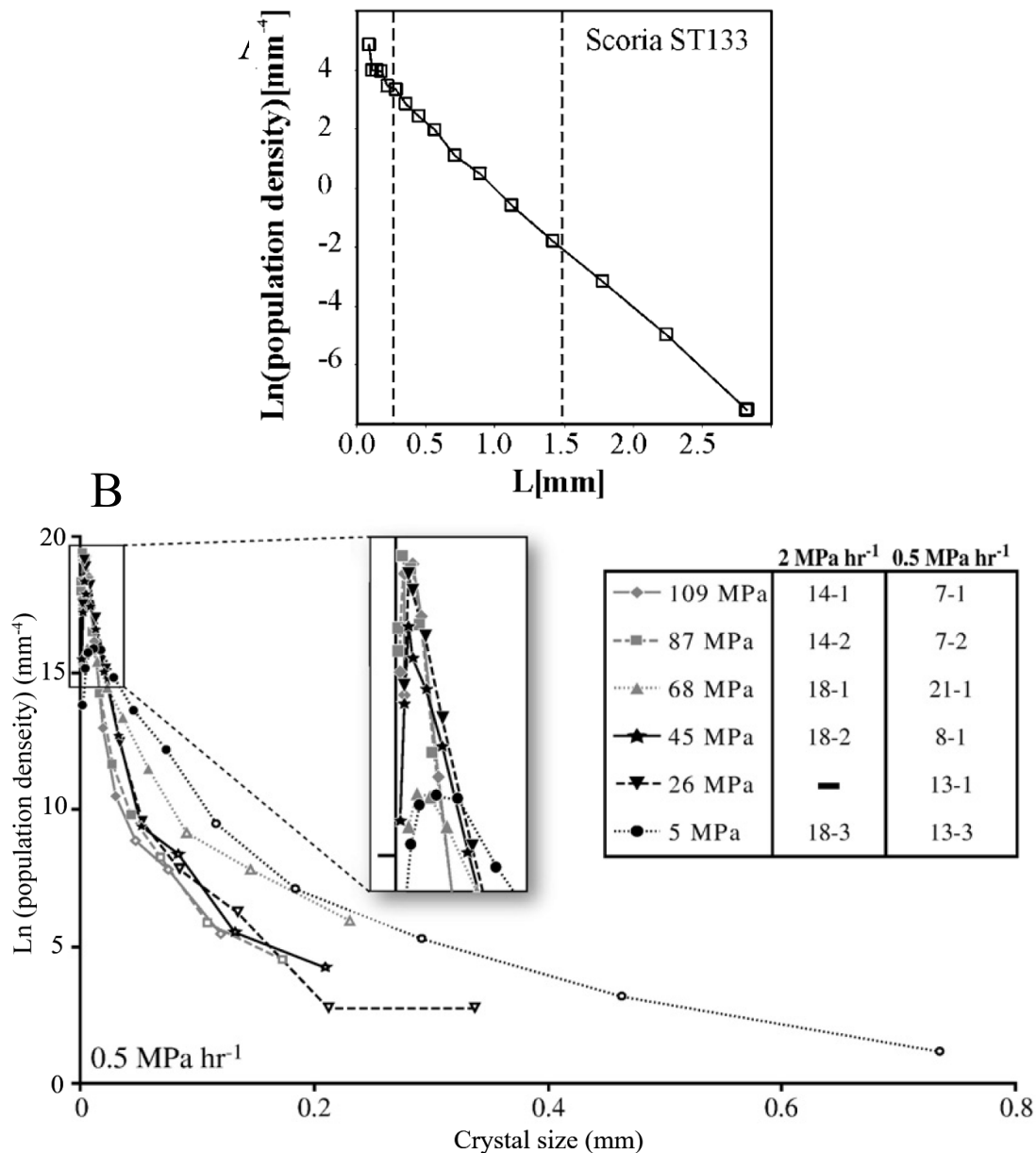


Figure 3.3. Shapes of crystal size distributions found in natural and experimental samples. (A) Figure 3 of Fornaciai *et al.* (2009) representing a linear CSD of plagioclase from a scoria of the 2002-2003 eruption of Stromboli, Aeolian Islands, Italy. (B) Figure 2 of Brugger & Hammer (2010) demonstrating curved-upwards CSD of plagioclase formed during decompression experiments of hydrous rhyodacite magma at different decompression rates. Downturn at smallest size interpreted as intersection artefact.

CSDs may be acquired for any type of volcanic samples (lava, scoria, bomb, pumice, ash, etc.), and the traditional method involves manual outlining of imaged crystals (e.g. Brugger & Hammer, 2010; Higgins, 2000; Jerram *et al.*, 2009; McCanta *et al.*, 2007). The dimensions are typically measured with the public software Fiji (i.e. Fiji is just ImageJ), which provides long- and short-axes of best fitting ellipse and the area of each particle (i.e. crystal) from a binary image in which the crystals have previously been outlined. However, the crystal dimensions obtained represent two-dimensional- rather than three-dimensional-crystal shapes and are not representative of the natural sample. Thus, Higgins (2000) developed a program called *CSDCorrections* to convert 2D data to 3D crystal size distributions. This software requires some parameters before generating CSDs; the type of measurements (length or width or ellipse major/minor axis or maximum length), the type of fabric (massive/lineated/foliated), the roundness factor of the sample, the vesicles/voids correction if applicable, the measured area, the shape factors and the size scale. Shape factors represent the best fit crystal habits i.e. the short, intermediate, and long axes, and need to be estimated. Shape factor determination is facilitated by *CSDslice*, a Excel program developed by Morgan & Jerram (2006): this routine compares the input measurements with the database composed of 703 random slices of crystal of different shapes and gives the average best fit shape factors of the observed crystal population. However, this method assumes that all crystals have the same shape, which is highly unlikely because a magma usually contains crystals formed at various degrees of undercooling, which affects crystal shapes (Brugger & Hammer, 2010). The number of divisions into which one bins data depends on the total number of measurements whereas the absolute size range is given by the biggest crystals. Higgins (2000) suggests that logarithmic size intervals are the most relevant to use as each bin is ten times larger than the previous bin. Also, he stated that 4 to 5 bins per decade generally give a suitable

result. He also suggested that if a bin contains less than 5 crystals, it will result in an insignificant CSD and thus this bin will need to be removed. If there is a gap in the CSD, it might be due either to a lack of data or because the bin is too narrow and has to be widened.

In order to obtain CSDs, crystals have to be outlined as stated earlier. To date, this selection has typically been done manually using image processing software such as *Photoshop* and involves laborious and time-consuming lab work (e.g. Berger *et al.*, 2011; Hammer *et al.*, 1999; Suzuki & Fujii, 2010). Some work such as the one of Muir *et al.* (2012) provided encouraging results using element maps to select different mineral phases automatically, but this method requires significant instrument time. Further, the intersection-probability effect defined by the higher probability of a large crystal to intersect with a random 2D slice than a small crystal reveals issues when converting 2D to 3D measurements (e.g. Royet, 1991; Underwood, 1970). Indeed, as a grain is rarely cut through its centre, there is a cut-section effect especially for acicular crystals (Peterson, 1996; Sahagian & Proussevitch, 1998). It has been stated that *CSDCorrection* gives less reliable results for acicular crystals due to the wider variability of shape and the statistics of sectioning; a minimum of 75 crystal sections is required to obtain a robust CSD for circular/prismatic crystals e.g. pyroxene, compared to > 250 crystal sections for acicular crystals e.g. needle-like microlites (Higgins, 2000; Morgan & Jerram, 2006). The reliability of these results can be predicted when the user inputs the measurements data into the *CSDslice* Excel spreadsheet that provides the level of fit R^2 of the crystal population habits (Figure 3.4). Previous studies have highlighted limitations and disadvantages related to CSDs. First of all, they do not provide information about the conduit geometry and depths where magmatic processes revealed by the CSDs occur (Melnik *et al.*, 2011). To extract information from CSDs such as the timescales of

magmatic events, the slope, the intercept and the growth rate are needed. However, the growth rate, which may change from one magmatic system to another or even within a system itself, is challenging to constrain and has typically been assumed to be constant (Armienti, 2008; Bindeman, 2003; Blundy & Cashman, 2008; Cashman & Marsh, 1988; Cashman, 1992; Cashman & McConnell, 2005; Hammer *et al.*, 1999; Piochi *et al.*, 2005; Resmini, 2007). Models based on CSDs are thus only applicable to one particular volcanic system or to similar edifices; Melnik *et al.* (2011) have developed a model to image volcanic plumbing systems based on CSD interpretations, crystallisation kinetics and hydrodynamic flow simulation. This simple model with assumptions is valid for eruptions with steady-state magma ascent, but is not applicable to eruptions fed by pulses or to products from explosive eruptions.

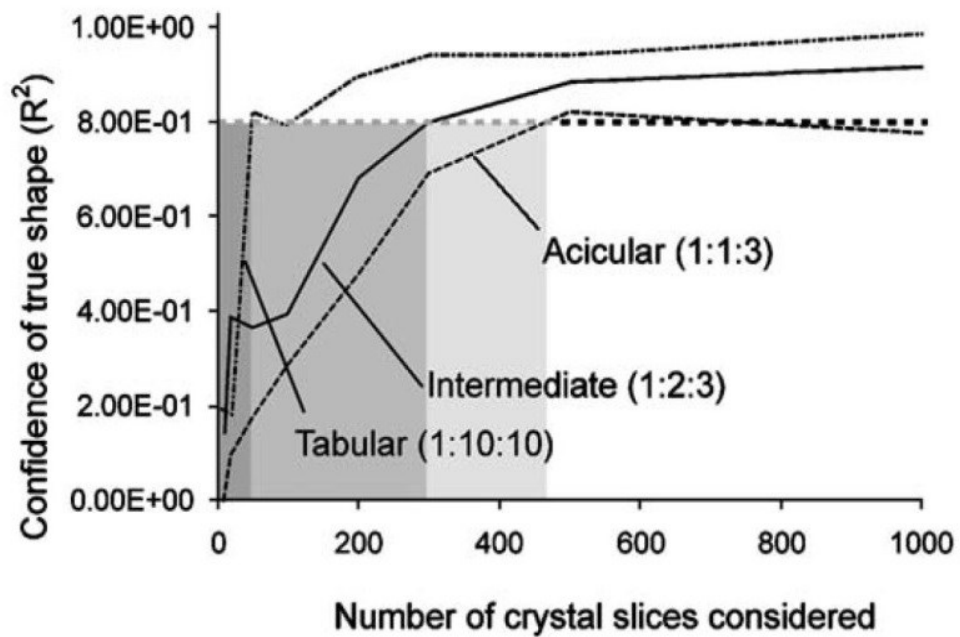


Figure 3.4. Figure 4d of Morgan & Jerram (2006) illustrating the level of fit (R^2) versus the number of crystal slices considered. Note that at least 300 crystals are required to obtain confident results for intermediate and acicular shapes.

3.3. Growth rate

The growth rate is an important parameter that elucidates the magmatic processes within both the magma chamber and the magmatic conduit. It depends on several parameters such as viscosity (e.g. high growth rates in low viscosity melts), magma composition (e.g. triggering crystallisation of different mineral phases at different growth rates) and can be controlled by several processes such as melt-crystal peritectic reaction, removal of latent heat of crystallisation and diffusion in the melt (e.g. Kirkpatrick, 1977) or even diffusion of the slowest species in the melt (Toramaru *et al.*, 2008). Experimentally, the rate of growth, e.g. for plagioclase, was interpreted to depend on the composition of the parental melt, the degree of undercooling and the conditions of experiments (Agostini *et al.*, 2013; Cashman, 1993; Conte *et al.*, 2006; Hammer & Rutherford, 2002; Muncill & Lasaga, 1988; Orlando *et al.*, 2008; Shea & Hammer, 2013). Eberl *et al.* (2002) have assumed the rate of growth to be proportional to the crystal size. This hypothesis has been questioned (e.g. Armienti *et al.*, 1994; Simakin & Bindeman, 2008) as small crystals can grow as fast as large crystals. However, a study conducted by Kile & Eberl (2003), comparing size-dependent and size-independent crystal growth, highlighted that these two processes are driven by, respectively, advection in a stirred system and diffusion in a non-stirred system and thus can both be applicable to a magmatic system. They also conclude their study by stating that advection and size-dependent crystal growth are the dominant process as it is the most common growth law revealed by natural crystal CSDs, which show lognormal distribution.

Early studies (e.g. Cashman & Blundy, 2000) have used time-averaged growth rates following the relation:

$$G = \frac{0.5L}{t} \quad (1)$$

where L is the crystal dimension (e.g. length) and t the time of growth. Time of growth is sometimes assumed to be similar to the time of ascent from the chamber to the surface. However, this assumption is controversial because the crystallisation process is not necessarily continuous; during their ascent magmas can be stored at several depths (Cichy *et al.*, 2011; Erlund *et al.*, 2009; Kuritani, 1999), where conditions of crystallisation (e.g. temperature, pressure, surrounding stress field, etc.) may change and where crystallisation may intermittently cease (Cashman & Blundy, 2000).

Growth rates are usually given as ranges or averages because they are challenging to determine (Hammer *et al.*, 1999; Preece *et al.*, 2016; Salisbury *et al.*, 2008). Cashman (1990) stated that growth rates under variable magmatic conditions generally range between 10^{-12} m s⁻¹ and 10^{-13} m s⁻¹. However, experiments to simulate ascending magma driven by decompression and water exsolution obtained microlite growth rates as fast as 10^{-9} m s⁻¹ (Couch *et al.*, 2003; Gardner *et al.*, 1998; Hammer *et al.*, 1999).

Many studies of CSDs (Bindeman, 2003; Blundy & Cashman, 2008; Cashman & Marsh, 1988; Cashman, 1992; Cashman & McConnell, 2005; Lentz & McSween, 2000; Piochi *et al.*, 2005; Resmini, 2007; Salisbury *et al.*, 2008) have been interpreted using constant crystal growth rates. Several methods have been used to define a crystal growth rate such as experimental and computational methods; (1) as stated earlier, using the slope and the intercept of a CSD allow the calculation of growth rate in experimental runs, where growth times are well-constrained. Armienti *et al.* (2007) have associated the result of this method to a mean or net growth rate due to potential dissolution episodes during ascent. Interpreting crystal growth rates from CSDs usually requires a contextual consideration; indeed, if crystals are thought to result from a rapid cooling associated with water exsolution, a high growth rate may be inferred (Cigolini *et al.*, 2008; Mastrolorenzo & Pappalardo, 2006). (2) Experimental methods of in-situ observation of growing crystals

are also used to determine growth rate (e.g. Gondé *et al.*, 2006; Means & Park, 1994; Schiavi *et al.*, 2009); a method called “ L_{\max} ”, which consists of measuring the largest four to ten crystals observed in a charge and dividing the length by the experimental duration can be used (Fenn, 1977; Gardner *et al.*, 1998; Hammer & Rutherford, 2002; Leshner *et al.*, 1999; Marsh, 1998a; McCanta *et al.*, 2007; Walker *et al.*, 1976). (3) The batch method has generally been used for studies of crystallisation kinetics in experimental and natural systems (e.g. Blundy & Cashman, 2008; Brugger & Hammer, 2010; Couch *et al.*, 2003; Larsen, 2005) and consists of averaging 2D bulk population characteristics using the simple following equations:

$$G = \frac{S_n}{t} \quad (2)$$

In which S_n is the characteristic crystal size, which can be obtained using:

$$S_n = \left(\frac{\varphi}{N_A} \right)^{1/2} \quad (3)$$

with φ the area fraction and N_A the number density.

The CSD method as well as the L_{\max} and batch methods were used and compared for several volcanic samples by Brugger & Hammer (2010). Their results give a wide range of growth rates, where the maximum is always obtained using the L_{\max} method, the minimum with the batch method and the CSD method gives intermediate growth rates. They also explain that depending on which part of the CSD is used, the resulting growth rate is different with the growth time being known. Steeper slopes, which are generally observed for smaller crystals will infer lower rates of growth and thus be closer to the value obtained with the batch method.

Also, relative change in growth rate can be interpreted from textural analysis of crystals; for instance, hopper morphology indicates a rapid increase in growth rate caused

by a high degree of undercooling (Viccaro *et al.*, 2010; Zellmer *et al.*, 2016b). More recently, a new method for rate of growth for microlites was published (Sano & Toramaru, 2017). By identifying micro-scale projection textures next to microlites of plagioclase, they have developed a model to estimate growth rate and time of growth from the instability theory between melt and crystals to understand the positive correlation of the length and the spacing of these needle-like textures. A peritectic reaction between olivine and the melt to form microlites of pyroxene has also been used to determine growth rate (Zellmer *et al.*, 2016c; Zellmer *et al.*, 2018); by modelling inter-diffusion at the olivine rim, they were able to determine the dissolution rate of olivine, which is intimately linked to the growth rate of the peritectic pyroxenes.

3.4. Thermodynamics in magmas

Commonly, thermodynamics are applied to a system in equilibrium as it allows the use of the classical theories of chemical thermodynamics to test, verify or discriminate between hypotheses (Ghiorso & Gualda, 2015). Thermodynamics can also be used to assess the energy of a system in disequilibrium, which in turn allows the quantification of energy needed to reach the equilibrium state, informing about the timescales of the system evolution and the rates of chemical reactions. It is common to find volcanic rocks with multiple crystal populations that have grown from diverse melts at different times, and under a range of temperatures, pressures and water contents (Cooper & Reid, 2003; Putirka, 2008; Streck, 2008). Indeed, compositional gradients and disequilibrium textures characterise volcanic rocks as magmas stall in the crust under the form of reservoirs that experience crustal contamination (e.g. Gómez-Tuena *et al.*, 2003; Jeffery *et al.*, 2013; Preston, 2001), magma mixing (e.g. Anderson, 1976; Schleider *et al.*, 2016; Sparks *et al.*, 1977), and remobilisation of crystal mush from previous intrusions (e.g. Cooper & Kent, 2014; Girard & Stix, 2009; Zellmer *et al.*, 2003b). However, for simplification and

because deviations from equilibrium can be quantified, thermodynamics applied to a magmatic system assumes local equilibrium as a reference state (Leshner & Spera, 2015). In the case of crystallisation, thermodynamics applied on the system are assumed at equilibrium to address the effect of the melt composition, the temperature, the pressure and the water content. At equilibrium, the equilibrium constant K accounts for differences in the standard Gibbs free energy (also called the free enthalpy) ΔG due to composition, and is expressed as follows:

$$\Delta G(T, X, P) = 0 = \Delta H^\circ(T) - T\Delta S^\circ(T) + RT\ln K + \int_0^P \Delta V_T^\circ(P) dP \quad (4)$$

where the standard state change in molar enthalpy and entropy for both the crystal and the melt are respectively ΔH° and ΔS° , and ΔV_T° is the change in molar volume for the reaction at a temperature T and a pressure P .

To elucidate the conditions under which the crystals grew, to estimate ascent rates, and to decipher magmatic and eruptive processes, intensive variables such as temperature, pressure and water content are essential to be retrieved. Thermobarometry is used to determine the P-T conditions at which the magma and the crystals were in equilibrium, crucial to elucidate magma storage conditions and magma ascent processes (e.g. Mollo *et al.*, 2013; Putirka & Condit, 2003). Hygrometry based on the equilibrium between a mineral-melt pair is a useful tool to estimate the water content at crystallisation and may also provide insights into eruptive dynamics upon magma ascent at the onset of explosive eruptions. Thermobarometers and hygrometers are based on empirical regression of thermodynamically derived expressions. Calibration of these models is done using large databases of phase-equilibrium experiments that crystallized the targeted mineral over a range of pressures, temperatures, and H₂O concentrations.

3.4.1. Thermobarometry

Geothermometers and geobarometers use equilibrium chemical reactions and compositional partitioning of elements between coexisting phases (e.g. mineral-melt or mineral-mineral pairs) to quantify the magmatic temperature and the pressure at which the targeted mineral crystallised. Many thermometers and barometers for volcanic rocks are available in the literature and here is a non-exhaustive list: the olivine-ilmenite thermometer (Sack & Ghiorso, 1991), the plagioclase-amphibole geothermometer (Holland & Blundy, 1994), the olivine- and orthopyroxene-liquid geothermometers of Beattie (1993), the Ti-in-quartz thermobarometer and the associated software TitaniQ (e.g. Huang & Audétat, 2012; Thomas *et al.*, 2015; Wark & Watson, 2006), Ti-in-zircon and Zr-in-rutile geothermometers (Fu *et al.*, 2008; Hayden & Watson, 2007), the sphene thermobarometer (Hayden *et al.*, 2008), the Fe-Ti oxide geothermometer (Ghiorso & Evans, 2008), the clinopyroxene-liquid thermobarometers (Masotta *et al.*, 2013; Neave & Putirka, 2017; Nimis, 1995; Nimis, 1999; Putirka *et al.*, 1996; Putirka *et al.*, 2003). Putirka (2008) provides an extensive review and summary of several geothermometers and geobarometers: clinopyroxene-liquid, orthopyroxene-liquid, two pyroxene, and feldspar-liquid thermobarometers, two feldspar-, olivine- and glass-based geothermometers, and a silica activity geobarometer. Although plagioclase is probably more sensitive to pressure, temperature and water content of magmatic systems than any other mineral phase (Mollo *et al.*, 2011), the relevant growth rate that will be used in Chapter 6 to calculate microlite residence time involves the pyroxene phase. The orthopyroxene-liquid geothermometer of Beattie (1993) is not ideal as it over-predicts the temperature. The clinopyroxene-liquid geobarometer of Nimis (1995) yields anomalously low P for high-P experiments, and the geobarometer of Putirka *et al.* (1996) yields higher systematic errors than that of Nimis. The clinopyroxene geothermometer of Nimis &

Taylor (2000) is calibrated from a more limited data set than that of Putirka (2008). The two-pyroxene thermobarometer of Putirka (2008) cannot be used as the microlite phases in the TgVC magmas studied usually contain plagioclase + orthopyroxene \pm clinopyroxene \pm pigeonite, and some tephra contain clinopyroxene instead of orthopyroxene \pm pigeonite. Hence, the orthopyroxene-liquid thermobarometer, the clinopyroxene-liquid geothermometer of Putirka (2008) and the clinopyroxene-liquid geobarometer of Neave & Putirka (2017) will be used in this study to determine the P-T conditions at which the microlites crystallised.

Equilibrium between the crystal-melt pair requires to be tested before retrieving the T and P outputs. The test is similar to the test proposed by Roeder & Emslie (1970), which compares the observed Fe-Mg exchange coefficient (i.e. $K_D(\text{Fe-Mg})$) with that of the

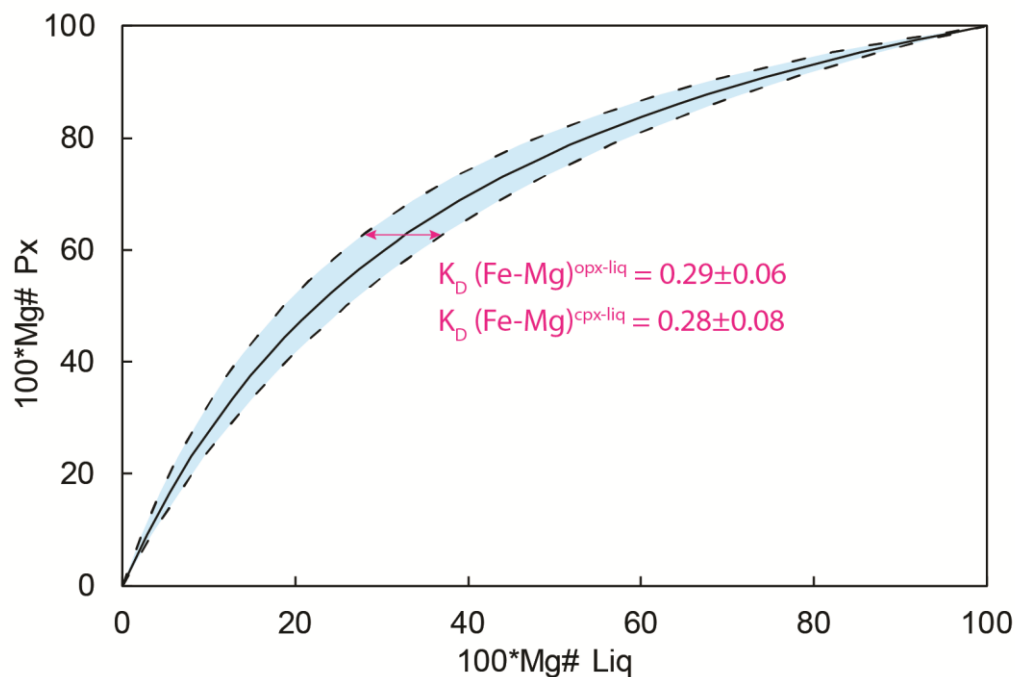


Figure 3.5. The Rhodes diagram presents tests of orthopyroxene- and clinopyroxene-melt equilibrium (Rhodes et al., 1979). It is based on 785 experimental data for orthopyroxene (opx) which yield $K_D(\text{Fe-Mg})^{\text{opx-liq}} = 0.29 \pm 0.06$, and based on 1245 experimental observations for clinopyroxene (cpx) which yield $K_D(\text{Fe-Mg})^{\text{cpx-liq}} = 0.28 \pm 0.08$. The blue area is the window where the putative pyroxene-melt should plot if in equilibrium.

experimental data. The Rhodes's diagram (Figure 3.5) graphically portrays this test (Rhodes *et al.*, 1979).

In the case of orthopyroxene, the K_D value decreases slightly with increasing silica content and it is expressed as:

$$K_D(Fe - Mg)^{opx-liq} = 0.4805 - 0.3733X_{Si}^{liq} \quad (5)$$

where X_{Si}^{melt} is the cation fraction of SiO₂ in the equilibrium liquid.

In the case of clinopyroxene, the K_D value accounts for a temperature dependency as follows:

$$\ln K_D(Fe - Mg)^{cpx-liq} = -0.107 - \frac{1719}{T(K)} \quad (6)$$

Liquid and orthopyroxene/clinopyroxene components are required to retrieve the temperature and pressure. The liquid components are SiO₂, TiO₂, Al₂O₃, FeO, MnO, MgO, CaO, Na₂O and K₂O. The pyroxene components are the same as the liquid components plus Cr₂O₃. Cations are calculated on the basis of 6 oxygens. The calculations of the components are reported in Appendix C1, C2 and C3.

The orthopyroxene-liquid geothermometer that will be used is defined by the Eq. 28a Putirka (2008). It was calibrated using 793 anhydrous and hydrous data, where orthopyroxenes had cations sums ranging between 3.97-4.03, providing a standard error estimation of SEE = ± 39 °C. This thermometer is applicable to the following ranges: pressures (1 atm-110 kbar), temperatures (750-1600 °C), and H₂O concentrations (0-14.2 wt%). It is expressed as follows:

$$\frac{10^4}{T(K)} = 4.07 - 0.329[P(GPa)] + 0.12(H_2O^{liq}) +$$

$$0.567 \ln \left[\frac{X_{EnFs}^{opx}}{(X_{SiO_2}^{liq})^2 (X_{FeO}^{liq} + X_{MnO}^{liq} + X_{MgO}^{liq})^2} \right] - 3.06(X_{MgO}^{liq}) -$$

$$6.17(X_{KO_{1.5}}^{liq}) + 1.89(Mg\#^{liq}) + 2.57(X_{Fe}^{opx}) \quad (7)$$

where EnFs stands for enstatite + ferrosilite. The details of the orthopyroxene component calculations can be found in Appendix C2. Terms under the form of X_{Fe}^{opx} are the number of cations of the element indicated in the phase mineral or liquid (e.g. in this case number of cations in Fe in orthopyroxene), calculated on the bases of 6 oxygens. Eq. 28b of Putirka (2008) was not used as it only uses the liquid components to calculate the temperature for a liquid saturated with orthopyroxene.

The orthopyroxene-liquid geobarometer that will be used is defined by the Eq. 29a of Putirka (2008), because it encompasses a larger number of experiments and a smaller systematic error than Eq. 29c. This calibration was derived from 592 hydrous and anhydrous experiments and yields a standard error estimate of SEE = ± 2.6 kbar (260 MPa). It is defined by:

$$P(kbar) = -13.97 + 0.0129T(^{\circ}C) + 0.001416T(^{\circ}C) \ln \left[\frac{X_{Jd}^{opx}}{X_{NaO_{0.5}}^{liq} X_{AlO_{1.5}}^{liq} (X_{SiO_2}^{liq})^2} \right] -$$

$$19.64(X_{SiO_2}^{liq}) + 47.49(X_{MgO}^{liq}) + 6.99(X_{Fe}^{opx}) + 37.37(X_{FmAl_2SiO_6}^{opx}) + 0.748(H_2O^{liq}) +$$

$$79.67(X_{NaO_{0.5}}^{liq} X_{KO_{0.5}}^{liq}) \quad (8)$$

where Jd is jadeite and Fm equals to Fe + Mg, which are the orthopyroxene components, calculated using the normative procedure outlined in Putirka *et al.* (2003). The details of the clinopyroxene component calculations can be found in Appendix C3

The clinopyroxene geothermometer that will be used in this study is defined by the Eq. 33 in Putirka (2008), which is based on the Jd-DiHd exchange of 1174 hydrous and anhydrous experiments, yielding error estimates of SEE = ± 45 °C. It calibrates the temperature as follows:

$$\begin{aligned} \frac{10^4}{T(K)} = & 7.53 - 0.14 \ln \left[\frac{X_{Jd}^{cpx} X_{CaO}^{liq} X_{Fm}^{liq}}{X_{DiHd}^{cpx} X_{Na}^{liq} X_{Al}^{liq}} \right] + 0.07 \ln(H_2O^{liq}) - 14.9 (X_{CaO}^{liq} X_{SiO_{1.5}}^{liq}) - \\ & 0.08 \ln(X_{TiO_2}^{liq}) - 3.62 (X_{NaO_{0.5}}^{liq} + X_{KO_{1.5}}^{liq}) - 1.1 (Mg\#^{liq}) - 0.18 \ln(X_{EnFs}^{cpx}) - \\ & 0.027P(kbar) \quad (9) \end{aligned}$$

where DiHd and EnFs are the clinopyroxene components and stand for diopside + hedenbergite and enstatite + ferrosilite, respectively, which are calculated using the normative procedure outlined in Putirka *et al.* (2003).

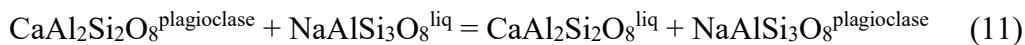
The clinopyroxene geobarometer of Neave and Putirka (2017) is calibrated from 113 hydrous and anhydrous experimental data for the 1 atm to 20 kbar range, saturated in clinopyroxene \pm olivine \pm plagioclase \pm orthopyroxene \pm spinel \pm hornblende \pm magnetite \pm ilmenite, and the 1-atm experiments included experienced negligible Na loss. The standard error estimate associated with this calibration is SEE = ± 1.4 kbar. The geobarometer is expressed as follows:

$$\begin{aligned} P(kbar) = & -26.27 + 39.16 \frac{T(K)}{10^4} \ln \left[\frac{X_{Jd}^{cpx}}{X_{NaO_{0.5}}^{liq} X_{AlO_{1.5}}^{liq} (X_{SiO_2}^{liq})^2} \right] - 4.22 \ln(X_{DiHd}^{cpx}) + \\ & 78.43 X_{AlO_{1.5}}^{liq} + 393.81 (X_{NaO_{0.5}}^{liq} X_{KO_{0.5}}^{liq})^2 \quad (10) \end{aligned}$$

Because the temperatures and pressures retrieved from the thermobarometers are dependent on H₂O, a hygrometer will be used iteratively with the thermobarometers to derive internally consistent solutions for P-T-X(H₂O).

3.4.2. Hygrometry

When data from melt inclusions are not available, mineral-liquid hygrometers can be used to provide an estimation of the water content of the magma. Geohygrometers quantify the effect of dissolved water in the liquid on the elemental partitioning between the melt and a mineral phase (Ghiorso & Gualda, 2015). Several mineral-melt hygrometers applicable to volcanic rocks are available in the literature and encompass the following mineral phases: plagioclase (Hamada *et al.*, 2013; Lange *et al.*, 2009; Ushioda *et al.*, 2014; Waters & Lange, 2015), amphibole (Ridolfi *et al.*, 2010), clinopyroxene (Perinelli *et al.*, 2016), and Ca-in-olivine (Gavrilenko *et al.*, 2016). Considering that the studied TgVC magmas are nearly aphyric, intermediate and contain plagioclase and mainly orthopyroxene as crystal phases, a plagioclase-liquid hygrometer will be used for this study. The recent plagioclase hygrometer of Lange *et al.* (2009), which was recalibrated, expanded and updated by Waters & Lange (2015) yields a relatively small standard error estimate of 0.35 wt%. Besides, this regression is based on 107 anhydrous and 107 hydrous phase-equilibrium experiments of basaltic to silicic compositions that crystallized plagioclase over a range of pressures (0-350 MPa), temperatures (750-1244 °C), and H₂O concentrations (0-8.3 wt%). The hydrous and anhydrous melts have plagioclase concentrations ranging respectively between An₁₇₋₉₅ and An₅₁₋₉₀. This model is based on the crystal-liquid exchange reaction between the components of albite (NaAlSi₃O₈, Ab) and anorthite (CaAl₂Si₂O₈, An).



At equilibrium, equation 1 is used with ΔH° and ΔS° , and ΔVS_T° being equivalent to the difference between the enthalpy, entropy and volume of fusion of pure An and pure Ab.

Both the enthalpy and entropy of fusion are temperature dependent and can be calculated as follows:

$$\Delta H_f(T) = \Delta H_f(T_f) + \int_{T_f}^T [C_P^{liq}(T) - C_P^{xtl}(T)] dT \quad (12)$$

$$\Delta S_f(T) = \Delta S_f(T_f) + \int_{T_f}^T \left[\frac{C_P^{liq}(T) - C_P^{xtl}(T)}{T} \right] dT \quad (13)$$

Where C_P, f, liq and xtl refer to heat capacity, fusion, liquid, and crystal, respectively.

This plagioclase-liquid hygrometer uses a regression equation to calibrate the water content, expressed as:

$$wt\% H_2O = m'x + a'' + \frac{b''}{T} + \sum X_i d_i'' \quad (14)$$

where

$$m' = -\frac{1}{d_{H_2O}}, a' = \frac{a}{-d_{H_2O}}, b' = \frac{b}{-d_{H_2O}}, d_i' = \frac{d_i}{-d_{H_2O}} \quad (15)$$

with the terms a, b and d_i being parameters fitted from the calibration of the experiment, and with x , which includes all the standard-state thermodynamics parameters, defined as follows:

$$x = \frac{\Delta H^\circ(T)}{RT} - \frac{\Delta S^\circ(T)}{R} + \frac{\int_1^P \Delta V_T^\circ(P) dP}{RT} + \ln \left(\frac{X_{Ab}^{ideal liq}}{X_{An}^{ideal liq}} \right) + \ln \left(\frac{a_{An}^{ideal liq}}{a_{Ab}^{ideal liq}} \right) \quad (16)$$

where the terms a_{Ab} and a_{An} are the activities of the anorthite and albite components in the liquid (i.e. silicate melt), which are functions of the mole fractions X and the activity coefficients γ (i.e. $a_i = \gamma_{x,i} X_i$, see more details in Waters & Lange, 2015). The activity coefficients for anorthite ($CaAl_2Si_2O_8$) and albite ($NaAlSi_3O_8$) are calculated as follows:

$$X_{CaAl_2Si_2O_8}^{ideal liq} = 64.0 (X_{CaO}^{liq}) (X_{Al_2O_3}^{liq}) (X_{SiO_2}^{liq})^2 \quad (17)$$

$$X_{NaAlSi_3O_8}^{ideal\ liq} = 18.963(X_{Na_2O}^{liq})^{0.5}(X_{Al_2O_3}^{liq})^{0.5}(X_{SiO_2}^{liq})^3 \quad (18)$$

All the thermodynamic data (e.g. temperature of fusion, enthalpy, entropy, heat capacity, crystal activities) used for this model are reported in Appendixes C4, C5 and C6.

As plagioclase-melt equilibrium are strongly dependent on both the temperature and the water content, this study adopted the strategy to iteratively use the pyroxene-liquid thermobarometer and the plagioclase-liquid hygrometer until unique solutions were found for pressure, temperature and water content. Similar strategy was previously used by Preece *et al.* (2016), which determined the temperature using the amphibole geothermometer and the water content with the plagioclase-liquid hygrometer of Waters & Lange (2015).

As the uncertainties on the pressure and the water content derived from the thermobarometers and the hygrometer are quite large, *MELTS* modelling is used to constrain these intensive variables further.

3.4.3. MELTS modelling

MELTS is a computational thermodynamic tool that combines multicomponent models applicable for silicate liquid, mineral and fluid phases. The calibrations were initially developed by Ghiorso & Sack (1995) and Asimow & Ghiorso (1998) to model equilibrium crystallisation or fractional crystallisation in closed or open systems buffered by oxygen (i.e. oxygen fugacity fO_2). These can be modelled at fixed temperature, pressure, or water content, and also at constant entropy (i.e. defined as the measure of the total heat content of a system; Ghiorso & Gualda, 2015) or enthalpy (i.e. defined as the “heat content” of a system at fixed pressure; Ghiorso & Gualda, 2015). *MELTS* allows the exploration of magmatic processes such as assimilation, adiabatic decompression

melting, or post-entrapment crystallisation in phenocryst-hosted melt inclusions. Computation of equilibrium phase relations for igneous systems using *MELTS* is applicable for wide range of temperature (500-2000 °C) and pressure (0-2 GPa). The models associated with the liquid phase were calibrated with low-P equilibrium experiments. Mineral phases, however, are calibrated using independent thermodynamic data and models. *pMELTS* is a revised version of *MELTS* by Ghiorso *et al.* (2002), optimised for mantle-like bulk compositions applicable for temperatures between 1000 °C and 2500 °C and pressure from 1 to 3 GPa. *RhyoliteMELTS* was later developed by Gualda *et al.* (2012) to provide models for silicic- and water-rich systems by correcting the enthalpies of formation of quartz and the potassic endmember of feldspar (i.e. orthoclase). *alphaMELTS*, previously referred as *phMELTS* and *Adiabat_1ph* (Smith & Asimow, 2005), adds trace element partitioning and H₂O partitioning into nominally anhydrous phases.

The TgVC magmas studied here are intermediate in composition and, according to previous studies, seem to be associated with unusually low magmatic water contents (i.e. < 1.5 wt%; e.g. Arpa *et al.*, 2017; Deering *et al.*, 2011a; Kilgour *et al.*, 2009). The version *alphaMELTS* 1.9 (from now on referred to as *MELTS* modelling) will be used as it is appropriate for the TgVC magmas. The tephtras will be modelled using fractional crystallisation, tested over a range of pressures (0.1-800 MPa) and water contents (0-2 wt%), and in agreement with the range of temperatures retrieved from the hydrothermobarometry calculations. Based on agreement with previous studies on TgVC (Arpa *et al.*, 2017; Kilgour *et al.*, 2013; Kilgour *et al.*, 2014; Kilgour *et al.*, 2016; Shane *et al.*, 2008a), the oxygen fugacity will be buffered at NNO (nickel-nickel-oxide).

3.5. Sample selection, preparation, and analysis

3.5.1. Sample selection

This study aims to obtain a better understanding of the magmatic processes involved in the explosive eruptions of variable eruptive styles from TgVC. Thus, we aimed to sample a wide selection of eruptive styles from different vents of the TgVC. All tephtras were sampled on the eastern side of the ring plane where they are clearly exposed due to the westerly prevailing winds. Twenty-four historical andesitic tephtras from Tongariro, Ngauruhoe and Ruapehu volcanoes were selected:

- Three distal tephtras from the Plinian Mangamate Formation (11-12 ka BP, Nairn *et al.*, 1998) from the early and the late petrological groups defined by Nakagawa *et al.* (1998). They consist of Te Rato (PM2), Ohinepango (PM4) and Wharepu (PM5), sourced respectively from proto-Ngauruhoe, Saddle Cone and Tama Lake.
- Ten distal tephtras from the Mangatawai Formation (3.4 – 2.8 c. ka BP, Moebis, 2010), which consisted of Strombolian to phreatomagmatic eruptions and were mainly sourced from Ngauruhoe.
- Five distal tephtras from the Tufa Trig Formation namely 108-131 (Tf8), 108-137 (Tf13), 108-138 (Tf14), 108-139 (Tf15) and 108-140 (Tf16) (as referred in Moebis, 2010, and in Donoghue *et al.*, 1997 between brackets), which consisted of Strombolian and possibly phreatomagmatic eruptions, sourced from Ruapehu.
- Four proximal tephtras and lapilli from the 1972-1975 eruptive sequence of Ngauruhoe. The eruptions of the 24th of March 1972 (Strombolian to Vulcanian), the 26th of October 1973 (Strombolian to Vulcanian), the 24th of January 1974 (Vulcanian) and the 19th of February 1975 (sub-Plinian) were selected for this study.

- Two tephras from the 1995-1996 eruptions of Ruapehu corresponding to the 12th of October 1995 sub-Plinian eruption and the 20th of July 1999 Strombolian eruption.

Sample locations and descriptions are reported in Figure 3.6 and Table 3.2, respectively. Te Rato was sampled along the State Highway 46 close to Lake Rotoaira, whereas Ohinepango and Wharepu were sampled along the desert road. Mangatawai and Tufa Trig were sampled along the desert road and prepared by Anja Moebis during her PhD thesis (Moebis, 2010). The 1972-1975 Ngauruhoe and the 1995-1996 Ruapehu samples were sampled by GNS Science at the time of the eruptions.

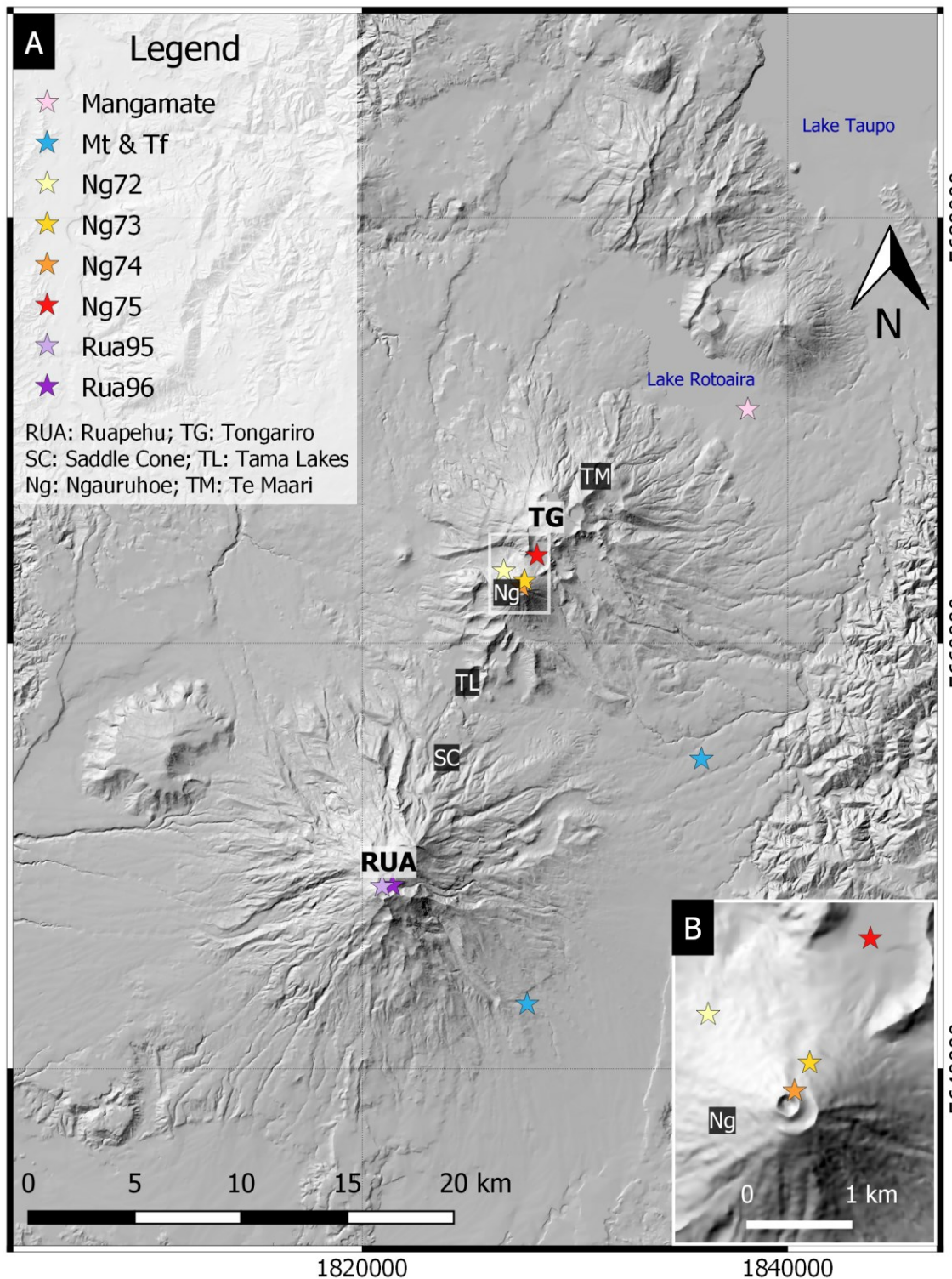


Figure 3.6. Sample location map of the tephras selected for this study. This is a shaded relief map derived from the 8-m-Digital-Elevation-Model (source: LINZ data). The colour gradient corresponds to the elevation variation. Georeference system: NZGD2000/New Zealand Transverse Mercator 2000.

Table 3.2. Descriptive table of the samples selected for this study. Mangamate (Mm) units were sampled and prepared during this study, and described by Donoghue *et al.* (1995). Mangatawai and Tufa Trig units were sampled, prepared and described by Moebis (2010). Ngauruhoe and Tufa Trig 19 units were sampled by GNS science, prepared and described during this study. Rua, Ng, TL, and SC stand for Ruapehu, Ngauruhoe, Tama Lakes and Saddle Cone, respectively. S, sP, V, pm, and P stand for Strombolian, sub-Plinian, Vulcanian, phreatomagmatic and Plinian, respectively.

Tephra formation	Tephra unit	Source	Description	Eruptive style
Tufa Trig 19	Rua96	Rua	20/07/1996; Dark grey fine ash	S
	Rua95	Rua	12/10/1995; Dark grey fine ash	sP
Ngauruhoe	Ng75	Ng	19/02/1975; Dark grey coarse ash and lapilli	sP
	Ng74	Ng	24/01/1974; Dark fine ash from the inner cone	V
	Ng73	Ng	26/10/1973; Dark greyish brown fine and coarse ash	S-V
	Ng72	Ng	24/03/1972; Dark greyish brown fine and coarse ash	S-V
Tufa Trig	108-140 (Tf16)	Rua	Tf16, light grey, fine ash, pocket	S-pm
	108-139 (Tf15)	Rua	Tf15, light grey, base coarser and darker	S-pm
	108-138 (Tf14)	Rua	Tf14, bluish black, wavy base, fine ash	S-pm
	108-137 (Tf13)	Rua	Tf13, black, pockets, discontinuous	S-pm
	108-131 (Tf8)	Rua	Tf9, black, medium ash, discontinuous	S-pm
Mangatawai	407-59	Ng	Black, vesicles, discontinuous	V-sP
	407-56	Ng	Black, fine ash	V-sP
	407-54	Ng	Grey - black, coarser fine sand	V-sP
	407-49	Ng	Steel grey, silt - fine ash	V-sP
	407-47	Ng	Black, fine sand, 1 mm round vesicles	V-sP
	407-18	Ng	Dark grey -black, fine - middle ash, lot leaves	V-sP
	407-17	Ng	Black, coarse sand, no real boundaries to top and bottom pocket	V-sP
	407-16	Ng	Dark grey -black, fine - medium ash, lot leaves	V-sP
	407-15	Ng	Brownish dark grey, lot leaves, fine ash	V-sP
	407-14	Ng	Black, leaves at the bottom, 26cm elongate pocket, normal graded	V-sP
Mangamate	Mm-Wh	TL	Bedded grey fine and very fine lapilli; upper bed: dark greyish brown and olive brown lithic and few yellowish brown pumice lapilli	P
	Mm-Oh	SC	Alternance of black and orange lithic-rich coarse ash layer	P
	Mm-TR	Ng	Dark grey coarse ash and lapilli	P

N/A: not available

3.5.2. Sample preparation

Although the Mangatawai and Tufa Trig samples were already prepared and mounted into epoxy plugs, all samples followed the same sample preparation. The deposits were thoroughly washed with distilled water while being sieved through 1 mm, 500 μm and 250 μm sieves. They were then dried for two days in an oven at 40 °C. Glass shards of sizes between 250 and 500 μm were then handpicked using a pair of tweezers and a Leica MZ8 stereoscopic microscope at Massey University. Depending on the shards size, 15 to 20 picked grains per tephra were mounted onto epoxy plugs and polished down to a sub-micron finish using diamond paste, until the grains intersected the flat surface.

3.5.3. Analytical techniques used for this study

To complete textural and chemical analyses of the selected volcanic tephra shards of TgVC, high-resolution imaging instruments were used. BSE images of the glass shards were acquired using Scanning Electron Microscope (SEM) in order to generate CSD and to identify regions of interests for further analyses. The JEOL JSM-7000F Field-Emission (FE) SEM of the Isotope Imaging Laboratory (IIL) at Hokkaido University, Sapporo, Japan, was used to acquire high-resolution BSE images ($4,096 \times 3,072$). A beam current of 10 nA and an accelerating voltage of 15 kV were used for these analyses. Chemical maps of pyroxene crystals to identify textures and zonations were also performed using the FE-SEM for the following elements: Al, Ca, Cr, Fe, Mg, Na, K, Si and Ti. To test the segmentation method (cf. 3.3), the FE-SEM of IIL was used as well as two other SEMs of lower resolution. The FEI Quanta 200 environmental SEM at Massey University, Palmerston North, New Zealand, with a beam current of 5 nA and an accelerating voltage of 20 kV was used to obtain medium-resolution BSE images ($2,048 \times 1,886$). BSE images with the smallest resolution ($1,280 \times 960$) were retrieved with the JEOL NEOSCOPE

6000plus desktop SEM at GNS Science Wairakei Research Centre, Taupo, New Zealand, using a beam current of 20 nA and an accelerating voltage of 10 kV.

The ultra-high resolution Cameca IMS-1270 SIMS instrument equipped with a Stacked CMOS-type Active Pixel Sensor (SCAPS) of the IIL was used to obtain semi-quantitative concentration maps for plagioclase crystals. This facility allows the visualisation at high magnification of the elemental distribution on the sample surface (i.e. isotopography; Yurimoto *et al.*, 2003). An O⁻ primary beam with an accelerating voltage of 23 keV was irradiated on the sample surface of 80-100 μm in diameter using a 7 nA beam current. Before the analysis, a 20 nA beam current was used on the sample surface of the area for ten minutes. Collection of positive secondary ion images of ^{23}Na , ^{24}Mg , ^{27}Al , ^{28}Si , ^{39}K , ^{40}Ca , ^{56}Fe and ^{88}Sr on the plagioclase surface were retrieved by the SCAPS detector, with exposure times of 50, 500, 50, 25, 50, 250 and 500 seconds, respectively, yielding a sub-micron spatial resolution for each image. Normalisation of the concentration ratio images to a major element such as Si were necessary to discriminate elemental zoning and textures of plagioclase crystals.

Mineral and glass compositions of Mangatawai and Tufa Trig samples were analysed using a JEOL JXA-8900R electron microprobe equipped with four wavelength-dispersive spectrometers at the Institute of Earth Sciences, Academia Sinica, Taipei, Taiwan. A 2- μm -defocused beam with a current of 12 nA and an acceleration voltage of 15 kV were set for these analyses. Mineral and glass analyses of 1972-1975 Ngauruhoe and 1995-1996 Ruapehu tephras were performed using a JEOL JXA-8800R electron microprobe equipped with four wavelength-dispersive spectrometers at the Graduate School of Science, Hokkaido University, Sapporo, Japan. An acceleration voltage of 15 kV was used for the analyses. A 10- μm -defocused beam with a current of 7 nA were used for

glass, whereas the mineral analyses were performed using a spot beam with a current of 10 nA for plagioclases, 20 nA for pyroxenes.

Chapter 4. Semi-automatic segmentation of crystals in BSE images for Crystal Size Distributions purposes

This chapter is based on a published article (Appendix A1):

Lormand C., Georg F. Zellmer G.F., Németh K., Kilgour G., Mead S., Palmer A.S., Sakamoto N., Yurimoto H., Moebis A. (2018) Weka Trainable Segmentation plugin in ImageJ: a semi-automatic tool applied to Crystal Size Distributions of microlites in volcanic rocks. *Microscopy and Microanalysis*, **24**: 667–675.

DOI: <https://doi.org/10.1017/S1431927618015428>

Participating authors:

- ✚ **Charline Lormand** (Massey University, New Zealand): field work, lab work, data analysis and processing, manuscript writing and editing
- ✚ **Georg F. Zellmer** (Massey University, New Zealand): manuscript editing and discussion, help to design the method
- ✚ **Károly Németh** (Massey University, New Zealand): assisting in the field, manuscript editing and discussion
- ✚ **Geoff Kilgour** (GNS Scienc Wairakei, New Zealand): manuscript editing and discussion
- ✚ **Stuart Mead** (Massey University, New Zealand): help to assess the accuracy performance tests, manuscript editing and discussion
- ✚ **Alan S. Palmer** (Massey University, New Zealand): assisting in the field, manuscript editing and discussion
- ✚ **Naoya Sakamoto** (assisting with image acquisition)
- ✚ **Hisayoshi Yurimoto** (assisting with image acquisition)
- ✚ **Anja Moebis** (Massey University, New Zealand): providing samples and assisting with sample preparation)

Chapter content:

4.1. Introduction	80
4.2. Materials and Methods	81
4.2.1. Image acquisition and cleaning (Steps 1-2)	82
4.2.2. Image segmentation (Steps 3-5).....	85
4.2.3. Generation (Steps 6-8)	86
4.2.4. Manual Segmentation versus Trainable Weka Segmentation: a comparison	90
4.3. Results	92
4.4. Discussion and implications	99

Abstract

Crystals within volcanic rocks record geochemical and textural signatures during magmatic evolution before eruption. Clues to this magmatic history can be examined using crystal size distribution (CSD) studies. The analysis of CSDs is a standard petrological tool, but laborious due to manual hand-drawing of crystal margins. The trainable Weka segmentation (TWS) plugin in ImageJ is a promising alternative. It uses machine learning and image segmentation to classify an image. We recorded back-scattered electron (BSE) images of three volcanic samples with different crystallinity (35, 50 and ≥ 85 vol. %), using scanning electron microscopes (SEM) of variable image resolutions, which we then tested using TWS. Crystal measurements obtained from the automatically segmented images are compared with those of the manual segmentation. Samples up to 50 vol. % crystallinity are successfully segmented using TWS. Segmentation at significantly higher crystallinities fails, as crystal boundaries cannot be distinguished. Accuracy performance tests for the TWS classifiers yield high F-scores (>0.930), hence, TWS is a successful and fast computing tool for outlining crystals from BSE images of glassy rocks. Finally, reliable CSD's can be derived using a low-cost desktop SEM, paving the way for a wide range of research to take advantage of this new petrological method.

Key words: crystal size distributions, microlites, electron microprobe, image segmentation, automation

4.1. Introduction

One of the most promising aspects of modern research is the ability to automate processes or analyses. Time-consuming, costly, difficult, or repetitive manual tasks all lend themselves to automation. In the geosciences, some processes or tools are already automated such as geochemical studies of tephrochronology (Petrelli *et al.*, 2017), the detection of lithological boundaries for geological interpretations (Vasuki *et al.*, 2017), the study of volcanic eruption precursors using seismic and remote sensing data (Chardot *et al.*, 2015; Hibert *et al.*, 2017; Meyer *et al.*, 2015) and automation of seismic waveform detections using machine learning algorithms (Riggelsen & Ohrnberger, 2014). Crystal Size Distributions (CSDs) in volcanic rocks are a useful tool to infer space- and time-integrated information about volcanic plumbing systems such as storage and mixing (e.g. Armienti *et al.*, 1994; Armienti *et al.*, 2007; Gutierrez & Parada, 2010; Higgins & Roberge, 2007; Magee *et al.*, 2010; Simakin & Bindeman, 2008) and detailed eruptive histories of magmas (Bindeman, 2003; Cato *et al.*, 2016; Hammer *et al.*, 1999; Mangan, 1990). Kinetics extracted from CSDs also provides identification of crystal nucleation and growth mechanisms (e.g. Berger *et al.*, 2011; Brugger & Hammer, 2010; Kile & Eberl, 2003; Rannou & Caroff, 2010; Szramek *et al.*, 2010), determine magma cooling rates, and thus elucidate the timescales of these events (e.g. Cashman & McConnell, 2005; Higgins, 1996a; Jerram *et al.*, 2009; Muir *et al.*, 2012). However, despite the low acquisition cost and the simplicity of the data collection process, generating CSD's rely on time-consuming image processing. Previous studies provided encouraging results from an automated method to quantify mineral phases from element mappings of volcanic samples (Cheng *et al.*, 2017; Drignon *et al.*, 2016; Muir *et al.*, 2012), but the data acquisition requires costly and significant time on the instrument (i.e., element mapping) or methods involving the use of proprietary software (i.e., Matlab).

The Trainable Weka Segmentation (TWS) plugin, available in the open source image processing package Fiji and installable on the free-access software ImageJ, consists of a combination of image segmentation and machine learning (Arganda-Carreras *et al.*, 2017). Image segmentation involves partitioning of an image into multiple segments or classes of similar attributes (e.g. pixel color, shape of object) and it has been commonly used in several fields such as remote sensing as an aid to landscape change detection and land use/cover classification (e.g. Benz *et al.*, 2004; Blaschke *et al.*, 2008; Blaschke, 2010; Pedersen, 2016), and medical-imaging to automate the delineation of anatomical structures or to track the evolution of cells (e.g. Chen *et al.*, 2006; Hance *et al.*, 1996; Pham *et al.*, 2000). TWS is based on machine learning algorithms for data mining tasks available in Weka that stands for Waikato Environment for Knowledge Analysis (Witten *et al.*, 1999). It was developed at Waikato University in New Zealand and is at present one of the most well-known workbenches for data mining using machine learning.

Here, we will show how the TWS plugin can be used to generate microlite (i.e., crystals $< 50 \mu\text{m}$; Crabtree & Lange, 2011) CSDs by providing a more accessible and fast computing automated method for segmenting crystals from back-scattered electron (BSE) images using an open access software (i.e., ImageJ).

4.2. Materials and Methods

The automated segmentation and CSD generation process are outlined in Figure 4.1. It comprises three broad steps: image acquisition and cleaning (Figure 4.1, steps 1 and 2), image segmentation (including training and post-segmentation image processing; Figure 4.1, steps 3-5) and generation of CSDs (Figure 4.1, steps 6-8).

4.2.1. Image acquisition and cleaning (Steps 1-2)

This study focuses on three volcanic samples from New Zealand of different crystallinities (Table 4.1): (1) a Ngauruhoe-sourced glass-rich ash shard (*c.* 35 vol. % of crystals) from a Mangatawai tephra dated 3.52 cal. ka (Moebis et al., 2011); (2) an intermediately crystal-rich glass shard (*c.* 50 vol. % of crystals) from the Te Rato member, part of the *c.* 10 ka Mangamate eruptive sequence erupted from a proto-Ngauruhoe source (Auer et al., 2015); and (3) an aphyric basaltic microlite-rich welded spatter sample (85 – 99 vol. % of microlites; Sable et al., 2009) from a Strombolian explosion of the 1886 eruption of Mt. Tarawera. All samples have plagioclase and pyroxene as the most abundant microlite phases (Table 4.1). The few olivine crystals were removed manually from the segmented image.

Back-scattered electron images of the samples are obtained using three different scanning electron microscopes (SEM) that offer three degrees of image resolution (Figure 4.1 step 1). High-resolution BSE images (i.e., image resolution: 4,096 x 3,072) were acquired using a Field Emission SEM (FE-SEM; JEOL JSM-7000F) at the Isotope Imaging Laboratory of Hokkaido University, in Sapporo, Japan, with an accelerating voltage of 15 kV and a 10 nA beam current. Medium-resolution BSE images (i.e., image resolution: 2,048 x 1,886) of the Tarawera sample were taken using the Environmental-SEM (FEI Quanta 200) at Massey University in Palmerston North, New Zealand, using an accelerating voltage of 20 kV and a beam current of 5 nA. Finally, the JEOL NEOSCOPE 6000plus Desktop SEM (i.e., image resolution: 1,280 x 960) at GNS Science Wairakei Research Centre in Taupo, New Zealand, was employed using an accelerating voltage of 10 kV and a high probe current of 20 nA.

A brief step of manual cleaning in ImageJ or image processing software may be needed (Figure 4.1, step 2) if the user estimates that an adjustment of the brightness and

contrast would provide more distinction between the phases to segment. A noise reduction filter such as “Despeckle” or “Salt and pepper” operations can also be applied. For glass shards, as we use in this study, the Lasso tool in Adobe Photoshop was used to select and then fill in black the heterogeneities (e.g. sample dust) in the background.

Table 4.1. Descriptive table of the samples used in this study and their segmentation characteristics: crystallinity, mineral assemblages, and the duration of segmentation, the number of crystals segmented and the best-fit crystal habit with level of fit for both manual and automatic (i.e., TWS) segmentations.

Sample	Mangatawai ash shard 407-18-05	Mangamate - Te Rato ash shard	Tarawera lava flow
Crystallinity (vol. %)	351	501	85 - 99 ²
Mineral assemblages (microelite)	plag + opx ± cpx	plg + opx ± cpx ± ol	plg + opx + ol
Area of the image or particle (µm ²)	92,535	223,227	368,206
Manual segmentation duration (s)	1,800	2,700	Unable to process
TWS segmentation duration (s)	410	260	145
	Plagioclase	Plagioclase	Plagioclase
	Pyroxene	Pyroxene	Pyroxene
Number of crystals manually segmented	423	855	N/A
Number of crystals segmented with TWS	423	1245	1771
Best-fit crystal habit for manual segmentation	x=1 y=1.4 z=9; R ² =0.73	x=1 y=1.25 z=5.5; R ² =0.85	x=1 y=1.4 z=8; R ² =0.87
Best-fit crystal habit for TWS segmentation	x=1 y=1.8 z=9; R ² =0.86	x=1 y=1.4 z=2.5; R ² =0.82	x=1 y=1.25 z=7; R ² =0.81
			x=1 y=1.6 z=3.6; R ² =0.82

¹ this study; ² Sable *et al.*, 2009; N/A: not applicable.

4.2.2. Image segmentation (Steps 3-5)

The image segmentation is achieved using the TWS plugin that uses machine learning algorithms to classify a Red-Green-Blue or greyscale image into different classes (Arganda-Carreras *et al.*, 2017). The classes (e.g. here different minerals or phases such as background, remaining gold coating in the vesicles, groundmass, crystals) comprise sets of pixels that share similar visual characteristics (e.g. colour). Before the image is segmented, the user needs to train the classifier by drawing traces - defined here as sets of training pixels (STP) - over regions of interest (ROI) for each class (Figure 4.1, step 3). One STP of two classes is the minimum required to start the segmentation. We recommend use of the “Freehand line” to trace lines over ROI while covering the entire range of greyscale for a specific class (e.g. as crystals can display zonation, a STP would need to cover pixels from the core to the rim of the crystal). We recommend at least ten STPs to obtain an acceptable classification.

Once the user has provided the STP for each class, the most suitable training features (e.g. filters applied on the image to assist the segmentation) and the algorithm offered by the plugin have to be selected (Figure 4.1, step 4). The Lipschitz (i.e., noise reduction filter, elimination of a slowly varying image background), Gabor (i.e., texture filter, edge detection), Bilateral and/or Neighbors (i.e., noise reduction filters, averaging the pixel values around the current pixel that are close in greyscale value) training features were found to provide the best balance of efficiency and classification accuracy for images studied here. Several other training features are available in TWS that may be suitable depending on individual image characteristics such as contrast and acquisition settings.

Image segmentation is achieved using the FastRandomForest algorithm, a parallel implementation of the random forest classification technique (Breiman, 2001). Random forest is a machine learning technique that uses an ensemble of decision trees to classify

data (pixels of an image in this case) from the user-defined input features (training features) and labelled sample data (the STP's). Decision trees are constructed from randomly selected STP's, with decision splits using randomly selected input features at each node in the tree. Final classification is then determined as the average classification of all tree. The random forest algorithm was chosen for its accuracy, speed and multi-class segmentation capabilities demonstrated for image segmentation tasks in other fields (e.g. Belgiu & Drăguț, 2016; Mahapatra, 2014). Readers may refer to Arganda-Carreras *et al.* (2017) and Witten *et al.* (1999) for more details about the Weka segmentation process, the training features and other algorithms that may be suitable.

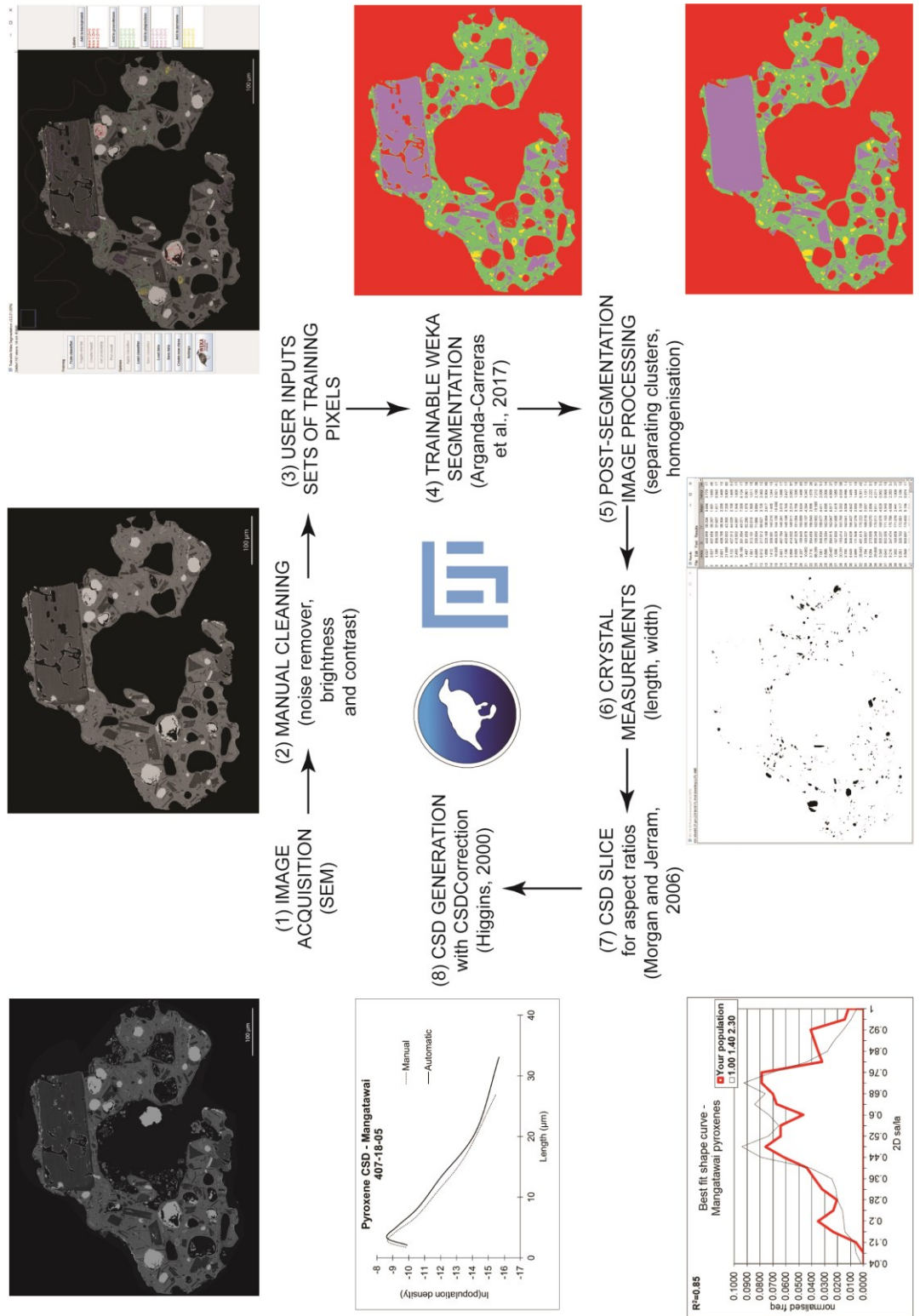
When the segmentation is successful, the result is overlain above the original image with the corresponding class colours. The result can be extracted to an image (Figure 4.1, step 4) and the “classic” CSD generation method can then be completed (Figure 4.1 steps 6-8 and Figure 4.2; e.g. Higgins, 2000; Marsh, 1988; Morgan & Jerram, 2006). A classifier used for one image can be applied to more images as long as they all have the same crystal phases and similar brightness and contrast. Once the image is fully segmented, it is recommended to briefly process it manually using image processing software (e.g. Adobe Photoshop) as (1) TWS cannot easily separate touching crystals, and/or (2) to homogenise crystals affected by fractures and cracks (Figure 4.1, step 5).

4.2.3. Generation (Steps 6-8)

A CSD is a powerful measure used to visualise pre-eruptive processes such as crystal growth and nucleation rates, petrological processes (e.g. crystal accumulation, crystal fractionation), degassing and cooling mechanisms, and may elucidate the timescales of these events (Brugger & Hammer, 2010; Higgins, 1996a; Higgins, 2002; Lentz & McSween, 2000; Marsh, 1988; Marsh, 1998b; Morgan *et al.*, 2007). Higgins (2000) developed CSDCorrections to convert 2D slices into 3D crystal shapes. To do so, the 2D

morphological parameters of the crystals (i.e., long- and short-axes of best fitting ellipse for each microlite) are required and are obtained automatically from the binary image using *ImageJ*. *CSDCorrections* also requires the best-fit crystal habits (i.e., aspect ratios of the crystal population; Figure 4.1, step 6), which can be retrieved using the Excel database *CSDslice* developed by Morgan & Jerram (2006) (Figure 4.1, step 7) which compares the input crystal population with 703 discrete crystal habits. Each crystal habit was randomly sectioned 10,000 times to produce highly representative 2D shape curves. However, for acicular shapes, that display a wide variety of aspect ratios, *CSDslice* tends to result in less reliable crystal shape habits due to the statistics of sectioning a crystal through its center, resulting in a lower level of fit (R^2). Indeed, if the 3D shape of the crystal is tabular then a minimum sample size of 75 crystals can be shown to obtain an accurate estimate of 3D shape. However, where the shape tends to acicular, at least 200-300 measurements are required to estimate the 3D shape accurately (Morgan & Jerram, 2006). This value (200-300) is similar to that obtained by Mock & Jerram (2005), as the minimum number of crystals that need to be measured to accurately produce a true 3D CSD from 2D measurements based on a known 3D distribution. Finally, the length measurements, the area of the sample, and the best-fit crystal habits can be implemented into *CSDCorrections* to generate the CSD curve (Figure 4.1, step 8).

Figure 4.1. (Figure in the next page) Automation protocol to derive robust crystal size distributions using the Trainable Weka Segmentation (TWS) plugin of ImageJ. (1) BSE images of the samples are obtained using a scanning electron microscope. (2) Adobe Photoshop is used for image processing to make the background of the image homogeneous (i.e., black) and to remove noise (i.e., dust, scratch) using a despeckle filter. (3) The interface of the TWS plugin, where the cleaned image is loaded for input of sets of training pixels (STP's) of each class by the user. (4) Result of the TWS using the input STP's. Red, green, purple, and yellow are, respectively, background, groundmass (i.e., volcanic glass), plagioclase, and pyroxene microlites. (5) The segmented image is the post-segmentation image processed manually using Adobe Photoshop to separate clusters and to homogenise crystals. (6) Measurements of crystals (e.g., length and width) are obtained using the Analyze Particles tool in ImageJ. (7) Lengths and widths are implemented into CSDSlice (Morgan and Jerram, 2006) to obtain the five best matching crystal shapes (i.e., aspect ratios) for the studied crystal population. The one with the best level of fit is chosen and integrated into CSDCorrections (Higgins, 2000). (8) The CSD plot is obtained with CSDCorrections by using length, the best-fit shape factors and the area of the sample. I) Interpretations from CSD slope and intercept are made.



4.2.4. Manual Segmentation versus Trainable Weka Segmentation: a comparison

The images are processed both manually (i.e., manual segmentation of crystals using an image processing software, e.g. Adobe Photoshop) and automatically using the TWS plugin in Fiji, to estimate the accuracy of the automatic segmentation. We quantitatively compared the two methods in terms of segmentation duration, crystal population (i.e., number of crystals segmented, best-fit crystal habits), and shapes of the resulting CSD curves. We also compared the TWS segmented image to that of the manual segmentation. We evaluate the TWS classifier performance using a R-based code (Appendix A2) using the “ROCR” package (Sing *et al.*, 2005). The binary images resulting from the segmentation are analysed and a number of performance measures relevant to this study are used to evaluate the performance i.e., the positive predictive value, the true positive rate, the false positive rate, and the precision-recall F measure (Fawcett, 2006). The positive predictive value (ppv) also called precision (Prec) indicates the proportion of crystal pixels identified by the classifier that are correct, estimated as:

$$PPV = Prec = TP/(TP + FP) \quad (1)$$

For which the true positives (TP) are the correctly classified pixels (i.e., plagioclase or pyroxene correctly identified; Figure 4.2) and false positives (FP) are the pixels incorrectly classified (i.e., a pixel classified as plagioclase or pyroxene where it does not exist).

The true positive rate also called recall (Rec) is the proportion of crystal pixels in the manually segmented image that are correctly classified by TWS and can be calculated as:

$$TPR = Rec = TP/(TP + FN) \quad (2)$$

For which the false negatives (FN) are the incorrectly classified pixels of any non-crystal phase (e.g. glass, groundmass, background or vesicle).

These two performance measures (Equations 1 and 2) indicate the level of over-prediction (precision) and under-prediction (recall) in the classifier. To evaluate overall classifier performance, the precision-recall F measure, also called F-score, is used. The F-score is defined as the weighted harmonic mean of precision and recall by van Rijsbergen (1979) as:

$$F = 1/(\alpha 1/Prec + (1 - \alpha)1/Rec) \quad (3)$$

where α indicates the desired balance between precision and recall. When $\alpha = 0.5$, the balance between over- and under- prediction is equal, offering the best compromise to identify crystal sizes for CSDs.

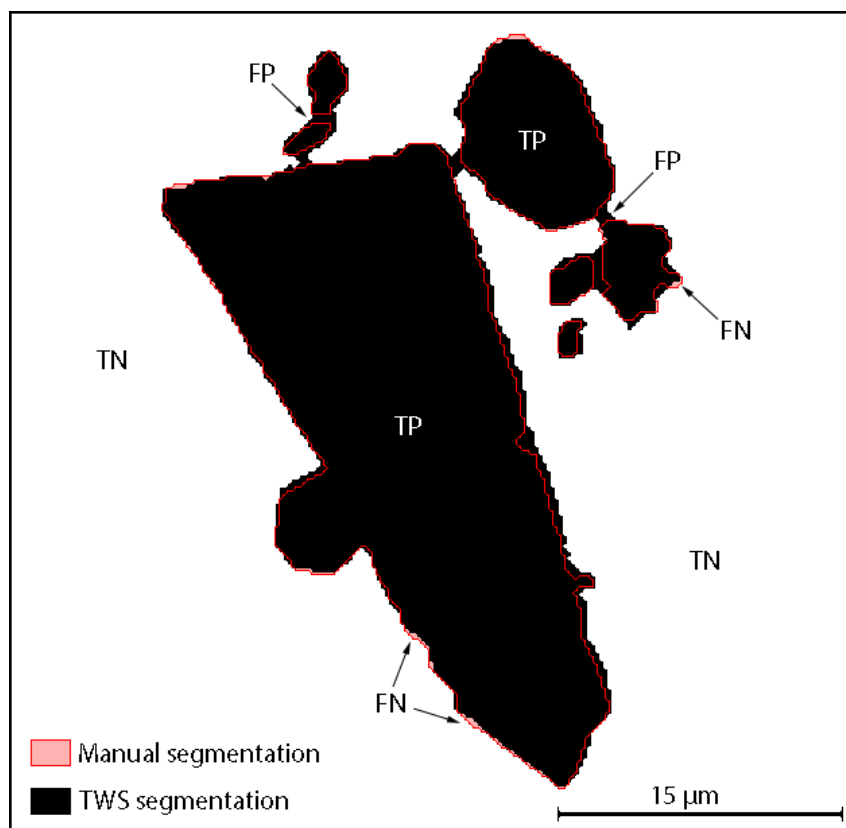


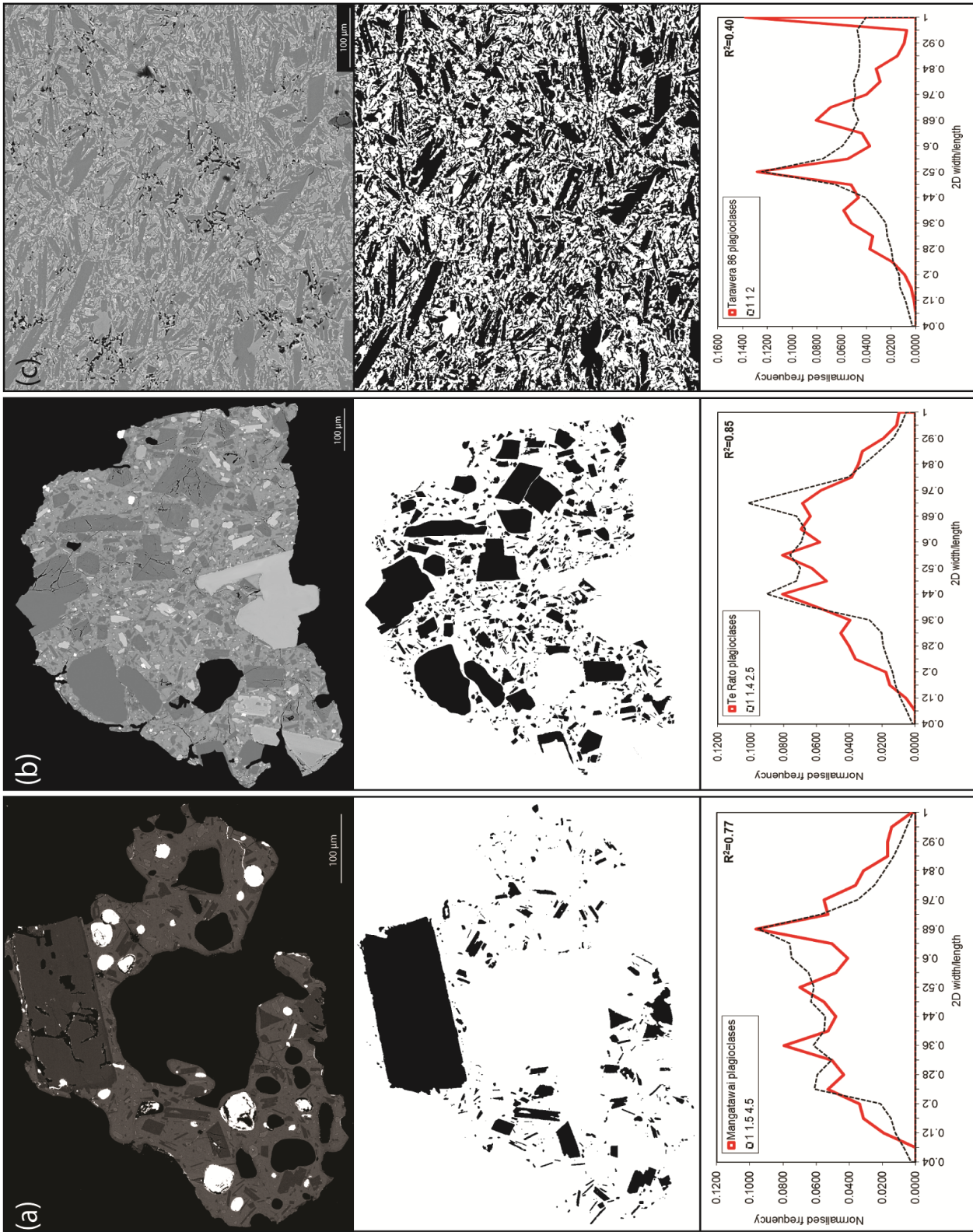
Figure 4.2. Example of pyroxene microlites of Mangamate – Te Rato classified using both manual and TWS segmentations, and the associated terms related to the performance evaluation of the automatic classifier. TN, TP, FN, and FP, respectively, stand for true negative, true positive, false negative, and false positive.

4.3. Results

The automatic segmentations for the glass shards of Mangatawai and Mangamate are successful and result in similar levels of fit for crystal habits as that of the manual segmentations for both plagioclase and pyroxene ($0.81 < R^2 < 0.86$ with TWS versus $0.73 < R^2 < 0.87$ with manual segmentation; Table 4.2). The manual segmentation is unsuccessful for the welded spatter sample of Tarawera, as crystal boundaries are difficult to distinguish due to the high crystallinity (Figure 4.3). The TWS for this sample gives a poor level of fit for crystal habits for the plagioclase population ($R^2=0.40$) but an

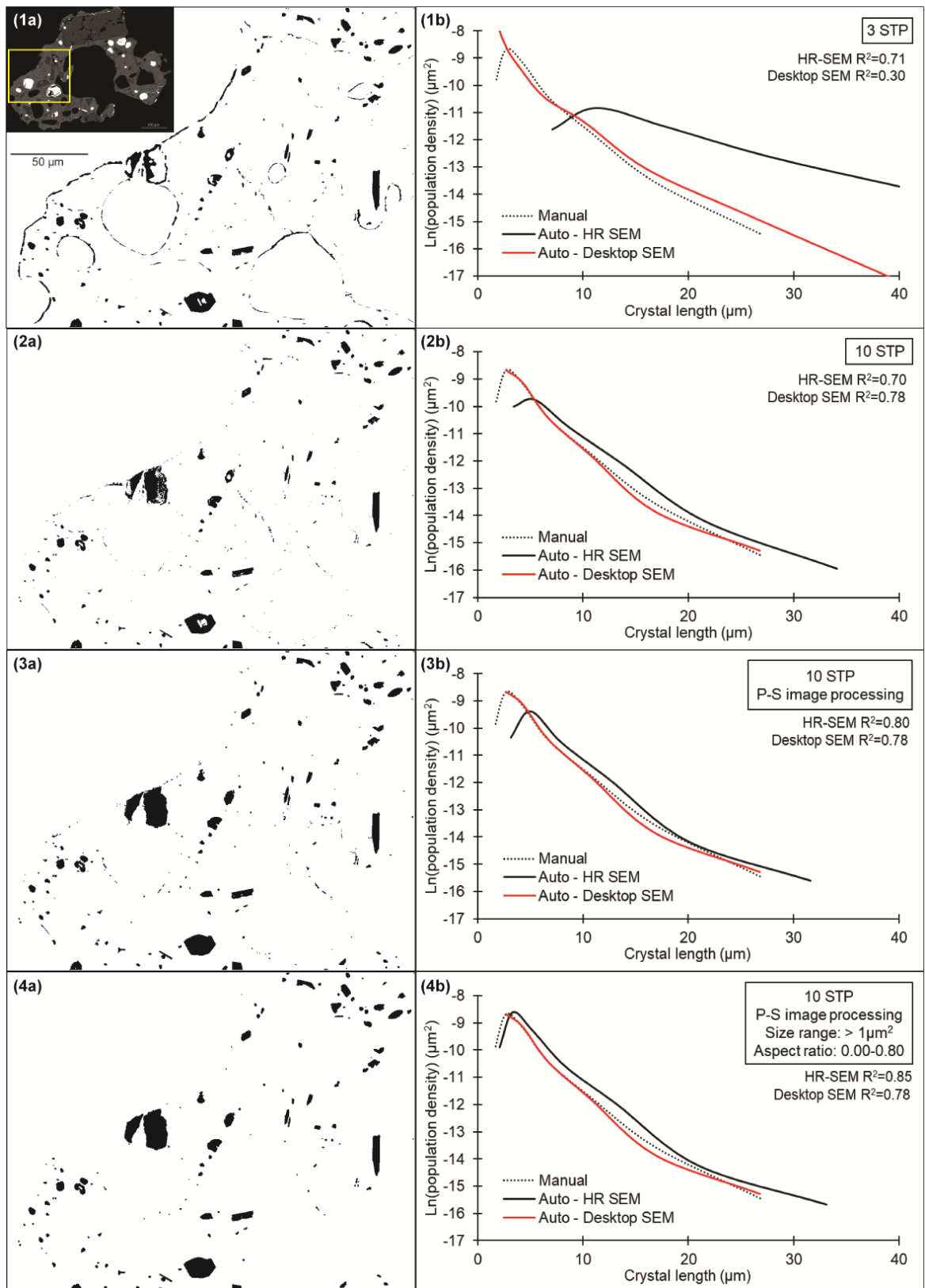
acceptable level of fit for crystal habit for the pyroxene population ($R^2=0.82$). The counted number of crystals is variable between manual and automatic segmentation for all samples. To emphasise the time saved using the automated method, we calculate that the TWS provides a segmentation four times faster for Mangatawai and up to ten times faster for Mangamate than outlining the crystals manually using image processing software.

Figure 4.3. (Figure in the next page) Examples of BSE images, binary images, and the best-fit shape curves of the plagioclase populations obtained from *CSDSlice* (Morgan & Jerram, 2006). a: BSE image of the Mangatawai glass shard captured using a JEOL NEOSCOPE 6000plus desktop-SEM, and its associated binary image and best-fit crystal habits. The bright white areas are due to residual gold coating in the vesicles. b: BSE image of the Mangamate – Te Rato glass shard, captured using a high resolution JEOL JSM-7000F FE-SEM, and its associated binary image and best-fit crystal habits. c: BSE image of a lava flow from the 1886 Tarawera eruption, captured using the FEI Quanta 200 Environmental SEM, and its associated binary image and best-fit crystal habits curve.



Variation in the number of STP input by the user before segmentation results in differences in the CSDs generated (Figure 4.4): the classifier based on three STP provides a relatively-poor fit CSD curve and a lower level of fit for crystal habit ($R^2 < 0.75$, Figure 4.4-1b) compared to that resulting from a classifier based on ten STP ($R^2 \geq 0.78$, Figure 4.4-2b). Post-segmentation image processing results in a CSD curve closer to that resulting from manual segmentation with a better level of fit for crystal habit (HR-SEM $R^2 = 0.80$; Figure 4.4-3b). Setting ranges of crystal size (i.e., to exclude isolated pixels that have been misclassified) and aspect ratio (i.e., to exclude segmented fractures or edges of vesicles that tend to display a wide range of greyscale values), implemented in the tool “Analyze Particles” in ImageJ, also provides a better level of fit for crystal habit (HR SEM $R^2 = 0.85$; Figure 4.4-4b). The CSD curve resulting from automatic segmentation of the image acquired with the desktop SEM fits almost perfectly to the manual CSD curve. However, it does not replicate the downturn at smaller size unlike the CSD curve resulting from automatic segmentation of the image acquired with the high-resolution SEM. The slopes of both the HR-SEM and desktop-SEM CSDs coincide with that of the manual CSD curve (Figure 4.4-4b). The HR-SEM CSD is constantly offset to higher population densities for all crystal size bins until it forms a downturn at smallest size (Figure 4.4-1b, -2b, -3b and -4b); because of the higher image resolution, the segmentation from the HR-SEM image picks up a larger number of particles than that of the lower resolution desktop-SEM.

Figure 4.4. (Figure in the next page) Binary images of the pyroxene population for a selected part of the Mangatawai glass shard (see (1a) in the upper left corner) with the associated CSD curves resulting from both manual and TWS segmentations. The manual CSD curve results from the manual segmentation of the image acquired with a high-resolution SEM (HR-SEM; JEOL JSM-7000F FE-SEM). The automatic CSD curves result from the segmentation using TWS of (1) the image acquired with the HR-SEM (i.e., Auto - HR SEM) and (2) the image acquired using the desktop SEM (i.e., Auto – Desktop SEM; JEOL NEOSCOPE 6000plus). The R^2 values are the level of fit for crystal habits of the pyroxene population extracted from *CSDslice* (Morgan and Jerram, 2006). STP stands for set (A) CSD curves resulting from manual segmentation and automatic segmentation with three STP by the user. (B) CSD curves resulting from manual segmentation and automatic segmentation with ten input STP by the user. The edges of the shard are less visible as in the segmented image (1a) as a new STP was added to classify them as the background. (C) CSD curves resulting from manual segmentation and automatic segmentation with ten STP and after post-segmentation image processing (P-S image processing; see step 5 from Figure 4.1). (D) CSD curves resulting from manual segmentation and automatic segmentation with ten STP and after post-segmentation image processing and setting a particle size range of $> 1\mu\text{m}^2$.



The performance of the TWS classifier is tested for both Mangatawai and Mangamate – Te Rato glass shards, including the pyroxene and the plagioclase microlite populations, with and without post-segmentation image processing (Table 4.2). For all performance measures, a value of 1.0 indicates perfect classification. The PPV, which indicates the rate of over-prediction in crystal pixel, varies between 0.761 and 0.989. The TPR, which indicates the rate of under-prediction in crystal pixels, varies between 0.833 and 0.985. The accuracy of the TWS classifier (i.e., F-score) varies between 0.795 and 0.987 with an average of 0.930 ± 0.070 (2σ) without post-segmentation image processing and an average of 0.951 ± 0.057 (2σ) with post-segmentation image processing. All the measures give a better performance for segmented images with post-segmentation image processing.

Table 4.2. Results of the classifier performance for the Trainable Weka Segmentation (TWS) tested on two volcanic glass shards. The predictive positive value (PPV), the true positive rate (TPR) and the precision-recall F measure (F-score) are calculated using the ROCR package in RStudio for resulting binary images of plagioclase and pyroxene microlite populations.

TWS performance	PPV	TPR	F-score
Mangatawai plagioclase	0.925	0.869	0.896
Mangatawai P-SIP plagioclase	0.967	0.985	0.976
Mangatawai pyroxene	0.761	0.833	0.795
Mangatawai P-SIP pyroxene	0.863	0.869	0.866
Mangamate plagioclase	0.969	0.957	0.963
Mangamate P-SIP plagioclase	0.984	0.963	0.973
Mangamate pyroxene	0.987	0.975	0.981
Mangamate P-SIP pyroxene	0.989	0.982	0.987
Average and standard deviation (2σ)	0.931 ± 0.081	0.929 ± 0.062	0.930 ± 0.070
Average P-SIP and standard deviation (2σ)	0.951 ± 0.059	0.950 ± 0.055	0.951 ± 0.057

P-SIP: post-segmentation image processing

4.4. Discussion and implications

The comparison of the manual and the automatic method confirms that the TWS plugin provides encouraging results for the generation of CSDs. Here we demonstrate that the TWS method is reliable for glass-rich samples with up to 50 vol% microlites, but yields inconsistent segmentation for significantly more crystal-rich rocks (e.g. at ≥ 85 vol. %, as in the case of the Tarawera sample). Although the level of fit for crystal habit using TWS is acceptable for the pyroxene population of the Tarawera sample, the amount of touching plagioclase crystals is significant and thus, the automatic segmentation cannot be considered to provide robust results. BSE images of samples exceeding the maximum packing fraction (i.e., 0.74 for spherical particles, between 0.50 and 0.60 for cubic particles; Leshner & Spera, 2015), in which a large amount of crystals share edges, cannot be successfully segmented using TWS, as this would require extensive and time-consuming post-segmentation image processing. In such cases where a significant amount of touching crystals is found (e.g. lava flow samples), 2D editing may be required (e.g. Jerram *et al.*, 2009), or the true 3D CSD can be obtained using serial grinding or X-ray tomography techniques and methods (e.g. Jerram & Higgins, 2007; Jerram *et al.*, 2018; Mock & Jerram, 2005).

Glassy volcanic samples (e.g. tephra), for which each phase is characterised by distinct greyscales, provide high levels of fit for crystal population habits, regardless of the resolution of SEM used for image acquisition ($R^2=0.78$ with the use of the desktop SEM and $R^2 > 0.81$ with the use of a higher resolution SEM; Table 4.2.; Figures 4.3 and 4.4). Depending on the image resolution and the greyscale, the segmentation time is four to ten times faster using TWS than by manual outlining. Post-segmentation image processing is required to obtain more reliable 3D CSDs. However, even without post-segmentation image processing, the automatically calculated CSD slopes match those

calculated manually and therefore can be used to elucidate residence time of the crystals if the growth rate is constrained (e.g. Higgins & Roberge, 2007; Marsh, 1988; Muir *et al.*, 2012).

The image resolution used for acquisition (i.e., intermediate resolution with the desktop SEM and high resolution with the FE-SEM) does not affect the aspect ratio and the CSD shape. The best fit of the manual CSD curve and the best level of fit for the pyroxene population of the Mangatawai glass shard are obtained with the segmented image acquired with the desktop-SEM as the lower resolution tends to homogenise chemical gradients in the phases (e.g. poor contrast of chemical zonation so less variation of the greyscale within one crystal, poor contrast of variations of melt boundary layer around the crystals, etc.). However, due to the lower resolution, the CSD curve resulting from the image acquired with the desktop SEM is not affected by the downturn at smaller size, previously interpreted as an artefact due to image resolution (Hammer *et al.*, 1999; Vona & Romano, 2013). The downturn is likely to be due to the intersection probability effect when converting 2D to 3D measurements (Brugger & Hammer, 2010; Cashman & McConnell, 2005) or due to a lack of late crystallisation resulting from quenching (Armienti *et al.*, 2007).

Analyses of CSDs provide essential information about the kinetics, magmatic histories and timing of eruptive processes. The potential time-consuming aspect of this robust method has to date been its major drawback. This study offers an adequate semi-automated tool for crystal shape and CSD generation. Indeed, TWS provides a fast-computing segmentation that will save a tremendous amount of time to the user. It can be used to outline phenocrysts or microlites from glass-rich to medium-crystalline samples (e.g. volcanic glass shards) and can produce crystal habit information with little additional image editing. With some additional manual image processing, good CSD analysis is also

realised, highlighting the potential value of TWS in speeding up the image preparation stage prior to image analysis and quantification of the crystal population.

Chapter 5. Textures of the crystal cargos

This chapter will be submitted for publication under the title of “*Intermittent ascent of aphyric andesitic melts revealed by cryptic micro-antecryst textures*”.

Participating authors:

- ✚ **Charline Lormand** (Massey University, New Zealand): sampling, sample preparation, data acquisition and processing, manuscript writing and editing)
- ✚ **Georg F. Zellmer** (Massey University, New Zealand): manuscript editing and discussion
- ✚ **Naoya Sakamoto** (Hokkaido University, Japan): assisting with sample preparation, data acquisition and data processing
- ✚ **Hisayoshi Yurimoto** (Hokkaido University, Japan): assisting with data acquisition, manuscript editing and discussion
- ✚ **Geoff Kilgour** (GNS Science Wairakei, New Zealand): providing samples, manuscript editing and discussion
- ✚ **Alan S. Palmer** (Massey University, New Zealand): assisting in the field, manuscript editing and discussion
- ✚ **Károly Németh** (Massey University, New Zealand): assisting in the field, manuscript editing and discussion
- ✚ **Teresa Ubide** (The University of Queensland, Australia): manuscript editing and discussion
- ✚ **Yoshiyuki Iizuka** (Academica Sinica, Taiwan): assisting with data acquisition
- ✚ **Anja Moebis** (Massey University, New Zealand): providing samples and assisting with sample preparation)

Chapter content:

5.1. Introduction	108
5.1.1. Magmatic processes	108
5.1.2. Crystal textures	109
5.1.3. Crystal sizes and origins	111
5.2. Geological setting.....	113
5.3. Analytical methods.....	114
5.3.1. Tephra selection and sample preparation.....	114
5.3.2. Mineral and glass major element analysis and equilibrium.....	115
5.3.3. Tephra imaging	116
5.3.3.1. Scanning Electron Microscopy (SEM)	116
5.3.3.2. Secondary Ion Mass Spectroscopy (SIMS)	118
5.3.4. Crystal texture classification.....	118
5.4. Results	120
5.4.1. Major element chemistry	120
5.4.2. Plagioclase textures and zonations.....	130
5.4.2.1. Resorption and overgrowth.....	130
5.4.2.2. Oscillatory zoning.....	130
5.4.2.3. Single compositional jump.....	130
5.4.2.4. Featureless crystals	131
5.4.2.5. Sieve texture.....	133
5.4.2.6. Fractured crystals and overgrowth.....	133
5.4.2.7. Strontium zonation.....	133
5.4.3. Pyroxene textures and zonations.....	135
5.4.3.1. Resorption and overgrowth.....	135
5.4.3.2. Calcium-rich rims	135
5.4.3.3. Magnesian core and calcic rim.....	135
5.4.3.4. Fractured crystals and overgrowth.....	138
5.4.3.5. Aluminum zonation.....	138
5.5. Discussion	140
5.5.1. A diversity of magmatic processes	140
5.5.2. Magma recharge and mixing.....	140
5.5.3. Recycling of crystals.....	141
5.5.4. (Over)growth in aphyric magmas	142

5.5.5. Rapid decompression events	143
5.5.6. Rapid cooling-induced crystallisation.....	144
5.5.7. Dyking of magma.....	145
5.5.8. Entrainment of crystals into aphyric to sparsely phyrlic ascending melts ...	146
5.6. Conclusions	150

Abstract

Crystal cargos transported by arc magmas upon eruption often consist of complexly zoned phenocrysts with diverse histories. While these crystals record the early stage of magma formation and evolution, they are not ideal recorders of ascent processes, which are the keys to useful constraints for adequate volcano monitoring. Conversely, microlites and micro-phenocrysts, frequently associated with decompression-induced degassing or cooling, are relevant recorders of late-stage ascent processes. Our study focusses on the active Tongariro Volcanic Centre (TgVC), located at the southern end of the Taupo Volcanic Zone; an active volcanic complex that has produced a wide range of explosive eruption styles fed by intermediate magmas. Scoriae from these volcanoes contain glassy and nearly-aphyric tephra, carrying microlites of plagioclase and pyroxene (mostly orthopyroxene). Major element analyses, combined with textural information, are used to assess equilibrium between the microlites/micro-phenocrysts and the groundmass glass. Chemical disequilibrium of some plagioclase and pyroxene crystals with the surrounding glass is common in most tephra. To investigate this further, we mapped plagioclase and pyroxene phenocrysts, micro-phenocrysts and microlites at submicron resolution for major and trace element distributions via chemical mapping and SIMS-SCAPS imaging. From a total of 105 images, six plagioclase textural patterns are noted: resorption and overgrowth, oscillatory zoning, single compositional jump, sieve textures, fractures, and strontium zonation; while in pyroxene microlites the following textures are found: resorption and overgrowth, calcium-rich rims, magnesian core and calcic rims, fractures, and aluminium zonation. Microlite textures are observed down to $<30\ \mu\text{m}$ in most tephra from TgVC, and interpreted in the context of an interplay of magmatic processes involving multiple events of magma recharge/mixing, pressure fluctuations, fracturing, and rapid cooling and crystal growth. Since TgVC is located in an extensional tectonic

setting, we envision a vertically oriented magma plumbing system, where short-lived and nearly-aphyric magma injections accommodate crustal extension through dyking. Explosive eruptions occur when a hot magma batch fractures through previous intrusions, recycling a variety of small crystals grown under diverse physico-chemical conditions and stored in rapidly cooled, previously intruded dykes. Thus, textures cryptic to conventional imaging indicate that a significant proportion of the microlitic and micro-phenocrystic mineral cargo is of antecrystic origin (i.e. hence referred as “micro-antecrysts”) and cannot be attributed to late-stage nucleation and growth at the onset of volcanic eruptions.

Keywords: microlites, micro-phenocrysts, zonations, intermediate magmas, magma ascent

5.1. Introduction

5.1.1. Magmatic processes

To better understand the processes driving volcanic unrest, geophysical and geochemical tools as well as field observations are used to build a greater understanding of the magmatic system beneath a restless volcano. Volcano monitoring employs a wide range of techniques with a wide array of data streams, including deformation (e.g., Nakao *et al.*, 2013; Ueda *et al.*, 2005), remote sensing (e.g., Burton *et al.*, 2000; Meyer *et al.*, 2015) and seismicity (e.g., Dawson *et al.*, 2004; Kim *et al.*, 2018). Real time data are interpreted in the context of magmatic processes and eruptive behaviour recorded in past eruptive products, including isotopic investigations (Sosa-Ceballos *et al.*, 2014; Zellmer *et al.*, 2014a), petrological descriptions (e.g., Jerram *et al.*, 2018; Saubin *et al.*, 2016), melt inclusion analyses (e.g., Kilgour *et al.*, 2013; Roberge *et al.*, 2014), and interpretation of deposits (e.g., Donoghue *et al.*, 1995; Geoffroy *et al.*, 2018; Hamilton *et al.*, 2017). For instance, magma mixing, regarded as a frequent eruption trigger, is commonly interpreted from a wide range of methodologies and can be observed at different scales using detailed petrological analyses; indeed, first observed in hand specimen of rocks as a sharp contact between two magma types (e.g., Lai *et al.*, 2008; Walker & Skelhorn, 1966; Wiesmaier *et al.*, 2011), magma mixing is also observed and interpreted at the crystal scale (e.g., Coombs & Gardner, 2004; Schleider *et al.*, 2016). Mineral textures and compositions can not only record magma mixing/recharge, but also changes in pressure and temperature that occur during the final stage of magma ascent to eruption (e.g., Coote & Shane, 2016; Ginibre *et al.*, 2002; Sparks *et al.*, 1977).

Many models of magmatic plumbing systems have been presented to explain the complexity of crystal cargos. Single magma reservoir (Costa *et al.*, 2009a; Wilson *et al.*, 2003), layered magma chambers (Civetta *et al.*, 1991), and multiple interconnected small

storage regions (Hobden *et al.*, 1999; Longpré *et al.*, 2009; Ubide & Kamber, 2018) have all been envisioned as potential architectures of magmatic plumbing systems, which may be fed from a single source (Bennett *et al.*, 2019b; Kahl *et al.*, 2011) or multiple sources (Annen *et al.*, 2006). Within a single pyroclast or lava fragment, crystal cargos are often composed of multiple crystal textures with differing histories and ages. Such diversity has led to the identification of long-lived crystal mush zones (Bach *et al.*, 2012; Gregg & Smith, 2003; Pyle *et al.*, 1988; Smith & Lofgren, 1982). The mush model contends that the magma reservoir consists of a high crystal content with small volumes of interstitial melt, where crystals accumulate and continue to grow and diffusively equilibrate (e.g., Allan *et al.*, 2013; Bachmann & Bergantz 2003; Bachmann & Bergantz, 2006; Costa *et al.*, 2010; Nakamura, 1995). Crystals may come from different intrusions and may develop various textures depending on their local environment and location within the crystal mush body. Because they typically reach high packing fractions, crystal mushes are difficult to mobilise (Marsh, 1981). However, mush fragments can be erupted when entrained by a percolating magma batch, moving upwards towards shallower levels and eventually reaching the surface upon eruption (Cashman *et al.*, 2017). Hence, crystals that reach the surface provide a partial but rich window into the textures that can develop within a magma reservoir at depth (e.g. Jerram & Martin, 2008; Salisbury *et al.*, 2008).

5.1.2. Crystal textures

The investigation of crystal textures is one of the key analyses done on natural rock samples, because crystals record the magmatic processes and the history of the magma in which they grew (e.g., Agostini *et al.*, 2013; Allan *et al.*, 2013; Couch *et al.*, 2003; Hammer & Rutherford, 2002; Riker *et al.*, 2015; Sano & Toramaru, 2017; Simakin & Bindeman, 2008; Wright *et al.*, 2012; Zellmer *et al.*, 2016b). From their storage to eruption, crystals record the varying conditions that surrounded them such as the intrusion

of a compositionally distinct magma (Clynne, 1999; Koyaguchi, 1986; Rae *et al.*, 2016; Schleider *et al.*, 2016; Snyder, 1997; Sparks *et al.*, 1977), pressure and temperature fluctuations (Coote & Shane, 2016; Métrich *et al.*, 2001; Nelson & Montana, 1992; Woods & Bower, 1995), cooling rate (Gibb, 1974; Kirkpatrick *et al.*, 1983; Pankhurst *et al.*, 2018; Toramaru, 1991), degassing (Cashman & Blundy, 2000; Giuffrida *et al.*, 2017; Hammer *et al.*, 1999; Lindoo *et al.*, 2017; Stevenson & Blake, 1998), late-stage volatile saturation (e.g., Stock *et al.*, 2016a; Zellmer *et al.*, 2015a), and initial conditions of magma ascent and growth kinetics (e.g. rapid growth, high/low undercooling; Lasaga, 1982; Muncill & Lasaga, 1988; Sparks, 1978; Zellmer *et al.*, 2016b).

Disequilibrium textures such as sieve, resorption and dissolution are common in volcanic crystals and have previously been attributed to pressure and temperature fluctuations (e.g. Cashman & Blundy, 2000; Nelson & Montana, 1992), magma mixing/recharge (Agostini *et al.*, 2013; Bennett *et al.*, 2019b; Cassidy *et al.*, 2018; Crummy *et al.*, 2014; Hobden *et al.*, 2002; Shane *et al.*, 2017; Tost *et al.*, 2016), and recycling of old crystals (Armienti *et al.*, 2007). Oscillatory zoning has been associated with growth kinetics such as high degree of undercooling and thus rapid crystal growth (Ginibre *et al.*, 2002; L'Heureux & Fowler, 1994; L'Heureux & Fowler, 1996) and may also reflect fluctuations of the intensive parameters in the magma reservoir such as pressure and temperature (Cashman & Blundy, 2000; Holten *et al.*, 1997; Wilkinson & Johnston, 1996). Other causes such as temporal variations in the melt compositions (e.g., Chen *et al.*, 2015), variations in growth rate (e.g., Halden & Hawthorne, 1993) and diffusion-induced chemical gradients between the melt and the mineral (e.g., Grove *et al.*, 1984; Higman & Pearce, 1993; Hills, 1936) have also been suggested to explain oscillatory zoning.

Numerical modelling of magmatic processes using crystal textures has become a powerful tool to constrain timescales and to access the kinetics of magmatic plumbing systems (e.g., Blundy & Cashman, 2008; Bradshaw & Kent, 2017; Chakraborty, 1997; Chakraborty, 2008; Cooper *et al.*, 2017; Cooper *et al.*, 2016). Elemental diffusion in crystals, which can be modelled using known diffusion coefficients combined with gradient profiles across crystals has been studied for a range of elements and minerals, such as Fe-Mg, Ni, H and Ca in olivine, (Chakraborty, 2010; Demouchy *et al.*, 2006; Dohmen & Chakraborty, 2007; Mackwell & Kohlstedt, 1990; Shea *et al.*, 2015), Mg, Sr, Ba and Li in plagioclase (Cherniak & Watson, 1994; Costa *et al.*, 2003; Giletti & Shanahan, 1997; Liu & Yund, 1992; Morse, 1984; Zellmer *et al.*, 1999), Pb, U and Th in zircon (Cherniak *et al.*, 1997; Lee *et al.*, 1997), and Fe-Mg and Pb in pyroxene (Cherniak, 1998; Cherniak & Dimanov, 2010; Flaherty *et al.*, 2016; Krimer & Costa, 2017; Petrone *et al.*, 2016). The modelling of diffusion is referred to as geospeedometry if used to constrain timescales such as crystal residence time (e.g., Costa *et al.*, 2003; Morgan *et al.*, 2004; Morgan & Blake, 2006; Zellmer *et al.*, 1999), ascent rate (e.g., Demouchy *et al.*, 2006; Humphreys *et al.*, 2008) and cooling rate (e.g., Grove *et al.*, 1984). Modelling diffusion in crystals has provided essential constraints on geochemical kinetics (Dohmen & Chakraborty, 2007; Kile & Eberl, 2003; Shea *et al.*, 2015), and magma plumbing systems (Morgan *et al.*, 2004; Morgan & Blake, 2006; Nakamura, 1995).

5.1.3. Crystal sizes and origins

Image resolution of volcanic rocks is continually increasing, allowing the observation of ever smaller-scale heterogeneities. Magmatic crystals can be classified into phenocrysts, micro-phenocrysts and microlites, depending on size and/or genesis. At first glance, crystal populations can be distinguished by their size, with microlites usually not larger than 100 μm (e.g., < 30 μm in Castro & Mercer, 2004; < 50 μm in McCanta *et*

al., 2007; < 50 μm in Melnik *et al.*, 2011; < 100 μm in length in Murphy *et al.*, 2000), Upon imaging and chemical analysis, crystals can be described further in terms of their origin. For instance, Salisbury *et al.* (2008) in their study on magmatic processes of the 1915 eruption of Lassen Peak in California, recognised three populations of crystals with diverse origins: phenocrysts grew in an isolated dacitic magma, while micro-phenocrysts were the results of magma mixing, and groundmass microlites formed at a late-stage in response to degassing and/or decompression during magma ascent. Microlites often lack complex textures and are associated with late-stage crystallisation upon magma ascent and eruption (e.g., Armienti *et al.*, 1994; Cashman *et al.*, 1999; Castro *et al.*, 2003; Couch *et al.*, 2003; Cox *et al.*, 1979; Geschwind & Rutherford, 1995; Hammer *et al.*, 1999; Jerram *et al.*, 2018; Martel *et al.*, 2006; Noguchi *et al.*, 2006; Pompilio *et al.*, 2017; Sano & Toramaru, 2017; Shane *et al.*, 2017; Toramaru, 1991; Toramaru *et al.*, 2008).

In the present study, we focus on microlites and micro-phenocrysts erupted from andesitic vents in the Tongariro Volcanic Centre (TgVC) to explore the response of crystal textures and compositions to the final stages of magma ascent, degassing and eruption in an active volcanic arc. Indeed, TgVC has produced a wide range of eruption styles from which microlite-rich and mysteriously phenocryst-poor juvenile glassy shards were erupted. Previous work by Lormand *et al.* (2018a) is applied to classify microlite populations on crystal size distributions (CSDs) of the same set of samples. These authors used changes in CSD slopes to define the following size threshold regardless of origin: 30 μm in length to distinguish between microlites and micro-phenocrysts, and 100 μm to separate micro-phenocrysts from phenocrysts, which are scarce. For the intermediate magmas of TgVC, we will show that micro-phenocrysts and even some of the microlites present a wide spectrum of different zoning patterns, , only visible when applying high-resolution imaging. The range of zonations suggests a wide range of magmatic processes,

indicating a long history of subvolcanic residence in vertical conduits (i.e. dykes) prior to entrainment and eruption. Our data indicate that a significant portion of small crystals have an antecrystic origin, calling for a reappraisal of the petrogenetic processes at work in the subvolcanic crust beneath TgVC, and possibly at other arc volcanic centres globally.

5.2. Geological setting

The TgVC is the most frequently active volcanic centre of the Taupo Volcanic Zone, located in the North Island of New Zealand (Figure 2.2). It is undergoing extension and rotation due to the oblique subduction of the Pacific Plate beneath the Zealandia continent (e.g., Cole & Lewis, 1981; Mortimer, 2004; Wilson & Rowland, 2016). The TgVC is composed of two volcanic centres – Ruapehu and Tongariro – and over 30 volcanic vents including the Ngauruhoe volcanic cone. Over the past 26,000 years, the TgVC has produced a variety of eruptions from Strombolian to Plinian in size, providing a wide range of eruptive products. The westerly prevailing winds have led to a well-preserved and well-exposed stratigraphy of tephra from these eruptions along an eastern ring plain (e.g., Cronin *et al.*, 1996; Donoghue *et al.*, 1995; Herzer, 1995; Rowlands *et al.*, 2005).

Previous studies of TgVC have revealed different eruptive scenarios and magmatic processes based on the petrology of historical deposits. Several studies have described disequilibrium textures on phenocrysts, including sieve-textured plagioclases as result of mixing and/or rapid decompression of magma; indeed, sieve textures were observed in Pukeonake lavas (Beier *et al.*, 2017), Ngauruhoe lavas (Hobden *et al.*, 2002), Ruapehu andesite-hosted rhyolitic xenoliths (Price *et al.*, 2005), Ruapehu andesites (Cronin *et al.*, 2003; Donoghue *et al.*, 1997), Ruapehu-sourced mass flow deposits (Tost *et al.*, 2016), and Red Crater lavas (Shane *et al.*, 2017). Oscillatory zoning is also commonly found in

many TgVC andesites (Cole, 1978) especially in plagioclase phenocrysts of Pukeonake lavas (Beier *et al.*, 2017), Ngauruhoe lavas (Coote & Shane, 2016), Tufa Trig tephra (Donoghue *et al.*, 1997) and Red Crater lavas (Shane *et al.*, 2017). In fact, plagioclase phenocrysts from Red Crater present diverse textures and compositional growth patterns such as resorption, oscillatory zoning, and sieve textures, suggesting a liquid-dominated reservoir or a crystal mush origin, where crystals of differing ages and histories coexist before being erupted. Furthermore, resorbed crystals/cores with oscillatory-zoned mantles have previously been described in the TgVC as part of the 1996 deposits of Mt. Ruapehu (Kilgour *et al.*, 2014; Kilgour *et al.*, 2016), the Ngauruhoe Formation (Coote & Shane, 2016), the Red Crater lavas (Shane *et al.*, 2017), the 27-11 cal. ka BP Bullock Formation from Ruapehu (Pardo *et al.*, 2014b), and the 26-16.6 ka BP pyroclastic deposits from Mt. Tongariro (Shane *et al.*, 2008a).

Despite their volcanological interest, microlite and micro-phenocryst textures of TgVC products have remained understudied. Previously described as “groundmass crystals” and “featureless” using traditional petrography and electron microscope imaging in Red Crater lavas (Shane *et al.*, 2017), microlites and micro-phenocrysts from volcanic tephra, quenched at the onset of the eruptions, may provide rich insights into the subvolcanic plumbing system when observed with novel, high-resolution imaging techniques, as explored here.

5.3. Analytical methods

5.3.1. Tephra selection and sample preparation

Five tephra formations were selected from TgVC, ranging from *c.* 10,000 years BP to 1996 and from Strombolian to Plinian in style: the 11 ka BP Plinian eruptions of the Mangamate Formation (i.e., Te Rato and Ohinepango units referred to as PM2 and PM4

respectively in Auer *et al.* 2015; e.g., Nairn *et al.*, 1998; Nakagawa *et al.*, 1998), the 1.7-3.5 ka BP Strombolian to Vulcanian eruptions of the Mangatawai Formation (Donoghue *et al.*, 1995; Donoghue & Neall, 1996), the 0-1.7 ka BP Strombolian to sub-Plinian eruptions of the Tufa Trig Formation (Donoghue *et al.*, 1997), the 1972-1975 Strombolian to Vulcanian eruptions of the Ngauruhoe Formations (Nairn & Self, 1978; Self, 1975) and the 1995-1996 sub-Plinian eruptions of Ruapehu (i.e., referred here as Rua95 and Rua96, also referred as Tf 19 in Auer *et al.*, 2015). These deposits represent a broad range of eruption sizes ranging from Strombolian to Plinian and originating from different vents of the Tongariro Volcanic Centre. Tephra samples were sieved wet and dried in the oven. Glass shards ranging between 500 μm and 250 μm in diameter were handpicked and mounted into epoxy plugs. Microlites and micro-phenocrysts for all these tephra are mostly plagioclases and pyroxenes (mostly orthopyroxene, subordinate clinopyroxene and/or pigeonite).

5.3.2. Mineral and glass major element analysis and equilibrium

Major element compositions of microlites, micro-phenocrysts and groundmass glass were analysed to assess equilibrium between the melts and the minerals. Mangatawai and Tufa Trig tephra were analysed at the Institute of Earth Sciences, Academia Sinica, Taipei, Taiwan, using a JEOL JXA-8900R electron microprobe equipped with four wavelength-dispersive spectrometers. These analyses were performed with an acceleration voltage of 15 kV and a 2- μm -defocused beam with a current of 12 nA. Tephra from the 1972-1975 Ngauruhoe and the 1995-1996 Ruapehu eruptions were analysed at the Graduate School of Science, Hokkaido University, Sapporo, Japan, using a JEOL JXA-8800R electron microprobe equipped with four wavelength-dispersive spectrometers. The analyses were performed using an acceleration voltage of 15 kV and a 10- μm -defocused beam with a current of 7 nA for glass, whereas the mineral analyses

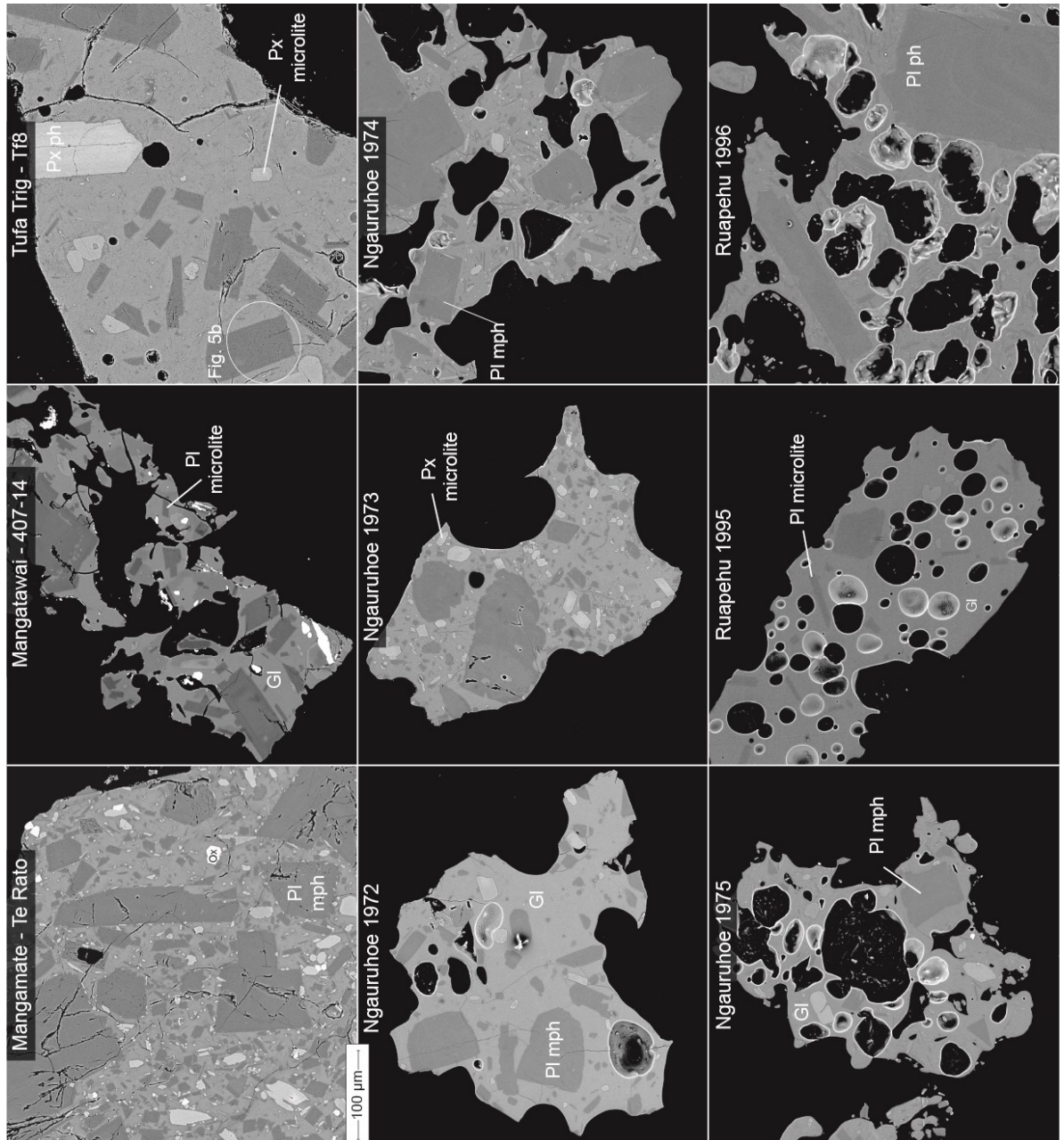
were performed using a spot beam with a current of 10 nA for plagioclases, 20 nA for pyroxenes. Glass and mineral compositions were not measured for the Mangamate eruptive sequence. Plagioclase-liquid equilibria were assessed based on the experimental calibration of the plagioclase hygrometer of Waters and Lange (2015), valid for intermediate magmas. Pyroxene-liquid equilibria were assessed using the Fe-Mg exchange coefficient determined by Putirka (2008) for both orthopyroxene [$K_d(\text{Fe-Mg})^{\text{opx-liq}} = 0.29 \pm 0.06$] and clinopyroxene [$K_d(\text{Fe-Mg})^{\text{cpx-liq}} = 0.28 \pm 0.08$]. Each mineral analysis is paired and tested with all glass compositions analysed in the same tephra.

5.3.3. Tephra imaging

5.3.3.1. Scanning Electron Microscopy (SEM)

Back-scattered electron (BSE) images were obtained for all the tephtras (see examples in Figure 5.1) using either (1) the Field Emission Scanning Electron Microscope (FE-SEM; JEOL JSM-7000F) of the Isotope Imaging Laboratory (IIL) of Hokkaido University in Sapporo, Japan; (2) the Environmental-SEM (FEI Quanta 200) of Massey University in Palmerston North, New Zealand; or (3) the JEOL NEOSCOPE 6000plus desktop SEM of GNS Science Wairakei Research Centre in Taupo, New Zealand. BSE images were used to gain an overview of the sample textures and to select regions of interests for further imaging/analysis. At IIL, SEM elemental maps of pyroxene microlites to micro-phenocrysts were obtained for Al, Ca, Cr, Fe, Mg, Na, K, Si and Ti.

Figure 5.1. Typical back-scattered electron images of the tephras from the Tongariro Volcanic Centre of this study: Mangamate, Mangatawai, Tufa Trig, Ngauruhoe 1972-1975 and Ruapehu 1995-1996. The Mangamate image was captured using the FE-SEM JEOL JSM-7000F of the Isotope Imaging Laboratory at Hokkaido University, Japan. Mangatawai and Tufa Trig images were captured using the Environmental-SEM (FEI Quanta 200) of Massey University in Palmerston North, New Zealand. Ngauruhoe and Ruapehu images were captured using the JEOL NEOSCOPE 6000plus desktop SEM of GNS Science Wairakei Research Centre in Taupo, New Zealand. Ox, plg, px, mph, ph and gl stand for oxide, plagioclase, pyroxene, micro-phenocryst, phenocryst and glass, respectively.



5.3.3.2. Secondary Ion Mass Spectroscopy (SIMS)

Semi-quantitative concentration maps for plagioclase crystals were obtained at ILL using a Cameca IMS-1270 SIMS instrument equipped with a Stacked CMOS-type Active Pixel Sensor (SCAPS). Preferred sites for SCAPS imaging were those containing euhedral crystals or crystals with observed zonation/shading in BSE. This microscope system is applied to visualise the elemental distribution on the sample surface at high magnification (i.e., isotopography, Yurimoto et al., 2003) for Al, Ca, Fe, Mg, Na, K, Si and Sr. SCAPS images were captured for phenocrysts, and especially micro-phenocrysts and microlites of plagioclase.

An O⁻ primary beam of 23 keV was irradiated on the sample surface of 80-100 μm in diameter using a 7 nA beam current. The sample surface of the area was sputtered with a 20 nA beam current for ten minutes before the analysis. The positive secondary ion images of ^{23}Na , ^{24}Mg , ^{27}Al , ^{28}Si , ^{39}K , ^{40}Ca , ^{56}Fe and ^{88}Sr on the sample surface were collected by the SCAPS detector, with exposure times of 50, 500, 50, 25, 50, 250 and 500 seconds, respectively. A submicron spatial resolution was achieved on individual images. Concentration ratio images normalised to Si were used to discriminate elemental zoning and textures of plagioclase crystals.

5.3.4. Crystal texture classification

84 images targeting plagioclase and 21 images targeting pyroxene crystals were acquired using SCAPS and SEM elemental imaging, respectively (Table 5.1). The images were used to define textural type of plagioclase (seven textures on 84 images) and pyroxene (five textures on 21 images), where a given crystal often displayed more than one texture.

Table 5.1. Summary table of number of images acquired using (1) the Cameca IMS-1270 SIMS instrument equipped with a Stacked CMOS-type Active Pixel Sensor (SCAPS) and (2) the FE-SEM; JEOL JSM-7000F at IIL, Hokkaido University, Japan. Crystals were

	Mangamate	Mangatawai	Tufa Trig	1972-1975 Ngauruhoe	1995-1996 Ruapehu
Plagioclases	15	23	30	8	8
<i>Resorption & overgrowth</i>	7	11	17	3	1
<i>Oscillatory zoning</i>	1	5	17	3	3
<i>Single comp. jump</i>	7	6	1	4	
<i>Featureless</i>	4	4	1		
<i>Sieve texture</i>		3	4	1	1
<i>Fracture</i>	1		3	1	
<i>Strontium zoning</i>	1	6	9	3	7
Total	21	35	52	15	12
Pyroxenes	1	9	3	8	
<i>Resorption & overgrowth</i>		5	1	4	
<i>Ca-rich rims</i>	1	3	1	5	
<i>Mg-core and Ca-rim</i>		3			
<i>Fracture</i>		2			
<i>Aluminum zoning</i>		7	3	2	
Total	1	20	5	11	

classified into different categories based on their texture. N/A stands for non-applicable/no analysis.

5.4. Results

5.4.1. Major element chemistry

Microprobe analyses demonstrate that glasses (n=127; see Appendix C7) from Mangatawai (n=70), Tufa Trig (n=32), Ngauruhoe (n=19) and Ruapehu (n=6) tephras are compositionally intermediate with 65% being andesitic, 33% dacitic and 2% basaltic-andesitic (Figure 5.2a).

Microprobe analyses on plagioclases (n=524; see Appendix C8) from Mangatawai (n=321), Tufa Trig (n=176), Ngauruhoe (n=21) and Ruapehu (n=6) consist of a main population of bytownites (i.e., *c.* 80% of the total population), and two smaller populations of labradorites (i.e., *c.* 13%) and anorthites (i.e., *c.* 7%; Figure 5.2b). Plagioclase microlites and micro-phenocrysts have An of An₂₋₄₉ (Figure 5.2d and Table 5.2). Specifically, plagioclase compositions are increasing with time as the averages are An₂₈ for Mangatawai Lower, An₃₃ for Mangatawai Upper, An₃₆ for Tufa Trig, An₃₉ for Ngauruhoe 1972-1975 and An₄₁ for Ruapehu 1995-1996 (Table 5.2). Standard deviations of Mg# and anorthite contents are large (Table 5.2).

Microprobe analyses of pyroxenes (n=294; see Appendix C9) from Mangatawai (n=124), Tufa Trig (n=143), Ngauruhoe (n=20) and Ruapehu (n=7) tephras define a main population of orthopyroxenes (i.e., *c.* 66% of clinoenstatite), a secondary population of pigeonites (*c.* 24%) and a smaller population of clinopyroxenes (i.e., *c.* 7% augite and *c.* 2% diopside; Figure 5.2c). Pyroxene microlites and micro-phenocrysts have Mg# ranging from 59 (i.e., Ngauruhoe 1974) to 86 (i.e., Mangatawai; Table 5.2). They have Mg# averages of 73 ± 7 (1 σ), 73 ± 3 (1 σ), 71 ± 6 (1 σ), 73 and 76 ± 4 (1 σ) for, respectively, Mangatawai Lower, Mangatawai Upper, Tufa Trig, Ngauruhoe 1972-1975 and Ruapehu

1995-1996 (Figure 5.2e). The clinopyroxenes have Mg# averages of 80 ± 4 (1σ), 74 ± 2 (1σ), 75 ± 5 (1σ), 64 ± 4 (1σ) and 74 ± 1 (1σ) for, respectively Mangatawai Lower, Mangatawai Upper, Tufa Trig, Ngauruhoe 1972-1975 and Ruapehu 1995-1996.

Among 527 plagioclases and 266 orthopyroxenes and 28 clinopyroxenes tested for assessment of equilibrium, 95 (i.e., c. 20%; Figure 5.3), 32 (c. 10%; Figure 5.4) and 11 (c. 40%; Figure 5.5) are in disequilibrium with their surrounding melt, respectively. Plagioclase-liquid equilibria are assessed based on the assumption that the TgVC magmas are H₂O-poor rather than H₂O saturated, as indicated by previous studies (Arpa *et al.*, 2017; Deering *et al.*, 2011a; Kilgour *et al.*, 2013): in fact, c. 55% of the plagioclase-liquid pairs are in equilibrium when assuming TgVC magmas are H₂O-poor, whereas less than 30% are in equilibrium when assuming TgVC are H₂O-saturated. As disequilibrium is not uncommon, it is essential to investigate the textures of small crystals using detailed imaging.

Table 5.2. (Table in the next page) Anorthite content (An) and Mg number (Mg#) of the plagioclases and the pyroxenes, respectively, for all tephra formations but Mangamate. The tephra member labels for Mangatawai (e.g. 407-14) and Tufa Trig (e.g. Tf8) correspond to the sample names used in Moebis *et al.* (2011) and Donoghue *et al.* (1997), respectively. N/A, n, E, P, A and D respectively stand for non-applicable/no analysis, number of analyses, enstatite, pigeonite, augite and diopside.

	PLAGIOCLASES						PYROXENES								
	An average	An maximum	An minimum	Std dev (1σ)	n		Mg# average	Mg# maximum	Mg# minimum	Std dev (1σ)	n	E	P	A	D
Mangatawai Lower	70.7	87.0	55.1	8.8	194		74	85.9	63.0	4	83	50	46	0	4
407-14	70.4	80.6	59.0	6.5	18		74	79.3	70.7	3	14	79	14	0	7
407-15	69.9	83.5	58.3	8.5	37		76	85.9	70.2	4	23	78	17	0	4
407-16	68.8	86.5	58.7	8.7	44		73	78.9	66.9	4	15	20	80	0	0
407-17	72.6	87.0	55.1	8.6	56		73	79.0	68.8	3	14	31	62	0	8
407-18	71.1	86.4	59.6	9.6	39		72	79.1	63.0	4	17	29	71	0	0
Mangatawai Upper	65.7	85.1	42.1	6.4	133		73	76.5	64.2	3	43	56	26	19	0
407-47	66.4	83.8	48.9	7.1	37		75	76.5	72.0	1	11	82	9	9	0
407-49	62.1	85.1	42.1	9.6	22		72	75.3	64.2	1	10	60	40	0	0
407-54	67.2	75.7	58.5	3.2	30		72	74.2	68.0	2	7	29	0	71	0
407-56	66.0	75.9	57.1	4.2	24		72	73.8	69.2	2	2	0	50	50	0
407-59	65.5	74.2	56.4	4.8	20		73	75.9	65.4	3	13	0	75	25	0
Tufa Trig	62.3	83.8	50.5	8.5	181		72	87.2	20.0	6	149	83	7	7	3
Tf8	59.8	73.1	51.5	4.5	43		71	79.2	20.0	9	39	79	11	10	0
Tf13	59.1	65.4	51.0	3.4	29		74	87.2	66.1	6	27	67	4	15	15
Tf14	66.0	83.5	53.7	9.8	38		71	79.5	65.0	3	29	93	3	3	0
Tf15	61.0	83.8	51.6	8.2	33		72	79.3	68.3	3	29	81	9	9	0
Tf16	64.8	83.8	50.5	10.8	38		71	79.4	68.3	2	25	50	25	25	0
Ngauruhoe 1972-1975	58.5	66.8	52.2	3.8	15		65	72.7	58.7	4	13	8	85	8	0
Ng72	57.2	58.8	56.0	1.2	3		64	69.5	61.8	4	3	0	67	33	0
Ng73	57.9	65.4	52.2	5.1	4		63	65.8	59.7	3	3	0	100	0	0
Ng74	59.2	66.8	55.5	4.1	5		66	69.5	58.7	4	4	0	100	0	0
Ng75	59.5	61.8	55.7	2.7	3		65	72.7	61.2	5	3	33	67	0	0
Ruapehu 1995-1996	57.4	61.2	56.0	1.8	6		75	81.6	72.1	3	6	67	17	17	0
Rua95	58.2	61.2	56.5	2.2	3		76	81.6	72.1	4	3	100	0	0	0
Rua96	56.6	57.6	56.0	0.7	3		74	74.7	72.9	1	3	33	33	33	0

Figure 5.2. Comparison of glass and mineral major elements: (a) TAS diagram (Le Bas *et al.*, 1986), (b) histogram of anorthite contents of plagioclase microlites and (c) discriminating chart for pyroxenes (Morimoto, 1989). Data for plagioclases and pyroxenes involve microlites and micro-phenocrysts only, except the field for Mangamate (data of Auer *et al.* 2015). All plotted compositions are recalculated to 100% anhydrous.

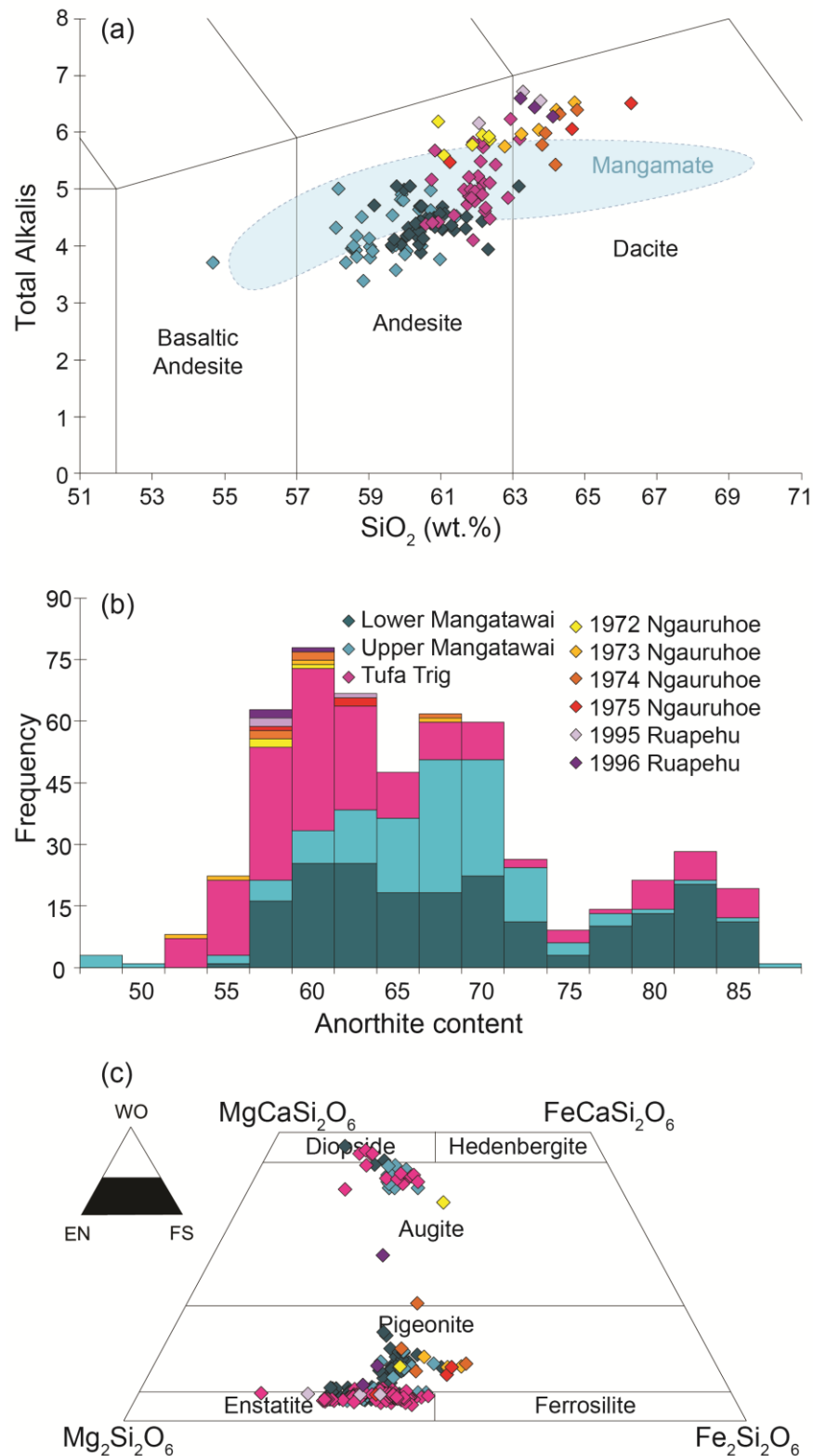


Figure 5.3. (Figure in the next page) Rhodes diagram to assess the equilibrium of the rims of plagioclase microlites from TgVC tephras using the anorthite content [$An\# = 100 \times Ca / (Ca + Na + K)$] of the plagioclase and melt compositions. Each horizontal bar is a range in glass An hosting a single mineral grain. The blue and grey fields in a-c represent the H₂O-saturated and dry experiments from basaltic to rhyolitic melts used in Figure 3a of Waters and Lange (2015), excluding the anhydrous felsic melts from the synthetic experiments of Brugger *et al.* (2003). According to previous studies (Arpa *et al.*, 2017; Deering *et al.*, 2011a; Kilgour *et al.*, 2009; Kilgour *et al.*, 2013), TgVC magmas are water-poor magmas, which is confirmed by the prevalence of plagioclase-liquid pairs in equilibrium. Note that disequilibrium is not uncommon, especially for the Mangatawai and Tufa Trig tephras.

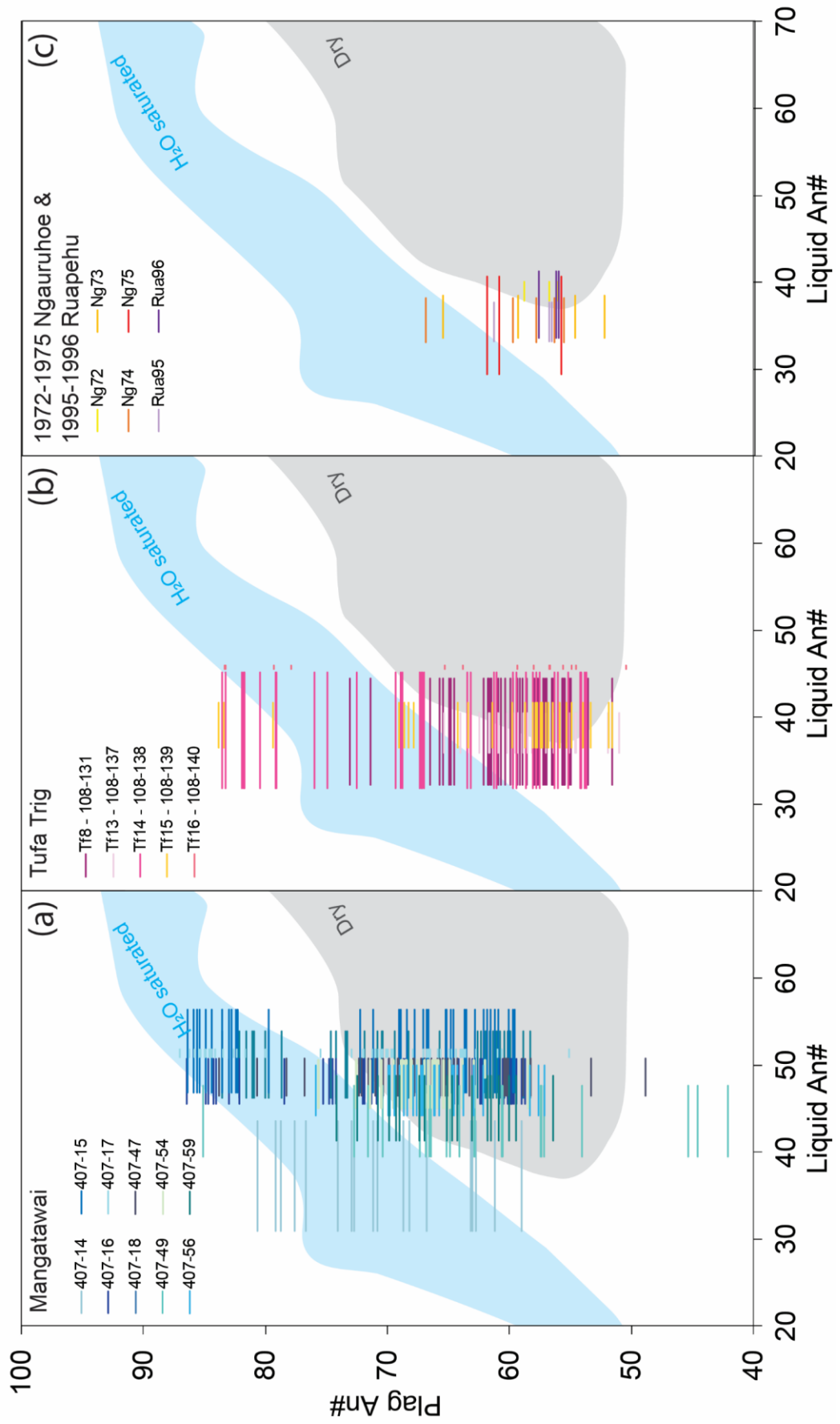


Figure 5.4. (Figure in the next page) Rhodes diagram to assess the equilibrium of the rims of orthopyroxene microlites from TgVC tephras using the Mg# [$\text{Mg\#} = 100 \times \text{Mg} / (\text{Mg} + \text{Fe}^{2+})$] of the orthopyroxene and glass compositions. Each horizontal bar is a range in glass Mg# hosting a single mineral grain. Orthopyroxene-liquid and clinopyroxene-liquid equilibria were assessed using the Fe-Mg exchange coefficients determined by Putirka (2008) i.e. $K_d(\text{Fe-Mg})^{\text{opx-liq}} = 0.29 \pm 0.06$. Note that disequilibrium is not uncommon, especially for the Mangatawai and Tufa Trig tephras.

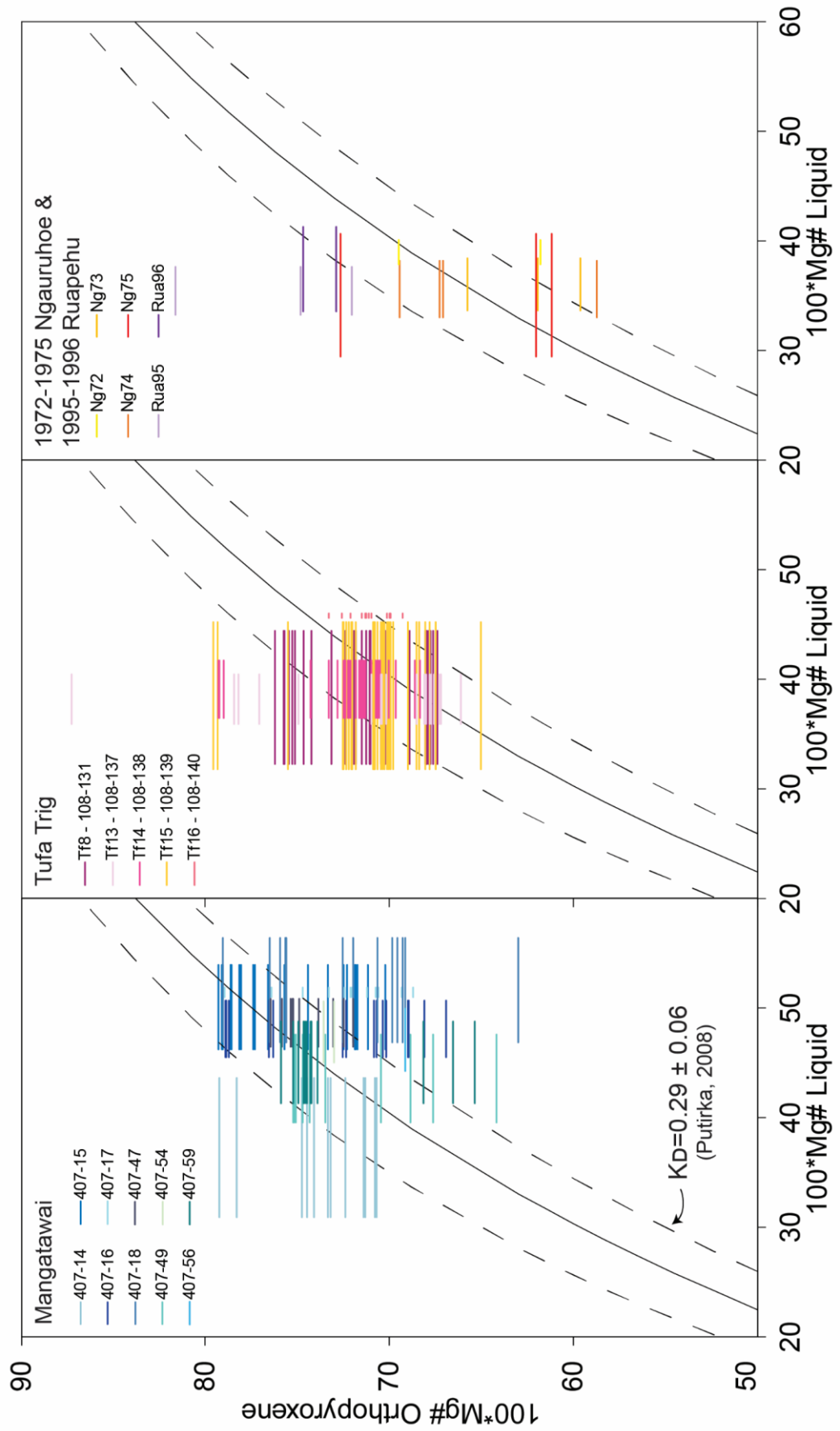
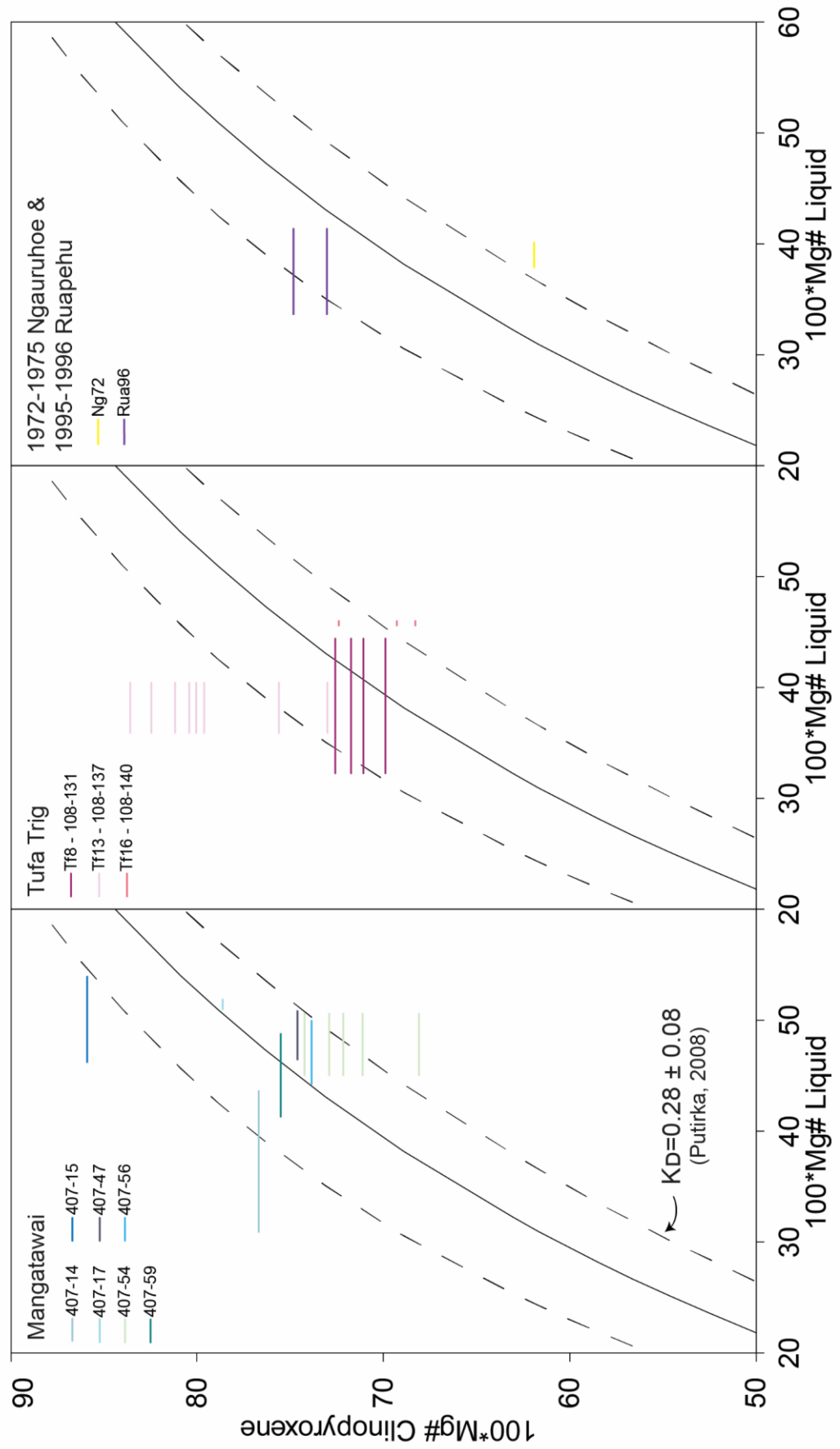


Figure 5.5. (Figure in the next page) Rhodes diagram to assess the equilibrium of the rims of clinopyroxene microlites from TgVC tephras using the Mg# [$Mg\# = 100 \times Mg / (Mg + Fe^{2+})$] of the clinopyroxene and glass compositions. Each horizontal bar is a range in glass Mg# hosting a single mineral grain. Clinopyroxene-liquid equilibria were assessed using the Fe-Mg exchange coefficients determined by Putirka (2008) i.e. $Kd(Fe-Mg)^{cpx-liq} = 0.28 \pm 0.08$. Note that disequilibrium is not uncommon, especially for the Mangatawai and Tufa Trig tephras.



5.4.2. Plagioclase textures and zonations

5.4.2.1. Resorption and overgrowth

Resorption and overgrowth is the most common texture observed in plagioclase micro-phenocrysts and microlites (Table 5.1, Figure 5.6a, and Appendix B1). Two levels of resorption can be identified: some crystals are affected by limited resorption (e.g. rounded corners of the crystal with oscillatory zoning in Figure 5.6) while others show more complex, extended resorption (e.g. resorbed core in Figure 5.6). Crystals with limited resorption are characterised by a rounded anhedral core and continuous overgrowth layers of euhedral to subhedral oscillatory zoning, where the crystal edges can also be truncated. Crystals with extended resorption have discontinuous and patchy resorbed zones.

5.4.2.2. Oscillatory zoning

Oscillatory zoning is common, especially in the Tufa Trig tephtras (see Table 5.1, Figure 5.6b, and Appendix B2). They are characterised by various amplitudes and frequencies of compositional cycles of up to 30 μm wide, usually parallel to crystal edges and with rounded corners (Figure 5.6b). According to the definition of Viccaro *et al.* (2010), most of the TgVC plagioclases yield the oscillatory pattern LAHF (Low Amplitude-High Frequency oscillations). Commonly, plagioclase rim zones display oscillatory zoning and they mantle a wide unzoned core, which may be resorbed. In some crystals, resorption, fracturing or truncating of crystal edges may have also occurred.

5.4.2.3. Single compositional jump

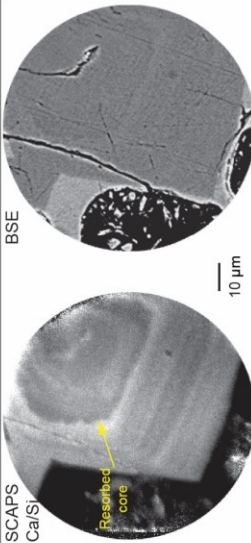
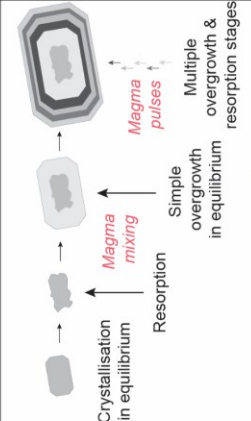
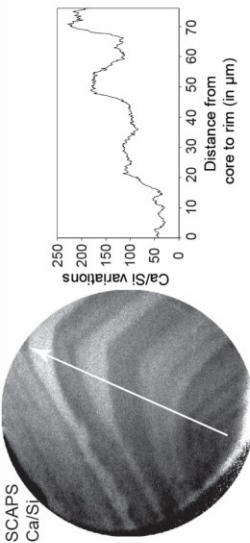
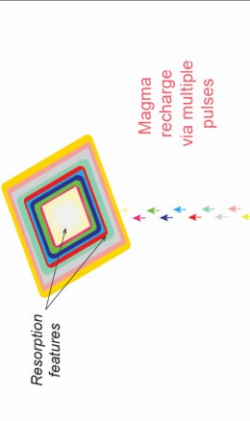
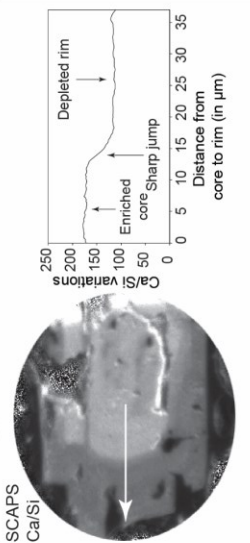
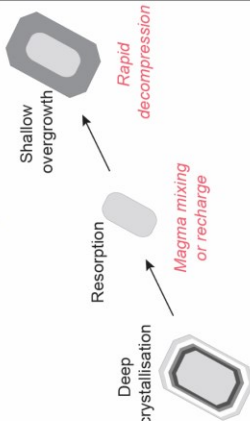
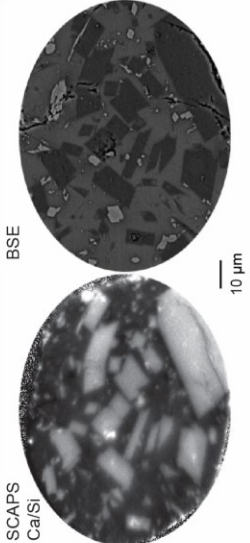
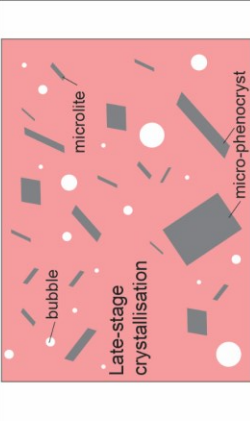
Single compositional jump in crystals is defined when the crystal has a sharp boundary between the core and the rim (see Figure 5.6c and Appendix B3). The rim can reach up to 20 μm in width in some micro-phenocrysts and phenocrysts. About 50% of

the crystals identified with this texture present a rounded core, indicating that it may have undergone resorption before growth of the outer layer. This texture is observed for all sizes of crystal and is common in the Mangamate and Mangatawai formations. All samples have plagioclases with calcic cores and sodic rims except for Mangamate tephras, which have plagioclases with sodic cores and more calcic rims.

5.4.2.4. Featureless crystals

Featureless plagioclase crystals are also present in Mangamate, Mangatawai and Tufa Trig tephras (Figure 5.6d and Appendix B4). Featureless plagioclases are euhedral to subhedral and do not show zonation or any kind of internal structure. They are generally 30 μm or less across i.e. classified as microlites, but can also occur as microphenocrysts.

Figure 5.6. Four of the seven main observed textures with descriptions and sketches of potential processes explaining the texture in plagioclase phenocrysts, but especially in plagioclase microlites and micro-phenocrysts, of the Tongariro Volcanic Centre andesitic tephra: (a) resorption and overgrowth textures and (b) oscillatory zoning, indicating multiple events of magma mixing and recharge; (c) single compositional jump that develops after resorption and rapid decompression events; (d) featureless crystals due to late-stage crystallisation. The black scale at the bottom left corner of each SCAPS image is 10 µm in size. Ca, Si, Sr, Na, and BSE respectively stand for calcium, silica, strontium, sodium, and back-scattered electron images.

TEXTURE	DESCRIPTION	INTERPRETATION
<p>(a) Resorption & overgrowth</p> 	<ul style="list-style-type: none"> • Very likely: single stage of resorption and multiple stages of overgrowth • Likely: multiple stages of both resorption and overgrowth • Observed in microlites, micro-phenocrysts and phenocrysts 	
<p>(b) Oscillatory zoning</p> 	<ul style="list-style-type: none"> • Very likely: resorbed core and oscillatory-zoned mantle • Low-amplitude-high-frequency zonation • Growth layers may have different thicknesses • Observed in: microlites, micro-phenocrysts and phenocrysts 	
<p>(c) Single compositional jump</p> 	<ul style="list-style-type: none"> • Sharp boundary between a calcic core and reverse zoned rim • No gradient observed in each zone, homogeneous crystallisation • Observed in: microlites, micro-phenocrysts and phenocrysts 	
<p>(d) Featureless</p> 	<ul style="list-style-type: none"> • No gradient or zonation observed • Euhedral to subhedral • Observed in: microlites and micro-phenocrysts 	

5.4.2.5. *Sieve texture*

Micro-phenocrysts and phenocrysts show sieve textures (Figure 5.7a and Appendix B5). Sieve textured crystals may also display complex zoning and resorption features. Typically, these textures are observed in the cores but they are also seen in the overgrowing outer zones.

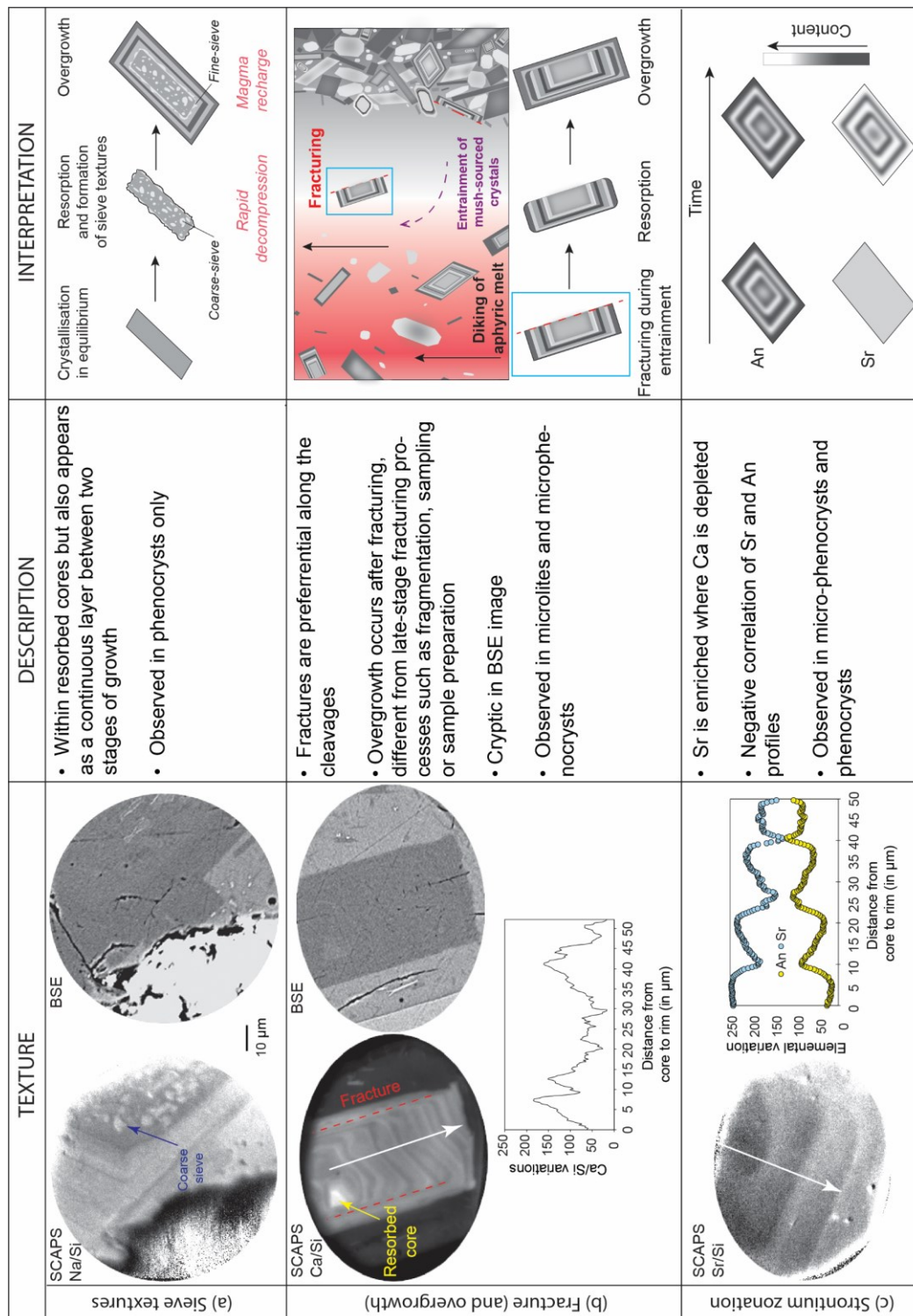
5.4.2.6. *Fractured crystals and overgrowth*

Crystals ranging from 40 μm to *c.* 100 μm in length show evidence of fracturing followed by overgrowth (see Figure 5.7b and Appendix B6). Fracturing is identified when the crystal displays missing or discontinuous zonation along certain crystal faces. Typically, fractures seem to follow the main cleavage planes of the crystal. Crystal cores appear rounded or may even be missing due to resorption before fracturing and crystal overgrowth.

5.4.2.7. *Strontium zonation*

Crystals showing zonation in strontium are observed in 26 images of micro-phenocrysts (see Figure 5.7c and Appendix B7). Most of the crystals have sharp zonation in strontium and may also display resorption textures. As Sr is intimately related to An (e.g., Cherniak & Watson, 1994; Cherniak, 1996; Giletti & Casserly, 1994), profiles of Sr and An are compared: the strontium signal is negatively correlated with the anorthite signal in all of the crystals.

Figure 5.7. Three of the seven main observed textures with descriptions and sketches of potential processes explaining the texture in plagioclase microlites, micro-phenocrysts and phenocrysts of the Tongariro Volcanic Centre andesitic tephra: (a) sieve textures resulting from rapid decompression; (b) fracture (and overgrowth) triggered by entrainment of crystals from a crystal-mush-like environment; (c) strontium zonation (Sr) associated with a negative correlation with An suggesting recycling of old crystals. Ca, Si, Sr, Na, BSE and An stand, respectively, for calcium, silica, strontium, sodium, back-scattered electron and anorthite content.



5.4.3. Pyroxene textures and zonation

5.4.3.1. Resorption and overgrowth

Resorption and overgrowth are features observed in all sizes of pyroxenes, in tephra from Mangatawai, Tufa Trig and Ngauruhoe 1972-1975 (Figure 5.8a and Appendix B8). Unlike the plagioclases, pyroxenes typically have a resorbed rounded core with euhedral overgrowth.

5.4.3.2. Calcium-rich rims

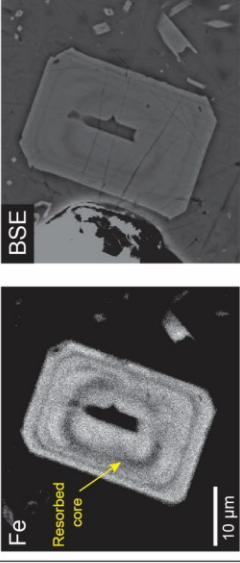
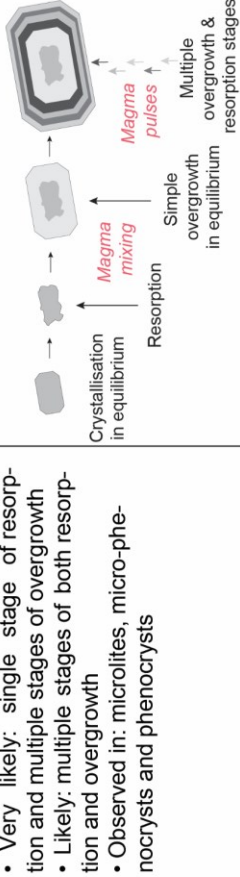
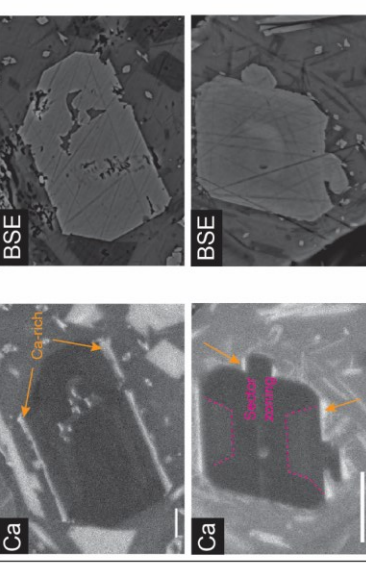
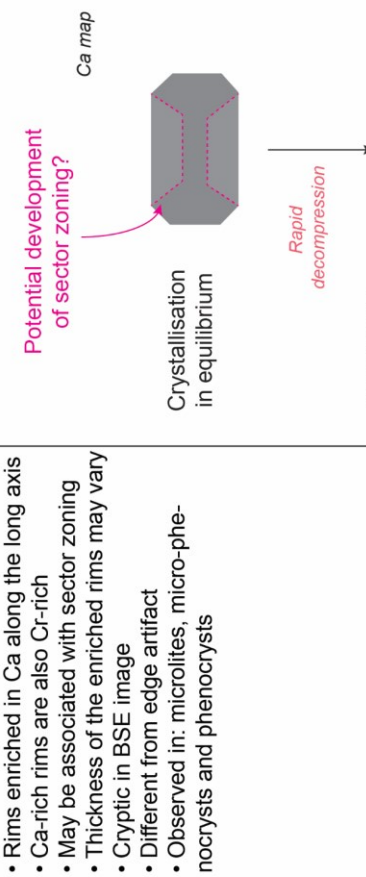
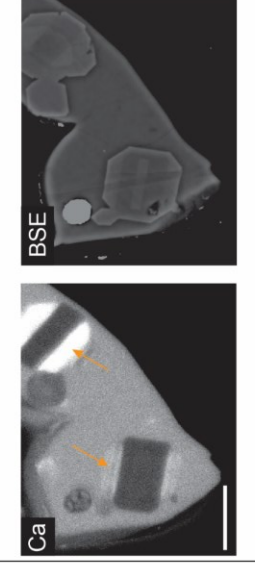

Quite commonly, several orthopyroxenes of sizes varying from one hundred micrometres to tens of micrometres and from different tephra formations, exhibit thin Ca-rich rims, but they may also appear across the whole crystal as parallel layers in basal cuts (Krimer & Costa, 2017; Ubide *et al.*, 2019; Table 5.1, Figure 5.8, and Appendix B9). In such cases, Ca-rich rims are also enriched in chromium, but not in magnesium. However, two crystals also show zonation in Ca within the crystal along elongated cuts. Considering the probe analyses and the tephra exhibiting this texture (e.g. 407-15 and 407-17 from Mangatawai, Tufa-Trig 14, Ng74 and Ng75), the Ca-rich rims compositionally constitute pigeonites (Figure 5.2c and Appendix B9). In addition to Ca-rich rims, some crystals may have developed discrete sector zoning (Figure 5.8b and Appendix B9 i.e., Te Rato and Ngauruhoe 1975 pyroxene crystals). We also observe a Ca-rich line running through the centre of some crystals and parallel to the Ca-rich rims (see dotted lines in Appendix B9). These features are invisible in BSE (Figure 5.8b) and are observed in Mangamate, Mangatawai, Tufa Trig and Ngauruhoe tephra.

5.4.3.3. Magnesian core and calcic rim

Some Mangatawai pyroxenes exhibit a peculiar texture where the cores are enriched in magnesium (Mg) and the rims are enriched in calcium (Ca) and chromium (Cr; see

Figure 5.8c and Appendix B10). The calcic rims are not always homogeneous and are usually observed along the long axis (b-axis, c-axis or transversal). The magnesian cores are euhedral and do not show any gradient. This texture affects micro-phenocrysts and microlites as small as 10 μm . These zonations are not visible on BSE and are observed in the Mangatawai tephra only.

Figure 5.8. Three of the five main observed textures with descriptions and sketches of potential processes explaining the texture in pyroxene microlites, micro-phenocrysts and phenocrysts of the Tongariro Volcanic Centre andesitic tephra: (a) resorption and overgrowth textures indicating multiple events of magma mixing; (b) Ca-rich rims and (c) magnesian-core and calcic-rim demonstrating a shift of mineral phase (i.e. orthopyroxene to clinopyroxene) resulting from rapid decompression. Fe, Ca and BSE respectively stand for iron, calcium and back-scattered electron images. The white scale at the bottom left corner of each map is 10 µm in length.

TEXTURE	DESCRIPTION	INTERPRETATION
<p>(a) Resorption & overgrowth</p> 	<ul style="list-style-type: none"> • Very likely: single stage of resorption and multiple stages of overgrowth • Likely: multiple stages of both resorption and overgrowth • Observed in: microlites, micro-phenocrysts and phenocrysts 	
<p>(b) Ca-rich rims</p> 	<ul style="list-style-type: none"> • Rims enriched in Ca along the long axis • Ca-rich rims are also Cr-rich • May be associated with sector zoning • Thickness of the enriched rims may vary • Cryptic in BSE image • Different from edge artifact • Observed in: microlites, micro-phenocrysts and phenocrysts 	
<p>(c) Mg-core and Ca-rim</p> 	<ul style="list-style-type: none"> • Sharp boundary between Mg-rich core and Ca-rich rims • Ca-rich rims are also Cr-rich • Likely to be observed along the basal cuts {100} • Observed in: microlites and micro-phenocrysts from Mangatawai only 	

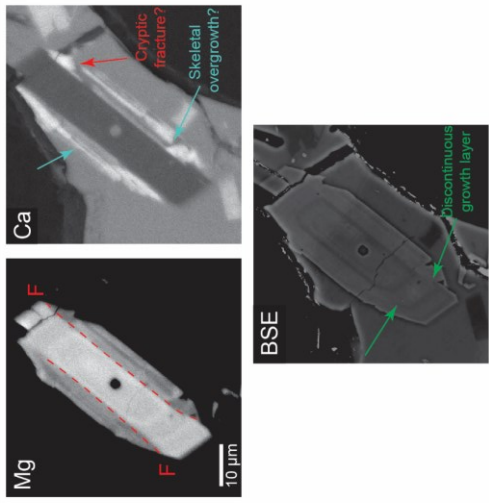
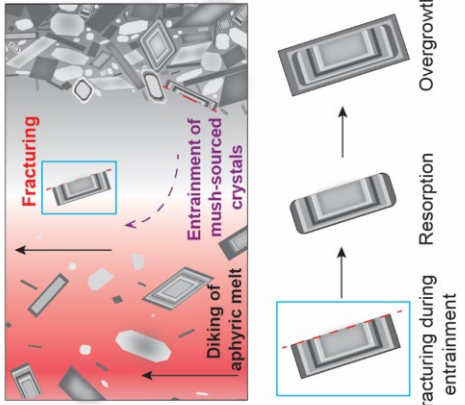
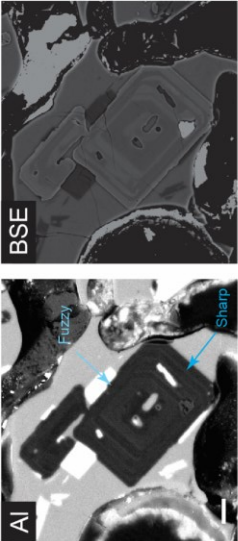
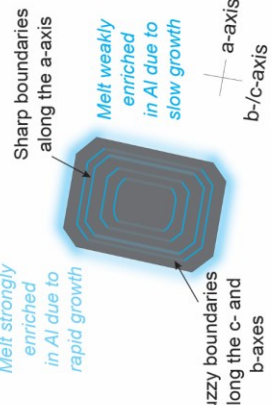
5.4.3.4. *Fractured crystals and overgrowth*

Two crystals of Mangatawai show evidence of fracturing and overgrowth (Table 5.1, Figure 5.9a and Appendix B11). The micro-phenocrysts are also associated with complex zoning and occasional resorption, which have affected the crystals before the fracturing and overgrowth events. The fractures, similar to the fractured plagioclases, follow the cleavage planes.

5.4.3.5. *Aluminum zonation*

The most common texture observed in pyroxenes is the zonation of aluminum (Al; Table 5.1, Figure 5.9b, and Appendix B12). Enriched and depleted growth layers of Al are observed in phenocrysts, micro-phenocrysts and even microlites. Interestingly, these zonations do not correlate with any other elements analysed here. In some instances, resorption events erased parts of growth layers. In some instances, resorption events erased parts of growth layers. Using schematic mineral models, pyroxene crystals are usually observed as cut along the a- and b-axes and parallel to the c-axis (Krimer & Costa, 2017). Clinopyroxene crystals are mainly cut along the a- and b-axes or a- and c-axes (Leung, 1974; Ubide *et al.*, 2019). Commonly, the zonations in Al are fuzzier parallel to the b-axis or c-axis compared to the a-axis. Al zonation is observed in Mangatawai, Tufa Trig and Ngauruhoe tephros.

Figure 5.9. Two of the five main observed textures with descriptions and sketches of potential processes explaining the texture in pyroxene microlites, micro-phenocrysts and phenocrysts of the Tongariro Volcanic Centre andesitic tephra: (a) fracture (and overgrowth) triggered by entrainment of crystals from a crystal-mush-like environment; (b) aluminium zonation with sharp and fuzzy zonation boundaries suggesting rapid growth kinetics rather than diffusion-controlled zonation. Mg, F, Ca, Al and BSE respectively stand for magnesium, fracture, calcium, aluminum and back-scattered electron images. The white scale at the bottom left corner of each map is 10 μm in length.

TEXTURE	DESCRIPTION	INTERPRETATION
<p>(a) Fracture (and overgrowth)</p> 	<ul style="list-style-type: none"> • Fractures are preferential along the cleavages • Fractures may occur within the overgrowing zones and appear cryptic in BSE • Overgrowth occurs after fracturing, different from late-stage fracturing processes such as fragmentation, sampling or sample preparation • Observed in microlites and micro-phenocrysts 	
<p>(b) Aluminium zonation</p> 	<ul style="list-style-type: none"> • More preserved towards the rim • Resorption may have affected the core, erasing any concentric Al zonation • Cryptic in BSE image • Fuzzier boundaries along the b- and c-axes compared to a-axis • Observed in: microlites, micro-phenocrysts & phenocrysts 	

5.5. Discussion

5.5.1. A diversity of magmatic processes

The tangible disequilibrium inferred from the mineral-liquid pair compositions and the large standard deviations of the anorthite content and the Mg# indicate that complex processes were occurring during the genesis of TgVC microlites and micro-phenocrysts or that crystallisation was occurring over a range of magmatic conditions. Such a variety of compositions within the same eruptive deposit is consistent with previous studies of phenocrysts from lavas of Ngauruhoe, Red Crater and Pukeonake (Coote & Shane, 2016; Shane *et al.*, 2017; Shane *et al.*, 2019). Furthermore, *c.* 15-20% of the microlites are not in chemical equilibrium with their surrounding melts. Although there are caveats regarding the small population of crystals investigated (*i.e.*, low number of analysed and imaged pyroxenes, Table 5.1 and 5.2), and thus, straight comparison between each tephra formation sourced from different vents would be undue, the existence of most textures across all volcanic systems is clear. This indicates that similar magmatic processes must have affected the magmatic plumbing systems of these eruptions. Hence, we discuss magmatic processes that are relevant to the textures observed in our case study to provide constraints on the magmatic plumbing system.

5.5.2. Magma recharge and mixing

Many plagioclase and pyroxene microlites show evidence of oscillatory zoning (Figure 5.6b and Appendix B2) and resorption followed by overgrowth, where a resorbed core is mantled by several concentric overgrowing layers (Figures 5.6a, 5.8a and Appendixes B1 and B8). This texture has been attributed to magma mixing or magma recharge (Agostini *et al.*, 2013; Ubide *et al.*, 2019), which would lead to (over-)growth of more mafic plagioclase. Disequilibrium textures are also consistent with magma mixing as sieve textures have previously been attributed to re-heating or a change to a

more mafic environment (Nakamura & Shimakita, 1998). Furthermore, the large standard deviations of An contents and Mg# (Figure 5.2b) and the 10-40% of mineral-liquid pairs in disequilibrium (Figures 5.3, 5.4 and 5.5) imply that the crystal cargo originated from different magma batches. The feeding magmas may thus have been compositionally heterogeneous due to the mixing of several magma batches before eruption.

5.5.3. Recycling of crystals

Several crystals show Sr concentration gradients. It has been shown previously that crystals typically grow without Sr concentration gradients (Cooper & Kent, 2014; Zellmer *et al.*, 2003a), and that gradients develop with time due to Sr diffusion down chemical potential gradients (Cherniak & Watson, 1992; Cherniak & Watson, 1994; Cherniak & Dimanov, 2010; Giletti & Casserly, 1994; Giletti & Shanahan, 1997). The latter exists due to variations in anorthite content, which is essentially unaffected by diffusion due to the extremely low interdiffusion of NaSi-CaAl (Grove *et al.*, 1984; Morse, 1984). The reason for the initial absence of Sr zonation is the increase in compatibility of Sr in plagioclase with decreasing anorthite content (Bindeman *et al.*, 1998; Blundy & Wood, 1991; McKay *et al.*, 1994), which counterbalances the Sr depletion in the melt (Kent *et al.*, 2008) during progressive plagioclase crystal fractionation (Cooper & Kent, 2014; Zellmer *et al.*, 2003b). The observed Sr concentration profiles in the studied microphenocrysts are anti-correlated with anorthite content. If this is due to diffusive equilibration during residence at magmatic temperatures, as proposed for larger crystals, quantification of crystal residence times may be possible. A fully quantitative geospeedometric analysis is beyond the scope of the present work. However, at magmatic temperatures of *c.* 1100 °C, as determined for these magmas (Graham *et al.*, 1995; Lormand *et al.*, 2018a; Tost *et al.*, 2016), full equilibration of Sr in small crystals with a zoning wavelength of 15 microns is expected to take five to six days at $X_{An} = 0.3$ and

about one month at $X_{An} = 0.5$. In this case, these crystals would not have grown in response to rapid decompression in the hours or possibly few days before the eruption. Instead, they would likely be recycled from previous intrusive bodies, in which they equilibrated during cooling, prior to their uptake into the magma that carried them to the surface. Also, at a broader magnification, the variety of textures in individual glass ash shards imaged initially confirms recycling of volcanic particles from previous eruptions (Taddeucci *et al.*, 2004; Wright *et al.*, 2012). Recycling of phenocrysts has previously been inferred for TgVC magmas (Auer *et al.*, 2013; Coote & Shane, 2016; Shane *et al.*, 2019), but this study extends the process down to micrometer-sized crystals, thus implying that remobilisation of antecrysts also happens at shallower depths from finely crystalline intrusives.

5.5.4. (Over)growth in aphyric magmas

Plagioclase from all tephras but especially from the Mangatawai and Ngauruhoe formations, are characterised by compositional jumps between a calcic core and a sodic rim, except for crystals from the Mangamate Formation, which show the opposite. Single compositional jumps between the core and the rim are further evidence of crystal entrainment in a foreign melt. The sodic rim of up to 20 μm did not develop a gradient (i.e., no normal or reverse zoning within each zone), therefore the magmas in which the crystals grew did not change composition during crystallisation. To maintain constant rim composition, the volume of the melt in which the crystals rims grew must have been large relative to the mush, because the overgrowth of the few existing crystals did not significantly affect the composition of the remaining silicate melt. This implies that the melts, in which the crystal rims grew, were aphyric or very sparsely phyric. A similar texture was also observed in plagioclase phenocrysts from Stromboli, Italy (Armienti *et al.*, 2007), in plagioclase phenocrysts of mid-ocean ridge basalt from the Gakkel Ridge

(Bennett *et al.*, 2019b), and also in plagioclase phenocrysts from monogenetic volcanoes of the Kaikohe-Bay of Islands field, New Zealand (Coote *et al.*, 2018). These observations imply that in the case of at least these settings, the propagation of aphyric or sparsely aphyric melt bodies are a key aspect of crustal magma ascent processes. By extension, the ascent of largely aphyric melts into dykes transporting foreign crystals may occur more readily than previously known.

5.5.5. Rapid decompression events

Several textures point towards pressure fluctuations associated with rapid decompression events. Resorption in plagioclase, for instance can be triggered by volatile-undersaturated decompression events, during which the plagioclase stability field contracts (Bennett *et al.*, 2019b; Nelson & Montana, 1992): this is consistent with the findings of Lormand *et al.* (2018a), which used hygrometry to constrain depths of microlite crystallisation (i.e. > 550 MPa) and water contents (< 1.7 wt% H₂O). Sieve textures are also common in plagioclases and can be related to pressure changes: indeed, they are the results of dissolution due to rapid volatile-undersaturated decompression (Nelson & Montana, 1992), or due to re-heating by injection of a more mafic melt (Nakamura & Shimakita, 1998). Disequilibrium patterns such as resorption and sieve textures have previously been described as dominant features in plagioclase phenocrysts of lavas from Red Crater and Pukeonake (Shane *et al.* 2019), confirming that pressure fluctuation is common within the TgVC plumbing system, regardless of eruption style (i.e. explosive and effusive).

Sector zoning in pyroxene has recently been observed but not explained (Barnes *et al.*, 2016; Zellmer *et al.*, 2016c; Zellmer *et al.*, 2018). In phenocrysts, sector zoning occurs during crystal growth, where surface kinetic processes such as diffusion in the melt boundary layer take place (e.g. Downes, 1974; Ferguson, 1973; Leung, 1974; Nakamura,

1973). We infer that in TgVC magmas, sector-zoned orthopyroxene microlites may be the result of a pressure decrease, which can shift phase relations in magmas to produce supercooled or superheated conditions for a mineral (Nelson & Montana, 1992). This process could also explain the pyroxenes displaying intergrowth of orthopyroxene and clinopyroxene, as they consist of Mg-rich cores (orthopyroxene) and Ca-rich rims (clinopyroxene) along the b- and c-axes. Hence, the Ca-rich rims on orthopyroxene could have developed at the initial stage of such a pressure change and would then have crystallised to form Ca-rich rims (clinopyroxene), and potentially sector zoning, around the Mg-rich core (orthopyroxene).

5.5.6. Rapid cooling-induced crystallisation

The substantial proportion of plagioclase-liquid pairs in disequilibrium (i.e. *c.* 20%; Figure 5.3c) and the abundance of disequilibrium textures observed in the TgVC plagioclases (e.g. resorption, single compositional jump, sieve textures) may be another piece of evidence for cooling-induced crystallisation as disequilibrium is favoured by high cooling rate (Mollo *et al.*, 2011). Notably, the steep boundary between the cores and rims of some plagioclase crystals (see Figure 5.6c and Appendix B3) may reflect growth near chilled margins of dykes where such textures are prevalent (Chistyakova & Latypov, 2010; Loomis & Welber, 1982).

Orthopyroxenes, mainly from the Mangatawai tephra, demonstrate that the boundary along the long-axis in the Al map is fuzzy parallel to b- and c-axes and sharp along the a-axis (Figure 5.8b). As Al is an extremely slow diffusing element in orthopyroxene (e.g., Freer, 1981; Freer *et al.*, 1982; Witt-Eickschen & Seck, 1991), the fuzzy boundaries could not have been the result of diffusion considering the time available (i.e. < 10,000 years; Smith & Barron, 1991), but rather suggest that the Al zonation must reflect rapid crystal growth (Allan *et al.*, 2013). Although Al is moderately

incompatible in orthopyroxene (i.e. $K_{d_{Al}^{opx-liq}} = 0.43$; Adam and Greene, 2006), some orthopyroxenes incorporate Al due to rapid growth and the formation of melt boundary layer, which in turn lead to local partitioning effects at the crystal-melt interface.

Ubide *et al.* (2019) have also associated sector-zoned-clinopyroxene phenocrysts with kinetic effects such as low degrees of undercooling and slow growth rates resulting from cooling. Such processes can be expected during slow magma ascent through dykes (e.g. Taisne & Jaupart, 2011; Weinberg, 1996).

Clinopyroxene incorporating Al has been interpreted to be strongly controlled by magma undercooling (Mollo *et al.*, 2010; Ubide & Kamber, 2018; Ubide *et al.*, 2019); indeed, Al incorporation into the tetrahedral site of clinopyroxene has been observed at the chilled margins of dykes due to higher cooling rate compared to that of the interior (Coish & Taylor, 1979; Mollo *et al.*, 2011).

5.5.7. Dyking of magma

Fractures have been described in previous studies (e.g., Higgins & Roberge, 2003; Jordan *et al.*, 2016; Kennedy *et al.*, 2005; Rosi *et al.*, 2004), and some rare published works such as Ohnenstetter & Brown (1992) have observed – but not explained – the presence of zonation or overgrowth after fracturing. Here, we find evidence of fractures followed by overgrowth, which thus cannot be associated to a late stage or even post-eruptive event. Instead, the crystals were subjected to environments with high rates of local pressure changes or high rates of collision, involving the risk of fracturing. Such a scenario may be associated with the injection of a magma as a dyke travelling through a previously solidified or nearly solidified intrusion as a particle-rich environment, where fracturing and entrainment of crystals with different histories and ages would occur (Oppenheimer *et al.*, 2015). A similar model has been developed to explain the diversity

of olivine core compositions of Llaima volcano, where largely solidified prehistoric intrusions are acting as shallow reservoirs (Bouvet de Maisonneuve *et al.*, 2012).

A vertical magmatic plumbing system consisting of dykes is also consistent with the tectonic regime in the southern TVZ; indeed, a recent study of the Tongariro graben (Gómez-Vasconcelos *et al.*, 2017) has defined an extension rate of $c. 7 \pm 1.2$ mm/yr since 20 ka, which is partly accommodated by dyke intrusions. That study also identified earthquakes associated with dyke formation, which may be related to fracturing associated with the injection of new magma.

5.5.8. Entrainment of crystals into aphyric to sparsely phyric ascending melts

The heterogeneous crystal cargo described in this study consists of a wide range of disequilibrium textures conveying a variability of magmatic processes and thus crystal histories within the same tephra, seen in all tephras. Such variability within single eruption deposits has previously been described, e.g. in arc volcanoes in the Trans-Mexican Volcanic Belt (Zellmer *et al.*, 2016a), and also in the TgVC for Ngauruhoe lavas (Coote & Shane, 2016). A study of the mid-oceanic basalts of the Gakkel Ridge (Bennett *et al.*, 2019b) also suggested that entrainment of crystals from a mush into ascending melts would produce a cargo of crystals, which are not in equilibrium with the melts.

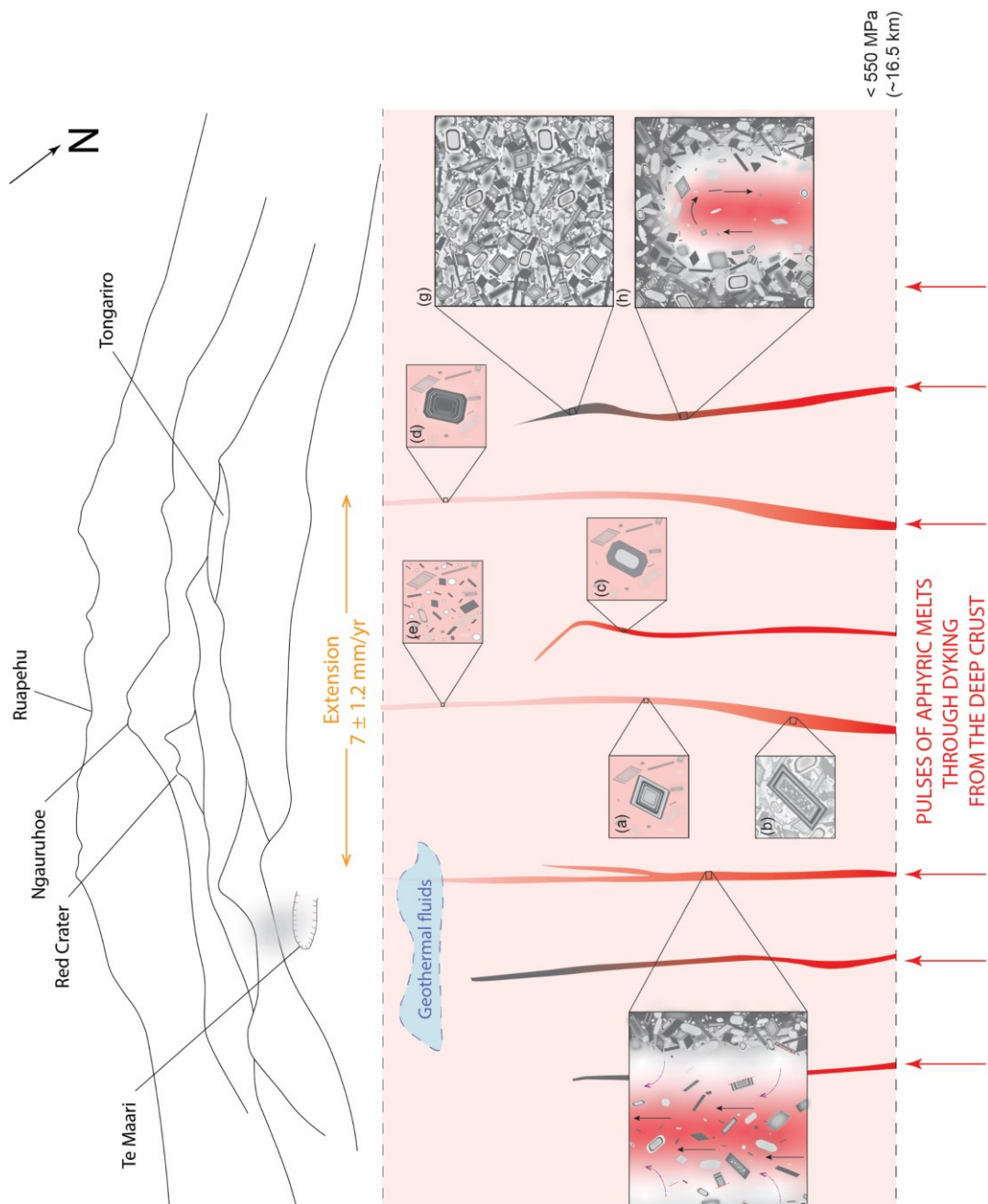
In the present study, different tephras from different sources all display similar textures and thus are all affected by similar magmatic processes, which indicates a commonality in time and space of the shallow magma plumbing systems allowing us to envisage a conceptual model (Figure 5.10). While previous studies described an interaction of ascending melts with crystal mush zones as a possible scenario beneath TgVC (Beier *et al.*, 2017; Kilgour *et al.*, 2013; Kilgour *et al.*, 2014; Nakagawa *et al.*, 1999; Shane *et al.*, 2008a; Shane *et al.*, 2017), the present observations and interpretations imply

a far more complex scenario, where crystals of differing histories, sizes and potentially ages developed and resided in intrusions of various states of solidification before being remobilised and picked up by a new and unusually hot (Lormand *et al.*, 2018a) injection of magma. Such a process was experimentally tested for crystal-rich magmas reaching high packing fraction, generating fracturing events when gas was injected into the system (Oppenheimer *et al.*, 2015). Similarly, a new injection of magma, which is travelling through previously intruded dykes, would trigger fracturing and entrainment of crystals.

This petrogenetic scenario is consistent with the texturally inferred (from the diversity of the crystal cargo) variability of magmatic processes, involving magma mixing and magma recharge due to frequent injections of small aphyric magma batches through dyking (Figure 5.10a), pressure and temperature fluctuations (Figure 5.10b), and rapid-cooling induced crystallisation (Figure 5.10c-d). Most of the intruded dykes would not reach the surface and thus, solidify in the upper crust. In this case, such intrusions coupled with an active hydrothermal system may be responsible for triggering phreatic eruptions such as the Upper Te Maari eruption in 2012 (Breard *et al.*, 2014; Lube *et al.*, 2014) and the heating cycles of Ruapehu's Crater Lake (Christenson *et al.*, 2010). Eventually, a larger crystal-poor magma injection will fracture upwards through this environment, recycling a wide spectrum of crystal textures while crystallising featureless microlites in equilibrium with the melt prior to ascent to the surface. This scenario is also consistent with the findings in Lormand *et al.* (2018a), which argues for dyke ascent of unusually hot aphyric magmas for the same range of eruptions at TgVC. More generally, studies of plutonic rocks have also identified a range of crystallisation processes occurring at depths through the mixed crystal populations: McCarthy and Müntener (2016; 2017), for instance, have associated the mineral and textural diversity of comb layering and orbicules found in the arc pluton of Fisher Lake, Sierra Nevada, USA, with individual

melt pulses within a shallow and vertical crustal reservoir. Similarly, the crystal cargo from the Tuolumne batholiths in Sierra Nevada, USA, found in multiple vertical structures (e.g. migrating tubes, pipes, diapirs), suggests the commonality of mixed crystal populations within subvolcanic chambers (Paterson, 2009). We reinforce the interpretation of the later study, which envisages that crystals within reservoirs (i.e. dykes here) form a framework and clusters that prevent chemical connection between the crystals and the freshly injected mafic melt, promoting mineral-liquid disequilibrium.

Figure 5.10. Conceptual model of the magma plumbing system feeding the explosive eruptions of the Tongariro Volcanic Centre. Considering the crustal extension of the TgVC at a rate of $c. 7 \pm 1.2$ mm/yr since 20 ka (Gómez-Vasconcelos *et al.*, 2017), we infer a vertical geometry, where magma ascends via dykes. The windows (a-h) are representative of processes occurring within the dykes and places randomly into the figure as examples. The various textures observed in microlites, micro-phenocrysts, and phenocrysts of the crystal cargos from TgVC intermediate magmas result from a variety of magmatic processes: (a) magma mixing, (b-c) pressure and temperature fluctuations, (d) high undercooling, and (e) shallow degassing-induced crystallization. Batches of aphyric magmas enter the upper crust through previously intruded semi-solidified dykes (g-h), which occasionally reach the surface, resulting in a wide variety of eruption styles. The phreatic eruption of Upper Te Maari and the heating cycles of Mt. Ruapehu's Crater Lake may be related to failed eruptions triggered by magma injections.



5.6. Conclusions

The Tongariro Volcanic Centre tephrae have crystal cargos with various and complex textures, recording a range of magmatic processes.

- A significant proportion (*c.* 10-40%) of microlite (< 30 μm) and micro-phenocryst (30-100 μm) rims from tephrae of the TgVC are not in chemical equilibrium with their surrounding glass.
- Micro-phenocrysts, and some microlites, display textural complexities that are similar in number and type to those commonly recorded by phenocrysts (> 100 μm). These complexities indicate that the small crystals have a growth history that is as complex as that of the larger crystals.
- Disequilibrium textures described in these small crystals are resorption and overgrowth, strontium zoning, oscillatory zoning, compositional jump without gradient, sector zoning, sieve textures and fractures. The most common textures found (*i.e.*, resorption and overgrowth, strontium zoning, oscillatory zoning and compositional jump without gradient) are attributed to magma mixing, multiple magma recharge events and recycling of crystals. None of these textures have previously been described in microlites from TgVC andesites, and some have never been described in microlitic or micro-phenocrystic crystals elsewhere.
- Remobilisation of microlitic and micro-phenocrystic crystal cargo implies uptake of crystals from fine grained intrusives, likely dykes that were previously injected into the subvolcanic system and solidified rapidly. This is opposed to the interpretation of uptake of antecrystic larger crystals, which is attributed to disaggregation of deep-seated magmatic mush zones with interstitial melts.
- Our data imply a complex subvolcanic system dominated by dyking events of small, sparsely phryic magma batches that solidify rapidly. In the extensional

setting of the TgVC, larger magma reservoirs that may contribute a few larger antecrysts ($> 100 \mu\text{m}$) to volcanic eruptives are likely restricted to the lower crust, e.g. a deep crustal hot zone. Eruptions occur when dykes reach the surface, carrying with them a largely antecrystic crystal cargo.

This study provides new insights into magmatic processes through micron-scale textures of crystal cargo. We infer that the use of high-resolution imaging technique such as elemental maps and SCAPS detectors in SIMS for microlites and micro-phenocrysts is relevant to link cryptic internal crystal structures and textures to the growth dynamics within magmatic system, as microlites typically appear simple, euhedral and featureless in conventional BSE images.

Chapter 6. Crystal Size Distributions and magma ascent rates

This chapter has been submitted and reviewed for publication in Journal of Petrology, under the title of “*Slow ascent of unusually hot intermediate magmas triggering Strombolian to sub-Plinian eruptions*” and was deemed acceptable pending minor revisions.

Participating authors:

- ✚ **Charline Lormand** (Massey University, New Zealand): sampling, sample preparation, data acquisition and processing, manuscript writing and editing
- ✚ **Georg F. Zellmer** (Massey University, New Zealand): manuscript editing and discussion
- ✚ **Geoff Kilgour** (GNS Science Wairakei, New Zealand): providing samples, manuscript editing and discussion
- ✚ **Károly Németh** (Massey University, New Zealand): assisting in the field, manuscript editing and discussion
- ✚ **Alan S. Palmer** (Massey University, New Zealand): assisting in the field, manuscript editing and discussion
- ✚ **Naoya Sakamoto** (Hokkaido University, Japan): assisting with sample preparation, data acquisition and data processing
- ✚ **Hisayoshi Yurimoto** (Hokkaido University, Japan): assisting with data acquisition, manuscript editing and discussion
- ✚ **Takeshi Kuritani** (Hokkaido University, Japan): assisting with data acquisition
- ✚ **Yoshiyuki Iizuka** (Academica Sinica, Taiwan): assisting with data acquisition
- ✚ **Anja Moebis** (Massey University, New Zealand): providing samples and assisting with sample preparation

Chapter content:

7.1. Introduction	155
7.2. Geological background and sample selection	157
7.3. Methods	162
7.3.1. Tephra sampling and image acquisition.....	162
7.3.2. Crystal Size Distributions (CSDs)	163
7.3.3. Compositional characterisation using Electron Probe Micro-Analysis (EPMA).....	165
7.3.4. Hygrothermobarometry.....	165
7.3.5. MELTS modelling	166
7.4. Results	167
7.4.1. Petrography	167
7.4.2. Texture and CSDs	167
7.4.3. Combining hygrothermobarometry and MELTS modelling to constrain magmatic P-T-X(H ₂ O) conditions	172
7.5. Discussion	178
7.5.1. Petrography and CSD shape	178
7.5.2. Microlite population growth time and plagioclase crystal growth rate	180
7.5.3. Unusually high temperature and quasi-anhydrous andesite magmas	184
7.5.4. Influence of regional tectonic setting and conduit geometry	187
7.5.5. Correlating geophysical signals and timescales.....	190
7.6. Conclusions	191

6.1. Introduction

Deciphering timescales and rates of magmatic and eruptive processes is critical for understanding volcanic eruption triggers and volcano monitoring, as well as to improve evacuation plans and hazard mitigation in anticipation of future eruptions (Cooper *et al.*, 2016; Finney *et al.*, 2003; Hughes & Hawkesworth, 2000; Kilgour *et al.*, 2014; Morgan *et al.*, 2004; Zellmer *et al.*, 2003b). Magma residence time, the interval between injection and expulsion of a magma batch, and magma ascent rate are two fundamental parameters to determine for a magmatic system. From minutes to thousands of years, residence times are commonly determined using chemical gradients in crystals (i.e. diffusion or geospeedometry; e.g. Costa *et al.*, 2003; Morgan *et al.*, 2004; Morgan & Blake, 2006; Zellmer *et al.*, 1999), using decay series disequilibria and isotopic dating (e.g. U-series; Black *et al.*, 1998; Bourdon *et al.*, 2000; Charlier *et al.*, 2000; Scheibner *et al.*, 2008; Turner *et al.*, 1996; Zellmer *et al.*, 2015b) and also by using textural tools such as analysis of crystal size distribution (CSD; e.g. Armienti *et al.*, 1994; Bindeman, 2003; Brugger & Hammer, 2010; Kile & Eberl, 2003; Mock & Jerram, 2005; Piochi *et al.*, 2005). Previous studies focusing on experimental petrology and crystal size distribution have indicated that magma ascent rates vary from 10^{-6} to 30 m s^{-1} (e.g. Armienti *et al.*, 1994; Befus *et al.*, 2015; Devine *et al.*, 1998; Lloyd *et al.*, 2014; Sano *et al.*, 2015) before accelerating near the surface due to volatile exsolution, late-stage degassing, and fragmentation (Taisne & Jaupart, 2011). Thus, ascent rates are thought to play a major role in modulating eruption style and dynamics. Several techniques have been used to estimate magma ascent rates, such as determining the thickness of breakdown rims around amphiboles (Buckley *et al.*, 2006; Rutherford & Hill, 1993), water speciation in andesitic melts (Ni *et al.*, 2009), and modelling elemental diffusion such as H_2O diffusion in melt inclusions (Humphreys *et al.*, 2008), lithium diffusion in feldspar and quartz revealing the final minutes of an

explosive super-eruption (Charlier *et al.*, 2012), and Ti-Fe interdiffusion in titanomagnetite (Morgado *et al.*, 2019). Geophysical work uses hypocentre propagation of seismic signals through time to determine ascent rates (Aki & Koyanagi, 1981; Endo *et al.*, 1996). Microlite textures and growth measurements compared with data from decompression experiments (Cashman, 1992; Geschwind & Rutherford, 1995; Martel, 2012) also provide estimates on magma ascent rates.

Microlites are small crystals arbitrarily defined as $< 100 \mu\text{m}$ in length (Murphy *et al.*, 2000) or $< 50 \mu\text{m}$ in width (McCanta *et al.*, 2007; Melnik *et al.*, 2011) or $< 30 \mu\text{m}$ (Castro & Mercer, 2004; Mujin *et al.*, 2017). Although the maximum size of microlites is not well-defined, it is widely accepted that their formation occurs in the conduit and is due to decompression-induced degassing during magma ascent (e.g. Befus *et al.*, 2015; Blundy *et al.*, 2006; Couch *et al.*, 2003; Geschwind & Rutherford, 1995; Hammer *et al.*, 1999; Hammer & Rutherford, 2002; Lipman & Banks, 1987; Nicholis & Rutherford, 2004; Pinkerton & Sparks, 1978; Swanson *et al.*, 1989). Previous studies have used microlite textures to infer eruptive styles (Martel & Poussineau, 2007; Szramek *et al.*, 2006; Wright *et al.*, 2012), thermal and degassing histories of lava flows (Lesher *et al.*, 1999), magma cooling rate and initial condition of magma ascent (Noguchi *et al.*, 2006; Noguchi *et al.*, 2008; Toramaru, 1991; Toramaru *et al.*, 2008), and undercooling ($\Delta T = T_m - T$, where T_m is the liquidus temperature) during decompression and cooling (Mollard *et al.*, 2012; Sano & Toramaru, 2017). The occurrence of microlites has also been used to infer timescales of magma ascent within the crust to the fragmentation level near the surface using microlite size distribution analysis (e.g. Cashman & Marsh, 1988; Castro *et al.*, 2003; Marsh, 1998a; Marsh, 1988; Pappalardo *et al.*, 2018).

Studying CSDs in volcanic rocks is one method to obtain an overview of the crystal population(s) and insights into the magmatic processes that lead to such a population.

While it is based on several assumptions such as the simplification of distribution of crystal shapes and the presence or absence of a fabric, it allows the calculation of the timescales of growth of a crystal population if the growth rate can be constrained (Cashman & Marsh, 1988; Higgins, 2002; Marsh, 1988; Morgan *et al.*, 2007; Muir *et al.*, 2011). Microlite CSD slopes have been correlated with eruption styles, where steeper CSD slopes (implying shorter residence times) have been associated with explosive eruptions, intermediate CSD slopes with Strombolian activity, and more gentle CSD slopes with lava effusions (Mastrolorenzo & Pappalardo, 2006).

In this study, we investigate petrographic, geochemical, and size distribution characteristics of microlites to characterize the timescales and P-T-X(H₂O) conditions of their formation and to constrain the dynamics of magma ascent at the onset of explosive volcanic eruptions of arc andesites, using deposits from the Tongariro Volcanic Centre (TgVC), located in the Southern Taupo Volcanic Zone, as an example. TgVC has produced a wide range of explosive eruption styles (Strombolian to Plinian eruptions) and may thus expose visitors of the highly frequented Tongariro Alpine Crossing to the risk of associated volcanic hazards (Jolly *et al.*, 2014). Thus, estimating the timescales and deciphering the pre- and syn-eruptive processes associated with TgVC eruptions is instructive for assessment of likely event scenarios.

6.2. Geological background and sample selection

The Tongariro Volcanic Centre in the North Island of New Zealand is part of an active volcanic arc and is composed of two major volcanoes, namely Ruapehu and Tongariro, with a large number of vents sites, including the prominent Ngauruhoe vent (Cole, 1978; Donoghue *et al.*, 1995; Topping, 1973). During the Holocene, TgVC activity produced frequent, well-documented and even observed volcanic events of differing

intensities and styles. Geological evidence from tephra deposit thickness and distribution show that eruptions from the TgVC have been Strombolian (e.g. the 1995 eruption of Ruapehu) to Plinian (e.g. the Mangamate eruptions) sized throughout its history. The complete stratigraphy of these volcanic events has been described in several previous studies (Auer *et al.*, 2015; Donoghue *et al.*, 1995; Donoghue & Neall, 1996; Moebis *et al.*, 2011; Nairn *et al.*, 1998; Nakagawa *et al.*, 1998; Topping, 1973; Topping & Kohn, 1973). The most recent eruption of the TgVC occurred during the night of 6 August 2012 after about three weeks of precursory seismicity (Hurst *et al.*, 2014), at the Upper Te Maari Crater, close to the track of the highly popular Tongariro Alpine Crossing trail (e.g. Breard *et al.*, 2014; Lube *et al.*, 2014; Procter *et al.*, 2014).

The tectonic setting of New Zealand and the TVZ has been thoroughly studied and elucidated, including its role in the volcanism of the TgVC (e.g. Ballance, 1976; Davey *et al.*, 1986; Karig, 1970; Lillie, 1980; Reyners, 1983; Smith *et al.*, 1989; Stern, 1987; Stern, 1985). Indeed, evidence of extension and dyking in the southern Taupo Volcanic Zone has previously been observed and explained (Gómez-Vasconcelos *et al.*, 2017; Gómez-Vasconcelos *et al.*, 2018; Villamor *et al.*, 2007): in this complex area, where normal faults and dyking are accommodating the rifting, the rate of crustal extension has been estimated to about 7.4 mm/yr during the last 20 ka (Gómez-Vasconcelos *et al.*, 2017).

The selection of tephtras studied here was based on the completeness of the stratigraphic description, the well-preserved aspect of the tephra layers, and the range of eruption styles. Five eruption sequences including a total of 22 tephtras were chosen for this study: three tephtra members of the Mangamate eruptive sequence (namely Te Rato, Wharepu and Ohinepango), ten tephtras from the Mangatawai Formation (mostly Ngauruhoe-sourced), three tephtra members from the Tufa Trig Formation (likely

Ruapehu-sourced), four tephra from the 1972-1975 eruptive period of Mt. Ngauruhoe, and two tephra from the 1995-1996 eruptions of Mt. Ruapehu (see Table 6.1 for more details and references). The Mangamate eruptive sequence is thought to have produced Plinian eruptions over a period of 200-400 years related to a regional extension event *c.* 9.5 ka ago (Nairn *et al.*, 1998; Nakagawa *et al.*, 1998). The three tephra members chosen from Mangamate, namely Te Rato, Ohinepango and Wharepu, were sourced from proto-Ngauruhoe, Saddle cone and Tama Lakes, respectively (Auer *et al.*, 2015). The Mangatawai Formation, ¹⁴C-dated at 3.52 cal. ka (Moebis *et al.*, 2011), was associated with the first and most intense eruptive period of Ngauruhoe, producing explosions up to sub-Plinian in size. The Tufa Trig Formation corresponds to the last 1.85 ka of volcanic activity of Ruapehu, consisting mainly of Strombolian style explosive eruptions and some small-volume, low energy phreatomagmatic and phreatic explosive eruptions (e.g. Donoghue *et al.*, 1997; Nakagawa *et al.*, 1998). Here, we focus on three members defined by Donoghue *et al.* (1995), namely Tf8, Tf13 and Tf14 (Table 6.1). Tf8 is one of the larger members of Tufa Trig with a volume of *< c.* 0.1 km³. Tf13 and Tf14 are smaller members, more representative of the entire eruptive sequence. The 1972-1975 eruptive period of Ngauruhoe was initially characterised by a series of semi-continuous small volume eruptions that culminated in a period of Vulcanian style eruptions between 1974 and 1975, associated with ash venting, and block and ash ejection, resulting in the formation of successive pyroclastic density currents through partial collapse of 3 to 7 km high eruptive columns (Hobden *et al.*, 2002; Lube *et al.*, 2007; Nairn & Self, 1978). Here, we refer to the entire eruptive period as “1972-1975”, including a total of 4 samples from 1972, 1973, 1974 and 1975. The 1995-1996 eruptive episode of Ruapehu was a combination of Strombolian, phreatomagmatic and sub-Plinian explosive events

(Christenson, 2000). The samples used for this study represent a sub-Plinian event with phreatomagmatism for the 1995 sample, and a Strombolian event for the 1996 sample.

Table 6.1. Descriptive table of the TgVC tephtras selected for this study. Plg, ens, pg, aug and ox stand for plagioclase, enstatite, pigeonite, augite and oxide, respectively.

Eruptive sequence	Age	Main eruption style	Source	Microlitic mineralogy	Crystal content (% 2D area)	Comments	References
Ruapehu 1995 - 1996 (2 samples)	1995 - 1996 AD	Strombolian, phreatomagmatic and sub-Plinian	Ruapehu	Plg + ens (1995) Plg + ens + pg + aug (1996)	5-36	Samples from the sub-Plinian phase in 1995 and ash and bomb explosion in 1996	Christenson, 2000
Ngauruhoe 1972 - 1975 (4 samples)	1972 - 1975 AD	Gas steaming, Strombolian and Vulcanian (Self 1974)	Ngauruhoe	Plg + pg ± aug*	14-24	Associated with steaming, block and ash ejections and flows, and eruptive columns	Nairn & Self, 1978; Hobden <i>et al.</i> , 2002
Tufa Trig (3 samples: Tf8, Tf13 and Tf14)	0 - 1.7 ka BP	Small volume Strombolian/phreatomagmatic	Ruapehu	Plg + ens	8-13	Rarely sub-Plinian, greater event every 100 years	Donoghue <i>et al.</i> , 1995; Donoghue <i>et al.</i> , 1997; Moebis <i>et al.</i> , 2011; Nakagawa <i>et al.</i> , 1998
Mangatawai (10 samples)	1.7 - 3.5 ka BP	Frequent, intermittent small explosive eruptions of up to sub-Plinian	Ngauruhoe	Plg + ens ± aug*	9-36	Deposit contains beech leaves	Donoghue <i>et al.</i> , 1995; Hobden <i>et al.</i> , 2002; Topping, 1973
Mangamate (3 samples: Te Rato, Wharepu and Ohinepango)	10 ka BP	Sub-Plinian to Plinian	Tongariro	Plg + ens ± ox	50	Large eruptions over a short period and from several vents along a fissure	Donoghue <i>et al.</i> , 1995; Nairn <i>et al.</i> , 1998; Nakagawa <i>et al.</i> , 1998

*rare

6.3. Methods

6.3.1. Tephra sampling and image acquisition

Tephra were sampled in the Tongariro National Park along Desert Road (SH1), State Highway 46 and near the vents (Figure 3.6). The glass shards were handpicked, polished, and mounted into epoxy plugs. BSE images of the glass shards were acquired using three different Scanning Electron Microscopes (SEM; Figure 6.1): (1) a Field Emission SEM with Energy Dispersive X-ray Spectrometers (FE-SEM-EDS; JEOL JSM-7000F with Oxford X-Max 150) at the Isotope Imaging Laboratory (IIL), Hokkaido University, Sapporo, Japan, using an accelerating voltage of 15 kV and a beam current of 13 nA; (2) an Environmental-SEM (FEI Quanta 200) at Massey University, Palmerston North, New Zealand, using an accelerating voltage of 20 kV and a beam current of 5 nA; and a JEOL NEOSCOPE 6000plus desktop SEM at GNS Science Wairakei Research Centre, Taupo, New Zealand, using an accelerating voltage of 10 kV and a high probe current of 20 nA. X-ray elemental mapping was conducted for pyroxene grains using the FE-SEM at Hokkaido University. Element maps of pyroxene were obtained for the following elements: Al, Ca, Cr, Fe, Mg, Na, Si and Ti.

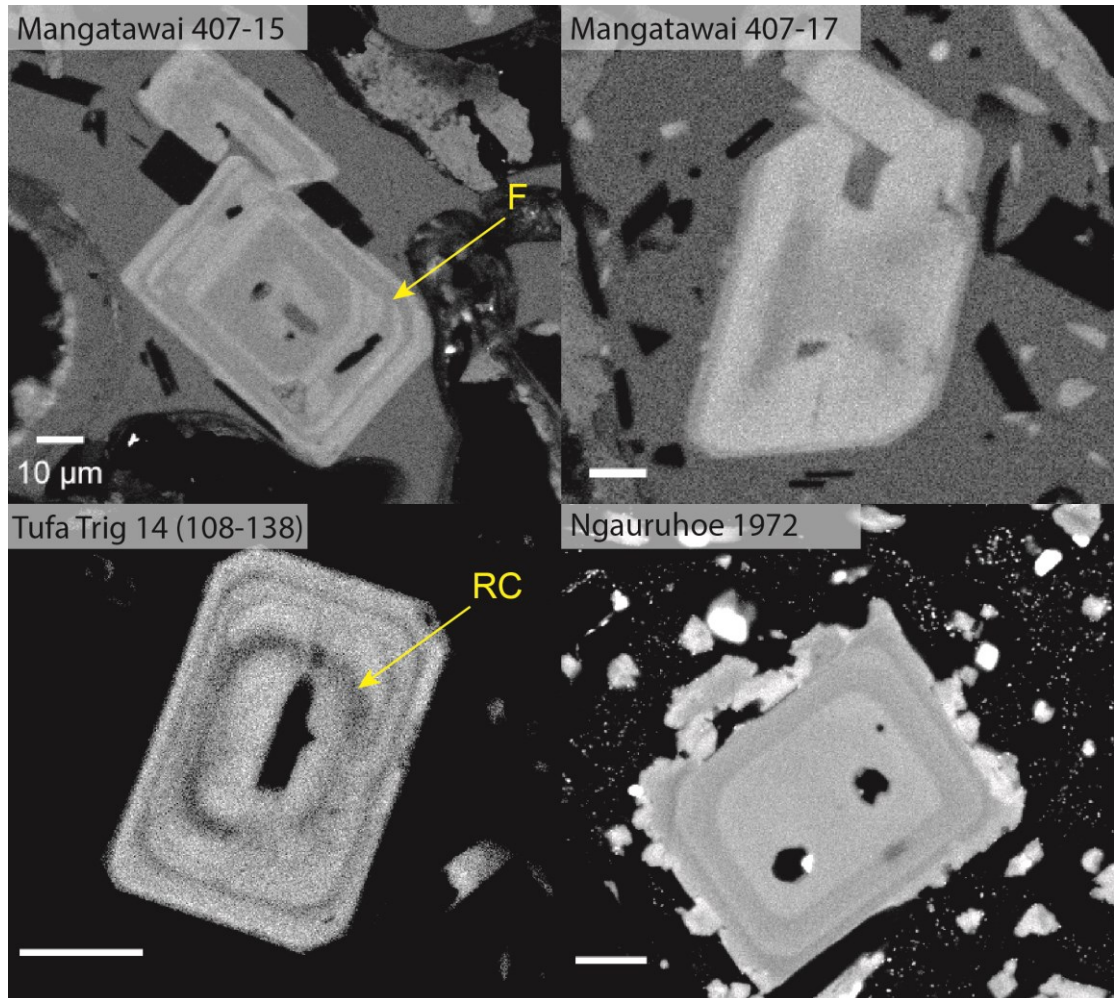


Figure 6.1. Fe-maps of some orthopyroxene microlites obtained using the FE-SEM JEOL JSM-7000F at the Isotope Imaging Laboratory of Hokkaido University in Sapporo, Japan. Note the resorbed cores and the complex zonations in iron (arrows) where RC and F stand for resorbed core and fracture, respectively. The scale of 10 μm is represented by a white bar at the left bottom corner of each image.

6.3.2. Crystal Size Distributions (CSDs)

Two-dimensional sections of separated tephra shards were imaged for measuring geometrical parameters of crystals (e.g. length, width, area), although generating CSDs implies the input of three-dimensional measurements, which are representative of the crystal 3D distribution within the rock. Using 3D direct measurements such as microtomography for textural purposes would be preferable (e.g. Jerram & Higgins, 2007; Jerram *et al.*, 2009; Mock & Jerram, 2005), but because measuring a large dataset

of microlites was required for the present work, 2D imaging was the method of choice. Besides, x-ray microtomography of microlites would also pose resolution issues (Jerram & Higgins, 2007). Computing 3D values from 2D measurements involves two effects that need to be corrected for: (1) the intersection probability, expected because a random 2D slice section is less likely to intersect a small crystal than a large one and (2) the cut-section effect, which produces slices of crystal of various orientations and dimensions, because a crystal is rarely cut through its centre (Brugger & Hammer, 2010). Crystals measurements of individual glass shard from the same tephra were combined and retrieved using *ImageJ*, which provides 2D length and width of binary images previously segmented following the method of Lormand *et al.* (2018b). This technique uses the FastRandomForest algorithm to classify the BSE images of glass shards according to pixel greyscale. The accuracy performance tests of this classifier for two glass shards from the Mangamate and Mangatawai Formations yield F-scores (i.e. the precision-recall measure) above 0.93, which we trust to use for this study. We then input the crystal measurements of microlites (2D length of 1-30 μm) into the Excel database *CSDSlice* of Morgan & Jerram (2006), which compares the aspect ratio of the measurements with those from a database composed of 703 random slices of known crystal shapes and determines the best fit crystal habits for the observed crystal population. By thresholding the 2D input parameters between 1 and 30 μm , we minimised the effect of (1) nanolites (Mujin & Nakamura, 2014), which may have grown under more extreme undercooling than microlites and thus would be expected to have a different morphology, dictated by higher surface area to volume ratio of the crystal lattice; and (2) the effect of microphenocrysts and phenocrysts which have grown previously, thus, representing deeper processes than those recorded by the microlites. We accept the inherent assumption of having a single set of shape factors applied to the entire microlite population of one

tephra. Finally, the software *CSDCorrections* (version 1.6; Higgins, 2000) was used to convert apparent crystal dimensions to 3D crystal shapes by integrating corrections of the intersection probability effect and the cut-section effect. For this, our samples contained no perceptible fabric, and a visual inspection indicated a roundness factor of 0.1 for all samples.

6.3.3. Compositional characterisation using Electron Probe Micro-Analysis (EPMA)

Glasses and mineral compositions from Mangatawai and Tufa Trig were analysed at the Institute of Earth Sciences, Academia Sinica, Taipei, Taiwan, using a JEOL JXA-8900R electron microprobe equipped with four wavelength-dispersive spectrometers. An acceleration voltage of 15 kV and a 2 μm defocused beam with a current of 12 nA were set for the analyses. Glasses and mineral compositions from the 1972-1975 Ngauruhoe eruptions and the 1995-1996 Ruapehu eruptions were analysed at the Graduate School of Science, Hokkaido University, Sapporo, Japan, using a JEOL JXA-8800R electron microprobe equipped with four wavelength-dispersive spectrometers. An acceleration voltage of 15 kV and a 10 μm defocused beam with a current of 7 nA for glass was set for the analyses. The same acceleration voltage conditions were used with a spot beam and a current of 10 nA for plagioclase and 20 nA for pyroxenes rims. The microlites selected for these analyses were homogeneous in the BSE image and did not show any zonation. No glass and mineral compositions were measured for the Mangamate eruptive sequence.

6.3.4. Hygrothermobarometry

To gain a better understanding of the magmatic and eruptive processes of the eruptions studied, water content, temperature and pressures during microlite crystallisation are essential parameters to determine. Equilibria were determined using

the orthopyroxene-liquid and the clinopyroxene-liquid thermobarometers from Putirka (2008). From the microlites in equilibrium with the glass, those in equilibrium with most compositions from the range analysed were selected. We then iteratively calculated water contents of the melt during crystallisation using plagioclase hygrometry, which is P-T dependent (Waters & Lange, 2015), and pressures and temperatures using pyroxene-liquid thermobarometry, which is affected by liquid H₂O content (Putirka, 2008).

6.3.5. MELTS modelling

Guided by the hydrothermobarometric results, the software *MELTS* (Asimow & Ghiorso, 1998; Ghiorso & Sack, 1995) was used to more tightly constrain pressure, temperature and water content during crystallisation through forward-modelling the observed microlite phase assemblage and compositions. The version *alphaMELTS* 1.9 was used as it was the latest version available at the time of modelling for mafic to intermediate magmatic systems, and it is appropriate for our study as it does not require modelling of volatile exsolution such as conducted in *rhyoliteMELTS*. To assess whether spinel would crystallize from the magmas, we first used the software *Spinmelts* (Nikolaev *et al.*, 2018a; <https://comagmat.web.ru/apps-spinmelt.html>; Nikolaev *et al.*, 2018b) as *MELTS* tends to overestimate the spinel liquidus temperatures. All tephra were modelled using fractional crystallisation at 0, 0.5, 1, 1.5 and 2 wt% water for pressures ranging from 0.1 to 800 MPa at 25 MPa intervals. We used glass compositions as starting material (see Appendix C10) and manually suppressed spinel crystallisation. Oxygen fugacity was buffered at NNO (i.e. nickel-nickel-oxide), based on agreement with previous studies of the TgVC magmas (Arpa *et al.*, 2017; Kilgour *et al.*, 2013; Kilgour *et al.*, 2014; Kilgour *et al.*, 2016; Shane *et al.*, 2008a).

6.4. Results

6.4.1. Petrography

Glass shards generally present abundant euhedral microlites ($< 30 \mu\text{m}$) and scarce subhedral to anhedral micro-phenocrysts ($> 30\text{-}100 \mu\text{m}$) of plagioclase and pyroxene. All tephra are dominated by orthopyroxene (i.e. enstatite; opx) over clinopyroxene, except the 1972-1975 Ngauruhoe eruptions and the 1996 Ruapehu eruption, which contain a larger proportion of clinopyroxene. In most of the other glass shards, antecrysts or xenocrysts of clinopyroxene can also be found (see Appendix B14). The 2-dimensional crystal contents by area vary between c. 20 % and 50 %. However, when excluding all the 2-dimensional measurements above the microlite size threshold (i.e. $< 30 \mu\text{m}$), the proportion of microlites completely surrounded by melt range from 8 % to 24 %, with an average of 15 %. The plagioclase proportion is consistently greater than that of the pyroxene, averaging 11 % and 5 %, respectively. The pyroxene microlites are generally smaller (2D length of c. 4 to 7 μm), but almost as abundant as plagioclase microlites (2D length of c. 6 to 10 μm). Crystals larger than 30 μm display complex zoning patterns observed through chemical mapping, and are then classified as micro-phenocrysts. Some micro-phenocrysts contain resorption patterns or evidence of fracturing events (Figure 6.1). BSE images of plagioclase micro-phenocrysts also show evidence of complex zoning (see Chapter 6). Thus, micro-phenocrysts are excluded from the following findings.

6.4.2. Texture and CSDs

A total of 42 CSDs (i.e. 20 pyroxene CSDs and 22 plagioclase CSDs; see Appendix A3 for an example of CSD generation) of volcanic tephra involving more than 60,000 crystals of plagioclase and pyroxene were segmented to generate CSDs (Figures 6.2 and

6.3). Pyroxene CSDs were not performed for Te Rato and Wharepu from the Mangamate Formation as the free hornblende, which was reported as a microlite phase in a previous study (Nakagawa *et al.*, 1998), was not distinguishable from the pyroxene in BSE images. CSD output parameters, including number of crystals, shape factors, coefficient of determination (R^2), and crystal content, are reported in Table 6.2. Due to the complex zonations and the possible antecrystic or xenocrystic origin of the micro-phenocrysts (Figure 6.1 and Chapter 5), a 2D length cut-off of the crystal measurements of 1-30 μm was chosen. There are no concerns regarding the potential impingement of crystals, because the microlite contents do not exceed 24% in any tephra. The R^2 values of the shape factors vary from 0.79 to 0.84 for pyroxene and from 0.77 to 0.87 for plagioclase, with averages of 0.82 for both mineral phases. Most CSDs exhibit sublinear curves, with some showing a change of slopes at c. 10 μm . Downturn at smallest size ($< 10 \mu\text{m}$) is sporadic for the studied populations. Broader variations in CSD slopes and curvatures are distinguishable for Mangatawai, 1972-1975 Ngauruhoe, and 1995-1996 Ruapehu, in both plagioclase and pyroxene, and for Mangamate plagioclase CSDs. No correlation between CSD slopes and eruption styles is observed (Figure 6.4), which is consistent with the CSD and compositions results for Shinmoedake (Kirishima volcano) eruption in 2011 (Mujin & Nakamura, 2014). *CSDCorrections* return volume percentages varying from 2.3 to 15.1 vol. % for pyroxene and from 8.9 to 35.2 vol. % for plagioclase, resulting in microlite 3D contents (i.e. pyroxene and plagioclase) between 11.8 vol. % and 44.3 vol. %.

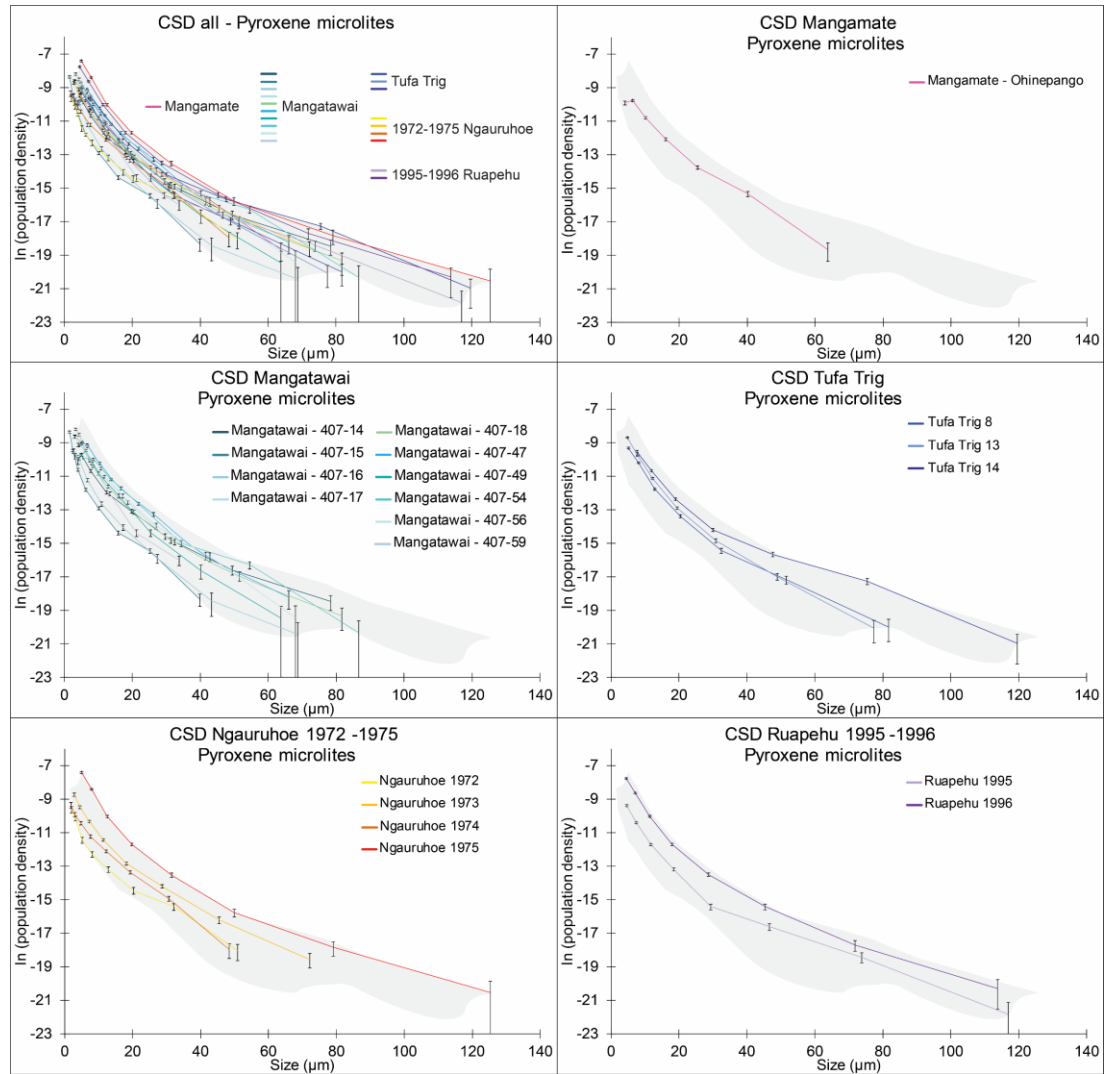


Figure 6.2. Pyroxene crystal size distributions (logarithm of the population density versus the size in μm) of various historical tephra from the Tongariro Volcanic Centre, New Zealand. The grey field represents the full range covered by the CSD plots. CSD parameters such as the number of crystals, the best fit shape factors for the studied crystal population and their associated coefficient of determination obtained with *CSDslice* (Morgan & Jerram, 2006), and the crystal content from *CSDCorrections* (Higgins, 2000) are reported in Table 6.2.

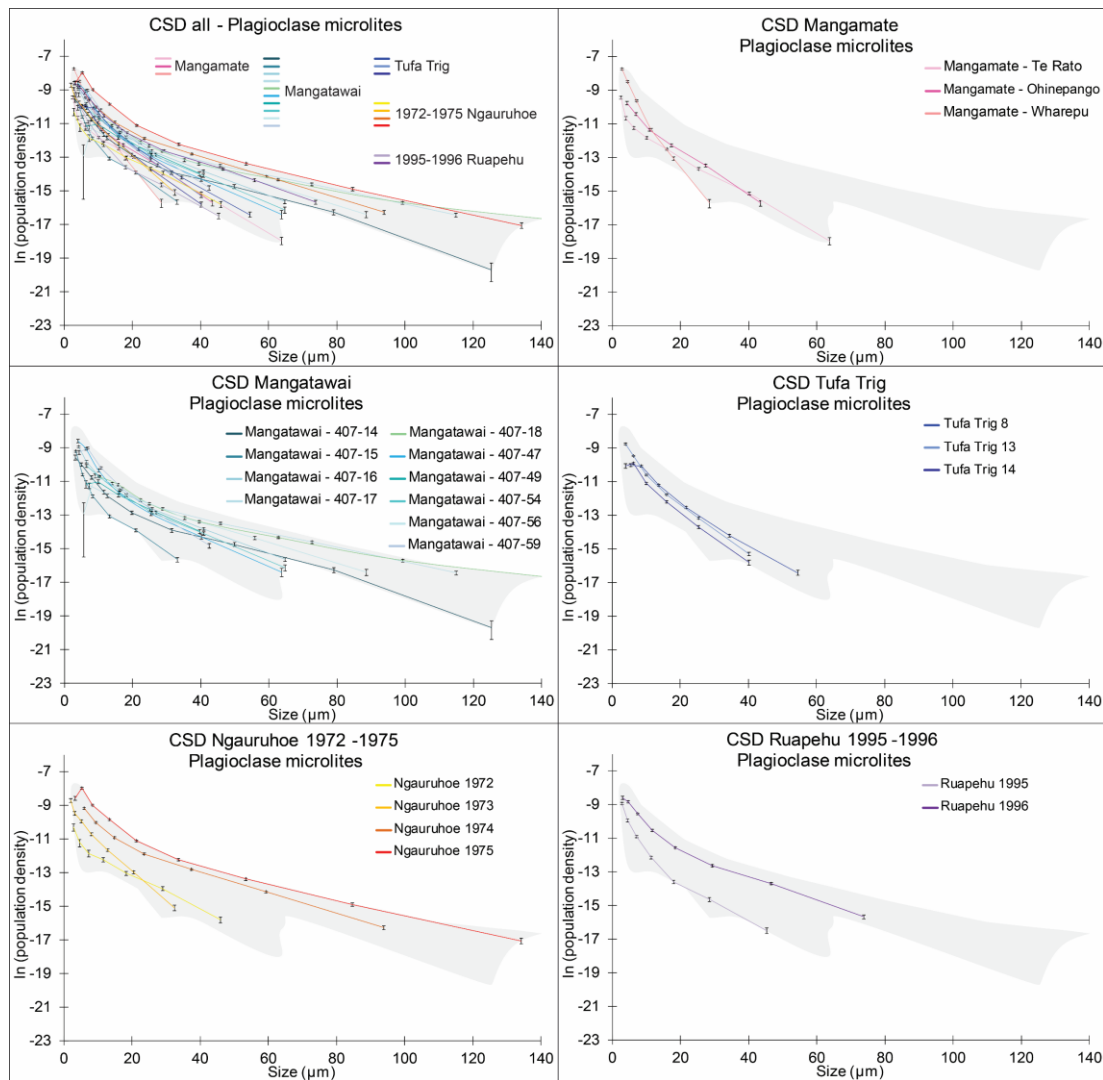


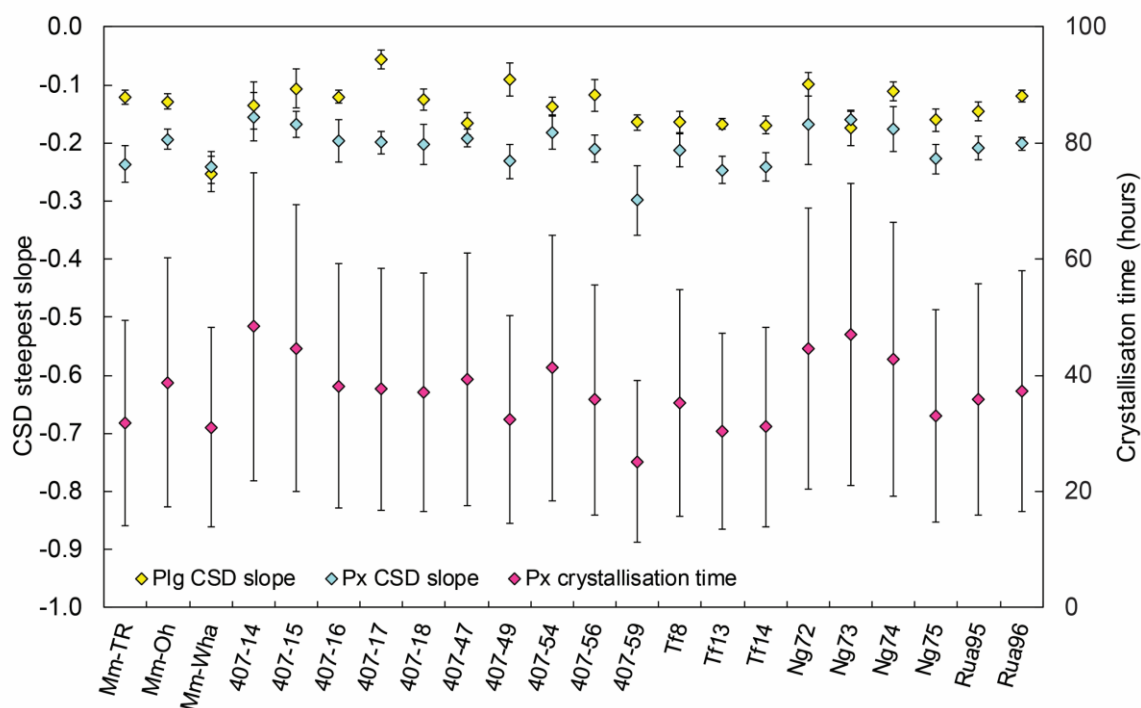
Figure 6.3. Plagioclase crystal size distributions (logarithm of the population density versus the size in μm) of various historical tephra from the Tongariro Volcanic Centre, New Zealand. The grey field represents the full range covered by the CSD plots. CSD parameters such as the number of crystals, the best fit shape factors for the studied crystal population and their associated coefficient of determination obtained with *CSDslice* (Morgan & Jerram, 2006), and the crystal content from *CSDCorrections* (Higgins, 2000) are reported in Table 6.2.

Table 6.2. CSD parameters for TgVC pyroxene and plagioclase microlite populations, i.e. the number of crystals considered for CSD generation, the best fit shape factors and the associated coefficient of determination retrieved from *CSDslice* (Morgan & Jerram, 2006), and the crystal content (vol. %) calculated by *CSDCorrections* (Higgins, 2000).

Glass shard	Number of crystals				Shape factors								R ²				Crystal content from CSD (vol. %)			
	Pyroxene		Plagioclase		Pyroxene				Plagioclase				Pyroxene		Plagioclase		Pyroxene		Plagioclase	
	x	y	z	x	y	z	x	y	z	x	y	z	Content	σ	Content	σ	Content	σ		
Te Rato	N/A	N/A	N/A	1	1.40	2.8	1	1.40	2.8	N/A	N/A	0.84	N/A	N/A	15.7	1.6	N/A	N/A	1.6	
Ohinepango	1158	989	1	1.40	2.8	2.7	1	1.25	2.7	2.8	2.7	0.84	15.1	2.0	14.6	1.3	15.1	2.0	1.3	
Wharepu	N/A	2078	N/A	N/A	1	1.20	1.7	1.40	1.7	N/A	N/A	0.78	N/A	N/A	15.3	1.4	N/A	N/A	1.4	
407-14	666	709	1	1.30	3.2	5.5	1	1.40	5.5	3.2	5.5	0.82	9.8	2.1	16.1	2.6	9.8	2.1	2.6	
407-15	1208	1448	1	1.20	1.5	2.3	1	1.40	2.3	1.5	2.3	0.83	4.6	0.7	21.2	1.5	4.6	0.7	1.5	
407-16	500	2118	1	1.30	2.8	4.5	1	1.40	4.5	2.8	4.5	0.81	2.3	0.7	25.5	2.0	2.3	0.7	2.0	
407-17	1046	1048	1	1.20	2.8	8.0	1	1.40	8.0	2.8	8.0	0.80	9.1	1.0	35.2	3.2	9.1	1.0	3.2	
407-18	1236	1596	1	1.25	3.2	9.0	1	1.15	9.0	3.2	9.0	0.81	9.6	1.8	25.3	5.2	9.6	1.8	5.2	
407-47	1299	985	1	1.40	2.9	3.0	1	1.50	3.0	2.9	3.0	0.82	8.9	1.8	20.8	4.3	8.9	1.8	4.3	
407-49	645	542	1	1.50	3	5.0	1	1.60	5.0	3	5.0	0.79	8.7	1.8	11.8	1.2	8.7	1.8	1.2	
407-54	995	973	1	1.40	3.8	4.5	1	1.40	4.5	3.8	4.5	0.84	7.2	1.9	11.9	2.1	7.2	1.9	2.1	
407-56	954	735	1	1.50	3.2	5.5	1	1.25	5.5	3.2	5.5	0.82	13.9	2.5	28.9	3.4	13.9	2.5	3.4	
407-59	1091	1568	1	1.25	2.1	3.8	1	1.80	3.8	2.1	3.8	0.83	9.8	1.4	24.0	2.2	9.8	1.4	2.2	
Tufa Trig 8	1649	2221	1	1.25	3.2	3.8	1	1.40	3.8	3.2	3.8	0.82	7.1	1.1	14.1	1.1	7.1	1.1	1.1	
Tufa Trig 13	3223	3728	1	1.40	3.4	2.8	1	1.40	2.8	3.4	2.8	0.82	9.1	1.0	19.0	1.2	9.1	1.0	1.2	
Tufa Trig 14	1923	1371	1	1.20	4.5	3.6	1	1.80	3.6	4.5	3.6	0.82	10.4	1.4	13.6	1.6	10.4	1.4	1.6	
Ngauruhoe 1972	305	429	1	1.25	2	3.2	1	1.40	3.2	2	3.2	0.83	7.0	1.7	13.9	2.5	7.0	1.7	2.5	
Ngauruhoe 1973	1112	1134	1	1.15	2.6	2.1	1	1.30	2.1	2.6	2.1	0.82	13.2	2.2	14.9	1.5	13.2	2.2	1.5	
Ngauruhoe 1974	748	2921	1	1.25	1.9	7.0	1	1.50	7.0	1.9	7.0	0.84	12.4	1.9	24.3	2.3	12.4	1.9	2.3	
Ngauruhoe 1975	2335	2764	1	1.40	5.5	10.0	1	1.50	10.0	5.5	10.0	0.82	10.3	2.5	27.6	3.6	10.3	2.5	3.6	
Ruapehu 1995	1326	1229	1	1.50	5.5	3.6	1	1.60	3.6	5.5	3.6	0.84	3.0	0.6	8.9	1.3	3.0	0.6	1.3	
Ruapehu 1996	2716	2480	1	1.40	5	5.5	1	1.50	5.5	5	5.5	0.82	12.4	1.7	28.5	2.2	12.4	1.7	2.2	
Total	26135	34908											9.2	1.6	19.6	2.2	9.2	1.6	2.2	
Average	1307	1587	1	1.33	3.2	4.5	1	1.43	4.5	3.2	4.5	0.82	3.4		6.9		3.4			
Standard deviation (2σ)	741	852.26		0.11	1.1	2.2		0.17	2.2	1.1	2.2	0.01								

N/A: not analysed because the classifier could not differentiate pyroxene from hornblende in BSE images

Figure 6.4. Pyroxene and plagioclase CSD slopes (left y-axis), and residence time (right y-axis) derived from the slope and a well-constrained growth rate. Plagioclase CSD slopes are indicated by yellow diamonds, orthopyroxene CSD slopes by light blue diamonds. Residence time calculated from the pyroxene slopes and an orthopyroxene growth rate determined for Mangatawai 407-17 (Zellmer *et al.*, 2016c; Zellmer *et al.*, 2018), are represented by magenta triangles. As orthopyroxene and plagioclase were crystallising concomitantly, a plagioclase growth rate range is derived ($1.65 \times 10^{-11} \text{ m s}^{-1}$ to $6.43 \times 10^{-11} \text{ m s}^{-1}$). Mm, TR, Oh, Wha, Ng, Rua respectively stand for Mangamate, Te Rato, Ohinepango, Wharepu, Ngauruhoe and Ruapehu.



6.4.3. Combining hygrothermobarometry and MELTS modelling to constrain magmatic P-T-X(H₂O) conditions

The glass data for the analysed tephra are mostly andesitic. All the Mangatawai and Tufa Trig glass compositions are andesitic, whereas 1972-1975 Ngauruhoe and 1995-1996 Ruapehu glasses are andesitic to dacitic in composition (see Figure 6.2a; Le Bas *et al.*, 1986; Le Maitre, 2005). The 1972 Ngauruhoe glasses are all andesitic, while those of the 1973 eruption are andesitic and dacitic. The 1974 and 1975 Ngauruhoe glasses, however, fall into the dacite field. The 1995 and 1996 eruption deposits from Ruapehu have similar dacitic glass composition.

A total of 238 pyroxenes, 460 plagioclases and 117 glass compositions were analysed (see Appendices C11, C12 and C13). The plagioclase X_{An} and pyroxene Mg# range from 0.59 to 0.87 and from 13 to 49, respectively. From the pyroxene analysed, 82 % are orthopyroxenes, 13% are clinopyroxenes (augite and diopside) and 5% are pigeonites. Only pigeonites were found for Ngauruhoe 1973 and Ngauruhoe 1974 products.

Among 75 pyroxene microlite compositions implemented in the thermobarometers, 19 were not in equilibrium (i.e. $K_D(\text{Fe-Mg})^{\text{opx-liq}} \neq 0.29 \pm 0.06$ and $K_D(\text{Fe-Mg})^{\text{cpx-liq}} \neq 0.27 \pm 0.03$) with a range of glass compositions from the same tephra. Equilibrium for seventy three plagioclase microlite compositions was also assessed and resulted in eight microlites that were not in equilibrium (i.e. $K_D(\text{An-Ab})^{\text{plg-liq}} \neq 0.27 \pm 0.11$) with a range of glass compositions. Crystal-glass pairs in equilibrium yielded temperatures ranging from 1078 °C to 1149 °C (SEE = ± 39 °C; see Figure 6.5a-b, and Table 6.3). Hygrometer-derived water contents at plagioclase crystallisation varied from -0.92 wt% to +0.26 wt% (SEE= ± 0.35 wt%) with an average of -0.19 wt%. Negative water contents are an artefact of the calculation method used in the hygrometer (Waters & Lange, 2015) and thus, these results simply imply very low water contents (i.e. anhydrous). Ngauruhoe 1973 and 1974 are not included, as the pyroxenes measured are pigeonites, which do not permit thermobarometric constraints. Due to the large uncertainties of thermobarometry and hygrometry, we employ *MELTS* modelling to assess permissible P-T-X(H₂O) conditions, although this assumes equilibrium in what may be a dynamic environment with changeable conditions.

Those *MELTS* runs that led to crystallisation of the observed (and only the observed) mineral phases (i.e. orthopyroxene and/or clinopyroxene and/or pigeonite, and plagioclase feldspar) were regarded as returning permissible conditions, reported in Table 6.3. Mineral compositions produced by *MELTS* overlap with the range of analysed

compositions. Generally, pyroxene and plagioclase appear concomitantly in the system, although pyroxene appears at slightly greater pressure than plagioclase in some cases. *MELTS* modelling narrows the range in temperatures, water contents, and pressures compared to using hygrometry alone (Figure 6.5c-d). The permissible pressures range from 0.1 MPa to 550, with an average of *c.* 140 MPa (i.e. *c.* 4 km). The permissible temperatures vary between 1005-1130 °C, with an average of 1076 °C. The permissible water contents are between 0.00 wt% (i.e. anhydrous) and 1.50 wt%, with an average of 0.40 wt% H₂O. The Mangatawai magmas were generally crystallising microlites at lower pressures (average of 105 MPa, *c.* 3 km) but higher temperatures (average of *c.* 1090 °C) and thus lower water contents (average of *c.* 0.20 wt% H₂O) than the Tufa Trig (averages of *c.* 180 MPa, i.e. *c.* 5.5 km, 1050 °C and 0.60 wt% H₂O), the 1972 and 1975 Ngauruhoe magmas (averages of *c.* 270 MPa, i.e. *c.* 8 km, 1050 °C and 0.50 wt% H₂O), and the 1995-1996 Ruapehu magmas (averages of *c.* 180 MPa, i.e. *c.* 5.5 km, 1040 °C and 0.70 wt% H₂O). No permissible case was found for 2.00 wt% H₂O and no *MELTS* runs were performed for the 1973 and the 1974 Ngauruhoe magmas, because no constraints could be retrieved from hygrometry for pigeonite (Putirka, 2019). According to *MELTS* modelling, decompression-induced exsolution of water from the investigated samples starts between 3 and 33 MPa (i.e. between *c.* 100 m and *c.* 1 km below the surface).

Figure 6.5. P-T-X(H₂O) plots retrieved from hydrothermobarometry (Putirka, 2008; Waters & Lange, 2015) and *MELTS* modelling (Asimow & Ghiorso, 1998; Ghiorso & Sack, 1995) for the TgVC deposits studied. Parameters for *MELTS* were fixed at 0, 0.5, 1, 1.5 and 2 wt.% for the water contents and from 0.1 to 800 MPa at 25 MPa intervals for pressures. Grey plots in (c) and (d) are copies of plots in (a) and (b). Note that *MELTS* data points (plots c and d) indicate the average (in color) and their range (i.e. not uncertainties).

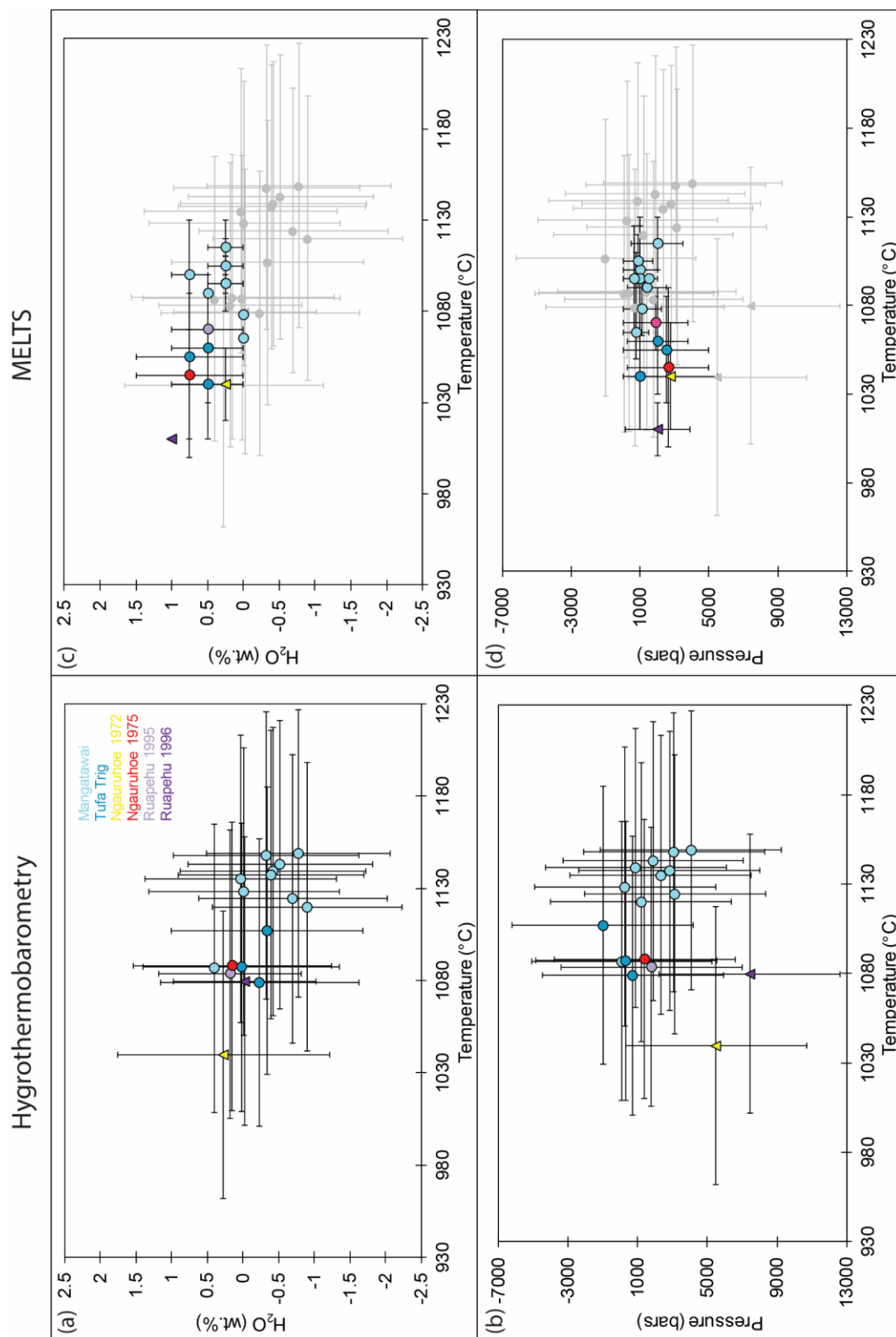


Table 6.3. (Table in the next page) Temperature (T), pressure (P), and water content (H₂O) ranges of crystallisation obtained from hygrometry and MELTS for the TgVC tephra. The temperatures and pressures were calculated using the orthopyroxene-liquid thermometer of Putirka (2008), namely the Eq. 28a and Eq. 29a (SEE=39 °C and SEE=±210 MPa), and the clinopyroxene-liquid thermometer from Putirka (2008; Eq. 33) and the clinopyroxene-liquid barometer of Neave & Putirka (2017) for Ng72* (SEE=±45 °C and SEE=±140 MPa). The water content was determined by the plagioclase hygrometer (SEE=±0.35 wt. %; Waters & Lange, 2015). Guided by the hygrometric results, *MELTS* modelling was performed (Asimow & Ghiorso, 1998; Ghiorso & Sack, 1995). The temperatures, pressures and water contents reported correspond to ranges for which *MELTS* successfully reproduce the minerals observed. The maximum ascent rates were calculated using the minimum residence time derived from the CSD slope and a well-constrained orthopyroxene growth rate (Zellmer et al., 2016c; Zellmer et al., 2018), and the maximum depth derived from hygrometry and *MELTS* modelling. Mangatawai Formation: 407-14 to 407-59. Tf, Ng and Rua stand for Tufa Trig, Ngauruhoe and Ruapehu, respectively.

Sample	Hygrothermobarometry				MELTS				Ascent rate max (cm.s ⁻¹)
	T (°C)	P (MPa)	H ₂ O (wt. %)	T (°C)	P (MPa)	H ₂ O (wt%)*	T (°C)		
407-14	1147	308	-0.35	1090	25-250	0.5	1090	2.7	
407-15	1124	233	0.02	1060-1100	0.1-200	0.5-1.0	1060-1100	2.4	
407-16	1135	313	-0.87	1080	0.1-225	0	1080	3.2	
407-17	1124	90	-0.21	1080-1110	0.1-150	0.0-0.5	1080-1110	2.2	
407-18	1139	406	-0.17	1100-1130	0.1-300	0.0-0.5	1100-1130	4.8	
407-47	1149	189	-0.62	1080-1110	0.1-200	0.0-0.5	1080-1110	2.8	
407-49	1120	119	-0.92	1065	0.1-150	0	1065	2.5	
407-54	1129	26	-0.03	1090-1120	0.1-175	0.0-0.5	1090-1120	2.3	
407-56	1137	281	-0.41	1080-1110	0.1-125	0.0-0.5	1080-1110	1.9	
407-59	1087	80	0.38	1080-1110	0.1-300	0.0-0.5	1080-1110	6.4	
Tufa Trig 8	1106	-99	-0.34	1030-1090	25-375	0.0-1.0	1030-1090	5.6	
Tufa Trig 13	1078	71	-0.25	1005-1065	0.1-200	0.0-1.0	1005-1065	3.5	
Tufa Trig 14	1087	33	0.00	1010-1100	0.1-500	0.0-1.5	1010-1100	8.7	
Ngauruhoe 1972	1040	549	0.26	1020-1060	0.1-550	0.0-1.0	1020-1060	6.7	
Ngauruhoe 1975	1088	138	0.13	1030-1090	25-500	0.0-1.0	1030-1090	2.0	
Ruapehu 1995	1083	178	0.16	1040-1100	0.1-375	0.0-1.0	1040-1100	1.9	
Ruapehu 1996	1080	743	-0.04	1010	0.1-350	1	1010	1.8	
Average	1109	215	-0.19	1076	141	0.4	1076	3.6	

6.5. Discussion

6.5.1. Petrography and CSD shape

The TgVC magmas are composed of two crystal populations of pyroxene and plagioclase, where the largest ($> 30 \mu\text{m}$) are complexly zoned and the smallest ($< 30 \mu\text{m}$) are microlites that grew from the melt during ascent. This combination of crystal populations (i.e. abundant microlites and less abundant zoned micro-phenocrysts) in the same magma have also been described in andesites in previous studies (e.g. Cashman & Blundy, 2000; Higgins & Roberge, 2003), and the origin of the micro-phenocrysts has been associated with crystallisation at higher pressures. The largest crystals have developed complex oscillatory zonings and resorption patterns which could be due to pressure fluctuations and/or multiple decompression steps (Zellmer *et al.*, 2003b). Alternatively, oscillatory zoning could also be the result of a series of cooling and heating events (Bergantz *et al.*, 2015; Couch *et al.*, 2001), likely to have occurred during long residence times. Considering the complex zoning, an antecrystic or xenocrystic origin for the micro-phenocrysts is likely. Fe-Mg interdiffusion in orthopyroxene is extremely slow (Cherniak & Dimanov, 2010), and at magmatic temperatures of *c.* 1100 °C, as determined for these magmas, diffusion lengthscales of $> 1 \mu\text{m}$ would require more than a month to be achieved, and the sharp compositional zoning observed in Figure 6.1 suggests that these crystals experienced high temperatures for shorter periods of time, and were likely kept in cold storage. The complexity of the zoning patterns (Chapter 5) indicate that these crystals did not grow in response to rapid decompression in the hours or days before the eruption. Thus, we infer that the micro-phenocrysts are old and were picked up by hot, initially aphyric magmas during their ascent (Humphreys *et al.*, 2016; Zellmer *et al.*, 2016a), whereas the microlites grew during magma ascent from mid-crust to the surface.

CSDs of plagioclase and pyroxene microlites yield unexpected similarities for eruptions of a wide range of eruption styles (e.g. Strombolian for Tufa Trig to Plinian for Mangamate) and from different sources. The concave-up shape of the CSDs has previously been associated with changes of crystal growth, cooling rate (Marsh, 1988) and dissolved water during ascent (Armienti *et al.*, 1994), or with a complex crystallisation history such as crystal accumulation and crystal removal (Marsh, 1998a). It was then attributed to textural coarsening (Armienti *et al.*, 1994), and to mixing of crystal populations (Jerram *et al.*, 2003; Turner *et al.*, 2003). Recent studies interpreted this shape as a consequence of crystallisation by decompression, triggering a rapid change in undercooling (Brugger & Hammer, 2010; Fornaciai *et al.*, 2015; Shea *et al.*, 2010a). The change of slope towards the smallest crystals (i.e. $< 10 \mu\text{m}$) is related to the late-stage crystallisation of nanolites under extreme undercooling (Mujin & Nakamura, 2014; Mujin *et al.*, 2017). We interpret that the change of slope towards the largest crystals (i.e. $> 30 \mu\text{m}$) for TgVC magmas, is related to scavenging of micro-phenocrysts, which, as mentioned earlier, have not crystallised during ascent. The downturn at smaller size is not common and is often accompanied with larger error bars. It was previously described as the result of the intersection artefact when converting 2D to 3D measurements, ripening, artefact of image processing, a lack of late nucleation, or insufficient resolution (e.g. Brugger & Hammer, 2010; Cashman & McConnell, 2005; Higgins & Roberge, 2003). Because the image resolution used was ideal to capture crystals larger than $1 \mu\text{m}$, we interpret the downturn as an intersection artefact. Finally, the similarity in shape and slope of the CSDs and the overlapping of these CSDs implies similar crystallisation processes and timescales at the onset of each of these explosive eruptions.

6.5.2. Microlite population growth time and plagioclase crystal growth rate

We evaluated crystallisation times using the sublinear slopes of the CSDs between 10 and 30 μm (Figures 6.6 and 6.7), to avoid (i) syn-eruptive crystallisation, which corresponds to the steepest slopes at microlite/nanolite sizes (usually $< 10 \mu\text{m}$), and (ii) contributions of older micro-phenocrysts ($> 30 \mu\text{m}$). Given a known growth rate, average crystallisation duration of a microlite population can be calculated (Marsh, 1988). The slopes of the considered populations range from -0.30 to $-0.06 \mu\text{m}^{-1}$ and have averages of -0.20 and $-0.14 \mu\text{m}^{-1}$, for pyroxene (Figure 6.6) and plagioclase (Figure 6.7) microlites, respectively. A growth rate that can be used was determined from the peritectic opx in a Mangatawai tephra (i.e. 407-17; Zellmer *et al.*, 2016c; Zellmer *et al.*, 2018): the peritectic reaction between an olivine phenocryst and the melt led to the crystallisation of opx microlites at the rim of the olivine. By modelling Fe-Mg inter-diffusion at the olivine rim, the dissolution rate of olivine and the growth rate of the peritectic opx were determined. This growth rate was estimated at $3.7 (\pm 2.6) \times 10^{-11} \text{ m s}^{-1}$ (2σ) based on a temperature of $1137 \pm 41 \text{ }^\circ\text{C}$ (Zellmer *et al.*, 2016c; Zellmer *et al.*, 2018), but based on the MELTS-derived temperature of $1095 \pm 15 \text{ }^\circ\text{C}$ for sample 407-17 with improved precision, determined here, the growth rate of opx microlites was recalculated to $1.80 (\pm 0.60) \times 10^{-11} \text{ m s}^{-1}$ (2σ). Growth rate determination considered both linear and volumetric growth, and found that these could not be distinguished within uncertainty even at the smallest crystals sizes of less than $20 \mu\text{m}$ (Zellmer *et al.*, 2016c; Zellmer *et al.*, 2018). Combined with the slope of the CSDs (reported in Table 6.4), pyroxene growth times vary from 52 ± 14 hours (2σ , i.e. Mangatawai 407-59) to 99 ± 27 hours (2σ , i.e. Mangatawai 407-14; see Figure 6.4, and Table 6.4) with an average of 76 ± 21 hours (2σ). In experimental petrology, equilibrium conditions for plagioclase microlites are typically achieved within *c.* 260 mins (i.e. 4-5 hours; Hammer *et al.*, 1999). Given the timescales

of 3 ± 1 days yielded by the considered microlite population, assessment of equilibrium using hygrometry and *MELTS* modelling for microlites is considered faithful. Besides, as *MELTS* runs suggest, pyroxene and plagioclase microlites usually grow concomitantly, so we can use these crystallisation timescales obtained from opx to derive the growth rates of plagioclase microlites. These range from $1.65 \times 10^{-11} \text{ m s}^{-1}$ to $6.43 \times 10^{-11} \text{ m s}^{-1}$ (average of c. $2.94 \times 10^{-11} \text{ m s}^{-1}$), within the range of experimental growth rates of plagioclase determined in previous studies (Cashman, 1990; Couch *et al.*, 2003; Hammer & Rutherford, 2002; Mollard *et al.*, 2012), in support of the reliability of the pyroxene growth timescales calculated above. Given timescales of 2-4 days for the growth of the microlite populations from TgVC, this growth may be considered to occur close to equilibrium condition, making the crystals amenable to traditional geothermometric and hygrometric calculations.

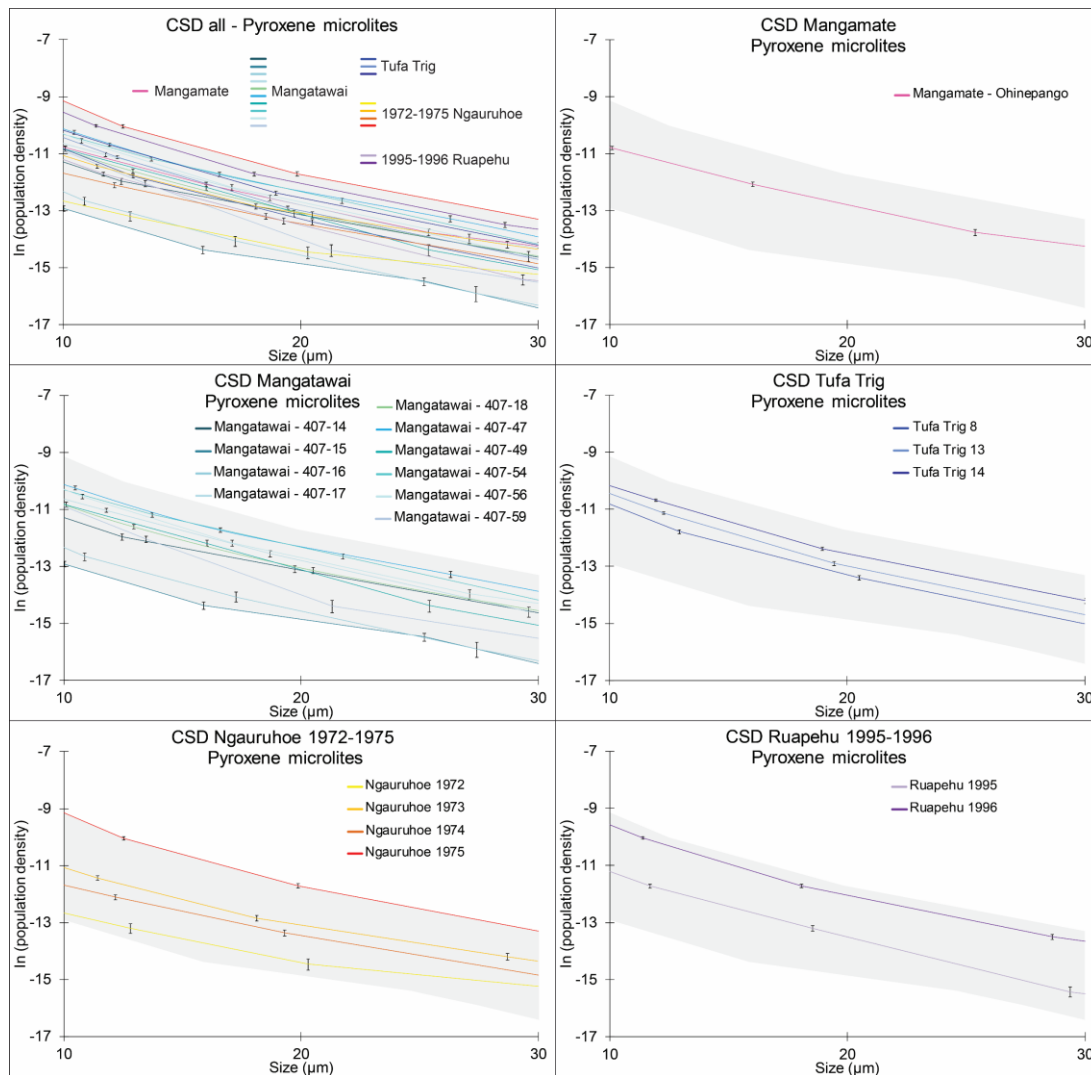


Figure 6.6. Crystal size distributions of the pyroxene microlite population. Slopes used to derive microlite crystallisation times (reported in Table 6.4) were calculated from this size section (10-30 μm). See text for discussion. The grey field represents the full range covered by the CSD plots.

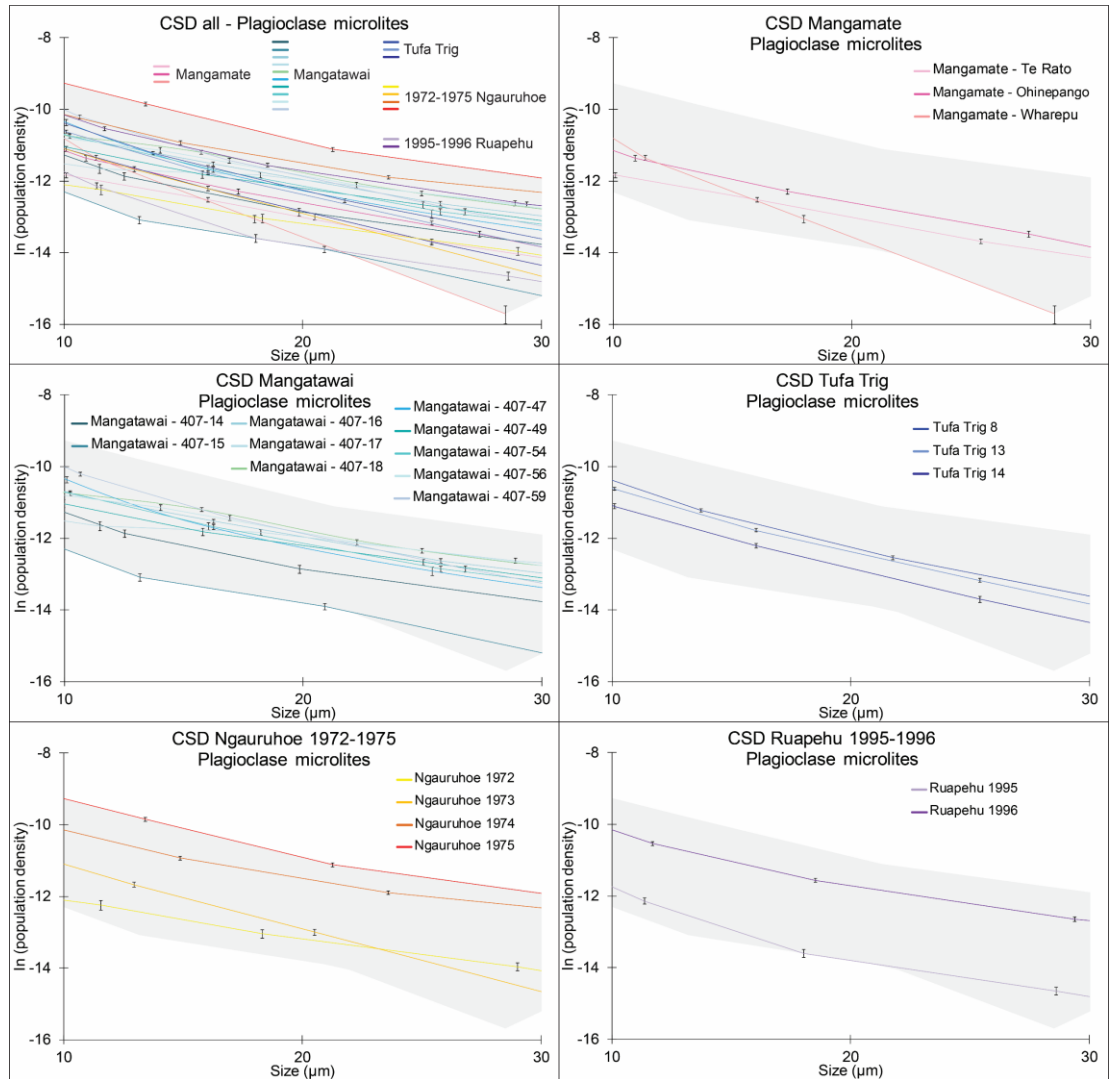


Figure 6.7. Crystal size distributions of the plagioclase microlite population. Slopes used to derive microlite crystallisation times (reported in Table 6.4) were calculated from this size section (10-30 μm). See text for discussion. The grey field represents the full range covered by the CSD plots.

Table 6.4. Microlite population CSD slopes, crystallisation time and plagioclase growth rate for the TgVC tephra. The slope was calculated from the average CSD slope between 10 and 30 μm . The microlite crystallisation time was calculated using the slope and a constrained orthopyroxene growth rate for Mangatawai (Zellmer *et al.*, 2016c; Zellmer *et al.*, 2018).

Sample	Pyroxene CSD slope (μm^{-1})	Std dev (2σ)	Plagioclase CSD slope (μm^{-1})	Std dev (2σ)	Microlite crystallisation time (hours)	Std dev (2σ)	Plagioclase growth rates (m s^{-1})
Te Rato	N/A	N/A	-0.12	0.01	78*	N/A	N/A
Ohinepango	-0.19	0.02	-0.13	0.01	80	21	2.71E-11
Wharepu	N/A	N/A	-0.25	0.03	37*	N/A	N/A
407-14	-0.16	0.04	-0.14	0.04	99	27	2.07E-11
407-15	-0.17	0.02	-0.11	0.03	92	25	2.85E-11
407-16	-0.20	0.04	-0.12	0.01	78	21	2.94E-11
407-17	-0.20	0.02	-0.06	0.02	77	21	6.43E-11
407-18	-0.20	0.04	-0.12	0.02	76	21	2.92E-11
407-47	-0.19	0.02	-0.17	0.02	81	22	2.07E-11
407-49	-0.23	0.03	-0.09	0.03	67	18	4.58E-11
407-54	-0.18	0.03	-0.14	0.02	85	23	2.39E-11
407-56	-0.21	0.02	-0.12	0.03	74	20	3.20E-11
407-59	-0.30	0.06	-0.16	0.01	52	14	3.27E-11
Tufa Trig 8	-0.21	0.03	-0.16	0.02	73	20	2.33E-11
Tufa Trig 13	-0.25	0.02	-0.17	0.01	63	17	2.65E-11
Tufa Trig 14	-0.24	0.02	-0.17	0.02	64	17	2.57E-11
Ngauruhoe 1972	-0.17	0.07	-0.10	0.02	92	24	3.07E-11
Ngauruhoe 1973	-0.16	0.02	-0.17	0.03	97	26	1.65E-11
Ngauruhoe 1974	-0.18	0.04	-0.11	0.02	88	24	2.84E-11
Ngauruhoe 1975	-0.23	0.03	-0.16	0.02	68	18	2.55E-11
Ruapehu 1995	-0.21	0.02	-0.15	0.02	74	20	2.58E-11
Ruapehu 1996	-0.20	0.01	-0.12	0.01	77	21	3.04E-11
Average	-0.20	0.03	-0.14	0.02	76	21	2.93E-11
Std dev (2σ)	0.03		0.04		12		1.01E-11

* indirectly determined using the calculated average plagioclase growth rate assuming pyroxene and plagioclase microlites have crystallised concomitantly

6.5.3. Unusually high temperature and quasi-anhydrous andesite magmas

Our data indicate that microlites started crystallising in near-anhydrous magmas (*c.* 0 to 1.5 wt% H₂O at microlite crystallisation) of high temperature (i.e. *c.* 1065 ± 65 °C) at approximately 3 days before eruption. The low water contents and the unusually high temperatures are consistent with previous studies of TgVC magmas (Arpa *et al.*, 2017; Deering *et al.*, 2011a; Kilgour *et al.*, 2009; Kilgour *et al.*, 2013), and indicate that the microlites of these magmas do not grow in response to degassing, but that cooling during magma ascent is the only way to form them. While cooling-induced crystallisation in magma reservoirs typically promotes growth rather than nucleation and thus occurs at low degrees of undercooling (Mollo & Hammer, 2017), melt ascent in narrow dykes would instead occur under high degrees of undercooling due to rapid heat loss through the dyke walls (Gray, 1970; Schaubroth *et al.*, 2016; Wadsworth *et al.*, 2015; Webber *et al.*, 1999) and lead to microlite nucleation. Previous studies have shown that a high degree of undercooling would produce crystal textures such as skeletal, swallowtail, dendritic and hopper (Faure *et al.*, 2003; Masotta *et al.*, 2020; Shea & Hammer, 2013; Vona & Romano, 2013), consistent with some high long-axis shape factors obtained from *CSDSlice* for the TgVC tephra (e.g. Mangatawai 407-17 and 407-18, Tufa trig 14, Ngauruhoe 1975 and Ruapehu 1995-1996).

Using the crystallisation times and the pressures of crystallisation (up to 550 MPa ≈ 16.5 km), we infer a range of maximum magma ascent rates of 4 to 18 cm s⁻¹ (i.e. considering the crystallisation time and the maximum pressure value for each tephra). Strombolian, Vulcanian and sub-Plinian explosive eruptions are fed by magmas exiting vents at much higher sonic to supersonic velocities from a few tens of up to 400 m s⁻¹ (e.g. Gaudin *et al.*, 2014; Morrissey & Mastin, 1999; Self *et al.*, 1978; Taddeucci *et al.*, 2012; Woods & Bower, 1995). Nevertheless, these exit velocities measured at the vent

are expected to be greater than the mean ascent velocity integrated on the whole conduit, and thus, it would not be surprising to obtain ascent rates much lower than the actual exit velocities for these eruptions. However, if the microlites had crystallised due to degassing, the microlite growth timescales would be much lower than those we inferred from the CSDs. This model is thus inconsistent with our data, implying that microlites have instead crystallised due to decompression-induced cooling.

Relatively low ascent rates followed by rapid acceleration of magma is well known and commonly linked to gas exsolution (e.g. Burgisser & Degruyter, 2015; Papale & Polacci, 1999). The exsolution of water in the magmas considered here occurs at a maximum of 33 MPa (i.e., *c.* 1 km below the surface), which triggers volume expansion at shallow depth. Assuming 1 wt% of water in these andesites of a density of *c.* 2.7 g L⁻¹ (Christenson, 2000), and considering water vapour density of 0.804 g L⁻¹ at 0 °C and 0.1 MPa, if all water turns into vapour, 0.027 g of water will take up to *c.* 33.5 cm³ at 0 °C (= 273 K). Using the ideal gas law, for which *V* scales linearly with *T*, and considering a temperature of *c.* 1100 °C (=1373 K), the volume of exsolved water will increase by a factor of about 5, which leads to an exsolved volume of 167.5 cm³ of vapour for 1 cm³ of melt. Assuming an incompressible vent, and complete retention of all vapour in the melt, the initial ascent rate will thus increase by a factor of approximately 150, i.e. 9 cm s⁻¹ will result in a final ascent rate of 13 m s⁻¹, still much too low to explain the observed sonic to supersonic exit velocities of Vulcanian and sub-Plinian explosive eruption products, as for example reported during the 1975 eruption of Ngauruhoe (Nairn & Self, 1978). Volatile exsolution alone thus cannot explain the range of explosive eruption styles reported at TgVC.

Finally, our data provide a minimum crystallisation depth (*c.* 16.5 km) on the basis of microlite formation by cooling. Because cooling is less efficient at great pressures,

where the crust is hot, magma may have been ascending from even deeper levels. Indeed, crystallisation of micro-phenocrysts of TgVC magmas have been interpreted to be sourced from depths greater than 20 km (Arpa *et al.*, 2017; Nakagawa *et al.*, 1998). However, shallow (*c.* 5 km) and small interconnected magma chambers beneath Tongariro and Ngauruhoe, where magma would reside before erupting, was previously interpreted from isotope data (Hill *et al.*, 2015; Hobden *et al.*, 1999; Rowlands *et al.*, 2005). A slow ascent from such great depth is inconsistent with the latter geometry, which is also inconsistent with the tectonic setting of the region. Isotopic variations found for the TgVC thus likely reflect deeper level processes.

6.5.4. Influence of regional tectonic setting and conduit geometry

As described earlier, the TgVC experiences extension accommodated by faults and dyke formation. Cassidy *et al.* (2009) showed that faults and eruptive vents at the TgVC coincide, and thus confirms that historical eruptions may have been fed by dykes. Solidification fronts in intrusions are a common physical model associated with volcanic eruptions or laccoliths formation (Marsh, 1996; Taisne & Tait, 2011). For dry magmas, solidification fronts are associated with crystallisation along the margins of the dyke caused by heat loss (e.g. cooling) through the surrounding host rock (Currier & Marsh, 2015). However, this type of crystallisation would result in viscous and crystal-rich magmas, which is inconsistent with the crystal contents (8-24 % of microlites), the high magmatic temperature at crystallisation (*c.* 1076 °C), and the low water content (*c.* 0.4 wt%) derived in the present study.

Another model for dyke propagation involves the pulsed ascent of an intrusion due to solidification effects (Taisne & Tait, 2011), which could explain the successive bursts in precursory seismic signals, involving a magma that may or may not reach the surface.

Failed magmatic eruptions, when magma gets close to but does not reach the surface, are dependent on many competing parameters and are often associated with dyke intrusions (Moran *et al.*, 2011). This is consistent with the frequent observations of precursory phenomena at TgVC such as increasing number of seismic tremors, ground deformation, increasing of degassing – or of lake temperature for Ruapehu Crater Lake, for instance – which do not always result in volcanic eruptions (e.g. Jolly *et al.*, 2010; Jolly *et al.*, 2014a; Rowlands *et al.*, 2005; Sherburn *et al.*, 1999).

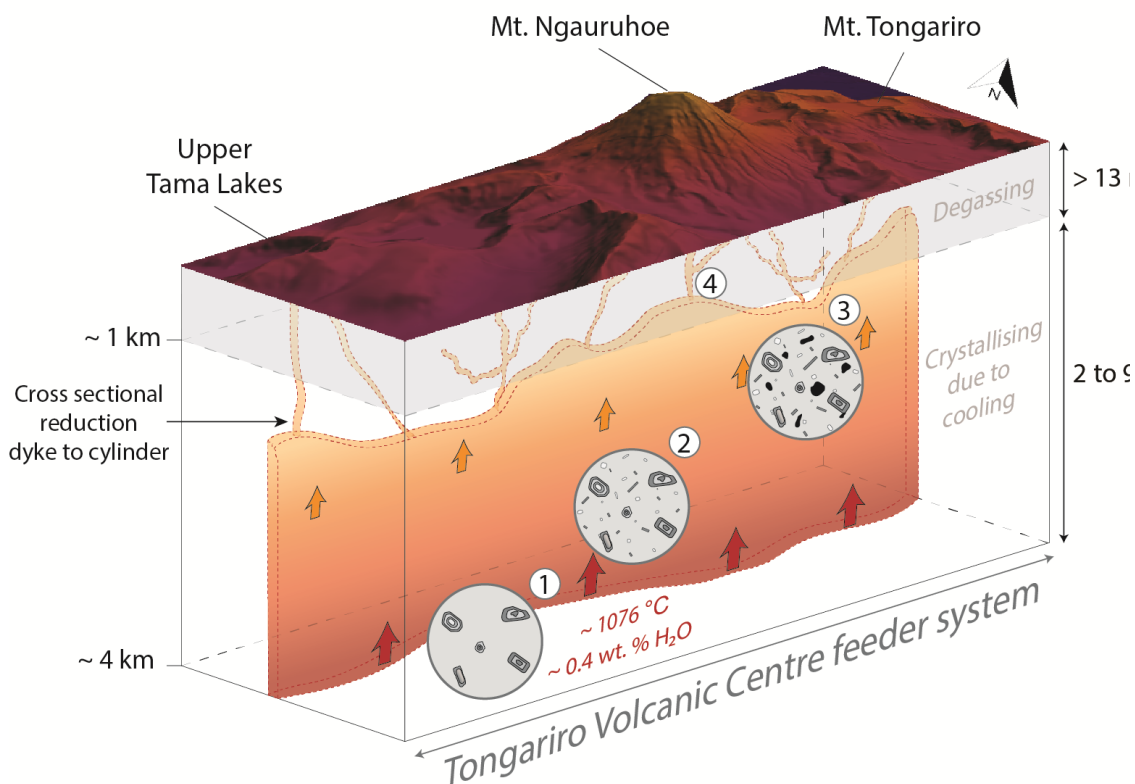
Further, previous studies have related the conduit geometry with the ascent and eruptive processes for explosive eruptions. Indeed, models on explosive and dome-forming eruptions (Costa *et al.*, 2009b; de' Michieli Vitturi *et al.*, 2008; Wilson *et al.*, 1980) have investigated the change in conduit geometry from a deep dyke to a shallower cylindrical conduit (Schauroth *et al.*, 2016; Wadsworth *et al.*, 2015), and have found that eruption dynamics would be affected: although the system would develop overpressure, the eruption would be more stable, mass fluxes would be four to six times larger compared to eruptions fed by a pure dyke or cylindrical system, and fragmentation would occur in the conduit, i.e. above the transition from dyke to cylindrical conduit. Cylindrical conduits are likely to develop early in phreatic and phreatomagmatic explosions before the dyke reaches the surface. A more recent study by Taisne & Jaupart (2011) demonstrated that for water-poor magmas such as those of the TgVC (Arpa *et al.*, 2017; Deering *et al.*, 2011a; Kilgour *et al.*, 2013), fragmentation is unlikely and the propagation of the ascending dyke tends to thin and thus accelerates due to magma expansion.

We infer a similar scenario for the shallow magmatic plumbing system of the TgVC (Figure 6.8). Hot (i.e. *c.* 1076 °C), nearly anhydrous (i.e. *c.* 0.4 wt% H₂O) intermediate magmas below TgVC are ascending slowly from the mantle or deep crust, taking up complexly zoned micro-phenocrysts of plagioclase and pyroxene from conduit walls. At

an average depth of *c.* 4 km and a mid-crustal maximum depth (*c.* 16.5 km), cooling leads to slow microlite nucleation and growth of smaller microlites of pyroxene and plagioclase at growth rates of $1.80 (\pm 0.60) \times 10^{-11} \text{ m s}^{-1} (2\sigma)$ and $2.93 (\pm 1.01) \times 10^{-11} \text{ m s}^{-1} (2\sigma)$, respectively. Due to the regional tectonic setting, the magma rises through dykes near the surface. At shallower depth (e.g. *c.* 1 km), water exsolution, bubble nucleation and thus volume expansion occur, resulting in faster ascent rates. The dyke becomes more channelised and starts funneling into narrower cylinders below eruptive vents to reach supersonic eruption velocities upon exit. This scenario is also compatible with shallow magma-water interaction (e.g. the 1995 Ruapehu phreatomagmatic eruption, Christenson, 2000).

Many studies have agreed on H₂O content being the principle driver of the explosivity of eruptions (Cashman & McConnell, 2005; Hammer *et al.*, 1999; Sparks, 2003; Zhang, 2008), however, our study shows that for nearly anhydrous magmas, the geometry of the conduit strongly controls vent exit velocities and thus volcanic explosivity.

Figure 6.8. Conceptual model of the shallow magma plumbing system beneath the TgVC. Temperatures, pressures and water contents are based on the results obtained with *MELTS*. (1) Hot (*c.* 1076 °C) andesitic/dacitic magmas ascending with microphenocrysts displaying complex oscillatory zonings. Nuclei sites for microlites of orthopyroxene and plagioclase at an average of 4 km depth and with water contents of *c.* 1 wt. %. (2) Microlite nucleation and growth due to cooling. (3) Microlites keep on nucleating and growing while degassing at *c.* 1 km yields to bubble nucleation and volume expansion and thus faster ascent rates, but not fast enough to feed the most explosive eruptions. (4) A change in geometry of the conduit cross-section (from dyke to cylinder) is thus required to accelerate these magmas to up to 400 m s⁻¹ upon exit.



6.5.5. Correlating geophysical signals and timescales

The most recent eruption investigated here is the 1995-1996 eruption of Mt. Ruapehu. It was the largest eruption of the stratovolcano in the past 50 years with a volume of erupted material of *c.* 0.1 km³ through phreatic, phreatomagmatic and ash eruptions (Johnston *et al.*, 2000). Predominant depths for earthquake swarms preceding the 1995 eruptions of Ruapehu were localised between 10 and 16 km depth (Hurst & McGinty, 1999). These volcanic tremors are interpreted as the result of slow rock failure,

fluid flow processes or magma motion (Aki *et al.*, 1977; Aki & Koyanagi, 1981; Chardot *et al.*, 2015; Mordensky *et al.*, 2019). Furthermore, a low resistivity and velocity zone was identified using tomography and magnetotelluric imaging at about 5 km depth beneath Ruapehu and Tongariro (Hill *et al.*, 2015; Rowlands *et al.*, 2005), which was interpreted as a zone of magma accumulation. These depths determined using geophysical tools are consistent with the range of the permissible pressures determined using both thermobarometry (i.e. 178 MPa *c.* 5.3 km) and *MELTS* modelling (i.e. 188 MPa *c.* 5.6 km) for the Ruapehu 1995 tephra. Previous studies have related the vesicle number density and the water content in glassy ash with duration of low-frequency earthquakes suggesting migration of deep-gas and vesicle-rich-magma to the surface (Miwa & Toramaru, 2013). Such studies show the relevance of evaluating the relation between microlite crystallisation and precursory seismic signals for recent and well-documented eruptions. In the case of TgVC, we would expect to see signals of geophysical unrest due to dyke injections 2-4 days prior to the next eruption.

6.6. Conclusions

1. Microlites (< 30 μm) have grown in the conduit and consist of orthopyroxene and plagioclase for most of the tephras considered here. Ngauruhoe 1972, 1973 and 1974 are composed of pigeonite and/or augite and plagioclase, and no orthopyroxene was analysed for these samples. Most micro-phenocrysts (> 30 μm) are complexly zoned and contain resorption patterns, and are thus of antecrystic or xenocrystic origin.
2. CSD plots show that late-stage processes of microlite crystallisation were similar and independent of the ensuing eruption styles (Tongariro, Ngauruhoe) and compositions (i.e. andesitic or dacitic). Similar slopes at smallest crystal size indicate analogous crystallisation processes.

3. During crystallisation, TgVC andesites and dacites were unusually hot (between 1005 °C and 1130 °C) and poor in water (≤ 1.50 wt%), consistent with previous studies (e.g. Kilgour *et al.*, 2013). Low water content and great depth of crystallisation are however inconsistent with microlite crystallisation by decompression-induced degassing (e.g. Hammer *et al.*, 1999; Noguchi *et al.*, 2006; Szramek *et al.*, 2006). Thus microlites instead crystallised due to cooling during slow magma ascent in dykes.
4. Pressures of up to 550 MPa (i.e. *c.* 16.5 km) during microlite crystallisation cannot be reconciled with the model suggested previously, consisting of small and shallow interconnected magma chambers in which magmas stall and differentiate (Hobden *et al.*, 1999; Rowlands *et al.*, 2005).
5. Timescales of microlite crystallisation ranging from 52 ± 38 (2σ) hours to 99 ± 73 (2σ) hours lead to ascent rates of up to 9 cm s^{-1} , too slow to feed explosive eruptions, even if complete exsolution of water and magma expansion prior to eruption are taken into account (i.e. maximum vent exit of up to 13 m s^{-1}). Eruption styles for past explosive eruptions at TgVC were thus regulated by a reduction of the conduit size (transition from dyke to cylindrical conduits) to yield faster vent exit velocities.

Chapter 7. Discussion: Dynamics and Geometry of Arc Magmatic Systems

Chapter content:

7.1. Geochemical constraints on magmatic processes and plumbing system architectures.....	194
7.1.1. Common architectural models of magmatic reservoirs	194
7.1.1.1. Single stratified magma chamber.....	196
7.1.1.2. Independent magmatic chambers.....	202
7.1.1.3. The “crystal mush” model.....	206
7.1.2. Mafic, intermediate and felsic magmatic systems	210
7.1.2.1. Mafic systems	210
7.1.2.2. Intermediate systems.....	217
7.1.2.3. Felsic systems	225
7.1.3. Reflection on the existing conceptual models.....	231
7.2. A new architectural model beneath the Tongariro Volcanic Centre.....	236
7.2.1. Magma mixing	239
7.2.2. Crystal uptake from a crystal mush.....	239
7.2.3. Cooling-induced microlite crystallisation.....	240
7.2.4. Pulsatile regime of ascent.....	241
7.2.5. Ascent through dykes.....	242
7.3. Implications of new results and hazard assessment	244
7.3.1. Implications.....	244
7.3.2. Monitoring and hazard assessment	247

7.1. Geochemical constraints on magmatic processes and plumbing system architectures

Most existing models for magmatic plumbing systems using geochemical and petrological evidence typically put constraints on dynamics of magmatic processes rather than geometry and architecture where these processes are taking place. Many of these visualise literally extensive chambers (e.g. sills, laccoliths) where melts segregate and evolve before being remobilised upon eruption (e.g. Cartwright & Hansen, 2006; Cashman *et al.*, 2017; Coote *et al.*, 2018; Davidson *et al.*, 2007; Nairn *et al.*, 2004; Pappalardo & Mastrolorenzo, 2012; Price *et al.*, 2005; Shane *et al.*, 2019; Tibaldi, 2015; Viccaro *et al.*, 2012; Voloschina *et al.*, 2018). On the contrary, the microlitic crystal cargos the TgVC investigated in this study point to vertical foliation of the upper crust, consistent with the extensional tectonic setting of the southern TVZ (Gómez-Vasconcelos *et al.* 2017). This chapter will first review the most common models invoked in the literature based on geochemical data of well-known examples. Finally, the new proposed model for the TgVC will be explained in conjunction with the few other existing models that suggest vertically-fed magmatic systems.

7.1.1. Common architectural models of magmatic reservoirs

Previous studies have interpreted magmatic plumbing systems beneath volcanoes based on several geophysical and geochemical techniques and evidence of various kinds. Textural analysis such as CSD, qualitative description of high-resolution images and *MELTS* modelling have previously been used, but not with the microlitic crystal cargo as target. Along with geophysical tools such as seismic tomography (Hirose *et al.*, 2008; Rowlands *et al.*, 2005; Zellmer *et al.*, 2019), magnetotulleric surveys (Hill *et al.*, 2015), and remote sensing (e.g. Benz *et al.*, 2004; Blaschke, 2010; Burton *et al.*, 2003; Marzocchi, 2002; Meyer *et al.*, 2015; Wadge & Haynes, 1998), numerical (Annen *et al.*,

2001; Bindeman & Simakin, 2014; Cheng *et al.*, 2017; Costa *et al.*, 1998; Turner *et al.*, 2010) and thermodynamic modelling as well as geochemical and petrological studies have used experiments (Faure & Schiano, 2005; Gondé *et al.*, 2006; Jenner *et al.*, 1994; Kinzler *et al.*, 1990; Martel, 2012; Mourtada-Bonnefoi & Laporte, 1999; Orlando *et al.*, 2008; Riker *et al.*, 2015; Wyllie, 1984), mineral and glass major, minor, trace and isotopic concentrations (e.g. Kepezhinskas *et al.*, 1997; Masotta *et al.*, 2020; Orozco-Esquivel *et al.*, 2007; Shibata *et al.*, 2005; Tamura & Nakamura, 1996; Taran & Zelenski, 2014; Ubide *et al.*, 2019; Verma & Luhr, 2010; Zellmer *et al.*, 2012a), and melt inclusions (e.g. Bégué *et al.*, 2014; Chen *et al.*, 2013; Danyushevsky *et al.*, 2002; Danyushevsky *et al.*, 2004; Humphreys *et al.*, 2008; Kilgour *et al.*, 2013; Kohut *et al.*, 2006) to constrain specific key parameters such as dynamics, geometry, temperature, depth, volatile content and oxygen fugacity of magmatic systems. Textures of the juvenile erupted materials such as crystals and bubbles have refined our understanding of the magmatic dynamics that led to their formation. Previous studies have attempted to provide conceptual models of dynamics and geometry of a magmatic system based on their data. However, these studies have focussed on the phenocryst crystal cargo to gain insights into deep processes (e.g. Berlo *et al.*, 2007; Browne *et al.*, 2006; Coote *et al.*, 2018; Crabtree & Lange, 2011; Viccaro *et al.*, 2010). The present chapter reviews and discusses the most common models interpreted for various arc volcanic systems across the globe, and how they relate to the resulting conceptual model from this study.

Although they may have differing eruptive dynamics, compositions, shapes, frequency and intensity of eruptions, and eruption style, arc volcanoes are ultimately the result of the same tectonic setting, namely subduction. Two common conceptual models for magmatic plumbing systems can be highlighted from the literature; a single stratified magma chamber with differing layers, which may or may not homogenise through

convection, and separate small and interconnected magma chambers and conduits which evolve independently. Within these structures, several processes can control the dynamics and the geometry and will be discussed here.

7.1.1.1. Single stratified magma chamber

The model of a single stratified, or zoned or layered magma chamber was proposed following the model of Eichelberger (1980), in which the density of the upper part of the mafic magma at the bottom of a stratified chamber may decrease due to vesiculation, and thus plumes of this magma may rise and become dispersed in the overlying more silicic magma. This model was later evoked due to the presence of nodules or inclusions of more mafic magmas into intermediate to silicic deposits (Bacon, 1986). These were attributed to amalgamation of magma pulses, intermittent replenishment of mafic intrusions, continuous upward flow (Coleman *et al.*, 2004; Parada *et al.*, 2005; Pitcher, 1979), and convection at the lower part of the storage by ascending plumes (Figure 7.1; Huppert & Sparks, 1980; Huppert & Sparks, 1984). The initial magma batch ascends from depth, stalls in the crust, and starts degassing, cooling and crystallising to progressively become more and more evolved. The replenishment by mafic batches yields to accumulation of layers of distinct compositions, densities, viscosities and temperatures. The density and the viscosity of two magma bodies, i.e. a more silicic and viscous magma overlying a hotter and denser mafic magma, may prevent mixing between them (Bacon, 1986). However, Huppert & Sparks (1984) suggested that the heat transfer leading to crystallisation and volatile exsolution from the intrusion of a mafic layer would trigger mixing of the dense mafic magma with the overlying more viscous and felsic magma via convection. Later, experiments of Turner & Campbell (1986) inferred that the stratification and the degree of mixing between the pre-existing magma and the intruding magma depend on the flow rate and on the density and the viscosity of the two bodies.

Indeed, fast upwards intrusion is a more efficient mechanism for mixing than a slow dense input of magma. Mt. Pelée in Martinique (Fichaut *et al.*, 1989), Mount Mazama (Crater Lake) in Oregon, USA (Bacon, 1986), Tarawera volcano in New Zealand (Leonard *et al.*, 2004; Nairn *et al.*, 2004), Mt Aso in Japan (Kaneko *et al.*, 2007), Campi Flegrei Volcanic Field and Sabatini Volcanic District in Italy (Mollo & Masotta, 2014), are some of the examples for which stratified magma chambers were proposed.

The study by Fichaut *et al.* (1989) of the eruptions of Mt Pelée, namely of the ash-and-scoria flows from *c.* 0.1 Ma to 19,500 yrs BP and the 1902 and 1929 block-and-ash flows, highlights heterogeneity in the mineral and chemical compositions of the erupted lavas. Although the magmas emplaced remained constant and cogenetic over time, they were characterised by a wide variation of SiO₂ (54-63 wt%) in both the bulk rock and associated variation in the mineral phases (i.e. olivine, plagioclase, clinopyroxene, orthopyroxene, amphibole and magnetite), a broad variability of the An content of plagioclase (i.e. *c.* An₅₀₋₉₆) and Fo content in olivines (*c.* Fo₆₀₋₈₅), and a variety of phenocryst textures (e.g., normally zoned, resorption, oscillatory). Fractional crystallisation (Bowen, 1956; O'Hara, 1977) and magma mixing (Anderson, 1976) were the two main magmatic processes proposed to explain these data. Such dynamics were associated with periodic mafic recharge from deeper levels triggering magma mixing, and eventually explosive eruptions producing pyroclastic density currents (Druitt, 1998). The authors proposed vertically elongated bodies of *c.* 25 km deep in shape of cylinders with small horizontal cross sections (i.e. *c.* 300-400 m in diameter), chemically stratified, consistent with geobarometric estimates and the centrally localised activity of Mt Pelée (i.e. no flank eruption or secondary vent).

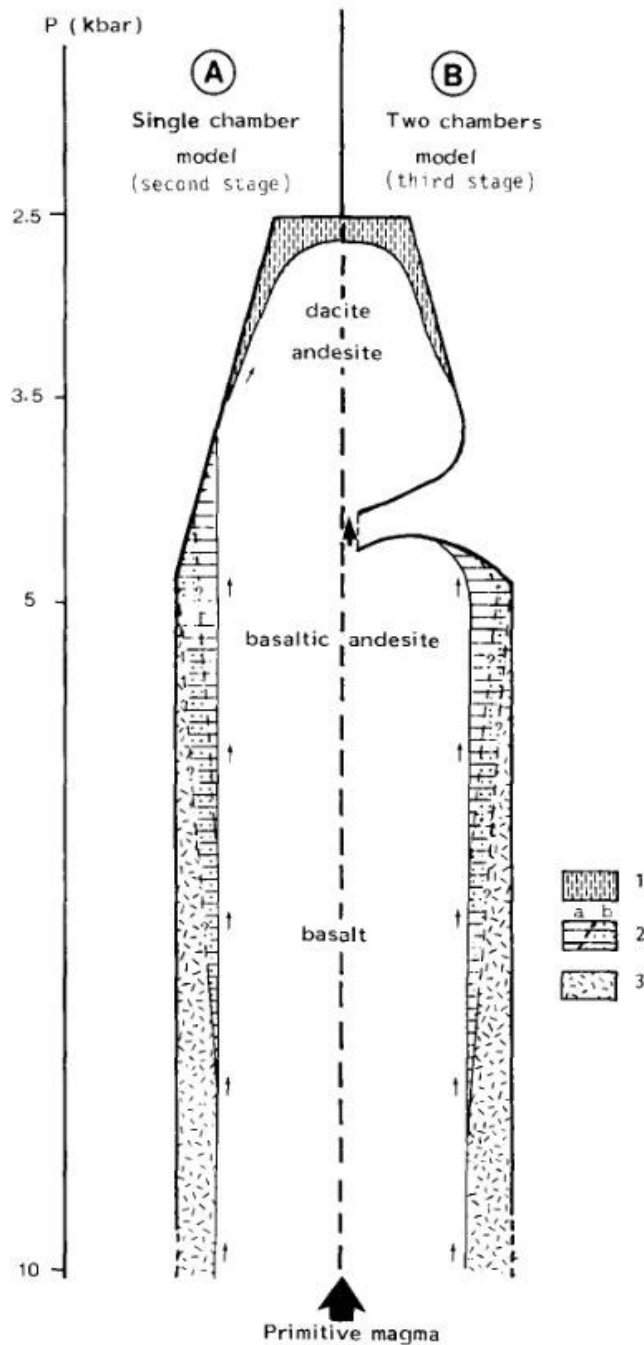


Figure 7.1. Figure 16 of Fichaut *et al.* (1989) representing the magma chamber(s) beneath Mt. Pelée. 1, 2 and 3 are symbols for various dioritic and gabbroic cumulates.

Andesitic inclusions or nodules found in porphyritic rhyodacitic lava flows of Mount Mazama at Crater Lake caldera are another example, which was attributed to compositional zonation in the magma reservoir (Bacon & Druitt, 1988). More abundant towards the head of the flows, the inclusions found have ellipsoidal to spheroidal shapes

and vary from < 2 cm to *c.* 1 m in size. These are more mafic than their host lavas (54-61.5 wt% SiO₂ versus *c.* 75 wt% SiO₂) and contain sieve-textured plagioclases. A compositional gap between the lavas, the inclusions and residual glasses from the *c.* 70,000 years BP Mount Mazama andesites are associated with magma mixing induced by mafic magma with its overlying more silicic and viscous magma. However, the mafic inclusions found in these lavas are explained by the decrease in density of the mafic magma at the interface with the overlying more silicic layer due to vesiculation resulting in gravitational instability. Thus, this process may have triggered convection and homogenisation of the single stratified magma chamber. No clear information about the geometry of the feeding magmatic system is given in this study, stating that it probably varies from system to system. However, the single magma chamber is thought to be bound by hydrothermally cooled roof rocks and wall rocks, and an underlying zone of dyke injections.

The 1315 Kaharoa eruption, part of the Okataina Volcanic Centre (OVC) in New Zealand, produced a large volume [*c.* 5 km³ dense rock equivalent (DRE)] of rhyolitic magma, but also involved a small portion of rhyodacitic pyroclasts mingled with basalt (Nairn *et al.*, 2004). The geometry of the magma reservoir, being 8 km long, 1 km wide and 1.4 km thick, is consistent with the dynamics of the eruption, which involved a *c.* 8 km long linear vent zone with 7 active vents (Figure 7.2). The main argument against a vertical geometry is the lack of evidence for sidewall crystallisation, which is enhanced in vertically structured chambers (Blake *et al.*, 1992; de Silva & Wolff, 1995).

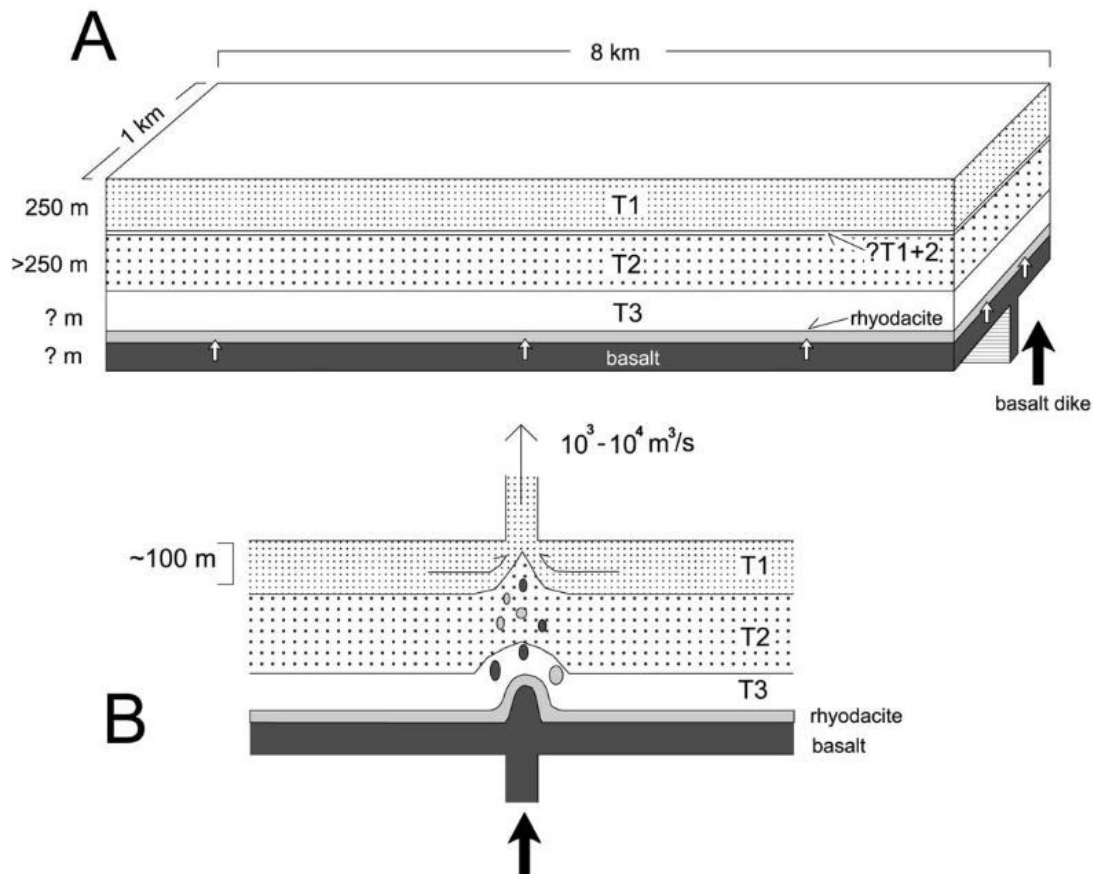


Figure 7.2. Figure 9 of Nairn *et al.* (2004) representing the conceptual model of the stratified plumbing system beneath Tarawera volcano (A) before and (B) during the *c.* 1315 AD Kaharoa eruption. The 8 km linear vent zone involved during the eruption suggests vertical magma rise. T1, T2 and T3 are three magma layers of distinct crystallinities, and compositions. The white arrows in (A) represent the uprising siliceous melt expelled from the fractional crystallisation of the deeper mafic magma.

The latest eruption cycle of the Mt. Aso caldera, located in SW Japan, has produced more than 600 km^3 of pyroclasts over the last 90,000 years. Kaneko *et al.* (2007) divided this period into two sub-cycles, which both consist of a voluminous silicic eruption followed by eruption of mafic magma. The whole-rock chemistry and the phenocryst mineralogy are converging towards a pre-eruptive stratified magma chamber composed of three main layers, consisting of a silicic magma layer at the top and a mafic magma layer at the bottom, separated by a hybrid layer in between. In this model, the hybrid layer resulted from the mixing of the lowermost part of the silicic layer and the uppermost part of the mafic layer. The upper part of the silicic layer was homogeneous whereas the mafic

layer was zoned, i.e. more silicic towards shallower depth. Mafic recharge triggered the evacuation of the upper silicic magma, which was successively followed by the eruption of the underlying hybrid and mafic magmas, without completely emptying the reservoir. After replenishment of the feeding system and mixing of the remaining hybrid and new mafic injections, the second subcycle started with evacuation of the new hybrid followed by eruption of the mafic magma. The single stratified magmatic chamber has an estimated extent of *c.* 10 km, based on the width of the caldera, and a depth of > 3 km, estimated from the minimum H₂O saturation pressure.

The 39 ka BP Campanian Ignimbrite (CI), produced during one caldera forming eruption of Campi Flegrei, Italy, is one of the most studied eruptive sequences in the world. Several studies have agreed on a zoned magma chamber as a source of the CI (Mollo & Masotta, 2014; Pabst *et al.*, 2008; Pappalardo *et al.*, 2002; Pappalardo & Mastrolorenzo, 2012). Two cogenetic magmas with different densities and separated by a compositional gap due to side-wall crystallisation are inferred as the source of four pyroclastic flow units of the CI (Pappalardo *et al.*, 2002). Evidence of mingling, a progressive decrease of Sr isotopes (⁸⁷Sr/⁸⁶Sr) in the whole pumice, and the eruption of progressively more mafic magmas with time indicate that the feeding reservoir was zoned. The Sr isotopic ratio in plagioclase seems to be constant over the course of the eruption and thus indicates a cogenetic source for both layers. Before the caldera collapse event, there was simultaneous tapping of the two magma layers during the Plinian and the pyroclastic flow phases of the eruption, generating late-stage mingling during ascent. No evidence was found for injection of mafic magma to trigger the eruption. Instead, interaction of the upper magma layer with geothermal fluids at shallow depth after plagioclase crystallisation, evidenced through the Sr isotopic increase in the most silicic glass sample, is the interpreted eruption trigger. More recently, Mollo & Masotta (2014)

investigated crystallisation temperatures of phenocrysts from heterogeneous magmas of CI. The clinopyroxene-melts pairs tested for equilibrium show a broad distribution of compositions, resulting from a thermally and chemically zoned magma chamber. Indeed, 60% of the cpx from CI were not in equilibrium with the glass at the time of the eruption, which is consistent with a thermally and chemically zoned magma chamber as a feeding source of CI.

The model of a stratified magma chamber has also been inferred for many other arc magmatic systems of variable volumes such as a small-volume monogenetic scoria cone called Uchino, Japan, (Kawamoto, 1992), Vesuvius, Italy with a magma chamber volume of *c.* 1-4 km³ for Plinian eruptions (Civetta *et al.*, 1991), the Hokkaido-Komagatake stratovolcano, Japan, which produced Plinian eruption in 1640 AD associated with an estimated volume of 2.9 km³ (Takahashi & Nakagawa, 2012), and the large La Pacana caldera, Chile (Lindsay *et al.*, 2001; Schmitt *et al.*, 2003) which produced ignimbrites of a total volume of 2,700 km³. However, the currently more common perception of plumbing system architecture is characterised by numerous small magma bodies stalling in the crust, evolving independently from each other.

7.1.1.2. Independent magmatic chambers

The presence of multiple smaller chambers, that evolve independently, is the model favoured for eruptions fed by small volume or short-lived magma reservoirs. The independent magma chambers may be linked and thus form a network of chambers and conduits, which may remain independent from each other, but may also coalesce at shallower depths during ascent.

A study by Carrasco-Núñez *et al.* (2012) focusses on Los Humeros, located in the Mexican volcanic belt, which is a volcano that has produced a caldera-forming eruption.

Zaragoza was its second largest eruption, which occurred 0.1 Ma ago. It was associated with two Plinian pumice-fall layers and a zoned intra-Plinian ignimbrite. This eruption was fed by two main magma types, namely a rhyodacitic magma reservoir and an intruding hybridized andesitic magma, with overlapping Sr-Nd-Pb isotopic signatures, similar phenocrysts assemblages, and similar major- and trace-element covariation patterns. Although both magmas originated from the same source, some geochemical and petrological evidence such as the chaotic and incoherent vertical variation in the relative abundance of both magmas, disequilibrium textures in plagioclase and a mixture of crystals that show equilibrium and disequilibrium, decoupling of bulk incompatible trace elements, a compositional gap, as well as a distinct magmatic temperature and oxygen fugacity for each magma type, suggest that there was no interaction between the two feeding magmas (Figure 7.3). Indeed, there is no evidence of pre-eruptive interaction of these two magmas, and the mingling observed in the erupted pumices may have resulted from syn-eruptive interaction during ascent. It is thought that this eruption was fed by two main reservoirs, which were spatially separated and sequentially tapped during the eruption. Interconnected sills rather than dykes are evoked as feeders to Los Humeros caldera volcano, although no clear supporting evidence for this specific geometry was provided in this study.

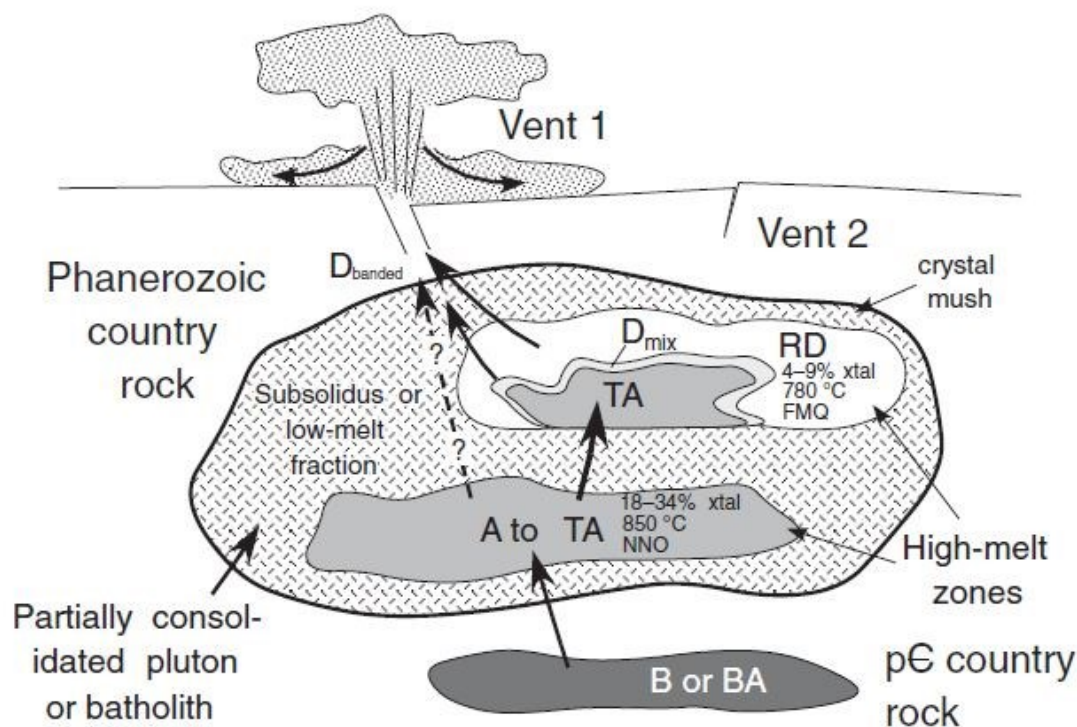


Figure 7.3. Figure 14 of Carrasco-Núñez *et al.* (2012) illustrating a cross section of Los Humeros volcano at the onset of the c. 0.1 Ma BP Zaragoza eruption, which was fed by two main magma reservoirs of distinct chemistry and petrology suggesting separate evolutions. D, RD, BA, B, A, TA, FMQ, NNO and xtal stand for dacite, rhyodacite, basaltic andesite, basalt, andesite, trachyandesite, fayalite-magnetite-quartz, nickel-nickel-oxide and crystal, respectively.

The caldera-forming eruption of Aniakchak volcano, Alaska (3.4 ka BP), was characterised by the eruption of a rhyodacitic and andesitic magma (Larsen, 2006). Although the analysis of melt inclusions provided similar entrapment depth, similar residence time, similar temperatures, and similar mineral compositions, divergence in the degree of crustal assimilation (e.g. Dreher *et al.*, 2005) indicated that these two magmas were not directly related. Thus, adjacent and separated magma reservoirs are the preferred model for the feeding system of the caldera-forming eruption of Aniakchak. Both reservoirs may have previously evolved within an extensive and common crystal mush, which built up over time through mafic injections from a deeper source. The magma dynamics related to this eruption may be related to the ascent of the rhyodacite magma,

either due to an earthquake that impacted the regional tectonic stress, or due to overpressure in the magma chamber allowing the passage of the magma through fractures. By assuming that these two magmas were proximal, the ascent of the rhyodacite may have triggered the destabilisation of the adjacent andesite reservoir, ascending simultaneously. No evidence is discussed in terms of the geometry of the feeding magma chambers.

A study by Larsen *et al.* (2013) focussed on the 2008 phreatomagmatic eruption of Okmok volcano in Alaska, which ejected phenocryst-poor basaltic andesite ejecta containing basaltic groundmass glasses and olivines hosting melt inclusions. The basaltic andesite magma transported olivine phenocrysts that are not in equilibrium with the glass from the juvenile samples. The whole rock compositions are clustered at 52 wt% SiO₂, and the olivine-hosted melt inclusions are more mafic (i.e. 47 wt%). The previous 1997 eruption was distinct in composition, in mineralogy, eruption style (i.e. effusive, blocky lava flow) and exited from a different vent located *c.* 3 km southward. However, the whole-rock major and trace elements overlap with the olivine-hosted melt inclusions found in the 2008 deposits. The sharp difference in composition from 1997 to 2008 indicates that the magmatic system beneath Okmok volcano is laterally heterogeneous, but it is rather composed of small shallow magma bodies fed by a deeper basaltic chamber at 3-6 km beneath the centre of the caldera. Small magma batches rise from this basaltic chamber through dykes to feed individual cones at the surface. The 2008 eruption was fed by the rejuvenation of an old stagnant magma, which had evolved during the past *c.* 1000 years. InSAR and seismic tomography identified two low velocity zones at 2 km and 4-6 km below the surface (Masterlark *et al.*, 2010). The shallow zone is interpreted as a groundwater-saturated caldera fill whereas the 4-6 km zone, which extends laterally

across *c.* 10 km, is associated with the deeper basaltic magma chamber interpreted by Larsen *et al.* (2013).

Another model for Campi Flegrei was proposed by Pabst *et al.* (2008), where multiple magma chambers with distinct compositions fed the pre-CI and the pre-Neapolitan Yellow Tuff caldera-forming eruptions. Major, minor, trace elements and isotopic compositions all point to the formation of different magma batches, which evolved in separate magma chambers with differing degree of differentiation, assimilation and storage duration. These magma chambers remained separated until a large and new magma recharge from a deeper differentiating reservoir into one of the chambers would have resulted in coalescence of the initially separated shallow reservoirs into one large chamber, which fed the cataclysmic eruption of CI. In this case, the Campi Flegrei magmatic plumbing system is characterised by the evolution of individual, separated magma batches, interrupted by large deeper intrusions that trigger their coalescence into a short-lived large magma chamber, which ultimately feeds the cataclysmic eruptions.

7.1.1.3. The “crystal mush” model

Many recent studies, independent of the preferred geometry and conceptual model of the magmatic plumbing system, have adopted the model of crystal mush to explain the long-lived magmatic bodies that get rejuvenated and from which crystals get recycled. The crystal mush model was first defined by Marsh (1981) for the Hawaiian plumbing system. Crystal mush was initially defined as partially molten rock, which reaches a crystal volume of 25-55%, enough to increase the viscosity of the magma, although it was initially not seen to behave like a rigid body. More recently, the distinction between magma and mush is defined at the transition of 55-65 vol. % of crystals (Cashman *et al.*, 2017). Several observations led to the proposal of the crystal mush model. First, it is

consistent with the presence of a few ten percent of melts in magma reservoirs from seismic imaging (e.g. Manga & Brodsky, 2006; Wilcock *et al.*, 1992). Second, there is a large variability of compositions (i.e. major, minor, trace and isotopic composition) and age both within and between crystals within volcanic rocks (e.g. Cooper, 2015; Cooper *et al.*, 2016; Macdonald *et al.*, 2008), again suggesting a long-lived crystal-rich magmatic body beneath volcanoes. Also, melt-dominated zones within a partially molten body over long periods of time are consistent with the results of numerical models of periodic magma recharge into a reservoir (Annen *et al.*, 2015; Huber *et al.*, 2012). Thus, a crystal mush model was initially defined as partially molten rock, which reaches a crystal volume of 25-55 %, enough to increase the viscosity of the magma, although it was initially not seen to behave like a rigid body. More recent work suggests that the distinction between magma and mush occurs at the transition of 55-65 vol. % of crystals (Figure 7.4; Cashman *et al.*, 2017).

A crystal mush may be formed incrementally, with small episodic magma recharge sometimes occurring over millions of years (Annen *et al.*, 2015; Paterson *et al.*, 2011). Crystal mushes are long-lived bodies that link volcanoes to plutons, which are non-eruptible by themselves. The presence of a lasting crystal mush is consistent with the lack of seismic signals during geophysical surveys. Whenever the system becomes liquid-dominant (i.e. after a magma injection), it becomes unstable and gets erupted (Barboni & Schoene, 2014). Indeed, melt-rich segregations are unstable and move through crystal mush regions quite rapidly if multiple vertical intrusions of melt funnel into a single magma chamber. Crystal mush can be erupted as glomerocrysts or cumulate nodules, which are typically characterized by very diverse crystals with complex textures (Fulignati *et al.*, 2000; Wolff *et al.*, 1999). Complex compositional zoning patterns in plagioclase, such as those identified in TgVC and described in Chapter 5, are commonly

thought to have formed in dynamic environments such as crystal mushes, where pressure and temperature fluctuations trigger resorption and disequilibrium features, and recharge events of more mafic magma result in repeated cycles of partial melting and fractional crystallisation (e.g. Zellmer *et al.*, 2003b). An extensive variety of crystal cargo can originate from crystal mushes, as their wide spatial and temporal distributions lead to a mixture of crystals of differing growth histories (e.g. Cooper *et al.*, 2017; Deering *et al.*, 2011b). Crystal mushes can be found in distinct parts of a magmatic reservoir, such as at the base of a stratified magma chamber that has previously undergone fractional crystallisation (Gutierrez & Parada, 2010), but also at the roof and the walls of a magma body because of the solidification fronts propagating inwards from the boundary of a chamber with the cooler crust (Marsh, 1996).

The crystal mush model is currently the most widely accepted model for a large range of tectonomagmatic environments. It has been invoked for many volcanic systems, independently of their compositions (i.e. mafic, intermediate or felsic).

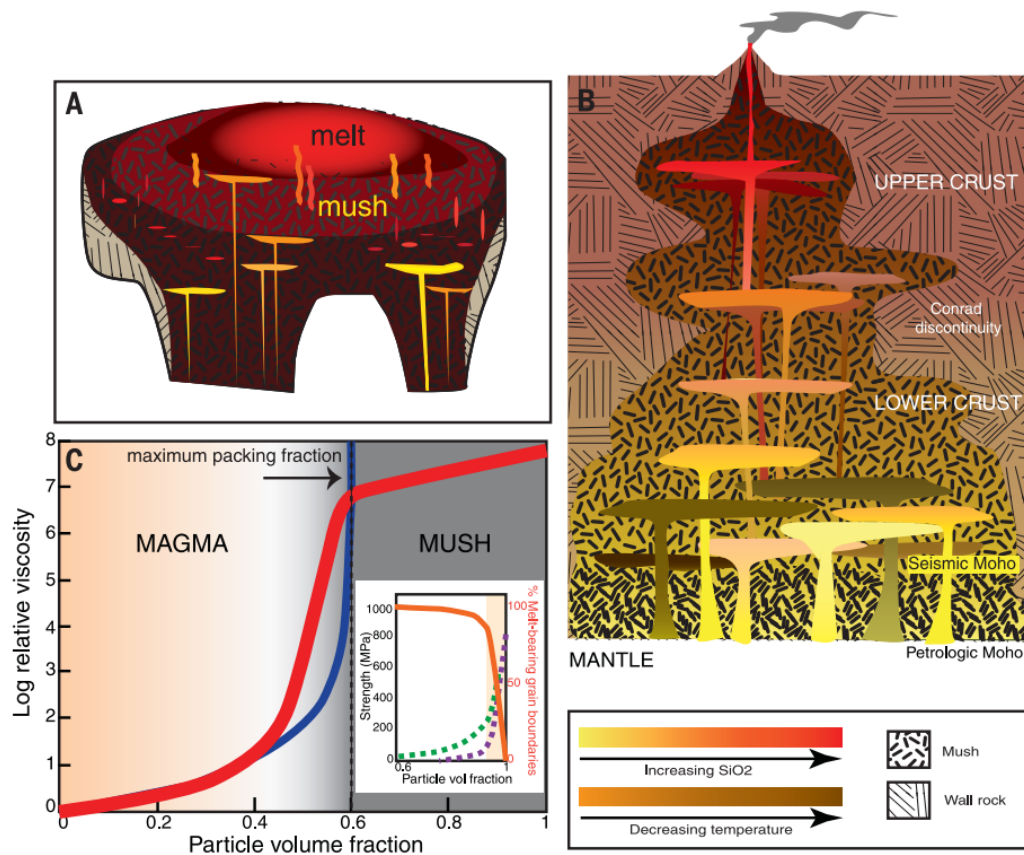


Figure 7.4. Figure 1 of Cashman *et al.* (2017) illustrating the common view of magmatic system with crystal mush based on previous works. (A) Upper crustal magmatic system mostly composed of a large crystal mush and smaller melt silicic melt pods which result from the frequent replenishment of mafic magma inspired from the study of Hildreth (2004). (B) Schematic representation of a trans-crustal magmatic systems with interconnected magma batches resulting from the destabilisation of melt lenses (Christopher *et al.*, 2015). (C) The effect of the particle volume fraction on the change of rheology from magma (orange) to mush (grey). The blue and red curves are calculated using different rheological models (red curve based on the model of Costa *et al.*, 2009a; blue curve based on the model of Marsh, 1981). The insert represents the changes in mush strength as a function of the particle volume fraction where the green dashed curve is based on the experimental data using the Westerly granite and the purple-dashed curve is based on experimental data using Delegate aplite (Rosenberg & Handy, 2005).

7.1.2. Mafic, intermediate and felsic magmatic systems

Although magmatic systems of distinct compositions may present similar inner magmatic processes, the overall geometry of their plumbing systems and the magmatic processes at the origin of their eruptive dynamics differ. The following subsections discuss the main models found in the literature for arc volcanism associated with mafic, intermediate and felsic magmas.

7.1.2.1. Mafic systems

Volcanoes producing mafic compositions (e.g. basalt, basaltic andesite and trachybasalt), are often associated with vigorous and frequent activity. Yasur (Vanuatu), Stromboli (Aeolian Islands, Italy) and Etna (Sicily, Italy) are some examples, and are associated with frequent Strombolian style activity interrupted by paroxysmal events (Figure 7.5; Cigolini *et al.*, 2008). Such volcanoes can be very hazardous as the precursory activity of paroxysmal eruptions (e.g. volcanic tremors, deformation, gas emission) are typically difficult to detect. Because of their frequent activity and their nearly constant magmatic recharge, the feeding conduits and chambers are continuously remobilised, which makes it challenging to detect any profound change in the magmatic feeding system. Also, because these systems are already active, major switches in activity may be implemented rapidly, hence leaving a short time, if any, for evacuation responses. This is well illustrated by the 2018 paroxysmal event at Fuego volcano (Guatemala), where no precursory activity was noticeable (Naismith *et al.*, 2019).

Explosive eruptions of basaltic arc volcanoes are driven by their high volatile content and their high magma flux, leading to rapid magma ascent to the surface. A recent study by Plank *et al.* (2013), which collated data of olivine-hosted melt inclusions from several volcanoes, found that mafic arc magmas contain *c.* 4 wt% water on average, varying from 2 to 6 wt%. A study by Zellmer *et al.* (2016) of mafic magmas from the Trans-Mexican

Volcanic Belt has correlated water content with the stalling depth of ascending magma batches, i.e. more hydrous and cooler melts start degassing and crystallizing deeper, leading to deeper stalling depths due to concomitant viscosity increase.



Figure 7.5. Paroxysmal activity of Stromboli volcano in July 2019 generating a pyroclastic flow after the crater collapse. Photo credits: Sailactive I Segelreisen & Yachtcharter.

In the literature there are two principal models for the eruption of mafic magmas: (i) a single upper crustal magma chamber hosting mafic melts with high volatile content and short magma residence time, and (ii) multiple short-lived and small interconnected magma chambers. These are discussed here using two examples.

(i) The first model is perhaps best represented by Stromboli volcano, located on the Aeolian Islands of Italy, which has been active over a long period of time, with its current eruptive regime starting in 1934 (Capaldi *et al.*, 1978). Stromboli typically behaves as a “steady” volcano with frequent Strombolian explosions, but has also demonstrated

paroxysmal and phreatomagmatic events (Armienti *et al.*, 2007). This is well illustrated by the recent paroxysmal event at Stromboli in July 2019, where no precursory activity was noticeable, except the opening of a vent an hour before the paroxysm (VolcanoDiscovery, 2019). It was characterised by a sudden exceptionally large magma bubble explosion, which triggered the emission of lava flows from all the vents, the ejection of ballistics, and the production of blasts spreading laterally down the island and beyond the shoreline.

A study by Bragagni *et al.* (2014) has characterised U-series disequilibria in the 1996-2007 scoria and lavas (associated with the so called *hp* magma, which stands for highly porphyritic) and pumices (associated with the Ca-rich so called *lp* magma), as well as the 1930 paroxysmal event. They suggested, based on their data and on the previous literature (e.g. Cigolini *et al.*, 2008; Francalanci *et al.*, 2007; Landi *et al.*, 2004; Métrich *et al.*, 2001), that the magma plumbing system consists of a deeper magma chamber at 7-10 km depth and a shallower reservoir at 2-3 km depth, which is characterized by a melt lens within a crystal mush. The *c.* 0.5 km³ deeper reservoir is fed by the *lp* magma, which stalls there for up to 55 years, but periodically feeds the shallower reservoir. During its ascent to the shallow reservoir, the *lp* magma picks up antecrysts, which formed up to 2.5 ka ago in the crystal mush. Subsequently, the volatile-rich *lp* magma and the *hp* magma mix and crystallise due to degassing before ascending to feed the frequent steady Strombolian activity. During paroxysmal events, vigorous pulses of the deep volatile-rich *lp* magma are rapidly percolating through the shallow reservoir without degassing and mixing with the crystal mush and the *hp* magma (Figure 7.6).

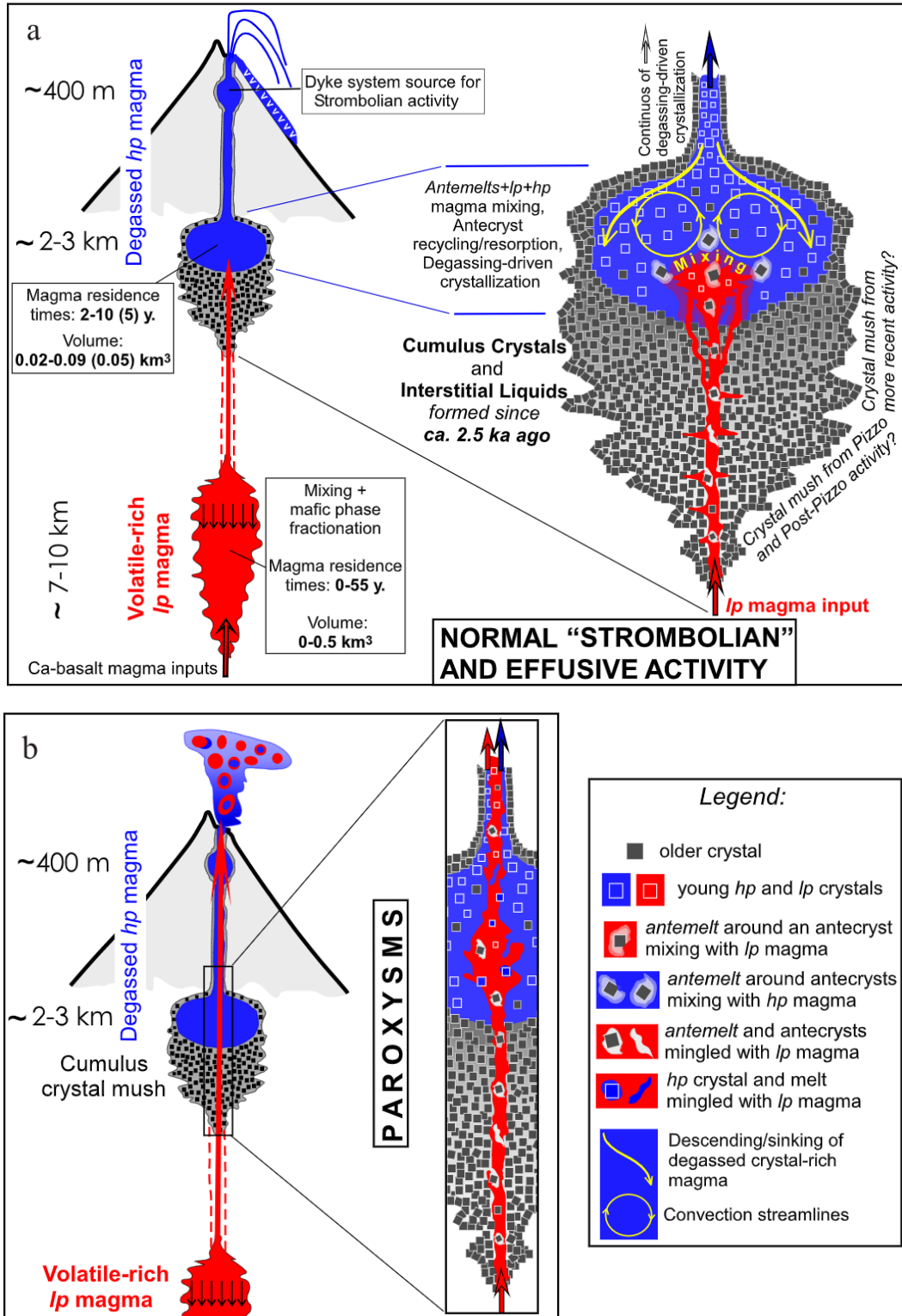


Figure 7.6. Figure 9 of Bragagni *et al.*, (2014) illustrating a conceptual model of the feeding system beneath Stromboli volcano during normal Strombolian and effusive activity (a) and during paroxysm events (b).

(ii) The second model commonly found for mafic arc systems consists of the presence of several small magma batches in the lower and upper crusts. This model was devised to explain the observations of eruptive activity of Etna volcano, Italy (e.g. Kahl *et al.*, 2011; Kahl *et al.*, 2017; La Delfa *et al.*, 2001; Ubide *et al.*, 2019). Mt. Etna has been the focus of much attention due to its frequent activity and the associated hazards it imposes on the nearby town of Catania. A study by Kahl *et al.* (2015) of 180 olivine crystals erupted from 1991 to 2008 has defined at least five compositionally different magmatic environments, which may be interconnected by passageways that are highly active weeks to days prior to an eruptive event. The main five different environments of olivine growth are characterised by distinct temperatures, water contents, and fO_2 conditions. Studies by Giacomoni *et al.* (2014; 2016) looked at the phenocryst textures in lavas and used thermobarometry to determine crystallisation depths. Periodic injections of mafic magma, as well as magma mixing between hydrous and degassed magmas, are recorded in the phenocryst textures, displaying oscillatory, inverse and dusty zoning. Clinopyroxene nucleation occurs at depths of up to *c.* 25 km, whereas plagioclase nucleate at a maximum of 12 km, but at an average of 5-6 km depth, where H_2O in basaltic magmas exsolves. Finally, one of the most recent studies on Mt. Etna employed high resolution imaging of Cr in clinopyroxenes of the eruptions from 1974 to 2014 (Ubide & Kamber, 2018). This new technique shows that titanogaugite can record sharp zoning in the trace element Cr, as it is compatible in the clinopyroxene lattice, and because the melt gets depleted in Cr when clinopyroxene and titanomagnetite crystallise soon after a mafic recharge. The oscillatory Cr-rich zones are located at the rims of clinopyroxene phenocrysts, suggesting late-stage growth before an eruption (Kent *et al.* 2010). Cr-poor cores and Cr-rich rims found in clinopyroxene are not in equilibrium with the same melts, indicating crystallisation from melts of differing compositions. The increase of metal (i.e. Ni and Sc) concentration and

the decrease in rare earth elements (i.e. La and Nd) and high field strength elements (i.e. Zr and Nb) contents in the Cr-rich rims suggest the arrival of a new mafic magma into the system. The growth timescales retrieved for the clinopyroxene, using a constrained growth rate for Etnean clinopyroxenes, imply timescales of 2 weeks from recharge to eruption, originating from 10 km depth using thermobarometers of Purтика (2008) and Neave and Putirka (2017).

These studies, along with those of Kahl *et al.* (2017), Giuffrida *et al.* (2017), and Mollo *et al.* (2015), have used mineral thermodynamics and chemistry, and all arrive at a similar geometry and dynamics for the magmatic plumbing system of Mt. Etna. Except for flank eruptions, for which magma rises quickly through a dyke from a deep reservoir (c. 10 km; Ubide & Kamber, 2018), summit eruptions are fed by magmas that ascend through an architecture of interconnected shallow magma reservoirs (Kahl *et al.*, 2015), in which the polybaric crystallisation of the phenocryst cargo (i.e. plagioclase, olivine and clinopyroxene) records evidence (e.g. patchy cores, oscillatory zoning, reverse zoning, clear dissolved cores, dusty rims; Giacomoni *et al.*, 2014; Giacomoni *et al.*, 2016) of magma mixing and degassing (Ferlito *et al.*, 2012; Mollo *et al.*, 2015) across the entire crustal column.

The spatial distributions of small magma batches that spread laterally are consistent with the multiple discontinuities within the bedrock beneath Mt. Etna (Figure 7.7; Ubide & Kamber, 2018). This model is also consistent with the local tectonic setting, where gravitational spreading and downward sliding of the eastern flank of a few centimetre per year are occurring (Acocella & Neri, 2003; Chiocci *et al.*, 2011; Froger *et al.*, 2001).

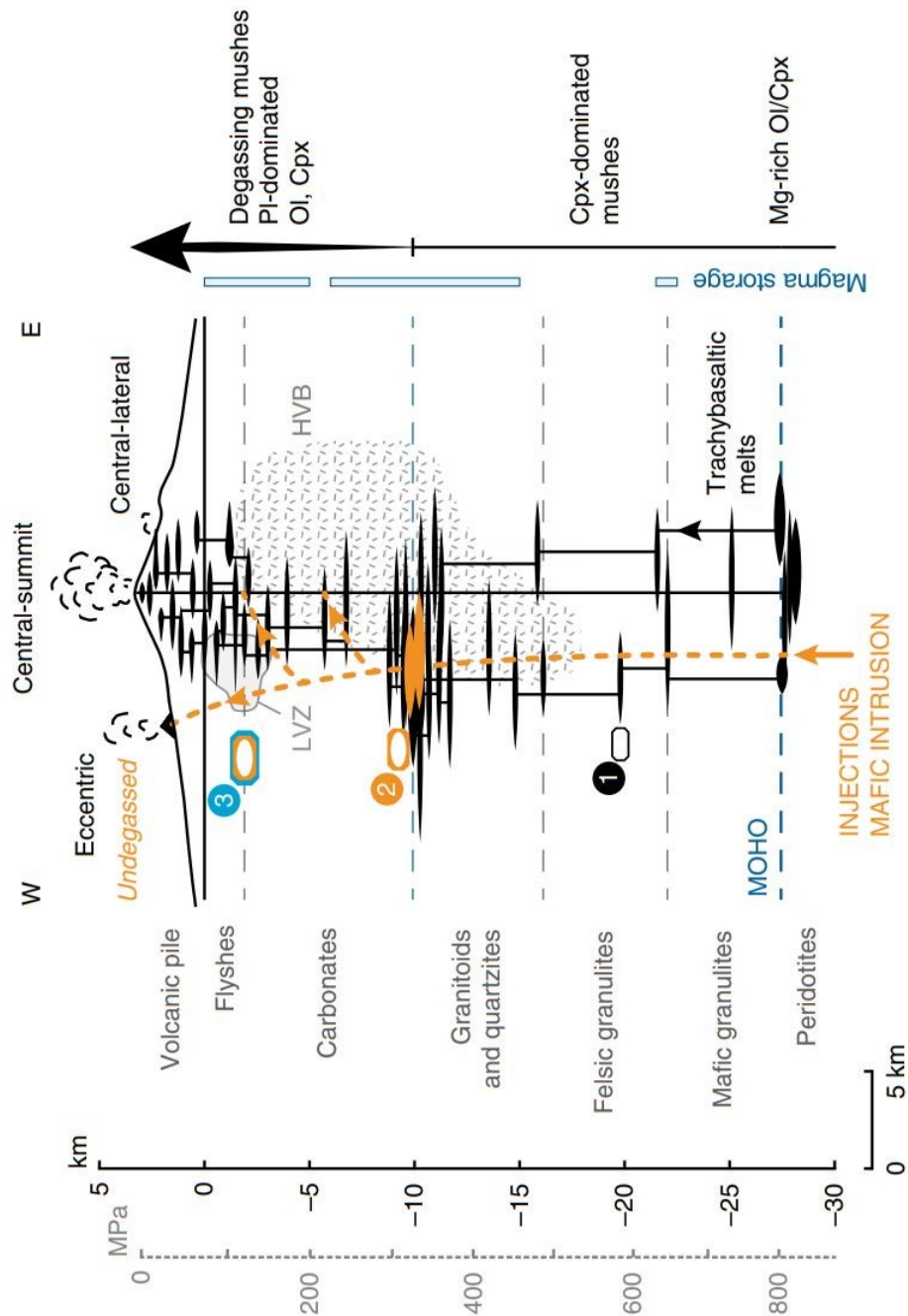


Figure 7.7. Figure 7 of Ubide & Kamber (2018) representing the magmatic plumbing system beneath Mt. Etna composed of multilevel interconnected magma chambers interpreted by the study of Ubide & Kamber (2018) and references therein. A main storage region is at *c.* 10 km depth at the interface between the crystalline basement and the shallower sedimentary sequence. The blue bars represent the magma storage depths inferred from geophysical data. Detected high-VP body (HVP) and the shallow low-Vp zone (LVZ) are used to interpret the magma ascent rates. The magmatic system consists of the accumulation of intruding repeated batches of new mafic magmas, which mix with the resident crystal mush. Injections of mafic intrusions either feed progressively the main central conduit or may feed eccentric eruptions (yellow dashed line).

7.1.2.2. Intermediate systems

The generation of intermediate arc magmatic systems have created profound debates within the scientific community. Their formation is either attributed to the mixing of mafic and felsic magmas (e.g. Mashima, 2004), or to fractional crystallisation of a system, which has progressively evolved (e.g. Grove *et al.*, 2005). For instance, Reubi & Blundy (2009) focus on melt inclusions from intermediate volcanic arc samples, which indicate strong evidence for intermediate magmas being the result of the mixing of mafic and felsic melts. Unlike the bulk-rock, the melt inclusions compositions are associated with a bimodal distribution of silica content, where a lack of intermediate inclusions exist. However, other studies have argued for the formation of intermediate magmas through fractional crystallisation, which is characterized by intrusion of a mafic magma batch that stalls, crystallises and evolves into intermediate compositions (e.g. Tait *et al.*, 1989).. In both cases, the erupted crystal cargo will consist of normally zoned crystals, in which the core is not in equilibrium with the surrounding melt.

Different styles of effusive eruptions occur at intermediate volcanoes involving extrusion of lava flows or growth of lava domes. Some examples of intermediate lava flows in the world include the Tumbre-Talabre andesitic lava flow from Lascar volcano, Chile, which was dated *c.* 7.1 ± 1.25 ka BP (Wörner *et al.*, 2000), the andesitic lava flows of Ngauruhoe volcano, New Zealand, extruded over the past 2 ka (Price *et al.*, 2010), the andesitic lava flows of Ceboruco volcano, Mexico, emitted in 1870 (Böhnelt *et al.*, 2016), the basaltic-andesite lava flow at Arenal volcano, Costa Rica, observed in September 1983 (Gill *et al.*, 1985), the dacitic lava flows of Santiaguito volcano, Guatemala, such as the *c.* 4-km-long flow in 1986-1987 and 1999-2002 (e.g. Harris *et al.*, 2003), and the andesitic lava flows of Bagana volcano, Papua New Guinea, erupted between 2010 and 2011 (Wadge *et al.*, 2012).

The difference between lava flow and lava dome has not clearly been defined in terms of which parameter control their distinction. However, the viscosity of the magma has been shown to have a great impact on whether an effusive eruption will lead to a lava flow or if a dome or a spine will form, potentially followed by an explosive eruption (Rhodes *et al.*, 2018). The viscosity of the magma is a function of temperature, magma compositions and crystal content (e.g. Costa, 2005; Giordano *et al.*, 2008). However, the crystallinity of the magma becomes the foremost factor when increasing from 40 to 60 vol. % (Giordano & Dingwell, 2003; Lejeune & Richet, 1995), contributing three times more than a change in magmatic composition. A study by Zellmer (2008) reports parameters such as the surface heat flux, the convergence rate, and a dimensionless proxy of lava dome proportion, for effusive eruptions from 29 subduction zones to identify the first-order differences between them. One of the main findings is that stalling of high viscosity magmas in a cold crust before eruption is envisaged for arc systems where the rate of mantle melting is low, and the magma transfer from the mantle to the crust is inefficient and slow, hence, resulting in a dominance of lava domes compared to lava flows. This is for example the case for the Lesser Antilles and the Aegean arcs (Zellmer *et al.*, 2000a; Zellmer *et al.*, 2000b). Indirectly, such conditions (i.e., high viscosity magma stalling in a cold crust) indicate that crystallisation and hence viscosity play a major role in the formation of lava domes.

Viscous lava flows and volatile-rich domes may be associated with transitions forth and back to explosive eruptions (e.g. Castro & Gardner, 2008; Preece *et al.*, 2016; Williamson *et al.*, 2010). However, due to the degassing ability of lava flows, the eruption of the pressurized magma within a lava dome is more likely to trigger a shift in activity, i.e. from effusive to explosive (e.g. Cassidy *et al.*, 2018; Voight & Elsworth, 2000; Williamson *et al.*, 2010).

Andesitic to dacitic lava domes are very unstable and are challenging to understand as their behaviour can rapidly change. Initially effusive, dome-forming activity can rapidly change to explosive activity (e.g. Cassidy *et al.*, 2018; Sparks *et al.*, 1977) generating lateral volcanic blasts and pyroclastic flows from collapsing flow fronts (e.g. Cole *et al.*, 1998), sector collapse leading to debris avalanches (e.g. Clavero *et al.*, 2008), and sub-Plinian and Vulcanian eruptions (e.g. Nakada *et al.*, 2019). Some well-studied dome eruptions include the 1980-1986 and 2000-2004 eruptive periods of Mount St. Helens, Oregon, United States (e.g. Berlo *et al.*, 2006; Berlo *et al.*, 2007; Blundy & Cashman, 2001; Geschwind & Rutherford, 1995; Klug & Cashman, 1994; Muir *et al.*, 2012), the 1989-1990 eruptions of Redoubt volcano, Alaska (e.g. Lahr *et al.*, 1994; Miller, 1994; Miller & Chouet, 1994) the 1991-1995 eruptions of Unzen, Japan (e.g. Cichy *et al.*, 2011; Nakada & Motomura, 1999; Nakamura, 1995; Noguchi *et al.*, 2008), the 1995-2002 dome growth and collapse of Soufrière Hills, Montserrat (e.g. Buckley *et al.*, 2006; Couch *et al.*, 2003; Melnik & Sparks, 2002; Robertson *et al.*, 2000; Rutherford & Devine, 2003; Voight *et al.*, 1998; Young *et al.*, 1998), the 2007-2008 dome-forming eruption of Kelut volcano, East Java, Indonesia (Jeffery *et al.*, 2013), and the 2013-2016 lava dome and flow complex of Mount Sinabung, North Sumatra, Indonesia (Hotta *et al.*, 2019; Nakada *et al.*, 2019). Eruptions fed by mafic magma do not usually extrude viscous dome because of the low viscosity and high temperature of the magma. On the contrary, post-caldera endogenous dome formations fed by felsic magma are naturally associated with the melt itself being very viscous due to the high silica content (> 68 wt% SiO₂) and due to the low temperature (*c.* 800 °C), independent of the crystal content (e.g. post Mamaku Ignimbrite domes; Murphy, 1977; Wilson *et al.*, 1984). However, for intermediate magmas, the alternation between effusive (lava domes and flows) and explosive eruptions imply complex processes. Some parameters which may play an important role in the

transition of dome activity to explosive activity are the volatile content, the conduit geometry, the ascent dynamics and whether the system is open or closed.

The 18 May 1980 eruption of Mount St. Helens (MSH) started with a failure of the north flank due to intrusion of a dacitic cryptodome, which triggered a lateral blast followed by 9 hours of sub-Plinian to Plinian activity (Lipman *et al.*, 1982). Donnadieu & Merle (1998) modelled scaled experiments of deformation of a volcanic edifice and found that for the dome preceding the May 1980 flank collapse, the rising magma was accommodated by elastic strain and became channelised following the formation of major shear faults originating from one side of the ascending magmatic body and the surface of the northern flank. After May 1980, MSH entered a period of intermittent lava-dome formation and collapse, accompanied by occasional Vulcanian to sub-Plinian style explosive events (Cashman, 1988). The dome-formation events became less frequent, but extruded larger volumes throughout 1981-1986. The study by melt inclusions by Cashman & McConnell (2005) identified magmas sourced from multiple levels of storage during the 1980 summer eruptions. An increase in cumulative volumes of extruded lava

in domes was also reported for eruptions from Redoubt, Unzen, and Mount Sinabung (Figure 7.8; Nakada *et al.*, 2019).

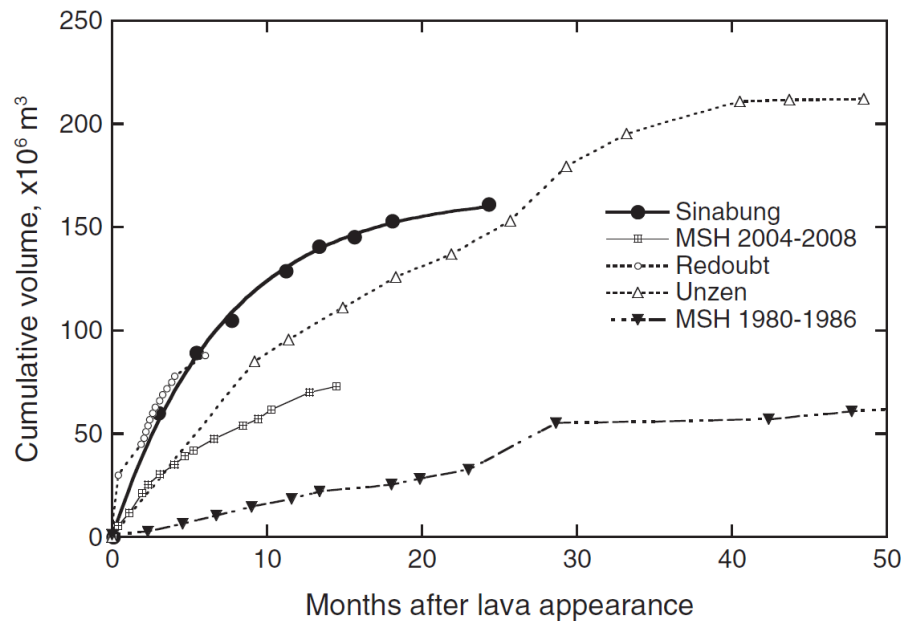


Figure 7.8. Figure 13 of Nakada *et al.* (2019) illustrating the cumulative volume of dome growth formation over time for different eruptions.

Several factors have been proposed as causes of the transition between effusive dome-formation and explosive events feeding Vulcanian and sub-Plinian eruptions. These are (i) shallow change of conduit geometry, (ii) changes in magma ascent rate, and (iii) open- versus closed-system behaviour. These will be discussed below.

(i) *Shallow change of conduit geometry.* One key factor that may explain the transition between dome extrusion and explosive activity has been attributed to a shallow change of conduit geometry. Some studies have highlighted that magmatic properties (such as temperature and composition) remained unchanged during the 1980-1986 activity of MSH (e.g. Browne & Szramek, 2015; Geschwind & Rutherford, 1995) suggesting that the conduit geometry must have been the controlling factors between effusive (i.e. dome) and explosive (e.g. Vulcanian or sub-Plinian) activity. This is especially the case

throughout 1980, during which the decrease in mass flux by three orders of magnitude and the similar temperature, composition, crystal content and water content of the magmas until at least March 1982 implied a decrease in conduit cross-section estimated from 35 m to 7 m (Geschwind & Rutherford, 1995). A more recent study of Cashman & McConnell (2005), which has looked at variations in the textures, compositions and volatile contents of melt inclusions from the 1980 eruptions of MSH, suggests that the conduit evolved from a dyke-like to a more cylindrical geometry through time. Another example is Soufrière Hills volcano, located on the island of Montserrat in the British West Indies, where recent volcanic activity was initiated by phreatic explosions on 18 of July 1995. The first andesitic lava dome began to extrude in mid-November 1995. The change of conduit geometry as a control of transitions between effusive and explosive activity was emphasised for the 1995-1998 Soufrière Hills eruptive period, during which the magma flux decreased over time and led to a slower ascent of a more degassed magma (Sparks *et al.*, 1998). Further, the change of geometry of the conduit has been modelled to assess its effect on magma ascent dynamics in dome-forming eruptions (de' Michieli Vitturi *et al.*, 2008; de' Michieli Vitturi *et al.*, 2010). Their findings indicate that changes in conduit geometry such as widening or constriction, caused by erosion during explosive eruption or by propagation of new magma pathways for instance, play an important role in magma ascent and eruptive dynamics.

(ii) *Magma ascent rates.* The change of ascent rates has previously been mentioned as a cause for transition from effusive to explosive eruptions. For Soufrière Hills volcano, the effect of the ascent rate has been discussed by Rutherford & Devine (2003), as the ascent rates derived from the hornblende reaction rims indicate that dome collapses and Vulcanian explosions coincide with the fastest ascent rates ($> 0.02 \text{ m s}^{-1}$). As the dome grows, the magma ascent rate increases progressively until the domes collapses. In the

case of MSH, it was shown that volatiles can escape from the system faster than they are exsolved from the magma for slow ascent velocity (e.g. $< 0.01 \text{ m s}^{-1}$; Eichelberger et al. 1986). Conversely, if the magma ascent velocity reaches $2\text{-}3 \text{ m s}^{-1}$, volatiles will exsolve from the magma faster than they can escape from the system leading to over-pressurisation, and thus triggering explosive eruptions (e.g. Vulcanian or sub-Plinian eruptions; Geschwind and Rutherford, 1995).

(iii) *Open versus closed system.* Degassing is thought to be one of the main driving forces for magma ascent during explosive eruptions (e.g. Burgisser & Degruyter, 2015; Castro & Gardner, 2008; Crabtree & Lange, 2011; Eichelberger *et al.*, 1986; Jaupart & Allègre, 1991; Shinohara, 2008). As the magma is ascending, the pressure reduces and the volatile solubility drops, triggering volatile exsolution into a gas phase. However, due to the high viscosity of intermediate magmas, the gas phase (present as bubbles) is trapped and the system behaves like a closed-system (Sparks, 2003). In such a system, the volatiles keep on exsolving, leading to growth of bubbles, increasing the volume of the flow, triggering faster ascent velocity and thus fragmentation and eruption (e.g. Cashman & Blundy, 2000; Holland *et al.*, 2011; Magee *et al.*, 2010). Kennedy *et al.* (2016) have experimentally shown that volatile-rich rhyodacite pumice can erupt effusively due to magma outgassing controlled by bubble interconnectivity and surface tension. Similarly, porosity, permeability and water content of the conduit wall rocks may vary over time and even during the same eruptive event (Kennedy *et al.*, 2010): for instance, the unusual explosivity of the 1886 basaltic eruption at Tarawera volcano was interpreted to be partially controlled by heat transfer that sealed the conduit, thereby inhibiting volatile loss. At MSH, in addition to the decrease in ascent rate and conduit radius, the change from closed-system to open-system degassing could have been a controlling factor in the shift from explosive to effusive eruptive activity in 1980 (Geschwind & Rutherford,

1995). From 1980 to 1986, a decrease in dissolved water, and hence explosivity, was associated with an increase of degassing during ascent (Rutherford & Hill, 1993). There was a noticeable decrease in emission of SO₂ and CO₂ in the week prior to the eruptions of July, August and October 1980 (Casadevall *et al.*, 1981). Between major eruptions, gas and entrained ash were commonly emitted. Conservative estimates indicated that the volume of magma degassed was 5-6 times greater than that of the erupted magma. In the case of the 2014 eruption of Kelut volcano in Indonesia, explosive eruptions were alternated by effusive dome-formation and collapse events (Jeffery *et al.*, 2013). It was inferred that the transition between these two types of activity was governed by the dynamics of magma renewal to the system and the degassing conditions, during which the volatiles escaped via permeable conduits in the wall rocks.

In the case of TgVC lava domes are quite uncommon and are mostly controlled by surface processes. In 1945, Ruapehu was characterised by the formation of lava domes interrupted by explosive eruptions with widespread ash emissions (Figure 7.9; Johnston *et al.*, 2000). Crater Lake was emptied by the growth of a dome at the beginning of the eruption in March, which was destroyed by subsequent explosive eruptions. A second dome appeared in May and grew steadily until being subsequently destroyed by explosive activity. Lava domes within the Taupo Volcanic Zone are more commonly associated with the felsic magmatic systems, especially calderas (e.g. Taupo, Maroa and Okataina), suggesting that intermediate and felsic magmatic systems involve different processes, geometries and compositions, even within the same volcanic arc.

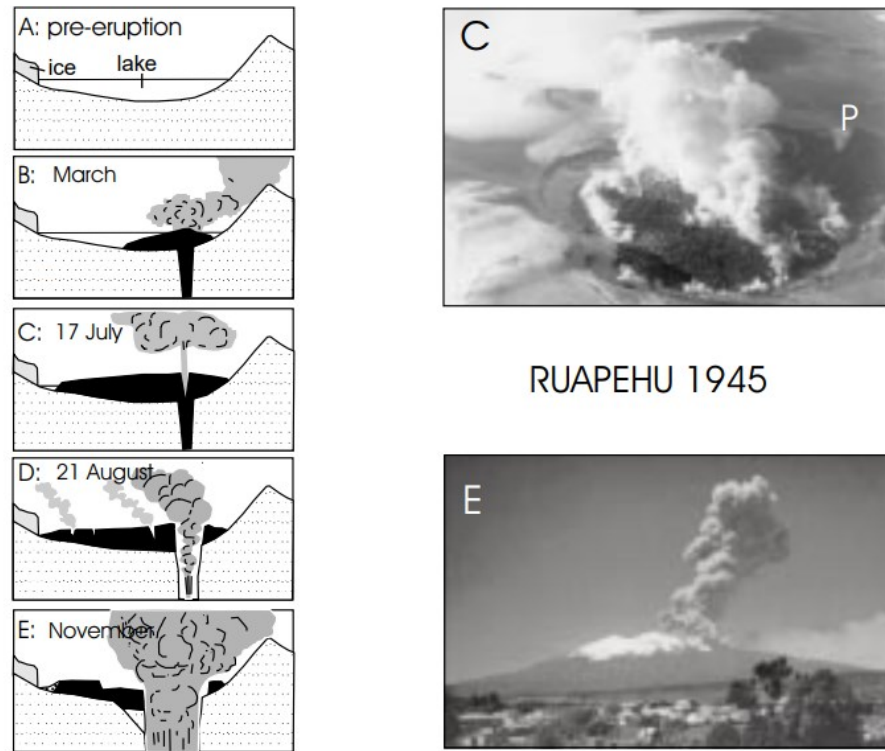


Figure 7.9. Figure 1 of Johnston *et al.* (2000) representing schematic cross sections and photographs from the 1945 activity at Mt. Ruapehu. P is a reference of Pyramid peak.

7.1.2.3. Felsic systems

Magmatic systems involving eruption of felsic magmas have been widely studied as they can be associated with caldera-forming eruptions, including super-eruptions, presenting the deadliest volcanic hazards despite their extremely rare occurrence and thus low likelihood. Felsic magmatic systems can erupt several hundreds of cubic kilometres of magma at once, generating pyroclastic density currents and voluminous ash clouds (Breard *et al.*, 2016). These large eruptions also can reach distances of hundreds of kilometres from their source, and have global effects on the atmosphere (Rampino & Self, 1992). Some examples include the Oruanui eruption of Taupo caldera, New Zealand, *c.* 25 ka BP (*c.* 530 km³; e.g. Wilson 2001); one of the world's largest eruption, which occurred at *c.* 75 ka BP at the lake Toba (*c.* 2,800 km³ including 800 km³ as ash falls; e.g.

Rose & Chesner, 1987); and the formation of the Silver Creek caldera, California, *c.* 18.8 Ma ago ($> 1,300 \text{ km}^3$; Roche *et al.*, 2016). Although these magmatic systems are much larger than TgVC, they share similar magmatic processes as those interpreted for TgVC magmas.

Magmatic systems of such voluminous eruptions have been intensely studied, to understand which processes are controlling the evolution of felsic magmas and their eruption at the surface. Long crystal residence time, often spanning from 10^3 to 10^4 years before the eruption, and zoning hiatus within crystals indicate that felsic eruptions are fed by long-lived magmatic systems that are episodically rejuvenated by intrusions (Storm *et al.*, 2010). Three main current petrogenesis models have been identified for felsic magmatic systems (Sas, submitted): remobilisation (e.g. via heat, volatile and/or mixing) of the felsic reservoir by underplating of mafic intrusions (Deering *et al.*, 2011b; Suzuki & Nakada, 2007); stalling of previously fractionated mafic batches, potentially contaminated by crustal components (via assimilation or mixing; e.g. Montanini *et al.*, 1994); and a magmatic reservoir that develops as a crystal mush, in which melt pods from intrusions ascend upwards and stall near the roof of the storage region (Bachmann, 2010). However, two main geometries in which these processes occur are distinguishable. We discuss here two principal ideas of the production of high-volume felsic magmatic systems: (i) the development of one big magma chamber associated with magmatic underplating, and (ii) multiple independent magma batches becoming amalgamated at the onset of eruption.

(i) The most common model for felsic magmatic systems consists of a very large and old magma chamber, which has evolved over long periods of time. The enormous erupted volumes as well as the crater collapses or caldera-forming events are visible consequences of a large magma chamber. Seismic imaging and gravity data also point to this geometry.

The Altiplano-Puna volcanic complex in central Andes is located above a laterally extensive (500,000 km³; Ward et al., 2014) low velocity zone at *c.* 15 km below sea level (e.g. Chmielowski *et al.*, 1999; Leidig & Zandt, 2003). Considering this sill-like geometry as a single voluminous magma chamber, two end-members of the dynamics occurring within the reservoir have been mentioned: a zoned magma chamber that becomes more mafic from top to bottom, and a globally silicic reservoir with a thinner underplating layer of more mafic magmas. Whether a magma chamber is zoned or not will depend on the ability of intruding melt to percolate through, which in turn depends on the viscosity and the crystallinity of the intruded magma body. Bachmann & Bergantz (2004) present a model of melt expulsion from crystal mush in discussing the origin of crystal-poor rhyolites. At crystallinities above 45 %, and where the interstitial melt is rhyolitic, the crystals form a framework, which allows melt extraction to occur towards the roof of the chamber, above the crystalline residue and below a solidification front. This is also consistent with the trend of zoned rhyolitic eruptions like the Bishop Tuff, which first extruded crystal-poor felsic magma, before tapping into less evolved crystal-rich magma (Hildreth, 1981). This was also observed for the 1912 eruption of Katmai, which showed an abrupt change of crystal content from nearly-aphyric to 40-50 % of crystals towards the end of the eruption (Hildreth & Fierstein, 2000; Turner *et al.*, 2010). For magmatic reservoirs with crystallinities below 55 %, the crystals are kept in suspension due to convection, and thus the magma chamber is mostly felsic, underplated by mafic intrusions (e.g. Bachmann & Bergantz, 2004). Mafic underplating will likely cause heating and remobilisation of the overlying crystal-rich mush (e.g. Cooper & Kent, 2014; Zellmer *et al.*, 2012b). The difference in temperature between the hot mafic intrusions and the “cold” stalling felsic reservoir triggers quenching and outgassing of the mafic magma causing the crystal mush to partially melt. If the intrusion is large and volatile-rich enough, or if

the gradient in temperature between the mafic and felsic bodies is large enough, this process could potentially trigger eruption of the felsic magma (e.g. Deering *et al.*, 2011b). Crystals of previous eruptions have recorded replenishment and remobilisation induced by mafic magma underplating. The presence of a zoning hiatus between growth layers and the varying rim ages of quartz crystals found in the 21.9 ka BP Okareka eruption of OVC, located in the central North Island of New Zealand, provide evidence for a felsic chamber underplated by mafic intrusions (Storm *et al.*, 2011). Quartz crystals were resorbed and contained melt inclusions that were compositionally more evolved than the surrounding melt (Shane *et al.*, 2008b). It is inferred that a crystal mush, which is episodically rejuvenated by mafic underplating, is the best explanation for silicic magmas with complex crystal growth histories.

(ii) Due to the heterogeneity found in erupted deposits from felsic eruptions, a second main model has been proposed, where multiple independent magma batches that previously stalled in the crust are feeding simultaneously the eruption at the surface. Syn-eruptive mingling of the individual magma batches is eventually occurring in the conduit shortly before the eruption starts, without resulting in an efficient mixing. In the case of Tarawera volcano, quartz melt inclusions from pumice clasts erupted over the past *c.* 22 ka, reveal crystallisation from different felsic pods with differing histories, but existing contemporaneously within an upper-crustal mush zone (Shane *et al.*, 2008). Considering the chemistry and thermometry of quartz, the vent locations and the hiatus in time between eruption sequences, distinct magma bodies are thought to be laterally separated. This is also corroborated by the late-stage mingling between co-erupted magmas, evidenced through the disequilibrium between Fe-Ti oxides and the mingled glasses in some samples. Presence of subordinate mafic components in the pumices indicate that the final trigger of the rhyolitic eruptions was the intrusion of mafic magmas into the

felsic magma pods. The melt inclusions, the Fe-Ti oxides and the temperature fluctuations retrieved from the quartz crystals suggest that the magmatic system beneath Tarawera volcano is fed by recurring intrusions and thus incremental growth, which recycles crystal mush upon ascent. A more recent study, which focusses on the Okataina Volcanic Centre, i.e. the broader system beneath Tarawera volcano, has investigated the phenocryst textures, the Sr and Pb isotopic ratios of plagioclase phenocrysts, and the oxygen isotopic ratio in quartz phenocrysts from rhyolitic deposits of caldera eruptions and dome-building episodes (Sas *et al.*, 2019). Phenocrysts exhibit normal and reverse zonings, sometimes both, and a wide range of anorthite contents (i.e. An_{19-77}) and trace element concentrations (e.g. Sr varying from 370 to 1250 ppm), suggesting diverse sources. Taking into consideration previous geophysical studies and petrological models, Sas (submitted) supports the model (Figure 7.10) where the felsic magmatic system beneath OVC was fed by many mafic magmas that stalled at *c.* 10-15 km depth, where they evolved by assimilation, fractionation and contamination of mid-crustal materials. The heat and the volatiles provided to the overlying silicic crystalline mush generate the formation of interconnected felsic melt pods, which ultimately may trigger eruption.

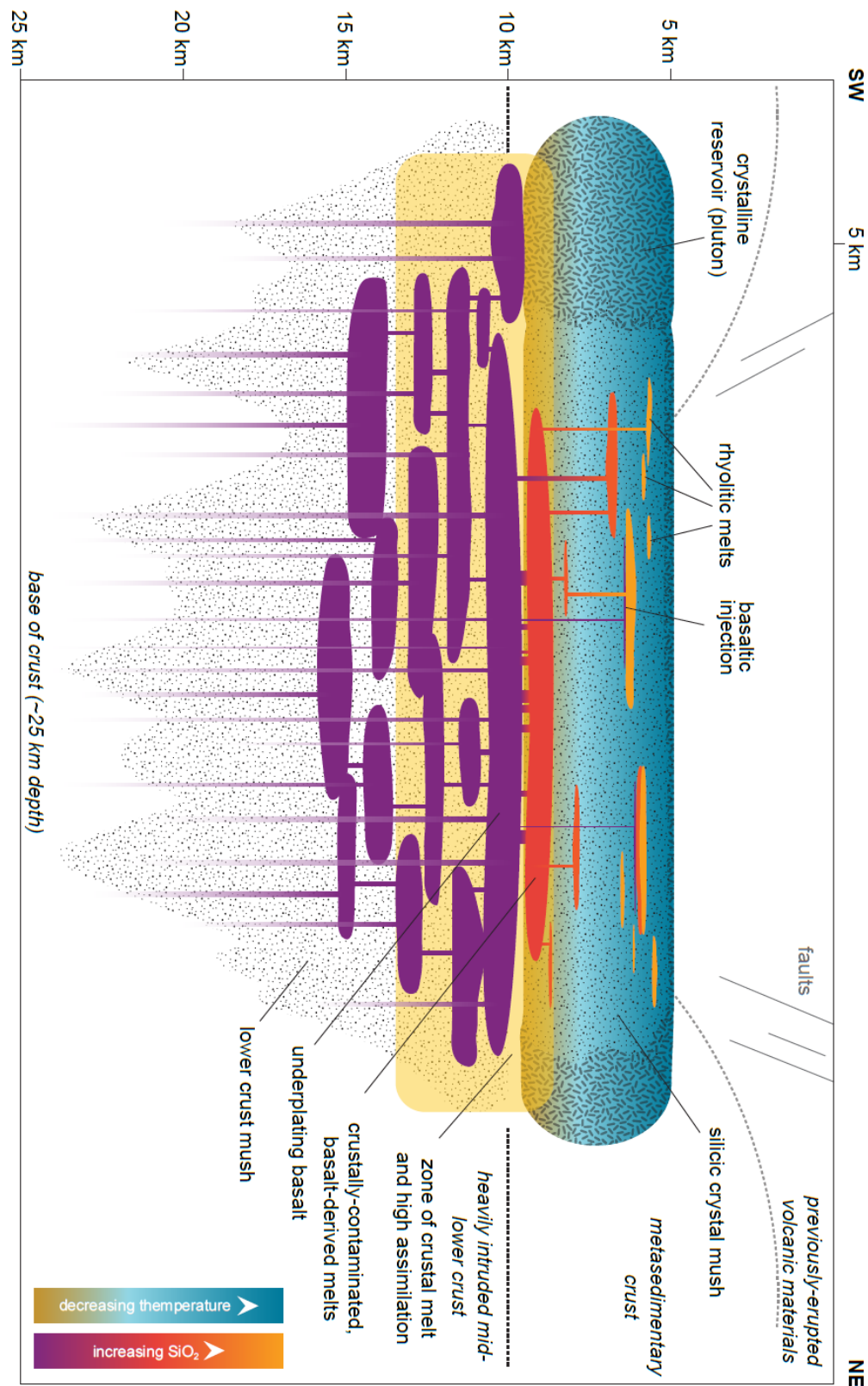
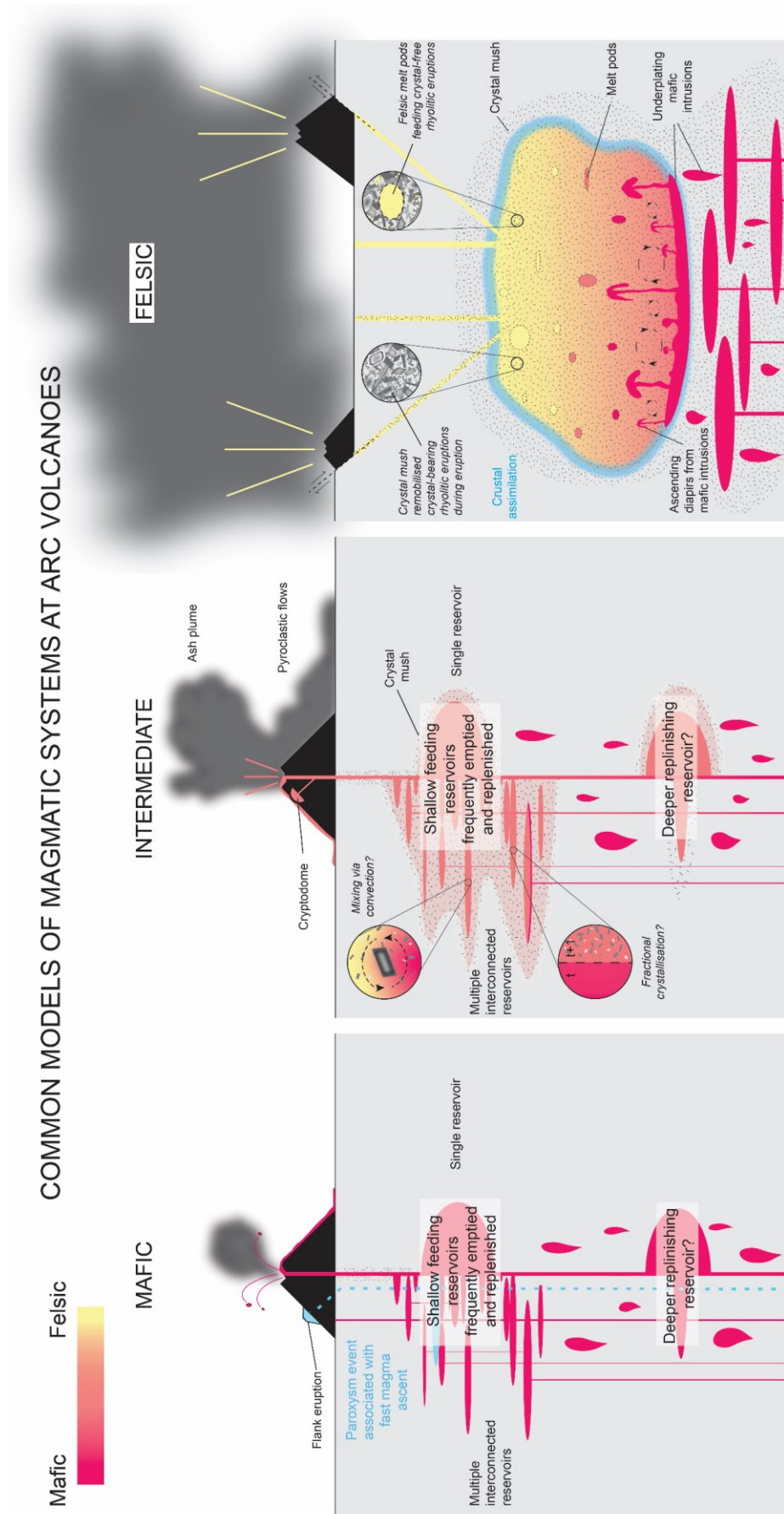


Figure 7.10. Figure 5.6 of Sas (submitted) illustrating a conceptual model of the magmatic system of Okataina Volcanic Centre, New Zealand, that is largely intruded by mafic underplating intrusions, which differentiate by assimilating mid-crustal components. The intrusions transfer heat and volatile to the overlying silicic crystal mush, forming rhyolitic melt pods which eventually feed explosive eruptions and domes.

7.1.3. Reflection on the existing conceptual models

In summary, main trends of the mafic, intermediate and felsic systems studied worldwide can be distinguished (Figure 7.11). Mafic magmatic systems usually erupt relatively frequently (e.g. Stromboli, Etna, Fuego, Paricutin, Karymsky), are fed by a single or multiple interconnected magma reservoir(s) which are continuously recharged by intrusions of small magma batches stalling following either a sill-like or a dyke-like structure. In contrast, felsic magmatic systems are more mature, rarely erupt, and are characterised by a large lateral magmatic reservoir composed of a crystal mush composed of small magma batches which have accumulated in the crust over millions of years (e.g. Taupo, Campi Flegrei, Yellowstone). In between, intermediate magmatic systems are complex, characterised by a single or multiple interconnected reservoir(s) with a crystal mush that formed due to the accumulation of mafic intrusions into the crust. Intermediate compositions develop due to fractional crystallisation of the mafic intrusions or due to the mixing of the silicic crystal mush and the mafic intrusions. Associated eruptions can rapidly switch from effusive (e.g. lava flow or lava domes) to explosive activity (Vulcanian and sub-Plinian style eruptions), depending on volatile content, shallow structure of the system (e.g. MSH cryptodome that formed along a major shear fault) and the degree of remobilisation of the crystal mush (i.e. crystal content), which affects the viscosity and thus the resulting eruption style. In most cases, whether a magmatic system is mafic, intermediate or felsic, the processes invoked for the origin of the eruptive and ascent dynamics include fractional crystallisation, remobilisation, crystal mush formation, magma mixing, changing P-T-X(H₂O) conditions, degassing, etc.

Figure 7.11. (Figure in the next page) Common magmatic plumbing systems beneath arc volcanoes. Mafic magmatic systems are composed of a single or multiple interconnected reservoir(s) which is/are frequently replenished by deep mafic intrusions, feeding mostly effusive (lava flows and Strombolian style) eruptions, and sometimes explosive eruptions (paroxysms). Flank eruptions are common and may be fed by rapidly ascending magma (e.g. Ubide & Kamber, 2018). Intermediate magmatic systems are composed of a single or multiple interconnected reservoir(s) which is/are frequently replenished by deep mafic intrusions which stall, evolve and form a crystal mush in the crust. Intermediate compositions are reached either due to convection between the silicic crystal mush and the replenished mafic intrusions (Reubi & Blundy, 2009), or due to fractional crystallisation (Tait *et al.*, 1989). The entire range of eruption styles can be associated with intermediate magmatic systems, from effusive eruptions (lavas and domes) to Plinian with formation of pyroclastic density currents and high eruptive column. Viscous lava flows and volatile-rich domes may be associated with transitions forth and back to explosive eruptions (Preece *et al.*, 2016). Felsic magmatic systems are fed by a large reservoir which consists of a crystal mush which has experienced crustal assimilation and fractional crystallisation. Melt pods form within this framework due to underplating of mafic intrusions causing heating and remobilisation of the crystal mush. Eventually, mafic intrusions trigger climatic eruptions of up to ultra-Plinian in style (e.g. Wilson, 2001) fed by crystal-bearing or crystal-free rhyolites, possibly mingled with more mafic magma(s).



Many of these conceptual models present sill-like and horizontal structures to represent the magmatic plumbing systems, even when the regional stress distribution may suggest otherwise. Learnt from the first textbooks and because the lower crust is often modelled to be heated by sill injections, many previous studies have presumed horizontal reservoirs to dominate in the upper crustal plumbing systems (e.g. Cartwright & Hansen, 2006; Edmonds *et al.*, 2019; Maccaferri *et al.*, 2011; Resmini, 2007; Tibaldi, 2015). However, the regional tectonic setting and stress field might have a significant effect on the composition, the dynamics and the eruptive processes at work beneath arc volcanoes (e.g. Cembrano & Lara, 2009; Frazzetta & Villari, 1981; Galland *et al.*, 2014; Gudmundsson *et al.*, 1999; Lavenu & Cembrano, 1999). This is often reflected in the shape and the geometry of the edifice or the volcanic complex at the surface. This is especially obvious for (1) flank eruptions on large stratovolcanoes, which are fed by dykes (e.g. 1669 and 1974 eruptions on the flanks of Mt. Etna; e.g. Branca *et al.*, 2013; Corsaro *et al.*, 2009; Favalli *et al.*, 2018), for (2) eruptive fissures such as the 1914 Taisho eruption at Sakurajima volcano, Japan, which developed parallel to the caldera rim (see Figure 1a of Todde *et al.*, 2017), and the 1981 eruption at Mount Pagan, Mariana Islands, where the major fissure developed in a stress field experiencing lateral shear. The kinematically-coupled systems identified by Cembrano & Lara (2009) in the Southern Andes Volcanic Zone, are linked to the current compressional or dextral transpressional tectonic regime, where the spatial distribution of the volcanic vents is governed by the upper crustal stress field (Figure 7.12). Tension fractures, extensional-shear fractures and tail cracks are reflected in clusters of flank vents and minor eruptive centres. These involve isolated pyroclastic cones that are related to active thrusts and thus have triggered large landslides (e.g. Las Hoyadas cones; Naranjo *et al.*, 1997), pyroclastic cones on stratovolcanoes that either follow the NE-SW trend (e.g. Lonquimay and Callaqui) or a

sigmoidal pattern such as those on Villarica and Moco-Choshuenco (e.g. Cembrano & Lara, 2009), and that have mostly produced basaltic and andesitic lava flows.

Finally, it is apparent from the existing models that felsic volcanoes are usually fed by very large magmatic plumbing systems, involving an extensive volume of crystal mush, which has evolved over long periods of time, while mafic and intermediate systems seem to be comparable in terms of size, involving an individual smaller magma reservoir (e.g. Calbuco volcano in Chile, and Shiveluch, Kamchatka in Russia; Castruccio *et al.*, 2016; Humphreys *et al.*, 2006) or multiple discrete magma batches stalling at mid-crustal depths (e.g. Etna and MSH, Cashman & McConnell, 2005; Ubide & Kamber, 2018). Likewise, mafic and intermediate systems generate comparable eruption styles: Strombolian style eruptions, e.g. Pacaya volcano (Dalton *et al.*, 2010) and White Island (Houghton & Nairn, 1991), Vulcanian eruptions e.g. Fuego volcano (Lloyd *et al.*, 2014) and Shinmoedake, Kirishima volcano (Mujin *et al.*, 2017; Shinohara, 2013), sub-Plinian eruptions, e.g. Fuji volcano (Suzuki & Fujii, 2010) and Tutupaca, Peru (Samaniego *et al.*, 2015), and Plinian e.g. Fontana Lapilli, near Masaya (Costantini *et al.*, 2008) and Tungurahua (Wright *et al.*, 2012).

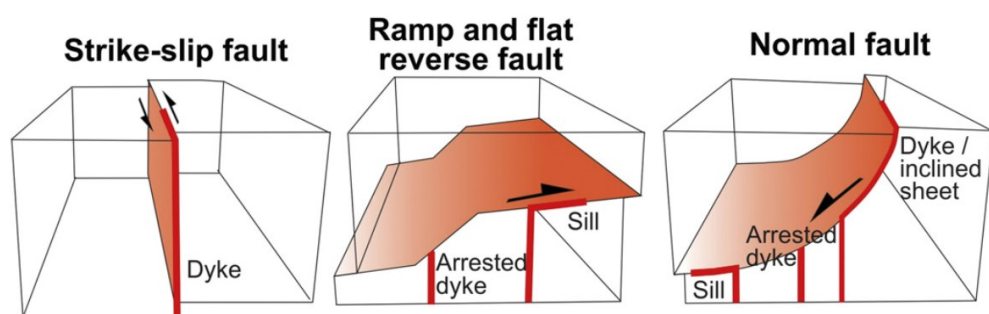


Figure 7.12. Figure 6 of Tibaldi (2015) representing the the preferential geometry of the magma plumbing system in the lower crust governed by the local stress field. Strike-slip fault would enhance the formation of dyke, whereas reverse faults would preferentially develop sill and arrest dyke propagation, and a normal fault will likely develop sill at depth and dyke towards the surface where the dip is increasing.

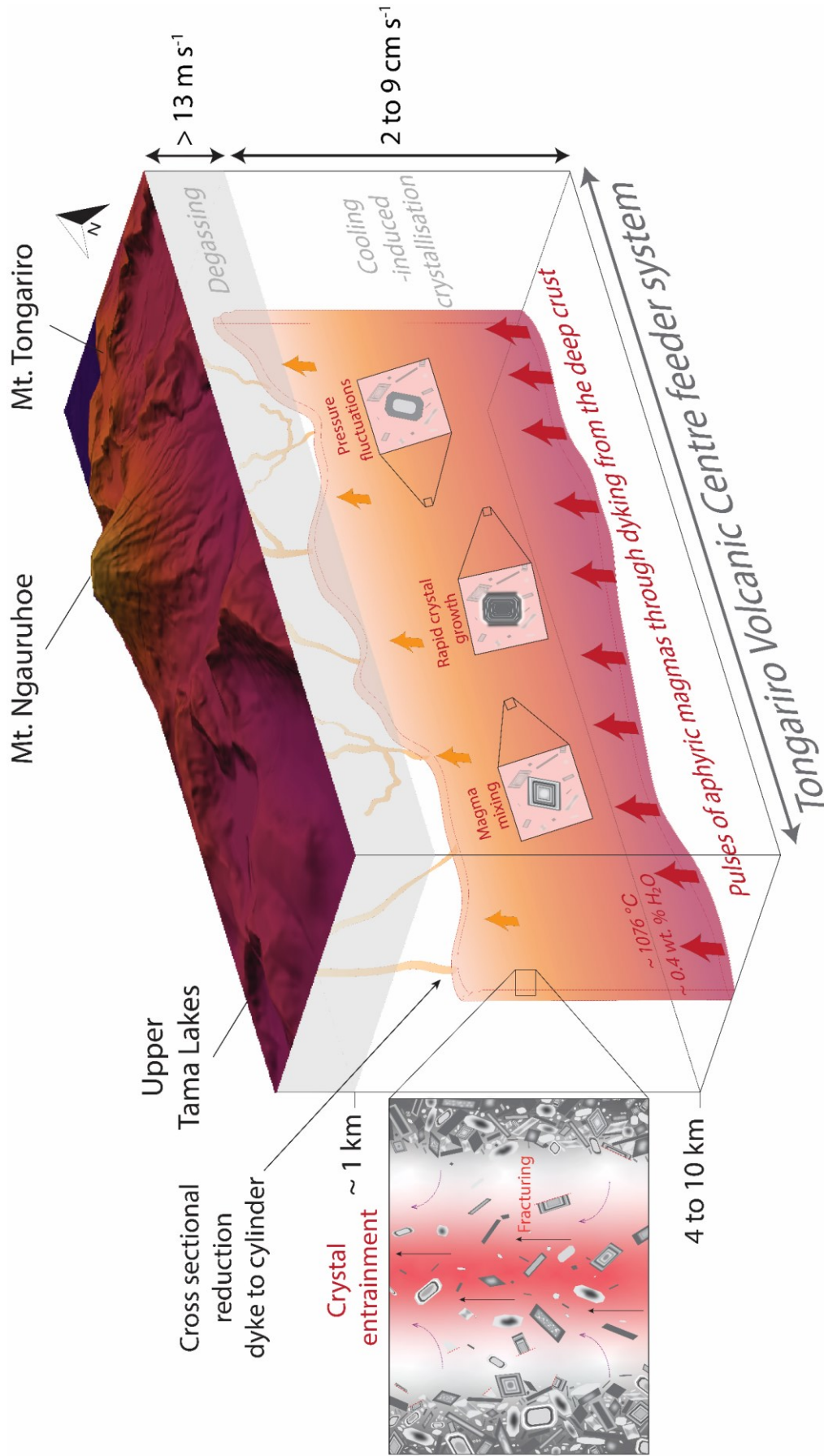
However, the exact geometry of the systems often remains uncertain, the microlitic crystal cargo is often associated with shallow magmatic processes, and both are rarely the main focus of most of the discussed studies. Geochemical and petrological studies, which take into account previous geophysical findings or the local tectonic setting, provide better constraints on the geometry of the magmatic plumbing system (e.g. Brocher, 1981; Leonard *et al.*, 2004; Ubide & Kamber, 2018; Viccaro *et al.*, 2012; Zellmer *et al.*, 2019). Finally, studies that have focussed on microlites and smaller crystal cargos have revealed key information related to late-stage processes leading to a diverse range of eruption styles (e.g. Cichy *et al.*, 2010; Martel, 2012; Mujin & Nakamura, 2014; Mujin *et al.*, 2017; Murch & Cole, 2019; Renjith, 2014; Sano & Toramaru, 2017; Szramek *et al.*, 2010), but these information are currently missing for the Tongariro Volcanic Centre, New Zealand.

7.2. A new architectural model beneath the Tongariro Volcanic Centre

TgVC is a polyvalent volcanic system, which has involved a wide range of explosive eruption styles from phreatic (e.g. Te Maari 2012; Pardo *et al.*, 2014a), Strombolian (e.g. Tufa Trig; Donoghue *et al.*, 1997), Vulcanian (Ngauruhoe 1974; Jolly *et al.*, 2012; Krippner, 2009) sub-Plinian (e.g. Ruapehu 1995; Johnston *et al.*, 2000; Kilgour *et al.*, 2016), and up to Plinian (e.g. the Mangatame Formation; Auer *et al.*, 2015; Nakagawa *et al.*, 1998). Besides, In addition to the three main cones (i.e. Ruapehu, Tongariro and Ngauruhoe), satellite cones (e.g. Pukeonake; Shane *et al.*, 2019), monogenetic volcanoes (i.e. the Ohakune Volcanic Complex; Kósik *et al.*, 2016), and growth of short-lived lava domes (e.g. Ruapehu 1945; Johnston *et al.*, 2000) have formed at TgVC. The extrusions of andesitic lavas is also common at TgVC such as the *c.* 250-275 ka BP lavas of Tongariro (Hobden *et al.*, 1996), the *c.* 2-0 ka BP lavas of Ngauruhoe (Price *et al.*, 2010), and the *c.* 3.4 ka BP lavas from Red Crater (Shane *et al.*, 2017; Topping, 1973). Ruapehu has also produced many effusive events during cone-building episodes e.g. the *c.* 160-

115 ka BP Wahianoa lavas (Gamble *et al.*, 2003; Hackett & Houghton, 1989). Some of the recent explosive eruptions of Ruapehu (e.g. 1945, 1966, 1969, 1995, 1996 eruptions; Gamble *et al.*, 1999) and Ngauruhoe (e.g. 1949 and 1975 eruptions; Hobden *et al.*, 2002) were also followed by lava extrusions. The study by the microlitic and micro-phenocrysts of TgVC has allowed the proposition of a new petrogenetic conceptual model for the feeding systems of explosive eruptions of the Tongariro Volcanic Centre, based on several processes interpreted from the crystal cargos (Figure 7.13).

Figure 7.13. (Figure in the next page) The conceptual model of the shallow magma plumbing system beneath TgVC inferred from this study. The magmas that feed explosive eruptions at TgVC are nearly phenocryst-free and are composed of micro-phenocrysts and large microlites with complex textures and zonations suggesting an antecrystic origin (Chapter 5). Microlites consist of plagioclases and pyroxenes that grew concomitantly due to cooling during magma ascent. Unusually high temperatures and low water contents at microlite crystallisation suggest that cooling drove microlite crystallisation (section 5.4.3). Microlite crystallisation time inferred from CSDs (section 5.4.2) are used with the depth constraint from MELTs modelling and thermobarometry calculations (section 5.4.3) to calculate magma ascent rates, which are too slow to feed explosive eruptions. Thus, a reduction of the conduit cross-section (from dyke to cylinder) is required to accelerate the magmas feeding explosive eruptions at TgVC (Vulcanian eruption with exit velocities of up to 400 m s^{-1}), consistent with the extensional tectonic setting of the region which is accommodated by dyke intrusions (Gómez-Vasconcelos *et al.*, 2017).



7.2.1. Magma mixing

The anorthite contents from the plagioclase crystal cargo present broad variations in compositions (i.e. An₅₅₋₉₉, see Chapter 5), highlighting the different physicochemical properties of the melts from which they crystallised. Besides, disequilibrium textures observed in the large microlites and micro-phenocrysts, such as resorption, overgrowth and sieve textures, are common in the TgVC crystal cargo and may have formed due to rapid decompression (Nelson & Montana, 1992), but also in response to re-heating or a change to a more mafic melt environment during magma recharge and/or magma mixing (Nakamura & Shimakita, 1998). For some tephra, the pyroxenes and the plagioclases were in equilibrium with different glass compositions within the same tephra, suggesting that magma mixing was a key process during crystallisation, or that crystallisation occurred in individual magma batches, distinct in composition, from which crystals were picked up upon ascent to feed explosive eruptions. Magma mixing has also been inferred from the textures found in the phenocrystic cargo of the lavas from Red Crater (Shane *et al.*, 2019) and Pukeonake (Beier *et al.*, 2017).

7.2.2. Crystal uptake from a crystal mush

The variety of crystal compositions (i.e. An content in plagioclase and Mg# in pyroxenes) and the disequilibrium of about 60 % of the adjacent crystal-glass pairs assessed for equilibrium (cf. Chapter 5), suggests that crystal uptake is a major process during ascent of magmas that fed the explosive eruptions at TgVC. Although not frequent, fracture and overgrowth in both plagioclase and pyroxene is identified, suggesting that these crystals experienced high rate of collision or they may have been torn apart from a nearly solidified crystal mush by a hot ascending magma batch. Crystal uptake from crystal mush has been inferred in previous studies (Costa & Morgan, 2010; Girard & Stix, 2009; Hartley *et al.*, 2016), notably from the 2005-2006 eruption at c. 9°50'N in the East

Pacific Rise, where the plagioclase outermost rims were not in equilibrium with the surrounding melts, and have been interpreted to be entrained less than a few days before or during the eruption (Moore *et al.*, 2014). The study by Humphreys *et al.* (2009) on the andesitic magmas of Soufrière Hills, Montserrat, investigated strongly zoned microlites (i.e. $< 100 \mu\text{m}$ in their study, corresponding to the size of micro-phenocrysts in this study), which have crystallised at higher temperatures and in a more mafic magma than that of the micro-phenocrysts (i.e. $100\text{-}300 \mu\text{m}$ in their study, corresponding to the size of phenocrysts in this study). The mafic microlites were incorporated through mixing into the andesitic magmas that fed the eruptions of domes and pyroclastic flows at Montserrat. Thus, the entrainment of large microlites may be a common process occurring at intermediate arc volcanoes.

7.2.3. Cooling-induced microlite crystallisation

The CSD slopes retrieved for pyroxene and plagioclase microlites are similar, regardless of the eruption style (Strombolian, to sub-Plinian), the source (Tongariro, Ngauruhoe or Ruapehu) and the compositions (andesitic or dacitic). This implies that both pyroxene and plagioclase microlites crystallised concomitantly and in response to the same process(es). The hygrometric calculations paired with MELTS modelling resulted in a maximum and an average depth for crystallisation of microlites of 550 MPa (i.e. 16.5 km below sea level) and 140 MPa (i.e. 4.5 km below sea level), respectively. Also, unusually high temperatures for intermediate magmas (i.e. $\leq 1080 \text{ }^\circ\text{C}$) and low water contents (i.e. $\leq 1.50 \text{ wt}\%$) were constrained during microlite crystallisation. These results indicated that microlites did not crystallise as the result of degassing. The water contents retrieved for the TgVC magmas are consistent with the low water contents ($< 2 \text{ wt}\%$) inferred from the phenocryst-hosted melt inclusions of the 1945 to 1996 eruptions of Mt. Ruapehu (Kilgour *et al.* 2013). However, low volatile contents are

unusual in arc settings, where volatiles in the parental magmas are typically the result of the incorporation of fluids (i.e. mainly H₂O) from the dehydrating subducting slab into the overlying mantle wedge (e.g. England & Katz, 2010; Grove *et al.*, 2009; Grove *et al.*, 2012; Kushiro, 1987; Zellmer *et al.*, 2015a). At TgVC, the low water contents and the pressures during microlite crystallisation are inconsistent with the model of microlite crystallisation by decompression-induced degassing (Geschwind & Rutherford, 1995; Hammer *et al.*, 1999; Noguchi *et al.*, 2006; Szramek *et al.*, 2006), and thus, cannot be the driving force of Vulcanian (e.g. Ngauruhoe 1974) and sub-Plinian eruptions (i.e. 1995 Ruapehu). Instead, we propose that the microlite crystallisation was driven by cooling, consistent with the slow magma ascent rates (i.e. < 13 cm s⁻¹ before water exsolution, see Chapter 5).

7.2.4. Pulsatile regime of ascent

Oscillatory zoning is commonly found in the studied tephra, even observed at microlite scale (see Appendix B2), and indicate that crystallisation occurred in a dynamic environment with frequent cycles of re-heating and cooling-induced growth. Remobilisation of a stalling crystal mush prior to eruption is recurrent and coherent with the high proportion of intrusions or failed eruptions, where up to 3 out of 10 intrusions make it to the surface (White *et al.*, 2006; Zellmer *et al.*, 2019 and Figure 7.14). Such a pulsating regime is also in agreement with the tephra stratigraphy of the studied eruptions; the frequent and small-volume eruptions of Mangatawai and Tufa Trig, well-preserved in the field, consist of multiple layered fine ash (e.g. Donoghue *et al.*, 1997; Moebis *et al.*, 2011). Strombolian and Vulcanian style eruptions are also fed by pulses of magmas, such as the frequent Strombolian style explosions of Stromboli and Yasur volcanoes (Gaudin *et al.*, 2014), and the recent Vulcanian activity of Volcán de Colima, Mexico (e.g. Cassidy *et al.*, 2015).

7.2.5. Ascent through dykes

Textures such as the Al-rich rim layers observed in clinopyroxene (cf. Chapter 5, Figure 5.9b) are characteristic of rapid cooling, because incompatible elements such as Al, are incorporated into the tetrahedral site of clinopyroxene during disequilibrium growth triggered by a high degree of undercooling (Mollo *et al.*, 2010; Mollo *et al.*, 2013; Ubide & Kamber, 2018; Ubide *et al.*, 2019). High cooling rates, usually caused by degassing at shallow depth (Crabtree & Lange, 2011), promote nucleation rather than growth (e.g. Armienti *et al.*, 1994; Kirkpatrick, 1977; Mollo & Hammer, 2017), and thus microlite crystallisation. Because the data presented here indicates that cooling was the driving force of crystallisation, due to the volatile-poor characteristic of the TgVC magmas, a narrow geometry of a stalling reservoir must have been in place during crystallisation. Thus, we infer that the magmas stalled in dyke-like structures, where high degrees of undercooling are common due to rapid heat loss through the dyke walls (Gray, 1970; Webber *et al.*, 1999). This is consistent with previous volcano-tectonic studies in the southern TVZ, such as that of Gómez-Vasconcelos *et al.* (2017), which stated that dyke intrusions accommodate 5–22% of the total extension of the Tongariro graben, of which 4–5% may be associated with volcanic eruptions, and 18–19% may be associated with arrested dyke intrusions (Wadsworth *et al.*, 2015). Besides, the high long-axis shape factors obtained from *CSDslice* for some of the TgVC magmas (Table 6.2), are likely to represent a high degree of undercooling, resulting in crystal textures such as hopper, swallowtail and dendritic (Conte *et al.*, 2006; Faure *et al.*, 2003; Humphreys *et al.*, 2006; Shea & Hammer, 2013; Vona & Romano, 2013). This is also consistent with the NNE-striking dykes exposed within Red Crater, which fed the basaltic andesite lavas (Wadsworth *et al.*, 2015). We thus infer a pulsating ascent of magmas through vertical structures, i.e. dykes. This is also consistent with the model of crystal recycling described

by Storm *et al.* (2011), as dyke intrusions of magma through a crystal mush would erode and transport diverse crystal populations.

Funneling into cylinder. Finally, the slow ascent rates calculated for the studied tephtras (i.e. 3 to 13 m s⁻¹, see Chapter 5), even after water exsolution, are too slow to feed the most explosive eruptions. As demonstrated in the work of Taisne & Jaupart (2011), fragmentation, one of the main shallow process accounting for the explosivity of an eruption (e.g. Bindeman, 2005; Martel *et al.*, 2001), in water-poor magmas is unlikely, and the ascending dyke tends to thin when approaching the surface, leading to faster ascent rates. Along these lines, we conclude that the feeder dykes, while propagating towards the surface, experienced a reduction of their cross-section and funnel into narrower conduits, similar to cylinders, to reach exit velocities feeding up to sub-Plinian eruptions (i.e. 50-400 m s⁻¹; Nairn & Self, 1978; Self *et al.*, 1978). If conduit constriction is ineffective, e.g. widening of conduit that may result in late effusion of lavas, or narrowing of initially wide conduits that lead to transitioning of effusive eruption style to more explosive over time (e.g. the 1886 eruption of Tarawera; Houghton *et al.*, 2004), effusive activity would be favoured at TgVC.

Altogether, the data from this study infer that the TgVC magmatic system consists of vertically oriented reservoirs with multiple dykes that are fed by pulses of aphyric melts. This plumbing system recycles complexly-textured micro-antecrysts/-xenocrysts upon ascent to feed explosive eruptions. Most of the intrusions stop propagating in the upper- to mid-crust, where they crystallise. Unlike the previous studies for TgVC based on phenocrysts (Coote & Shane, 2016; Hill *et al.*, 2015; Kilgour *et al.*, 2014; Rowlands *et al.*, 2005; Shane *et al.*, 2017; Shane *et al.*, 2019), this study provides a unique constraint on the origin of the microlites and micro-phenocrysts at TgVC. Our study is in agreement with the most recent study on Tongariro lavas from Shane *et al.* (2019) where textures of

phenocrysts from Red Crater lavas record magma mixing and an antecrystic origin, and for which they deduce a crystal-poor magma entraining phenocrysts during ascent from the mantle to upper-crustal depths. However, in the case of explosive eruptions, if the ascending magmas from the mantle are entraining phenocrysts, most of them remain in the magmatic system. Although dykes are the major structures to transport magma vertically, sills and batholiths are generally the most popular geometry adopted to store magmas at depth. Dykes require accommodation space, which is generally limited to continental rifting (Cashman *et al.*, 2017). However, vertically fed-systems have been inferred for arc volcanoes such as Etna (Giacomoni *et al.*, 2018), Vesuvius (Morgan *et al.*, 2004), Stromboli (Cigolini *et al.*, 2008), Popocatepetl (Martin-Del Pozzo *et al.*, 2008), Mt. Pelée (Fichaut *et al.*, 1989), Soufrière Hills (Paulatto *et al.*, 2019), and Agung volcano during the pre-eruptive seismic swarm in 2017 (Albino *et al.*, 2019). Also, maar eruptions are commonly fed by dykes as the diatreme is often exposed by subsequent half sectioning of entire volcanic edifices (White & Ross, 2011). Diatremes are exposed at many places such as the Barombi Mbo Maa maar in Cameroon (Chako Tchamabé *et al.*, 2015), Miyakejima in Japan (Geshi *et al.*, 2011), Hopi Buttes, Navajo Station, USA (Lefebvre *et al.*, 2013), and the monogenetic Mt Gambier Volcanic Complex, South Australia (van Otterloo & Cas, 2016).

7.3. Implications of new results and hazard assessment

7.3.1. Implications

The study by petrological evidence retrieved from volcanic rocks is an expanding area of research as it provides key information on the kinetics and processes occurring within magmatic systems. Although the current number of citations per annum has doubled in 10 years' time (2010-2020; Scopus research with key words: crystals, volcanic and/or eruption), the amount of available literature that focusses on microlites remains

poor (i.e. *c.* 20 per annum). This study demonstrates the importance of the understanding of microlite ($< 30 \mu\text{m}$) formation to obtain a full picture of the processes at work beneath volcanic systems. As arc magmas are usually carriers of a high content of volatiles (e.g. Wallace, 2005; Zellmer *et al.*, 2015a), microlite crystallisation is commonly associated with decompression-induced degassing (e.g. Cichy *et al.*, 2010; Hammer *et al.*, 1999; Noguchi *et al.*, 2006; Szramek *et al.*, 2006). However, this study questions this mechanism as the permissible depths during microlite crystallisation are as deep as 16.5 km (i.e. 550 MPa), hence, unlikely to be linked to degassing, which is reinforced by the low water contents derived for these magmas.

Previous studies have used CSDs of phenocrysts and microlites to unravel the link between crystal populations and eruption styles (e.g. Murch & Cole, 2019). In this study, however, 60,000 microlites from 22 eruptions were used to generate CSDs for explosive eruptions of TgVC, and they displayed similar slopes. Thus, we infer that microlite CSDs should not be used as discriminant for eruption styles. Instead, we recommend to focus on nanolites ($< 10 \mu\text{m}$) to identify the shallow physicochemical conditions during crystallisation associated with different eruption styles (Mujin & Nakamura, 2014).

Similarly, the inferred plagioclase growth rates derived from the CSD slope and the concomitantly crystallising orthopyroxene microlite crystallisation time (e.g. *c.* $2.94 \times 10^{-11} \text{ m s}^{-1}$), are very similar, irrespective of the eruption styles, and in the range of the existing growth rates from the literature (e.g. Cashman & Blundy, 2000; Geschwind & Rutherford, 1995; Kirkpatrick, 1977). In particular, the study by McCanta *et al.* (2007) derived a very similar plagioclase microlite growth rate for Black Butte dacitic lava flows of $2.50 \times 10^{-11} \text{ m s}^{-1}$, located on the flank of Mount Shasta, CA, USA. Despite eruption styles within TgVC eruptions are different to that of Black Butte, the plagioclase growth

rates derived are similar. Thus, the crystallisation processes may be very similar during microlite crystallisation, which implies that the eruption style is governed by shallower processes, such as the change of geometry of the conduit proposed in this study (i.e. narrowing versus widening of the conduit). The recent study of Murch & Cole (2019) supports this statement, as Vulcanian style explosions and lava dome formations of Soufrière Hills volcano also displayed similar CSDs for large microlites ($> 84 \mu\text{m}$), suggesting that the eruption style is controlled at shallower depths ($< 2 \text{ km}$).

Ascent rate variations are still widely called upon to explain the different eruption styles (Gonnermann & Manga, 2007). However, CSDs and the resulting slow ascent rates derived for TgVC magmas clearly demonstrate that ascent rate at depth is not a key factor to moderate the eruption style within the range investigated. This was also inferred for the 0.5 ka BP eruption of the Inyo volcanic chain, California, which led to comparable ascent and effusion rates for sub-Plinian explosions and extrusion of lavas (Castro & Gardner, 2008). We thus highlight that the variation of conduit geometry at shallow depths for water-poor magmas, such as those of the TgVC, likely dominates the control of the resulting eruption style.

Finally, this study implies that microlites are not necessarily grown within the erupting magmas. The equilibrium assessment failed for 60% of the microlite-glass pairs of TgVC magmas, inferring that the micro-phenocrysts (i.e. $> 30 \mu\text{m}$, considered as microlites in most of the existing literature) have an antecrystic or a xenocrystic origin. This is also confirmed by the complex textures identified for this size range (e.g. oscillatory zoning, resorbed cores, sieve textures). Future studies should not assume that microlite compositions are necessarily in equilibrium with the melt composition, as they

may have grown deeper than volatile exsolution depths and may have even been recycled from previous intrusions (e.g. Humphreys *et al.*, 2009).

7.3.2. Monitoring and hazard assessment

In terms of monitoring and hazard assessment, this study provides an indication of the expected time window between volcanic-related geophysical unrest and eruption, which was unknown until now. Based on the explosive eruptions of the past *c.* 10,000 years, when the magma is ascending to the surface, microlite crystallisation starts 2 to 4 days before an imminent eruption. Crystallisation typically occurs at 4 km beneath the surface, but may start as deep as mid-crustal depths (*c.* 16 km). Microlite crystallisation can be linked to seismic signals, as it increases the viscosity of the magma and might trigger fracturing and fault formation, which in turn triggers volcano-tectonic earthquakes (Stix, 2018). TgVC has been host of all kind of eruption styles e.g. phreatic (e.g. the 2012 Te Maari eruption, Pardo *et al.*, 2014a), phreatomagmatic (e.g. events during the 1995-1996 eruptive period of Ruapehu, Cronin *et al.*, 2003), Strombolian (e.g. the Tufa Trig Formation, Donoghue *et al.*, 1997), Vulcanian (e.g. the 1974-1975 eruptions of Ngauruhoe, Self *et al.*, 1978), sub-Plinian (e.g. the 11-12 October 1995 eruption of Ruapehu, Kilgour *et al.*, 2016) or Plinian eruption (e.g. the Mangamate Formation, Auer *et al.*, 2015). However, the eruptions at TgVC are not always associated with detectable seismic signals. For instance, the 2012 phreatic eruption of Te Maari was preceded by three weeks of precursory gas emission (Christenson *et al.*, 2013) and seismic activity with most of the events located between 1 and 1.5 km beneath the volcano (Hurst *et al.*, 2014), but no clear precursors preceded the explosion. This lack of precursory activity was associated with the sudden decompression of the shallow hydrothermal system that was heated by a deeper magmatic intrusion (Pardo *et al.*, 2014a). Unless the feeding magma is transporting more volatiles than the studied eruptions, only shallow processes

such as the conduit geometry and the potential hydrothermal systems, are likely to control the eruption styles at TgVC. Thus, considering all the potential scenario for a future explosive eruption at TgVC, the next step to mitigate the volcanic hazards will be the detection of the geophysical signals associated with the inferred early ascent from this study.

Chapter 8. Conclusions and outlook

Chapter content:

8.1. Summary of results and implications	250
8.2. Future directions of research	256
8.3. Concluding remark	262

8.1. Summary of results and implications

The main purpose of this study was to unravel the pre- and syn-eruptive ascent of magma and magmatic processes associated with explosive eruptions at the Tongariro Volcanic Centre, New Zealand, through the investigation of the micro-crystal cargo of andesitic tephtras. The tephtras selected for this research were erupted during eruptions of Strombolian to Plinian in style, from different sources and at different times over the past 10,000 years. We focussed on three tephtras from the *c.* 10 ka BP Mangamate Formation (Plinian, erupted from several vents between Ruapehu and Tongariro), ten tephtras from the *c.* 1.7-3.5 ka BP Mangatawai Formation (small volume Vulcanian up to sub-Plinian, erupted mostly from Ngauruhoe), seven tephtras from the *c.* 0-2 ka Tufa Trig Formation (Strombolian to sub-Plinian, erupted from Ruapehu, and including the 1995-1996 AD eruptions), and four tephtras from the 1972-1975 AD eruptions of Ngauruhoe (Strombolian and Vulcanian). These andesitic tephtras glassy-rich, nearly phenocryst-free, and thus offered the ideal foundation to study the micrometre-sized populations of crystals. To this aim, multiple analytical, petrological, and textural approaches were used to address four objectives:

1. Development of an automated method to characterise microlite crystal size distributions (CSDs) from back-scattered electron (BSE) images.

Time-consuming image processing is normally required to generate a CSD, which requires outlining at least 300 crystals (Morgan & Jerram, 2006) from BSE images, usually done manually using image processing software (e.g. *Adobe Photoshop*). The Weka Trainable Segmentation plugin on *ImageJ* was applied for the first time on volcanic rocks (cf. Chapter 3). It consists of a semi-automatic segmentation tool, which uses semi-supervised learning techniques to train an algorithm that in turns classifies the remaining data automatically. This

segmentation technique was used on a set of three images of volcanic rocks (i.e. two individual andesitic tephra from Mangatawai and Mangamate formations, and a welded spatter sample from Tarawera) with differing crystallinities (35%, 50%, $\geq 85\%$ by area) and captured using three Scanning Electron Microscopes of different resolutions (SEM; Field Emission SEM with an image resolution of $4,096 \times 3,072$, Environmental SEM with a resolution of $2,048 \times 1,886$, and a Desktop SEM with a resolution of $1,280 \times 960$). The software successfully classified the plagioclase and pyroxene microlites for the two images with the lowest crystal contents, four to ten times faster compared to the time spent processing the images manually. The crystal-rich sample yielded poor segmentation results due to crystal impingement. The accuracy performance test of the successful classifiers led to F-scores > 0.93 (i.e. the precision-recall F measure), regardless of the resolution of the SEM used. This enhances the reliability of Trainable Weka Segmentation to segment crystals from BSE images of volcanic rocks with up to 50% of crystals. However, it is pertinent to mention that this method is not successful for images in which two objects (e.g. two minerals, or one mineral and the glass) have very similar greyscales, as these will not be distinguished. This study was published in *Microscopy and Microanalysis* (Lormand et al., 2018).

2. Characterisation of the origin of microlites and micro-phenocrysts of TgVC through high resolution imaging.

The textures of the microlites ($< 30 \mu\text{m}$) and micro-phenocrysts ($30\text{-}100 \mu\text{m}$) were investigated to identify the processes at work during crystallisation (cf. Chapter 5). The FE-SEM and the 1270 Secondary Ion Mass Spectrometer (SIMS)

equipped with a stacked CMOS active pixel sensor (SCAPS) provided high resolution elemental maps for plagioclase and pyroxene crystals. Six textures for each mineral were identified down to 30 micrometres and consisted of: resorption and overgrowth, oscillatory zoning, single compositional jump, sieve textures, fractures, and strontium zonation in plagioclase; and resorption and overgrowth, calcium-rich rims, magnesium core and calcic rims, fractures, and aluminium zonation in pyroxene. Additionally, the anorthite content (X_{An}) of the plagioclase and the magnesium number (Mg#) were analysed. Crystal chemical and textural observations were interpreted to indicate the operation of multiple magmatic processes including magma recharge/mixing, pressure fluctuations, fracturing, and rapid cooling and crystal growth. These processes suggest that the microlites and micro-phenocrysts cargo of the feeding magmas of TgVC explosive eruptions have not crystallised from the host magma during its ascent, but instead are relics from previous intrusions, highlighting their antecrystic or xenocrystic origin. We infer that these crystals were entrained by the ascending magma upon ascent. This study has prepared for publication in *Frontiers in Earth Science*, under the title of “*Intermittent ascent of aphyric andesitic melts revealed by cryptic micro-antecryst textures*”..

3. Usage of microlite CSDs to estimate the timescales of magma transfer through the volcanic conduit at the onset of explosive eruptions of TgVC.

Crystal size distributions is a line based on the assumption that for a crystal population with a simple and common history, the logarithm of the population density is inversely proportional to the crystal length. This line can be curved or linear and can provide key information regarding the crystallisation and

nucleation processes of crystals. In this study, CSDs were generated for 22 andesitic tephra of differing sources and eruption styles (cf. Chapter 6). CSDs were created from the morphological measurements of a total of *c.* 60,000 microlites, outlined using the semi-automatic segmentation technique developed for objective 1. Irrespective of the eruption styles, CSDs of all plagioclase and pyroxene microlites (10-30 μm) generated have comparable slopes and thus microlites crystallised under similar conditions and processes. The magma transfer time t from the crystallisation of these microlites to eruption was calculated by combining the CSD slopes and a known growth rate G , as it follows:

$$t = -\frac{1}{G \times \text{slope}}$$

In this case, a well-constrained growth rate of orthopyroxene previously calculated for one of the studied tephra (i.e. Mangatawai 407-17) was used. It was calculated from the orthopyroxene microlites that crystallised at the rim of an olivine phenocryst during its reaction with the surrounding melt (Zellmer et al., 2016; Zellmer et al., 2018). The resulting microlite population growth times vary between 52 ± 14 (2σ) to 99 ± 27 (2σ), implying crystallisation of microlites *c.* 2 to 4 days before an explosive eruption at TgVC. Assuming the pyroxene and the plagioclase microlites crystallised concomitantly, the growth rates derived for plagioclase using the CSD slopes range from 1.65×10^{-11} to $6.43 \times 10^{-11} \text{ m s}^{-1}$. Within the range of experimental growth rates determined for plagioclase, these growth rates corroborate the notion of simultaneous crystallisation of plagioclases and pyroxenes.

4. Identification of the P-T-X(H₂O) conditions during microlite crystallisation to understand the magmatic processes at work during magma ascent.

To fully understand the conditions in which the microlite cargos of TgVC magmas have grown, thermodynamic models such as hygrometry and MELTS were combined to determine pressure, temperature and water content at which the microlites crystallised (cf. Chapter 6). To this aim, mineral and glass compositions retrieved were used for equilibrium assessment of mineral-glass pairs (i.e. $K_D(\text{Fe-Mg})^{\text{opx-liq}} = 0.29 \pm 0.06$ and $K_D(\text{Fe-Mg})^{\text{cpx-liq}} = 0.27 \pm 0.03$), required to validate the output of the hygrometry and MELTS modelling. The orthopyroxene-liquid and clinopyroxene-liquid thermobarometers from Putirka (2008) providing pressure and temperature were iteratively calculated with the water content retrieved from the plagioclase hygrometer of Waters and Lange (2015). MELTS modelling was subsequently tested to narrow the P-T-X(H₂O) ranges obtained by hygrometry. Combined hygrometry and MELTS led to permissible temperatures between 1005 °C and 1130 °C (average of 1076 °C), permissible pressures between 0.1 MPa and 550 MPa (average of 140 MPa i.e. c. 4 km), and water contents between 0.00 wt% and 1.50 wt% (average of 0.40 wt%). During microlite crystallisation, the TgVC magmas were unusually dry and thus hot, and started crystallising microlites at relatively great depths.

Chapter 6 has been reviewed for publication in Journal of Petrology, was deemed acceptable pending minor revisions. The revised script will be resubmitted under the title of “*Slow ascent of unusually hot intermediate magmas triggering Strombolian to sub-Plinian eruptions*”.

The microlite crystallisation times derived from objective 3 and the crystallisation depths derived from objective 4 led to maximum magma ascent rates of 9 cm s^{-1} . Although these ascent rates are calculated assuming constant ascent rates, acceleration is likely at shallower depths. However, the maximum ascent rate after water exsolution of 18 m s^{-1} is still too slow to feed explosive eruptions requiring supersonic exit velocities of *c.* 400 m s^{-1} . Taking the tectonic setting into account, these results have allowed the proposition of a new conceptual model of the magmatic plumbing system feeding explosive eruption at TgVC. The large microlites and micro-phenocrysts have witnessed an environment, where multiple events of recharge, pressure fluctuations, high rate of collision and rapid cooling under high degree of undercooling are occurring, suggesting crystallisation in narrow conduits. Besides, the polybaric crystallisation of microlites favours a vertical system where dykes are intruding the crust. Such a geometry is consistent with the diversity of crystals, which have locally experienced varying magmatic events, e.g. compression and fracturing near the walls and the top of the dyke, and magma recharge events associated with re-heating deeper within the dyke, leading to disequilibrium and oscillatory zoning. Considering the extensional setting, the slow magma ascent and the low water content of these magmas, the ascent and the microlite crystallisation were not driven by decompression-induced degassing; hence, we infer a narrowing of the feeder dyke into a constricted conduit towards the surface, which will allow acceleration of the erupting magma. It appears that in the TgVC, conduit geometry is the ultimate regulator of the explosivity of Holocene volcanism.

Regarding the existing models for magmatic plumbing systems at arc volcanoes reviewed in Chapter 7, it appears that vertically oriented reservoirs are under-represented in the literature, although this study implied that they could be a more common feeding source, especially domains where extensional/transensional tectonic regime prevails e.g.

Cerro Negro volcano (La Femina *et al.*, 2004) and Chiltepe volcano (Freundt & Kutterolf, 2019) in Nicaragua, Mount Mazama in the Cascades, USA (Bacon & Robinson, 2019), Ubinas in southern Peru (Lavallée *et al.*, 2009), Akutan volcano in the Aleutian volcanic arc in Alaska (Lu *et al.*, 2000), Caviahue-Copahue Volcanic Complex at the border of Chile and Argentina (Agusto *et al.*, 2013), and the submarine Hachijo NW volcanic chain in Japan (Ishizuka *et al.*, 2008).

8.2. Future directions of research

During the course of this study, several possible directions for future research were identified, applicable to the current data set and selected samples, but also for other volcanic systems in similar tectonic settings (e.g. an extensional back arc environment):

- Model the Sr diffusion in the 24 plagioclase (micro-)phenocrysts to constrain the timescales of crystallisation of the antecrysts/xenocrysts. The elemental maps obtained with the 1270 SIMS equipped with SCAPS yield ultra-high resolution at submicron scale. The chemical gradient within the imaged crystal will be estimated from the greyscale intensity values (e.g., Kilgour *et al.*, 2014; Morgan *et al.*, 2004) combined with the compositional profiles retrieved across crystals. A forward modelling approach will be used to model the diffusion profiles observed in the crystals.

- Further investigation of the cryptic microlite textures using high-resolution instruments (cf. Chapter 5) may provide a better understanding of the growth kinetics and the processes at work during microlite crystallisation. For instance, the low-Ca pyroxene cores surrounded by high-Ca pyroxene rims have never been targeted in microlites prior to this study (Figure 8.1).

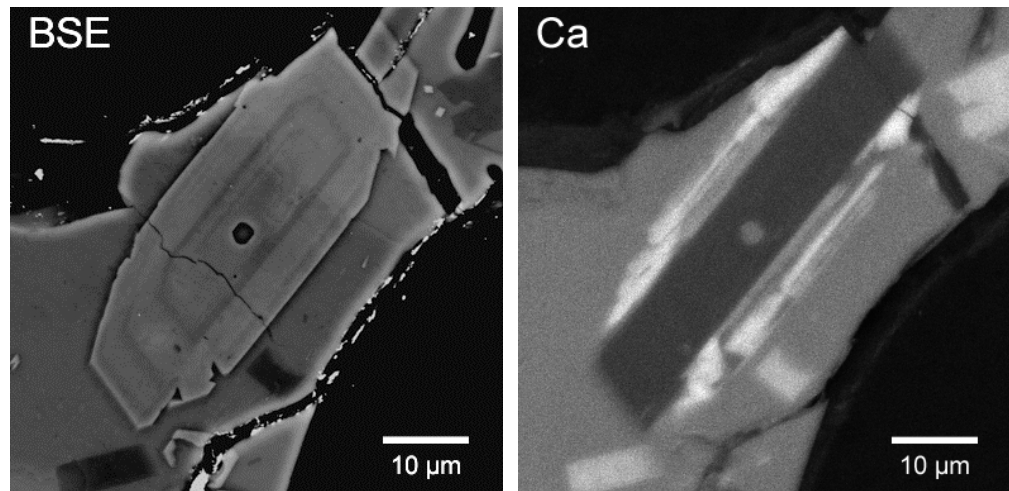


Figure 8.1. Ca (calcium) map of a large microlite of pyroxene from Mangatawai showing Ca-rich rims, cryptic in BSE image.

- One of the main implications of this study is that eruption style is governed by late-stage and shallow processes, following microlite crystallisation, and thus not recorded by microlite crystallisation. Indeed, all TgVC microlite CSDs have similar slopes, regardless of the eruption style. The nanolites ($< 1 \mu\text{m}$) however, exhibit steeper CSDs, due to the extreme undercooling, and may show a dependence related to the eruption style. The studies of Mujin & Nakamura (2014, 2017) have focused on the eruption style transition from the 2011 eruption of Shinmoedake, recorded by the nanolite population. They found that the mineral assemblages of the nanolites change with explosivity, as a consequence of the differing residence time of the magma near the surface. Expanding this

work to the nanolites may reveal similar relationships for the Holocene TgVC explosive eruption record, and this should be tested.

- During analytical sessions, melt inclusions were identified within some microlites and micro-phenocrysts (Figure 8.2). With the exponential improvement of the technology and the resolution of analytical instruments, the measurement of volatile content and compositions in microlite-hosted melt inclusions may provide a better understanding of the rate of volatile degassing in the magma. Indeed, if feasible, the volatile content in the phenocryst-hosted melt inclusions could be compared with that of the microlite-hosted melt inclusions. In the case of TgVC, we found that microlites form 2-4 days prior to an eruption in a nearly anhydrous magma using thermodynamic models. However, given some assumptions and uncertainties, retrieving H₂O from microlite melt inclusions would be valuable to check for consistency with the data presented here.

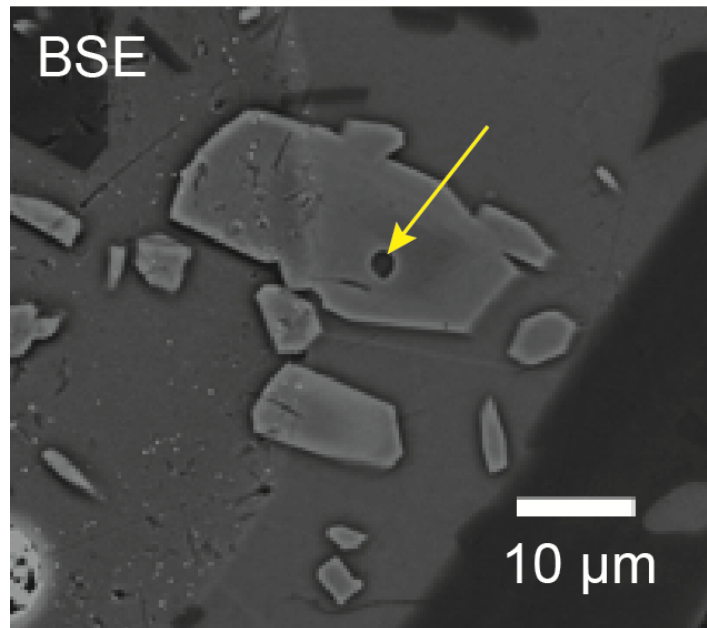


Figure 8.2. Melt inclusion observed (yellow arrow) in a pyroxene microlite from Mangatawai 407-17.

- Although the growth rate used to calculate the microlite population growth time for TgVC magmas was within the range of the existing growth rates, growth rate was assumed linear and constant. However, growth rates are unlikely to be linear and constant under dynamic conditions such as those found in many magmatic systems (e.g. irregular decompression rate, increase of the crystallinity over time), and thus, may not be applicable when the geometry of the conduit is narrowing towards the surface or when the magma displays an irregular ascent behaviour. Verifying the growth rate variation under such conditions with variable decompression rate, mimicking the narrowing of the dyke and therefore the acceleration of the magma, and the associated microlite textures and aspect ratios may provide an even more detailed understanding of the crystallisation processes and timescales.
- To verify the depths resulting from the thermodynamic models, and the validity of using such models applied to microlites, the microlite number density (MND)

could be examined for the studied tephras, where we would expect a high MND for tephras that supposedly started crystallised deeper (e.g. Ngauruhoe 1975) than for those that have crystallised shallower (e.g. Mangatawai 407-56). Additionally, as MND has been interpreted as a function of the water exsolution rate from a magma (Toramaru *et al.*, 2008), we might be able to use it to estimate the water exsolution rate for the TgVC magmas to constrain further the magma ascent velocities at the shallowest depths.

- The vesicle morphology of some of the studied samples varied greatly from one to another. For instance, the vesicles from the 1995 sub-Plinian eruption of Ruapehu are numerous, small and spherical, whereas the vesicles from the 1996 Strombolian eruption of Ruapehu show evidence of coalesced vesicles (Figure 8.3). Such morphologies can be linked to the eruption styles and can provide a better understanding of the late-stage outgassing, and the fragmentation processes and depth (Moitra *et al.*, 2013; Shea *et al.*, 2010b; Shea, 2017). Along these lines, the ash shard morphology may be investigated, especially for the Mangatawai and Tufa Trig eruptions, which require better constraints of their associated eruption styles (Liu *et al.*, 2015).

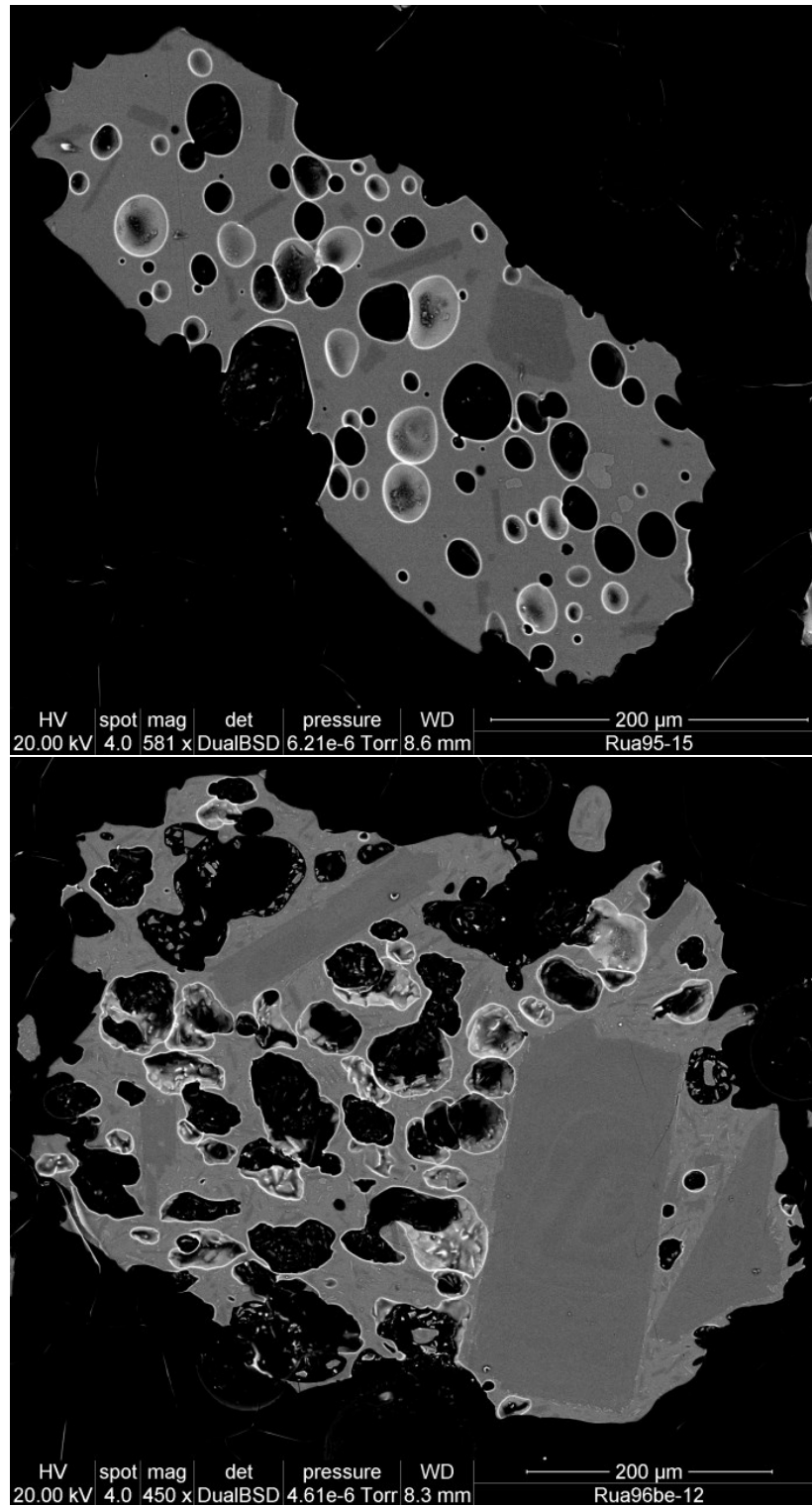


Figure 8.3. BSE images of two glass shards from (a) the 1995 Ruapehu (sub-Plinian) and (b) the 1996 Ruapehu (Strombolian) eruptions. Note the different morphology of the vesicles between the two eruptions.

8.3. Concluding remark

Deep processes in the lower crust (> 15 km) occurring beneath arc volcanoes have been identified and are now well understood thanks to the extensive amount of literature focussing on phenocrysts ($> 100 \mu\text{m}$), such as the analysis of their melt inclusions (e.g. Humphreys *et al.*, 2008), or their isotopic signatures (e.g. Shane *et al.*, 2019). Similarly, near-surface processes are also well constrained by means of geophysical detection tools such as seismic tomography (e.g. Koulakov & Vargas, 2018), and easier access such as the conduit drilling of active volcanoes (e.g. Sakuma *et al.*, 2008). This research fills the gap between deep and eruptive processes by providing a comprehensive investigation of the microlites and micro-phenocrysts, which record upper-crustal processes.

This study contributes to the expansion of the scientific knowledge and provides relevant information to be included in future hazard assessments and evacuation planning, required by the decision makers and stakeholder agencies. The Tongariro Volcanic Centre is one of the most visited spots in New Zealand and requires appropriate and reliable information regarding the potential hazards and risks associated to an explosive eruption.

References

- Acocella, V. and Neri, M. (2003). What makes flank eruptions? The 2001 Etna eruption and its possible triggering mechanisms. *Bulletin of Volcanology*, **65**(7): 517-529.
- Adam, J. and Green, T. (2006). Trace element partitioning between mica- and amphibole-bearing garnet lherzolite and hydrous basanitic melt: 1. Experimental results and the investigation of controls on partitioning behaviour. *Contributions to Mineralogy and Petrology*, **152**(1): 1-17.
- Agostini, C., Fortunati, A., Arzilli, F., Landi, P. and Carroll, M., R. (2013). Kinetics of crystal evolution as a probe to magmatism at Stromboli (Aeolian Archipelago, Italy). *Geochimica et Cosmochimica Acta*, **110**: 135-151.
- Ague, J. J. and Baxter, E. F. (2007). Brief thermal pulses during mountain building recorded by Sr diffusion in apatite and multicomponent diffusion in garnet. *Earth and Planetary Science Letters*, **261**(3-4): 500-516.
- Agusto, M., Tassi, F., Caselli, A. T., Vaselli, O., Rouwet, D., Capaccioni, B., Caliro, S., Chiodini, G. and Darrah, T. (2013). Gas geochemistry of the magmatic-hydrothermal fluid reservoir in the Copahue-Caviahue Volcanic Complex (Argentina). *Journal of Volcanology and Geothermal Research*, **257**: 44-56.
- Ágústsdóttir, T., Woods, J., Greenfield, T., Green, R. G., White, R. S., Winder, T., Brandsdóttir, B., Steinhórsson, S. and Soosalu, H. (2016). Strike-slip faulting during the 2014 Bárðarbunga-Holuhraun dike intrusion, central Iceland. *Geophysical Research Letters*, **43**(4): 1495-1503.
- Aki, K., Fehler, M. and Das, S. (1977). Source mechanism of volcanic tremor: Fluid-driven crack models and their application to the 1963 kilauea eruption. *Journal of Volcanology and Geothermal Research*, **2**: 259-287.
- Aki, K. and Koyanagi, R. Y. (1981). Deep volcanic tremor and magma ascent mechanism under Kilauea, Hawaii. *Journal of Geophysical Research*, **86**: 7095-7110.
- Albino, F., Biggs, J. and Syahbana, D. K. (2019). Dyke intrusion between neighbouring arc volcanoes responsible for 2017 pre-eruptive seismic swarm at Agung. *Nature Communications*, **10**(748).
- Allan, A. S. R., Morgan, D. J., Wilson, C. J. N. and Millet, M.-A. (2013). From mush to eruption in centuries: assembly of the super-sized Oruanui magma body. *Contrib Mineral Petrol*, **166**: 143-164.
- Anderson, A. T. (1976). Magma mixing — petrological process and volcanological tool. *Journal of Volcanology and Geothermal Research*, **1**: 3-33.
- Anderson, A. T. (1984). Probable relations between plagioclase zoning and magma dynamics Fuego Volcano, Guatemala. *American Mineralogist*, **69**: 660-676.
- Annen, C., Lenat, J.-F. and Provost, A. (2001). The long-term growth of volcanic edifices: numerical modelling of the role of dyke intrusion and lava-flow emplacement. *Journal of Volcanology and Geothermal Research*, **105**: 263-289.
- Annen, C., Blundy, J. D. and Sparks, R. S. J. (2006). The genesis of intermediate and silicic magmas in deep crustal hot zones. *Journal of Petrology*, **47**: 505-539.
- Annen, C., Blundy, J. D., Leuthold, J. and Sparks, R. S. J. (2015). Construction and evolution of igneous bodies: Towards an integrated perspective of crustal magmatism. *Lithos*, **230**: 206-221.

- Arganda-Carreras, I., Kaynig, V., Rueden, C., Eliceiri, K. W., Schindelin, J., Cardona, A. and Seung, H. S. (2017). TrainableWeka Segmentation: a machine learning tool for microscopy pixel classification. *Bioinformatics*, **33**(15): 2424-2426.
- Armienti, P., Pareschi, M., T., Innocenti, F. and Pompilio, M. (1994). Effects of magma storage and ascent on the kinetics of crystal growth. *Contrib Mineral Petrol*, **115**: 402-414.
- Armienti, P., Francalanci, L. and Landi, P. (2007). Textural effects of steady state behaviour of the Stromboli feeding system. *Journal of Volcanology and Geothermal Research*, **160**(1-2): 86-98.
- Armienti, P. (2008). Decryption of Igneous Rock Textures: Crystal Size Distribution Tools. *Reviews in Mineralogy and Geochemistry*, **69**: 623-649.
- Arpa, M. C., Zellmer, G. F., Christenson, B. W., Lube, G. and Shellnutt, J. G. (2017). Variable magma reservoir depths for Tongariro Volcanic Complex eruptive deposits from 10,000 years to present. *Bulletin of Volcanology*, **79**(56).
- Asimow, P. D. and Ghiorso, M. S. (1998). Algorithmic modifications extending MELTS to calculate subsolidus phase relations, *American Mineralogist*, pp. 1127.
- Auer, A., White, J. D. L., Nakagawa, M. and Rosenberg, M. D. (2013). Petrological record from young Ruapehu eruptions in the 4.5 ka Kiwikiwi Formation, Whangaehu Gorge, New Zealand. *New Zealand Journal of Geology and Geophysics*, **56**(3): 121-133.
- Auer, A., Martin, C. E., Palin, J. M., White, J. D. L., Nakagawa, M. and Stirling, C. (2015). The evolution of hydrous magmas in the Tongariro Volcanic Centre: the 10 ka Pahoka-Mangamate eruptions. *New Zealand Journal of Geology and Geophysics*, **58**(4): 364-384.
- Bach, P., Smith, I. E. M. and Malpas, J. G. (2012). The origin of garnets in adesitic rocks from the Northland arc, New Zealand, and their implication for sub-arc processes. *Journal of Petrology*, **53**: 1169-1195.
- Bachmann, O. and Bergantz, G. W. (2003). The origin of rhyolites in continental settings: escaping from batholithic crystal mushes, State of the Arc.
- Bachmann, O. and Bergantz, G. W. (2004). On the origin of crystal-poor rhyolites: Extracted from batholithic crystal mushes. *Journal of Petrology*, **45**(8): 1565-1582.
- Bachmann, O. and Bergantz, G. W. (2006). Gas percolation in upper-crustal silicic crystal mushes as a mechanism for upward heat advection and rejuvenation of near-solidus magma bodies. *Journal of Volcanology and Geothermal Research*, **149**(1-2): 85-102.
- Bachmann, O. (2010). The petrologic evolution and pre-eruptive conditions of the rhyolitic Kos Plateau Tuff (Aegean arc), *Open Geosciences*, pp. 270.
- Bacon, C. R. (1986). Magmatic inclusions in silicic and intermediate volcanic rocks. *Journal of Geophysical Research*, **91**: 6091-6112.
- Bacon, C. R. and Druitt, T. H. (1988). Compositional evolution of the zoned calcalkaline magma chamber of Mount Mazama, Crater Lake, Oregon. *Contributions to Mineralogy and Petrology*, **98**(2): 224-256.
- Bacon, C. R. and Robinson, J. E. (2019). Postglacial faulting near Crater Lake, Oregon, and its possible association with the Mazama caldera-forming eruption. *Bulletin of the Geological Society of America*, **131**(9-10): 1440-1458.

- Ballance, P. F. (1976). Evolution of the Upper Cenozoic Magmatic Arc and plate boundary in northern New Zealand. *Earth and Planetary Science Letters*, **28**(3): 356-370.
- Barboni, M. and Schoene, B. (2014). Short eruption window revealed by absolute crystal growth rates in a granitic magma. *Nature Geoscience*, **7**(7): 524-528.
- Barnes, P. M. and Lépinay, B. M. (1997). Rates and mechanics of rapid frontal accretion along the very obliquely convergent southern Hikurangi margin, New Zealand. *Journal of Geophysical Research: Solid Earth*, **102**(B11): 24931–24952.
- Barnes, S. J., Mole, D. R., Le Vaillant, M., Campbell, M. J., Verrall, M. R., Roberts, M. P. and Evans, N. J. (2016). Poikilitic Textures, Heteradcumulates and Zoned Orthopyroxenes in the Ntaka Ultramafic Complex, Tanzania: Implications for Crystallization Mechanisms of Oikocrysts. *Journal of Petrology*, **57**(6): 1171-1198.
- Beattie, P. (1993). Olivine-melt and orthopyroxene-melt equilibria. *Contributions to Mineralogy and Petrology*, **115**(1): 103-111.
- Bebout, G. E. (2012). Metasomatism in Subduction Zones of Subducted Oceanic Slabs, Mantle Wedges, and the Slab-Mantle Interface, Metasomatism and the Chemical Transformation of Rock. Springer.
- Befus, K. S., Manga, M., Gardner, C. A. and Williams, M. (2015). Ascent and emplacement dynamics of obsidian lavas inferred from microlite textures. *Bulletin of Volcanology*, **77**(88).
- Bégué, F., Gravley, D. M., Chambefort, I., Deering, C. D. and Kennedy, B. M. (2014). Magmatic volatile distribution as recorded by rhyolitic melt inclusions in the Taupo Volcanic Zone, New Zealand. In: G.F. Zellmer, M. Edmonds and S.M. Straub (Editors), The role of volatiles in the genesis, evolution and eruption of arc magmas. Geological Society, London, Special Publications.
- Beier, C., Haase, K. M., Brandl, P. A. and Krumm, S. H. (2017). Primitive andesites from the Taupo Volcanic Zone formed by magma mixing. *Contributions to Mineralogy and Petrology*, **172**(5).
- Belgiu, M. and Drăguț, L. (2016). Random forest in remote sensing: A review of applications and future directions. *ISPRS Journal of Photogrammetry and Remote Sensing*, **114**: 24-31.
- Bennett, E. N., Lissenberg, C. J. and Cashman, K. V. (2019a). The significance of plagioclase textures in mid-ocean ridge basalt (Gakkel Ridge, Arctic Ocean). *Contributions to Mineralogy and Petrology*, **174**(6): 49.
- Bennett, E. N., Lissenberg, C. J. and Cashman, K. V. (2019b). The significance of plagioclase textures in mid-ocean ridge basalt (Gakkel Ridge, Arctic Ocean). *Contributions to Mineralogy and Petrology*, **174**(49).
- Benz, U. C., Hofmann, P., Willhauck, G., Lingenfelder, I. and Heynen, M. (2004). Multi-resolution, object-oriented fuzzy analysis of remote sensing data for GIS-ready information. *ISPRS Journal of Photogrammetry and Remote Sensing*, **58**(3-4): 239-258.
- Bergantz, G. W., Schleicher, J. M. and Burgisser, A. (2015). Open-system dynamics and mixing in magma mushes. *Nature Geoscience*, **8**: 793-796.
- Berger, A., Herwegh, M., Schwarz, J.-O. and Putlitz, B. (2011). Quantitative analysis of crystal/grain sizes and their distributions in 2D and 3D. *Journal of Structural Geology*, **33**(12): 1751-1763.

- Berlo, K., Turner, S., Blundy, J., Black, S. and Hawkesworth, C. (2006). Tracing pre-eruptive magma degassing using ($^{210}\text{Pb}/^{226}\text{Ra}$) disequilibria in the volcanic deposits of the 1980-1986 eruptions of Mount St. Helens. *Earth and Planetary Science Letters*, **249**: 337-349.
- Berlo, K., Blundy, J., Turner, S. and Hawkesworth, C. (2007). Textural and chemical variation in plagioclase phenocrysts from the 1980 eruptions of Mount St. Helens, USA. *Contributions to Mineralogy and Petrology*, **154**: 291-308.
- Bindeman, I. N., Davis, A. M. and Drake, M. J. (1998). Ion microprobe study of plagioclase-basalt partition experiments at natural concentration levels of trace elements. *Geochimica et Cosmochimica Acta*, **62**(7): 1175-1193.
- Bindeman, I. N. (2003). Crystal sizes in evolving silicic magma chambers. *Geology*, **31**(4): 367-370.
- Bindeman, I. N. (2005). Fragmentation phenomena in populations of magmatic crystals. *American Mineralogist*, **90**: 1801-1815.
- Bindeman, I. N. and Simakin, A. G. (2014). Rhyolites - Hard to produce, but easy to recycle and sequester: Integrating microgeochemical observations and numerical models. *Geosphere*, **10**(5): 1-27.
- Black, S., Macdonald, R., De Vivo, B., Kilburn, C. R. J. and Rolandi, F. (1998). U-series disequilibria in young (A.D. 1944) Vesuvius rocks: preliminary implications for magma residence times and volatile addition. *Journal of Volcanology and Geothermal Research*, **82**: 97-111.
- Blackburn, E. A., Wilson, L., . and Sparks, R. S. J. (1976). Mechanisms and dynamics of strombolian activity. *Journal of the Geological Society of London*, **132**: 429-440.
- Blake, S., Wilson, C. J. N., Smith, I. E. M. and Walker, G. P. L. (1992). Petrology and dynamics of the Waimihia mixed magma eruption, Taupo Volcano, New Zealand. *Journal of the Geological Society*, **149**(2): 193-207.
- Blaschke, T., Lang, S. and Hay, G. J. (2008). Object-Based Image Analysis: Spatial Concepts for Knowledge-Driven Remote Sensing Applications. Springer.
- Blaschke, T. (2010). Object based image analysis for remote sensing. *ISPRS Journal of Photogrammetry and Remote Sensing*, **65**(1): 2-16.
- Blundy, J. and Wood, B. J. (1991). Crystal-chemical controls on the partitioning of Sr and Ba between plagioclase feldspar, silicate melts, and hydrothermal solutions. *Geochimica et Cosmochimica Acta*, **55**(1): 193-209.
- Blundy, J. and Cashman, K. V. (2001). Ascent-driven crystallisation of dacite magmas at Mount St Helens, 1980-1986. *Contributions to Mineralogy and Petrology*, **140**: 631-650.
- Blundy, J., Cashman, K. V. and Humphreys, M. (2006). Magma heating by decompression-driven crystallization beneath andesite volcanoes. *Nature*, **443**: 76-80.
- Blundy, J. and Cashman, K. V. (2008). Petrologic Reconstruction of Magmatic System Variables and Processes. *Reviews in Mineralogy and Geochemistry*, **69**(1): 179-239.
- Blundy, J. D. and Annen, C. J. (2016). Crustal Magmatic Systems from the Perspective of Heat Transfer. *Elements*, **12**(2): 115-120.
- Böhnel, H., Pavón-Carrasco, F. J., Sieron, K. and Mahgoub, A. N. (2016). Palaeomagnetic dating of two recent lava flows from Ceboruco volcano, western Mexico. *Geophysical Journal International*, **207**(2): 1203-1215.

- Bonaccorso, A., Bonforte, A., Calvari, S., Del Negro, C., Di Grazia, G., Ganci, G., Neri, M., Vicari, A. and Boschi, E. (2011). The initial phases of the 2008–2009 Mount Etna eruption: A multidisciplinary approach for hazard assessment. *Journal of Geophysical Research: Solid Earth*, **116**(B3).
- Bouhifd, M. A. and Jephcoat, A. P. (2011). Convergence of Ni and Co metal–silicate partition coefficients in the deep magma–ocean and coupled silicon–oxygen solubility in iron melts at high pressures. *Earth and Planetary Science Letters*, **307**(3-4): 341-348.
- Bourdon, B., Wörner, G. and Zindler, A. (2000). U-series evidence for crustal involvement and magma residence times in the petrogenesis of Paríacota volcano, Chile. *Contributions to Mineralogy and Petrology*, **139**: 458-469.
- Bouvet de Maisonneuve, C., Dungan, M. A., Bachmann, O. and Burgisser, A. (2012). Insights into shallow magma storage and crystallization at Volcán Llaima (Andean Southern Volcanic Zone, Chile). *Journal of Volcanology and Geothermal Research*, **211-212**: 76-91.
- Bowen, N. L. (1956). *The Evolution of the Igneous Rocks*. Dover, Canada.
- Bradshaw, R. W. and Kent, A. J. (2017). The analytical limits of modeling short diffusion timescales. *Chemical Geology*, **466**: 667-677.
- Bragagni, A., Avanzinelli, R., Freymuth, H. and Francalanci, L. (2014). Recycling of crystal mush-derived melts and short magma residence times revealed by U-series disequilibria at Stromboli volcano. *Earth and Planetary Science Letters*, **404**: 206-209.
- Branca, S., De Beni, E. and Proietti, C. (2013). The large and destructive 1669 AD eruption at Etna volcano: reconstruction of the lava flow field evolution and effusion rate trend. *Bulletin of Volcanology*, **75**(2): 694.
- Breard, E. C. P., Lube, G., Cronin, S. J., Fitzgerald, R., Kennedy, B., Scheu, B., Montanaro, C., White, J. D. L., Tost, M., Procter, J. N. and Moebis, A. (2014). Using the spatial distribution and lithology of ballistic blocks to interpret eruption sequence and dynamics: August 6 2012 Upper Te Maari eruption, New Zealand. *Journal of Volcanology and Geothermal Research*, **286**: 373-386.
- Breard, E. C. P., Lube, G., Jones, J. R., Dufek, J., Cronin, S. J., Valentine, G. A. and Moebis, A. (2016). Coupling of turbulent and non-turbulent flow regimes within pyroclastic density currents. *Nature Geoscience*, **9**(10): 767-771.
- Breiman, L. (2001). Random Forests. *Machine Learning*, **45**(1): 5-32.
- Brocher, T. M. (1981). Geometry and physical properties of the Socorro, New Mexico, Magma bodies. *Journal of Geophysical Research*, **86**(NB10): 9420-9432.
- Browne, B. and Szramek, L. (2015). Chapter 9: Rates of Magma Ascent and Storage. In: H. Sigurdsson, B. Houghton, S.R. McNutt, H. Rymer and J. Stix (Editors), *The Encyclopedia of Volcanoes*. Elsevier.
- Browne, B. L., Eichelberger, J., C., Patino, L. C., Vogel, T. A., Uto, K. and Hoshizumi, H. (2006). Magma mingling as indicated by texture and Sr/Ba ratios of plagioclase phenocrysts from Unzen volcano, SW Japan. *Journal of Volcanology and Geothermal Research*, **154**: 103-116.
- Brugger, C. and Hammer, J. (2010). Crystal size distribution analysis of plagioclase in experimentally decompressed hydrous rhyodacite magma. *Earth and Planetary Science Letters*, **300**(3-4): 246-254.

- Brugger, C. R., Johnston, A. D. and Cashman, K. V. (2003). Phase relations in silicic systems at one-atmosphere pressure. *Contribution to Mineralogy and Petrology*, **146**: 356-369.
- Bryan, C. J. and Sherburn, S. (1999). Seismicity associated with the 1995–1996 eruptions of Ruapehu volcano, New Zealand: narrative and insights into physical processes. *Journal of Volcanology and Geothermal Research*, **90**(1): 1-18.
- Buckley, V. J. E., Sparks, R., S, J. and Wood, B. J. (2006). Hornblende dehydration reactions during magma ascent at Soufrière Hills Volcano, Montserrat. *Contribution to Mineralogy and Petrology*, **151**(2): 121-140.
- Burgisser, A. and Degruyter, W. (2015). Chapter 11 - Magma Ascent and Degassing at Shallow Levels. In: H. Sigurdsson (Editor), *The Encyclopedia of Volcanoes*, pp. 225-236.
- Burton, M. R., Oppenheimer, C., Horrocks, L. A. and Francis, P. W. (2000). Remote sensing of CO₂ and H₂O emission rates from Masaya volcano, Nicaragua. *Geology*, **28**: 915-918.
- Burton, M. R., Allard, P., Murè, F. and Oppenheimer, C. (2003). FTIR remote sensing of fractional magma degassing at Mount Etna. In: C. Oppenheimer, D.M. Pyle and J. Barclay (Editors), *Volcanic degassing*, Geological Society, London, Special Publication, pp. 281-293.
- Capaldi, G., Guerra, I., Lo Bascio, A., Luongo, G., Pece, R., Rapolla, A., Scarpa, R., Del Pezzo, E., Martini, M., Ghiara, M. R., Lirer, L., Munno, R. and La Volpe, L. (1978). Stromboli and its 1975 eruption. *Bulletin Volcanologique*, **41**(3): 259-285.
- Carrasco-Núñez, G. and Riggs, N. R. (2008). Polygenetic nature of a rhyolitic dome and implications for hazard assessment: Cerro Pizarro volcano, Mexico. *Journal of Volcanology and Geothermal Research*, **171**(3): 307-315.
- Carrasco-Núñez, G., McCurry, M., Branney, M. J., Norry, M. and Willcox, C. (2012). Complex magma mixing, mingling, and withdrawal associated with an intra-Plinian ignimbrite eruption at a large silicic caldera volcano: Los Humeros of central Mexico. *GSA Bulletin*, **124**(11-12): 1793-1809.
- Cartwright, J. and Hansen, D. M. (2006). Magma transport through the crust via interconnected sill complexes. *Geology*, **34**(11): 929-932.
- Casadevall, T. J., Johnston, D. A., Harris, D. M., Rosie, W. I., Malincocino, J. L. L., Stoiber, R. E., Bornhost, T. J., Williams, S. N., Woodruff, L. and Thompson, J. M. (1981). SO₂ emission rates at Mount St. Helens from March 29 through December, 1980. In: U.G. Survey (Editor), *The 1980 Eruptions of Mount St. Helens*, Washington, DC., pp. 193-200.
- Cashman, K. V. (1988). Crystallization of Mount St. Helens 1980–1986 dacite: A quantitative textural approach. *Bulletin of Volcanology*, **50**(3): 194-209.
- Cashman, K. V. and Marsh, B. D. (1988). Crystal size distribution (CSD) in rocks and the kinetics and dynamics of crystallisation. II: Makaopuhi lava lake. *Contributions to Mineralogy and Petrology*, **99**: 292-305.
- Cashman, K. V. (1990). Textural constraints on the kinetics of crystallization of igneous rocks. *Reviews in Mineralogy and Geochemistry*, **24**(1): 259-314.
- Cashman, K. V. (1992). Groundmass crystallization of Mount St. Helens dacite, 1980–1986: a tool for interpreting shallow magmatic processes. *Contrib Mineral Petrol*, **109**(4): 431-449.
- Cashman, K. V. (1993). Relationship between plagioclase crystallization and cooling rate in basaltic melts. *Contrib Mineral Petrol*, **113**(1): 126-142.

- Cashman, K. V., Thornber, C. and Kauahikaua, J. P. (1999). Cooling and crystallization of lava in open channels, and the transition of Pahoehoe Lava to 'A'a. *Bulletin of Volcanology*, **61**: 306-323.
- Cashman, K. V. and Blundy, J. (2000). Degassing and crystallization of ascending andesite and dacite. *Philosophical Transactions of the Royal Society of London A*, **358**: 1443-1464.
- Cashman, K. V. and McConnell, S. M. (2005). Multiple levels of magma storage during the 1980 summer eruptions of Mount St. Helens, WA. *Bulletin of Volcanology*, **68**: 57-75.
- Cashman, K. V., Sparks, R., S, J. and Blundy, J. (2017). Vertically extensive and unstable magmatic systems: A unified view of igneous processes. *Science*, **355**(1280).
- Cassidy, J., Ingham, M., Locke, C. A. and Bibby, H. (2009). Subsurface structure across the axis of the Tongariro Volcanic Centre, New Zealand. *Journal of Volcanology and Geothermal Research*, **179**(3-4): 233-240.
- Cassidy, M., Cole, P. D., Hicks, K. E., Varley, N. R., Peters, N. and Lerner, A. H. (2015). Rapid and slow: varying magma ascent rates as a mechanism for Vulcanian explosion. *Earth and Planetary Science Letters*, **420**: 73-84.
- Cassidy, M., Manga, M., Cashman, K. V. and Bachmann, O. (2018). Controls on explosive-effusive volcanic eruption styles. *Nature Communications*, **9**(2839).
- Castro, J., Cashman, K. V. and Mangan, M. T. (2003). A technique for measuring 3D crystal size distributions of prismatic microlites in obsidian. *American Mineralogist*, **88**.
- Castro, J. M. and Mercer, C. (2004). Microlite textures and volatile contents of obsidian from the Inyo volcanic chain, California. *Geophysical Research Letters*, **31**(18).
- Castro, J. M. and Gardner, J. E. (2008). Did magma ascent rate control the explosive-effusive transition at the Inyo volcanic chain, California? *Geology*, **36**(4): 279-282.
- Castruccio, A., Clavero, J., Segura, A., Samaniego, P., Roche, O., Le Pennec, J.-L. and Droguett, B. (2016). Eruptive parameters and dynamics of the April 2015 sub-Plinian eruptions of Calbuco volcano (southern Chile). *Bulletin of Volcanology*, **78**(9): 62.
- Cato, M., J., Fagan, A., L. and Gross, J. (2016). Crystal size distribution of low-Ti lunar basalt Northwest-Africa 8632, 47th Lunar and Planetary Science Conference.
- Cembrano, J., González, G., Lara, L., Medina, E., Aron, E., M., B., Ortega, V., Pérez, P. and Sielfeld, G. (2008). The interplay between crustal tectonics and volcanism in the Central and Southern Volcanic zones of the Chilean Andes, International Symposium on Andean Geodynamics, Nice.
- Cembrano, J. and Lara, L. (2009). The link between volcanism and tectonics in the southern volcanic zone of the Chilean Andes: A review. *Tectonophysics*, **471**: 96-113.
- Chako Tchamabé, B., Ohba, T., Kereszturi, G., Németh, K., Aka, F. T., Youmen, D., Issa, Miyabuchi, Y., Ooki, S., Tanyileke, G. and Hell, J. V. (2015). Towards the reconstruction of the shallow plumbing system of the Barombi Mbo Maar (Cameroon) Implications for diatreme growth processes of a polygenetic maar volcano. *Journal of Volcanology and Geothermal Research*, **301**: 293-313.
- Chakraborty, S. (1997). Rates and mechanisms of Fe-Mg interdiffusion in olivine at 980°C-1300°C. *Journal of Geophysical Research*, **102**(B6): 12317-12331.

- Chakraborty, S. (2008). Diffusion in Solid Silicates: A Tool to Track Timescales of Processes Comes of Age. *Annual Review of Earth and Planetary Sciences*, **36**(1): 153-190.
- Chakraborty, S. (2010). Diffusion coefficients in olivine, wadsleyite and ringwoodite. *Reviews in Mineralogy and Geochemistry*, **72**: 603-639.
- Chardot, L., Jolly, A. D., Kennedy, B. M., Fournier, N. and Sherburn, S. (2015). Using volcanic tremor for eruption forecasting at White Island volcano (Whakaari), New Zealand. *Journal of Volcanology and Geothermal Research*, **302**: 11-23.
- Charlier, B. L. A., Blake, S., van Calsteren, P. and Wilson, C. J. N. (2000). ^{230}Th - ^{238}U magma residence times for the voluminous 26.5 ka Oruanui eruption, Taupo volcano, New Zealand: a multi-grain zircon study. In: I.E.M. Smith, J.P. Davidson, J.A. Gamble and R.C. Price (Editors), State of the Arc 2000 - Processes and time scales. The Royal Society of New Zealand, The Grand Chateau, Ruapehu, New Zealand, pp. 32-35.
- Charlier, B. L. A., Morgan, D. J., Wilson, C. J. N., Wooden, J. L., Allan, A. S. R. and Baker, J. A. (2012). Lithium concentration gradients in feldspar and quartz record the final minutes of magma ascent in an explosive supereruption. *Earth and Planetary Science Letters*, **319-320**: 218-227.
- Chen, W. T., Zhou, M.-F., Gao, J.-F. and Zhao, T.-P. (2015). Oscillatory Sr isotopic signature in plagioclase megacrysts from the Damiao anorthosite complex, North China: Implication for petrogenesis of massif-type anorthosite. *Chemical Geology*, **393-394**: 1-15.
- Chen, X., Zhou, X. and Wong, S. T. C. (2006). Automated segmentation, classification, and tracking of cancer cell nuclei in time-lapse microscopy. *IEEE Transactions on Biomedical Engineering*, **53**(4): 762-766.
- Chen, Y., Provost, A., Schiano, P. and Cluzel, N. (2013). Magma ascent rate and initial water concentration inferred from diffusive water loss from olivine-hosted melt inclusions. *Contributions to Mineralogy and Petrology*, **165**: 525-541.
- Cheng, L., Costa, F. and Carniel, R. (2017). Unraveling the presence of multiple plagioclase populations and identification of representative two-dimensional sections using a statistical and numerical approach. *American Mineralogist*, **102**: 1894-1905.
- Cherniak, D. J. and Watson, E. B. (1992). A study of strontium diffusion in K-feldspar, Na-K feldspar and anorthite using Rutherford Backscattering Spectroscopy. *Earth and Planetary Science Letters*, **113**: 411-425.
- Cherniak, D. J. and Watson, E. B. (1994). A study of strontium diffusion in plagioclase using Rutherford backscattering spectroscopy. *Geochimica et Cosmochimica Acta*, **58**(23): 5179-5190.
- Cherniak, D. J. (1996). Strontium diffusion in sanidine and albite, and general comments on strontium diffusion in alkali feldspars. *Geochimica et Cosmochimica Acta*, **60**: 5037-5043.
- Cherniak, D. J., Hanchar, J. M. and Watson, E. B. (1997). Diffusion of tetravalent cations in zircon. *Contributions of Mineralogy and Petrology*, **127**: 383-390.
- Cherniak, D. J. (1998). Pb diffusion in clinopyroxene. *Chemical Geology*, **150**: 105-117.
- Cherniak, D. J. and Dimanov, A. (2010). Diffusion in pyroxene, mica and amphibole. *Reviews in Mineralogy and Geochemistry*, **72**: 641-690.

- Chiocci, F. L., Coltelli, M., Bosman, A. and Cavallaro, D. (2011). Continental margin large-scale instability controlling the flank sliding of Etna volcano. *Earth and Planetary Science Letters*, **305**(1): 57-64.
- Chistyakova, S. and Latypov, R. (2010). On the development of internal chemical zonation in small mafic dykes. *Geological Magazine*, **147**(1): 1-12.
- Chmielowski, J., Zandt, G. and Haberland, C. (1999). The Central Andean Altiplano-Puna magma body. *Geophysical Research Letters*, **26**(6): 783-786.
- Christenson, B. W. (2000). Geochemistry of fluids associated with the 1995–1996 eruption of Mt. Ruapehu, New Zealand: signatures and processes in the magmatic-hydrothermal system. *Journal of Volcanology and Geothermal Research*, **97**(1): 1-30.
- Christenson, B. W., Reyes, A. G., Young, R., Moebis, A., Sherburn, S., Cole-Baker, J. and Britten, K. (2010). Cyclic processes and factors leading to phreatic eruption events: Insights from the 25 September 2007 eruption through Ruapehu Crater Lake, New Zealand. *Journal of Volcanology and Geothermal Research*, **191**(1-2): 15-32.
- Christenson, B. W., Britten, K. W., Mazot, A. and Fitzgerald, J. (2013). The 2012 Eruption of Te Maari: Pre- and Post-eruption Gas Signatures from the Magmatic-Hydrothermal System, Te Maari day – a workshop to discuss scientific advances from the 2012 Te Maari eruption. GNS Science Miscellaneous Series, Council Office, Turangi, pp. 28.
- Christopher, T. E., Blundy, J., Cashman, K., Cole, P., Edmonds, M., Smith, P. J., Sparks, R. S. J. and Stinton, A. (2015). Crustal-scale degassing due to magma system destabilization and magma-gas decoupling at Soufrière Hills Volcano, Montserrat. *Geochemistry, Geophysics, Geosystems*, **16**(9): 2797-2811.
- Cichy, S. B., Botcharnikov, R. E., Holtz, F. and Behrens, H. (2010). Vesiculation and Microlite Crystallization Induced by Decompression: a Case Study of the 1991-1995 Mt Unzen Eruption (Japan). *Journal of Petrology*, **52**(7-8): 1469-1492.
- Cichy, S. B., Botcharnikov, R. E., Holtz, F. and Behrens, H. (2011). Vesiculation and Microlite Crystallization Induced by Decompression: a Case Study of the 1991-1995 Mt Unzen Eruption (Japan). *Journal of Petrology*, **52**(7-8): 1469-1492.
- Cigolini, C., Laiolo, M. and Bertolino, S. (2008). Probing Stromboli volcano from the mantle to paroxysmal eruptions. In: C. Annen and G.F. Zellmer (Editors), Dynamics of crustal magma transfer, storage and differentiation. Special Publications. Geological Society, London, pp. 33-70.
- Cioni, R. and Funedda, A. (2005). Structural geology of crystal-rich, silicic lava flows: A case study from San Pietro Island (Sardinia, Italy). In: M. Manga and G. Ventura (Editors), Kinematics and dynamics of lava flows.
- Cioni, R., Pistolesi, M. and Rosi, M. (2015). Plinian and Subplinian Eruptions. In: H. Sigurdsson (Editor), The Encyclopedia of Volcanoes. Academic Press.
- Civetta, L., Galati, R. and Santacroce, R. (1991). Magma mixing and convective compositional layering within the Vesuvius magma chamber. *Bulletin of Volcanology*, **53**(4): 287-300.
- Clarke, A. B., Esposti Ongaro, T. and Belousov, A. (2015). Vulcanian Eruptions. In: H. Sigurdsson (Editor), The Encyclopedia of Volcanoes. Academic Press.
- Clavero, J., Godoy, E., Arancibia, G., Rojas, C. and Moreno, H. (2008). Multiple Holocene sector collapses at Calbuco volcano, Southern Andes, IAVCEI General Assembly, Reykjavik, Iceland.

- Cleere, H. (1995). Cultural landscapes ad World Heritage. *Conservation and Management of archaeological sites*: 63-68.
- Clynne, M. A. (1999). A complex magma mixing origin for rocks erupted in 1915, Lassen Peak, California. *Journal of Petrology*, **40**: 105-132.
- Coish, R. A. and Taylor, L. A. (1979). The effects of cooling rate on texture and pyroxene chemistry in DSDP Leg 34 basalt: A microprobe study. *Earth and Planetary Science Letters*, **42**(3): 389-398.
- Cole, J. W. (1978). Andesites of the Tongariro Volcanic Centre, North Island, New Zealand. *Journal of Volcanology and Geothermal Research*, **3**: 121-153.
- Cole, J. W. and Lewis, K. B. (1981). Evolution of the Taupo-Hikurangi subduction system. *Tectonophysics*, **72**(1-2): 1-21.
- Cole, J. W., Graham, I. J., Hackett, W. R. and Houghton, B. F. (1986). Volcanology and petrology of the Quaternary composite volcanoes of Tongariro volcanic centre, Taupo volcanic zone. *The Royal Society of New Zealand Bulletin*, **23**: 224-249.
- Cole, P. D., Calder, E. S., Druitt, T. H., Hoblitt, R., Robertson, R., Sparks, R. S. J. and Young, S. R. (1998). Pyroclastic flows generated by gravitational instability of the 1996-97 lava dome of Soufriere Hills Volcano, Montserrat. *Geophysical Research Letters*, **25**(18): 3425-3428.
- Coleman, D. S., Gray, W. and Glazner, A. F. (2004). Rethinking the emplacement and evolution of zoned plutons: Geochronologic evidence for incremental assembly of the Tuolumne Intrusive Suite, California. *Geology*, **32**(5): 433-436.
- Conte, A. M., Perinelli, C. and Trigila, R. (2006). Cooling kinetics experiments on different Stromboli lavas: Effects on crystal morphologies and phases composition. *Journal of Volcanology and Geothermal Research*, **155**: 179-200.
- Conway, C. E., Leonard, G. S., Townsend, D. B., Calvert, A. T., Wilson, C. J. N., Gamble, J. A. and Eaves, S. R. (2016). A high-resolution $^{40}\text{Ar}/^{39}\text{Ar}$ lava chronology and edifice construction history for Ruapehu volcano, New Zealand. *Journal of Volcanology and Geothermal Research*, **327**: 152-179.
- Conway, C. E., Gamble, J. A., Wilson, C. J. N., Leonard, G. S., Townsend, D. B. and Calvert, A. T. (2018). New petrological, geochemical, and geochronological perspectives on andesite-dacite magma genesis at Ruapehu volcano, New Zealand. *American Mineralogist*, **103**(4): 565-581.
- Coombs, M. L. and Gardner, J. E. (2004). Reaction rim growth on olivine in silicic melts: implications for magma mixing. *American Mineralogist*, **89**: 748-759.
- Cooper, G. F., Morgan, D. J. and Wilson, C. J. N. (2017). Rapid assembly and rejuvenation of a large silicic magmatic system: Insights from mineral diffusive profiles in the Kidnappers and Rocky Hill deposits, New Zealand. *Earth and Planetary Science Letters*, **473**: 1-13.
- Cooper, K. M. and Reid, M. R. (2003). Re-examination of crystal ages in recent Mount St. Helens lavas: Implications for magma reservoir processes. *Earth and Planetary Science Letters*, **213**: 149-167.
- Cooper, K. M. and Kent, A. J. (2014). Rapid remobilization of magmatic crystals kept in cold storage. *Nature*, **506**(7489): 480-483.
- Cooper, K. M. (2015). Timescales of crustal magma reservoir processes: insights from U-series crystal ages. *Geological Society, London, Special Publications*, **422**(1): 141-174.

- Cooper, K. M., Sims, K. W. W., Eiler, J. M. and Banerjee, N. (2016). Timescales of storage and recycling of crystal mush at Krafla Volcano, Iceland. *Contributions to Mineralogy and Petrology*, **171**(6).
- Coote, A., Shane, P., Stirling, C. and Reid, M. (2018). The origin of plagioclase phenocrysts in basalts from continental monogenetic volcanoes of the Kaikohe-Bay of Islands field, New Zealand: implications for magmatic assembly and ascent. *Contribution to Mineralogy and Petrology*, **173**(14).
- Coote, A. C. and Shane, P. (2016). Crystal origins and magmatic system beneath Ngauruhoe volcano (New Zealand) revealed by plagioclase textures and compositions. *Lithos*, **260**: 107-119.
- Corrigan, G. M. (1982). Supercooling and crystallization of plagioclase, olivine and clinopyroxene from basaltic magmas, Mineral Magazine, pp. 31-42.
- Corsaro, R. A., Métrich, N., Allard, P., Andronico, D., Miraglia, L. and Fourmentraux, C. (2009). The 1974 flank eruption of Mount Etna: An archetype for deep dike-fed eruptions at basaltic volcanoes and a milestone in Etna's recent history. *Journal of Geophysical Research: Solid Earth*, **114**(B7).
- Costa, A. (2005). Viscosity of high crystal content melts: dependence on solid fraction, Geophysical Research Letters.
- Costa, A., Caricchi, L. and Bagdassarov, N. (2009a). A model for the rheology of particle-bearing suspensions and partially molten rocks. *Geochemistry Geophysics Geosystems*, **10**: 1-13.
- Costa, A., Sparks, R., S, J., Macedonio, G. and Melnik, O. (2009b). Effects of wall-rock elasticity on magma flow in dykes during explosive eruptions. *Earth and Planetary Science Letters*, **288**(3-4): 455-462.
- Costa, F., Chakraborty, S. and Dohmen, R. (2003). Diffusion coupling between trace and major elements and a model for calculation of magma residence times using plagioclase. *Geochimica et Cosmochimica Acta*, **67**: 2189-2200.
- Costa, F. and Chakraborty, S. (2004). Decadal time gaps between mafic intrusion and silicic eruption obtained from chemical zoning patterns in olivine. *Earth and Planetary Science Letters*, **227**(3-4): 517-530.
- Costa, F. and Dungan, M. (2005). Short time scales of magmatic assimilation from diffusion modeling of multiple elements in olivine. *Geology*, **33**: 837-840.
- Costa, F., Dohmen, R. and Chakraborty, S. (2008). Time Scales of Magmatic Processes from Modeling the Zoning Patterns of Crystals. *Reviews in Mineralogy and Geochemistry*, **69**(1): 545-594.
- Costa, F., Coogan, L. A. and Chakraborty, S. (2010). The time scales of mixing and mingling involving primitive melts and melt-mush interaction at Mid-Ocean Ridges. *Contributions to Mineralogy and Petrology*, **159**: 371-387.
- Costa, F. and Morgan, D. J. (2010). Time Constraints from Chemical Equilibration in Magmatic Crystals. In: A. Dosseto, S.P. Turner and J.A. Van Orman (Editors), Timescales of Magmatic Processes: From Core to Atmosphere. John Wiley & Sons, Ltd, Chichester, UK.
- Costa, M., Buddhi, D. and Oliva, A. (1998). Numerical simulation of a latent heat thermal energy storage system with enhanced heat conduction. *Energy Conversion and Management*, **39**: 319-330.
- Costantini, L., Bonadonna, C., Houghton, B. F. and Wehrmann, H. (2008). New physical characterization of the Fontana Lapilli basaltic Plinian eruption, Nicaragua. *Bulletin of Volcanology*, **71**(3): 337.

- Couch, S., Sparks, R. S. J. and Carroll, M. R. (2001). Mineral disequilibrium in lavas explained by convective self-mixing in open magma chambers. *Nature*, **411**: 1037-1039.
- Couch, S., Sparks, R., S, J. and Carroll, M., R. (2003). The Kinetic of degassing-induced crystallization at Soufriere Hills volcano, Montserrat. *Journal of Petrology*, **44**(8): 1477-1502.
- Cox, K. G., Bell, J. D. and Pankhurst, R. J. (1979). The interpretation of igneous rocks. Chapman and Hall, 450 pp.
- Crabtree, S. M. and Lange, R. A. (2011). Complex phenocryst textures and zoning patterns in andesites and dacites: evidence of degassing-induced rapid crystallization? *Journal of Petrology*, **52**: 3-38.
- Cronin, S. J., Neall, V. E. and Palmer, A. S. (1996). Geological history of the north-eastern ring plain of Ruapehu Volcano, New Zealand. *Quaternary International*, **34-36**: 21-28.
- Cronin, S. J., Hedley, M. J., Neall, V. E. and Smith, R. G. (1998). Agronomic impact of tephra fallout from the 1995 and 1996 Ruapehu Volcano eruptions, New Zealand. *Environmental Geology*, **34**(1): 21-30.
- Cronin, S. J., Neall, V. E., Lecointre, J. A. and Palmer, A. S. (1999). Dynamic interactions between lahars and stream flow: A case study from Ruapehu volcano, New Zealand *Geological Society of America*, **111**(1): 28-38.
- Cronin, S. J., Neall, V. E., Lecointre, J. A., Hedley, M. J. and Loganathan, P. (2003). Environmental hazards of fluoride in volcanic ash: a case study from Ruapehu volcano, New Zealand. *Journal of Volcanology and Geothermal Research*, **121**: 271-291.
- Crummy, J. M., Savov, I. P., Navarro-Ochoa, C., Morgan, D. J. and Wilson, M. (2014). High-KMafic Plinian Eruptions of Volcanc̃nde Colima, Mexico. *Journal of Petrology*, **55**(11): 2155-2192.
- Currier, R. M. and Marsh, B., D. (2015). Mapping real time growth of experimental laccoliths: The effect of solidification on the mechanics of magmatic intrusion. *Journal of Volcanology and Geothermal Research*, **302**: 211-224.
- Dalton, M. P., Waite, G. P., Watson, I. M. and Nadeau, P. A. (2010). Multiparameter quantification of gas release during weak Strombolian eruptions at Pacaya Volcano, Guatemala. *Geophysical Research Letters*, **37**(9).
- Danyushevsky, L. V., Sokolov, S. and Falloon, T. J. (2002). Melt inclusions in olivine phenocrysts: Using diffusive re-equilibration to determine the cooling history of a crystal, with implications for the origin of olivine-phyric volcanic rocks. *Journal of Petrology*, **43**: 1651-1671.
- Danyushevsky, L. V., Leslie, R. A. J., Crawford, A. J. and Durance, P. (2004). Melt inclusions in primitive olivine phenocrysts: the role of localized reaction processes in the origin of anomalous compositions. *Journal of Petrology*, **45**: 2531-2553.
- Davey, F. J., Hampton, M., Childs, J., Fisher, M. A., Lewis, K. and Pettinga, J. R. (1986). Structure of a growing accretionary prism, Hikurangi margin, New Zealand. *Geology*, **14**(8).
- Davidson, J., Turner, S., Handley, H., Macpherson, C. and Dosseto, A. (2007). Amphibole "sponge" in arc crust? *Geology*, **35**: 787-790.

- Dawson, P., Whilldin, D. and Chouet, B. (2004). Application of near real-time radial semblance to locate the shallow magmatic conduit at Kilauea Volcano, Hawaii. *Geophysical Research Letters*, **31**(21).
- de' Michieli Vitturi, M., Clarke, A. B., Neri, A. and Voight, B. (2008). Effects of conduit geometry on magma ascent dynamics in dome-forming eruptions. *Earth and Planetary Science Letters*, **272**(3-4): 567-578.
- de' Michieli Vitturi, M., Clarke, A. B., Neri, A. and Voight, B. (2010). Transient effects of magma ascent dynamics along a geometrically variable dome-feeding conduit. *Earth and Planetary Science Letters*, **295**(3): 541-553.
- de Silva, S. L. and Wolff, J. A. (1995). Zoned magma chambers: the influence of magma chamber geometry on sidewall convective fractionation. *Journal of Volcanology and Geothermal Research*, **65**(1): 111-118.
- Deering, C. D., Bachmann, O., Dufek, J. and Gravelly, D. M. (2011a). Rift-related transition from andesite to rhyolite volcanism in the Taupo Volcanic Zone (New Zealand) controlled by crystal-melt dynamics in mush zones with variable mineral assemblages. *Journal of Petrology*, **52**: 2243-2263.
- Deering, C. D., Bachmann, O. and Vogel, T. A. (2011b). The Ammonia Tanks Tuff: Erupting a melt-rich rhyolite cap and its remobilized crystal cumulate. *Earth and Planetary Science Letters*, **310**(3): 518-525.
- Demouchy, S., Jacobsen, S. D., Gaillard, F. and Stem, C. R. (2006). Rapid magma ascent recorded by water diffusion profiles in mantle olivine. *Geology*, **34**: 429-432.
- Devine, J. D., Rutherford, M. J. and Gardner, J. E. (1998). Petrologic determination of ascent rates for the 1995-1997 Soufriere Hills Volcano andesitic magma. *Geophysical Research Letters*, **25**: 3673-3676.
- DOC. (2017). Strategic review of Tongariro Alpine Crossing.
- Dohmen, R. and Chakraborty, S. (2007). Fe-Mg diffusion in olivine II: point defect chemistry, change of diffusion mechanisms and a model for calculation of diffusion coefficients in natural olivine. *Physics and Chemistry of Minerals*, **34**: 409-430.
- Donnadieu, F. and Merle, O. (1998). Experiments on the indentation process during cryptodome intrusions: new insights into Mount St. Helens deformation. *Geology*, **26**(1): 79-82.
- Donoghue, S. L., Neall, V. E. and Palmer, A. S. (1995). Stratigraphy and chronology of late Quaternary andesitic tephra deposits, Tongariro Volcanic Centre, New Zealand. *Journal of the Royal Society of New Zealand*, **25**: 115-206.
- Donoghue, S. L. and Neall, V. E. (1996). Tephrostratigraphic studies at Tongariro Volcanic Centre, New Zealand: an overview. *Quaternary International*, **34-36**: 13-20.
- Donoghue, S. L., Neall, V. E., Palmer, A. S. and Stewart, R. B. (1997). The volcanic history of Ruapehu during the past 2 millennia based on the record of Tufa Trig tephra. *Bulletin of Volcanology*, **59**: 136-146.
- Downes, M. J. (1974). Sector and oscillatory zoning in calcic augites from M. Etna, Sicily. *Contributions to Mineralogy and Petrology*, **47**(3): 187-196.
- Dowty, E. (1980). Crystal growth and nucleation theory and the numerical simulation of igneous crystallization. In: R.B. Hargraves (Editor), *Physics of Magmatic Processes*, Princeton, pp. 419-485.

- Dreher, S. T., Macpherson, C. G., Pearson, D. G. and Davidson, J. P. (2005). Re-Os isotope studies of Mindanao adakites: Implications for sources of metals and melts. *Geology*, **33**: 957–960.
- Drignon, M. J., Bechon, T., Arbaret, L., Burgisser, A., Komorowski, J., Martel, C., Miller, H. and Yapura, R. (2016). Preexplosive conduit conditions during the 2010 eruption of Merapi volcano (Java, Indonesia). *Geophysical Research Letters*, **43**(22): 11595-11602.
- Druitt, T. H. (1998). Pyroclastic density currents. *Geological Society, London, Special Publications*, **145**(1): 145-182.
- Druitt, T. H., Costa, F., Deloule, E., Dungan, M. and Scaillet, B. (2012). Decadal to monthly timescales of magma transfer and reservoir growth at a caldera volcano. *Nature*, **482**(7383): 77-80.
- Duncan, A. R. (1970). The Petrology and Petrochemistry of Andesite and Dacite Volcanoes in Eastern Bay of Plenty, New Zealand, Victoria University.
- Dvorak, J. J. (1992). Mechanism of explosive eruptions of Kilauea Volcano, Hawaii. *Bulletin of Volcanology*, **54**(8): 638-645.
- Eberl, D. D., Kile, D. E. and Drits, V. A. (2002). On geological interpretations of crystal size distributions: Constant vs. proportionate growth. *American Mineralogist*, **87**(8-9): 1235-1241.
- Edmonds, M., Cashman, K. V., Holness, M. and Jackson, M. (2019). Architecture and dynamics of magma reservoirs. *Philosophical Transactions of the Royal Society A: Mathematical, Physical and Engineering Sciences*, **377**.
- Eichelberger, J. (1980). Vesiculation of mafic magma during replenishment of silicic magma reservoirs. *Nature*, **288**: 446-450.
- Eichelberger, J. C., Carrigan, C. R., Westrich, H. R. and Price, R. H. (1986). Non-explosive silicic volcanism. *Nature*, **323**: 598-602.
- Endo, E. T., Murray, T. L. and Power, J. A. (1996). A comparison of pre-eruption, real-time seismic amplitude measurements for eruptions at Mount St. Helens, Redoubt Volcano, Mount Spurr, and Mount Pinatubo. In: C.G.P. Newhall, R. S. (Editor), Eruptions and Lahars of Mount Pinatubo, Philippines, University of Washington press, pp. 233-246.
- England, P. C. and Katz, R. F. (2010). Melting above the anhydrous solidus controls the location of volcanic arcs. *Nature*, **467**: 700-703.
- Erdmann, S., Scaillet, B. and Kellett, D. A. (2012). Textures of peritectic crystals as guides to reactive minerals in magmatic systems: new insights from melting experiments. *Journal of Petrology*, **53**: 2231-2258.
- Erlund, E. J., Cashman, K. V., Wallace, P. J., Pioli, L., Rosi, M., Johnson, E. and Granados, H. D. (2009). Compositional evolution of magma from Parícutin Volcano, Mexico: The tephra record. *Journal of Volcanology and Geothermal Research*, **197**(1-4): 167-187.
- Ewart, A., Brothers, R. N. and Mategan, A. (1977). An outline of the geology and geochemistry, and the possible petrogenetic evolution of the volcanic rocks of the Tonga-Kermadec-New Zealand island arc. *Journal of Volcanology and Geothermal Research*, **2**(3): 205-250.
- Faure, F., Trolliard, G., Nicollet, C. and Montel, J.-M. (2003). A developmental model of olivine morphology as a function of the cooling rate and the degree of undercooling. *Contributions to Mineralogy and Petrology*, **145**: 251-263.

- Faure, F. and Schiano, P. (2005). Experimental investigation of equilibration conditions during forsterite growth and melt inclusion formation. *Earth and Planetary Science Letters*, **236**: 882-898.
- Favalli, M., Chirico, G. D., Papale, P., Pareschi, M., T. and Boschi, E. (2009). Lava flow hazard at Nyiragongo volcano, D.R.C. *Bulletin of Volcanology*, **71**(4): 363-374.
- Favalli, M., Fornaciai, A., Nannipieri, L., Harris, A., Calvari, S. and Lormand, C. (2018). UAV-based remote sensing surveys of lava flow fields: a case study from Etna's 1974 channel-fed lava flows. *Bulletin of Volcanology*, **80**(3): 29.
- Fawcett, T. (2006). An introduction to ROC analysis. *Pattern Recognition Letters*, **27**: 861-874.
- Fenn, P. M. (1977). The nucleation and growth of alkali feldspars from hydrous melts. *Journal of the Mineralogical Association of Canada*, **15**: 135-161.
- Ferguson, A. K. (1973). On hour-glass sector zoning in clinopyroxene. *Mineralogical Magazine*, **39**(303): 321-325.
- Fergusson, G. J. and Rafter, T. A. (1959). New Zealand ¹⁴C age measurements-4. *New Zealand Journal of Geology and Geophysics*, **2**: 208-241.
- Ferlito, C., Viccaro, M., Nicotra, E. and Cristofolini, R. (2012). Regimes of magma recharge and their control on the eruptive behaviour during the period 2001–2005 at Mt. Etna volcano. *Bulletin of Volcanology*, **74**(2): 533-543.
- Fichaut, M., Maury, R. C., Traineau, H., Westercamp, D., Joron, J. L., Gourgaud, A. and Coulon, C. (1989). Magmatology of Mt. Pelée (Martinique, F.W.I.). III: Fractional crystallization versus magma mixing,. *Journal of Volcanology and Geothermal Research*, **38**(1-2): 189-213.
- Finney, B. M., Turner, S. P., Hawkesworth, C. J., George, R. M. M., Zellmer, G. F., Nye, C. J., Eichelberger, J. and Larson, J. F. (2003). Timescales of Magmatic Processes at Okmok Caldera, Aleutian Islands, Alaska, State of the Arc 2003.
- Flaherty, T., Druitt, T. H., Fabbro, G., Costa, F., Preece, K. and Deering, C. (2016). Fe-Mg diffusion chronometry in orthopyroxene from the Minoan eruption of Santorini, Greece, EGU General Assembly 2016, Vienna, Austria.
- Ford, C. E., Russell, D. G., Craven, J. A. and Fisk, M. R. (1983). Olivine-Liquid Equilibria: Temperature, Pressure and Composition Dependence of the Crystal/Liquid Cation Partition Coefficients for Mg, Fe²⁺, Ca and Mn. *Journal of Petrology*, **24**: 256-265.
- Fornaciai, A., Landi, P. and Armienti, P. (2009). Dissolution/crystallization kinetics recorded in the 2002–2003 lavas of Stromboli (Italy). *Bulletin of Volcanology*, **71**(6): 631-641.
- Fornaciai, A., Perinelli, C., Armienti, P. and Favalli, M. (2015). Crystal size distributions of plagioclase in lavas from the July–August 2001 Mount Etna eruption. *Bulletin of Volcanology*, **77**(8).
- Francalanci, L., Varekamp, J. C., Vougioukalakis, G. E., Innocenti, F. and Manetti, P. (2007). Is there a compositional gap at Nisyros volcano? A Comment on: *Magma generation at the easternmost section of the Hellenic arc: Hf, Nd, Pb and Sr isotope geochemistry of Nisyros and Yali volcanoes (Greece)* [Lithos 83 (2005) 29-46]. *Lithos*, **95**: 458-461.
- Frazzetta, G. and Villari, L. (1981). The feeding of the eruptive activity of Etna volcano. The regional stress field as a constraint to magma uprising and eruption. *Bulletin Volcanologique*, **44**(3): 269-282.

- Freer, R. (1981). Diffusion in silicate minerals and glasses: A data digest and guide to the literature. *Journal of Petrology*, **76**: 440-454.
- Freer, R., Carpenter, M. A., Long, J. V. P. and Reed, S. J. B. (1982). "Null result" diffusion experiments with diopside: implications for pyroxene equilibria. *Earth and Planetary Science Letters*, **58**: 285-292.
- Freundt, A. and Kutterolf, S. (2019). The long-lived Chiltepe volcanic complex, Nicaragua: magmatic evolution at an arc offset. *Bulletin of Volcanology*, **81**(10).
- Frey, H. M. and Lange, R. A. (2011). Phenocryst complexity in andesites and dacites from the Tequila volcanic field, Mexico: resolving the effects of degassing vs. magma mixing. *Contributions to Mineralogy and Petrology*, **162**(2): 415-445.
- Froger, J. L., Merle, O. and Briole, P. (2001). Active spreading and regional extension at Mount Etna imaged by SAR interferometry. *Earth and Planetary Science Letters*, **187**(3): 245-258.
- Fu, B., Page, F. Z., Cavosie, A. J., Fournelle, J., Kita, N. T., Lackey, J. S., Wilde, S. A. and Valley, J. W. (2008). Ti-in-zircon thermometry: applications and limitations. *Contributions to Mineralogy and Petrology*, **156**(2): 197-215.
- Fulignati, P., Marianelli, P. and Sbrana, A. (2000). Glass-bearing felsic nodules from the crystallizing sidewalls of the 1944 Vesuvius magma chamber, *Mineralogical Magazine*, pp. 481.
- Galland, O., Burchardt, S., Hallot, E., Mourgues, R. and Bulois, C. (2014). Dynamics of dikes versus cone sheets in volcanic systems. *Journal of Geophysical Research: Solid Earth*, **119**(8): 6178-6192.
- Gamble, J. A., Wood, C. P., Price, R. C., Smith, I. E. M., Stewart, R. B. and Waight, T. (1999). A fifty year perspective of magmatic evolution on Ruapehu Volcano, New Zealand: verification of open system behaviour in an arc volcano. *Earth and Planetary Science Letters*, **170**: 301-314.
- Gamble, J. A., Price, R. C., Smith, I. E. M., McIntosh, W. C. and Dunbar, N. W. (2003). $^{40}\text{Ar}/^{39}\text{Ar}$ geochronology of magmatic activity, magma flux and hazards at Ruapehu volcano, Taupo Volcanic Zone, New Zealand. *Journal of Volcanology and Geothermal Research*, **120**: 271-287.
- Gardner, J. E., Carey, S. and Sigurdsson, H. (1998). Plinian eruptions at Glacier Peak and Newberry volcanoes, United States: Implications for volcanic hazards in the Cascade Range. *Geological Society of America*, **110**(2): 173-187.
- Gaudin, D., Taddeucci, A., Scarlato, P., Moroni, M., Freda, C., Gaeta, M. and Palladino, D. M. (2014). Pyroclast Tracking Velocimetry illuminates bomb ejection and explosion dynamics at Stromboli (Italy) and Yasur (Vanuatu) volcanoes. *Journal of Geophysical Research: Solid Earth*, **119**(7): 5384-5397.
- Gavrilenko, M., Herzberg, C., Vidito, C., Carr, M. J., Tenner, T. and Ozerov, A. (2016). A Calcium-in-Olivine Geohygrometer and its Application to Subduction Zone Magmatism. *Journal of Petrology*, **57**(9): 1811-1832.
- Geoffroy, C. A., Alloway, B. V., Amigo, A., Parada, M. A., Gutierrez, F., Castruccio, A., Pearce, N. J. G., Morgado, E. and Moreno, P. I. (2018). A widespread compositionally bimodal tephra sourced from Volcan Melimoyu (44°S, Northern Patagonian Andes): Insights into magmatic reservoir processes and opportunities for regional correlation. *Quaternary Science Reviews*, **200**: 141-159.
- Geschwind, C.-H. and Rutherford, M. J. (1995). Crystallization of microlites during magma ascent: the fluid mechanics of 1980-1986 eruptions at Mount St Helens. *Bulletin of Volcanology*, **57**: 356-370.

- Geshi, N., Németh, K. and Oikawa, T. (2011). Growth of phreatomagmatic explosion craters: A model inferred from Suoana crater in Miyakejima Volcano, Japan. *Journal of Volcanology and Geothermal Research*, **201**(1-4): 30-38.
- Ghiorso, M. S. and Sack, R. O. (1995). Chemical mass transfer in magmatic processes IV. A revised and internally consistent thermodynamic model for the interpolation and extrapolation of liquid-solid equilibria in magmatic systems at elevated temperatures and pressures. *Contributions to Mineralogy and Petrology*, **119**: 197-212.
- Ghiorso, M. S., Hirschmann, M. M., Reiners, P. W. and Kress III, V. C. (2002). The pMELTS: A revision of MELTS for improved calculation of phase relations and major element partitioning related to partial melting of the mantle to 3 GPa. *Geochemistry, Geophysics, Geosystems*, **3**(5): 1-35.
- Ghiorso, M. S. and Evans, B. W. (2008). Thermodynamics of Rhombohedral Oxide Solid Solutions and a Revision of the FE-TI Two-Oxide Geothermometer and Oxygen-Barometer. *American Journal of Science*, **308**(9): 957-1039.
- Ghiorso, M. S. and Gualda, G. A. R. (2015). Chapter 6. Chemical Thermodynamics and the Study of Magmas. In: H. Sigurdsson, B. Houghton, S.R. McNutt, H. Rymer and J. Stix (Editors), *The Encyclopedia of Volcanoes*. Elsevier.
- Giacomoni, P. P., Ferlito, C., Coltorti, M., Bonadiman, C. and Lanzafame, G. (2014). Plagioclase as archive of magma ascent dynamics on “open conduit” volcanoes: The 2001–2006 eruptive period at Mt. Etna. *Earth-Science Reviews*, **138**: 371-393.
- Giacomoni, P. P., Coltorti, M., Bryce, J. G., Fahnstock, M. F. and Guitreau, M. (2016). Mt. Etna plumbing system revealed by combined textural, compositional, and thermobarometric studies in clinopyroxenes. *Contributions to Mineralogy and Petrology*, **171**(4): 34.
- Giacomoni, P. P., Coltorti, M., Mollo, S., Ferlito, C., Braiato, M. and Scarlato, P. (2018). The 2011–2012 paroxysmal eruptions at Mt. Etna volcano: Insights on the vertically zoned plumbing system. *Journal of Volcanology and Geothermal Research*, **349**: 370-391.
- Gibb, F. G. F. (1974). Supercooling and the crystallization of plagioclase from a basaltic magma, *Mineral Magazine*, pp. 641-653.
- Giletti, B. J. and Casserly, J. E. D. (1994). Strontium diffusion kinetics in plagioclase feldspars. *Geochimica et Cosmochimica Acta*, **58**(18): 3785-3793.
- Giletti, B. J. and Shanahan, T. M. (1997). Alkali Diffusion in plagioclase feldspar. *Chemical Geology*, **139**: 3-20.
- Gill, J., Williams, R. and Bruland, K. (1985). Eruption of basalt and andesite lava degasses ²²²Rn and ²¹⁰Po. *Geophysical Research Letters*, **12**(1): 17-20.
- Ginibre, C., Worner, G. and Kronz, A. (2002). Minor- and trace-element zoning in plagioclase: implications for magma chamber processes at Parinacota volcano, northern Chile. *Contribution to Mineralogy and Petrology*, **143**: 300-315.
- Giordano, D. and Dingwell, D. W. (2003). Non-Arrhenian multicomponent melt viscosity: a model. *Earth and Planetary Science Letters*, **208**: 337-349.
- Giordano, D., Russell, J. K. and Dingwell, D. B. (2008). Viscosity of magmatic liquids: a model. *Earth and Planetary Science Letters*, **271**: 123-134.
- Girard, G. and Stix, J. (2009). Buoyant replenishment in silicic magma reservoirs: Experimental approach and implications for magmadynamics, crystal

- mush remobilization, and eruption. *Journal of Geophysical Research*, **114**(B08203).
- Giuffrida, M., Holtz, F., Vetere, F. and Viccaro, M. (2017). Effects of CO₂ flushing on crystal textures and compositions: experimental evidence from recent K-trachybasalts erupted at Mt. Etna. *Contribution to Mineralogy and Petrology*, **172**(90).
- Gómez-Tuena, A., LaGatta, A. B., Langmuir, C. H., Goldstein, S. L., Ortega-Gutiérrez, F. and Carrasco-Núñez, G. (2003). Temporal control of subduction magmatism in the eastern Trans-Mexican Volcanic Belt: Mantle sources, slab contributions, and crustal contamination. *Geochemistry Geophysics Geosystems*, **4**(8): 8912.
- Gómez-Vasconcelos, M. G., Villamor, P., Cronin, S. J., Procter, J. N., Palmer, A. S., Townsend, D. B. and Leonard, G. (2017). Crustal extension in the Tongariro graben, New Zealand: Insights into volcano-tectonic interactions and active deformation in a young continental rift. *Geological Society of America*, **129**(9/10): 1085-1099.
- Gómez-Vasconcelos, M. G., Villamor, P., Procter, J. N., Palmer, A. S., Cronin, S. J., Wallace, C., Townsend, D. and Leonard, G. (2018). Characterisation of faults as earthquake sources from geomorphic data in the Tongariro Volcanic Complex, New Zealand. *New Zealand Journal of Geology and Geophysics*.
- Gondé, C., Massare, D., Bureau, H., Martel, C., Pichavant, M. and Clocchiatti, R. (2006). In situ study of magmatic processes: a new experimental approach. *High Pressure Research*, **26**(3): 243-250.
- Gonnermann, H. M. and Manga, M. (2007). The Fluid Mechanics Inside a Volcano. *Annual Review of Fluid Mechanics*, **39**(1): 321-356.
- Gottsmann, J. and Dingwell, D. B. (2001). The cooling of frontal flow ramps: a calorimetric study on the Rocche Rosse rhyolite flow, Lipari, Aeolian Islands, Italy. *Terra Nova*, **13**(3): 157-164.
- Graham, I. J. and Hackett, W. R. (1987). Petrology of Calc-alkaline Lavas from Ruapehu Volcano and Related Vents, Taupo Volcanic Zone, New Zealand. *Journal of Petrology*, **28**(3): 531-567.
- Graham, I. J., Cole, J. W., Briggs, R. M., Gamble, J. A. and Smith, I. E. M. (1995). Petrology and petrogenesis of volcanic rocks from the Taupo Volcanic Zone: a review. *Journal of Volcanology and Geothermal Research*, **68**: 59-87.
- Graham, I. J. (2008). A continent on the move: New Zealand Geoscience into the 21st Century. The Geological Society of New Zealand in association with GNS Science, Wellington, New Zealand, 377 pp.
- Grange, L. I. (1931). Volcanic ash showers: a geological reconnaissance of volcanic ash showers of the central part of the North Island. *New Zealand Journal of Science*, **12**: 228-240.
- Gravley, D. M., Deering, C. D., Leonard, G. S. and Rowland, J. V. (2016). Ignimbrite flare-ups and their drivers: A New Zealand perspective. *Earth-Science Reviews*, **162**: 65-82.
- Gray, N. H. (1970). Crystal growth and nucleation in flash-injected diabase dikes. *Canadian Journal of Earth Sciences*, **15**(12): 1904-1923.
- Gregg, T. K. P. and Smith, D. K. (2003). Volcanic investigations of the Puna Ridge, Hawaii: Relations of lava flow morphologies and underlying slopes. *Journal of Volcanology and Geothermal Research*, **126**: 63-77.

- Grove, T. L., Baker, M. B. and Kinzler, R. J. (1984). Coupled CaAl-NaSi diffusion in plagioclase feldspar: experiments and applications to cooling rate speedometry. *Geochimica et Cosmochimica Acta*, **48**: 2113-2121.
- Grove, T. L., Baker, M. B., Price, R. C., Parman, S. W., Elkins-Tanton, L. T., Chatterjee, N. and Müntener, O. (2005). Magnesian andesite and dacite lavas from Mt. Shasta, northern California: products of fractional crystallization of H₂O-rich mantle melts. *Contributions to Mineralogy and Petrology*, **148**: 542-565.
- Grove, T. L., Till, C. B., Lev, E., Chatterjee, N. and Médard, E. (2009). Kinematic variables and water transport control the formation and location of arc volcanoes. *Nature*, **459**: 649-679.
- Grove, T. L., Till, C. B. and Krawczynski, M. J. (2012). The role of H₂O in subduction zone magmatism. *Annual Review of Earth and Planetary Sciences*, **40**: 413-439.
- Gualda, G. A. R., Ghiorso, M. S., Lemons, R. V. and Carley, T. L. (2012). Rhyolite-MELTS: a Modified Calibration of MELTS Optimized for Silica-rich, Fluid-bearing Magmatic Systems. *Journal of Petrology*, **53**(5): 875-890.
- Gudmundsson, A., Marinoni, L. B. and Marti, J. (1999). Injection and arrest of dykes: implications for volcanic hazards. *Journal of Volcanology and Geothermal Research*, **88**(1): 1-13.
- Guo, C. and Zhang, Y. (2016). Multicomponent diffusion in silicate melts: SiO₂-TiO₂-Al₂O₃-MgO-CaO-Na₂O-K₂O System. *Geochimica et Cosmochimica Acta*, **195**: 126-141.
- Gutierrez, F. and Parada, M. A. (2010). Numerical Modeling of Time-dependent Fluid Dynamics and Differentiation of a Shallow Basaltic Magma Chamber. *Journal of Petrology*, **51**(3): 731-762.
- Haase, C. S., Chadam, J., Feinn, D. and Ortoleva, P. (1980). Oscillatory Zoning in Plagioclase Feldspar. *Science*, **209**(4453): 272-274.
- Hackett, W. R. (1985). Geology and Petrology of Ruapehu Volcano and Related Vents, Victoria University.
- Hackett, W. R. and Houghton, B. F. (1989). A facies model for a quaternary andesitic composite volcano: Ruapehu, New Zealand. *Bulletin of Volcanology*, **51**(1): 51-68.
- Halden, N. M. and Hawthorne, F. C. (1993). The fractal geometry of oscillatory zoning in crystals: Application to zircon *American Mineralogist*, **78**(9-10): 1113-1116.
- Hamada, M., Ushioda, M., Fujii, T. and Takahashi, E. (2013). Hydrogen concentration in plagioclase as a hygrometer of arc basaltic melts: Approaches from melt inclusion analyses and hydrous melting experiments. *Earth and Planetary Science Letters*, **365**: 253-262.
- Hamilton, C. W., Fitch, E. P., Fagents, S. A. and Thordarson, T. (2017). Rootless tephra stratigraphy and emplacement processes. *Bulletin of Volcanology*, **79**(11).
- Hammer, J., Cashman, K. V., Hoblitt, R., P. and Newman, S. (1999). Degassing and microlite crystallization during pre-climatic events of the 1991 eruption of Mt. Pinatubo, Philippines. *Bulletin of Volcanology*, **60**: 355-380.
- Hammer, J. E. and Rutherford, M. J. (2002). An experimental study of the kinetics of decompression-induced crystallization in silicic melt. *Journal of Geophysical Research: Solid Earth*, **107**(B1): ECV8-1 - ECV8-24.
- Hance, G. A., Umbaugh, S. E., Moss, R. H. and Stoecker, W. V. (1996). Unsupervised color image segmentation with application to skin tumor borders. *IEEE Engineering in Medicine and Biology*: 104-111.

- Harris, A. J. L., Flynn, L. P., O., M. a. and Rose, W. I. (2002). The thermal stealth flows of Santiaguito dome, Guatemala: Implications for the cooling and emplacement of dacitic block-lava flows. *Geological Society of America*, **114**(5): 533-546.
- Harris, A. J. L., Rose, W. I. and Flynn, L. P. (2003). Temporal trends in lava dome extrusion at Santiaguito 1922–2000. *Bulletin of Volcanology*, **65**: 77-89.
- Hartley, M. E., Morgan, D. J., MacLennan, J., Edmonds, M. and Thordarson, T. (2016). Tracking timescales of short-term precursors to large basaltic fissure eruptions through Fe–Mg diffusion in olivine. *Earth and Planetary Science Letters*, **439**: 58-70.
- Hayden, L. A. and Watson, E. B. (2007). Rutile saturation in hydrous siliceous melts and its bearing on Ti-thermometry of quartz and zircon. *Earth and Planetary Science Letters*, **258**(3): 561-568.
- Hayden, L. A., Watson, E. B. and Wark, D. A. (2008). A thermobarometer for sphene (titanite). *Contributions to Mineralogy and Petrology*, **155**(4): 529-540.
- Herzer, R. H. (1995). Seismic stratigraphy of a buried volcanic arc, Northland, New Zealand and implications for Neogene subduction. *Marine and Petroleum Geology*, **12**(5): 511-531.
- Hibert, C., Mangeney, A., Grandjean, G. and Shapiro, N. M. (2017). Slope instabilities in Dolomieu crater, Réunion Island: From seismic signals to rockfall characteristics. *Journal of Geophysical Research: Earth Surface*, **116**(F4).
- Higgins, M. D. (1996a). Crystal size distributions and other quantitative textural measurements in lavas and tuff from Egmont volcano (Mt. Taranaki), New Zealand. *Bulletin of Volcanology*, **58**: 194-204.
- Higgins, M. D. (1996b). Magma dynamics beneath Kameni volcano, Thera, Greece, as revealed by crystal size and shape measurements. *Journal of Volcanology and Geothermal Research*, **70**: 37-48.
- Higgins, M. D. (2000). Measurement of crystal size distributions. *American Mineralogist*, **85**: 1105-1116.
- Higgins, M. D. (2002). Closure in crystal size distributions (CSD), verification of CSD calculations, and the significance of CSD fans. *American Mineralogist*, **87**(171-175): 171.
- Higgins, M. D. and Roberge, J. (2003). Crystal size distribution (CSD) of plagioclase and amphibole from Soufriere Hills volcano, Montserrat: Evidence for dynamic crystallisation / textural coarsening cycles. *Journal of Petrology*, **44**: 1401-1411.
- Higgins, M. D. (2006). Verification of ideal semi-logarithmic, lognormal or fractal crystal size distributions from 2D datasets. *Journal of Volcanology and Geothermal Research*, **154**(1-2): 8-16.
- Higgins, M. D. and Roberge, J. (2007). Three magmatic components in the 1973 eruption of Eldfell volcano, Iceland: Evidence from plagioclase crystal size distribution (CSD) and geochemistry. *Journal of Volcanology and Geothermal Research*, **161**(3): 247-260.
- Higgins, M. D. (2009). The Cascadia megathrust earthquake of 1700 may have rejuvenated an isolated basalt volcano in western Canada: Age and petrographic evidence. *Journal of Volcanology and Geothermal Research*, **179**(1-2): 149-156.
- Higman, S. L. and Pearce, T. H. (1993). Spatiotemporal dynamics in oscillatory zoned magmatic plagioclase. *Geophysical Research Letters*, **20**(18): 1935-1938.
- Hildreth, W. (1981). Gradients in silicic magma chambers: implications for lithospheric magmatism. *Journal of Geophysical Research*, **86**(B11): 10153-10192.

- Hildreth, W. and Fierstein, J. (2000). Katmai volcanic cluster and the great eruption of 1912. *GSA Bulletin*, **112**(10): 1594-1620.
- Hildreth, W. (2004). Volcanological perspectives on Long Valley, Mammoth Mountain, and Mono Craters: several contiguous but discrete systems. *Journal of Volcanology and Geothermal Research*, **136**(3): 169-198.
- Hill, G. J., Bibby, H. M., Ogawa, Y., Wallin, E. L., Bennie, S. L., Caldwell, T. G., Keys, H., Bertrand, E. A. and Heise, W. (2015). Structure of the Tongariro Volcanic system: Insights from magnetotelluric imaging. *Earth and Planetary Science Letters*, **432**: 115-125.
- Hills, E. S. (1936). Reverse and Oscillatory Zoning in Plagioclase Felspars., *The Geological Magazine*, pp. 46-56.
- Hirose, F., Nakajima, J. and Hasegawa, A. (2008). Three-dimensional velocity structure and configuration of the Philippine Sea slab in southwestern Japan estimated by double-difference tomography. *Journal of Geophysical Research*, **113**: B09315.
- Hitchcock, D. W. and Cole, J. W. (2007). Potential impacts of a widespread subplinian andesitic eruption from Tongariro volcano, based on a study of the Poutu Lapilli. *New Zealand Journal of Geology and Geophysics*, **50**(2): 53-66.
- Hobden, B. J., Houghton, B. F., Lanphere, M. A. and Nairn, I. A. (1996). Growth of the Tongariro volcanic complex: New evidence from K-Ar age determinations. *New Zealand Journal of Geology and Geophysics*, **39**: 151-154.
- Hobden, B. J., Houghton, B. F., Davidson, J. P. and Weaver, S. D. (1999). Small and short-lived magma batches at composite volcanoes: time windows at Tongariro volcano, New Zealand. *Journal of the Geological Society, London*, **156**: 865-868.
- Hobden, B. J., Houghton, B. F. and Nairn, I. A. (2002). Growth of a young, frequently active composite cone: Ngauruhoe volcano, New Zealand. *Bulletin of Volcanology*, **64**(6): 392-409.
- Hogg, A. G., Lowe, D. J., Palmer, J., Boswijk, G. and Ramsey, C. B. (2011). Revised calendar date for the Taupo eruption derived by ¹⁴C wiggle-matching using a New Zealand kauri ¹⁴C calibration data set. *The Holocene*, **22**(4).
- Holland, A. S. P., Watson, I. M., Phillips, J. C., Caricchi, L. and Dalton, M. P. (2011). Degassing processes during lava dome growth: Insights from Santiaguitolava dome, Guatemala. *Journal of Volcanology and Geothermal Research*, **202**: 153-166.
- Holland, T. J. B. and Blundy, J. D. (1994). Non-ideal interactions in calcic amphiboles and their bearing on amphibole-plagioclase thermometry. *Contributions to Mineralogy and Petrology*, **116**: 433-447.
- Holness, M. B., Martin, V. M. and Pyle, D. M. (2005). Information about open-system magma chambers derived from textures in magmatic enclaves: the Kamani Islands, Santorini, Greece. *Geological Magazine*, **142**: 637-649.
- Holten, T., Jamtveit, B., Meakin, P., Cortini, M., Blundy, J. and Austrheim, H. (1997). Statistical characteristics and origin of oscillatory zoning in crystals. *American Mineralogist*, **82**: 596-606.
- Hotta, K., Iguchi, M., Ohkura, T., Hendrasto, M., Gunawan, H., Rosadi, U. and Kristawi, E. (2019). Magma intrusion and effusion at Sinabung volcano, Indonesia, from 2013 to 2016, as revealed by continuous GPS observation *Journal of Volcanology and Geothermal Research*, **382**: 173-183.

- Houghton, B., White, J. D. L. and Van Eaton, A. R. (2015). Phreatomagmatic and related eruption styles. In: H. Sigurdsson (Editor), *The Encyclopedia of Volcanoes*. Academic Press.
- Houghton, B. F. and Nairn, I. A. (1991). The 1976–1982 Strombolian and phreatomagmatic eruptions of White Island, New Zealand: eruptive and depositional mechanisms at a ‘wet’ volcano. *Bulletin of Volcanology*, **54**(1): 25-49.
- Houghton, B. F., Wilson, C. J. N., Del Carlo, P., Coltelli, M., Sable, J. E. and Carey, R. (2004). The influence of conduit processes on changes in style of basaltic Plinian eruptions: Tarawera 1886 and Etna 122 BC. *Journal of Volcanology and Geothermal Research*, **137**(1): 1-14.
- Huang, R. and Audétat, A. (2012). The titanium-in-quartz (TitaniQ) thermobarometer: A critical examination and re-calibration. *Geochimica et Cosmochimica Acta*, **84**: 75-89.
- Huber, C., Bachmann, O., Vigneresse, J.-L., Dufek, J. and Parmigiani, A. (2012). A physical model for metal extraction and transport in shallow magmatic systems. *Geochemistry, Geophysics, Geosystems*, **13**(8).
- Hughes, R. and Hawkesworth, C. (2000). Timescales of andesite generation at Mount Ruapehu. In: I.E.M. Smith, J.P. Davidson, J.A. Gamble and R.C. Price (Editors), *State of the Arc 2000: Processes and Timescales*. The Royal Society of New Zealand, P. O. Box 598, Wellington, New Zealand, Mt. Ruapehu, New Zealand, pp. 115-117.
- Humphreys, M. C. S., Blundy, J. D. and Sparks, R. S. J. (2006). Magma evolution and open-system processes at Shiveluch volcano: insights from phenocryst zoning. *Journal of Petrology*, **47**: 2303-2334.
- Humphreys, M. C. S., Menand, T., Blundy, J. D. and Klimm, K. (2008). Magma ascent rates in explosive eruptions: Constraints from H₂O diffusion in melt inclusions. *Earth and Planetary Science Letters*, **270**: 25-40.
- Humphreys, M. C. S., Christopher, T. and Hards, V. (2009). Microlite transfer by disaggregation of mafic inclusions following magma mixing at Soufrière Hills volcano, Montserrat. *Contributions to Mineralogy and Petrology*, **157**: 609-624.
- Humphreys, M. C. S., Edmonds, M. and Klöcking, M. S. (2016). The validity of plagioclase-melt geothermometry for degassing-driven magma crystallization. *American Mineralogist*, **101**(4).
- Huppert, H. E. and Sparks, R. S. J. (1980). The fluid dynamics of a basaltic magma chamber replenished by influx of hot dense ultrabasic magma. *Contributions to Mineralogy and Petrology*, **75**: 279-289.
- Huppert, H. E. and Sparks, R., S, J. (1984). Double-diffusive convection due to crystallization in magmas. *Annual Review of Earth and Planetary Science*, **12**: 11-37.
- Hurst, A. W., Bibby, H. M., Scott, B. J. and McGuinness, M. J. (1991). The heat source of Ruapehu crater lake; deductions from the energy and mass balances. *Journal of Volcanology and Geothermal Research*, **46**(1-2): 1-20.
- Hurst, A. W. and McGinty, P. J. (1999). Earthquake swarms to the west of Mt Ruapehu preceding its 1995 eruption. *Journal of Volcanology and Geothermal Research*: 19-28.

- Hurst, T., Jolly, A. D. and Sherburn, S. (2014). Precursory characteristics of the seismicity before the 6 August 2012 eruption of Tongariro volcano, North Island, New Zealand. *Journal of Volcanology and Geothermal Research*, **286**: 294-302.
- Ishizuka, O., Geshi, N., Itoh, J., Kawanabe, Y. and TuZino, T. (2008). The magmatic plumbing of the submarine Hachijo NW volcanic chain, Hachijojima, Japan: Long-distance magma transport? *Journal of Geophysical Research: Solid Earth*, **113**(8).
- Izbekov, P. E., Eichelberger, J. C., Patino, L. C., Vogel, T. A. and Ivanov, B. V. (2002). Calcic cores of plagioclase phenocrysts in andesite from Karymsky volcano: Evidence for rapid introduction by basaltic replenishment. *Geology*, **30**(9): 799-802.
- Jaupart, C. and Vergnolle, S. (1988). Laboratory models of Hawaiian and Strombolian eruptions. *Nature*, **331**: 58-60.
- Jaupart, C. and Allègre, C. J. (1991). Gas content, eruption rate and instabilities of eruption regime in silicic volcanoes *Earth and Planetary Science Letters*, **102**: 413-429.
- Jeffery, A. J., Gertisser, R., Troll, V. R., Jolis, E. M., Dahren, B., Harris, C., Tindle, A. G., Preece, K., O'Driscoll, B., Humaida, H. and Chadwick, J. P. (2013). The pre-eruptive magma plumbing system of the 2007–2008 dome-forming eruption of Kelut volcano, East Java, Indonesia. *Contributions to Mineralogy and Petrology*, **166**(1): 275-308.
- Jenner, G. A., Foley, S. F., Jackson, S. E., Green, T. H., Fryer, B. J. and Longerich, H. P. (1994). Determination of partition-coefficients for trace elements in high pressure temperature experimental run products by laser-ablation microprobe inductively-coupled plasma-mass spectrometry (LAM-ICP-MS). *Geochimica et Cosmochimica Acta*, **57**(23-24): 5099-5103.
- Jerram, D. and Higgins, M. D. (2007). 3D Analysis of Rock Textures: Quantifying Igneous Microstructures. *Elements*, **3**(4): 239-245.
- Jerram, D., Dobson, K. J., Morgan, D. and Pankhurst, M. J. (2018). Chapter 8. The Petrogenesis of Magmatic Systems: Using Igneous Textures to Understand Magmatic Processes. In: S. Burchardt (Editor), *Volcanic and Igneous Plumbing Systems*. Elsevier.
- Jerram, D. A., Cheadle, M. J. and Philpotts, A. R. (2003). Quantifying the building blocks of igneous rocks: are clustered crystal frameworks the foundation. *Journal of Petrology*, **44**(11): 2033-2051.
- Jerram, D. A. and Martin, V. M. (2008). Understanding crystal populations and their significance through the magma plumbing system. In: C. Annen and G.F. Zellmer (Editors), *Dynamics of crustal magma transfer, storage and differentiation*. Special Publications. Geological Society, London, pp. 133-148.
- Jerram, D. A., Mock, A., Davis, G., Field, M. and Brown, R. (2009). 3D crystal size distributions: A case study on quantifying olivine populations in kimberlites. *Lithos*, **112**: 223-235.
- Johnston, D. M., Houghton, B. F., Neil, V. E., Ronan, K. R. and Paton, D. (2000). Impacts of the 1945 and 1995-1996 Ruapehu eruptions, New Zealand.: An example of increasing societal vulnerability. *Geological Society of America Bulletin*, **112**: 720-726.
- Jolly, A. D., Sherburn, S., Jousset, P. and Kilgour, G. (2010). Eruption source processes derived from seismic and acoustic observations of the 25 September 2007

- Ruapehu eruption - North Island, New Zealand. *Journal of Volcanology and Geothermal Research*, **191**: 33-45.
- Jolly, A. D., Neuberg, J., Jousset, P. and Sherburn, S. (2012). A new source process for evolving repetitive earthquakes at Ngauruhoe volcano, New Zealand. *Journal of Volcanology and Geothermal Research*, **215-216**: 26-39.
- Jolly, A. D., Lokmer, I., Kennedy, B., Keys, H. J. R., Proctor, J., Lyons, J. J. and Jolly, G. E. (2014a). Active seismic sources as a proxy for seismic surface processes: An example from the 2012 Tongariro volcanic eruptions, New Zealand. *Journal of Volcanology and Geothermal Research*, **286**: 317-330.
- Jolly, G. E., Keys, H., Proctor, J. N. and Deligne, N. I. (2014b). Overview of the coordinated risk-based approach to science and management response and recovery for the 2012 eruptions of Tongariro volcano, New Zealand. *Journal of Volcanology and Geothermal Research*, **286**: 184-207.
- Jordan, S. C., Le Pennec, J. L., Gurioli, L., Roche, O. and Boivin, P. (2016). Highly explosive eruption of the monogenetic 8.6ka BP La Vache et Lassolas scoria cone complex (Chaîne des Puys, France). *Journal of Volcanology and Geothermal Research*, **313**: 15-28.
- Kahl, M., Chakraborty, S., Costa, F. and Pompilio, M. (2011). Dynamic plumbing system beneath volcanoes revealed by kinetic modeling, and the connection to monitoring data: An example from Mt. Etna. *Earth and Planetary Science Letters*, **308**(1): 11-22.
- Kahl, M., Chakraborty, S., Pompilio, M. and Costa, F. (2015). Constraints on the Nature and Evolution of the Magma Plumbing System of Mt. Etna Volcano (1991–2008) from a Combined Thermodynamic and Kinetic Modelling of the Compositional Record of Minerals. *Journal of Petrology*, **56**(10): 2025-2068.
- Kahl, M., Viccaro, M., Ubide, T., Morgan, D. J. and Dingwell, D. B. (2017). A Branched Magma Feeder System during the 1669 Eruption of Mt Etna: Evidence from a Time-integrated Study of Zoned Olivine Phenocryst Populations. *Journal of Petrology*, **58**(3): 443-472.
- Kaneko, K., Kamata, H., Koyaguchi, T., Yoshikawa, M. and Furukawa, K. (2007). Repeated large-scale eruptions from a single compositionally stratified magma chamber: An example from Aso volcano, Southwest Japan. *Journal of Volcanology and Geothermal Research*, **167**: 160-180.
- Karig, D. E. (1970). Kermadec arc—New Zealand tectonic confluence. *New Zealand Journal of Geology and Geophysics*, **13**(1): 21-29.
- Kawamoto, T. (1992). Dusty and honeycomb plagioclase: indicators of processes in the Uchino stratified magma chamber, Izu Peninsula, Japan. *Journal of Volcanology and Geothermal Research*, **49**(3): 191-208.
- Kelsey, H. M., Cashman, S. M., Beanland, S. and Berryman, K. R. (1995). Structural evolution along the inner forearc of the obliquely convergent Hikurangi margin, New Zealand. *Tectonics*, **14**(1).
- Kennedy, B., Spieler, O., Scheu, B., Kueppers, U., Taddeucci, J. and Dingwell, D. B. (2005). Conduit implosion during Vulcanian eruptions. *Geology*, **33**: 581-584.
- Kennedy, B. M., Jellinek, A. M., Russell, J. K., Nichols, A. R. L. and Vigouroux, N. (2010). Time- and temperature-dependent conduit wall porosity: a key control on degassing and explosivity at Tarawera volcano, New Zealand. *Earth and Planetary Science Letters*, **299**: 126-137.

- Kennedy, B. M., Wadsworth, F. B., Vasseur, J., Schipper, C. I., Jellinek, A. M., Von Auloc, F. W., Hess, K.-U., Russell, J. K., Lavallée, Y., Nichols, A. R. L. and Dingwell, D. B. (2016). Surface tension driven processes densify and retain permeability in magma and lava. *Earth and Planetary Science Letters*, **433**: 116-124.
- Kent, A. J. R., Rowe, M. C., Thornber, C. and Wortel, M. (2008). Trace Element and Pb Isotope Composition of Plagioclase from Dome Samples from the 2004–2005 Eruption of Mount St. Helens, Washington. In: D.R. Sherrod, W.E. Scott and P.H. Stauffer (Editors), *A Volcano Rekindled: The Renewed Eruption of Mount St. Helens, 2004–2006*, U.S. Geological Survey Professional Paper, pp. 809-826.
- Kepezhinskas, P., McDermott, F., Defant, M. J., Hochstaedter, A., Drummond, M. S., Hawkesworth, C. J., Koloskov, A., Maury, R. C. and Bellon, H. (1997). Trace element and Sr-Nd-Pb isotopic constraints on a three-component model of Kamchatka Arc petrogenesis. *Geochimica et Cosmochimica Acta*, **61**(3): 577-600.
- Kereszturi, G., Cappello, A., Ganci, G., Procter, J. N., Nemeth, K., Del Negro, C. and Cronin, S. J. (2014). Numerical simulation of basaltic lava flows in the Auckland Volcanic Field, New Zealand—implication for volcanic hazard assessment. *Bulletin of Volcanology*, **76**(879).
- Kile, D. E. and Eberl, D. D. (2003). On the origin of size-dependent and size-independent crystal growth; influence of advection and diffusion. *American Mineralogist*, **88**: 1514–1521.
- Kilgour, G. N., Della Pasqua, F. and Jolly, G. E. (2009). Magma ascent during eruptions at Mt. Ngauruhoe: insight from xenolith fluid inclusions. GNS Science Consultancy Report, 2009/168, 20 p.
- Kilgour, G. N., Blundy, J., Cashman, K. V. and Mader, H. M. (2013). Small volume andesite magmas and melt–mush interactions at Ruapehu, New Zealand: evidence from melt inclusions. *Contrib Mineral Petrol*, **166**: 371-392.
- Kilgour, G. N., Saunders, K. E., Blundy, J. D., Cashman, K. V., Scott, B. J. and Miller, C. A. (2014). Timescales of magmatic processes at Ruapehu volcano from diffusion chronometry and their comparison to monitoring data. *Journal of Volcanology and Geothermal Research*, **288**: 62-75.
- Kilgour, G. N., Mader, H. M., Blundy, J. D. and Brooker, R. A. (2016). Rheological controls on the eruption potential and style of an andesite volcano: A case study from Mt. Ruapehu, New Zealand. *Journal of Volcanology and Geothermal Research*, **327**: 273-287.
- Kim, D., Brown, L. D., Árnason, K., Gudmundsson, O., Ágústsson, K. and Flóvenz, O. G. (2018). Magma “bright spots” mapped beneath Krafla, Iceland, using RVSP imaging of reflected waves from microearthquakes. *Journal of Volcanology and Geothermal Research*.
- Kinzler, R. J., Grove, T. L. and Recca, S. I. (1990). An experimental study on the effect of temperature and melt composition on the partitioning of nickel between olivine and silicate melt. *Geochimica et Cosmochimica Acta*, **54**: 1255-1265.
- Kirkpatrick, R. J. (1977). Nucleation and growth of plagioclase, Makaopuhi and Alae lava lakes, Kilauea Volcano, Hawaii. *Geological Society of America*, **88**: 78-84.
- Kirkpatrick, R. J., Reck, B. H., Pelly, I. Z. and Kuo, L.-C. (1983). Programmed cooling experiments in the system MgO-SiO₂: kinetics of a peritectic reaction. *American Mineralogist*, **68**: 1095-1101.

- Klug, C. and Cashman, K. V. (1994). Vesiculation of May 18, 1980, Mount St. Helens magma. *Geology*, **22**: 468-472.
- Kohn, B. P. and Topping, W. W. (1978). Time-space relationships between late Quaternary rhyolitic and andesitic volcanism in the southern Taupo volcanic zone, New Zealand. *Geological Society of America*, **89**: 1265-1271.
- Kohut, E. J., Stern, R. J., Kent, A. J. R., Nielsen, R. L., Bloomer, S. H. and Leybourne, M. (2006). Evidence for adiabatic decompression melting in the Southern Mariana Arc from high-Mg lavas and melt inclusions. *Contributions to Mineralogy and Petrology*, **152**: 201-221.
- Konrad-Schmolke, M., O'Brien, P. J., de Capitani, C. and Carswell, D. A. (2008). Garnet growth at high- and ultra-high pressure conditions and the effect of element fractionation on mineral modes and composition. *Lithos*, **103**(3-4): 309-332.
- Kósik, S., Nemeth, K., Kereszturi, G., Procter, J. N., Zellmer, G. F. and Geshi, N. (2016). Phreatomagmatic and water-influenced Strombolian eruptions of a small-volume parasitic cone complex on the southern ringplain of Mt. Ruapehu, New Zealand: Facies architecture and eruption mechanisms of the Ohakune Volcanic Complex controlled by an unstable fissure eruption. *Journal of Volcanology and Geothermal Research*, **327**: 99-115.
- Koulakov, I. and Vargas, C. A. (2018). Evolution of the Magma Conduit Beneath the Galeras Volcano Inferred From Repeated Seismic Tomography. *Geophysical Research Letters*, **45**(15): 7514-7522.
- Koyaguchi, T. (1986). Textural and compositional evidence for magma mixing and its mechanism, Abu volcano group, Southwestern Japan. *Contributions to Mineralogy and Petrology*, **93**: 33-45.
- Krimer, D. and Costa, F. (2017). Evaluation of the effects of 3D diffusion, crystal geometry, and initial conditions on retrieved time-scales from Fe–Mg zoning in natural oriented orthopyroxene crystals. *Geochimica et Cosmochimica Acta*, **196**: 271-288.
- Krippner, J. B. (2009). Ngauruhoe inner crater volcanic processes of the 1954-1955 and 1974-1975 eruptions, The University of Waikato.
- Kuritani, T. (1999). Phenocryst crystallization during ascent of alkali basalt magma at Rishiri Volcano, northern Japan. *Journal of Volcanology and Geothermal Research*, **88**: 77-97.
- Kushiro, I. (1987). A petrological model of the mantle wedge and lower crust in the Japanese island arcs. In: B.O. Mysen (Editor), *Magmatic processes: physicochemical principles*. The Geochemical Society Special Publication Vol. 1, pp. 165-181.
- L'Heureux, I. and Fowler, A. D. (1994). A nonlinear dynamical model of oscillatory zoning in plagioclase. *American Mineralogist*, **79**(9-10): 885-891.
- L'Heureux, I. and Fowler, A. D. (1996). Dynamical model of oscillatory zoning in plagioclase with nonlinear partition relation. *Geophysical Research Letters*, **23**(1): 17-20.
- La Delfa, S., Patane, G., Clocchiatti, R., Joron, J. L. and Tanguy, J. C. (2001). Activity of Mount Etna preceding the February 1999 fissure eruption: inferred mechanism from seismological and geochemical data. *Journal of Volcanology and Geothermal Research*, **105**(1-2): 121-139.
- La Femina, P. C., Connor, C. B., Hill, B. E., Strauch, W. and Saballos, J. A. (2004). Magma-tectonic interactions in Nicaragua: The 1999 seismic swarm and eruption

- of Cerro Negro volcano. *Journal of Volcanology and Geothermal Research*, **137**(1-3 SPEC. ISS.): 187-199.
- Lahr, J. C., Chouet, B. A., Stephens, C. D., Power, J. A. and Page, R. A. (1994). Earthquake classification, location and error analysis in a volcanic environment - implications for the magmatic system of the 1989-1990 eruptions at Redoubt volcano, Alaska. *Journal of Volcanology and Geothermal Research*, **62**(1-4): 137-151.
- Lai, Y.-M., Song, S.-R. and Iizuka, Y. (2008). Magma mingling in the Tungho area, coastal range of eastern Taiwan. *Journal of Volcanology and Geothermal Research*, **178**: 608-623.
- Lamb, S., Moore, J. D. P., Smith, E. G. C. and Stern, T. A. (2017). Episodic kinematics in continental rifts modulated by changes in mantle melt fraction. *Nature*, **547**.
- Landi, P., Metrich, N., Bertagnini, A. and Rosi, M. (2004). Dynamics of magma mixing and degassing recorded in plagioclase at Stromboli (Aeolian Archipelago, Italy). *Contrib Mineral Petrol*, **147**: 213-227.
- Lange, R. A., Frey, H. M. and Hector, J. (2009). A thermodynamic model for the plagioclase-liquid hygrometer/thermometer. *American Mineralogist*, **94**: 494-506.
- Larsen, J. F. (2005). Experimental study of plagioclase rim growth around anorthite seed crystals in rhyodacitic melt. *American Mineralogist*, **90**(2-3): 417-427.
- Larsen, J. F. (2006). Rhyodacite magma storage conditions prior to the 3430 yBP caldera-forming eruption of Aniakchak volcano, Alaska. *Contributions to Mineralogy and Petrology*, **152**(4): 523-540.
- Larsen, J. F., Śliwiński, M. G., Nye, C., Cameron, C. and Schaefer, J. R. (2013). The 2008 eruption of Okmok Volcano, Alaska: Petrological and geochemical constraints on the subsurface magma plumbing system. *Journal of Volcanology and Geothermal Research*, **264**: 85-106.
- Lasaga, A. C. (1982). Toward a master equation in crystal growth. *American Journal of Science*, **282**: 1264-1288.
- Lasaga, A. C. (1983). Geospeedometry: an extension of geothermometry. In: S.K. Saxena (Editor), *Kinetics and Equilibrium in Mineral Reactions*, New York, pp. 82-114.
- Lavallée, Y., de Silva, S. L., Salas, G. and Byrnes, J. M. (2009). Structural control on volcanism at the Ubinas, Huaynaputina, and Ticsani Volcanic Group (UHTVG), southern Peru. *Journal of Volcanology and Geothermal Research*, **186**(3-4): 253-264.
- Lavenu, A. and Cembrano, J. (1999). Compressional and transpressional-stress pattern for Pliocene and Quaternary brittle deformation in fore arc and intra-arc zones (Andes of Central and Southern Chile). *Journal of Structural Geology*, **21**: 1669-1691.
- Le Bas, M. J., Le Maitre, R. W., Streckeisen, A. and Zanettin, P. (1986). A chemical classification of volcanic rocks based on the total alkali-silica diagram. *Journal of Petrology*, **27**: 745-750.
- Le Maitre, R. W. (2005). *A Classification of Igneous Rocks and Glossary of terms: Recommendations of the International Union of Geological Sciences Subcommission on the Systematics of Igneous Rocks*. Cambridge University Press.
- Lee, J. K. W., Williams, I. S. and Ellis, D. J. (1997). Pb, U and Th diffusion in natural zircon. *Nature*, **390**: 159-162.

- Lefebvre, N. S., White, J. D. L. and Kjarsgaard, B. A. (2013). Unbedded diatreme deposits reveal maar-diatreme-forming eruptive processes: Standing Rocks West, Hopi Buttes, Navajo Nation, USA. *Bulletin of Volcanology*, **75**(8): 739.
- Leidig, M. and Zandt, G. (2003). Modeling of highly anisotropic crust and application to the Altiplano-Puna volcanic complex of the central Andes. *Journal of Geophysical Research: Solid Earth*, **108**(B1): ESE 5-1-ESE 5-15.
- Lejeune, A. and Richet, P. (1995). Rheology of crystal-bearing silicate melts: An experimental study at high viscosity. *Journal of Geophysical Research*, **100**: 4215–4229.
- Lentz, R. C. F. and McSween, Y. (2000). Crystallization of the basaltic shergottites: Insights from crystal size distribution (CSD) analysis of pyroxenes. *Meteoritics and Planetary Science*, **35**(919-927).
- Leonard, G. S. (2003). The evolution of Maroa Volcanic Centre, Taupo Volcanic Zone, New Zealand, University of Canterbury.
- Leonard, G. S., Cole, J. W., Nairn, I. A. and Self, S. (2004). Basalt triggering of the c. AD 1305 Kaharoa rhyolite eruption, Tarawera Volcanic Complex, New Zealand. *Journal of Volcanology and Geothermal Research*, **115**(3-4): 461-486.
- Leshner, C. E., Cashman, K. V. and Mayfield, J. D. (1999). Kinetic controls on crystallization of Tertiary North Atlantic basalt and implications for the emplacement and cooling history of lava at Site 989, Southeast Greenland rifted margin. *Proc. ODP, Sci. Results*, **163**: 135–148.
- Leshner, C. E. and Spera, F. J. (2015). Thermodynamic and Transport Properties of Silicate Melts and Magma. In: H. Sigurdsson (Editor), *The Encyclopedia of Volcanoes*. Elsevier.
- Leung, I. S. (1974). Sector-Zoned Titanaugites: Morphology, Crystal Chemistry, and Growth *American Mineralogist*, **59**(1-2): 127-138.
- Lillie, A. R. (1980). *Strata and Structure in New Zealand*. The Tohunga Press, Auckland, New Zealand.
- Lindoo, A., Larsen, J. F., Cashman, K. V. and Oppenheimer, J. (2017). Crystal controls on permeability development and degassing in basaltic andesite magma. *HGeology*, **45**(9): 831-834.
- Lindsay, J. M., de Silva, S., Trumbull, R., Emmermann, R. and Wemmer, K. (2001). La Pacana caldera, N. Chile: a re-evaluation of the stratigraphy and volcanology of one of the world's largest resurgent calderas. *Journal of Volcanology and Geothermal Research*, **106**(1): 145-173.
- Lipman, P. W., Mullineaux, D. R. and Survey, G. (1982). *The 1980 Eruptions of Mount St. Helens*, Washington. U.S. Department of the Interior, U.S. Geological Survey.
- Lipman, P. W. and Banks, N. G. (1987). Aa flow dynamics, Mauna Loa 1984. . *USGS Prof. Paper*, **1350**: 1527-1567.
- Liu, E. J., Cashman, K. V., Rust, A. C. and Gislason, S. R. (2015). The role of bubbles in generating fine ash during hydromagmatic eruptions. *Geology*, **43**(3): 239-242.
- Liu, M. and Yund, R. (1992). NaSi-CaAl interdiffusion in plagioclase. *American Mineralogist*, **77**: 275-283.
- Lloyd, A. S., Ruprecht, P., Hauri, E. H., Rose, W., Gonnermann, H. M. and Plank, T. (2014). NanoSIMS results from olivine-hosted melt embayments: Magma ascent rate during explosive basaltic eruptions. *Journal of Volcanology and Geothermal Research*, **283**: 1-18.

- Lofgren, G. E. (1980). Experimental studies on the dynamic crystallization of silicate melts. In: R.B. Hargraves (Editor), *The Physics of Magmatic Processes*, Princeton, pp. 487–551.
- Longpré, M.-A., Troll, V. R., Walter, T. R. and Hansteen, T. H. (2009). Volcanic and geochemical evolution of the Teno massif, Tenerife, Canary Islands: Some repercussions of giant landslides on ocean island magmatism. *Geochemistry Geophysics Geosystems*, **10**(12).
- Loomis, T. P. and Welber, P. W. (1982). Crystallization processes in the Rocky Hill granodiorite Pluton, California: An interpretation based on compositional zoning of plagioclase. *Contributions to Mineralogy and Petrology*, **81**(3): 230-239.
- Lormand, C., Zellmer, G. F., Kilgour, G., Iizuka, Y., Mead, S., Sakamoto, N., Németh, K., Palmer, A. S., Moebis, A., Kuritani, T. and Yurimoto, H. (2018a). Microlite size distributions and P-T-t-X (H₂O) constraints of Central Plateau tephra, New Zealand: Implications for magma ascent processes of explosive eruptions, American Geophysical Union Fall Meeting 2019, San Francisco, USA.
- Lormand, C., Zellmer, G. F., Németh, K., Kilgour, G. N., Mead, S., Palmer, A. S., Sakamoto, N., Yurimoto, H. and Moebis, A. (2018b). Weka Trainable Segmentation Plugin in ImageJ: A Semi-Automatic Tool Applied to Crystal Size Distributions of Microlites in Volcanic Rocks. *Microscopy and Microanalysis*, **24**(6): 667-675.
- Loughlin, S. C., Miller, A. D. and Aspinall, W. P. (1998). World-wide dome-building eruptions: summary of dome growth, periods of dome repose and post-eruption characteristics. Montserrat Volcano Observatory (MVO), 98/15.
- Lu, Z., Wicks Jr, C., Power, J. A. and Dzurisin, D. (2000). Ground deformation associated with the March 1996 earthquake swarm at Akutan volcano, Alaska, revealed by satellite radar interferometry. *Journal of Geophysical Research: Solid Earth*, **105**(B9): 21483-21495.
- Lube, G., Cronin, S. J., Platz, T., Freundt, A., Procter, J. N., Henderson, C. and Sheridan, M. F. (2007). Flow and deposition of pyroclastic granular flows: A type example from the 1975 Ngauruhoe eruption, New Zealand. *Journal of Volcanology and Geothermal Research*, **161**: 165-186.
- Lube, G., Breard, E. C. P., Cronin, S. J., Procter, J. N., Brenna, M., Moebis, A., Pardo, N., Stewart, R. B., Jolly, A. and Fournier, N. (2014). Dynamics of surges generated by hydrothermal blasts during the 6 August 2012 Te Maari eruption, Mt. Tongariro, New Zealand. *Journal of Volcanology and Geothermal Research*, **286**: 348-366.
- Maccaferri, F., Bonafede, M. and Rivalta, E. (2011). A quantitative study of the mechanisms governing dike propagation, dike arrest and sill formation. *Journal of Volcanology and Geothermal Research*, **208**: 39-50.
- Macdonald, G. A. (1972). *Volcanoes*, Englewood Cliffs, NJ.
- Macdonald, R., Belkin, H. E., Fitton, J. G., Rogers, N. W., Nejbirt, K., Tindle, A. G. and Marshall, A. S. (2008). The Roles of Fractional Crystallization, Magma Mixing, Crystal Mush Remobilization and Volatile–Melt Interactions in the Genesis of a Young Basalt–Peralkaline Rhyolite Suite, the Greater Olkaria Volcanic Complex, Kenya Rift Valley. *Journal of Petrology*, **49**(8): 1515-1547.
- Mackwell, S. J. and Kohlstedt, D. L. (1990). Diffusion of hydrogen in olivine: implications for water in the mantle. *Journal of Geophysical Research*, **95**(B4): 5079-5088.

- Magee, C., O'Driscoll, B. and Chambers, A. D. (2010). Crystallization and textural evolution of a closed-system magma chamber: insights from a crystal size distribution study of the Lilloise layered intrusion, East Greenland, *Geological Magazine*, pp. 363-379.
- Mahapatra, D. (2014). Automatic Cardiac Segmentation Using Semantic Information from Random Forests. *Journal of Digital Imaging*, **27**(6): 794-804.
- Manga, M. and Brodsky, E. (2006). Seismic triggering of eruptions in the far field: volcanoes and geysers. *Annual Review of Earth and Planetary Sciences*, **2006**(34): 263-291.
- Mangan, M. T. (1990). Crystal size distribution systematics and the determination of magma storage times: The 1959 eruption of Kilauea volcano, Hawaii. *Journal of Volcanology and Geothermal Research*, **44**: 295-302.
- Marsh, B., D. (1998a). On the Interpretation of Crystal Size Distributions in Magmatic Systems. *Journal of Petrology*, **39**(4): 553-599.
- Marsh, B. D. (1981). On the Crystallinity, Probability of Occurrence, and Rheology of Lava and Magma. *Contributions to Mineralogy and Petrology*, **78**(1): 85-98.
- Marsh, B. D. (1988). Crystal size distribution (CSD) in rocks and the kinetics and dynamics of crystallisation. I: Theory. *Contributions to Mineralogy and Petrology*, **99**: 277-291.
- Marsh, B. D. (1996). Solidification fronts and magmatic evolution. *Mineralogical Magazine*, **60**: 5-40.
- Marsh, B. D. (1998b). On the interpretation of crystal size distributions in magmatic systems. *Journal of Petrology*, **39**: 553-599.
- Martel, C., Dingwell, D. B., Spieler, O., Pichavant, M. and Wilke, M. (2001). Experimental fragmentation of crystal- and vesicle-bearing silicic melts. *Bulletin of Volcanology*, **63**: 398-405.
- Martel, C., Radadi Ali, A., Poussineau, S., Gourgaud, A. and Pichavant, M. (2006). Basalt-inherited microlites in silicic magmas: Evidence from Mount Pelée (Martinique, French West Indies). *Geology*, **34**(11): 905-908.
- Martel, C. and Poussineau, S. (2007). Diversity of eruptive styles inferred from the microlites of Mt Pelée andesite (Martinique, Lesser Antilles). *Journal of Volcanology and Geothermal Research*, **166**(3-4): 233-254.
- Martel, C. (2012). Eruption Dynamics Inferred from Microlite Crystallization Experiments: Application to Plinian and Dome-forming Eruptions of Mt. Pelée (Martinique, Lesser Antilles). *Journal of Petrology*, **53**(4): 699-725.
- Martin-Del Pozzo, A. L., Cifuentes, G., Gonzalez, E., Martinez, A. and Mendiola, F. (2008). Magnetic signatures associated with magma ascent and stagnation at Popocatepetl volcano, Mexico: implications for eruption triggering mechanisms during 2006. In: C. Annen and G.F. Zellmer (Editors), Dynamics of crustal magma transfer, storage and differentiation. Special Publications. Geological Society, London, pp. 117-131.
- Marzocchi, W. (2002). Remote seismic influence on large explosive eruptions, *Journal of Geophysical Research*.
- Marzocchi, W., Sandri, L., Gasparini, P., Newhall, C. and Boschi, E. (2004). Quantifying probabilities of volcanic events: The example of volcanic hazard at Mount Vesuvius. *Journal of Geophysical Research: Solid Earth*, **109**(B11).

- Mashima, H. (2004). Time scale of magma mixing between basalt and dacite estimated for the Saga-Futagoyama volcanic rocks from northwest Kyushu, southwest Japan. *Journal of Volcanology and Geothermal Research*, **131**: 333-349.
- Masotta, M., Mollo, S., Freda, C., Gaeta, M. and Moore, G. (2013). Clinopyroxene–liquid thermometers and barometers specific to alkaline differentiated magmas. *Contributions to Mineralogy and Petrology*, **166**(6): 1545-1561.
- Masotta, M., Mollo, S., Gaeta, M. and Freda, C. (2016). Melt extraction in mush zones: The case of crystal-rich enclaves at the Sabatini Volcanic District (central Italy). *Lithos*, **248-251**: 288-292.
- Masotta, M., Pontesilli, A., Mollo, S., Armienti, P., Ubide, T., Nazzari, M. and Scarlato, P. (2020). The role of undercooling during clinopyroxene growth in trachybasaltic magmas: Insights on magma decompression and cooling at Mt. Etna volcano. *Geochimica et Cosmochimica Acta*, **268**: 258-276.
- Masterlark, T., Haney, M., Dickinson, H., Fournier, T. and Searcy, C. (2010). Rheologic and structural controls on the deformation of Okmok volcano, Alaska: FEMs, InSAR, and ambient noise tomography. *Journal of Geophysical Research: Solid Earth*, **115**(B2).
- Mastrolorenzo, G. and Pappalardo, L. (2006). Magma degassing and crystallization processes during eruptions of high-risk Neapolitan volcanoes: Evidence of common equilibrium rising processes in alkaline magmas. *Earth and Planetary Science Letters*, **250**: 164-181.
- McCanta, M., Rutherford, M. and Hammer, J. (2007). Pre-eruptive and syn-eruptive conditions in the Black Butte, California dacite: Insight into crystallization kinetics in a silicic magma system. *Journal of Volcanology and Geothermal Research*, **160**(3-4): 263-284.
- McCarthy, A. and Müntener, O. (2016). Comb layering monitors decompressing and fractionating hydrous mafic magmas in subvolcanic plumbing systems (Fisher Lake, Sierra Nevada, USA). *Journal of Geophysical Research: Solid Earth*, **121**(12): 8595-8621.
- McCarthy, A. and Müntener, O. (2017). Mineral growth in melt conduits as a mechanism for igneous layering in shallow arc plutons: mineral chemistry of Fisher Lake orbicules and comb layers (Sierra Nevada, USA). *Contributions to Mineralogy and Petrology*, **172**(7): 55.
- McKay, G., Le, L., Wagstaff, J. and Crozaz, G. (1994). Experimental partitioning of rare earth elements and strontium; constraints on petrogenesis and redox conditions during crystallization of Antarctic angrite Lewis Cliff 86010. *Geochimica et Cosmochimica Acta*, **58**(13): 2911-2919.
- Means, W. D. and Park, Y. (1994). New experimental approach to understanding igneous texture. *Geology*, **22**: 323-326.
- Melnik, O. and Sparks, R. S. J. (2002). Dynamics of magma ascent and lava extrusion at Soufrière Hills Volcano, Montserrat. In: T.H. Druitt and B.P. Kokelaar (Editors), The eruption of Soufrière Hills Volcano, Montserrat, from 1995 to 1999, Geological Society, London, Memoirs, pp. 153-171.
- Melnik, O. E., Blundy, J. D., Rust, A. C. and Muir, D. D. (2011). Subvolcanic plumbing systems imaged through crystal size distributions. *Geology*, **39**: 403-406.
- Menand, T., Annen, C. and de Saint Blanquat, M. (2015). Rates of magma transfer in the crust: Insights into magma reservoir recharge and pluton growth. *Geology*, **43**(3): 199-202.

- Métrich, N., Bertagnini, A., Landi, P. and Rosi, M. (2001). Crystallization Driven by Decompression and Water Loss at Stromboli Volcano (Aeolian Islands, Italy). *Journal of Petrology*, **42**(8): 1471-1490.
- Meyer, F. J., McAlpin, D. B., Gong, W., Ajadi, O., Arko, S., Webley, P. W. and Dehn, J. (2015). Integrating SAR and derived products into operational volcano monitoring and decision support systems. *ISPRS Journal of Photogrammetry and Remote Sensing*, **100**: 106-117.
- Miller, T. P. (1994). Dome growth and destruction during the 1989–1990 eruption of redoubt volcano. *Journal of Volcanology and Geothermal Research*, **62**(1-4): 197-212.
- Miller, T. P. and Chouet, B. A. (1994). The 1989–1990 eruptions of Redoubt Volcano: an introduction. *Journal of Volcanology and Geothermal Research*, **62**(1-4): 1-10.
- Miwa, T. and Toramaru, A. (2013). Conduit process in vulcanian eruptions at Sakurajima volcano, Japan: Inference from comparison of volcanic ash with pressure wave and seismic data. *Bulletin of Volcanology*, **75**(685).
- Mock, A. and Jerram, D. A. (2005). Crystal Size Distributions (CSD) in Three Dimensions: Insights from the 3D Reconstruction of a Highly Porphyritic Rhyolite. *Journal of Petrology*, **46**(8): 1525-1541.
- Moebis, A., Cronin, S. J. and Nemeth, K. (2007). Magmatic and phreatomagmatic tephra in fine ash successions of an arc volcanic complex, the Mangatawai Tephra Formation, Tongariro Volcanic Centre, New Zealand, Geological Society of New Zealand and New Zealand Geophysical Society Joint Annual Conference, Tauranga, New Zealand.
- Moebis, A. (2010). Understanding the Holocene explosive eruption record of the Tongariro Volcanic Centre, New Zealand, PhD thesis, Massey University, Palmerston North, New Zealand, 344 pp.
- Moebis, A., Cronin, S. J., Neall, V. E. and Smith, I. E. (2011). Unravelling a complex volcanic history from fine-grained, intricate Holocene ash sequences at the Tongariro Volcanic Centre, New Zealand. *Quaternary International*, **246**: 352-363.
- Moitra, P., Gonnermann, H. M., Houghton, B. F. and Giachetti, T. (2013). Relating vesicle shapes in pyroclasts to eruption styles. *Bulletin of Volcanology*, **75**(2): 691.
- Mollard, E., Martel, C. and Bourdier, J.-L. (2012). Decompression-induced Crystallization in Hydrated Silica-rich Melts: Empirical Models of Experimental Plagioclase Nucleation and Growth Kinetics. *Journal of Petrology*, **53**(8): 1743-1766.
- Mollo, S., Del Claudio, P., Ventura, G., Iezzi, G. and Scarlato, P. (2010). Dependence of clinopyroxene composition on cooling rate in basaltic magmas: Implications for thermobarometry. *Lithos*, **118**(3-4): 302-312.
- Mollo, S., Putirka, K., Iezzi, G., Del Gaudio, P. and Scarlato, P. (2011). Plagioclase–melt (dis)equilibrium due to cooling dynamics: Implications for thermometry, barometry and hygrometry. *Lithos*, **125**(1): 221-235.
- Mollo, S., Putirka, K. D., Iezzi, G. and Scarlato, P. (2013). The control of cooling rate on titanomagnetite composition: implications for a geospeedometry model applicable to alkaline rocks from Mt. Etna volcano. *Contrib Mineral Petrol*, **165**: 457-475.

- Mollo, S. and Masotta, M. (2014). Optimizing pre-eruptive temperature estimates in thermally and chemically zoned magma chambers. *Chemical Geology*, **368**: 97-103.
- Mollo, S., Giacomoni, P. P., Andronico, D. and Scarlato, P. (2015). Clinopyroxene and titanomagnetite cation redistributions at Mt. Etna volcano (Sicily, Italy): Footprints of the final solidification history of lava fountains and lava flows. *Chemical Geology*, **406**: 45-54.
- Mollo, S. and Hammer, J. E. (2017). Dynamic crystallization in magmas. In: W. Heinrich and R. Abart (Editors), *EMU Notes in Mineralogy*, pp. 373-418.
- Montanini, A., Barbieri, M. and Castorina, F. (1994). The role of fractional crystallisation, crustal melting and magma mixing in the petrogenesis of rhyolites and mafic inclusion-bearing dacites from the Monte Arci volcanic complex (Sardinia, Italy). *Journal of Volcanology and Geothermal Research*, **61**(1): 95-120.
- Moore, A., Coogan, L. A., Costa, F. and Perfit, M. R. (2014). Primitive melt replenishment and crystal-mush disaggregation in the weeks preceding the 2005–2006 eruption 9°50'N, EPR. *Earth and Planetary Science Letters*, **403**: 15-26.
- Moran, S. C., Newhall, C. and Roman, D. C. (2011). Failed magmatic eruptions: late-stage cessation of magma ascent. *Bulletin of Volcanology*, **2011**(73): 115-122.
- Mordensky, S. P., Heap, M. J., Kennedy, B. M., Gilg, H. A., Villeneuve, M. C., Farguharson, J. I. and Garvley, D. M. (2019). Influence of alteration on the mechanical behaviour and failure mode of andesite: implications for shallow seismicity and volcano monitoring. *Bulletin of Volcanology*, **81**(44).
- Morgado, E., Morgan, D. J., Castruccio, A., Ebmeier, S. K., Parada, M.-A., Brahm, R., Harvey, J., Gutierrez, F. and Walshaw, R. (2019). Old magma and a new, intrusive trigger: using diffusion chronometry to understand the rapid-onset Calbuco eruption, April 2015 (Southern Chile). *Contribution to Mineralogy and Petrology*, **174**(61).
- Morgan, D. and Jerram, D. (2006). On estimating crystal shape for crystal size distribution analysis. *Journal of Volcanology and Geothermal Research*, **154**(1-2): 1-7.
- Morgan, D. J., Blake, S., Rogers, N. W., De Vivo, B., Rolandi, G., Macdonald, R. and Hawkesworth, C. J. (2004). Timescales of crystal residence and magma chamber volume from modelling of diffusion profiles in phenocrysts: Vesuvius 1944. *Earth and Planetary Science Letters*, **222**: 933-946.
- Morgan, D. J. and Blake, S. (2006). Magmatic residence times of zoned phenocrysts: introduction and application of the binary element diffusion modelling (BEDM) technique. *Contributions to Mineralogy and Petrology*, **151**: 58-70.
- Morgan, D. J., Jerram, D. A., Chertkoff, D. G., Davidson, J. P., Pearson, D. G., Kronz, A. and Nowell, G. M. (2007). Combining CSD and isotopic microanalysis: Magma supply and mixing processes at Stromboli Volcano, Aeolian Islands, Italy. *Earth and Planetary Science Letters*, **260**(3-4): 419-431.
- Morimoto, N. (1989). Nomenclature of pyroxenes. *Mineralogical Journal*, **14**(5): 198-221.
- Morrissey, M. and Mastin, L. G. (1999). Vulcanian eruptions. In: H. Sigurdsson, B. Houghton, H. Rymer, J. Stix and S. McNutt (Editors), *Encyclopedia of Volcanoes*, pp. 463-476.
- Morse, S. A. (1984). Cation diffusion in plagioclase feldspar. *Science*, **225**: 504-505.

- Mortimer, N. (2004). New Zealand's Geological Foundations. *Gondwana Research*, **7**(1): 261-272.
- Mortimer, N., Herzer, R. H., Gans, P. B., Laporte-Magoni, C., Calvert, A. T. and Bosch, D. (2007). Oligocene–Miocene tectonic evolution of the South Fiji Basin and Northland Plateau, SW Pacific Ocean: Evidence from petrology and dating of dredged rocks. *Marine Geology*, **237**: 1-24.
- Mortimer, N., Gans, P. B., Palin, J. M., Meffre, S., Herzer, R. H. and Skinner, D. N. B. (2010). Location and migration of Miocene–Quaternary volcanic arcs in the SW Pacific region. *Journal of Volcanology and Geothermal Research*, **190**: 1-10.
- Mourtada-Bonnefoi, C. C. and Laporte, D. (1999). Experimental study of homogeneous bubble nucleation in rhyolitic magmas. *Geophysical Research Letters*, **26**(23): 3505-3508.
- Muir, D. D., Rust, A. C. and Blundy, J. D. (2011). Quantitative textural data from x-ray element maps: CSDs, crystallinity and mineral modes, Volcanic and Magmatic Studies Group Annual Meeting.
- Muir, D. D., Blundy, J. and Rust, A. C. (2012). Multiphase petrography of volcanic rocks using element maps: a method applied to Mount St. Helens, 1980–2005. *Bulletin of Volcanology*, **74**: 1101-1120.
- Mujin, M. and Nakamura, M. (2014). A nanolite record of eruption style transition. *Geology*, **42**.
- Mujin, M., Nakamura, M. and Miyake, A. (2017). Eruption style and crystal size distributions: Crystallization of groundmass nanolites in the 2011 Shinmoedake eruption. *American Mineralogist*, **102**: 2367-2380.
- Muncill, G. E. and Lasaga, A. C. (1988). Crystal-growth kinetics of plagioclase in igneous systems: Isothermal H₂O-saturated experiments and extension of a growth model to complex silicate melts. *American Mineralogist*, **73**: 982-992.
- Murch, A. P. and Cole, P. D. (2019). Using microlites to gain insights into ascent conditions of differing styles of volcanism at Soufrière Hills Volcano. *Journal of Volcanology and Geothermal Research*, **384**: 221-231.
- Murphy, M. D., Sparks, R. S. J., Barclay, J., Carroll, M. R. and Brewer, T. S. (2000). Remobilization of andesite magma by intrusion of mafic magma at the Soufrière Hills volcano, Montserrat, West Indies. *Journal of Petrology*, **41**: 21-42.
- Murphy, R. P. (1977). The volcanic geology of Matahina Basin, Victoria University, Wellington.
- Nagasawa, H. and Schnetzler, C. C. (1971). Partitioning of rare earth, alkali and alkaline earth elements between phenocrysts and acidic igneous magma. *Geochimica et Cosmochimica Acta*, **35**: 953-968.
- Nairn, I. A., Hewson, C., Latter, J. and Wood, C. (1976). Pyroclastic eruptions of Ngauruhoe volcano, central North Island, New Zealand, 1974 January and March. In: R.W. Johnson (Editor), *Volcanism in Australasia*. Elsevier, Amsterdam, pp. 385-405.
- Nairn, I. A. and Self, S. (1978). Explosive eruptions and pyroclastic avalanches from Ngauruhoe in February 1975. *Journal of Volcanology and Geothermal Research*, **3**: 39-60.
- Nairn, I. A., Kobayashi, T. and Nakagawa, M. (1998). The ~10 ka multiple vent pyroclastic eruption sequence at Tongariro Volcanic Centre, Taupo Volcanic Zone, New Zealand: Part 1. Eruptive processes during regional extension. *Journal of Volcanology and Geothermal Research*, **86**: 19-44.

- Nairn, I. A., Shane, P. R., Cole, J. W., Leonard, G. J., Self, S. and Pearson, N. (2004). Rhyolite magma processes of the VAD 1315 Kaharoa eruption episode, Tarawera volcano, New Zealand. *Journal of Volcanology and Geothermal Research*, **131**: 265-294.
- Naismith, A. K., Matthew Watson, I., Escobar-Wolf, R., Chigna, G., Thomas, H., Coppola, D. and Chun, C. (2019). Eruption frequency patterns through time for the current (1999–2018) activity cycle at Volcán de Fuego derived from remote sensing data: Evidence for an accelerating cycle of explosive paroxysms and potential implications of eruptive activity. *Journal of Volcanology and Geothermal Research*, **371**: 206-219.
- Nakada, S. and Motomura, Y. (1999). Petrology of the 1991–1995 eruption at Unzen: effusion pulsation and groundmass crystallization. *Journal of Volcanology and Geothermal Research*, **89**: 173-196.
- Nakada, S., Zaennudin, A., Yoshimoto, M., Maeno, F., Suzuki, Y., Hokanishi, N., Sasaki, M., Ohkura, T., Gunawan, H. and Triastuty, H. (2019). Growth process of the lava dome/flow complex at Sinabung Volcano during 2013–2016. *Journal of Volcanology and Geothermal Research*, **382**: 120-136.
- Nakagawa, M., Nairn, I. A. and Kobayashi, T. (1998). The ~10 ka multiple vent pyroclastic eruption sequence at Tongariro Volcanic Centre, Taupo Volcanic Zone, New Zealand: Part 2. Petrological insight into magma storage and transport during regional extension. *Journal of Volcanology and Geothermal Research*, **86**: 45-65.
- Nakagawa, M., Wada, K., Thordarson, T., Wood, C. P. and Gamble, J. A. (1999). Petrologic investigations of the 1995 and 1996 eruptions of Ruapehu volcano, New Zealand: Formation of discrete and small magma pockets and their intermittent discharge. *Bulletin of Volcanology*, **61**(1-2): 15-31.
- Nakamura, M. (1995). Continuous mixing of crystal mush and replenished magma in the ongoing Unzen eruption. *Geology*, **23**(9): 807-810.
- Nakamura, M. and Shimakita, D. (1998). Dissolution origin and syn-entrapment compositional change of melt inclusion in plagioclase. *Earth and Planetary Science Letters*, **161**(119-133).
- Nakamura, Y. (1973). Origin of sector-zoning of igneous clinopyroxenes. *American Mineralogist*, **58**(11-12): 986-990.
- Nakao, S., Morita, Y., Oikawa, J., Ueda, H., Takahashi, H., Ohta, Y., Matsushima, T. and Iguchi, M. (2013). Volume change of the magma reservoir relating to the 2011 Kirishima Shinmoe-dake eruption—Charging, discharging and recharging process inferred from GPS measurements. *Earth Planets Space*, **65**(3): 505-515.
- Naranjo, J. A., Lara, L. E. and Mazzoni, M. M. (1997). Late Quaternary monogenetic volcanoes along Río Salado, Southwest Mendoza Province, Argentina. *Acta Geologica Hispanica*, **32**: 113-122.
- Neave, D. A. and Putirka, K. D. (2017). A new clinopyroxene-liquid barometer, and implications for magma storage pressures under Icelandic rift zones. *American Mineralogist*, **102**(4): 777-794.
- Nelson, S. T. and Montana, A. (1992). Sieve-textured plagioclase in volcanic rocks produced by rapid decompression. *American Mineralogist*, **77**: 1242-1249.
- Ni, H., Liu, Y., Wang, L. and Zhang, Y. (2009). Water speciation and diffusion in haploandesitic melts at 743–873 K and 100 MPa. *Geochimica et Cosmochimica Acta*, **73**: 3630-3641.

- Nicholis, M. G. and Rutherford, M. J. (2004). Experimental constraints on magma ascent rate for the Crater Flat volcanic zone hawaiite. *Geology*, **32**(6): 489-492.
- Nicol, A., Seebeck, H. and Wallace, L. (2017). Chapter 1 Quaternary Tectonics of New Zealand. In: J. Shulmeister (Editor), *Landscape and Quaternary Environmental Change in New Zealand*. Atlantis Press.
- Nikolaev, G. S., Ariskin, A. A. and Barmina, G. S. (2018a). SPINMELT-2.0: Simulation of spinel–melt equilibrium in basaltic systems under pressures up to 15 kbar: I. Model formulation, calibration, and tests. *Geochemistry International*, **56**: 24-45.
- Nikolaev, G. S., Ariskin, A. A. and Barmina, G. S. (2018b). SPINMELT-2.0: Simulation of spinel–melt equilibrium in basaltic systems under pressures up to 15 kbar: II. Description of the program package, the topology of the Cr-spinel–melt model system, and petrological implications. *Geochemistry International*, **56**: 125-135.
- Nimis, P. (1995). A clinopyroxene geobarometer for basaltic systems based on crystal-structure modeling. *Contributions to Mineralogy and Petrology*, **121**(2): 115-125.
- Nimis, P. (1999). Clinopyroxene geobarometry of magmatic rocks. Part 2. Structural geobarometers for basic to acid, tholeiitic and mildly alkaline magmatic systems. *Contributions to Mineralogy and Petrology*, **135**(1): 62-74.
- Nimis, P. and Taylor, W. R. (2000). Single clinopyroxene thermobarometry for garnet peridotites. Part I. Calibration and testing of a Cr-in-Cpx barometer and an enstatite-in-Cpx thermometer. *Contributions to Mineralogy and Petrology*, **139**(5): 541-554.
- Noguchi, S., Toramaru, A. and Shimano, T. (2006). Crystallization of microlites and degassing during magma ascent: Constraints on the fluid mechanical behavior of magma during the Tenjo Eruption on Kozu Island, Japan. *Bulletin of Volcanology*, **68**(5): 432-449.
- Noguchi, S., Toramaru, A. and Nakada, S. (2008). Relation between microlite textures and discharge rate during the 1991–1995 eruptions at Unzen, Japan. *Journal of Volcanology and Geothermal Research*, **175**(1-2): 141-155.
- Norman, M., Garcia, M. O. and Pietruszka, A. J. (2005). Trace-element distribution coefficients for pyroxenes, plagioclase, and olivine in evolved tholeiites from the 1955 eruption of Kilauea Volcano, Hawai'i, and petrogenesis of differentiated rift-zone lavas. *American Mineralogist*, **90**(5-6): 888-899.
- O'Hara, M. J. (1977). Geochemical evolution during fractional crystallisation of a periodically refilled magma chamber. *Nature*, **266**: 503-507.
- Ohnenstetter, D. and Brown, W. (1992). Overgrowth Textures, Disequilibrium Zoning, and Cooling History of a Glassy Four-Pyroxene Boninite Dyke from New Caledonia. *Journal of Petrology*, **33**: 231-271.
- Oppenheimer, J., Rust, A., C., Cashman, K. V. and Sandnes, B. (2015). Gas migration regimes and outgassing in particle-rich suspensions. *Frontiers in Physics*, **3**(60).
- Orlando, A., D'Orazio, M., Armienti, P. and Borrini, D. (2008). Experimental determination of plagioclase and clinopyroxene crystal growth rates in an anhydrous trachybasalt from Mt Etna (Italy). *European Journal of Mineralogy*, **20**(4): 653-664.
- Orozco-Esquivel, T., Petrone, C. M., Ferrari, L., Tagami, T. and Manetti, P. (2007). Geochemical and isotopic variability in lavas from the eastern Trans-Mexican Volcanic Belt: slab detachment in a subduction zone with varying dip. *Lithos*, **93**: 149-174.

- Pabst, S., Wörner, G., Civetta, L. and Tesoro, R. (2008). Magma chamber evolution prior to the Campanian Ignimbrite and Neapolitan Yellow Tuff eruptions (Campi Flegrei, Italy). *Bulletin of Volcanology*, **70**(8): 961-976.
- Pallister, J. S., Hoblitt, R. P., Meeker, G. P., Knight, R. J. and Siems, D. F. (1996). Magma mixing at Mount Pinatubo; petrographic and chemical evidence from the 1991 deposits. In: C.G.N.R. Punongbayan (Editor), *Fire and mud*. Seattle: University of Washington Press., pp. 687-731.
- Palmer, B. A. and Neall, V. E. (1989). The Murimotu Formation—9500 year old deposits of a debris avalanche and associated lahars, Mount Ruapehu, North Island, New Zealand. *New Zealand Journal of Geology and Geophysics*, **32**(4): 477-486.
- Pamukcu, A. S., Gualda, G. A. R., Bégué, F. and Gravley, D. M. (2015). Melt inclusion shapes: Timekeepers of short-lived giant magma bodies. *Geology*, **43**(11): 947-950.
- Pankhurst, M. J., Morgan, D., Thordarson, T. and Loughlin, S. C. (2018). Magmatic crystal records in time, space, and process, causatively linked with volcanic unrest. *Earth and Planetary Science Letters*, **493**(231-241).
- Papale, P. and Polacci, M. (1999). Role of carbon dioxide in the dynamics of magma ascent in explosive eruptions. *Bulletin of Volcanology*, **60**: 583-594.
- Papale, P., Moretti, R. and Barbato, D. (2006). The compositional dependence of the saturation surface of H₂O + CO₂ fluids in silicate melts. *Chemical Geology*, **229**: 78-95.
- Pappalardo, L., Civetta, L., de Vita, S., Di Vito, M., Orsi, G., Carandente, A. and Fisher, R. V. (2002). Timing of magma extraction during the Campanian Ignimbrite eruption (Campi Flegrei Caldera). *Journal of Volcanology and Geothermal Research*, **114**(3): 479-497.
- Pappalardo, L. and Mastrolorenzo, G. (2012). Rapid differentiation in a sill-like magma reservoir: a case study from the campi flegrei caldera. *Scientific Reports*, **2**(1): 712.
- Pappalardo, L., Buono, G., Fanara, S. and Petrosino, P. (2018). Combining textural and geochemical investigations to explore the dynamics of magma ascent during Plinian eruptions: a Somma–Vesuvius volcano (Italy) case study. *Contributions to Mineralogy and Petrology*, **173**(61).
- Parada, M. A., Féraud, G., Fuentes, F., Aguirre, L., Morata, D. and Larrondo, P. (2005). Ages and cooling history of the Early Cretaceous Caleu pluton: testimony of a switch from a rifted to a compressional continental margin in central Chile. *Journal of the Geological Society*, **162**(2): 273-287.
- Pardo, N., Cronin, S. J., Palmer, A. S. and Németh, K. (2012). Reconstructing the largest explosive eruptions of Mt. Ruapehu, New Zealand: lithostratigraphic tools to understand subplinian–plinian eruptions at andesitic volcanoes. *Bulletin of Volcanology*, **74**(3): 617-640.
- Pardo, N., Cronin, S. J., Németh, K., Brenna, M., Schipper, C. I., Breard, E., White, J. D. L., Procter, J., Stewart, B., Agustín-Flores, J., Moebis, A., Zernack, A., Kereszturi, G., Lube, G., Auer, A., Neall, V. and Wallace, C. (2014a). Perils in distinguishing phreatic from phreatomagmatic ash; insights into the eruption mechanisms of the 6 August 2012 Mt. Tongariro eruption, New Zealand. *Journal of Volcanology and Geothermal Research*, **286**: 397-414.

- Pardo, N., Cronin, S. J., Wright, H. M. N., Schipper, C., Smith, I. and Stewart, B. (2014b). Pyroclast textural variation as an indicator of eruption column steadiness in andseitic Plinian eruptions at Mt. Ruapehu. *Bulletin of Volcanology*, **76**.
- Pardo, N., Wilson, H., Procter, J. N., Lattughi, E. and Black, T. (2015). Bridging Māori indigenous knowledge and western geosciences to reduce social vulnerability in active volcanic regions. *Journal of Applied Volcanology*, **4**(5).
- Paterson, S. R. (2009). Magmatic tubes, pipes, troughs, diapirs, and plumes: Late-stage convective instabilities resulting in compositional diversity and permeable networks in crystal-rich magmas of the Tuolumne batholith, Sierra Nevada, California. *Geosphere*, **5**(6): 496-527.
- Paterson, S. R., Okaya, D., Memeti, V., Economos, R. and Miller, R. B. (2011). Magma addition and flux calculations of incrementally constructed magma chambers in continental margin arcs: Combined field, geochronologic, and thermal modeling studies. *Geosphere*, **7**(6): 1439-1468.
- Paulatto, M., Moorkamp, M., Hautmann, S., Hooft, E., Morgan, J. V. and Sparks, R. S. J. (2019). Vertically Extensive Magma Reservoir Revealed From Joint Inversion and Quantitative Interpretation of Seismic and Gravity Data. *Journal of Geophysical Research: Solid Earth*, N/A.
- Pedersen, G. B. M. (2016). Semi-automatic classification of glaciovolcanic landforms: An object-based mapping approach base on geomorphology. *Journal of Volcanology and Geothermal Research*, **311**: 29-40.
- Perinelli, C., Mollo, S., Gaeta, M., De Cristofaro, S. P., Palladino, D. M., Armienti, P., Scarlato, P. and Putirka, K. D. (2016). An improved clinopyroxene-based hygrometer for Etnean magmas and implications for eruption triggering mechanisms. *American Mineralogist*, **101**(12): 2774-2777.
- Peterson, T. D. (1996). A refined technique for measuring crystal size distributions in thin section. *Contrib Mineral Petrol*, **124**: 395-405.
- Petrelli, M., Bizzarri, R., Morgavi, D., Baldanza, A. and Perugini, D. (2017). Combining machine learning techniques, microanalyses and large geochemical datasets for tephrochronological studies in complex volcanic areas: New age constraints for the Pleistocene magmatism of central Italy. *Quaternary Geochronology*, **40**: 33-44.
- Petrelli, M. and Zellmer, G. F. (in press). Rates and timescales of magma transfer, storage, emplacement, and eruption. In: F.P. Vetere and A. Fiege (Editors), *Dynamic Magma Evolution*. AGU Monograph Series.
- Petrone, C. M., Bugatti, G., Braschi, E. and Tommasini, S. (2015). Pre-eruptive magmatic processes re-timed using a non-isothermal approach to magma chamber dynamics. *Nature Communications*, **7**(12946).
- Petrone, C. M., Bugatti, Braschi and Tommasini. (2016). Pre-eruptive magmatic processes re-timed using a non-isothermal approach to magma chamber dynamics. *Nature Communications*, **7**: 12946.
- Pham, D. L., Xu, C. and Prince, J. L. (2000). Current Methods in Medical Image Segmentation. *Annual Review of Biomedical Engineering*, **2**: 315-337.
- Pinkerton, H. and Sparks, R. S. J. (1978). Field measurements of the rheology of flowing lava. *Nature*, **276**: 383-385.
- Piochi, M., Mastrolorenzo, G. and Pappalardo, L. (2005). Magma ascent and eruptive processes from textural and compositional features of Monte Nuovo pyroclastic products, Campi Flegrei, Italy. *Bulletin of Volcanology*, **67**(7): 663-678.

- Pistolesi, M., Cioni, R. and Aguilera, E. (2014). Lahar hazard assessment in the southern drainage system of Cotopaxi volcano, Ecuador: Results from multiscale lahar simulations. *Geomorphology*, **207**: 51-63.
- Pitcher, W. S. (1979). The nature, ascent and emplacement of granitic magmas. *Journal of the Geological Society*, **136**(6): 627-662.
- Plank, T., Kelley, K. A., Zimmer, M. M., Hauri, E. H. and Wallace, P. J. (2013). Why do mafic arc magmas contain ~ 4 wt% water on average? *Earth and Planetary Science Letters*, **364**: 168-179.
- Polacci, M., Papale, P. and Rosi, M. (2001). Textural heterogeneities in the pumices from the climactic eruption of Mount Pinatubo, 15 June 1991, and implications for magma ascent properties. *Bulletin of Volcanology*, **63**: 83-97.
- Pompilio, M., Bertagnini, A., Del Carlo, P. and Di Roberto, A. (2017). Magma dynamics within a basaltic conduit revealed by textural and compositional features of erupted ash: the December 2015 Mt. Etna paroxysms. *Scientific Report*, **7**(4805).
- Preece, K., Gertisser, R., Barclay, J., Charbonnier, S. J., Komorowski, J.-C. and Herd, R. A. (2016). Transitions between explosive and effusive phases during the cataclysmic 2010 eruption of Merapi volcano, Java, Indonesia. *Bulletin of Volcanology*, **78**(8).
- Preston, R. J. (2001). Composite minor intrusions as windows into subvolcanic magma reservoir processes: mineralogical and geochemical evidence for complex magmatic plumbing systems in the British Tertiary Igneous Province. *Journal of the Geological Society*, **158**: 47-58.
- Price, G. D., Gamble, J. A., Smith, I. E. M., Stewart, R. B., Eggins, S. and Wright, I. C. (2005). An integrated model for the temporal evolution of andesites and rhyolites and crustal development in New Zealand's North Island. *Journal of Volcanology and Geothermal Research*, **140**: 1-24.
- Price, R. C., R., G., Gamble, J. A., Turner, S., M., S. I. E., Cook, C., Hobden, B. and Dosseto, A. (2007). U-Th-Ra fractionation during crustal-level andesite formation at Ruapehu volcano, New Zealand. *Chemical Geology*, **244**: 437-451.
- Price, R. C., Turner, S., Cook, C., Hobden, B., Smith, I. E. M., Gamble, J. A., Handley, H., Maas, R. and Möbis, A. (2010). Crustal and mantle influences and U-Th-Ra disequilibrium in andesitic lavas of Ngauruhoe volcano, New Zealand. *Chemical Geology*, **277**(3): 355-373.
- Price, R. C., Gamble, J. A., Smith, I. E. M., Maas, R., Waight, T., Stewart, R. B. and Woodhead, J. (2012). The anatomy of an andesite volcano: a time-stratigraphic study of andesite petrogenesis and crustal evolution at Ruapehu volcano, New Zealand. *Journal of Petrology*, **53**(10): 2139-2189.
- Price, R. C., Smith, I. E. M., Stewart, R. B., Gamble, J. A., Gruender, K. and Maas, R. (2016). High-K andesite petrogenesis and crustal evolution: Evidence from mafic and ultramafic xenoliths, Egmont Volcano (Mt. Taranaki) and comparisons with Ruapehu Volcano, North Island, New Zealand. *Geochimica et Cosmochimica Acta*, **185**: 328-357.
- Procter, J. N., Cronin, S. J., Zernack, A. V., Lube, G., Stewart, R. B., Nemeth, K. and Keys, H. (2014). Debris flow evolution and the activation of an explosive hydrothermal system; TeMaari, Tongariro, New Zealand. *Journal of Volcanology and Geothermal Research*, **286**: 303-316.
- Putirka, K., Johnson, M., Kinzler, R., Longhi, J. and Walker, D. (1996). Thermobarometry of mafic igneous rocks based on clinopyroxene-liquid

- equilibria, 0–30 kbar. *Contributions to Mineralogy and Petrology*, **123**(1): 92-108.
- Putirka, K. and Condit, C. D. (2003). Cross section of a magma conduit system at the margin of the Colorado Plateau. *Geology*, **31**: 701–704.
- Putirka, K. (2019). Personal communication.
- Putirka, K. D., Mikaelian, H., Ryerson, F. and Shaw, H. (2003). New clinopyroxene-liquid thermobarometers for mafic, evolved, and volatile-bearing lava compositions, with applications to lavas from Tibet and the Snake River Plain, Idaho. *American Mineralogist*, **88**(10): 1542-1554.
- Putirka, K. D. (2008). Thermometers and barometers for volcanic systems. In: K.D. Putirka and F. Tepley (Editors), *Reviews in Mineralogy and Geochemistry*, pp. 61-120.
- Pyle, D. M., Ivanovich, M. and Sparks, R., S, J. (1988). Magma–cumulate mixing identified by U–Th disequilibrium dating. *Nature*, **331**: 157-159.
- Rae, A., Edmonds, M., MacLennan, J., Morgan, D., Houghton, B., Hartley, M. and Sides, I. (2016). Time scales of magma transport and mixing at Kīlauea Volcano, Hawai'i. *Geology*, **44**(6): 463-466.
- Rampino, M. R. and Self, S. (1992). Volcanic winter and accelerated glaciation following the Toba super-eruption. *Nature*, **359**(6390): 50-52.
- Randolph, A. D. and Larson, M. A. (1971). *Theory of particulate processes: analysis and techniques of continuous crystallization*. New York, Academic Press.
- Rannou, E. and Caroff, M. (2010). Crystal Size Distribution in Magmatic Rocks: Proposition of a Synthetic Theoretical Model. *Journal of Petrology*, **51**(5): 1087-1098.
- Renjith, M. L. (2014). Micro-textures in plagioclase from 1994–1995 eruption, Barren Island Volcano: Evidence of dynamic magma plumbing system in the Andaman subduction zone. *Geoscience Frontiers*, **5**(1): 113-126.
- Resmini, R. G. (2007). Modeling of crystal size distributions (CSDs) in sills. *Journal of Volcanology and Geothermal Research*, **161**(1-2): 118-130.
- Reubi, O. and Blundy, J. (2009). A dearth of intermediate melts at subduction zone volcanoes and the petrogenesis of arc andesites. *Nature*, **461**: 1269-1273.
- Reyners, M. (1983). Lateral segmentation of the subducted plate at the Hikurangi margin, New Zealand: seismological evidence. *Tectonophysics*, **96**: 203-223.
- Reyners, M. (2013). The central role of the Hikurangi Plateau in the Cenozoic tectonics of New Zealand and the Southwest Pacific. *Earth and Planetary Science Letters*, **361**: 460-468.
- Rhodes, E., Kennedy, B. M., Lavallée, Y., Hornby, A., Edwards, M. and Chigna, G. (2018). Textural insights into the evolving lava dome cycles at Santiaguito lava dome, Guatemala. *Frontiers in Earth Science*, **6**.
- Rhodes, J. M., Dungan, M. A., Blanchard, D. P. and Long, P. E. (1979). Magma mixing at mid-ocean ridges: Evidence from basalts drilled near 22° N on the Mid-Atlantic Ridge. *Tectonophysics*, **55**(1): 35-61.
- Ridolfi, F., Renzulli, A. and Puerini, M. (2010). Stability and chemical equilibrium of amphibole in calc-alkaline magmas: an overview, new thermobarometric formulations and application to subduction-related volcanoes. *Contributions to Mineralogy and Petrology*, **160**(1): 45-66.

- Riggelsen, C. and Ohrnberger, M. (2014). A Machine Learning Approach for Improving the Detection Capabilities at 3C Seismic Stations. *Pure and Applied Geophysics*, **171**: 395-411.
- Riker, J. M., Cashman, K. V., Rust, A., C. and Blundy, J. (2015). Experimental Constraints on Plagioclase Crystallization during H₂O- and H₂O–CO₂- Saturated Magma Decompression. *Journal of Petrology*, **56**(10): 1967-1998.
- Roberge, J., Guilbaud, M. N., Mercer, C. and Reyes-Luna, P. (2014). Insight on monogenetic eruption processes at Pelagatos volcano, Sierra Chichinautzin, Mexico: a combined melt inclusion and physical volcanology study. In: G.F. Zellmer, M. Edmonds and S.M. Straub (Editors), The role of volatiles in the genesis, evolution and eruption of arc magmas. Geological Society, London, Special Publications.
- Robertson, R. E. A., Aspinall, W. P., Herd, R. A., Norton, G. E., Sparks, R. S. J. and Young, S. R. (2000). The 1995-1998 eruption of the Soufriere Hills volcano, Montserrat, WI. *Philosophical Transactions of the Royal Society of London A*, **358**: 1619-1637.
- Roche, O., Buesch, D. C. and Valentine, G. A. (2016). Slow-moving and far-travelled dense pyroclastic flows during the Peach Spring super-eruption. *Nature Communications*, **7**(1): 10890.
- Roeder, P. L. and Emslie, R. F. (1970). Olivine-liquid equilibrium. *Contributions to Mineralogy and Petrology*, **29**: 275-289.
- Rose, W. I. and Chesner, C. A. (1987). Dispersal of ash in the great Toba eruption, 75 ka. *Geology*, **15**(10): 913-917.
- Rosenberg, C. L. and Handy, M. R. (2005). Experimental deformation of partially melted granite revisited: implications for the continental crust. *Journal of Metamorphic Geology*, **23**: 19-28.
- Rosi, M., Landi, P., Polacci, M., Di Muro, A. and Zandomenighi, D. (2004). Role of conduit shear on ascent of the crystal-rich magma feeding the 800-year-B.P. Plinian eruption of Quilotoa Volcano (Ecuador). *Bulletin of Volcanology*, **66**: 307-321.
- Rössler, M. (2006). World heritage cultural landscapes: A UNESCO flagship programme 1992–2006. *Landscape Research*, **31**(4): 333-353.
- Rowland, S. K., Garbeil, H. and Harris, A. J. L. (2005). Lengths and hazards from channel-fed lava flows on Mauna Loa, Hawai'i, determined from thermal and downslope modeling with FLOWGO. *Bulletin of Volcanology*, **67**(7): 634-647.
- Rowlands, D. P., White, R. S. and Haines, A. J. (2005). Seismic tomography of the Tongariro Volcanic Centre, New Zealand. *Geophysical Journal International*, **163**: 1180-1194.
- Royet, J., P. (1991). Sterology: a method for analyzing images. *Progress in Neurobiology*, **37**: 433-474.
- Rutherford, M. J. and Hill, P. M. (1993). Magma ascent rates from amphibole breakdown: An experimental study applied to the 1980–1986 Mount St. Helens eruptions. *Journal of Geophysical Research*, **98**(B11): 19667-19685.
- Rutherford, M. J. and Devine, J. D. (2003). Magmatic Conditions and Magma Ascent as Indicated by Hornblende Phase Equilibria and Reactions in the 1995–2002 Soufrière Hills Magma. *Journal of Petrology*, **44**(8): 1433-1453.
- Sable, J. E., Houghton, B. F., Wilson, C. J. N. and Carey, R. J. (2009). Eruption mechanisms during the climax of the Tarawera 1886 basaltic Plinian eruption

- inferred from microtextural characteristics of the deposits, *Studies in volcanology : the legacy of George Walker*, pp. 129-154.
- Sack, R. O. and Ghiorso, M. S. (1991). Chromian spinels as petrogenetic indicators: Thermodynamics and petrological applications. *American Mineralogist*, **76**(5-6): 827-847.
- Sahagian, D., L. and Proussevitch, A., A. (1998). 3D particle size distributions from 2D observations: stereology for natural applications. *Journal of Volcanology and Geothermal Research*, **84**: 173-196.
- Sakuma, S., Kajiwara, T., Nakada, S., Uto, K. and Shimizu, H. (2008). Drilling and logging results of USDP-4 — Penetration into the volcanic conduit of Unzen Volcano, Japan. *Journal of Volcanology and Geothermal Research*, **175**(1): 1-12.
- Salisbury, M. J., Bohron, W. A., Clyne, M. A., Ramos, F. C. and Hoskin, P. (2008). Multiple Plagioclase Crystal Populations Identified by Crystal Size Distribution and in situ Chemical Data: Implications for Timescales of Magma Chamber Processes Associated with the 1915 Eruption of Lassen Peak, CA. *Journal of Petrology*, **49**(10): 1755-1780.
- Samaniego, P., Valderrama, P., Mariño, J., van Wyk de Vries, B., Roche, O., Manrique, N., Chédeville, C., Liorzou, C., Fidel, L. and Malnati, J. (2015). The historical (218 ± 14 aBP) explosive eruption of Tutupaca volcano (Southern Peru). *Bulletin of Volcanology*, **77**(6): 51.
- Sandri, L., Thouret, J.-C., Constantinescu, R., Biass, S. and Tonini, R. (2014). Long-term multi-hazard assessment for El Misti volcano (Peru). *Bulletin of Volcanology*, **76**(771).
- Sano, K., Wada, K. and Sato, E. (2015). Rates of water exsolution and magma ascent inferred from microstructures and chemical analyses of the Tokachi–Ishizawa obsidian lava, Shirataki, northern Hokkaido, Japan. *Journal of Volcanology and Geothermal Research*, **292**: 29-40.
- Sano, K. and Toramaru, A. (2017). Cooling and crystallization of rhyolite–obsidian lava: Insights from micron-scale projections on plagioclase microlites. *Journal of Volcanology and Geothermal Research*, **341**: 158-171.
- Sas, M., Shane, P., Kuritani, T., Zellmer, G. F., Kent, A. J. and Nakagawa, M. (2019). Complex and dynamic magmatic processes captured in plagioclase and their implications for petrogenesis of Taupo Volcanic Zone rhyolites, AGU Fall Meeting 2019, San Francisco, CA.
- Sas, M. (submitted). Isotopic and geochemical records of magmatic processes captured in crystals from Okataina volcano, University of Auckland.
- Sato, H. (1995). Textural difference between pahoehoe and aa lavas of Izu-Oshima volcano, Japan — an experimental study on population density of plagioclase. *Journal of Volcanology and Geothermal Research*, **66**(1): 101-113.
- Saubin, E., Tuffen, H., Gurioli, L., Owen, J., Castro, J., Berlo, K., McGowan, E., Schipper, C. and Wehbe, K. (2016). Conduit Dynamics in Transitional Rhyolitic Activity Recorded by Tuffisite Vein Textures from the 2008–2009 Chaitén Eruption. *Frontiers in Earth Science*, **4**.
- Schauroth, J., Wadsworth, F. B., Kennedy, B., von Auloc, F. W., Lavallée, Y., Damby, D. E., Vasseur, J., Scheu, B. and Dingwell, D. B. (2016). Conduit margin heating and deformation during the AD 1886 basaltic Plinian eruption at Tarawera volcano, New Zealand. *Bulletin of Volcanology*, **78**(12).

- Scheibner, B., Heumann, A., Wörner, G. and Civetta, L. (2008). Crustal residence times of explosive phonolite magmas: U–Th ages of magmatic Ca-Garnets of Mt. Somma-Vesuvius (Italy). *Earth and Planetary Science Letters*, **276**: 293-301.
- Schiavi, F., Walte, N. and Keppler, H. (2009). First in situ observation of crystallization processes in a basaltic-andesitic melt with the moissanite cell. *Geology*, **37**: 963-966.
- Schleider, J. M., Bergantz, G. W., Breidenthal, R. E. and Burgisser, A. (2016). Time scales of crystal mixing in magma mushes. *Geophysical Research Letters*, **43**(4): 1543-1550.
- Schmitt, A. K., Lindsay, J. M., de Silva, S. and Trumbull, R. B. (2003). U–Pb zircon chronostratigraphy of early-Pliocene ignimbrites from La Pacana, north Chile: implications for the formation of stratified magma chambers. *Journal of Volcanology and Geothermal Research*, **120**(1): 43-53.
- Seebeck, H. and Nicol, A. (2009). Dike intrusion and displacement accumulation at the intersection of the Okataina Volcanic Centre and Paeroa Fault zone, Taupo Rift, New Zealand. *Tectonophysics*, **475**(3-4).
- Self, S. (1975). Explosive activity of Ngauruhoe, 27–30 March 1974. *New Zealand Journal of Geology & Geophysics*, **18**(1): 189-195.
- Self, S., Wilson, L. and Nairn, I. A. (1978). Vulcanian eruption mechanisms. *Nature*, **277**: 440-443.
- Sen, G. (2014). *Petrology: Principle and Practice*, 368 pp.
- Sepiol, B., Meyer, A., Vogl, G., Franz, H. and Ruffer, R. (1998). Diffusion in a crystal lattice with nuclear resonant scattering of synchrotron radiation. *Physical Review B*, **57**(17): 10433-10439.
- Shane, P., Doyle, L. R. and Nairn, I. A. (2008a). Heterogeneous andesite–dacite ejecta in 26–16.6 ka pyroclastic deposits of Tongariro Volcano, New Zealand: the product of multiple magma-mixing events. *Bulletin of Volcanology*, **70**(4): 517-536.
- Shane, P., Nairn, I. A., Smith, V. C., Darragh, M., Beggs, K. and Cole, J. W. (2008b). Silicic recharge of multiple rhyolite magmas by basaltic intrusion during the 22.6 ka Okareka Eruption Episode, New Zealand. *Lithos*, **103**(3): 527-549.
- Shane, P. (2017). Chapter 2 The Southern End of the Pacific Ring of Fire: Quaternary Volcanism in New Zealand. In: J. Shulmeister (Editor), *Landscape and Quaternary Environmental Change in New Zealand*. Atlantis Press.
- Shane, P., Maas, R. and Lindsay, J. M. (2017). History of Red Crater volcano, Tongariro Volcanic Centre (New Zealand): Abrupt shift in magmatism following recharge and contrasting evolution between neighboring volcanoes. *Journal of Volcanology and Geothermal Research*, **340**: 1-15.
- Shane, P., Cocker, K., Coote, A., Stirling, C. H. and Reid, M. R. (2019). The prevalence of plagioclase antecrysts and xenocrysts in andesite magma, exemplified by lavas of the Tongariro volcanic complex, New Zealand. *Contributions to Mineralogy and Petrology*, **174**(89).
- Shea, T., Gurioli, L., Larsen, J. F., Houghton, B. F., Hammer, J. E. and Cashman, K. V. (2010a). Linking experimental and natural vesicle textures in Vesuvius 79AD white pumice. *Journal of Volcanology and Geothermal Research*, **192**: 69-84.
- Shea, T., Houghton, B. F., Gurioli, L., Cashman, K. V., Hammer, J. E. and Hobden, B. J. (2010b). Textural studies of vesicles in volcanic rocks: An integrated methodology. *Journal of Volcanology and Geothermal Research*, **190**: 271-289.

- Shea, T. and Hammer, J. E. (2013). Kinetics of cooling- and decompression-induced crystallization in hydrous mafic-intermediate magmas. *Journal of Volcanology and Geothermal Research*, **260**: 127-145.
- Shea, T., Lynn, K. J. and Garcia, M. O. (2015). Cracking the olivine zoning code: Distinguishing between crystal growth and diffusion. *Geology*, **43**(10): 935-938.
- Shea, T. (2017). Bubble nucleation in magmas: A dominantly heterogeneous process? *Journal of Volcanology and Geothermal Research*, **343**: 155-170.
- Sherburn, S., Bryan, C. J., Hurst, A. W., Latter, J. H. and Scott, B. J. (1999). Seismicity of Ruapehu volcano, New Zealand, 1971–1996: a review. *Journal of Volcanology and Geothermal Research*, **88**: 255-278.
- Shibata, T., Itoh, J. and Takemura, K. (2005). Sr, Nd and Pb Isotopic compositions of Quaternary volcanics from Hime-Shima volcanic group, Japan Geoscience Union Meeting, Chiba City, Abstract J030-003.
- Shinohara, H. (2008). Excess degassing from volcanoes and its role on eruptive and intrusive activity. *Reviews of Geophysics*, **46**: RG4005.
- Shinohara, H. (2013). Composition of volcanic gases emitted during repeating Vulcanian eruption stage of Shinmoedake, Kirishima volcano, Japan. *Earth, Planets and Space*, **65**(6): 17.
- Shore, M. and Fowler, A. D. (1996). Oscillatory zoning in minerals; a common phenomenon. *The Canadian Mineralogist*, **34**(6): 1111-1126.
- Sielfeld, G., Cembrano, J. and Lara, L. (2017). Transtension driving volcano-edifice anatomy: Insights from Andean transverse-to-the-orogen tectonic domains. *Quaternary International*, **438**: 33-49.
- Sigurdsson, H., Houghton, B., McNutt, S., Rymer, H. and Stix, J. (2015). The Encyclopedia of Volcanoes. John Fedor.
- Simakin, A. G. and Bindeman, I. N. (2008). Evolution of crystal sizes in the series of dissolution and precipitation events in open magma systems. *Journal of Volcanology and Geothermal Research*, **177**(4): 997-1010.
- Sing, T., Sander, O., Beerenwinkel, N. and Lengauer, T. (2005). ROCr: visualizing classifier performance in R. *Bioinformatics Applications Note*, **21**(20): 3940-3941.
- Singer, B. S., Pearce, T. H., Kolisnik, A. M. and Myers, J. D. (1993). Plagioclase zoning in mid-Pleistocene lavas from the Seguan volcanic center, central Aleutian arc, Alaska. *American Mineralogist*, **78**: 143-157.
- Smith, D. and Barron, B. R. (1991). Pyroxene-garnet equilibration during cooling in the mantle. *American Mineralogist*, **76**(11-12): 1950-1963.
- Smith, E. G. C., Stern, T. A. and Reyners, M. (1989). Subduction and back-arc activity at the Hikurangi convergent margin, New Zealand. *Pure Appl. Geophys.*, **129**: 203-231.
- Smith, P. M. and Asimow, P. D. (2005). Adibat_1ph: A new public front-end to the MELTS, pMELTS, and pHMELTS models. *Geochemistry Geophysics Geosystems*, **6**: Q02004.
- Smith, R. K. and Lofgren, G. E. (1982). An analytical and experimental study of zoning in plagioclase. *Lithos*, **16**: 153-168.
- Smithsonian Institution's Global Volcanism Program. (2019). Ruapehu.
- Snyder, D. (1997). The mixing and mingling of magmas. *Endeavour*, **27**: 19-22.
- Sosa-Ceballos, G., Gardner, J. E. and Lassiter, J. C. (2014). Intermittent mixing processes occurring before Plinian eruptions of Popocatepetl volcano, Mexico: insights from

- textural-compositional variations in plagioclase and Sr-Nd-Pb isotopes. *Contributions to Mineralogy and Petrology*, **167**: 966.
- Sparks, R. S. J., Sigurdsson, H. and Wilson, L. (1977). Magma mixing: a mechanism for triggering acid explosive eruptions. *Nature*, **267**: 315-318.
- Sparks, R. S. J. (1978). The dynamics of bubble formation and growth in magmas: A review and analysis. *Journal of Volcanology and Geothermal Research*, **3**: 1-37.
- Sparks, R. S. J., Young, S. R., Barclay, J., Calder, E. S., Cole, P., Darroux, B., Davies, M., Druitt, T. H., Harford, C., Herd, R., James, M., Lejeune, A. M., Loughlin, S., Norton, G., Skerrett, G., Stasiuk, M. V., Stevens, N. S., Toothill, J., Wadge, G. and Watts, R. (1998). Magma production and growth of the lava dome of the Soufriere Hills volcano, Montserrat, West Indies: November 1995 to December 1997. *Geophysical Research Letters*, **25**(18): 3421-3424.
- Sparks, R. S. J. (2003). Dynamics of magma degassing. *Geological Society, London, Special Publications*, **213**(1): 5-22.
- Stern, I. A. (1987). Asymmetric back-arc spreading, heat flux and structure associated with the Central Volcanic Region of New Zealand. *Earth and Planetary Science Letters*, **85**: 265-276.
- Stern, R. J. (2002). Subduction zones. *Reviews of Geophysics*, **40**: (3)1-(3)37.
- Stern, T. A. (1985). A back-arc basin formed within continental lithosphere: the Central Volcanic Region of New Zealand. *Tectonophysics*, **112**: 385-409.
- Stern, T. A., Stratford, W. R. and Salmon, M. L. (2006). Subduction evolution and mantle dynamics at a continental margin: central North Island, New Zealand. *Reviews of Geophysics*, **44**: 2005RG000171.
- Stevenson, D. S. and Blake, S. (1998). Modelling the dynamics and thermodynamics of volcanic degassing. *Bulletin of Volcanology*, **60**: 307-317
- Stewart, R. B. (2010). Andesites as magmatic liquids or liquid-crystal mixtures; insights from Egmont and Ruapehu Volcanoes, New Zealand. *Central European Journal Of Geosciences*, **2**: 329-338.
- Stix, J. (2018). Understanding Fast and Slow Unrest at Volcanoes and Implications for Eruption Forecasting. *Frontiers in Earth Science*, **6**(56).
- Stock, M., Humphreys, M. C. S., Smith, V. C., Isaia, R. and Pyle, D. (2016a). Late-stage volatile saturation as a potential trigger for explosive volcanic eruptions. *Nature Geoscience*, **9**: 249-254.
- Stock, M. J., Humphreys, M. C. S., Smith, V. C., Isaia, R. and Pyle, D. M. (2016b). Late-stage volatile saturation as a potential trigger for explosive volcanic eruptions. *Nature Geoscience*, **9**(3): 249-254.
- Storm, S., Shane, P., Schmitt, A. K. and Lindsay, J. M. (2011). Contrasting punctuated zircon growth in two syn-erupted rhyolite magmas from Tarawera volcano: Insights to crystal diversity in magmatic systems. *Earth and Planetary Science Letters*, **301**(3-4): 511-520.
- Streck, M. J. (2008). Mineral Textures and Zoning as Evidence for Open System Processes. In: K. Putirka and F. Tepley (Editors), *Reviews in Mineralogy and Geochemistry*, pp. 595-622.
- Suzuki, A. M., Yasuda, A. and Ozawa, K. (2008). Cr and Al diffusion in chromite spinel: experimental determination and its implication for diffusion creep. *Physics and Chemistry of Minerals*, **35**: 433-445.
- Suzuki, Y. and Nakada, S. (2007). Remobilization of Highly Crystalline Felsic Magma by Injection of Mafic Magma: Constraints from the Middle Sixth Century

- Eruption at Haruna Volcano, Honshu, Japan. *Journal of Petrology*, **48**(8): 1543-1567.
- Suzuki, Y. and Fujii, T. (2010). Effect of syneruptive decompression path on shifting intensity in basaltic sub-Plinian eruption: Implication of microlites in Yufune-2 scoria from Fuji volcano, Japan. *Journal of Volcanology and Geothermal Research*, **198**(1-2): 158-176.
- Swanson, S., E., Naney, M., T., Westrich, H., R. and Eichelberger, J., C. (1989). Crystallization history of Obsidian Dome, Inyo Domes, California. *Bulletin of Volcanology*, **51**: 161-176.
- Szramek, L., Gardner, J. E. and Larsen, J. (2006). Degassing and microlite crystallization of basaltic andesite magma erupting at Arenal Volcano, Costa Rica. *Journal of Volcanology and Geothermal Research*, **157**: 182-201.
- Szramek, L., Gardner, J. E. and Hort, M. (2010). Cooling-induced crystallization of microlite crystals in two basaltic pumice clasts. *American Mineralogist*, **95**(4): 503-509.
- Taddeucci, J., Pompilio, M. and Scarlato, P. (2004). Conduit processes during the July–August 2001 explosive activity of Mt. Etna (Italy): inferences from glass chemistry and crystal size distribution of ash particles. *Journal of Volcanology and Geothermal Research*, **137**(1-3): 33-54.
- Taddeucci, J., Scarlato, P., Capponi, A., Del Bello, E., Cimarelli, C., Palladino, D. M. and Kueppers, U. (2012). High-speed imaging of Strombolian explosions: The ejection velocity of pyroclasts. *Geophysical Research Letters*, **39**(2).
- Taisne, B. and Jaupart, C. (2011). Magma expansion and fragmentation in a propagating dyke. *Earth and Planetary Science Letters*, **301**: 146-152.
- Taisne, B. and Tait, S. (2011). Effect of solidification on a propagating dike. *Journal of Geophysical Research: Solid Earth*, **116**(1).
- Tait, S. R., Wörner, G., Van Den Bogaard, P. and Schmincke, H.-U. (1989). Cumulate nodules as evidence for convective fractionation in a phonolite magma chamber. *Journal of Volcanology and Geothermal Research*, **37**(1): 21-37.
- Takahashi, R. and Nakagawa, M. (2012). Formation of a Compositionally Reverse Zoned Magma Chamber: Petrology of the ad 1640 and 1694 Eruptions of Hokkaido-Komagatake Volcano, Japan. *Journal of Petrology*, **54**(4): 815-838.
- Tamura, Y. and Nakamura, E. (1996). The arc lavas of the Shirahama Group, Japan: Sr and Nd isotopic data indicate mantle-derived bimodal magmatism. *Journal of Petrology*, **37**: 1307-1319.
- Taran, Y. and Zelenski, M. (2014). Systematics of the water isotopic composition and chlorine content in arc-volcanic gases. In: G.F. Zellmer, M. Edmonds and S.M. Straub (Editors), *The role of volatiles in the genesis, evolution and eruption of arc magmas*. Geological Society, London, Special Publications.
- Thomas, J. B., Watson, E. B., Spear, F. S. and Wark, D. A. (2015). Titanite recrystallized: experimental confirmation of the original Ti-in-quartz calibrations. *Contributions to Mineralogy and Petrology*, **169**(3): 27.
- Tibaldi, A. (2015). Structure of volcano plumbing systems: A review of multi-parametric effects. *Journal of Volcanology and Geothermal Research*, **298**: 85-135.
- Todde, A., Cioni, R., Pistolesi, M., Geshi, N. and Bonadonna, C. (2017). The 1914 Taisho eruption of Sakurajima volcano: stratigraphy and dynamics of the largest explosive event in Japan during the twentieth century. *Bulletin of Volcanology*, **79**(10): 72.

- Topping, W. W. (1973). Tephrostratigraphy and chronology of late quaternary eruptives from the Tongariro Volcanic Centre, New Zealand. *New Zealand Journal of Geology and Geophysics*, **16**(3): 397-423.
- Topping, W. W. and Kohn, B. P. (1973). Rhyolitic tephra marker beds in the Tongariro area, North Island, New Zealand. *New Zealand Journal of Geology and Geophysics*, **16**(3): 375-395.
- Toramaru, A. (1991). Model of nucleation and growth of crystals in cooling magmas. *Contribution to Mineralogy and Petrology*, **108**(1-2): 106-117.
- Toramaru, A., Noguchi, S., Oyoshihara, S. and Tsune, A. (2008). MND(microlite number density) water exsolution rate meter. *Journal of Volcanology and Geothermal Research*, **175**(1-2): 156-167.
- Tost, M., Price, G. D., Cronin, S. J. and Smith, I. E. M. (2016). New insights into the evolution of the magmatic system of a composite andesite volcano revealed by clasts from distal mass-flow deposits: Ruapehu volcano, New Zealand. *Bulletin of Volcanology*, **78**(38).
- Turcotte, D. L., Ockendon, H., Ockendon, J. R. and Cowley, S. J. (1990). A mathematical model of vulcanian eruptions. *Geophysical Journal International*, **103**(1): 211-217.
- Turner, J. S. and Campbell, I. H. (1986). Convection and mixing in magma chambers. *Earth Science Reviews*, **23**: 255-352.
- Turner, S., Hawkesworth, C., van Calsteren, P., Heath, E., Macdonald, R. and Black, S. (1996). U-series isotopes and destructive plate margin magma genesis in the Lesser Antilles. *Earth and Planetary Science Letters*, **142**: 191-207.
- Turner, S., George, R., Jerram, D. A., Carpenter, N. and Hawkesworth, C. (2003). Case studies of plagioclase growth and residence times in island arc lavas from Tonga and the Lesser Antilles, and a model to reconcile discordant age information. *Earth and Planetary Science Letters*, **214**: 279-294.
- Turner, S., Sandiford, M., Reagan, M., Hawkesworth, C. and Hildreth, W. (2010). Origins of large-volume, compositionally zoned volcanic eruptions: New constraints from U-series isotopes and numerical thermal modeling for the 1912 Katmai-Novarupta eruption. *Journal of Geophysical Research*, **115**: B12201.
- Ubide, T. and Kamber, B. S. (2018). Volcanic crystals as time capsules of eruption history. *Nature Communications*, **9**(326).
- Ubide, T., Mollo, S., Zhao, J., Nazzari, M. and Scarlato, P. (2019). Sector-zoned clinopyroxene as a recorder of magma history, eruption triggers, and ascent rates. *Geochimica et Cosmochimica Acta*, **251**: 265-283.
- Ueda, H., Fujita, E., Ukawa, M., Yamamoto, E., Irwan, M. and Kimata, F. (2005). Magma intrusion and discharge process at the initial stage of the 2000 activity of Miyakejima, Central Japan, inferred from tilt and GPS data *Geophysical Journal International*, **161**(3): 891-906.
- Underwood, E. E. (1970). *Quantitative Stereology*. Addison-Wesley, 274 pp.
- Ushioda, M., Takahashi, E., Hamada, M. and Suzuki, T. (2014). Water content in arc basaltic magma in the Northeast Japan and Izu arcs: an estimate from Ca/Na partitioning between plagioclase and melt. *Earth, Planets and Space*, **66**(1): 127.
- van Otterloo, J. and Cas, R. A. F. (2016). Low-temperature emplacement of phreatomagmatic pyroclastic flow deposits at the monogenetic Mt Gambier Volcanic Complex, South Australia, and their relevance for understanding some deposits in diatremes. *Journal of the Geological Society*, **173**(4): 701-710.

- van Rijsbergen, C. J. (1979). Information Retrieval. Butterworths.
- Vandergoes, M. J., Hogg, A. G., Lowe, D. J., Newnham, R. M., Denton, G. H., Southon, J., Barrell, D. J. A., Wilson, C. J. N., McGlone, M. S., Allan, A. S. R., Almond, P. C., Petchey, F., Dabell, K., Dieffenbacher-Krall, A. C. and Blauuw, M. (2013). A revised age for the Kawakawa/Oruanui tephra, a key marker for the Last Glacial Maximum in New Zealand. *Quaternary Science Reviews*, **74**: 195-201.
- Vasuki, Y., Holden, E.-J., Kovesi, P. and Micklethwaite, S. (2017). An interactive image segmentation method for lithological boundary detection: A rapid mapping tool for geologists. *Computers & Geosciences*, **100**: 27-40.
- Venugopal, S., Moune, S. and Williams-Jones, G. (2016). Investigating the subsurface connection beneath Cerro Negro volcano and the El Hoyo Complex, Nicaragua. *Journal of Volcanology and Geothermal Research*, **325**: 211-224.
- Vergnolle, S. and Brandeis, S. (1996). Strombolian explosions. 1. A large bubble breaking at the surface of a lava column as a source of sound. *Journal of Geophysical Research: Solid Earth*, **101**: 20433-20447.
- Verma, S. P. and Luhr, J. F. (2010). Sr, Nd, and Pb isotopic evidence for the origin and evolution of the Cántaro-Colima volcanic chain, Western Mexican Volcanic Belt. *Journal of Volcanology and Geothermal Research*, **197**: 33-51.
- Viccaro, M., Giacomoni, P. P., Ferlito, C. and Crisofolini, R. (2010). Dynamics of magma supply at Mt. Etna volcano (Southern Italy) as revealed by textural and compositional features of plagioclase phenocrysts. *Lithos*, **116**: 77-91.
- Viccaro, M., Giuffrida, M., Nicotra, E. and Ozerov, A. Y. (2012). Magma storage, ascent and recharge history prior to the 1991 eruption at Avachinsky Volcano, Kamchatka, Russia: Inferences on the plumbing system geometry. *Lithos*, **140-141**: 11-24.
- Villamor, P., Van Dissen, R., Alloway, B. V., Palmer, A. S. and Litchfield, N. (2007). The Rangipo fault, Taupo rift, New Zealand: An example of temporal slip-rate and single-event displacement variability in a volcanic environment. *Geological Society of America Bulletin*, **119**: 529-547.
- Voight, B., Sparks, R. S. J., Miller, A. D., Stewart, R. C., Hoblitt, R. P., Clarke, A., Ewart, J., Aspinall, W. P., Baptie, B., Calder, E. S., Cole, P., Druitt, T. H., Hartford, C., Herd, R. A., Jackson, P., Lejeune, A. M., Lockhart, A. B., Loughlin, S. C., Luckett, R., Lynch, L., Norton, G. E., Robertson, R., Watson, I. M., Watts, R. and Young, S. R. (1998). Magma flow instability and cyclic activity at Soufriere Hills volcano, Montserrat, British West Indies. *Science*, **283**: 1138-1142.
- Voight, B. and Elsworth, D. (2000). Instability and collapse of hazardous gas-pressurized lava domes. *Geophysical Research Letters*, **27**(1): 1-4.
- VolcanoDiscovery. (2019). The paroxysm of Stromboli on 3 July 2019 - a summary.
- Voloschina, M., Pistolesi, M., Bertagnini, A., Métrich, N., Pompilio, M., Di Roberto, A., Di Salvo, S., Francalanci, L., Isaia, R., Cioni, R. and Romano, C. (2018). Magmatic reactivation of the Campi Flegrei volcanic system: insights from the Baia-Fondi di Baia eruption. *Bulletin of Volcanology*, **80**(10): 75.
- Vona, A. and Romano, C. (2013). The effects of undercooling and deformation rates on the crystallization kinetics of Stromboli and Etna basalts. *Contrib Mineral Petrol*, **166**: 491-509.
- Voorhees, P. W. (1992). Ostwald ripening of two-phase mixtures. *Annual Review of Materials Research*, **22**: 197-215.

- Wadge, G. and Haynes, M. (1998). Radar images growth of Soufriere Hills Volcano, Montserrat. *International Journal of Remote Sensing*, **19**: 797-800.
- Wadge, G., Saunders, S. and Itikarai, I. (2012). Pulsatory andesite lava flow at Bagana Volcano. *Geochemistry, Geophysics, Geosystems*, **13**(11).
- Wadsworth, F. B., Kennedy, B. M., Branney, M. J., von Auloc, F. W., Lavallée, Y. and Menendez, A. (2015). Exhumed conduit records magma ascent and drain-back during a Strombolian eruption at Tongariro volcano, New Zealand. *Bulletin of Volcanology*, **77**(71).
- Walker, D., Hays, J. F., Longhi, J. and Kirkpatrick, R. J. (1976). Differentiation of an Apollo 12 picrite magma, 7th Lunar Science Conference, Texas, USA, pp. 1365-1389.
- Walker, G. P. L. and Skelhorn, R. R. (1966). Some associations of acid and basic igneous rocks. *Earth Science Reviews*, **2**: 93-109.
- Walker, G. P. L. (1973). Explosive volcanic eruptions—a new classification scheme. *Geologische Rundschau*, **62**: 431-446.
- Walker, G. P. L. (1980). The Taupo pumice: Product of the most powerful known (ultraplinian) eruption? *Journal of Volcanology and Geothermal Research*, **8**(1).
- Wallace, L. M., Beavan, J., McCaffrey, R. and Darby, D. (2004). Subduction zone coupling and tectonic block rotations in the North Island, New Zealand. *Journal of Geophysical Research: Solid Earth*, **109**(B12406).
- Wallace, P. J. (2005). Volatiles in subduction zone magmas: concentrations and fluxes based on melt inclusion and volcanic gas data. *Journal of Volcanology and Geothermal Research*, **140**: 217-240.
- Ward, K. M., Zandt, G., Beck, S. L., Christensen, D. H. and McFarlin, H. (2014). Seismic imaging of the magmatic underpinnings beneath the Altiplano-Puna volcanic complex from the joint inversion of surface wave dispersion and receiver functions. *Earth and Planetary Science Letters*, **404**: 43-53.
- Wark, D. A. and Watson, E. B. (2006). TitaniumQ: a titanium-in-quartz geothermometer. *Contributions to Mineralogy and Petrology*, **152**(6): 743-754.
- Waters, L. E. and Lange, R. A. (2015). An updated calibration of the plagioclase-liquid hygrometer-thermometer applicable to basalts through rhyolites. *American Mineralogist*, **100**(10): 2172-2184.
- Webber, K. L., Simmons, W. B., Falster, A. U. and Foord, E. E. (1999). Cooling rates and crystallization dynamics of shallow level pegmatite-aplite dikes, San Diego County, California. *American Mineralogist*, **84**: 708-717.
- Weinberg, R. F. (1996). Ascent mechanism of felsic magmas: news and views. *Earth and Environmental Science Transactions of the Royal Society of Edinburgh*, **87**(1-2): 95-103.
- White, J. D. L. (1996). Pre-emergent construction of a lacustrine basaltic volcano, Pahvant Butte, Utah (USA). *Bulletin of Volcanology*, **58**(4): 249-262.
- White, J. D. L. and Ross, P. S. (2011). Maar-diatreme volcanoes: A review. *Journal of Volcanology and Geothermal Research*, **201**(1): 1-29.
- White, S. M., Crisp, J. A. and Spera, F. J. (2006). Long-term volumetric eruption rates and magma budgets. *Geochemistry Geophysics Geosystems*, **7**(3): Q03010.
- Wiesmaier, S., Deegan, F. M., Troll, V. R., Carracedo, J. C., Chadwick, J. P. and Chew, D. M. (2011). Magma mixing in the 1100 AD Montaña Reventada composite lava flow, Tenerife, Canary Islands: interaction between rift zone and central volcano plumbing systems. *Contribution to Mineralogy and Petrology*, **162**: 651-669.

- Wilcock, W. S. D., Solomon, S. C., Purdy, G. M. and Toomey, D. R. (1992). The Seismic Attenuation Structure of a Fast-Spreading Mid-Ocean Ridge. *Science*, **258**(5087): 1470-1474.
- Wilkinson, J. J. and Johnston, J. D. (1996). Pressure fluctuations, phase separation, and gold precipitation during seismic fracture propagation. *Geology*, **24**(5): 395-398.
- Williamson, B. J., Di Muro, A., Horwell, C. J., Spieler, O. and Llewellyn, E. W. (2010). Injection of vesicular magma into an andesitic dome at the effusive–explosive transition. *Earth and Planetary Science Letters*, **295**(1): 83-90.
- Wilson, C. J. N., Rogan, A. M., Smith, I. E. M., Northey, D. J., Nairn, I. A. and Houghton, B. F. (1984). Caldera Volcanoes of the Taupo Volcanic Zone, New Zealand. *Journal of Geophysical Research*, **89**(B10): 8463-8484.
- Wilson, C. J. N., Houghton, B. F., McWilliams, M. O., Lanphere, M. A., Weaver, S. D. and Briggs, R. M. (1995). Volcanic and structural evolution of Taupo Volcanic Zone, New Zealand: a review. *Journal of Volcanology and Geothermal Research*, **68**: 1-28.
- Wilson, C. J. N. (2001). The 26.5ka Oruanui eruption, New Zealand: an introduction and overview. *Journal of Volcanology and Geothermal Research*, **112**(1): 133-174.
- Wilson, C. J. N. and Rowland, J. V. (2016). The volcanic, magmatic and tectonic setting of the Taupo Volcanic Zone, New Zealand, reviewed from a geothermal perspective. *Geothermics*: 168-187.
- Wilson, C. K., Jones, C. H. and Gilbert, H. (2003). Single-chamber silicic magma system inferred from shear wave discontinuities of the crust and uppermost mantle, Coso geothermal area, California. *Journal of Geophysical Research: Solid Earth*, **108**(B5).
- Wilson, L. (1980). Relationships between pressure, volatile content, and ejecta velocity in three types of volcanic explosions. *Journal of Volcanology and Geothermal Research*, **8**: 297-313.
- Wilson, L., Sparks, R., S, J. and Walker, G. P. L. (1980). Explosive volcanic eruptions — IV. The control of magma properties and conduit geometry on eruption column behaviour *Geophysical Journal International*, **63**(1): 117-148.
- Witt-Eickschen, G. and Seck, H. A. (1991). Solubility of Ca and Al in orthopyroxene from spinel peridotite: an improved version of an empirical geothermometer *Contribution to Mineralogy and Petrology*, **106**: 431-439.
- Witten, I. H., Frank, E., Trigg, L., Hall, M. and Holmes, G. (1999). Weka: Practical machine learning tools and techniques with Java implementations, Computer Science Working Papers. University of Waikato, Department of Computer Science, Hamilton, New Zealand.
- Wohletz, K. (1983). Mechanisms of hydrovolcanic pyroclast formation: Grain-size, scanning electron microscopy, and experimental studies. *Journal of Volcanology and Geothermal Research*, **17**(1-4): 31-63.
- Wolff, J. A., Ramos, F. C. and Davidson, J. P. (1999). Sr isotope disequilibrium during differentiation of the Bandelier Tuff: Constraints on the crystallization of a large rhyolitic magma chamber. *Geology*, **27**(6): 495-498.
- Woods, A. W. and Bower, S. M. (1995). The decompression of volcanic jets in a crater during explosive eruptions. *Earth and Planetary Science Letters*, **131**: 189-205.
- Wörner, G., Hammerschmidt, K., Henjes-Kunst, F., Lezaun, J. and Wilke, H. (2000). Geochronology ($^{40}\text{Ar}/^{39}\text{Ar}$, K-Ar and He-exposure ages) of Cenozoic magmatic

- rocks from Northern Chile (18-22°S): implications for magmatism and tectonic evolution of the central Andes. *Revista Geológica de Chile*, **27**(2): 205-240.
- Wright, H. M. N., Cashman, K. V., Mothes, P. A., Hall, M. L., Ruiz, A. G. and Le Pennec, J. L. (2012). Estimating rates of decompression from textures of erupted ash particles produced by 1999–2006 eruptions of Tungurahua volcano, Ecuador. *Geology*, **40**(7): 619-622.
- Wright, J. W., Smith, A. L. and Self, S. (1980). A working terminology of pyroclastic deposits. *Journal of Volcanology and Geothermal Research*, **8**: 315-336.
- Wyllie, P. J. (1984). Constraints imposed by experimental petrology on possible and impossible magma sources and products. *Philosophical Transactions of the Royal Society of London A*, **310**: 439-456.
- Young, S. R., Sparks, R. S. J., Aspinall, W. P., Lynch, L. L., Miller, A. D., Robertson, R. E. A. and Shepherd, J. B. (1998). Overview of the eruption of Soufriere Hills volcano, Montserrat, 18 July 1995 to December 1997. *Geophysical Research Letters*, **25**: 3389-3392.
- Yurimoto, H., Nagashima, K. and Kunihiro, T. (2003). High precision isotope micro-imaging of materials. *Applied Surface Science*, **203-204**: 793.
- Zealand, G. o. N. (1966). An Encyclopaedia of New Zealand.
- Zellmer, G., Turner, S. and Hawkesworth, C. (2000a). Timescales of destructive plate margin magmatism: new insights from Santorini, Aegean volcanic arc. *Earth and Planetary Science Letters*, **174**(3): 265-281.
- Zellmer, G. F., Blake, S., Vance, D., Hawkesworth, C. and Turner, S. (1999). Plagioclase residence times at two island arc volcanoes (Kameni islands, Santorini, and Soufriere, St. Vincent) determined by Sr diffusion systematics. *Contributions to Mineralogy and Petrology*, **136**(4): 345-357.
- Zellmer, G. F., Sparks, R. S. J., Hawkesworth, C. J., Thomas, L. E. and Brewer, T. S. (2000b). Petrogenetic processes and their timescales at Montserrat, Lesser Antilles Volcanic arc. *Eos*, **81**(48): 1359.
- Zellmer, G. F., Hawkesworth, C. J., Sparks, R. S. J., Thomas, L. E., Harford, C., Brewer, T. S. and Loughlin, S. (2003a). Geochemical evolution of the Soufrière Hills volcano, Montserrat, Lesser Antilles Volcanic Arc. *Journal of Petrology*, **44**: 1349-1374.
- Zellmer, G. F., Sparks, R. S. J., Hawkesworth, C. J. and Wiedenbeck, M. (2003b). Magma emplacement and remobilization timescales beneath Montserrat: insights from Sr and Ba zonation in plagioclase phenocrysts. *Journal of Petrology*, **44**: 1413-1431.
- Zellmer, G. F. (2008). Some first order observations on magma transfer from mantle wedge to upper crust at volcanic arcs. In: C. Annen and G.F. Zellmer (Editors), Dynamics of crustal magma transfer, storage and differentiation. Special Publications. Geological Society, London, pp. 15-31.
- Zellmer, G. F., Rubin, K. H., Dulski, P., Iizuka, Y., Goldstein, S. L. and Perfit, M. R. (2011). Crystal growth during dike injection of MOR basaltic melts: evidence from preservation of local Sr disequilibria in plagioclase. *Contributions to Mineralogy and Petrology*, **161**: 153-173.
- Zellmer, G. F., Dulski, P. and Iizuka, Y. (2012a). Combined major and trace element LA-ICP-MS analysis of compositional variations in simple solid solutions through cross-correlation with an EPMA-characterized working standard. *Microscopy and Microanalysis*, **18**: 852-859.

- Zellmer, G. F., Sheth, H. C., Iizuka, Y. and Lai, Y.-J. (2012b). Remobilization of granitoid rocks through mafic recharge: evidence from basalt-trachyte mingling and hybridization in the Manori-Gorai area, Mumbai, Deccan Traps. *Bulletin of Volcanology*, **74**: 47-66.
- Zellmer, G. F., Freymuth, H., Cembrano, J. M., Clavero, J. E., Veloso, E. A. E. and Sielfeld, G. G. (2014a). Altered mineral uptake into fresh arc magmas: insights from U-Th isotopes of samples from Andean volcanoes under differential crustal stress regimes. In: A. Gomez-Tuena, S.M. Straub and G.F. Zellmer (Editors), *Orogenic andesites and crustal growth*. Geological Society, London, Special Publications, pp. 185-208.
- Zellmer, G. F., Sakamoto, N., Iizuka, Y., Miyoshi, M., Tamura, Y., Hsieh, H.-H. and Yurimoto, H. (2014b). Crystal uptake into aphyric arc melts: insights from two-pyroxene pseudo-decompression paths, plagioclase hygrometry, and measurement of hydrogen in olivines from mafic volcanics of southwest Japan. In: A. Gomez-Tuena, S.M. Straub and G.F. Zellmer (Editors), *Orogenic andesites and crustal growth*. Geological Society, London, Special Publications, pp. 161-184.
- Zellmer, G. F., Edmonds, M. and Straub, S. M. (2015a). Volatiles in subduction zone magmatism. In: G.F. Zellmer, M. Edmonds and S.M. Straub (Editors), *The role of volatiles in the genesis, evolution, and eruption of arc magmas*. Geological Society, London, Special Publications, pp. 1-17.
- Zellmer, G. F., Rubin, K. H., Miller, C. A., Shellnutt, J. G., Belousov, A. and Belousova, M. (2015b). Resolving discordant U-Th-Ra ages: constraints on petrogenetic processes of recent effusive eruptions at Tatun Volcano Group, northern Taiwan. In: L. Caricchi and J.D. Blundy (Editors), *Chemical, physical and temporal evolution of magmatic systems*. Geological Society, London, Special Publications, pp. 175-188.
- Zellmer, G. F., Pistone, M., Iizuka, Y., Andrews, B. J., Gomez-Tuena, A., Straub, S. M. and Cottrell, E. (2016a). Petrogenesis of antecryst-bearing arc basalts from the Trans-Mexican Volcanic Belt: insights into along-arc variations in magma-mush ponding depths, H₂O contents, and surface heat flux. *American Mineralogist*, **101**(11): 2405-2422.
- Zellmer, G. F., Sakamoto, N., Hwang, S.-L., Matsuda, N., Iizuka, Y., Moebis, A. and Yurimoto, H. (2016b). Inferring the effects of compositional boundary layers on crystal nucleation, growth textures, and mineral chemistry in natural volcanic tephra through submicron-resolution imaging. *Frontiers in Earth Sciences*, **4**: 88.
- Zellmer, G. F., Sakamoto, N., Matsuda, N., Iizuka, Y., Moebis, A. and Yurimoto, H. (2016c). On progress and rate of the peritectic reaction Fo + SiO₂ → En in natural andesitic arc magmas. *Geochimica et Cosmochimica Acta*, **185**: 383-393.
- Zellmer, G. F., Sakamoto, N., Matsuda, N., Iizuka, Y., Moebis, A. and Yurimoto, H. (2018). Corrigendum to “On progress and rate of the peritectic reaction Fo + SiO₂ → En in natural andesitic arc magmas”. *Geochimica et Cosmochimica Acta*, **185**(383-393).
- Zellmer, G. F., Chen, K.-X., Gung, Y., Kuo, B.-Y. and Yoshida, T. (2019). Magma transfer processes in the NE Japan arc: insights from crustal ambient noise tomography combined with volcanic eruption records. *Frontiers in Earth Science*, **7**(40).
- Zhang, Y. (2008). *Geochemical Kinetics*. Princeton University Press, 660 pp.

Appendix A: Supplementary Data

Appendix A1. Published methodology: Lormand C., Georg F. Zellmer G.F., Németh K., Kilgour G., Mead S., Palmer A.S., Sakamoto N., Yurimoto H., Moebis A. (2018) Weka Trainable Segmentation plugin in ImageJ: a semi-automatic tool applied to Crystal Size Distributions of microlites in volcanic rocks. *Microscopy and Microanalysis*, **24**: 667–675.

DOI: <https://doi.org/10.1017/S1431927618015428>

Appendix A2. Performance evaluation code in RStudio – example for the classifier used for the TWS segmentation (section 3.3.2.4) of the plagioclase population of the Mangamate - Te Rato sample.

```
#Load the ROCR, raster and rgdal packages
library(ROCR)
library(raster)
library(rgdal)

#Load the images using readGDAL function
manual <- readGDAL("C:/Users/clormand/Desktop/Papers/4
weka/Data/Metrics/Mangamate/manual_plg.tif")

auto <- readGDAL("C:/Users/clormand/Desktop/Papers/4
weka/Data/Metrics/Mangamate/auto_plg.tif")

#Run the prediction using ROC predict function - order is
the automatic and then ground truth
rocPred <- prediction(auto$band1, manual$band1)

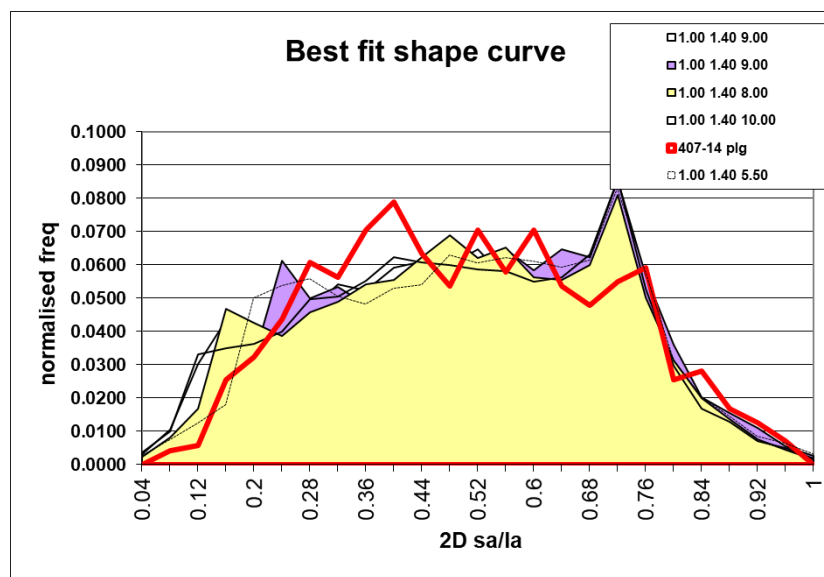
#Classify the performance using each metric
ppv <- performance(rocPred, "ppv")
tpr <- performance(rocPred, "tpr")
f <- performance(rocPred, "f")

#Build a data table
table1 = data.frame(classification = "Mangamate TWS plg",
ppv = ppv@y.values[[1]][2], tpr = tpr@y.values[[1]][2], f
= f@y.values[[1]][2])
```

Appendix A3. One example of the CSD output for one tephra (i.e. Mangatawai 407-14) consisting of the output parameters from *CSDslice* and *CSDCorrections*, and the crystal measurements output from *ImageJ*.

- *CSDslice* output:

Shape	x	y	z	Score (R ²)
best	1	1.7	6	0.795
2nd best	1	2	6	0.791
3rd	1	1.9	5.5	0.789
4th	1	1.9	6	0.789
5th	1	1.7	5.5	0.788



- *CSDCorrections* output:

Mid Inter	ln(pop den)	ln(min PD)	ln(max PD)	Cry Num	Vol%
125.3	-19.7	-20.4	-19.3	1.60E-07	1.46
79.1	-16.28	-16.44	-16.15	3.09E-06	7.06
49.9	-14.76	-14.88	-14.66	8.92E-06	5.13
31.48	-13.93	-14.06	-13.82	1.29E-05	1.87
19.86	-12.85	-12.97	-12.75	2.39E-05	0.87
12.53	-11.89	-12.01	-11.79	3.95E-05	0.36
7.91	-10.78	-10.88	-10.69	7.59E-05	0.17
4.99	-10.03	-10.14	-9.92	0.000102	0.06

- Crystal measurements output from *ImageJ*:

n	Major	Minor	n	Major	Minor	n	Major	Minor
1	1.003	0.461	237	2.353	0.554	474	6.343	3.447
2	1.017	0.662	238	2.370	1.189	475	6.433	1.621
3	1.022	0.864	239	2.373	1.293	476	6.441	2.272
4	1.025	0.410	240	2.389	1.796	477	6.483	2.381
5	1.025	0.410	241	2.394	1.177	478	6.489	1.815
6	1.035	0.731	242	2.404	1.347	479	6.525	3.841
7	1.035	0.731	243	2.405	1.399	480	6.539	4.328
8	1.041	0.605	244	2.420	2.294	481	6.541	0.932
9	1.043	0.726	245	2.420	0.939	482	6.619	3.247
10	1.045	0.563	246	2.422	1.511	483	6.659	3.833
11	1.079	0.390	247	2.435	1.227	484	6.736	1.055
12	1.086	0.581	248	2.443	0.671	485	6.764	1.051
13	1.086	0.581	249	2.455	2.244	486	6.831	2.223
14	1.094	0.807	250	2.459	1.659	487	6.860	2.556
15	1.094	0.807	251	2.464	1.212	488	6.933	4.282
16	1.094	0.807	252	2.465	0.955	489	6.947	3.378
17	1.094	0.807	253	2.488	0.811	490	6.962	4.488
18	1.095	0.768	254	2.502	1.311	491	6.968	2.969
19	1.105	0.495	255	2.504	0.923	492	7.019	2.475
20	1.108	0.683	256	2.512	1.323	493	7.027	1.604
21	1.111	0.909	257	2.515	0.903	494	7.041	3.375
22	1.111	0.909	258	2.532	1.595	495	7.064	2.500
23	1.111	0.909	259	2.541	0.695	496	7.075	4.084
24	1.111	0.909	260	2.550	1.896	497	7.081	2.465
25	1.111	0.909	261	2.577	0.865	498	7.089	3.079
26	1.121	0.975	262	2.582	2.378	499	7.138	2.309
27	1.122	0.825	263	2.587	1.301	500	7.183	4.988
28	1.125	0.823	264	2.596	2.106	501	7.209	3.955
29	1.125	0.449	265	2.596	1.523	502	7.211	2.765
30	1.133	0.445	266	2.602	0.824	503	7.337	4.551
31	1.137	0.961	267	2.612	2.045	504	7.338	5.559
32	1.140	0.553	268	2.622	1.331	505	7.393	0.791
33	1.144	0.588	269	2.627	2.257	506	7.520	5.128
34	1.144	0.588	270	2.632	1.119	507	7.547	4.613
35	1.149	0.733	271	2.641	1.210	508	7.552	3.051
36	1.165	0.831	272	2.653	2.409	509	7.574	2.293
37	1.167	0.865	273	2.665	1.878	510	7.603	2.887
38	1.167	0.685	274	2.667	1.041	511	7.636	3.150
39	1.175	0.715	275	2.674	1.384	512	7.713	3.719
40	1.179	0.927	276	2.677	1.948	513	7.722	2.663
41	1.180	0.784	277	2.679	1.177	514	7.743	2.161
42	1.187	0.851	278	2.696	1.981	515	7.809	6.074

43	1.194	0.810	279	2.749	1.913	516	7.821	4.560
44	1.197	0.843	280	2.757	2.013	517	7.850	3.648
45	1.204	0.489	281	2.773	0.576	518	7.879	2.311
46	1.207	0.383	282	2.787	2.339	519	7.929	2.959
47	1.213	0.693	283	2.788	0.513	520	7.941	2.214
48	1.219	0.655	284	2.812	1.989	521	7.943	3.876
49	1.227	0.789	285	2.823	2.443	522	7.963	5.175
50	1.232	0.921	286	2.843	1.819	523	8.005	2.480
51	1.235	0.715	287	2.873	2.064	524	8.014	1.023
52	1.239	0.543	288	2.890	2.648	525	8.057	2.505
53	1.243	0.879	289	2.908	1.273	526	8.091	4.418
54	1.243	0.541	290	2.913	1.963	527	8.143	1.905
55	1.244	0.507	291	2.925	2.171	528	8.257	1.843
56	1.244	0.879	292	2.939	1.717	529	8.327	2.237
57	1.245	0.743	293	2.941	0.958	530	8.348	3.501
58	1.245	0.574	294	2.949	1.355	531	8.427	4.042
59	1.247	0.439	295	2.963	2.498	532	8.449	1.021
60	1.248	1.011	296	2.969	0.694	533	8.455	3.268
61	1.253	0.771	297	2.975	1.809	534	8.494	2.446
62	1.259	0.367	298	2.979	0.381	535	8.625	1.414
63	1.264	0.433	299	2.993	1.321	536	8.687	4.067
64	1.264	0.433	300	2.995	1.811	537	8.689	2.270
65	1.287	0.719	301	3.000	0.897	538	8.702	1.754
66	1.294	0.943	302	3.006	2.434	539	8.732	3.405
67	1.297	0.843	303	3.007	1.889	540	8.776	2.281
68	1.298	0.777	304	3.020	1.629	541	8.781	0.929
69	1.298	0.972	305	3.057	2.091	542	8.894	3.055
70	1.300	0.970	306	3.058	2.228	543	8.964	5.611
71	1.301	0.711	307	3.087	1.021	544	9.065	1.577
72	1.303	0.613	308	3.101	0.868	545	9.084	4.648
73	1.305	0.515	309	3.116	1.701	546	9.129	4.091
74	1.309	0.963	310	3.140	1.875	547	9.200	1.933
75	1.317	0.703	311	3.155	1.119	548	9.287	8.436
76	1.325	0.445	312	3.162	2.341	549	9.309	2.837
77	1.328	0.791	313	3.163	1.781	550	9.331	1.009
78	1.331	0.759	314	3.179	1.825	551	9.352	4.479
79	1.331	0.759	315	3.189	1.925	552	9.399	4.277
80	1.339	0.785	316	3.203	2.127	553	9.464	4.083
81	1.339	0.534	317	3.222	1.383	554	9.498	7.359
82	1.339	0.534	318	3.267	0.965	555	9.555	3.552
83	1.341	0.533	319	3.267	0.721	556	9.667	3.415
84	1.346	1.000	320	3.304	1.285	557	9.765	3.781
85	1.352	0.933	321	3.309	1.868	558	9.787	6.711
86	1.356	0.744	322	3.356	2.895	559	9.792	5.626
87	1.366	1.016	323	3.365	0.913	560	9.809	3.456

88	1.374	0.581	324	3.399	0.866	561	9.847	0.705
89	1.388	1.182	325	3.410	0.863	562	9.850	3.428
90	1.390	0.999	326	3.419	0.996	563	9.850	6.079
91	1.400	0.571	327	3.434	1.702	564	9.993	4.007
92	1.410	0.507	328	3.459	1.471	565	10.111	4.492
93	1.417	0.564	329	3.469	2.376	566	10.123	3.439
94	1.433	0.734	330	3.481	0.435	567	10.211	3.081
95	1.437	0.644	331	3.496	2.983	568	10.231	6.428
96	1.439	0.877	332	3.501	0.841	569	10.262	7.630
97	1.442	0.992	333	3.501	1.213	570	10.348	2.007
98	1.448	0.959	334	3.504	2.256	571	10.386	7.924
99	1.453	1.186	335	3.519	2.425	572	10.422	8.155
100	1.471	0.572	336	3.536	2.141	573	10.534	6.220
101	1.471	0.686	337	3.540	1.378	574	10.631	3.560
102	1.482	0.993	338	3.544	1.780	575	10.647	5.336
103	1.493	1.212	339	3.591	2.553	576	10.656	6.413
104	1.496	0.619	340	3.601	2.757	577	10.657	4.881
105	1.497	0.534	341	3.620	1.266	578	10.694	4.349
106	1.504	0.531	342	3.639	0.797	579	10.739	6.861
107	1.509	0.613	343	3.640	1.329	580	10.784	4.336
108	1.510	0.585	344	3.646	3.207	581	10.785	4.191
109	1.517	0.887	345	3.669	1.868	582	10.847	4.211
110	1.524	0.414	346	3.677	2.151	583	10.875	1.875
111	1.543	1.091	347	3.697	1.274	584	10.921	4.544
112	1.544	0.681	348	3.709	1.349	585	11.030	1.987
113	1.547	0.707	349	3.729	0.778	586	11.093	4.799
114	1.550	0.869	350	3.731	2.965	587	11.177	0.737
115	1.555	1.163	351	3.741	1.214	588	11.239	6.017
116	1.559	1.430	352	3.751	2.343	589	11.299	7.299
117	1.561	0.512	353	3.765	0.971	590	11.303	7.996
118	1.568	0.643	354	3.781	2.803	591	11.428	2.429
119	1.575	0.801	355	3.804	0.939	592	11.429	6.707
120	1.581	1.038	356	3.817	1.212	593	11.522	3.365
121	1.591	1.190	357	3.821	0.671	594	11.553	5.260
122	1.591	0.925	358	3.844	1.477	595	11.606	6.848
123	1.592	1.215	359	3.849	2.787	596	11.667	2.091
124	1.593	0.766	360	3.880	0.802	597	11.719	4.687
125	1.594	1.029	361	3.887	1.049	598	11.758	2.421
126	1.599	1.053	362	3.900	2.922	599	11.778	2.663
127	1.603	0.708	363	3.902	2.403	600	11.789	1.527
128	1.605	1.231	364	3.915	1.009	601	11.840	3.378
129	1.613	0.599	365	3.929	1.809	602	11.991	6.397
130	1.615	1.433	366	3.948	3.259	603	12.001	8.099
131	1.620	1.116	367	3.970	2.341	604	12.019	5.091
132	1.628	0.517	368	3.973	0.836	605	12.033	6.811

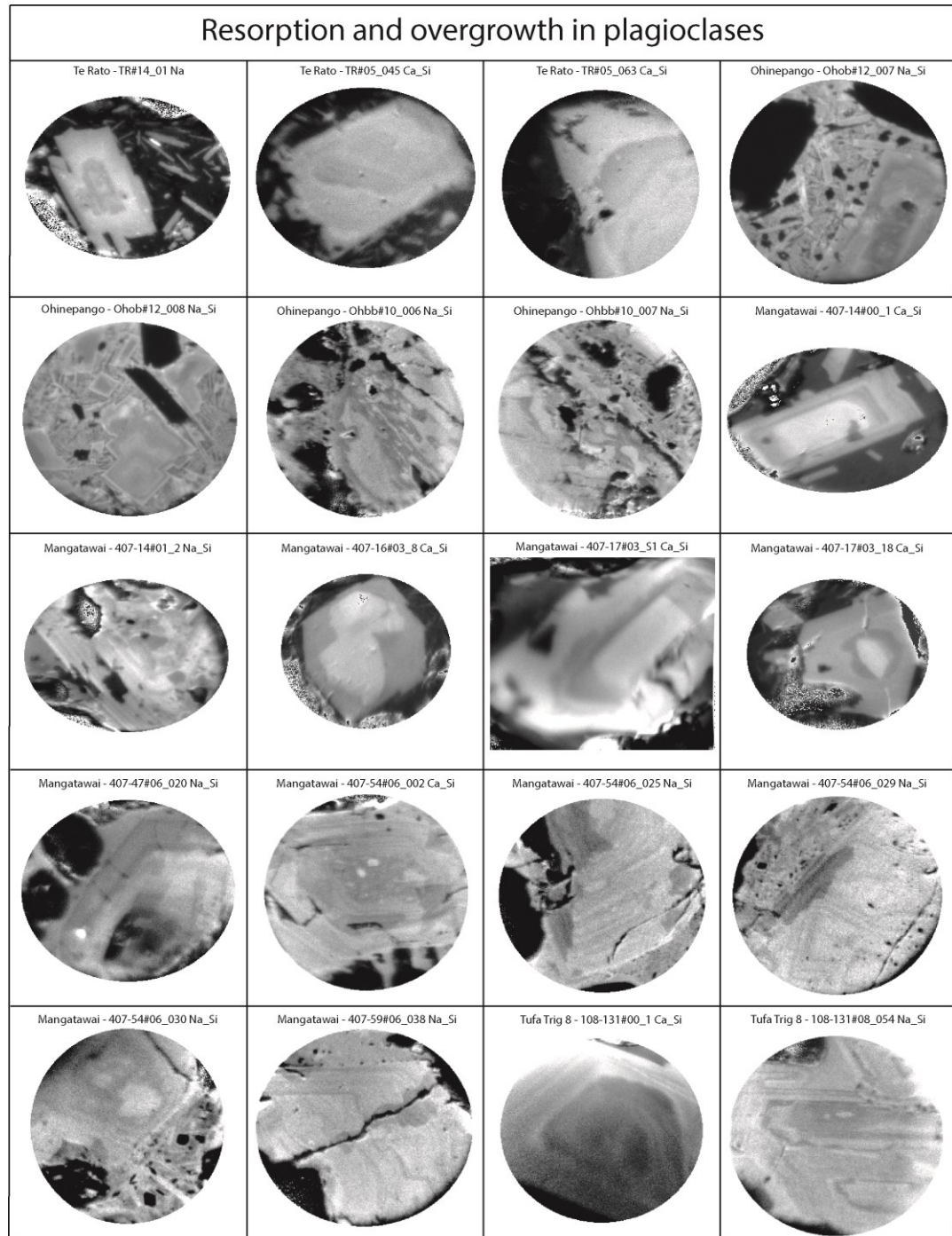
133	1.639	0.667	369	3.977	1.988	606	12.035	7.939
134	1.641	0.410	370	3.987	0.770	607	12.113	4.451
135	1.642	1.024	371	3.987	3.217	608	12.169	0.847
136	1.674	0.829	372	4.037	2.312	609	12.195	10.207
137	1.677	0.953	373	4.063	1.521	610	12.261	7.096
138	1.681	1.026	374	4.081	3.019	611	12.273	8.933
139	1.691	1.517	375	4.084	2.574	612	12.409	4.321
140	1.699	0.965	376	4.102	1.743	613	12.459	9.721
141	1.700	1.583	377	4.124	1.907	614	12.520	1.612
142	1.701	1.137	378	4.125	1.040	615	12.589	8.502
143	1.710	1.230	379	4.145	3.033	616	12.634	6.381
144	1.713	1.080	380	4.175	2.267	617	12.709	1.628
145	1.717	0.563	381	4.175	2.367	618	12.800	8.535
146	1.717	0.955	382	4.181	1.851	619	12.825	4.597
147	1.721	1.637	383	4.205	2.340	620	12.869	2.755
148	1.725	0.561	384	4.223	2.649	621	12.914	4.784
149	1.735	0.848	385	4.247	1.495	622	12.923	2.353
150	1.737	0.944	386	4.257	2.123	623	13.103	2.307
151	1.738	0.677	387	4.260	1.343	624	13.229	9.635
152	1.745	0.506	388	4.316	2.017	625	13.286	4.475
153	1.746	0.843	389	4.322	1.635	626	13.311	4.215
154	1.750	0.985	390	4.348	0.522	627	13.553	4.387
155	1.778	1.253	391	4.353	2.209	628	13.587	5.803
156	1.787	1.482	392	4.363	1.340	629	13.619	4.631
157	1.808	0.931	393	4.375	2.134	630	13.717	3.057
158	1.812	0.905	394	4.383	2.351	631	13.811	3.751
159	1.818	1.295	395	4.422	3.671	632	14.003	5.310
160	1.820	1.641	396	4.425	3.117	633	14.010	8.213
161	1.821	0.762	397	4.426	1.995	634	14.073	3.691
162	1.827	0.667	398	4.428	1.329	635	14.105	2.710
163	1.831	1.217	399	4.459	3.489	636	14.127	7.611
164	1.833	1.009	400	4.478	1.803	637	14.138	3.549
165	1.835	0.687	401	4.503	1.186	638	14.184	8.393
166	1.836	0.687	402	4.525	1.663	639	14.305	7.058
167	1.840	0.685	403	4.531	2.478	640	14.334	6.833
168	1.845	0.912	404	4.547	1.230	641	14.433	6.833
169	1.847	1.411	405	4.575	0.551	642	14.454	8.661
170	1.852	0.568	406	4.607	3.040	643	14.561	3.798
171	1.860	1.221	407	4.631	3.841	644	14.684	3.156
172	1.861	0.881	408	4.655	1.545	645	14.793	6.269
173	1.873	1.594	409	4.662	2.472	646	14.812	2.578
174	1.875	0.539	410	4.665	3.372	647	14.965	10.527
175	1.875	1.323	411	4.701	1.825	648	15.093	6.667
176	1.897	0.665	412	4.727	0.917	649	15.093	8.099
177	1.907	0.573	413	4.756	1.574	650	15.478	7.947

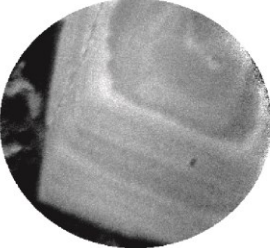
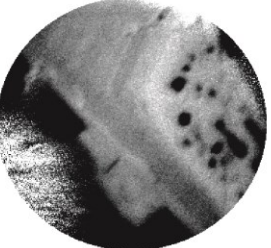
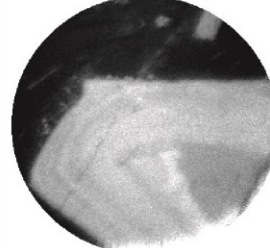
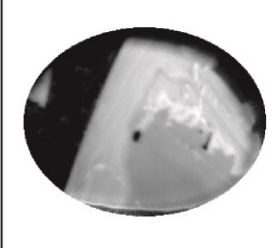
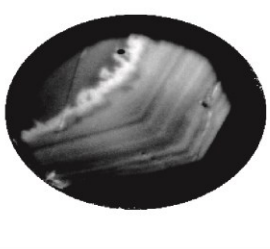
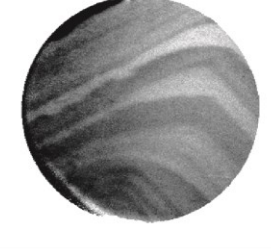

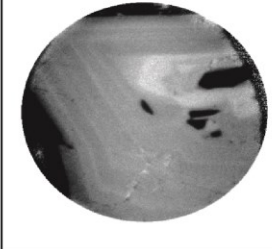
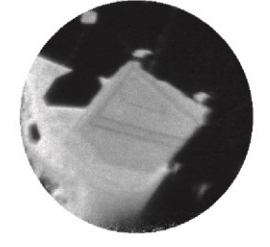
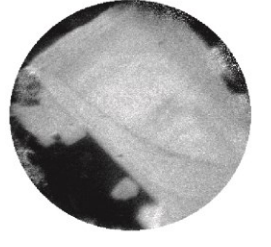
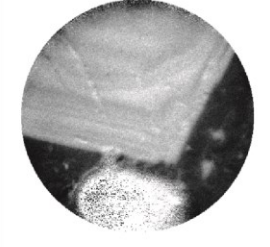

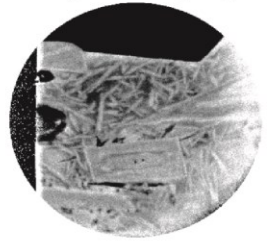
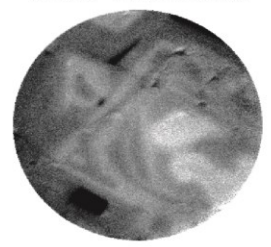
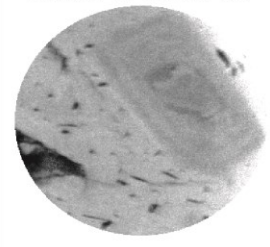
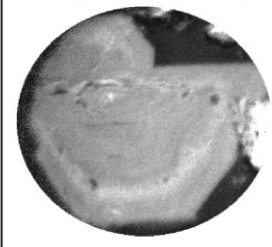
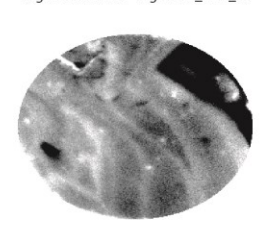
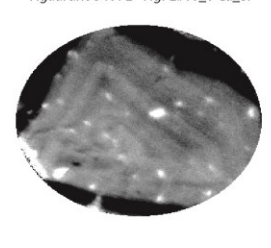
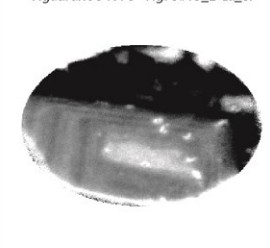
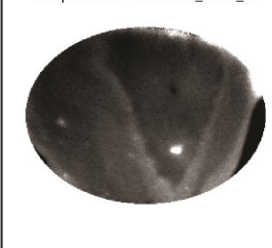
178	1.922	0.481	414	4.769	3.519	651	15.535	9.407
179	1.936	0.847	415	4.807	0.753	652	15.577	7.578
180	1.936	1.173	416	4.828	2.753	653	15.651	7.137
181	1.947	0.756	417	4.857	3.074	654	15.690	5.406
182	1.957	1.418	418	4.881	1.533	655	15.718	9.145
183	1.959	0.730	419	4.892	3.559	656	15.792	10.031
184	1.973	1.130	420	4.940	3.524	657	16.070	7.845
185	1.978	0.638	421	4.977	1.141	658	16.191	8.483
186	1.985	1.271	422	5.017	3.169	659	16.225	3.792
187	1.989	0.423	423	5.023	1.800	660	16.270	6.697
188	2.000	0.589	424	5.031	0.753	661	16.277	7.679
189	2.007	0.964	425	5.039	2.587	662	16.393	10.523
190	2.011	0.418	426	5.043	2.101	663	16.601	2.335
191	2.017	0.646	427	5.107	2.841	664	16.695	8.625
192	2.040	0.557	428	5.109	2.979	665	17.105	8.140
193	2.041	1.401	429	5.112	1.193	666	17.192	8.640
194	2.041	1.833	430	5.161	2.738	667	17.312	3.228
195	2.045	0.843	431	5.167	3.353	668	17.425	4.235
196	2.050	1.641	432	5.201	1.884	669	17.477	10.559
197	2.061	0.591	433	5.212	1.646	670	17.577	3.517
198	2.064	1.345	434	5.244	3.705	671	17.817	8.190
199	2.081	0.505	435	5.297	1.667	672	18.035	3.169
200	2.093	1.567	436	5.311	2.051	673	18.065	9.698
201	2.099	0.921	437	5.333	1.672	674	18.187	10.969
202	2.101	1.261	438	5.346	4.106	675	18.243	6.865
203	2.115	0.597	439	5.366	1.348	676	18.329	6.039
204	2.115	1.809	440	5.398	1.013	677	18.391	2.031
205	2.118	1.152	441	5.405	3.042	678	18.409	4.790
206	2.135	1.261	442	5.437	1.284	679	18.686	5.867
207	2.145	0.921	443	5.489	2.640	680	18.751	9.684
208	2.148	0.920	444	5.615	2.359	681	18.909	3.883
209	2.157	0.917	445	5.619	3.113	682	19.116	4.991
210	2.164	0.544	446	5.695	2.090	683	19.341	12.405
211	2.164	1.671	447	5.720	1.301	684	20.103	6.227
212	2.165	1.049	448	5.735	2.816	685	20.574	5.463
213	2.168	1.047	449	5.750	1.580	686	20.747	14.559
214	2.181	0.925	450	5.775	2.840	687	20.817	5.265
215	2.182	0.443	451	5.776	3.160	688	20.873	2.613
216	2.188	1.211	452	5.787	1.279	689	20.963	4.163
217	2.193	1.765	453	5.851	2.494	690	20.967	5.467
218	2.203	0.859	454	5.869	0.845	691	21.048	9.277
219	2.207	1.619	455	5.897	4.122	692	21.259	5.107
220	2.209	0.723	456	5.914	3.129	693	21.502	5.801
221	2.255	1.772	457	5.919	3.140	694	21.521	4.936
222	2.261	1.544	458	5.922	3.785	695	22.430	6.031

223	2.269	0.389	459	5.943	0.977	696	23.004	14.341
224	2.282	1.732	460	5.963	5.684	697	23.031	10.647
225	2.286	1.821	461	5.973	3.929	698	23.077	8.513
226	2.296	1.667	462	6.003	1.681	699	23.994	3.940
227	2.301	0.749	463	6.049	4.644	700	24.027	6.957
228	2.305	0.931	464	6.059	4.366	701	24.419	4.001
229	2.307	1.567	465	6.092	5.033	702	24.763	3.797
230	2.313	0.655	466	6.117	3.128	703	24.987	7.111
231	2.324	0.724	467	6.119	3.725	704	25.008	7.387
232	2.329	1.101	468	6.167	3.600	705	25.081	8.097
233	2.333	1.280	469	6.221	1.649	706	27.367	11.798
234	2.336	1.152	470	6.237	2.279	707	28.324	13.687
235	2.336	1.638	471	6.251	3.619	708	28.558	16.249
236	2.351	1.306	472	6.294	2.339	709	29.992	5.127
237	2.353	0.554	473	6.304	3.509			

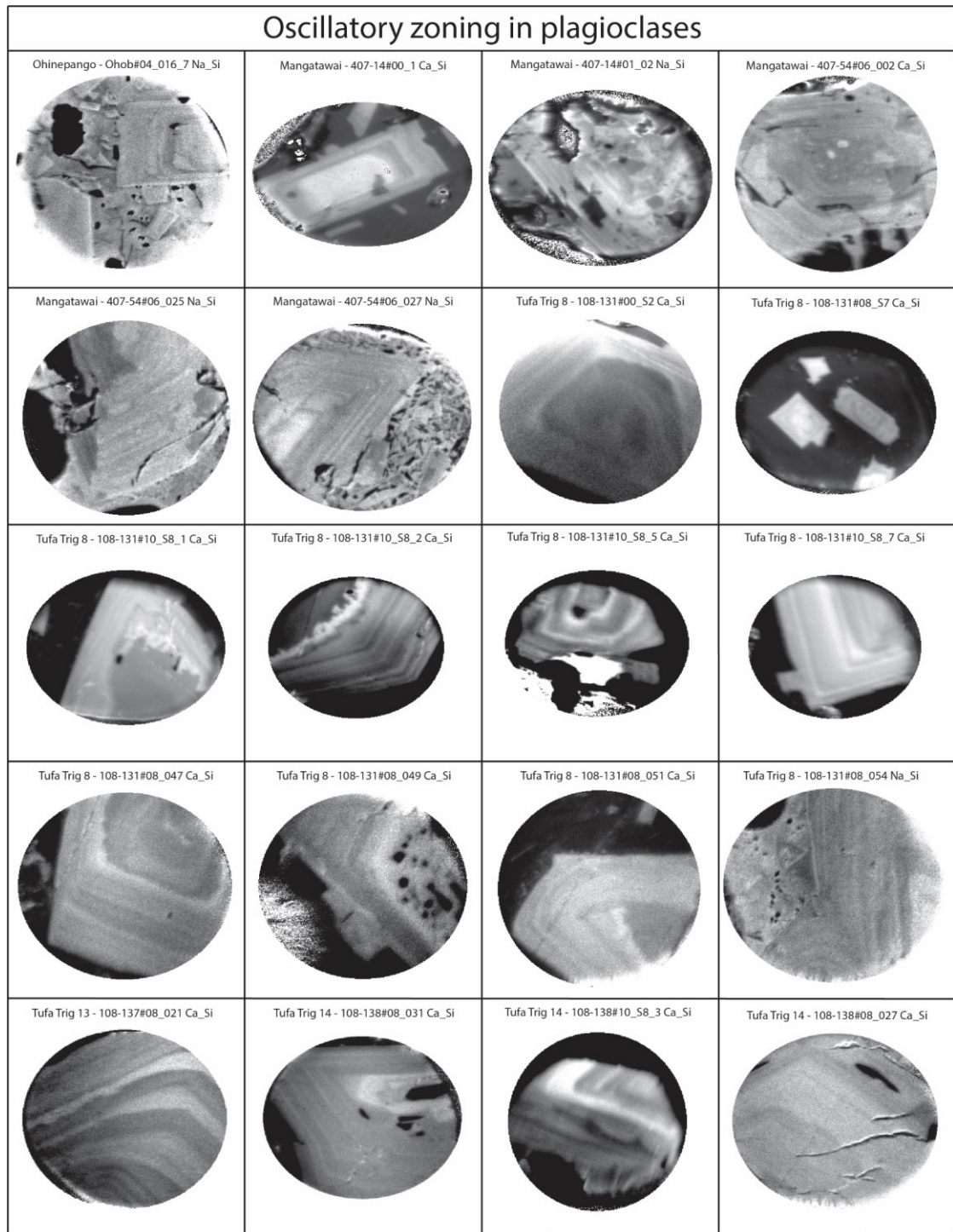
Appendix B: Supplementary Figures

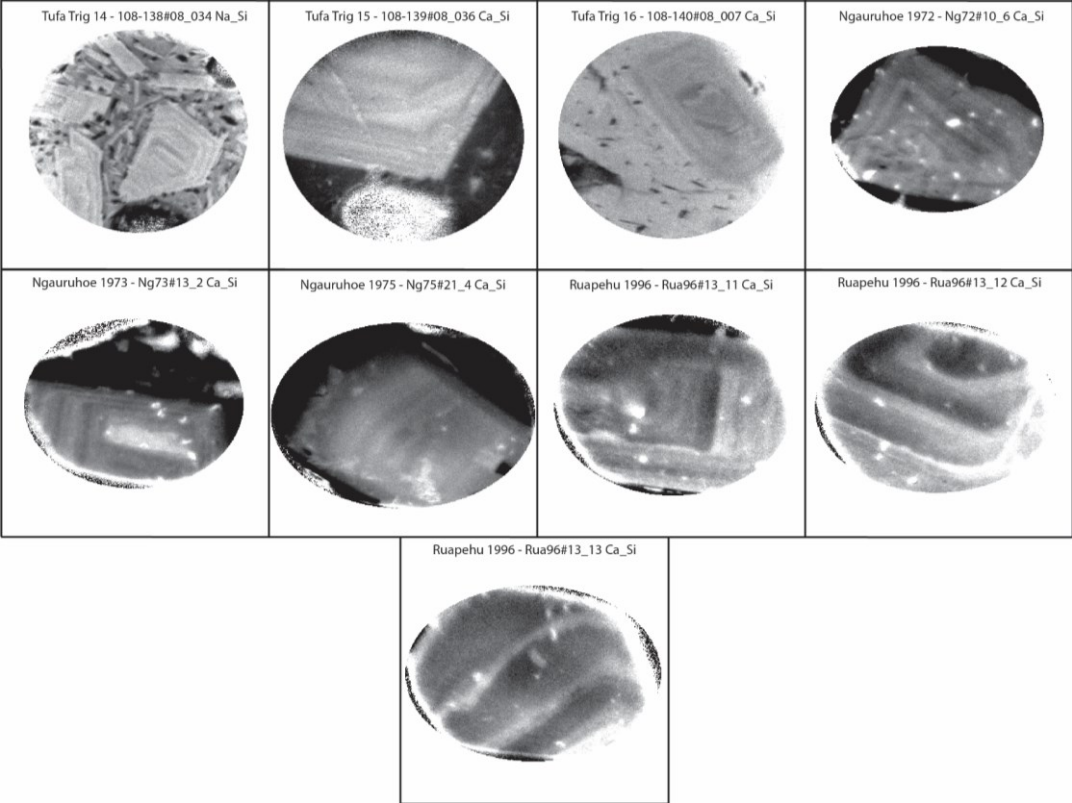
Appendix B1. SCAPS images of plagioclase crystals with resorption and overgrowth. All images are between 80 μm and 100 μm across.



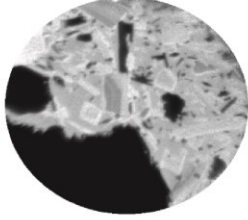
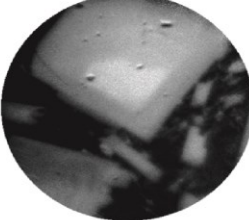
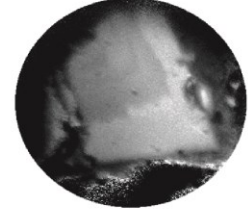
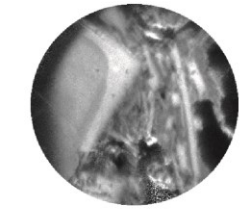
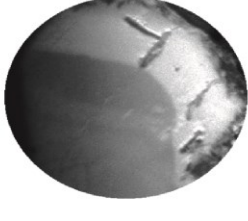
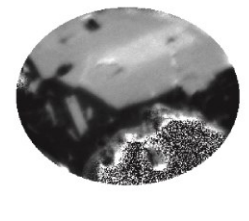
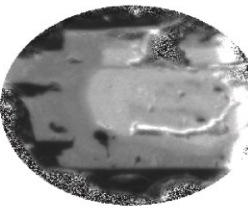
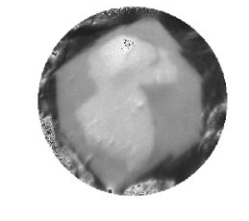
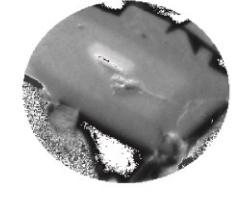
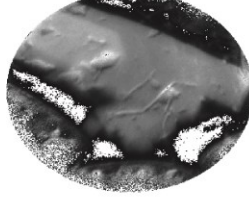

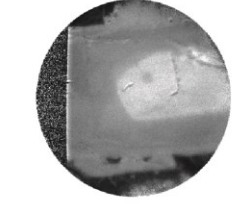
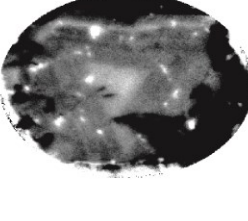
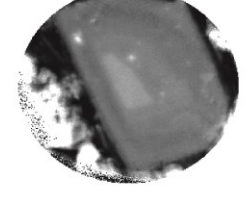
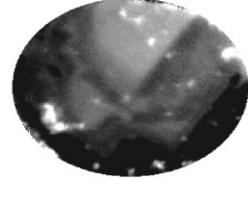
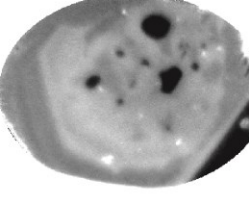
<p>Tufa Trig 8 - 108-131#08_047 Ca_Si</p> 	<p>Tufa Trig 8 - 108-131#08_049 Ca_Si</p> 	<p>Tufa Trig 8 - 108-131#08_051 Ca_Si</p> 	<p>Tufa Trig 8 - 108-131#10_S8_1 Ca_Si</p> 
<p>Tufa Trig 8 - 108-131#10_S8_2 Ca_Si</p> 	<p>Tufa Trig 13 - 108-137#08_021 Ca_Si</p> 	<p>Tufa Trig 14 - 108-138#08_027 Ca_Si</p> 	<p>Tufa Trig 14 - 108-138#08_031 Ca_Si</p> 
<p>Tufa Trig 14 - 108-138#08_038 Na_Si</p> 	<p>Tufa Trig 14 - 108-138#08_039 Na_Si</p> 	<p>Tufa Trig 15 - 108-139#08_036 Ca_Si</p> 	<p>Tufa Trig 15 - 108-139#08_046 Na_Si</p> 
<p>Tufa Trig 15 - 108-139#08_042 Na_Si</p> 	<p>Tufa Trig 16 - 108-140#08_002 Ca_Si</p> 	<p>Tufa Trig 16 - 108-140#08_007 Ca_Si</p> 	<p>Tufa Trig 16 - 108-140#08_011 Na_Si</p> 
<p>Ngauruhoe 1972 - Ng72#06_2 Ca_Si</p> 	<p>Ngauruhoe 1972 - Ng72#10_6 Ca_Si</p> 	<p>Ngauruhoe 1973 - Ng73#13_2 Ca_Si</p> 	<p>Ruapehu 1996 - Rua96-13_17 Ca_Si</p> 

Appendix B2. SCAPS images of plagioclase crystals with oscillatory zoning. All images are between 80 μm and 100 μm across.

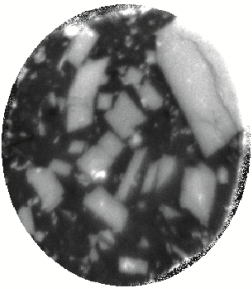

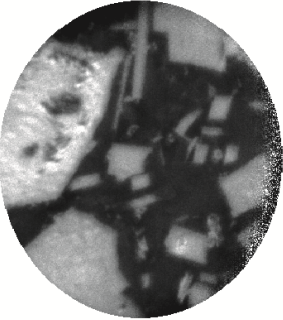
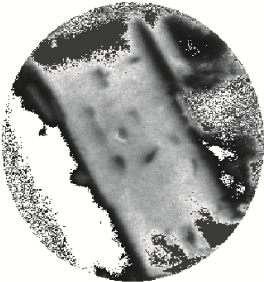

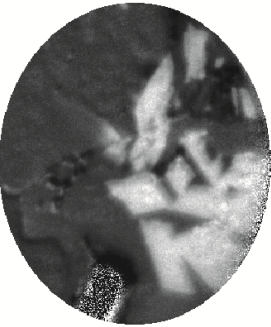
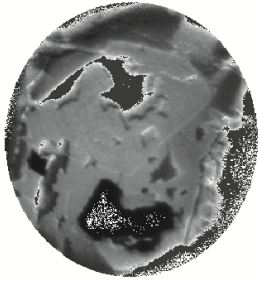
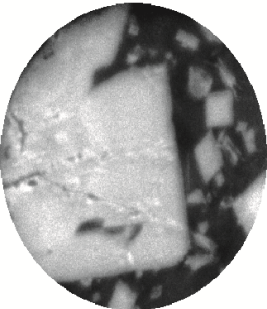





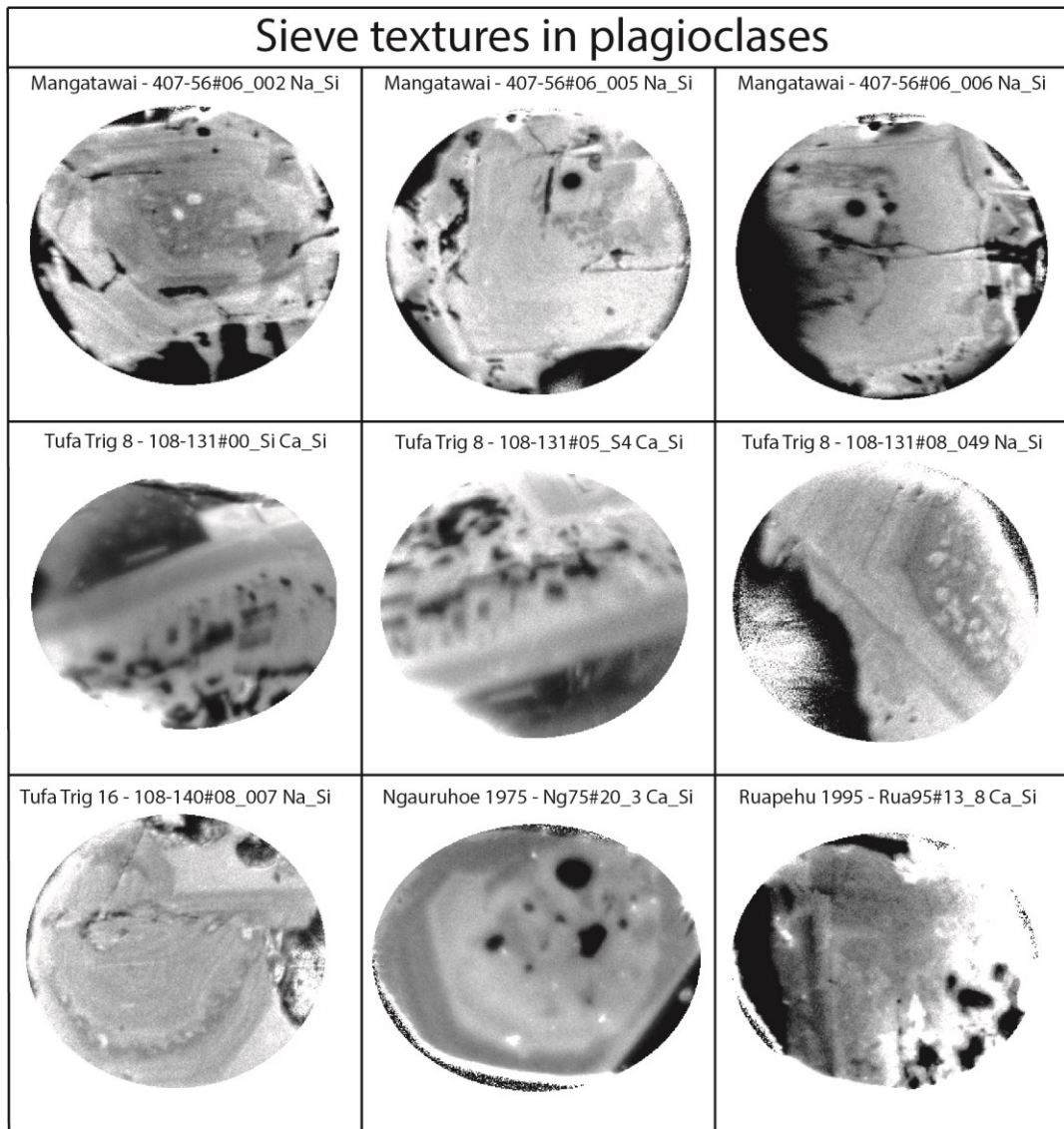
Appendix B3. SCAPS images of plagioclase crystals with single compositional jump. The single compositional jump texture is characterised by a sharp boundary between the (resorbed) core and the rim with no compositional gradient. All images are between 80 μm and 100 μm across.

Single compositional jump in plagioclases			
Ohinepango- Oh#04_021 Na_Si 	Te Rato - TR#05_054 Na_Si 	Te Rato - TR#05_062 Ca_Si 	Te Rato - TR#05_103 Ca_Si 
Te Rato - TR#05_104 Ca_Si 	Mangatawai - 407-14#02_5 Ca_Si 	Mangatawai - 407-14#02_6 Ca_Si 	Mangatawai - 407-16#03_8 Ca_Si 
Mangatawai - 407-16#03_9 Ca_Si 	Mangatawai - 407-16#03_10 Ca_Si 	Mangatawai - 407-17#03_18 Ca_Si 	Tufa Trig 14 - 108-138#08_041 Ca_Si 
Ngauruhoe 1972 - Ng72#08_4 Ca_Si 	Ngauruhoe 1975 - Ng75#12_2 Ca_Si 	Ngauruhoe 1975 - Ng75#14_1 Ca_Si 	Ngauruhoe 1975 - Ng75#20_3 Ca_Si 

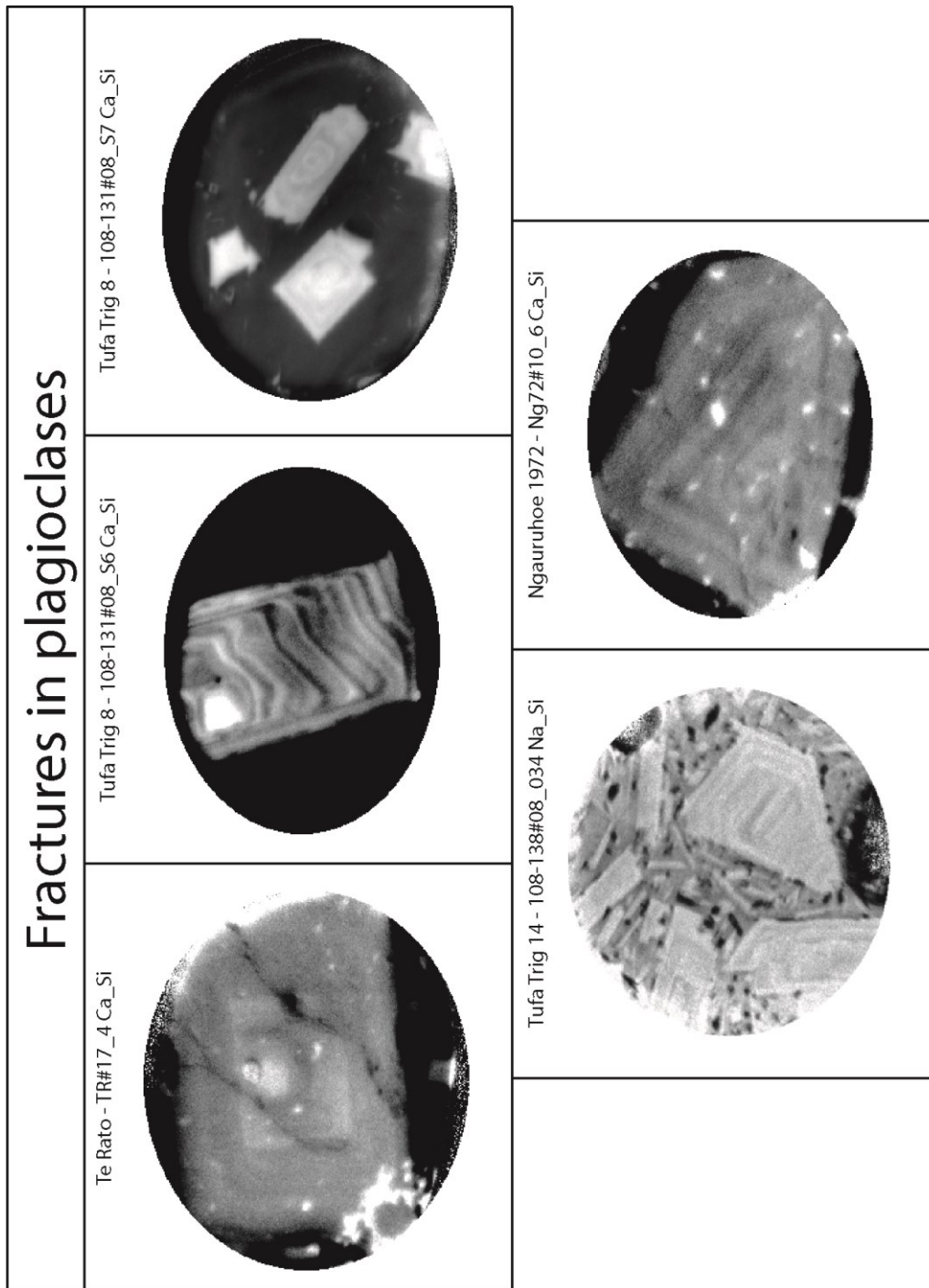
Appendix B4. SCAPS images of featureless plagioclases. All images are between 80 μm and 100 μm across.

<p>Featureless plagioclases</p>	<p>Te Rato - TR#19_6 Ca_Si</p> 	<p>Mangatawai - 407-17#03_21 Ca_Si</p> 	
	<p>Te Rato - TR#13_22 Ca_Si</p> 	<p>Mangatawai - 407-16#03_14</p> 	<p>Tufa Trig 13 - 108-138#08_13 Ca_Si</p> 
	<p>Te Rato - TR#13_20 Ca_Si</p> 	<p>Mangatawai - 407-16#11 Na_Si</p> 	
	<p>Te Rato - TR#13_16 Ca_Si</p> 	<p>Mangatawai - 407-14#02_7 Ca_Si</p> 	

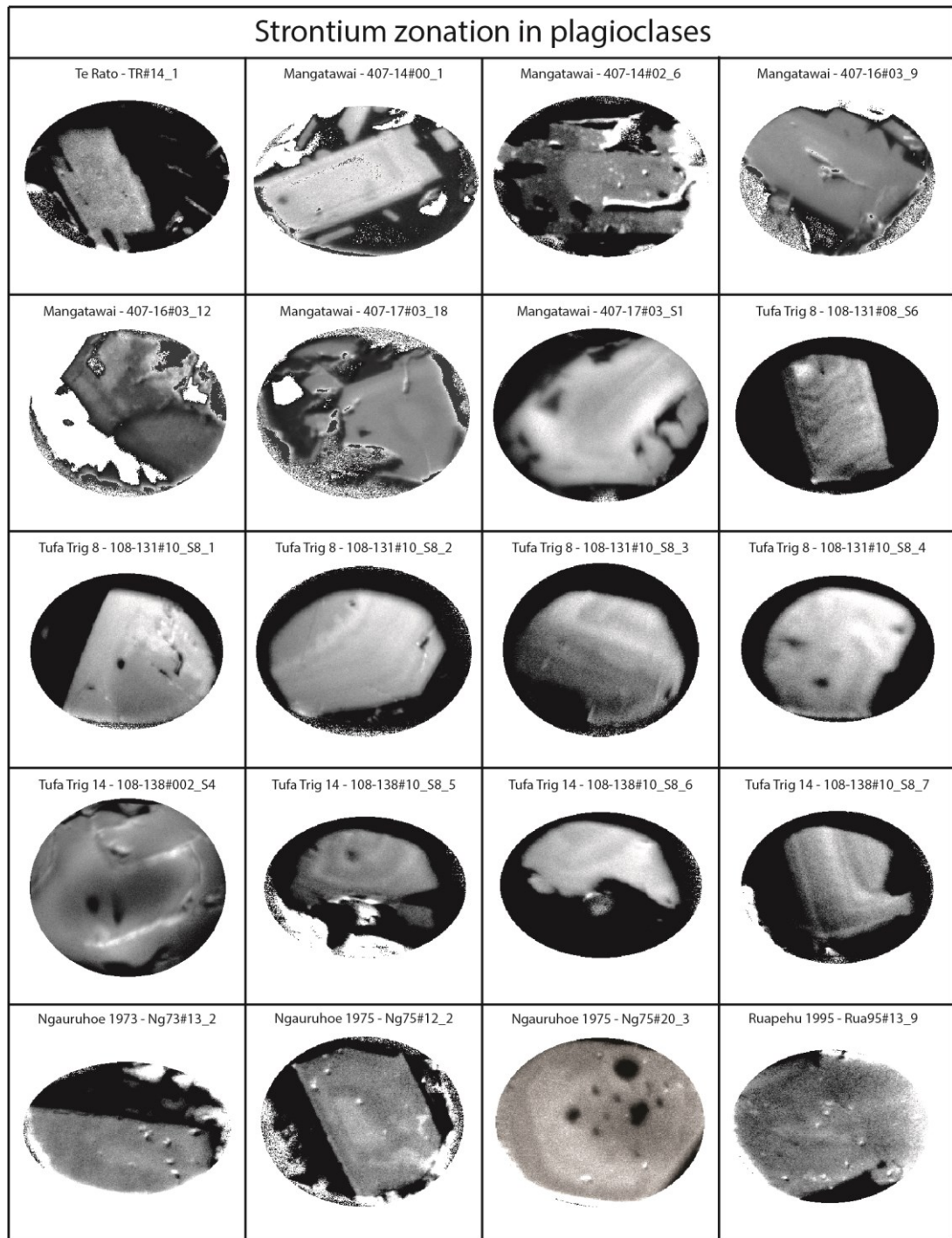
Appendix B5. SCAPS images of plagioclase crystals with sieve and dissolution textures. All images are between 80 μm and 100 μm across.

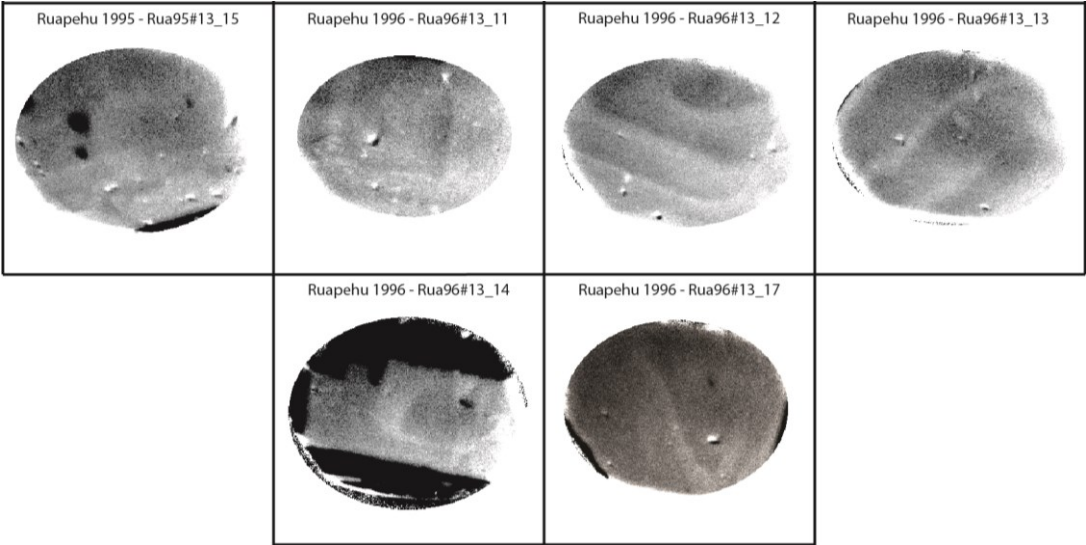


Appendix B6. SCAPS images of plagioclase crystals fractures. All images are between 80 µm and 100 µm across.

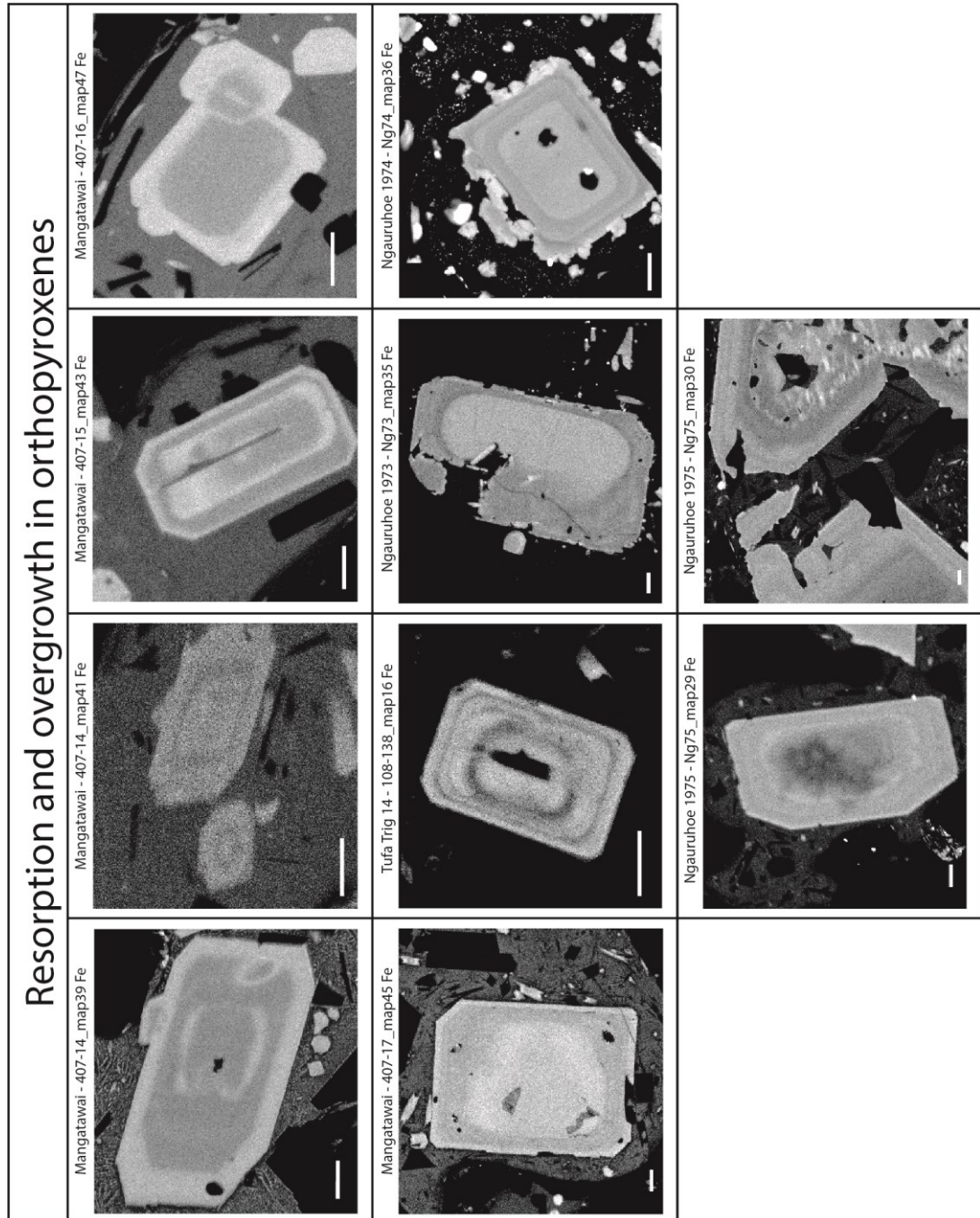


Appendix B7. SCAPS images of plagioclase crystals with zonation in strontium. All images are between 80 μm and 100 μm across.

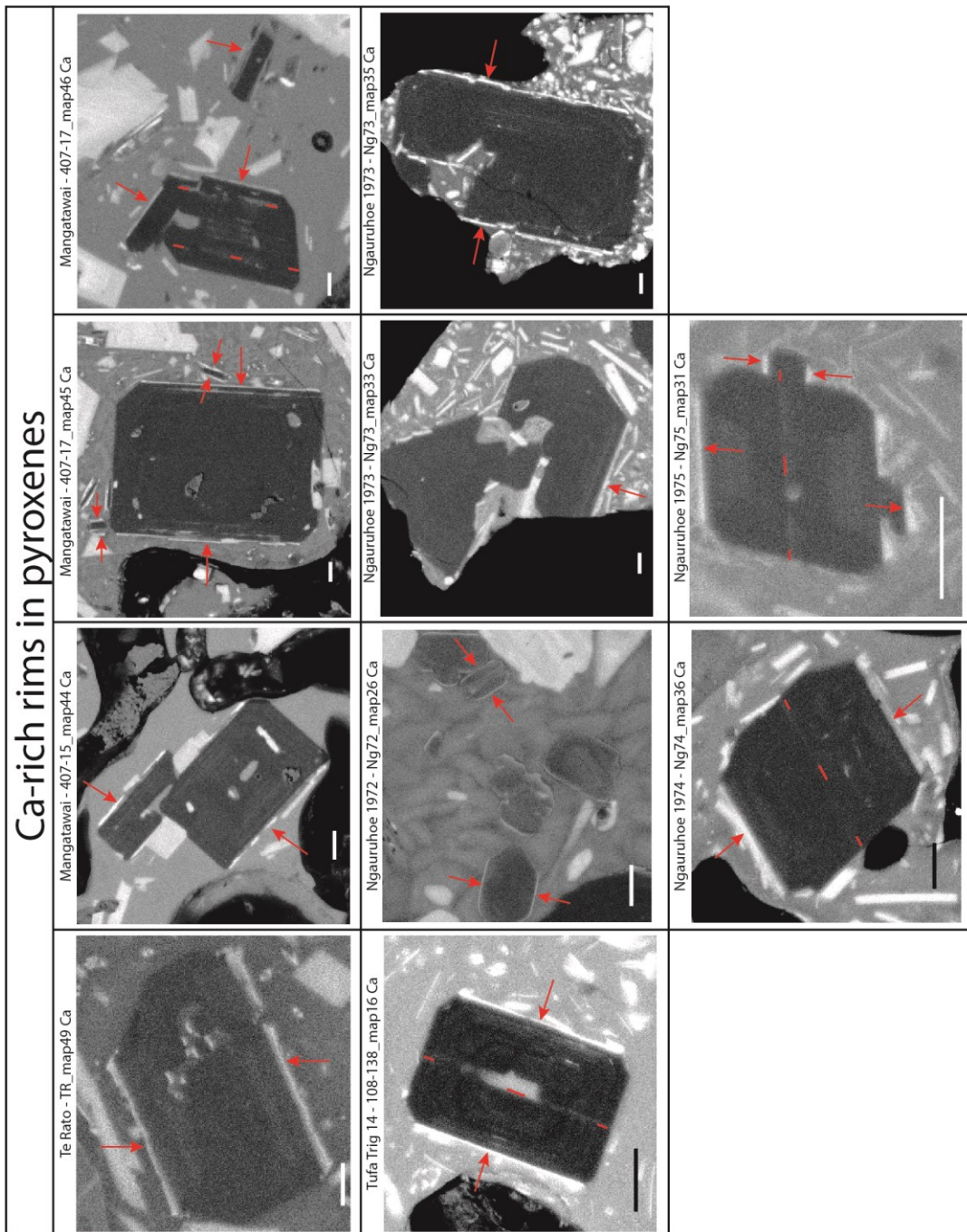




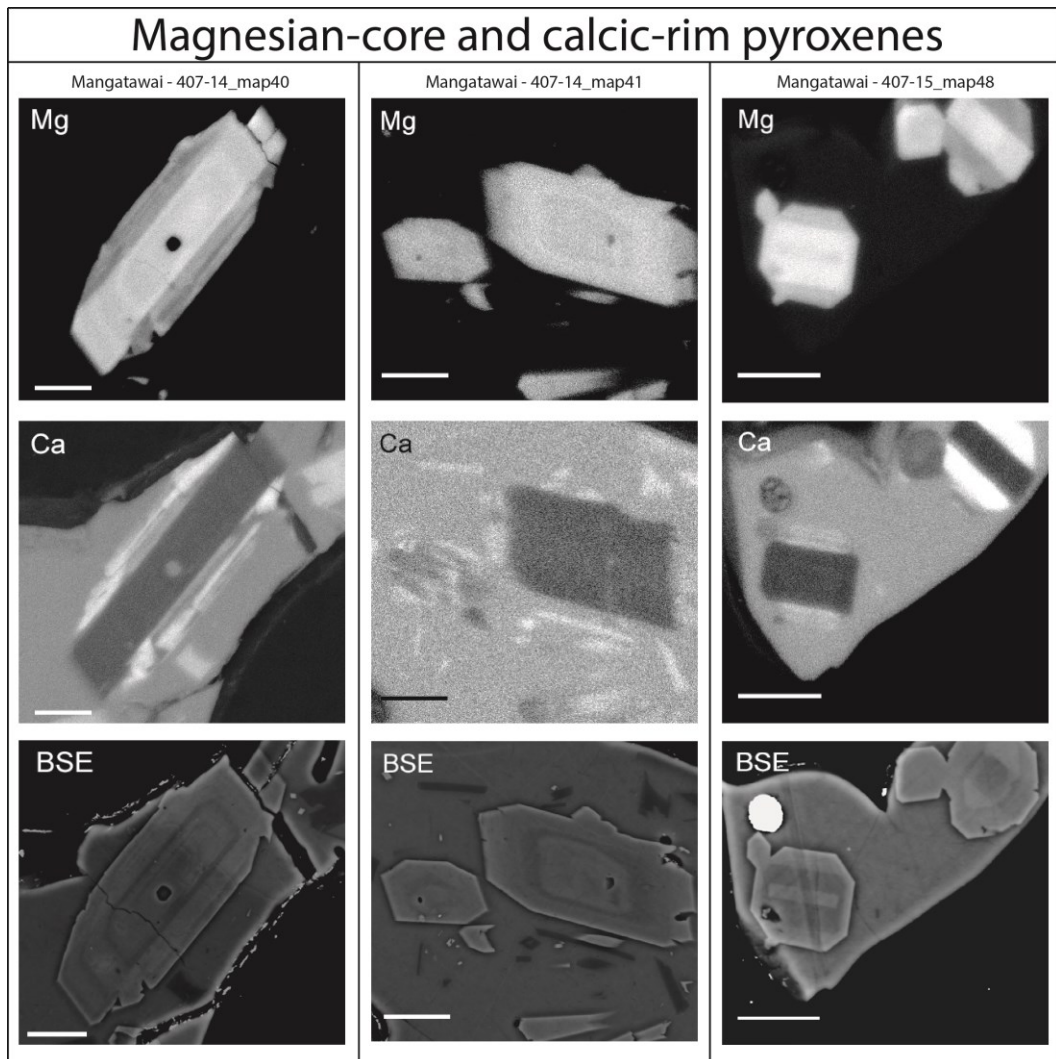
Appendix B8. Element maps of pyroxene crystals with resorption and overgrowth. The white scale bar at the bottom left corner is 10 μm in length.



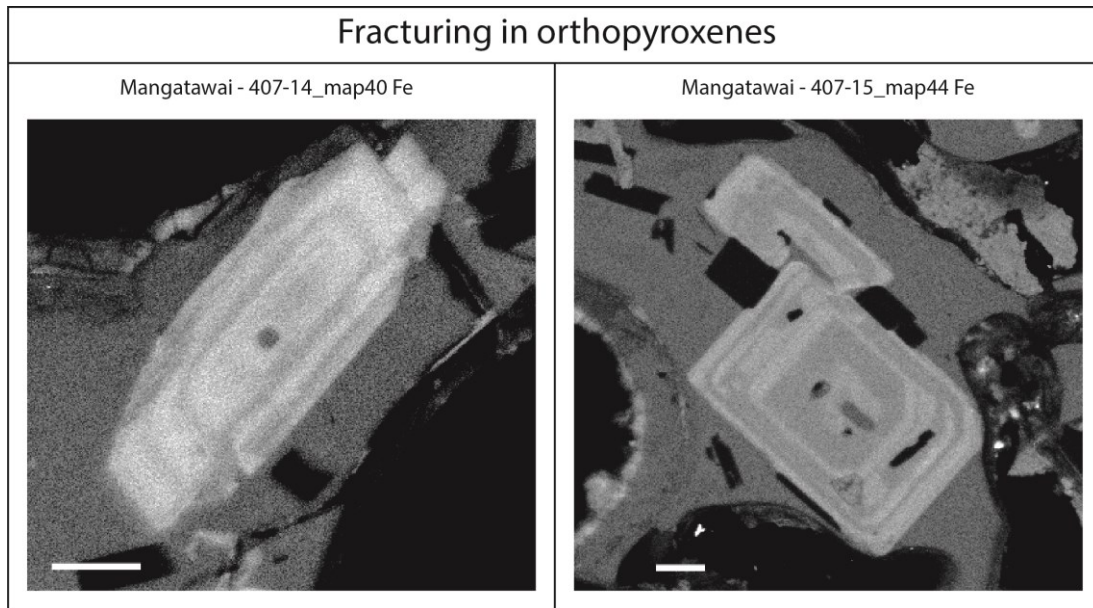
Appendix B9. Element maps of pyroxene crystals with calcium-rich rims along the long axis (see red arrows). The white/black scale bar as the bottom left corner is 10 μm in length.



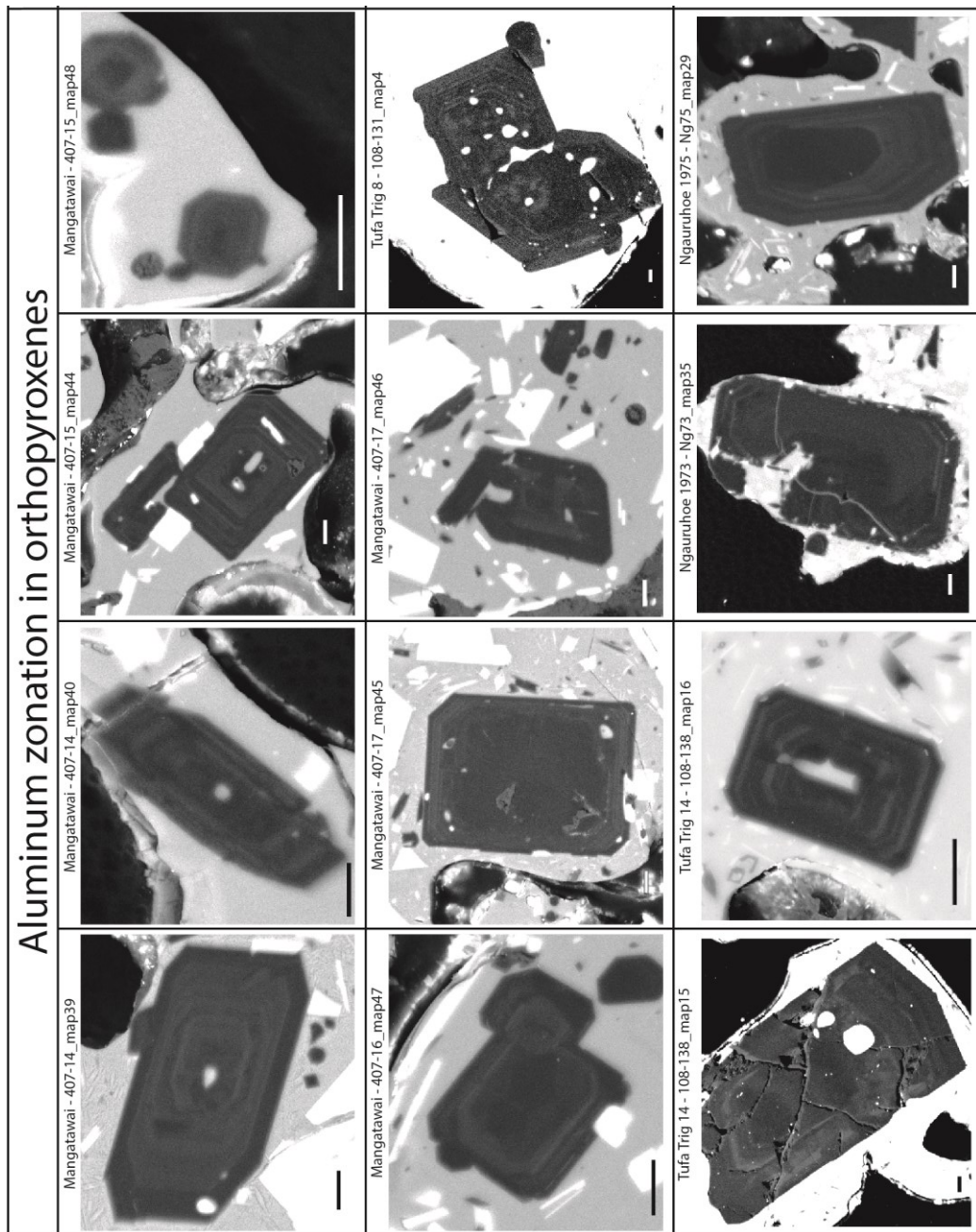
Appendix B10. Element maps and BSE images of pyroxene crystals with magnesian-core and calcic-rim. The white/black scale bar as the bottom left corner is 10 μm in length. Note that the Ca zonations are poorly visible in BSE image.



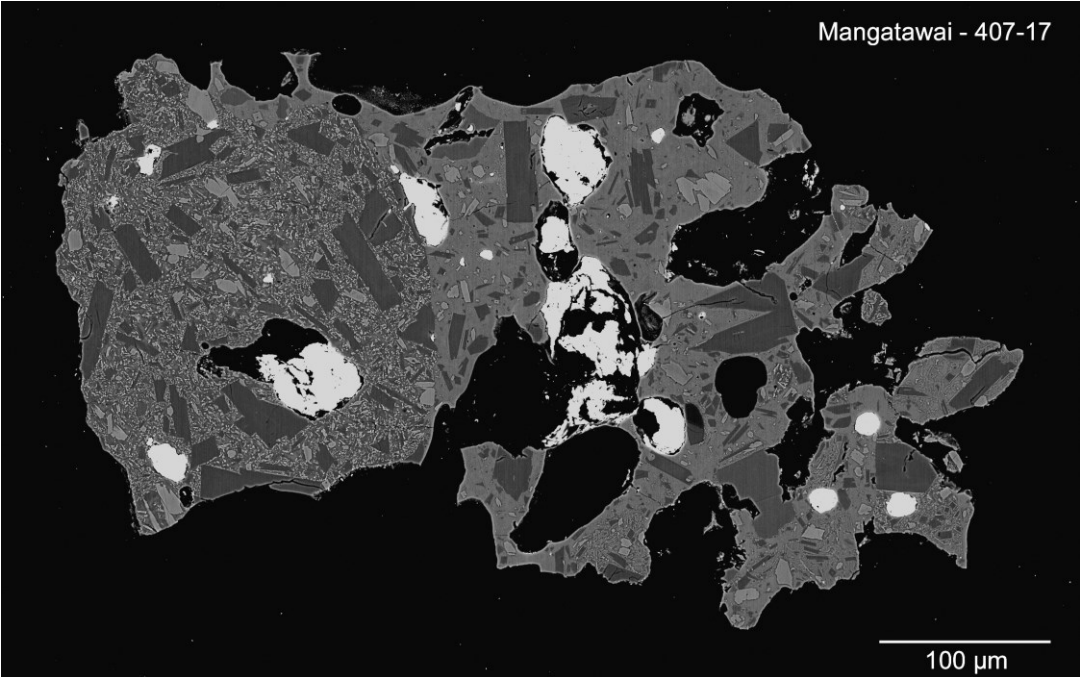
Appendix B11. Element maps of pyroxene crystals with fractures. The white scale bar as the bottom left corner is 10 μm in length.



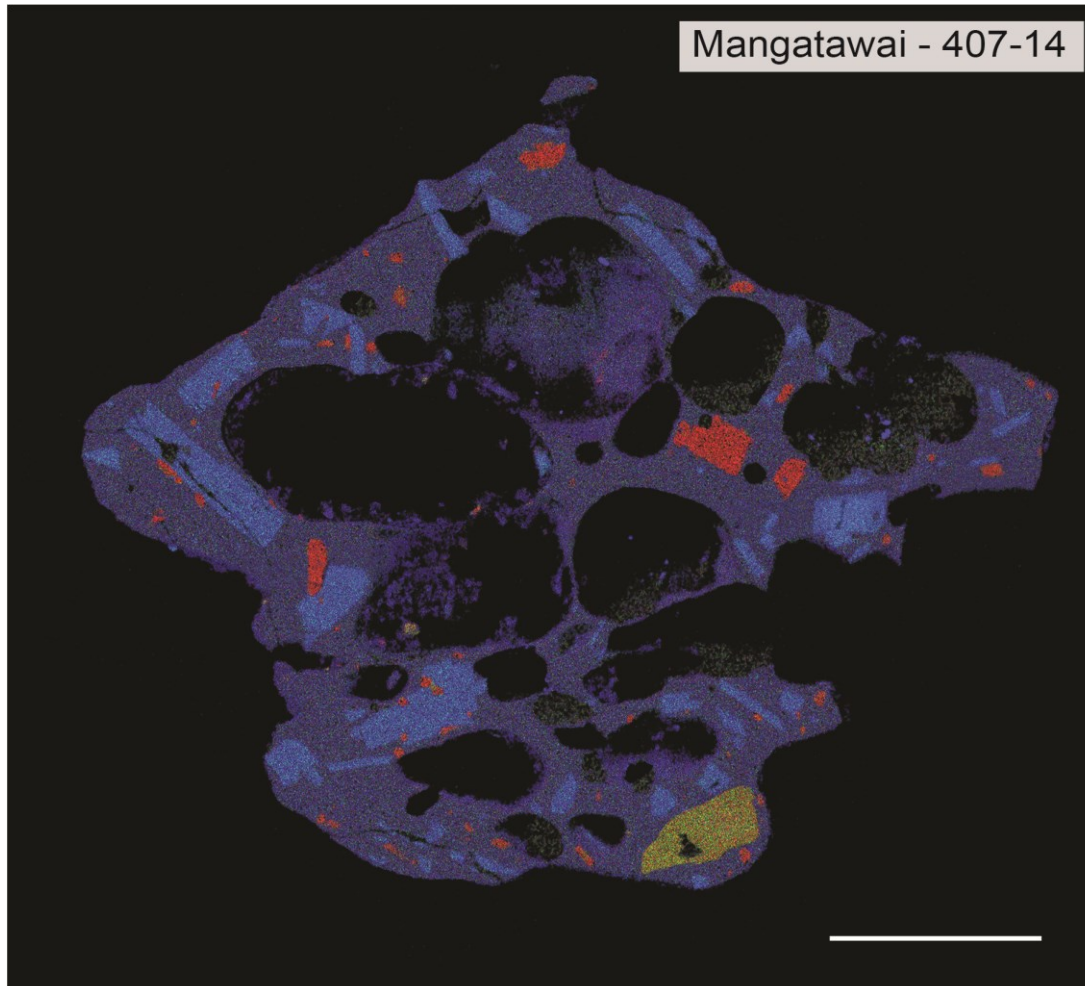
Appendix B12. Element maps of pyroxene crystals with fractures. The white/black scale bar as the bottom left corner is 10 μm in length.



Appendix B13. BSE image of a volcanic ash shard from Mangatawai (i.e., 407-17). Note the sharp contact between two different textures suggesting recycling of volcanic particle.



Appendix B14. Mg-Ca-Al chemical map of a Mangatawai glass shard imaged using the FE-SEM (JEOL JSM-7000F) at Hokkaido University, Japan. Plagioclases are in light blue, orthopyroxenes are in red and note the clinopyroxene in yellow, possibly antecryst or xenocryst. The white scale bar at the bottom right represents 100 μm .



Appendix C: Supplementary Tables

Appendix C1. Table 1 of Putirka (2008) describing the sample calculations for liquid components used to determine the orthopyroxene- and clinopyroxene-liquid thermobarometers (see section 3.5.1).

	SiO ₂	TiO ₂	Al ₂ O ₃	FeO	MnO	MgO	CaO	Na ₂ O	K ₂ O	total
1) Weight %	47.05	0.89	16.11	7.96	0.15	12.78	11.13	2.18	0.04	98.29
2) Molecular weights	60.08	79.9	101.96	71.85	70.94	40.3	56.08	61.98	94.2	
3) Mole proportions	0.7831	0.0111	0.1580	0.1108	0.0021	0.3171	0.1985	0.0352	0.0004	1.62
	$X_{SiO_2}^{liq}$	$X_{TiO_2}^{liq}$	$X_{Al_2O_3}^{liq}$	X_{FeO}^{liq}	X_{MnO}^{liq}	X_{MgO}^{liq}	X_{CaO}^{liq}	$X_{Na_2O}^{liq}$	$X_{K_2O}^{liq}$	
4) Mole fractions	0.4845	0.0069	0.0978	0.0685	0.0013	0.1962	0.1228	0.0218	0.0003	1.00
	SiO ₂	TiO ₂	AlO _{1.5}	FeO	MnO	MgO	CaO	NaO _{0.5}	KO _{0.5}	
5) Molecular weights	60.08	79.9	50.98	71.85	70.94	40.3	56.08	30.99	47.1	
6) Cation proportions	0.7831	0.0111	0.3160	0.1108	0.0021	0.3171	0.1985	0.0703	0.0008	1.81
	$X_{SiO_2}^{liq}$	$X_{TiO_2}^{liq}$	$X_{AlO_{1.5}}^{liq}$	X_{FeO}^{liq}	X_{MnO}^{liq}	X_{MgO}^{liq}	X_{CaO}^{liq}	$X_{NaO_{0.5}}^{liq}$	$X_{KO_{0.5}}^{liq}$	
7) Cation fractions	0.4327	0.0062	0.1746	0.0612	0.0012	0.1752	0.1096	0.0389	0.0005	1.00
			$C_{SiO_2}^{liq}$	C_{NM}^{liq}	C_{NF}^{liq}	NF				
8) Beattie (1993) components			0.4327	0.3472	0.4782	-0.7148				

Appendix C2. Table 1 of Putirka (2008) describing the sample calculations for orthopyroxene components used to determine the orthopyroxene-liquid thermobarometer (see section 3.5.1), based on six oxygens.

	SiO ₂	TiO ₂	Al ₂ O ₃	FeO	MnO	MgO	CaO	Na ₂ O	K ₂ O	Cr ₂ O ₃
1) Opx wt%	55.7	0.03	1.88	13.82	0	27.7	1.47	0.44	0	0
2) Mol wt	60.08	79.9	101.96	71.85	70.94	40.3	56.08	61.98	94.2	152.0
3) mole prop	0.9271	0.0004	0.0184	0.1923	0.0000	0.6873	0.0262	0.0071	0	0
4) # of oxygens	2(0.9271)	2(0.0004)	3(0.0184)	0.1923	0.00	0.6873	0.0262	0.0071	0.00	3(0.00)
5) # of oxygens	1.8542	0.0008	0.0553	0.1923	0.0000	0.6873	0.0262	0.0071	0.0000	0.0000
6) sum of row 5	2.8233									
7) ORF	6/(oxy sum) =	2.1252								
Cations on the basis of 6 oxygens										
	X _{Si} ^{opx}	X _{Ti} ^{opx}	X _{Al} ^{opx}	X _{Fe} ^{opx}	X _{Mn} ^{opx}	X _{Mg} ^{opx}	X _{Ca} ^{opx}	X _{Na} ^{opx}	X _K ^{opx}	X _{Cr} ^{opx}
8) cat/6 O	1.9703	0.0008	0.0784	0.4088	0	1.4607	0.0557	0.0302	0	0
9) cation sum	4.0048									
Orthopyroxene Components										
	X _{Al(IV)}} ^{opx}	X _{Al(VI)}} ^{opx}	X _{FeTiAlSiO₆} ^{opx}	X _{CrAl₂SiO₆} ^{opx}	X _{CaFms₂O₆} ^{opx}	X _{Fm₂Si₂O₆} ^{opx}	X _{Fm₂Si₂O₆} ^{opx}	X _{Fm₂Si₂O₆} ^{opx}	X _{Fm₂Si₂O₆} ^{opx}	total
10)	0.0297	0.0486	0.0008	0.0000	0.0185	0.0557	0.8973	0.0000	0.0302	1.0024

Appendix C3. Table 1 of Putirka (2008) describing the sample calculations for orthopyroxene components used to determine the orthopyroxene-liquid thermobarometer (see section 3.5.1), based on six oxygens.

	SiO ₂	TiO ₂	Al ₂ O ₃	FeO	MnO	MgO	CaO	Na ₂ O	K ₂ O	Cr ₂ O ₃
1) Cpx, wt%	52.5	0.33	1.58	9.89	0.24	13.29	22.5	0.37	0	0.05
2) mol. wt	60.08	79.9	101.96	71.85	70.94	40.3	56.08	61.98	94.2	152.0
3) mol. prop.	0.8738	0.0041	0.0155	0.1376	0.0034	0.3298	0.4012	0.0060	0.0000	0.0003
4) # of O	1.7477	0.0083	0.0465	0.1376	0.0034	0.3298	0.4012	0.0060	0.0000	0.0010
5) oxy sum	2.6814									
6) ORF	6/(oxy sum) =	2.2376								
Cations on the basis of 6 oxygens										
	X_{Si}^{cpx}	X_{Ti}^{cpx}	X_{Al}^{cpx}	X_{Fe}^{cpx}	X_{Mn}^{cpx}	X_{Mg}^{cpx}	X_{Ca}^{cpx}	X_{Na}^{cpx}	X_K^{cpx}	X_{Cr}^{cpx}
7) cat/6 Oxy	1.9553	0.0092	0.0694	0.3080	0.0076	0.7379	0.8978	0.0267	0.0000	0.0015
8) cation sum	4.0134									
Clinopyroxene Components										
	$X_{Al(IV)}^{cpx}$	$X_{Al(VI)}^{cpx}$	$X_{Fe(3+)}^{cpx}$	X_{Mg}^{cpx}	X_{CaTs}^{cpx}	X_{CaTi}^{cpx}	X_{CrCaTs}^{cpx}	X_{DiHd}^{cpx}	X_{EnFs}^{cpx}	total
9)	0.0447	0.0247	0.0268	0.0247	0.0000	0.0223	0.0007	0.8747	0.0856	1.0081

Appendix C4. Table 1a of Waters & Lange (2015) describing the albite thermodynamic data used in the hygrometer model (section 3.5.2)

Parameter	Value	Reference
T_f	1373 K	Boettcher et al. (1982)
$\Delta H_f(T_f)$	64.5 kJ/(mol·K)	Tenner et al. (2007)
$\Delta S_f(T_f)$	47.0 J/(mol·K)	Tenner et al. (2007)
C_p crystal	$393.64 - 2415.5T^{-0.5} - 7.8928 \cdot 10^6 T^{-2}$ $+ 1.07064 \cdot 10^9 T^{-3}$	Berman (1988)
C_p liquid	359 J/(mol·K)	Tenner et al. (2007)
V_{298K} crystal	100.57 cm ³ /mol	Wruck et al. (1991)
$\alpha(T)$ crystal	$2.68 \times 10^{-5} \text{ K}^{-1}$	Fei (1995)
$(\delta V/\delta P)^{\text{crystal}}$	-1.67 cm ³ /GPa	Tenner et al. (2007); Lange et al. (2009)
$V(T)$ liquid	$112.72 + 0.00382 (T-1373) \text{ cm}^3/\text{mol}$	Lange (1996)
$(\delta V/\delta P)^{\text{liquid}}$	$-6.379 - 0.00055 (T-1673) \text{ cm}^3/\text{GPa}$	Kress and Carmichael (1988)

Appendix C5. Table 1b of Waters & Lange (2015) describing the anorthite thermodynamic data used in the hygrometer model (section 3.5.2)

Parameter	Value	Reference
T_f	1373 K	Boettcher et al. (1982)
$\Delta H_f(T_f)$	64.5 kJ/(mol·K)	Tenner et al. (2007)
$\Delta S_f(T_f)$	47.0 J/(mol·K)	Tenner et al. (2007)
C_p crystal	$393.64 - 2415.5T^{-0.5} - 7.8928 \cdot 10^6 T^{-2} + 1.07064 \cdot 10^9 T^{-3}$	Berman (1988)
C_p liquid	359 J/(mol·K)	Tenner et al. (2007)
V_{298K} crystal	100.57 cm ³ /mol	Wruck et al. (1991)
$\alpha(T)$ crystal	$2.68 \times 10^{-5} \text{ K}^{-1}$	Fei (1995)
$(\delta V/\delta P)^{\text{crystal}}$	-1.67 cm ³ /GPa	Tenner et al. (2007); Lange et al. (2009)
$V(T)$ liquid	$112.72 + 0.00382 (T-1373) \text{ cm}^3/\text{mol}$	Lange (1996)
$(\delta V/\delta P)^{\text{liquid}}$	$-6.379 - 0.00055 (T-1673) \text{ cm}^3/\text{GPa}$	Kress and Carmichael (1988)

Appendix C6. Table 2 of Waters & Lange (2015) describing the model parameters used by the plagioclase-liquid hygrometer (section 3.5.2)

Parameter	Value	Reference
T_f	1373 K	Boettcher et al. (1982)
$\Delta H_f(T_f)$	64.5 kJ/(mol·K)	Tenner et al. (2007)
$\Delta S_f(T_f)$	47.0 J/(mol·K)	Tenner et al. (2007)
C_p crystal	$393.64 - 2415.5T^{-0.5} - 7.8928 \cdot 10^6 T^{-2} + 1.07064 \cdot 10^9 T^{-3}$	Berman (1988)
C_p liquid	359 J/(mol·K)	Tenner et al. (2007)
V_{298K} crystal	100.57 cm ³ /mol	Wruck et al. (1991)
$\alpha(T)$ crystal	$2.68 \times 10^{-5} \text{ K}^{-1}$	Fei (1995)
$(\delta V/\delta P)^{\text{crystal}}$	-1.67 cm ³ /GPa	Tenner et al. (2007); Lange et al. (2009)
$V(T)$ liquid	$112.72 + 0.00382 (T-1373) \text{ cm}^3/\text{mol}$	Lange (1996)
$(\delta V/\delta P)^{\text{liquid}}$	$-6.379 - 0.00055 (T-1673) \text{ cm}^3/\text{GPa}$	Kress and Carmichael (1988)

Appendix C7. Microprobe analyses of glass from intermediate tephra of the Tongariro Volcanic Centre. Mangatawai and Tufa Trig glasses were analysed using a JEOL JXA-8900R electron microprobe equipped with four wavelength-dispersive spectrometers at the Institute of Earth Sciences, Academia Sinica, Taipei, Taiwan. Ngauruhoe 1972-1975 and Ruapehu 1995-1996 glasses were analysed using a JEOL JXA-8800R electron microprobe equipped with four wavelength-dispersive spectrometers at the Graduate School of Science, Hokkaido University, Sapporo, Japan.

Tephra formation/sequence	Comment	SiO ₂	TiO ₂	Al ₂ O ₃	FeO	MgO	CaO	K ₂ O	Na ₂ O	Cr ₂ O ₃	P ₂ O ₅	Total
MANGATAWAI												
Mangatawai Lower	No14-10	59.91	1.13	13.94	9.38	2.84	6.25	3.38	1.54	0.00		98.36
	No14-11	59.90	1.15	14.19	8.84	2.74	6.24	3.25	1.58	0.01		97.89
	No14-12	60.72	1.04	13.97	9.38	2.74	5.73	3.19	1.46	0.01		98.23
	No14-21	54.71	0.63	20.44	6.06	2.65	9.93	2.74	0.98	0.00		98.14
	No14-51	58.68	1.17	13.99	9.02	2.92	6.54	2.48	1.71	0.03		96.54
	No15-2	59.97	1.13	14.36	8.23	2.61	6.54	3.04	1.77	0.00		97.65
	No15-9	60.05	1.30	13.60	9.57	2.48	6.03	2.06	1.88	0.01		96.98
	No15-12	60.02	1.24	13.43	9.64	2.44	5.84	1.97	1.90	0.00		96.48
	No15-14	58.55	1.07	14.49	8.79	3.21	6.71	2.38	1.59	0.00		96.78
	No15-15	58.39	0.99	14.78	8.49	3.16	6.71	2.12	1.60	0.00		96.26
	No15-17	58.60	0.96	14.67	8.78	3.26	6.68	2.43	1.54	0.00		96.90
	No15-22	58.65	1.08	14.48	8.72	3.17	6.75	2.34	1.60	0.00		96.79
	No15-41	59.06	1.04	14.28	8.74	3.08	6.59	2.19	1.63	0.00		96.61
	No15-52	59.67	1.20	13.83	8.85	2.74	6.21	2.22	1.78	0.03		96.52

Mangatawai Upper

No15-80	59.77	1.11	14.49	8.31	3.10	6.73	2.34	1.69	0.00	97.53
No15-81	59.05	1.07	14.54	8.54	3.23	6.67	2.38	1.62	0.00	97.09
No15-82	58.68	0.98	14.71	8.31	3.05	6.74	2.22	1.60	0.01	96.30
No16-9	60.42	1.22	13.99	8.89	2.51	6.33	2.47	1.80	0.00	97.63
No16-10	60.47	1.41	13.41	9.40	2.46	6.26	2.13	1.88	0.01	97.42
No16-21	61.44	1.34	13.23	9.22	2.36	5.81	2.53	2.00	0.00	97.93
No16-36	60.73	1.08	16.28	6.94	2.03	6.81	3.49	1.50	0.00	98.86
No16-75	60.40	1.22	14.19	8.49	2.92	5.89	2.37	2.28	0.00	97.76
No17-2	59.13	1.11	13.87	9.52	2.78	6.50	2.20	1.73	0.01	96.84
No17-47	60.97	1.32	13.06	9.15	2.48	5.74	1.63	2.16	0.00	96.50
No17-80	58.11	1.25	14.37	9.74	2.71	7.05	2.57	1.77	0.01	97.57
No18-15	58.87	1.15	14.17	9.54	2.91	6.81	1.96	1.46	0.00	96.86
No18-22	58.19	1.08	14.43	9.02	3.31	6.55	1.46	3.55	0.00	97.59
No18-42	59.66	1.40	13.52	8.81	2.52	6.14	2.52	2.03	0.02	96.62
No18-44	59.03	1.21	14.02	9.24	2.49	6.15	2.32	1.84	0.00	96.29
No18-48	58.60	1.14	14.37	8.92	2.76	6.47	2.25	1.77	0.00	96.27
No18-51	59.77	1.25	13.10	9.65	2.69	6.13	1.48	2.12	0.00	96.18
No47-12	60.59	1.03	14.17	8.07	2.81	6.04	2.61	1.89	0.00	97.20
No47-13	60.46	1.11	14.25	7.94	2.83	6.18	2.18	1.73	0.00	96.67
No47-14	60.23	1.00	14.29	8.23	2.91	6.01	2.53	1.76	0.00	96.97
No47-37	61.05	1.11	13.51	8.45	2.41	5.79	2.35	1.96	0.00	96.62
No49-5	63.17	1.34	13.00	9.27	1.40	5.01	2.64	2.43	0.02	98.28
No49-12	61.03	1.21	13.80	8.53	2.45	5.94	2.40	1.92	0.03	97.30

No49-13	61.36	1.12	13.94	8.42	2.70	5.97	2.36	1.94	0.00	97.80
No49-18	60.00	1.09	14.70	7.87	3.03	6.97	3.72	1.30	0.00	98.66
No49-32	60.81	1.19	13.93	8.29	2.58	5.79	2.57	1.94	0.01	97.12
No54-13	61.04	1.39	13.46	8.73	2.04	5.93	2.65	2.05	0.00	97.29
No54-25	59.89	1.19	13.32	8.70	2.89	6.11	2.27	1.77	0.00	96.14
No54-26	60.06	1.21	13.40	8.83	2.74	6.13	2.40	1.79	0.03	96.58
No54-27	60.40	1.26	13.40	8.90	2.78	6.38	2.29	1.76	0.00	97.17
No54-38	60.11	1.08	14.15	8.17	2.82	6.49	2.78	1.56	0.01	97.16
No54-39	59.65	1.08	13.73	8.68	2.93	6.35	2.41	1.63	0.01	96.46
No54-40	60.25	1.22	13.61	8.72	2.95	6.43	2.48	1.77	0.02	97.46
No54-41	60.31	1.27	13.54	8.73	2.82	6.29	2.39	1.81	0.00	97.15
No56-15	60.73	1.11	13.67	8.31	2.90	6.19	2.43	1.99	0.00	97.33
No56-18	60.83	1.12	13.66	8.13	2.66	6.20	2.39	1.96	0.00	96.96
No56-19	59.71	1.10	13.09	8.79	3.69	6.36	2.34	1.80	0.01	96.88
No56-20	62.15	1.24	13.50	7.90	2.38	5.82	2.45	2.01	0.00	97.43
No56-21	61.71	1.14	13.75	8.21	2.51	6.05	2.61	1.91	0.00	97.90
No56-22	61.12	1.21	13.86	8.12	2.63	5.99	2.58	2.00	0.00	97.52
No56-28	61.30	1.13	14.02	8.15	2.62	6.11	2.42	1.96	0.00	97.70
No56-29	60.70	1.15	13.72	8.59	2.67	6.12	2.50	1.99	0.00	97.44
No56-30	60.41	1.16	14.09	8.23	2.74	6.34	2.41	1.87	0.00	97.23
No56-34	60.40	1.12	14.10	8.49	2.70	6.17	2.53	1.91	0.00	97.41
No56-35	60.45	1.12	14.23	8.53	2.74	6.38	2.55	1.91	0.00	97.90
No56-40	62.31	1.32	12.99	8.50	2.09	5.45	1.79	2.17	0.00	96.62

TUFA TRIG

Tufa Trig 8

No56-42	60.97	1.16	14.11	8.14	2.72	5.52	2.43	2.16	0.00	97.21
No56-45	60.52	1.32	12.70	9.03	3.25	5.62	2.14	2.02	0.00	96.59
No56-46	61.68	1.33	13.10	8.46	2.46	5.94	2.29	2.04	0.01	97.31
No59-1	60.31	1.07	14.14	8.37	2.66	6.17	2.44	1.96	0.00	97.13
No59-2	60.12	1.02	14.27	8.10	2.66	6.19	2.38	1.84	0.00	96.58
No59-20	60.43	1.13	14.17	8.80	2.45	6.29	2.87	1.84	0.00	97.97
No59-22	59.78	1.17	13.57	9.20	2.82	6.31	3.13	1.93	0.00	97.89
No59-28	59.15	1.11	14.86	7.97	2.84	6.44	2.94	1.79	0.00	97.09
No59-36	60.14	1.13	13.98	7.73	2.71	5.10	1.98	3.09	0.02	95.89
No59-37	60.48	1.23	14.01	8.33	2.97	5.42	2.24	2.48	0.00	97.16

Tufa Trig 13

No131-3	61.36	1.07	15.03	6.39	2.60	5.53	2.43	2.12	0.02	96.56
No131-5	61.73	0.91	14.69	6.56	2.34	5.24	2.43	2.32	0.02	96.23
No131-26	63.19	1.00	14.25	6.31	2.25	4.46	3.79	2.10	0.00	97.35
No131-49	62.51	0.86	15.09	6.58	2.15	5.25	3.32	2.11	0.00	97.86
No131-51	62.17	0.91	14.71	6.90	2.36	5.02	2.58	2.54	0.00	97.19
No131-82	61.86	0.89	14.98	6.70	2.47	4.83	2.55	2.30	0.02	96.61
No137-12	62.04	1.10	14.82	7.05	2.23	4.96	2.64	2.61	0.02	97.45
No137-14	60.76	0.91	14.70	7.45	2.41	5.04	2.66	2.52	0.00	96.45
No137-26	62.17	0.99	14.22	6.76	2.12	4.77	2.70	3.05	0.00	96.78
No137-29	62.12	0.92	14.75	6.46	2.28	4.92	2.78	3.05	0.06	97.34
No137-71	62.35	0.97	14.71	6.72	2.09	4.97	2.52	2.60	0.00	96.93
No137-72	61.78	0.85	14.82	6.63	2.23	4.94	2.33	2.56	0.00	96.14

	No137-73	61.64	0.95	14.72	6.65	2.14	4.88	2.46	2.55	0.00	95.98
	No137-74	62.06	0.98	14.88	6.49	2.21	4.88	2.44	2.57	0.02	96.53
Tufa Trig 14	No138-1	62.04	1.09	14.56	6.87	2.20	4.81	2.68	2.56	0.00	96.81
	No138-4	62.85	1.03	14.73	6.75	2.13	4.93	2.35	2.51	0.00	97.27
	No138-47	62.94	0.99	15.19	6.25	2.06	4.56	3.77	2.48	0.00	98.22
	No138-100	62.35	1.04	15.01	6.73	2.20	5.17	1.85	2.64	0.03	97.02
	No138-101	62.21	1.04	15.19	6.79	2.23	4.79	1.97	2.65	0.00	96.87
	No138-102	61.95	1.08	15.07	7.05	2.22	4.95	2.06	2.74	0.00	97.13
	No138-103	61.89	1.12	14.56	7.11	2.60	4.96	1.82	2.29	0.00	96.35
Tufa Trig 15	No139-2	60.84	1.03	14.69	6.73	2.35	4.86	2.77	2.92	0.00	96.18
	No139-19	61.89	0.62	18.29	3.70	0.91	6.02	4.20	1.64	0.04	97.30
	No139-39	61.78	1.02	14.78	6.88	2.34	5.03	2.60	2.63	0.00	97.05
	No139-45	62.24	0.91	14.60	7.04	2.69	5.01	2.29	2.40	0.00	97.18
	No139-48	61.82	0.92	14.68	6.60	2.22	4.91	2.37	2.63	0.00	96.15
	No139-50	61.95	0.94	14.58	6.94	2.17	4.83	2.45	2.52	0.00	96.38
	No139-59	61.85	0.91	14.85	6.87	2.20	4.87	2.27	2.58	0.00	96.41
	No139-64	62.16	0.93	14.70	6.91	2.25	4.98	2.30	2.62	0.00	96.84
	No139-89	62.11	0.90	14.74	6.98	2.10	4.89	2.88	2.61	0.00	97.21
Tufa Trig 16	No140-48	60.93	0.95	14.94	7.25	2.71	5.65	2.37	2.08	0.01	96.89
	No140-49	60.60	0.90	14.70	7.17	2.58	5.66	2.29	2.11	0.01	96.01

1972-1975

NGAURUHOE

1972 Ngauruhoe	Ng72#1	60.93	1.40	13.34	8.85	2.38	5.86	3.62	2.57	0.30	98.96
	Ng72#7	61.09	1.36	12.09	9.76	3.66	5.82	3.31	2.29	0.24	99.38
	Ng72#8	62.35	1.45	13.20	8.96	2.37	5.64	3.34	2.54	0.30	99.86
	Ng72#9	62.15	1.35	13.27	8.95	2.27	5.77	3.41	2.55	0.28	99.72
	Ng72#12	61.88	1.41	13.86	8.65	2.38	5.92	3.46	2.33	0.28	99.88
	Ng72#13	62.34	1.33	13.46	8.94	2.49	5.84	3.52	2.41	0.30	100.33
1973 Ngauruhoe	Ng73#4	63.70	1.46	13.27	8.90	2.21	5.93	3.84	2.22	0.29	101.51
	Ng73#8	62.77	1.36	14.35	8.43	1.81	5.55	3.28	2.47	0.31	100.02
	Ng73#10	63.22	1.48	13.54	9.14	1.90	5.28	3.31	2.67	0.31	100.54
	Ng73#11	64.19	1.57	13.18	8.91	1.68	4.89	3.24	3.16	0.26	100.81
	Ng73#16	64.71	1.56	13.23	8.80	1.68	5.07	3.59	2.95	0.23	101.59
1974 Ngauruhoe	Ng74#3	64.16	1.44	14.14	8.64	1.58	5.45	3.79	1.65	0.27	100.85
	Ng74#8	64.77	1.50	13.50	8.73	1.57	4.81	3.39	3.01	0.31	101.28
	Ng74#12	63.91	1.45	13.48	8.62	1.65	5.18	3.17	2.81	0.26	100.26
	Ng74#14	63.81	1.42	12.83	9.62	2.56	4.95	3.30	2.49	0.33	100.98
	Ng74#19	64.29	1.50	13.19	9.24	1.54	4.83	3.63	2.69	0.25	100.92
1975 Ngauruhoe	Ng75#2	61.25	1.14	14.77	8.65	2.42	5.95	3.47	2.01	0.18	99.65
	Ng75#10	64.64	1.11	14.08	7.43	1.64	4.76	3.55	2.52	0.27	99.72
	Ng75#13	66.27	1.11	13.23	7.25	1.32	4.20	3.69	2.83	0.31	99.89

1995-1996 RUAPEHU

1995 Ruapehu	Rua95#1	63.76	1.03	15.04	6.19	2.35	5.11	3.93	2.64	0.21	100.03
--------------	---------	-------	------	-------	------	------	------	------	------	------	---------------

1996 Ruapehu

Rua95#8	62.06	0.91	15.69	5.97	2.95	5.89	3.90	2.27		0.17	99.64
Rua95#9	63.29	0.96	15.33	6.21	2.49	5.26	4.01	2.71		0.20	100.25
Rua96#6	64.11	1.19	14.28	6.70	2.01	4.85	3.39	2.89		0.18	99.42
Rua96#9	63.59	1.07	14.91	6.46	2.19	5.18	3.73	2.72		0.19	99.85
Rua96#16	63.21	1.03	15.12	6.43	2.11	5.23	3.87	2.74		0.23	99.74
Minimum	54.71	0.62	12.09	3.70	0.91	4.20	1.46	0.98	0.00	0.17	95.89
Maximum	66.27	1.57	20.44	9.76	3.69	9.93	4.20	3.55	0.06	0.33	101.59
Average	61.18	1.14	14.21	8.04	2.49	5.76	2.70	2.16	0.01	0.26	97.69
Std. dev.	1.69	0.18	0.95	1.09	0.46	0.76	0.59	0.46	0.01	0.05	1.40

Appendix C8. Microprobe analyses of plagioclase from intermediate tephras of the Tongariro Volcanic Centre. Mangatawai and Tufa Trig glasses were analysed using a JEOL JXA-8900R electron microprobe equipped with four wavelength-dispersive spectrometers at the Institute of Earth Sciences, Academia Sinica, Taipei, Taiwan. Ngauruhoe 1972-1975 and Ruapehu 1995-1996 glasses were analysed using a JEOL JXA-8800R electron microprobe equipped with four wavelength-dispersive spectrometers at the Graduate School of Science, Hokkaido University, Sapporo, Japan.

Tephra formation/sequence	Comment	SiO ₂	TiO ₂	Al ₂ O ₃	FeO	MgO	CaO	K ₂ O	Na ₂ O	Cr ₂ O ₃	P ₂ O ₅	Total
MANGATAWAI												
Mangatawai Lower	No14-6	50.93	0.06	30.29	0.01	0.61	0.00	0.14	13.72	3.45	0.13	99.34
	No14-7	48.38	0.00	32.21	0.00	0.64	0.03	0.11	15.65	2.29	0.07	99.38
	No14-8	51.36	0.07	30.09	0.01	0.73	0.00	0.13	13.60	3.33	0.15	99.46
	No14-9	49.94	0.09	30.68	0.00	0.71	0.00	0.14	14.62	2.93	0.11	99.21
	No14-19	53.37	0.01	28.38	0.00	0.71	0.04	0.16	12.07	4.11	0.18	99.02
	No14-22	50.06	0.02	30.79	0.00	0.69	0.00	0.12	14.77	2.99	0.10	99.53
	No14-23	48.53	0.03	32.11	0.00	0.86	0.05	0.15	15.83	2.25	0.08	99.88
	No14-24	51.99	0.02	29.52	0.00	0.91	0.00	0.19	13.36	3.59	0.13	99.70
	No14-27	53.84	0.05	28.15	0.05	0.90	0.01	0.23	11.62	4.32	0.22	99.40
	No14-29	52.21	0.03	28.91	0.00	0.89	0.00	0.18	12.70	3.98	0.17	99.08
	No14-39	52.42	0.04	28.77	0.00	0.96	0.00	0.16	12.54	3.95	0.17	99.01
	No14-40	48.75	0.03	32.02	0.00	0.68	0.04	0.14	15.30	2.39	0.08	99.42
	No14-41	48.32	0.00	32.01	0.00	0.63	0.00	0.16	15.47	2.56	0.06	99.21
	No14-48	50.02	0.02	30.96	0.00	0.85	0.00	0.16	14.89	2.79	0.14	99.84
	No14-49	52.98	0.04	29.14	0.00	0.93	0.00	0.18	12.58	4.00	0.19	100.05
	No14-50	50.25	0.10	30.59	0.00	0.69	0.00	0.13	14.21	3.17	0.10	99.25

No14-56	50.65	0.07	30.47	0.02	0.81	0.02	0.15	14.44	3.17	0.10	99.89
No14-57	47.89	0.03	32.31	0.00	0.80	0.02	0.13	16.00	2.07	0.09	99.34
No15-3	47.50	0.04	32.66	0.00	0.69	0.00	0.11	16.25	2.08	0.06	99.39
No15-4	47.41	0.05	32.50	0.00	0.80	0.00	0.14	16.31	2.20	0.08	99.49
No15-5	52.75	0.08	28.83	0.00	0.95	0.00	0.17	12.40	4.02	0.21	99.40
No15-7	53.39	0.10	28.07	0.00	0.96	0.00	0.16	12.02	4.08	0.24	99.03
No15-8	53.27	0.09	28.19	0.00	0.84	0.02	0.15	11.83	4.42	0.24	99.04
No15-10	53.34	0.04	28.63	0.00	0.92	0.00	0.16	12.11	4.10	0.20	99.49
No15-16	50.95	0.05	30.26	0.03	0.89	0.00	0.13	13.98	3.09	0.15	99.52
No15-21	53.42	0.00	28.50	0.00	0.95	0.06	0.19	12.14	4.17	0.24	99.67
No15-25	47.53	0.07	32.54	0.00	0.78	0.04	0.15	16.33	2.07	0.09	99.58
No15-31	51.87	0.05	30.35	0.00	0.92	0.02	0.16	13.66	3.42	0.13	100.57
No15-32	47.60	0.03	33.05	0.00	0.77	0.00	0.10	16.56	2.03	0.07	100.20
No15-33	54.10	0.09	28.58	0.00	0.91	0.00	0.22	12.40	4.08	0.21	100.58
No15-35	54.08	0.02	28.44	0.02	0.98	0.00	0.17	12.13	4.25	0.22	100.31
No15-38	53.07	0.03	29.91	0.00	0.80	0.00	0.19	13.21	3.71	0.15	101.07
No15-39	53.01	0.05	28.77	0.00	0.96	0.00	0.17	12.54	4.02	0.19	99.71
No15-42	51.25	0.07	30.36	0.00	0.69	0.00	0.16	14.12	3.20	0.12	99.98
No15-43	54.14	0.07	28.52	0.02	1.01	0.00	0.18	12.07	4.29	0.21	100.51
No15-51	53.61	0.10	28.61	0.00	0.90	0.05	0.20	12.47	4.13	0.25	100.32
No15-53	53.89	0.09	27.68	0.01	0.84	0.00	0.13	11.70	4.47	0.24	99.05
No15-56	49.59	0.09	31.12	0.00	0.83	0.02	0.18	14.74	2.76	0.10	99.44
No15-57	53.44	0.04	28.54	0.00	1.00	0.00	0.21	12.33	3.90	0.20	99.66
No15-58	53.64	0.06	28.63	0.00	0.81	0.00	0.19	12.37	4.05	0.23	99.98

No15-59	49.79	0.03	31.11	0.00	0.89	0.03	0.14	14.87	2.89	0.13	99.88
No15-60	50.64	0.04	30.22	0.00	0.79	0.04	0.19	14.14	3.19	0.12	99.38
No15-61	49.99	0.01	31.10	0.00	0.71	0.00	0.14	14.67	2.87	0.14	99.62
No15-62	48.13	0.01	32.55	0.00	0.69	0.04	0.13	16.12	2.04	0.06	99.78
No15-68	50.18	0.05	30.83	0.00	0.78	0.01	0.15	14.38	3.02	0.13	99.52
No15-69	47.84	0.00	32.64	0.01	0.76	0.04	0.12	16.66	1.96	0.07	100.08
No15-70	48.22	0.00	32.16	0.02	0.63	0.00	0.12	15.73	2.17	0.07	99.12
No15-71	47.47	0.00	32.82	0.01	0.68	0.05	0.13	16.58	1.77	0.06	99.55
No15-72	48.73	0.07	32.12	0.00	0.61	0.01	0.14	15.95	2.21	0.06	99.90
No15-75	48.96	0.00	32.22	0.02	0.89	0.00	0.15	15.81	2.32	0.08	100.45
No15-76	50.03	0.05	31.03	0.00	0.81	0.02	0.13	15.02	2.75	0.11	99.95
No15-78	51.57	0.04	30.48	0.01	1.00	0.01	0.18	13.88	3.29	0.14	100.60
No15-79	48.66	0.04	31.73	0.00	1.08	0.00	0.30	16.09	2.00	0.14	100.04
No15-83	53.92	0.05	27.90	0.00	1.12	0.01	0.29	12.05	4.28	0.27	99.87
No15-84	54.23	0.03	28.13	0.00	0.86	0.05	0.18	12.15	4.34	0.21	100.19
No16-1	54.18	0.06	28.10	0.00	0.88	0.01	0.13	11.92	4.34	0.24	99.85
No16-3	53.85	0.04	28.62	0.00	0.78	0.03	0.13	11.92	4.14	0.24	99.75
No16-4	53.35	0.07	28.89	0.00	0.97	0.00	0.21	12.64	3.95	0.23	100.30
No16-6	54.54	0.05	28.59	0.00	0.97	0.00	0.13	12.14	4.17	0.23	100.82
No16-8	54.01	0.06	28.25	0.00	0.94	0.00	0.18	12.15	4.21	0.24	100.03
No16-11	50.53	0.08	30.60	0.00	0.83	0.00	0.18	14.39	3.02	0.10	99.73
No16-12	51.56	0.02	29.98	0.00	0.82	0.00	0.20	13.87	3.39	0.15	100.00
No16-13	46.94	0.04	33.01	0.03	0.62	0.06	0.07	17.06	1.67	0.05	99.53
No16-14	52.38	0.06	29.64	0.00	0.70	0.04	0.17	13.52	3.59	0.13	100.22

No16-16	54.67	0.02	28.14	0.00	0.84	0.00	0.14	11.67	4.22	0.22	99.92
No16-18	53.86	0.08	28.09	0.00	0.82	0.00	0.17	11.97	4.24	0.22	99.46
No16-19	54.23	0.05	28.12	0.00	0.92	0.00	0.15	11.89	4.28	0.26	99.89
No16-20	53.11	0.06	28.74	0.00	1.10	0.05	0.20	12.64	4.06	0.22	100.18
No16-23	52.00	0.05	29.66	0.01	0.85	0.00	0.18	13.35	3.53	0.17	99.79
No16-24	49.95	0.01	30.92	0.00	0.80	0.00	0.14	15.28	2.71	0.10	99.91
No16-25	50.83	0.01	30.23	0.00	0.87	0.00	0.17	13.93	3.24	0.13	99.41
No16-27	53.45	0.03	28.66	0.00	0.85	0.02	0.19	12.53	4.07	0.20	99.99
No16-28	51.19	0.02	30.29	0.00	0.87	0.04	0.18	14.37	3.01	0.14	100.12
No16-31	53.58	0.19	27.15	0.02	2.01	0.03	0.70	12.70	3.65	0.31	100.34
No16-32	52.51	0.32	2.50	0.28	7.14	0.15	16.66	19.99	0.22	0.00	99.77
No16-33	52.46	0.04	29.60	0.00	0.84	0.01	0.17	13.56	3.57	0.14	100.37
No16-40	49.84	0.05	31.37	0.00	0.83	0.00	0.12	14.84	2.76	0.13	99.93
No16-41	50.17	0.08	31.22	0.00	0.86	0.00	0.14	14.90	2.74	0.13	100.24
No16-42	53.02	0.07	28.98	0.00	1.02	0.04	0.19	12.98	3.87	0.20	100.36
No16-43	54.41	0.03	28.12	0.00	0.95	0.00	0.18	11.93	4.17	0.21	99.98
No16-44	53.97	0.00	28.18	0.01	1.04	0.00	0.17	11.97	4.32	0.21	99.86
No16-47	54.39	0.04	27.72	0.04	0.89	0.02	0.17	11.83	4.37	0.27	99.73
No16-48	49.02	0.08	31.86	0.00	0.82	0.00	0.15	15.60	2.32	0.07	99.92
No16-49	51.25	0.05	30.75	0.00	0.91	0.03	0.18	14.54	3.15	0.13	100.98
No16-50	54.31	0.07	27.98	0.01	0.96	0.00	0.16	11.88	4.47	0.23	100.08
No16-52	50.70	0.01	30.24	0.00	0.81	0.00	0.18	14.40	3.04	0.12	99.50
No16-53	47.77	0.00	32.66	0.01	0.62	0.06	0.09	17.01	1.75	0.05	100.01
No16-54	47.25	0.00	32.99	0.00	0.67	0.00	0.10	17.09	1.74	0.03	99.87

No16-64	49.87	0.02	31.17	0.00	0.76	0.01	0.16	15.39	2.80	0.11	100.27
No16-65	46.64	0.01	33.35	0.01	0.56	0.00	0.11	17.34	1.68	0.03	99.73
No16-66	47.49	0.01	32.60	0.01	0.59	0.01	0.11	16.96	1.89	0.06	99.73
No16-67	47.86	0.04	32.68	0.00	0.63	0.02	0.11	16.42	1.93	0.06	99.75
No16-68	46.35	0.05	33.66	0.00	0.67	0.00	0.10	17.52	1.49	0.04	99.88
No16-69	51.88	0.07	30.24	0.00	0.92	0.00	0.14	13.88	3.41	0.17	100.71
No16-70	53.62	0.00	28.35	0.00	0.93	0.00	0.16	12.07	4.29	0.26	99.69
No16-71	54.12	0.03	28.31	0.00	0.95	0.02	0.17	12.11	4.34	0.22	100.26
No16-72	51.17	0.15	30.44	0.00	0.92	0.04	0.17	14.33	3.19	0.10	100.50
No16-73	51.23	0.05	29.88	0.00	0.83	0.00	0.16	13.92	3.42	0.13	99.62
No16-81	53.76	0.02	28.36	0.00	0.78	0.00	0.17	11.97	4.30	0.23	99.59
No17-1	51.84	0.05	29.78	0.01	0.86	0.00	0.17	13.38	3.61	0.16	99.86
No17-5	51.10	0.04	30.82	0.01	0.97	0.01	0.12	14.56	3.25	0.11	100.98
No17-6	51.47	0.00	30.72	0.00	0.96	0.03	0.16	14.38	3.31	0.15	101.18
No17-7	52.87	0.09	29.51	0.00	0.68	0.04	0.08	12.85	3.74	0.15	100.00
No17-8	51.14	0.05	30.17	0.00	0.90	0.04	0.14	14.06	3.30	0.13	99.90
No17-11	53.00	0.08	28.81	0.02	0.93	0.02	0.16	13.09	3.87	0.19	100.17
No17-12	52.81	0.08	29.15	0.00	0.76	0.04	0.11	12.79	3.89	0.15	99.77
No17-13	50.91	0.03	30.10	0.00	0.78	0.00	0.12	13.88	3.29	0.12	99.23
No17-15	51.67	0.06	29.10	0.00	0.90	0.00	0.16	13.46	3.62	0.17	99.13
No17-16	52.64	0.06	29.03	0.00	0.87	0.00	0.17	12.94	3.92	0.15	99.78
No17-21	46.48	0.04	33.60	0.00	0.47	0.03	0.08	17.50	1.40	0.06	99.65
No17-22	46.69	0.02	33.03	0.00	0.65	0.00	0.06	17.46	1.63	0.04	99.58
No17-23	51.02	0.00	30.26	0.02	0.76	0.00	0.16	13.97	3.32	0.10	99.61

No17-24	51.25	0.01	30.46	0.00	0.90	0.11	0.19	14.05	3.10	0.12	100.18
No17-25	52.15	0.06	29.88	0.00	1.01	0.00	0.20	13.55	3.47	0.11	100.42
No17-28	51.27	0.07	30.30	0.00	0.86	0.04	0.17	13.91	3.30	0.10	100.02
No17-29	46.94	0.00	33.46	0.00	0.70	0.00	0.08	17.32	1.51	0.03	100.03
No17-30	54.22	0.02	28.49	0.01	0.98	0.00	0.21	12.03	4.20	0.18	100.34
No17-31	51.00	0.05	30.90	0.00	0.79	0.00	0.13	14.48	3.05	0.11	100.50
No17-32	53.03	0.04	28.87	0.01	0.85	0.00	0.17	12.90	3.91	0.17	99.93
No17-33	51.08	0.03	30.20	0.00	0.80	0.00	0.12	14.40	3.12	0.13	99.89
No17-34	50.80	0.05	30.10	0.00	0.89	0.00	0.15	14.05	3.17	0.12	99.33
No17-36	50.25	0.02	30.39	0.00	0.83	0.00	0.13	14.73	2.97	0.08	99.39
No17-37	47.95	0.00	32.74	0.00	0.60	0.00	0.10	16.45	2.01	0.04	99.89
No17-38	48.12	0.00	32.75	0.00	0.70	0.02	0.09	16.68	1.90	0.07	100.33
No17-39	52.29	0.01	29.66	0.00	0.84	0.00	0.18	13.49	3.64	0.16	100.28
No17-40	52.47	0.05	28.98	0.00	0.71	0.05	0.17	13.08	3.70	0.12	99.33
No17-41	50.96	0.06	30.22	0.02	0.81	0.00	0.09	14.31	3.23	0.14	99.85
No17-42	51.46	0.07	29.84	0.00	0.90	0.06	0.13	13.47	3.62	0.14	99.67
No17-43	53.39	0.09	28.88	0.00	1.04	0.05	0.15	12.55	3.99	0.20	100.34
No17-44	52.36	0.01	29.27	0.00	0.84	0.00	0.20	13.39	3.59	0.14	99.81
No17-45	52.49	0.08	28.83	0.02	0.96	0.06	0.16	13.21	3.86	0.19	99.86
No17-46	47.89	0.00	32.55	0.00	0.86	0.03	0.09	16.77	1.94	0.07	100.20
No17-57	46.95	0.01	33.01	0.02	0.67	0.03	0.09	17.52	1.68	0.06	100.03
No17-58	47.58	0.01	33.37	0.02	0.67	0.02	0.10	17.25	1.66	0.05	100.73
No17-59	47.06	0.07	33.32	0.00	0.62	0.01	0.08	17.03	1.71	0.03	99.93
No17-61	51.12	0.07	30.27	0.00	0.62	0.00	0.16	14.24	3.14	0.10	99.72

No17-62	53.57	0.06	28.44	0.00	0.86	0.00	0.15	12.29	4.20	0.22	99.79
No17-64	52.27	0.06	28.86	0.00	1.00	0.00	0.21	13.19	3.46	0.18	99.23
No17-65	49.82	0.03	31.23	0.00	0.80	0.00	0.17	15.18	2.67	0.10	100.00
No17-66	50.78	0.07	30.58	0.00	0.78	0.00	0.18	14.51	3.05	0.11	100.05
No17-67	48.66	0.00	32.40	0.00	0.64	0.00	0.10	16.08	2.21	0.03	100.12
No17-68	46.88	0.03	32.93	0.00	0.60	0.00	0.10	16.72	1.80	0.04	99.10
No17-70	46.77	0.08	33.30	0.00	0.61	0.00	0.13	16.92	1.74	0.04	99.60
No17-71	48.60	0.04	32.42	0.00	0.61	0.03	0.14	16.04	2.17	0.07	100.11
No17-72	47.03	0.02	33.40	0.00	0.52	0.01	0.10	17.27	1.59	0.07	100.01
No17-73	47.40	0.03	33.51	0.03	0.61	0.00	0.07	17.38	1.57	0.03	100.62
No17-74	52.48	0.01	28.99	0.00	0.92	0.00	0.15	12.82	3.90	0.19	99.47
No17-75	53.10	0.04	28.92	0.04	0.81	0.02	0.22	12.86	3.93	0.16	100.08
No17-77	52.29	0.00	29.51	0.00	1.00	0.00	0.21	13.22	3.70	0.13	100.05
No17-81	55.75	0.12	26.18	0.03	1.94	0.01	1.00	10.60	4.49	0.42	100.54
No17-82	53.31	0.05	29.07	0.00	0.97	0.03	0.19	12.85	3.94	0.20	100.60
No17-83	46.79	0.05	33.08	0.01	0.67	0.01	0.08	17.34	1.67	0.04	99.73
No17-84	47.14	0.02	32.98	0.04	0.61	0.02	0.11	17.10	1.67	0.07	99.75
No17-85	47.07	0.00	32.99	0.02	0.58	0.01	0.09	17.05	1.71	0.05	99.57
No17-86	51.02	0.03	30.68	0.00	0.86	0.04	0.14	14.10	3.22	0.15	100.23
No18-7	53.34	0.08	28.72	0.00	0.80	0.01	0.11	12.45	4.16	0.21	99.88
No18-8	51.01	0.00	30.38	0.00	0.71	0.00	0.15	13.87	3.35	0.14	99.61
No18-9	51.56	0.06	29.49	0.00	1.09	0.00	0.16	13.47	3.58	0.18	99.59
No18-12	51.56	0.06	29.54	0.00	0.99	0.00	0.14	13.16	3.76	0.19	99.39
No18-16	51.23	0.00	29.61	0.00	0.87	0.00	0.27	13.67	3.37	0.17	99.20

No18-17	52.87	0.11	28.80	0.02	0.87	0.00	0.16	12.55	4.15	0.21	99.73
No18-18	51.14	0.08	29.56	0.00	0.84	0.04	0.19	13.43	3.62	0.15	99.04
No18-19	51.46	0.00	29.47	0.00	0.79	0.00	0.17	13.63	3.61	0.15	99.27
No18-23	52.89	0.04	28.79	0.00	0.91	0.00	0.16	12.39	4.21	0.21	99.59
No18-24	52.51	0.05	28.71	0.03	0.79	0.01	0.17	12.67	3.86	0.22	99.02
No18-25	53.67	0.05	28.39	0.00	0.81	0.00	0.14	11.77	4.27	0.22	99.33
No18-37	53.08	0.05	28.45	0.00	1.01	0.00	0.16	12.16	4.31	0.25	99.47
No18-38	51.45	0.09	29.25	0.00	1.13	0.00	0.21	13.24	3.84	0.21	99.40
No18-40	49.87	0.00	30.73	0.05	0.86	0.01	0.13	14.20	3.09	0.14	99.09
No18-41	54.12	0.03	28.27	0.00	0.87	0.00	0.18	11.95	4.29	0.25	99.97
No18-43	51.90	0.03	29.37	0.00	0.65	0.05	0.18	13.25	3.83	0.13	99.39
No18-45	52.01	0.00	28.93	0.00	0.89	0.02	0.25	12.81	3.97	0.16	99.02
No18-52	46.23	0.01	33.94	0.04	0.59	0.00	0.08	17.33	1.56	0.02	99.79
No18-53	51.67	0.09	29.19	0.00	0.69	0.02	0.18	13.07	4.06	0.14	99.09
No18-55	50.29	0.00	30.27	0.01	0.80	0.00	0.12	14.01	3.42	0.12	99.04
No18-61	49.80	0.05	30.95	0.00	0.71	0.00	0.18	14.46	3.01	0.10	99.25
No18-62	46.21	0.02	33.71	0.03	0.77	0.00	0.10	17.49	1.70	0.03	100.05
No18-63	51.07	0.04	29.92	0.00	0.86	0.01	0.18	13.61	3.47	0.16	99.32
No18-65	46.22	0.03	33.13	0.00	0.55	0.00	0.11	17.54	1.50	0.05	99.12
No18-66	46.23	0.03	33.75	0.00	0.60	0.03	0.11	17.53	1.61	0.03	99.90
No18-67	46.64	0.02	33.17	0.00	0.47	0.08	0.10	16.78	1.90	0.05	99.20
No18-68	46.55	0.08	32.85	0.00	0.57	0.00	0.11	16.90	1.98	0.05	99.08
No18-72	45.89	0.00	33.47	0.00	0.73	0.00	0.11	17.42	1.60	0.03	99.25
No18-74	52.01	0.06	29.37	0.00	0.99	0.00	0.19	12.63	3.86	0.19	99.29

Mangatawai Upper

No18-78	52.76	0.09	28.49	0.00	0.94	0.00	0.20	12.45	4.25	0.25	99.44
No18-81	47.23	0.05	32.42	0.00	0.70	0.02	0.10	16.22	2.24	0.07	99.05
No18-82	46.27	0.02	33.29	0.01	0.62	0.00	0.09	17.18	1.74	0.02	99.24
No18-83	46.40	0.04	33.14	0.00	0.62	0.01	0.13	17.02	1.83	0.04	99.22
No18-84	46.16	0.04	33.55	0.00	0.58	0.00	0.12	17.37	1.61	0.04	99.47
No18-86	47.09	0.01	33.11	0.00	0.60	0.01	0.07	16.68	1.94	0.04	99.53
No18-87	51.88	0.01	29.15	0.00	1.05	0.00	0.17	13.08	3.85	0.16	99.36
No18-89	47.10	0.05	32.68	0.00	0.64	0.04	0.10	16.74	1.86	0.05	99.26
No18-98	52.72	0.07	28.61	0.02	1.03	0.00	0.20	12.56	4.10	0.21	99.50
No18-100	52.03	0.06	28.87	0.00	1.09	0.04	0.24	12.79	4.09	0.15	99.36
No47-1	51.53	0.03	30.84	0.00	0.79	0.02	0.17	14.16	3.11	0.13	100.77
No47-2	53.91	0.05	29.18	0.00	0.96	0.00	0.20	12.69	3.93	0.23	101.15
No47-3	51.27	0.05	30.73	0.02	0.81	0.00	0.10	14.30	3.07	0.11	100.45
No47-4	54.65	0.04	28.24	0.02	0.84	0.00	0.14	11.61	4.34	0.20	100.08
No47-5	55.10	0.02	28.26	0.03	0.60	0.00	0.15	11.46	4.41	0.20	100.21
No47-6	52.18	0.00	30.21	0.00	0.65	0.00	0.11	13.68	3.28	0.14	100.25
No47-7	49.86	0.00	31.02	0.00	0.71	0.00	0.11	15.07	2.44	0.11	99.31
No47-8	52.71	0.06	29.22	0.02	0.68	0.00	0.10	12.97	3.72	0.16	99.62
No47-9	54.88	0.08	28.42	0.00	0.62	0.03	0.14	11.53	4.41	0.23	100.32
No47-10	53.44	0.03	28.90	0.00	0.78	0.00	0.15	12.94	3.85	0.19	100.29
No47-11	54.17	0.02	28.30	0.00	0.81	0.05	0.16	11.93	4.25	0.20	99.89
No47-22	57.25	0.09	26.61	0.00	0.80	0.01	0.11	9.77	5.42	0.36	100.42
No47-23	56.38	0.00	27.53	0.00	0.69	0.00	0.13	10.76	4.99	0.33	100.82
No47-25	52.41	0.05	30.12	0.00	0.82	0.00	0.12	13.43	3.52	0.15	100.61

No47-27	52.91	0.04	29.56	0.00	1.02	0.03	0.17	12.88	3.64	0.16	100.41
No47-28	52.72	0.00	29.34	0.00	0.82	0.00	0.17	13.01	3.75	0.19	99.98
No47-29	51.27	0.09	30.63	0.00	0.65	0.02	0.08	14.31	2.96	0.09	100.10
No47-30	52.49	0.04	29.89	0.00	0.69	0.00	0.13	13.45	3.66	0.16	100.51
No47-31	49.58	0.08	31.73	0.00	0.63	0.02	0.13	15.71	2.36	0.08	100.30
No47-32	51.56	0.03	30.56	0.00	0.75	0.01	0.13	13.78	3.21	0.12	100.13
No47-33	52.49	0.05	29.83	0.00	0.62	0.00	0.12	13.05	3.46	0.16	99.78
No47-34	52.12	0.09	30.41	0.01	0.60	0.00	0.08	13.86	3.32	0.16	100.65
No47-35	54.96	0.04	28.79	0.00	0.67	0.00	0.12	11.88	4.20	0.21	100.87
No47-36	55.03	0.06	27.98	0.01	0.99	0.00	0.23	11.56	4.43	0.25	100.52
No47-38	52.55	0.04	29.81	0.00	0.73	0.00	0.15	13.37	3.42	0.14	100.21
No47-39	54.37	0.02	28.27	0.03	0.66	0.00	0.07	12.11	4.25	0.21	100.01
No47-40	51.18	0.03	30.68	0.00	0.73	0.03	0.08	14.44	3.07	0.15	100.40
No47-41	51.62	0.02	30.25	0.00	0.68	0.01	0.11	14.11	3.20	0.12	100.13
No47-42	53.28	0.05	29.44	0.00	0.65	0.00	0.14	13.00	3.65	0.16	100.36
No47-43	53.20	0.06	29.66	0.00	0.77	0.07	0.11	12.98	3.81	0.19	100.84
No47-44	51.45	0.02	30.70	0.02	0.77	0.00	0.13	14.46	3.01	0.11	100.67
No47-45	48.46	0.02	32.59	0.00	0.71	0.06	0.07	16.64	1.73	0.07	100.34
No47-46	48.81	0.06	32.21	0.00	0.75	0.00	0.10	16.05	2.06	0.09	100.13
No47-49	52.40	0.03	29.92	0.00	0.78	0.00	0.14	13.70	3.49	0.15	100.61
No47-50	51.87	0.02	30.52	0.00	0.79	0.00	0.09	13.77	3.32	0.13	100.51
No47-51	52.85	0.05	29.33	0.00	0.93	0.00	0.12	13.15	3.65	0.18	100.25
No47-52	54.54	0.03	28.23	0.00	0.99	0.02	0.14	12.06	4.24	0.19	100.43
No49-1	52.67	0.01	29.92	0.00	0.79	0.00	0.15	13.49	3.50	0.17	100.69

No49-2	52.89	0.04	29.53	0.01	0.84	0.00	0.11	13.37	3.63	0.16	100.57
No49-3	51.33	0.03	30.85	0.00	0.74	0.00	0.10	14.48	2.90	0.14	100.57
No49-4	56.08	0.06	28.05	0.00	1.07	0.07	0.29	11.28	4.45	0.26	101.60
No49-14	55.85	0.05	27.79	0.00	0.91	0.00	0.18	11.33	4.49	0.26	100.86
No49-15	55.75	0.09	28.06	0.00	0.88	0.05	0.16	11.62	4.63	0.28	101.51
No49-16	60.58	1.11	14.73	0.00	7.73	0.16	3.09	6.87	3.68	1.36	99.30
No49-17	61.05	1.01	14.79	0.00	7.53	0.14	3.00	6.91	3.91	1.27	99.61
No49-19	59.34	0.90	14.45	0.00	8.43	0.16	3.97	8.51	3.12	1.34	100.21
No49-20	61.04	0.97	15.04	0.00	8.12	0.14	3.13	6.21	3.83	1.35	99.81
No49-22	52.93	0.03	29.41	0.05	0.86	0.00	0.10	12.89	3.87	0.18	100.32
No49-23	53.99	0.05	29.49	0.00	0.79	0.03	0.14	12.58	3.98	0.21	101.25
No49-24	54.40	0.09	28.79	0.01	0.82	0.00	0.09	12.30	4.29	0.21	101.00
No49-25	52.36	0.02	30.42	0.00	0.73	0.00	0.15	13.93	3.13	0.16	100.90
No49-26	53.39	0.00	29.39	0.00	0.69	0.00	0.13	12.99	3.77	0.18	100.53
No49-27	54.33	0.05	28.56	0.00	0.67	0.00	0.14	12.24	4.25	0.24	100.47
No49-28	47.44	0.05	33.12	0.00	0.63	0.00	0.07	16.93	1.62	0.02	99.88
No49-29	52.85	0.00	29.18	0.02	0.73	0.00	0.15	12.75	4.03	0.20	99.91
No49-34	51.55	0.09	29.94	0.00	0.88	0.00	0.15	13.36	3.57	0.15	99.69
No49-35	50.56	0.05	30.34	0.01	0.82	0.01	0.10	14.19	3.02	0.13	99.21
No49-37	51.99	0.06	29.42	0.00	0.87	0.02	0.13	12.88	3.68	0.19	99.25
No49-43	51.60	0.09	29.93	0.00	0.78	0.00	0.13	13.16	3.54	0.18	99.42
No54-3	52.51	0.05	29.77	0.00	0.91	0.07	0.13	13.94	3.60	0.16	101.12
No54-4	51.75	0.02	29.93	0.00	0.79	0.00	0.14	13.95	3.39	0.18	100.16
No54-5	49.36	0.00	31.03	0.00	0.72	0.00	0.09	15.20	2.61	0.13	99.15

No54-6	53.01	0.05	29.18	0.00	0.74	0.00	0.13	12.98	3.95	0.18	100.21
No54-8	51.99	0.03	29.87	0.05	1.00	0.00	0.13	13.83	3.47	0.19	100.56
No54-10	50.89	0.07	29.83	0.00	0.91	0.04	0.12	14.08	3.03	0.13	99.09
No54-14	52.93	0.04	28.80	0.03	0.98	0.00	0.14	13.47	3.73	0.18	100.30
No54-15	52.50	0.06	29.49	0.00	0.88	0.00	0.14	13.33	3.66	0.19	100.24
No54-16	53.50	0.04	28.75	0.00	0.70	0.00	0.14	12.73	4.03	0.17	100.06
No54-17	52.57	0.05	29.08	0.00	0.64	0.00	0.14	13.17	3.83	0.16	99.63
No54-18	52.28	0.00	29.52	0.00	0.78	0.00	0.11	13.49	3.56	0.18	99.91
No54-19	51.70	0.07	29.64	0.00	0.67	0.05	0.11	13.96	3.40	0.14	99.76
No54-20	52.04	0.07	30.06	0.00	0.81	0.00	0.13	13.83	3.44	0.13	100.50
No54-21	50.49	0.03	30.73	0.00	0.74	0.00	0.11	14.68	2.98	0.13	99.90
No54-22	52.68	0.08	29.69	0.00	0.85	0.00	0.13	13.54	3.77	0.18	100.91
No54-28	51.91	0.06	29.80	0.00	0.88	0.00	0.12	14.04	3.41	0.18	100.39
No54-29	52.51	0.08	29.06	0.00	0.72	0.00	0.09	13.45	3.62	0.14	99.67
No54-30	51.87	0.04	29.51	0.00	0.72	0.04	0.13	13.88	3.43	0.14	99.76
No54-31	52.47	0.02	29.08	0.01	0.69	0.00	0.12	13.17	3.73	0.18	99.48
No54-32	51.07	0.04	29.94	0.00	0.80	0.02	0.15	14.28	3.21	0.14	99.64
No54-33	51.85	0.00	29.92	0.04	0.80	0.04	0.15	13.78	3.47	0.14	100.19
No54-34	55.15	0.11	27.00	0.00	1.05	0.00	0.22	11.67	4.38	0.30	99.90
No54-42	52.19	0.06	29.16	0.00	0.97	0.00	0.13	13.49	3.67	0.17	99.85
No54-43	51.60	0.00	30.29	0.00	0.72	0.00	0.12	14.28	3.37	0.14	100.52
No54-44	52.01	0.07	29.24	0.00	0.83	0.01	0.11	13.38	3.64	0.19	99.49
No54-45	53.21	0.04	29.22	0.00	0.85	0.00	0.12	13.10	3.62	0.17	100.34
No54-46	53.71	0.03	28.47	0.00	0.84	0.01	0.09	12.48	4.08	0.22	99.93

No54-47	52.12	0.00	29.40	0.00	0.81	0.00	0.14	13.27	3.51	0.17	99.41
No54-48	52.07	0.02	29.68	0.00	0.83	0.00	0.10	13.77	3.46	0.16	100.09
No54-49	52.37	0.03	29.45	0.02	0.91	0.01	0.13	13.24	3.64	0.17	99.97
No56-1	50.81	0.01	29.87	0.00	0.79	0.01	0.12	13.95	3.30	0.15	99.01
No56-2	51.43	0.03	29.46	0.03	0.84	0.01	0.11	14.12	3.41	0.14	99.58
No56-3	52.30	0.02	29.02	0.00	0.73	0.00	0.12	12.92	3.94	0.18	99.22
No56-4	52.60	0.03	28.96	0.00	0.81	0.03	0.11	13.45	3.75	0.19	99.92
No56-5	52.26	0.07	28.65	0.00	0.79	0.00	0.12	13.14	3.85	0.21	99.08
No56-6	52.06	0.06	29.58	0.01	0.88	0.00	0.12	13.80	3.59	0.19	100.29
No56-7	52.30	0.04	29.08	0.01	0.79	0.01	0.14	13.07	3.89	0.19	99.52
No56-10	54.27	0.03	27.82	0.00	0.74	0.07	0.14	12.77	4.02	0.22	100.09
No56-12	52.14	0.10	28.50	0.00	0.97	0.02	0.18	13.99	3.29	0.18	99.37
No56-16	53.45	0.03	27.75	0.00	0.90	0.00	0.17	12.96	3.79	0.19	99.23
No56-23	55.50	0.07	26.92	0.00	0.98	0.06	0.20	11.45	4.47	0.28	99.92
No56-24	54.97	0.09	27.30	0.00	0.94	0.05	0.18	11.91	4.53	0.26	100.21
No56-25	53.07	0.08	28.73	0.00	0.78	0.01	0.13	13.46	3.70	0.19	100.15
No56-26	53.46	0.06	28.87	0.00	0.70	0.00	0.15	13.49	3.68	0.19	100.61
No56-27	52.61	0.04	29.04	0.01	0.80	0.06	0.12	13.60	3.59	0.15	100.02
No56-31	52.20	0.01	29.21	0.00	0.82	0.02	0.08	13.81	3.38	0.16	99.68
No56-32	50.08	0.03	31.13	0.00	0.77	0.02	0.10	15.45	2.65	0.10	100.32
No56-33	51.70	0.00	29.35	0.00	0.72	0.00	0.12	13.73	3.51	0.19	99.33
No56-37	52.13	0.04	29.62	0.00	0.93	0.00	0.13	13.65	3.39	0.14	100.03
No56-38	51.72	0.09	29.89	0.01	0.84	0.02	0.15	13.94	3.22	0.15	100.02
No56-39	53.15	0.05	28.55	0.05	0.80	0.03	0.15	12.68	4.14	0.20	99.79

No56-41	55.32	0.04	27.37	0.00	0.96	0.00	0.17	11.36	4.53	0.28	100.03
No56-43	51.20	0.00	29.99	0.00	0.77	0.00	0.09	14.05	3.25	0.17	99.52
No56-44	52.33	0.00	29.76	0.01	0.85	0.00	0.13	13.46	3.42	0.16	100.12
No59-3	53.18	0.04	29.53	0.00	0.85	0.00	0.12	13.24	3.78	0.21	100.94
No59-4	55.29	0.09	27.78	0.00	0.94	0.00	0.10	11.61	4.76	0.31	100.86
No59-11	52.17	0.03	30.01	0.00	0.71	0.00	0.04	14.29	3.41	0.14	100.79
No59-17	54.58	0.12	27.35	0.00	1.36	0.00	0.34	12.24	4.15	0.30	100.44
No59-21	50.64	0.04	30.69	0.02	0.68	0.00	0.10	14.77	3.01	0.13	100.08
No59-23	50.92	0.05	30.38	0.05	0.82	0.01	0.13	14.42	3.20	0.14	100.11
No59-24	51.15	0.03	29.85	0.00	0.69	0.01	0.12	13.70	3.57	0.15	99.26
No59-25	50.75	0.02	30.73	0.00	0.71	0.01	0.11	14.51	3.20	0.16	100.20
No59-26	51.40	0.03	29.96	0.00	0.82	0.00	0.12	14.02	3.37	0.17	99.89
No59-27	53.60	0.09	28.68	0.00	0.96	0.00	0.17	12.43	4.15	0.22	100.28
No59-29	53.49	0.06	28.12	0.00	0.68	0.03	0.10	12.07	4.39	0.24	99.16
No59-30	52.24	0.07	29.15	0.01	0.72	0.03	0.13	13.02	3.90	0.15	99.43
No59-31	52.99	0.00	28.77	0.00	0.74	0.00	0.10	12.56	4.17	0.19	99.52
No59-33	52.16	0.07	28.92	0.00	0.89	0.00	0.12	13.09	3.83	0.18	99.27
No59-34	52.61	0.08	28.95	0.01	1.00	0.00	0.13	12.83	4.01	0.22	99.82
No59-35	51.13	0.08	29.50	0.01	0.91	0.04	0.09	13.60	3.59	0.19	99.13
No59-38	49.82	0.02	30.89	0.04	0.85	0.00	0.09	15.06	2.81	0.14	99.71
No59-41	54.06	0.08	28.26	0.04	0.84	0.00	0.14	12.09	4.30	0.23	100.04
No59-42	53.66	0.07	28.28	0.01	0.85	0.03	0.16	12.43	4.12	0.20	99.81
No59-44	50.25	0.08	30.40	0.00	0.83	0.05	0.10	14.30	3.33	0.14	99.46

TUFA TRIG

Tufa Trig 8

No131-2	53.80	0.00	27.79	0.00	0.85	0.02	0.17	11.97	4.39	0.28	99.26
No131-4	54.32	0.04	27.77	0.03	0.91	0.01	0.17	11.69	4.51	0.28	99.72
No131-11	54.18	0.08	27.60	0.01	0.74	0.03	0.12	11.38	4.68	0.29	99.12
No131-12	53.82	0.05	27.65	0.00	0.86	0.02	0.16	11.66	4.62	0.29	99.13
No131-13	50.34	0.04	30.80	0.00	0.57	0.01	0.11	14.42	3.09	0.15	99.53
No131-14	49.77	0.00	31.22	0.00	0.68	0.03	0.09	14.78	2.91	0.14	99.63
No131-16	53.40	0.04	28.56	0.00	0.78	0.00	0.14	12.39	4.12	0.20	99.63
No131-17	53.39	0.06	28.12	0.00	0.86	0.04	0.12	12.00	4.42	0.25	99.25
No131-18	54.18	0.05	27.61	0.00	0.86	0.00	0.14	11.33	4.67	0.26	99.09
No131-19	53.32	0.04	28.86	0.00	0.73	0.00	0.16	12.23	4.10	0.20	99.65
No131-22	54.08	0.05	28.24	0.00	0.78	0.00	0.14	11.75	4.51	0.28	99.83
No131-23	55.05	0.09	27.17	0.00	0.82	0.04	0.15	10.75	4.93	0.35	99.35
No131-27	54.36	0.07	27.73	0.03	0.87	0.00	0.17	11.52	4.60	0.28	99.63
No131-28	53.78	0.10	27.78	0.00	0.83	0.00	0.14	11.61	4.53	0.26	99.04
No131-36	53.26	0.18	0.69	0.00	17.18	0.36	25.58	2.02	0.04	0.00	99.31
No131-37	54.26	0.12	27.66	0.01	0.92	0.05	0.13	11.09	4.76	0.35	99.34
No131-38	54.60	0.04	27.56	0.00	0.84	0.00	0.14	11.11	4.70	0.30	99.29
No131-39	53.09	0.00	28.61	0.00	0.82	0.04	0.11	12.38	4.04	0.21	99.30
No131-40	57.31	0.38	23.44	0.02	3.05	0.04	0.83	9.54	3.62	0.91	99.14
No131-41	53.49	0.05	28.43	0.02	0.65	0.00	0.08	11.90	4.27	0.25	99.14
No131-42	51.45	0.06	29.79	0.00	0.68	0.00	0.08	13.25	3.75	0.18	99.22
No131-43	52.71	0.06	28.96	0.00	0.63	0.04	0.12	12.32	4.21	0.25	99.30
No131-57	53.46	0.08	28.76	0.00	0.82	0.00	0.16	12.12	4.04	0.23	99.66
No131-58	55.90	0.08	26.89	0.00	0.67	0.00	0.08	10.42	5.17	0.38	99.59

Tufa Trig 13

No131-61	51.69	0.56	2.12	0.05	8.90	0.20	16.30	19.17	0.27	0.00	99.25
No131-64	51.94	0.01	29.76	0.00	0.66	0.00	0.12	13.05	3.50	0.20	99.24
No131-65	53.63	0.06	28.44	0.00	0.75	0.00	0.12	11.61	4.29	0.28	99.17
No131-66	53.54	0.04	28.31	0.04	0.76	0.00	0.15	11.97	4.38	0.24	99.44
No131-67	54.36	0.09	27.50	0.00	0.91	0.03	0.13	11.26	4.75	0.31	99.33
No131-71	54.54	0.04	28.17	0.00	0.72	0.06	0.13	11.30	4.62	0.28	99.85
No131-72	53.13	0.05	28.62	0.00	0.74	0.00	0.14	12.31	4.26	0.22	99.47
No131-73	53.74	0.03	28.16	0.00	0.79	0.00	0.11	11.85	4.46	0.28	99.42
No131-75	53.04	0.01	28.60	0.00	0.85	0.01	0.12	12.27	4.32	0.21	99.44
No131-79	52.31	0.03	29.16	0.00	0.59	0.00	0.12	12.98	3.76	0.21	99.15
No131-80	52.40	0.08	29.11	0.01	0.61	0.00	0.13	12.94	3.71	0.23	99.22
No131-86	55.00	0.10	27.84	0.00	1.02	0.00	0.14	10.75	4.58	0.30	99.74
No131-87	53.43	0.06	28.70	0.00	0.86	0.00	0.14	11.69	4.16	0.23	99.26
No131-88	54.51	0.07	27.72	0.00	0.82	0.03	0.15	11.40	4.59	0.26	99.53
No131-89	52.56	0.03	29.32	0.00	0.85	0.00	0.11	13.01	3.84	0.18	99.89
No131-90	51.91	0.05	29.87	0.00	0.70	0.00	0.11	13.50	3.76	0.21	100.10
No131-100	52.99	0.06	28.66	0.00	0.82	0.02	0.13	12.48	4.11	0.25	99.52
No131-101	53.88	0.07	28.04	0.00	0.85	0.04	0.13	11.51	4.51	0.22	99.24
No131-104	54.76	0.05	27.13	0.00	0.97	0.00	0.16	11.05	4.82	0.29	99.22
No137-8	55.12	0.08	27.62	0.00	0.97	0.00	0.12	11.12	4.87	0.38	100.27
No137-19	51.37	0.28	4.03	0.32	6.77	0.16	19.07	17.05	0.28	0.00	99.32
No137-20	53.01	0.05	28.46	0.00	0.81	0.03	0.10	12.12	4.43	0.24	99.25
No137-21	53.30	0.06	28.73	0.00	0.79	0.00	0.11	11.97	4.36	0.27	99.58
No137-27	53.00	0.04	28.96	0.00	0.75	0.01	0.13	12.47	4.09	0.29	99.72

No137-28	53.54	0.06	28.57	0.00	0.64	0.00	0.09	12.06	4.29	0.34	99.60
No137-30	55.63	0.05	27.08	0.00	0.59	0.02	0.10	10.38	5.28	0.35	99.48
No137-31	53.04	0.05	28.92	0.00	0.56	0.00	0.04	12.62	4.19	0.25	99.66
No137-32	53.77	0.07	28.71	0.00	0.70	0.00	0.07	11.79	4.37	0.29	99.75
No137-33	54.62	0.10	27.79	0.00	0.58	0.00	0.06	11.20	4.81	0.34	99.48
No137-34	54.64	0.08	27.75	0.00	0.63	0.00	0.06	11.07	4.84	0.37	99.44
No137-35	53.68	0.08	28.37	0.01	0.63	0.00	0.06	11.68	4.40	0.28	99.19
No137-36	53.29	0.10	28.37	0.00	0.69	0.00	0.11	12.14	4.40	0.27	99.36
No137-41	52.88	0.10	29.03	0.00	0.72	0.00	0.12	12.92	3.99	0.25	100.01
No137-45	53.12	0.07	28.05	0.00	0.83	0.00	0.15	12.56	4.13	0.28	99.20
No137-54	55.75	0.04	26.58	0.00	0.66	0.00	0.08	10.53	5.14	0.38	99.15
No137-57	53.95	0.03	27.59	0.02	0.73	0.00	0.12	11.94	4.57	0.27	99.22
No137-59	53.85	0.06	27.77	0.01	0.78	0.00	0.13	11.84	4.43	0.30	99.18
No137-61	53.80	0.05	27.87	0.00	0.79	0.00	0.07	11.98	4.39	0.25	99.19
No137-62	53.49	0.04	28.24	0.00	0.67	0.00	0.10	12.22	4.44	0.31	99.51
No137-64	52.67	0.05	29.07	0.00	0.74	0.01	0.09	12.76	4.05	0.28	99.72
No137-65	52.67	0.07	29.20	0.00	0.68	0.02	0.09	12.72	4.03	0.29	99.77
No137-68	53.14	0.05	28.90	0.02	0.94	0.00	0.08	12.31	4.20	0.25	99.87
No137-69	53.37	0.10	27.83	0.02	0.98	0.01	0.18	12.03	4.19	0.32	99.02
No137-82	53.09	0.09	28.67	0.00	0.76	0.00	0.13	12.42	4.22	0.27	99.65
No137-83	54.22	0.02	27.66	0.01	0.75	0.02	0.09	11.58	4.64	0.30	99.29
No137-84	51.90	0.03	29.79	0.00	0.67	0.00	0.13	13.26	3.79	0.14	99.71
No137-85	54.25	0.07	28.16	0.04	0.58	0.00	0.08	11.47	4.71	0.29	99.64
No137-86	53.07	0.03	29.58	0.00	0.66	0.00	0.13	13.11	3.94	0.20	100.71

Tufa Trig 14

No138-2	53.86	0.12	27.74	0.01	0.95	0.03	0.12	11.83	4.52	0.30	99.48
No138-6	53.52	0.06	28.40	0.00	0.76	0.09	0.12	12.20	4.42	0.29	99.85
No138-7	54.62	0.10	27.59	0.04	0.77	0.01	0.12	11.32	4.72	0.28	99.58
No138-8	54.19	0.11	28.11	0.00	0.84	0.01	0.12	11.77	4.60	0.30	100.05
No138-12	53.69	0.09	27.78	0.00	0.90	0.00	0.17	11.39	4.67	0.33	99.01
No138-24	53.73	0.06	28.62	0.00	0.75	0.00	0.11	11.93	4.33	0.27	99.79
No138-25	51.62	0.04	30.11	0.00	0.64	0.00	0.11	13.46	3.52	0.20	99.70
No138-26	49.24	0.01	31.25	0.00	0.58	0.02	0.11	15.29	2.74	0.14	99.37
No138-27	49.94	0.04	31.13	0.00	0.63	0.01	0.06	14.86	3.04	0.12	99.83
No138-28	50.85	0.00	30.73	0.00	0.66	0.00	0.09	14.06	3.40	0.17	99.95
No138-48	52.86	0.06	28.80	0.00	0.81	0.00	0.11	12.15	4.09	0.24	99.12
No138-51	54.52	0.07	27.37	0.00	0.84	0.00	0.12	11.13	4.80	0.31	99.15
No138-55	47.01	0.01	32.86	0.00	0.59	0.00	0.08	16.69	1.99	0.09	99.31
No138-56	48.03	0.03	32.25	0.00	0.61	0.00	0.06	16.16	2.31	0.08	99.53
No138-57	48.73	0.04	31.77	0.00	0.55	0.00	0.09	15.56	2.65	0.11	99.50
No138-58	48.25	0.06	32.78	0.00	0.56	0.00	0.08	15.91	2.26	0.08	99.99
No138-59	51.20	0.02	30.53	0.05	0.71	0.01	0.10	14.34	3.38	0.19	100.52
No138-61	47.57	0.03	32.33	0.01	0.58	0.01	0.09	16.22	2.13	0.07	99.03
No138-62	53.74	0.02	28.05	0.01	0.85	0.00	0.12	11.63	4.35	0.28	99.05
No138-63	55.19	0.03	27.44	0.00	1.05	0.00	0.12	10.95	5.01	0.34	100.11
No138-64	53.22	0.02	28.23	0.03	0.79	0.00	0.11	12.03	4.29	0.30	99.01
No138-65	54.60	0.04	27.71	0.00	0.91	0.01	0.09	11.08	4.95	0.35	99.73
No138-71	52.44	0.03	29.64	0.00	0.88	0.02	0.08	12.93	4.03	0.22	100.26
No138-72	53.22	0.07	28.64	0.02	0.87	0.05	0.12	12.12	4.41	0.25	99.77

Tufa Trig 15

No138-73	52.60	0.06	29.49	0.03	0.76	0.02	0.07	12.85	3.94	0.23	100.05
No138-74	53.35	0.00	29.09	0.00	0.69	0.02	0.10	12.25	4.17	0.22	99.90
No138-75	54.73	0.05	27.61	0.03	0.66	0.04	0.08	10.85	4.93	0.32	99.30
No138-79	51.35	0.01	30.04	0.02	0.60	0.00	0.11	13.50	3.51	0.16	99.30
No138-80	47.71	0.05	33.03	0.00	0.64	0.02	0.10	16.45	1.99	0.07	100.05
No138-81	46.83	0.00	33.04	0.02	0.59	0.01	0.08	16.91	1.84	0.07	99.38
No138-82	51.09	0.01	30.08	0.00	0.62	0.00	0.11	13.59	3.61	0.14	99.24
No138-83	51.07	0.02	30.51	0.00	0.70	0.00	0.13	13.99	3.41	0.17	99.99
No138-89	51.69	0.06	30.12	0.00	0.81	0.00	0.09	13.65	3.56	0.19	100.16
No138-90	46.71	0.00	33.06	0.02	0.55	0.00	0.09	16.75	1.79	0.06	99.03
No138-91	47.69	0.05	32.94	0.00	0.58	0.00	0.06	16.62	2.00	0.04	99.98
No138-104	53.47	0.10	28.21	0.00	0.72	0.00	0.12	11.68	4.54	0.27	99.11
No138-105	54.66	0.05	27.66	0.02	0.68	0.02	0.10	11.01	4.91	0.37	99.49
No138-106	54.28	0.00	28.19	0.00	0.77	0.04	0.10	11.43	4.69	0.31	99.82
No139-1	51.83	0.04	29.70	0.01	0.80	0.00	0.14	13.00	3.84	0.24	99.59
No139-4	54.65	0.07	27.80	0.01	0.68	0.00	0.12	10.92	4.90	0.37	99.52
No139-5	53.67	0.10	28.16	0.00	0.87	0.03	0.09	11.75	4.56	0.29	99.53
No139-8	53.55	0.03	28.73	0.02	0.78	0.03	0.11	12.21	4.38	0.25	100.09
No139-9	53.68	0.08	28.20	0.01	0.59	0.00	0.08	11.56	4.57	0.28	99.05
No139-10	54.54	0.08	27.79	0.00	0.71	0.00	0.08	11.12	4.84	0.34	99.48
No139-12	54.23	0.07	28.06	0.00	0.90	0.00	0.17	11.22	4.78	0.34	99.78
No139-13	54.14	0.03	28.51	0.00	0.61	0.02	0.04	11.61	4.48	0.29	99.74
No139-14	54.27	0.07	28.39	0.01	0.62	0.00	0.06	11.67	4.61	0.28	99.96
No139-15	55.02	0.08	27.36	0.00	0.63	0.00	0.10	10.69	4.97	0.32	99.17

No139-32	51.65	0.42	2.74	0.11	6.93	0.18	16.36	20.36	0.27	0.00	99.02
No139-36	50.97	0.01	30.07	0.01	0.99	0.00	0.18	13.72	3.44	0.14	99.54
No139-37	50.63	0.08	30.21	0.01	0.72	0.00	0.11	13.99	3.35	0.18	99.27
No139-38	51.05	0.05	30.19	0.06	0.58	0.00	0.10	13.78	3.36	0.18	99.35
No139-42	53.70	0.02	28.50	0.00	0.75	0.06	0.06	11.49	4.63	0.30	99.50
No139-43	53.53	0.07	28.97	0.00	0.74	0.04	0.05	11.89	4.44	0.28	100.00
No139-44	55.35	0.06	27.37	0.00	0.68	0.00	0.08	10.58	5.19	0.36	99.68
No139-47	54.31	0.01	27.51	0.00	0.97	0.00	0.13	11.26	4.58	0.33	99.08
No139-54	47.95	0.01	32.20	0.00	0.46	0.00	0.10	16.15	2.27	0.07	99.20
No139-55	46.78	0.02	32.84	0.02	0.55	0.00	0.10	16.91	1.78	0.04	99.02
No139-57	46.92	0.02	33.18	0.00	0.57	0.00	0.08	16.78	1.82	0.04	99.39
No139-60	52.40	0.08	29.21	0.00	0.67	0.00	0.12	12.72	3.91	0.24	99.35
No139-69	54.30	0.07	27.82	0.00	0.86	0.00	0.14	11.17	4.69	0.28	99.32
No139-70	53.86	0.07	27.96	0.00	0.87	0.00	0.14	11.62	4.56	0.30	99.38
No139-74	55.38	0.08	26.84	0.02	0.92	0.00	0.14	10.37	5.15	0.36	99.26
No139-81	53.67	0.12	28.36	0.02	0.69	0.00	0.12	11.62	4.45	0.28	99.32
No139-82	53.67	0.05	28.41	0.01	0.70	0.00	0.11	11.58	4.49	0.31	99.32
No139-83	53.71	0.06	28.36	0.01	0.66	0.00	0.10	11.65	4.53	0.29	99.36
No139-84	54.37	0.04	28.26	0.02	0.67	0.01	0.12	11.27	4.62	0.29	99.65
No139-85	54.09	0.06	28.14	0.00	0.70	0.00	0.10	11.68	4.47	0.30	99.53
No139-88	53.49	0.08	28.07	0.00	0.92	0.00	0.10	11.50	4.56	0.35	99.07
No139-96	52.39	0.05	28.85	0.00	0.99	0.00	0.16	12.33	4.13	0.24	99.14
No139-97	51.43	0.05	30.56	0.00	0.62	0.04	0.10	13.91	3.53	0.17	100.42
No140-1	55.49	0.09	26.95	0.00	0.92	0.03	0.11	10.40	5.43	0.33	99.75

Tufa Trig 16

No140-5	53.86	0.03	28.12	0.03	0.94	0.01	0.14	11.35	4.62	0.26	99.36
No140-6	54.06	0.06	28.19	0.00	0.77	0.00	0.12	10.89	4.83	0.30	99.21
No140-8	54.53	0.05	27.57	0.00	0.75	0.02	0.11	10.87	4.82	0.29	99.00
No140-9	54.79	0.08	28.15	0.01	0.82	0.00	0.12	11.31	4.81	0.26	100.36
No140-11	54.67	0.04	27.45	0.00	0.83	0.00	0.13	11.00	4.87	0.30	99.28
No140-13	53.47	0.07	28.65	0.00	0.69	0.01	0.11	12.27	4.48	0.25	100.00
No140-14	53.63	0.04	28.22	0.00	0.84	0.05	0.12	11.92	4.61	0.25	99.67
No140-15	55.02	0.01	27.73	0.00	0.82	0.00	0.08	10.98	4.80	0.28	99.71
No140-16	47.95	0.04	32.26	0.00	0.51	0.01	0.06	15.99	2.28	0.04	99.13
No140-17	46.87	0.05	33.07	0.00	0.54	0.00	0.05	17.25	1.86	0.07	99.76
No140-18	48.50	0.02	32.34	0.00	0.46	0.03	0.05	16.07	2.49	0.05	100.01
No140-19	52.26	0.09	29.57	0.01	0.77	0.00	0.06	13.21	3.77	0.17	99.90
No140-20	52.29	0.02	29.38	0.00	0.89	0.02	0.13	12.75	3.86	0.21	99.54
No140-21	47.12	0.00	33.30	0.00	0.71	0.00	0.04	16.99	1.86	0.04	100.06
No140-22	54.07	0.08	28.28	0.00	0.89	0.00	0.12	11.50	4.69	0.24	99.86
No140-23	52.91	0.04	28.63	0.01	0.88	0.00	0.11	12.33	4.32	0.23	99.45
No140-24	53.30	0.01	28.99	0.00	0.71	0.00	0.09	12.16	4.24	0.21	99.71
No140-30	47.58	0.00	32.87	0.00	0.65	0.00	0.07	16.32	2.08	0.06	99.63
No140-31	46.92	0.00	33.22	0.00	0.65	0.03	0.06	17.06	1.80	0.04	99.76
No140-37	53.15	0.04	28.97	0.00	0.88	0.00	0.10	12.32	4.18	0.18	99.82
No140-46	54.62	0.07	27.66	0.00	0.83	0.01	0.12	10.92	4.79	0.27	99.30
No140-51	55.77	0.06	27.09	0.04	0.76	0.01	0.12	10.61	5.16	0.32	99.94
No140-52	49.20	0.02	31.66	0.00	0.56	0.00	0.06	15.16	2.74	0.13	99.52
No140-53	50.80	0.14	30.26	0.00	0.62	0.02	0.07	14.04	3.19	0.21	99.36

No140-54	48.22	0.06	32.15	0.01	0.57	0.01	0.06	16.18	2.33	0.12	99.71
No140-55	54.84	0.03	27.72	0.00	0.55	0.02	0.09	10.90	4.79	0.27	99.20
No140-56	52.98	0.03	28.93	0.00	0.79	0.01	0.09	12.24	4.21	0.20	99.48
No140-57	53.76	0.01	28.77	0.00	0.85	0.00	0.12	12.18	4.16	0.22	100.05
No140-58	51.37	0.00	29.95	0.00	0.89	0.00	0.10	13.71	3.53	0.16	99.71
No140-61	47.88	0.04	32.48	0.00	0.58	0.00	0.05	16.25	2.21	0.07	99.56
No140-62	47.06	0.00	32.84	0.00	0.71	0.03	0.04	16.47	1.96	0.05	99.16
No140-65	48.01	0.02	32.53	0.03	0.60	0.00	0.09	16.23	2.06	0.06	99.62
No140-66	53.52	0.03	28.33	0.00	0.84	0.02	0.07	11.41	4.53	0.26	99.02
No140-67	53.16	0.09	28.68	0.00	0.71	0.02	0.10	12.19	4.23	0.23	99.41
No140-68	52.98	0.04	29.18	0.00	0.75	0.00	0.09	12.66	3.98	0.23	99.91
No140-70	54.49	0.04	27.73	0.05	0.74	0.00	0.10	11.20	4.81	0.23	99.38
No140-71	55.55	0.04	27.34	0.00	0.93	0.00	0.11	10.66	5.02	0.26	99.91

1972-1975 NGAURUHOE	Ng72#2	54.63	28.29	1.14	0.17	11.69	4.27	0.39	100.57
1972 Ngauruhoe	Ng72#5_2	56.25	27.88	1.05	0.20	12.05	4.48	0.37	102.29
	Ng72#6	55.60	27.45	0.99	0.18	11.75	4.39	0.38	100.73
	Ng72#6_2	55.59	27.10	0.95	0.18	11.45	4.71	0.39	100.37
	Ng72#10	55.83	27.76	1.07	0.21	11.55	4.58	0.44	101.45
1973 Ngauruhoe	Ng73#1	53.92	29.15	1.03	0.11	13.39	3.76	0.23	101.60
	Ng73#2	57.87	26.46	0.97	0.18	10.63	5.18	0.49	101.77
	Ng73#2_2	57.57	26.80	0.94	0.13	10.84	5.19	0.46	101.93
	Ng73#9	55.73	27.97	1.02	0.14	11.14	4.64	0.37	101.00

	Ng73#9_2	54.13	28.97	1.03	0.14	12.39	4.47	0.35	101.48			
	Ng73#14	56.44	28.12	1.01	0.12	11.34	4.94	0.43	102.40			
1974 Ngauruhoe	Ng74#2	57.57	25.01	2.04	0.37	10.84	4.26	0.60	100.68			
	Ng74#2_2	55.38	27.97	0.99	0.13	12.20	4.36	0.30	101.32			
	Ng74#9	55.70	28.21	1.10	0.16	11.95	4.64	0.28	102.05			
	Ng74#13	55.99	25.57	2.12	0.60	10.56	4.28	0.60	99.73			
1975 Ngauruhoe	Ng75#1	58.68	21.53	3.74	0.90	8.94	4.05	1.18	99.01			
	Ng75#1_2	54.50	27.76	1.04	0.11	12.44	4.25	0.26	100.34			
	Ng75#9	54.00	28.40	1.02	0.14	12.58	4.12	0.27	100.53			
	Ng75#12	56.10	28.63	0.89	0.08	11.80	4.81	0.31	102.61			
	Ng75#12_2	55.67	27.72	0.96	0.10	11.34	4.76	0.34	100.89			
	Ng74#18	52.60	30.16	1.05	0.15	13.87	3.67	0.21	101.70			
1995-1996 RUAPEHU												
1995 Ruapehu	Rua95#4	53.96	29.54	0.76	0.15	12.64	4.25	0.26	101.56			
	Rua95#5	56.21	28.65	0.89	0.15	11.91	4.77	0.38	102.95			
	Rua95#11	55.69	28.12	0.96	0.18	11.83	4.77	0.39	101.92			
1996 Ruapehu	Rua96#4	56.15	26.62	1.16	0.50	11.34	4.66	0.42	100.85			
	Rua96#10	56.31	27.58	0.93	0.25	11.71	4.79	0.40	101.96			
	Rua96#15	55.41	27.28	0.88	0.16	11.86	4.61	0.33	100.53			
	Minimum	45.89	0.00	0.69	0.00	0.46	0.00	0.04	2.02	0.04	0.00	99.00
	Maximum	61.05	1.11	33.94	0.32	17.18	0.36	25.58	20.36	5.43	1.36	102.95
	Average	52.19	0.06	29.19	0.01	0.95	0.01	0.34	13.30	3.61	0.20	99.85
	Std. dev.	2.59	0.10	3.39	0.02	1.12	0.03	1.85	1.99	0.97	0.15	0.62

Appendix C9. Microprobe analyses of pyroxene from intermediate tephra of the Tongariro Volcanic Centre. Mangatawai and Tufa Trig glasses were analysed using a JEOL JXA-8900R electron microprobe equipped with four wavelength-dispersive spectrometers at the Institute of Earth Sciences, Academia Sinica, Taipei, Taiwan. Ngauruhoe 1972-1975 and Ruapehu 1995-1996 glasses were analysed using a JEOL JXA-8800R electron microprobe equipped with four wavelength-dispersive spectrometers at the Graduate School of Science, Hokkaido University, Sapporo, Japan.

Tephra formation/sequence	Comment	SiO ₂	TiO ₂	Al ₂ O ₃	Cr ₂ O ₃	FeO	MnO	MgO	CaO	Na ₂ O	K ₂ O	NiO	Total
MANGATAWAI													
Mangatawai Lower	No14-52	51.17	0.39	3.61	0.11	8.49	0.15	15.65	19.82	0.33	0.00		99.72
	No15-40	53.15	0.26	2.47	0.33	5.16	0.12	17.61	20.69	0.21	0.01		100.00
	No17-14	52.33	0.40	2.84	0.13	7.92	0.16	16.33	19.39	0.22	0.00		99.71
	No14-1	54.36	0.17	1.28	0.10	13.24	0.23	28.40	1.69	0.06	0.00		99.53
	No14-2	53.47	0.20	1.41	0.01	16.95	0.34	26.04	1.71	0.04	0.00		100.15
	No14-3	53.76	0.31	1.34	0.04	17.86	0.37	25.05	1.93	0.02	0.00		100.67
	No14-4	55.24	0.16	1.06	0.10	13.84	0.30	28.09	1.92	0.04	0.00		100.74
	No14-25	54.38	0.27	0.67	0.01	16.82	0.31	26.01	2.11	0.03	0.00		100.61
	No14-26	53.64	0.27	1.37	0.03	15.61	0.28	25.97	2.38	0.02	0.00		99.57
	No14-35	54.03	0.26	1.13	0.08	15.75	0.33	25.80	2.56	0.02	0.00		99.94
	No14-36	53.78	0.32	0.93	0.03	17.20	0.29	25.33	2.29	0.06	0.00		100.24
	No14-42	53.36	0.21	1.41	0.17	16.00	0.33	26.21	1.73	0.01	0.00		99.42
	No14-43	53.33	0.29	1.39	0.00	17.87	0.34	24.99	1.82	0.02	0.00		100.04
	No14-44	54.05	0.17	0.83	0.04	16.51	0.32	26.52	1.68	0.01	0.00		100.13
	No14-45	53.02	0.24	0.96	0.01	17.09	0.33	23.18	4.30	0.07	0.00		99.19
	No14-55	54.18	0.27	1.47	0.00	16.60	0.42	22.60	3.96	0.06	0.13		99.68

No15-11	53.41	0.21	0.87	0.03	17.53	0.33	23.25	4.14	0.00	0.00	99.77
No15-13	54.36	0.25	0.80	0.00	17.49	0.32	25.13	2.29	0.04	0.00	100.66
No15-23	52.94	0.32	1.30	0.03	17.09	0.36	25.32	2.21	0.04	0.00	99.62
No15-24	53.84	0.23	1.91	0.20	13.44	0.27	27.75	2.50	0.05	0.00	100.19
No15-26	54.86	0.17	1.58	0.15	13.24	0.28	28.18	1.70	0.03	0.01	100.19
No15-27	54.78	0.20	1.80	0.06	14.18	0.26	27.33	1.72	0.04	0.00	100.36
No15-28	55.19	0.28	1.74	0.04	13.93	0.22	27.86	1.71	0.01	0.00	100.97
No15-29	55.77	0.14	0.92	0.00	13.23	0.30	28.07	1.83	0.00	0.00	100.27
No15-30	54.62	0.20	1.87	0.04	14.30	0.30	27.36	1.81	0.02	0.00	100.52
No15-34	54.57	0.31	1.49	0.08	14.43	0.33	26.56	2.55	0.06	0.00	100.37
No15-44	53.60	0.21	1.14	0.00	16.18	0.42	22.45	5.58	0.07	0.00	99.65
No15-45	55.04	0.29	2.00	0.03	15.82	0.33	22.70	3.11	0.23	0.17	99.73
No15-46	55.37	0.18	1.04	0.02	13.37	0.28	27.67	2.19	0.02	0.00	100.13
No15-47	53.93	0.26	1.01	0.00	17.40	0.35	24.85	2.28	0.04	0.00	100.11
No15-54	54.78	0.23	0.96	0.02	15.11	0.32	26.45	2.21	0.02	0.00	100.10
No15-55	54.59	0.19	1.78	0.12	13.57	0.34	27.30	2.46	0.04	0.00	100.40
No15-63	54.74	0.24	0.69	0.04	15.84	0.38	25.91	2.33	0.04	0.00	100.21
No15-64	53.70	0.20	1.18	0.03	16.42	0.30	25.36	2.35	0.05	0.00	99.57
No15-65	53.79	0.31	1.17	0.01	17.08	0.34	25.05	2.46	0.02	0.00	100.23
No15-73	55.04	0.21	1.49	0.09	13.41	0.31	27.67	2.21	0.04	0.00	100.45
No15-74	55.13	0.17	1.66	0.15	13.16	0.33	28.31	1.79	0.03	0.00	100.73
No15-77	53.91	0.28	1.26	0.05	17.22	0.41	22.82	5.05	0.09	0.00	101.08
No16-2	53.56	0.28	0.63	0.00	18.22	0.45	21.87	4.56	0.10	0.00	99.67
No16-7	53.76	0.25	0.78	0.00	18.47	0.39	20.99	5.16	0.09	0.00	99.89

No16-15	54.08	0.18	0.63	0.04	18.27	0.40	22.81	4.04	0.03	0.00	100.48
No16-17	53.63	0.37	1.49	0.05	17.57	0.35	23.82	2.59	0.06	0.00	99.93
No16-29	54.76	0.18	1.71	0.10	13.41	0.27	28.08	1.74	0.02	0.00	100.27
No16-30	55.04	0.15	1.64	0.09	13.56	0.29	28.17	1.65	0.02	0.00	100.61
No16-34	53.78	0.35	1.72	0.08	16.87	0.33	24.83	2.52	0.04	0.00	100.51
No16-35	55.03	0.20	0.98	0.03	14.76	0.33	26.73	2.25	0.02	0.00	100.32
No16-45	55.59	0.15	0.98	0.11	13.19	0.26	27.69	2.52	0.06	0.00	100.55
No16-46	54.75	0.26	1.81	0.19	14.51	0.31	26.63	2.03	0.05	0.01	100.56
No16-51	54.40	0.18	0.80	0.04	16.90	0.35	23.07	3.81	0.01	0.01	99.56
No16-56	54.25	0.21	0.87	0.01	17.13	0.47	22.64	4.20	0.07	0.00	99.84
No16-57	54.54	0.25	0.67	0.01	17.46	0.32	23.29	3.76	0.06	0.00	100.36
No16-74	54.02	0.26	1.05	0.03	16.09	0.34	23.87	3.84	0.07	0.00	99.56
No16-76	53.80	0.35	1.95	0.01	17.53	0.35	21.94	4.12	0.16	0.05	100.25
No17-4	53.68	0.24	1.41	0.02	16.31	0.32	25.18	2.62	0.09	0.00	99.86
No17-9	54.63	0.28	0.65	0.00	19.12	0.35	23.61	2.16	0.01	0.00	100.82
No17-10	54.25	0.19	0.65	0.00	18.77	0.40	23.80	2.15	0.03	0.00	100.24
No17-17	54.04	0.29	0.91	0.00	17.57	0.56	24.42	1.81	0.00	0.00	99.59
No17-18	54.94	0.20	0.84	0.00	15.49	0.31	25.74	2.30	0.03	0.00	99.84
No17-19	53.46	0.28	1.26	0.00	17.71	0.36	23.89	2.39	0.02	0.00	99.38
No17-26	54.82	0.19	1.62	0.08	13.27	0.30	27.98	1.73	0.01	0.00	100.00
No17-27	53.57	0.43	1.58	0.00	15.40	0.38	22.26	6.59	0.10	0.00	100.30
No17-35	55.24	0.16	0.91	0.07	14.84	0.24	27.01	2.16	0.04	0.00	100.68
No17-60	53.80	0.26	0.75	0.00	17.80	0.46	22.61	4.08	0.04	0.00	99.78
No17-63	54.16	0.22	0.63	0.01	17.29	0.32	25.15	2.31	0.03	0.00	100.11

	No17-76	53.17	0.32	1.55	0.06	17.64	0.28	23.98	2.95	0.04	0.00	99.98
	No17-87	54.03	0.26	0.92	0.01	16.73	0.39	24.73	2.24	0.04	0.00	99.33
	No18-10	51.91	0.42	1.64	0.04	17.51	0.36	22.19	4.81	0.09	0.03	99.00
	No18-21	53.71	0.22	0.76	0.03	17.32	0.35	23.45	4.08	0.08	0.00	99.99
	No18-30	53.39	0.20	0.69	0.00	17.79	0.46	22.40	4.12	0.09	0.00	99.14
	No18-31	52.95	0.30	1.07	0.03	17.10	0.51	22.24	5.36	0.06	0.00	99.63
	No18-32	53.18	0.38	1.38	0.07	17.89	0.37	24.20	2.28	0.05	0.00	99.80
	No18-33	52.43	0.35	1.34	0.00	17.34	0.34	21.84	5.32	0.05	0.00	99.00
	No18-34	52.77	0.32	1.25	0.04	17.59	0.39	22.59	4.09	0.09	0.00	99.12
	No18-35	53.03	0.22	0.61	0.00	18.17	0.42	23.01	3.91	0.05	0.00	99.41
	No18-47	53.49	0.27	0.63	0.00	17.42	0.34	25.11	2.23	0.05	0.00	99.53
	No18-58	53.25	0.21	1.33	0.05	15.21	0.37	26.47	2.20	0.00	0.00	99.08
	No18-59	53.59	0.24	1.63	0.10	15.16	0.38	26.45	2.21	0.04	0.00	99.79
	No18-93	53.50	0.23	0.96	0.00	17.07	0.42	25.34	2.15	0.02	0.01	99.70
	No18-95	53.82	0.22	1.71	0.01	15.05	0.34	26.71	1.71	0.03	0.00	99.58
	No18-96	53.76	0.21	1.72	0.04	14.70	0.39	26.90	1.78	0.03	0.00	99.54
	No18-97	53.81	0.21	1.70	0.13	13.18	0.24	27.99	1.79	0.01	0.00	99.05
	No18-103	52.31	0.36	0.76	0.00	21.19	0.36	20.27	4.31	0.09	0.00	99.65
	No18-104	52.55	0.31	1.71	0.03	15.15	0.45	22.49	6.91	0.12	0.02	99.74
Mangatawai Upper	No47-15	54.15	0.23	1.02	0.00	10.01	0.29	16.51	17.98	0.23	0.00	100.41
	No49-7	52.86	0.48	2.48	0.04	9.65	0.20	15.69	18.39	0.32	0.00	100.11
	No49-8	52.55	0.47	2.78	0.09	10.22	0.21	15.91	17.67	0.27	0.00	100.18
	No49-9	52.82	0.48	2.34	0.05	9.30	0.27	15.88	18.67	0.26	0.00	100.06
	No49-10	52.98	0.39	2.37	0.12	9.53	0.24	16.23	18.91	0.28	0.00	101.05

No49-11	53.40	0.34	1.98	0.05	9.80	0.28	16.26	18.19	0.28	0.00	100.58
No54-1	51.99	0.56	2.11	0.05	10.61	0.32	14.66	19.48	0.30	0.00	100.06
No54-2	52.19	0.62	2.07	0.00	12.09	0.37	14.48	18.02	0.33	0.00	100.16
No54-23	52.38	0.43	2.36	0.02	10.07	0.26	15.19	18.49	0.28	0.00	99.48
No54-24	52.11	0.55	2.76	0.04	10.50	0.26	15.26	18.24	0.36	0.00	100.07
No54-51	52.36	0.52	2.38	0.03	9.65	0.20	15.59	19.03	0.29	0.00	100.05
No56-36	52.47	0.42	2.52	0.02	9.57	0.22	15.15	19.63	0.31	0.00	100.28
No59-43	50.74	0.39	2.45	0.14	9.04	0.19	15.63	19.50	0.32	0.00	98.40
No47-16	54.12	0.20	1.61	0.02	16.21	0.38	25.77	1.83	0.02	0.00	100.16
No47-17	55.12	0.22	1.60	0.07	15.38	0.38	26.32	1.76	0.01	0.00	100.86
No47-18	55.19	0.23	1.55	0.06	14.98	0.41	27.35	1.57	0.02	0.00	101.35
No47-19	55.58	0.22	1.33	0.00	15.78	0.41	26.43	1.83	0.05	0.00	101.62
No47-20	55.17	0.17	1.31	0.02	15.47	0.37	26.61	1.70	0.03	0.00	100.86
No47-21	54.80	0.14	1.78	0.00	15.36	0.32	26.21	1.67	0.00	0.00	100.30
No47-24	56.04	0.24	1.99	0.05	14.36	0.32	25.31	1.99	0.14	0.06	100.50
No47-26	54.59	0.25	1.16	0.02	15.78	0.36	23.37	4.53	0.05	0.00	100.11
No47-47	54.61	0.24	1.13	0.02	17.29	0.43	24.95	2.02	0.03	0.00	100.70
No47-48	54.74	0.23	1.37	0.04	16.53	0.32	25.18	1.85	0.05	0.00	100.30
No49-21	54.68	0.38	1.66	0.06	17.07	0.42	22.86	3.32	0.12	0.05	100.60
No49-30	54.06	0.30	0.80	0.05	18.27	0.41	21.47	4.17	0.05	0.02	99.60
No49-31	53.95	0.28	0.70	0.01	18.05	0.47	22.42	4.07	0.05	0.00	99.99
No49-33	52.70	0.33	1.08	0.04	20.10	0.38	20.27	4.50	0.06	0.00	99.45
No54-9	54.37	0.30	1.35	0.01	16.13	0.36	25.22	2.33	0.00	0.00	100.07
No54-12	54.55	0.31	1.34	0.11	16.30	0.28	24.79	2.49	0.02	0.00	100.19

TUFA TRIG
Tufa Trig 8

No56-47	53.61	0.40	1.47	0.06	17.10	0.45	21.52	5.35	0.08	0.00	100.04
No59-5	55.01	0.22	0.68	0.00	18.97	0.42	22.83	2.20	0.05	0.00	100.38
No59-6	53.51	0.21	1.16	0.00	20.64	0.47	21.91	2.25	0.00	0.00	100.14
No59-7	54.30	0.33	1.19	0.01	19.89	0.48	22.22	2.20	0.00	0.00	100.62
No59-8	55.54	0.14	0.91	0.01	15.48	0.38	26.43	1.71	0.00	0.00	100.60
No59-9	55.41	0.20	1.00	0.01	16.10	0.34	26.12	1.68	0.03	0.02	100.92
No59-12	54.54	0.26	1.52	0.10	15.76	0.34	26.11	2.00	0.09	0.00	100.71
No59-13	54.73	0.28	1.64	0.06	15.73	0.26	25.80	1.92	0.04	0.01	100.47
No59-14	54.77	0.28	1.54	0.05	16.30	0.30	25.93	1.95	0.03	0.00	101.14
No59-15	54.91	0.29	1.55	0.11	16.03	0.32	25.95	2.08	0.06	0.00	101.27
No59-16	55.14	0.27	1.55	0.12	15.54	0.28	26.11	1.98	0.04	0.00	101.03
No59-18	55.10	0.19	0.88	0.07	15.17	0.28	26.86	1.99	0.03	0.00	100.56
No59-19	54.44	0.24	1.56	0.11	15.42	0.34	25.43	2.78	0.01	0.00	100.33
No131-54	53.36	0.29	0.47	0.00	11.07	0.29	15.25	18.79	0.25	0.00	99.77
No131-55	52.31	0.42	1.07	0.00	10.59	0.23	15.71	19.20	0.22	0.00	99.75
No131-56	51.21	0.72	2.22	0.04	10.95	0.24	15.58	18.47	0.26	0.00	99.68
No131-93	51.71	0.62	2.01	0.02	11.23	0.20	14.61	19.01	0.34	0.00	99.75
No137-4	51.75	0.25	2.01	0.42	7.45	0.18	17.13	19.52	0.32	0.00	99.01
No137-5	50.94	0.64	2.42	0.11	9.42	0.22	16.36	18.66	0.26	0.00	99.05
No137-7	51.35	0.60	1.94	0.06	10.38	0.23	15.73	18.82	0.20	0.00	99.31
No137-66	54.07	0.17	1.90	0.11	6.80	0.17	19.42	17.55	0.19	0.00	100.38
No137-67	51.41	0.49	4.66	0.34	6.35	0.20	16.73	19.95	0.32	0.00	100.44
No137-75	52.24	0.28	2.67	0.20	7.45	0.16	16.74	20.84	0.27	0.00	100.85

No137-76	52.61	0.31	2.69	0.17	6.87	0.20	16.62	20.73	0.31	0.00	100.51
No137-77	52.22	0.40	2.68	0.04	7.47	0.21	16.35	20.57	0.30	0.00	100.25
No140-50	51.47	0.55	1.98	0.01	10.33	0.26	15.21	19.17	0.28	0.00	99.27
No140-63	51.29	0.60	2.37	0.03	11.40	0.26	14.43	19.22	0.41	0.00	100.00
No140-64	50.55	0.61	2.70	0.11	11.89	0.21	14.35	18.56	0.42	0.00	99.40
No131-6	54.06	0.30	0.84	0.00	15.34	0.40	26.42	2.04	0.03	0.00	99.42
No131-8	53.82	0.19	1.20	0.05	15.54	0.28	26.35	2.03	0.01	0.00	99.46
No131-24	54.60	0.19	0.91	0.00	15.98	0.35	25.83	2.08	0.03	0.00	99.97
No131-25	54.06	0.28	1.13	0.04	15.40	0.44	26.29	2.14	0.00	0.00	99.76
No131-33	53.11	0.30	1.30	0.00	17.74	0.37	24.93	2.26	0.03	0.00	100.03
No131-34	53.74	0.28	1.14	0.03	17.68	0.34	24.59	2.30	0.06	0.00	100.16
No131-35	53.56	0.36	1.06	0.01	17.93	0.32	24.68	2.11	0.04	0.00	100.07
No131-44	53.84	0.27	1.35	0.02	15.07	0.34	26.35	2.48	0.08	0.00	99.78
No131-45	54.06	0.27	1.01	0.00	15.24	0.33	26.65	2.02	0.05	0.00	99.64
No131-46	53.90	0.18	1.28	0.01	17.65	0.36	25.33	1.43	0.00	0.00	100.13
No131-47	53.62	0.37	1.22	0.01	17.63	0.28	25.19	1.94	0.00	0.00	100.27
No131-48	54.86	0.16	0.68	0.00	15.08	0.28	27.09	1.85	0.04	0.00	100.02
No131-50	54.15	0.26	1.15	0.01	15.43	0.31	26.35	1.91	0.02	0.00	99.58
No131-52	53.71	0.08	27.98	0.00	0.89	0.00	0.13	11.86	4.48	0.29	99.42
No131-60	52.59	0.32	1.50	0.02	19.39	0.31	23.06	1.89	0.03	0.00	99.10
No131-62	54.61	0.36	1.31	0.02	15.16	0.25	26.56	1.95	0.02	0.00	100.25
No131-63	54.34	0.35	1.58	0.03	15.40	0.33	26.29	2.05	0.16	0.04	100.57
No131-68	53.29	0.34	1.31	0.03	18.32	0.42	24.50	1.94	0.01	0.00	100.17
No131-69	53.07	0.19	0.93	0.02	20.23	0.32	23.47	1.68	0.07	0.00	99.98

Tufa Trig 13

No131-77	52.85	0.35	1.09	0.03	19.68	0.38	23.23	1.73	0.06	0.00	99.38
No131-78	53.44	0.28	1.16	0.01	18.32	0.32	24.22	1.97	0.06	0.00	99.77
No131-81	52.97	0.35	1.75	0.01	16.78	0.43	24.66	2.33	0.05	0.00	99.32
No131-83	53.84	0.34	1.15	0.00	18.54	0.33	24.04	1.91	0.01	0.00	100.15
No131-84	53.94	0.23	0.95	0.02	17.88	0.38	24.58	1.94	0.04	0.00	99.96
No131-85	54.65	0.21	0.75	0.00	16.62	0.39	25.39	1.94	0.01	0.00	99.95
No131-91	53.24	0.32	1.20	0.00	19.18	0.30	23.85	1.77	0.06	0.00	99.94
No131-92	53.21	0.26	1.19	0.01	19.96	0.36	23.39	1.66	0.06	0.00	100.09
No131-94	52.76	0.31	1.32	0.05	20.26	0.41	23.49	1.74	0.04	0.00	100.38
No131-95	53.02	0.27	1.18	0.02	19.75	0.34	23.55	1.80	0.02	0.00	99.95
No131-96	53.21	0.35	1.17	0.00	20.09	0.42	23.80	1.80	0.02	0.00	100.85
No131-97	52.98	0.27	1.20	0.00	19.88	0.32	23.75	1.83	0.04	0.00	100.26
No131-98	54.49	0.28	0.88	0.02	15.88	0.28	26.26	1.85	0.05	0.00	99.98
No131-99	54.63	0.20	1.05	0.00	15.29	0.33	26.73	1.93	0.04	0.00	100.20
No131-102	54.77	0.22	0.78	0.00	15.70	0.28	26.80	1.94	0.07	0.00	100.56
No131-103	53.91	0.15	1.15	0.03	15.24	0.34	26.61	1.88	0.06	0.00	99.35
No137-9	52.56	0.45	1.32	0.02	20.80	0.32	22.76	1.92	0.03	0.00	100.18
No137-10	52.96	0.40	1.31	0.00	18.16	0.34	24.27	2.45	0.08	0.00	99.97
No137-11	53.11	0.29	1.10	0.01	18.51	0.39	24.45	2.07	0.02	0.00	99.95
No137-16	54.35	0.05	1.66	0.49	8.32	0.23	31.87	2.05	0.02	0.00	99.04
No137-22	54.08	0.20	0.88	0.00	15.74	0.40	26.42	2.02	0.03	0.00	99.75
No137-23	53.97	0.17	1.57	0.04	14.06	0.22	28.27	1.60	0.00	0.00	99.90
No137-24	54.02	0.21	1.72	0.08	14.70	0.31	27.68	1.66	0.01	0.00	100.37

Tufa Trig 14

No137-25	53.89	0.09	1.56	0.03	13.67	0.23	27.84	1.65	0.05	0.00	99.02
No137-37	52.98	0.32	1.13	0.00	19.73	0.38	23.33	1.99	0.04	0.00	99.89
No137-38	52.23	0.35	1.39	0.00	19.80	0.41	23.28	1.75	0.00	0.00	99.21
No137-39	52.94	0.22	1.35	0.04	20.27	0.42	23.39	1.73	0.01	0.00	100.37
No137-48	52.64	0.30	1.29	0.05	19.64	0.34	23.97	1.86	0.02	0.00	100.10
No137-49	52.53	0.26	1.15	0.00	20.35	0.40	23.80	1.81	0.04	0.00	100.34
No137-50	52.81	0.23	1.17	0.00	19.80	0.38	23.60	1.78	0.02	0.00	99.81
No137-51	52.88	0.23	1.21	0.00	20.65	0.36	23.72	1.79	0.01	0.00	100.84
No137-52	52.87	0.35	1.33	0.04	19.90	0.42	23.41	1.87	0.03	0.00	100.22
No137-55	53.03	0.33	1.08	0.01	19.64	0.51	23.53	2.12	0.04	0.00	100.27
No137-70	53.75	0.31	1.00	0.00	18.39	0.41	24.57	2.05	0.05	0.00	100.53
No137-81	54.13	0.20	0.75	0.01	18.37	0.33	25.17	1.93	0.03	0.00	100.93
No138-3	53.89	0.20	0.85	0.00	17.54	0.34	25.31	2.07	0.04	0.00	100.25
No138-9	54.00	0.27	0.90	0.00	17.77	0.33	25.42	2.02	0.05	0.00	100.74
No138-10	53.87	0.25	0.84	0.00	18.20	0.47	24.83	2.16	0.04	0.00	100.64
No138-11	52.82	0.36	2.51	0.03	17.26	0.33	24.69	2.53	0.04	0.01	100.58
No138-17	53.74	0.27	0.76	0.00	18.56	0.36	24.60	2.02	0.05	0.00	100.36
No138-19	52.76	0.33	1.24	0.03	19.90	0.36	23.53	1.82	0.02	0.00	99.98
No138-20	52.42	0.15	2.17	0.16	19.25	0.34	24.05	1.66	0.03	0.00	100.24
No138-21	52.70	0.24	1.89	0.13	18.53	0.32	24.82	1.45	0.03	0.00	100.11
No138-22	53.07	0.39	1.42	0.07	19.62	0.37	23.96	1.79	0.03	0.00	100.72
No138-23	53.43	0.31	0.75	0.00	18.36	0.30	24.44	1.94	0.03	0.00	99.55
No138-29	53.31	0.26	0.71	0.00	21.27	0.38	22.21	2.04	0.00	0.00	100.19
No138-30	54.51	0.16	1.54	0.16	13.09	0.18	28.53	1.52	0.03	0.00	99.73

Tufa Trig 15

No138-31	54.15	0.21	1.90	0.04	13.35	0.31	28.70	1.53	0.05	0.00	100.24
No138-32	53.57	0.22	1.71	0.00	15.64	0.31	27.06	1.51	0.03	0.00	100.05
No138-33	54.06	0.25	1.49	0.00	17.18	0.35	25.39	1.80	0.03	0.00	100.56
No138-34	53.51	0.40	1.20	0.00	19.92	0.40	23.82	1.79	0.03	0.00	101.08
No138-35	52.93	0.40	1.73	0.07	18.85	0.33	24.46	1.94	0.04	0.01	100.75
No138-49	53.51	0.29	1.00	0.04	18.55	0.41	24.29	2.14	0.04	0.00	100.26
No138-50	53.81	0.33	1.18	0.05	17.26	0.35	25.29	2.06	0.03	0.01	100.37
No138-53	54.43	0.27	0.76	0.00	17.40	0.36	25.36	1.90	0.02	0.01	100.50
No138-54	53.35	0.32	1.31	0.00	17.53	0.29	25.34	2.07	0.02	0.00	100.23
No138-67	53.48	0.32	0.96	0.00	18.87	0.39	24.86	1.94	0.03	0.00	100.86
No138-68	53.43	0.20	0.86	0.06	17.35	0.33	25.70	1.88	0.04	0.00	99.85
No138-69	53.25	0.34	1.31	0.02	18.35	0.32	25.02	1.93	0.06	0.00	100.58
No138-70	53.45	0.28	1.22	0.01	18.28	0.42	24.86	1.81	0.01	0.00	100.34
No138-84	53.57	0.26	0.89	0.04	18.85	0.29	24.57	1.94	0.05	0.00	100.45
No138-85	53.31	0.29	0.90	0.03	18.46	0.38	24.90	1.89	0.04	0.00	100.18
No138-87	53.03	0.21	1.08	0.00	20.52	0.38	23.90	1.33	0.03	0.00	100.48
No138-88	52.59	0.27	0.95	0.05	19.93	0.41	24.16	1.48	0.00	0.00	99.84
No139-6	53.10	0.34	1.24	0.00	18.33	0.37	24.01	2.25	0.04	0.00	99.68
No139-7	53.23	0.32	1.41	0.00	17.20	0.31	25.12	2.13	0.00	0.00	99.71
No139-11	53.63	0.31	1.16	0.00	17.27	0.33	25.13	2.18	0.01	0.00	100.01
No139-16	53.09	0.26	1.40	0.11	16.04	0.29	25.98	2.19	0.06	0.00	99.41
No139-17	53.57	0.30	1.14	0.05	16.84	0.35	25.27	2.11	0.01	0.00	99.64
No139-29	55.10	0.11	1.57	0.24	13.22	0.29	28.38	1.66	0.03	0.00	100.60
No139-30	54.58	0.18	1.86	0.02	13.45	0.28	28.37	1.67	0.03	0.00	100.43

No139-31	54.71	0.18	1.77	0.09	13.40	0.22	28.65	1.65	0.03	0.00	100.71
No139-33	53.12	0.32	1.41	0.00	17.45	0.41	25.28	2.23	0.04	0.00	100.26
No139-40	53.13	0.30	1.25	0.11	17.41	0.36	24.92	2.33	0.03	0.00	99.84
No139-46	53.43	0.23	1.20	0.00	17.69	0.38	25.09	2.07	0.00	0.00	100.10
No139-49	53.31	0.20	0.90	0.00	18.23	0.39	24.73	1.94	0.04	0.00	99.74
No139-51	53.12	0.20	0.99	0.04	18.33	0.39	24.84	2.06	0.02	0.00	99.99
No139-58	53.89	0.24	0.88	0.00	18.28	0.35	24.71	2.10	0.04	0.00	100.49
No139-61	51.92	0.35	2.49	0.00	19.47	0.42	23.59	2.37	0.06	0.00	100.68
No139-62	52.92	0.21	1.21	0.07	18.96	0.36	24.43	2.01	0.06	0.00	100.23
No139-63	53.49	0.30	1.13	0.00	18.69	0.40	24.52	2.06	0.02	0.00	100.60
No139-66	53.00	0.29	1.23	0.00	18.34	0.38	24.69	2.24	0.05	0.00	100.21
No139-67	53.23	0.23	1.32	0.00	17.19	0.40	25.39	2.19	0.07	0.00	100.02
No139-68	53.78	0.22	1.25	0.01	17.18	0.34	25.27	2.19	0.03	0.00	100.27
No139-73	54.25	0.24	1.26	0.00	17.51	0.37	24.59	2.16	0.02	0.04	100.43
No139-79	53.42	0.27	0.97	0.02	19.62	0.38	24.06	1.81	0.01	0.00	100.56
No139-80	53.98	0.27	0.80	0.05	18.14	0.36	25.27	1.92	0.01	0.00	100.80
No139-90	53.32	0.19	0.80	0.00	18.12	0.37	24.87	2.07	0.04	0.00	99.77
No139-91	53.68	0.27	1.07	0.03	17.74	0.42	25.05	2.15	0.07	0.00	100.47
No139-92	53.54	0.30	1.34	0.00	17.53	0.41	24.64	2.14	0.05	0.00	99.95
No139-93	54.10	0.20	0.68	0.04	18.43	0.35	24.71	1.85	0.03	0.00	100.39
No139-94	53.28	0.34	1.59	0.09	17.76	0.38	24.88	2.00	0.02	0.00	100.34
No139-95	53.64	0.26	1.42	0.08	16.63	0.34	25.60	2.08	0.05	0.00	100.11
No140-2	53.56	0.18	0.76	0.00	18.63	0.40	24.52	1.85	0.02	0.00	99.91
No140-3	53.11	0.28	1.43	0.10	17.29	0.31	25.09	2.39	0.04	0.00	100.04

Tufa Trig 16

No140-4	53.45	0.23	0.75	0.04	18.77	0.42	24.51	1.82	0.02	0.00	100.01	
No140-12	53.59	0.32	1.20	0.05	18.67	0.40	24.43	1.83	0.09	0.00	100.59	
No140-25	53.33	0.14	0.80	0.00	17.98	0.41	25.29	1.91	0.00	0.00	99.86	
No140-26	53.81	0.25	0.68	0.00	19.23	0.46	24.32	1.80	0.00	0.00	100.55	
No140-27	53.23	0.34	1.53	0.05	18.22	0.40	24.96	2.14	0.01	0.00	100.88	
No140-28	53.23	0.29	1.31	0.01	17.92	0.38	24.96	1.66	0.00	0.00	99.76	
No140-29	53.65	0.29	0.90	0.04	17.87	0.38	24.84	2.15	0.01	0.00	100.13	
No140-32	54.09	0.17	0.82	0.01	16.87	0.36	25.95	2.08	0.03	0.00	100.37	
No140-33	52.65	0.32	1.25	0.01	18.67	0.35	24.36	1.85	0.02	0.00	99.48	
No140-34	53.38	0.18	2.21	0.05	16.79	0.31	24.90	1.58	0.14	0.07	99.61	
No140-35	53.49	0.14	1.46	0.05	18.20	0.36	25.15	1.63	0.06	0.00	100.55	
No140-36	52.59	0.33	1.36	0.00	19.42	0.44	23.99	1.89	0.05	0.00	100.06	
No140-42	53.85	0.30	1.00	0.00	18.66	0.36	24.34	1.83	0.04	0.00	100.37	
No140-43	53.83	0.29	0.98	0.04	18.05	0.37	24.62	1.90	0.00	0.00	100.07	
No140-44	54.42	0.24	0.77	0.05	18.87	0.37	24.25	1.78	0.05	0.00	100.80	
No140-45	53.36	0.27	0.97	0.00	17.92	0.41	24.34	2.14	0.08	0.00	99.48	
No140-47	54.46	0.13	1.96	0.00	13.05	0.22	28.22	1.63	0.00	0.00	99.67	
No140-59	53.65	0.30	1.39	0.03	18.39	0.37	24.63	2.07	0.00	0.00	100.82	
No140-60	52.95	0.31	1.44	0.00	18.34	0.33	24.27	2.08	0.06	0.00	99.77	
No140-69	53.81	0.33	1.09	0.00	18.68	0.37	24.20	1.87	0.01	0.00	100.35	
1972-1975												
NGAURUHOE												
1972 Ngauruhoe	Ng72#3	55.37	0.25	0.64	0.07	18.60	0.47	22.38	4.30	0.05	0.00	102.13
	Ng72#3_2	54.75	0.36	1.37	0.07	18.45	0.47	21.93	4.05	0.10	0.00	101.54

	Ng72#3_3	55.01	0.24	0.71	0.10	17.73	0.47	22.67	4.28	0.08	0.06	101.34
	Ng72#4	53.91	0.24	0.61	0.06	22.13	0.52	20.11	4.21	0.09	0.01	101.89
1973 Ngauruhoe	Ng72#11	52.21	0.85	2.13	0.02	14.81	0.32	13.52	17.28	0.22	0.03	101.38
	Ng73#3	54.22	0.34	0.71	0.00	21.74	0.53	19.87	4.34	0.04	0.02	101.82
	Ng73#5_2	54.41	0.46	1.33	0.10	20.01	0.47	20.38	5.29	0.08	0.00	102.52
	Ng73#6	54.97	0.27	0.63	0.02	19.44	0.46	20.96	5.09	0.04	0.07	101.94
	Ng73#12_2	55.52	0.50	2.22	0.13	18.81	0.42	19.68	5.10	0.32	0.00	102.69
	Ng73#15	53.26	0.41	0.81	0.00	22.64	0.52	18.79	4.36	0.06	0.05	100.90
1974 Ngauruhoe	Ng74#1	52.70	0.58	2.48	0.04	16.35	0.44	18.87	9.04	0.16	0.00	100.65
	Ng74#6	54.29	0.38	1.60	0.08	17.21	0.46	21.96	5.65	0.08	0.00	101.70
	Ng74#10_2	56.08	0.58	3.43	0.03	18.12	0.42	18.02	5.51	0.35	0.00	102.54
	Ng74#11	53.28	0.42	1.23	0.00	22.19	0.55	18.20	4.93	0.10	0.01	100.92
	Ng74#11_2	53.95	0.39	0.68	0.00	23.13	0.56	18.48	4.63	0.07	0.01	101.90
1975 Ngauruhoe	Ng75#3	54.28	0.24	0.60	0.02	21.99	0.61	20.17	3.71	0.04	0.00	101.66
	Ng75#7	55.52	0.22	0.99	0.01	17.12	0.43	25.55	2.07	0.03	0.00	101.94
	Ng75#11	59.34	0.54	4.99	0.02	19.14	0.48	13.34	4.02	0.47	0.00	102.35
	Ng75#11_2	53.95	0.24	0.56	0.00	22.03	0.65	19.51	4.30	0.06	0.00	101.29
	Ng74#16	55.21	0.31	1.14	0.00	19.26	0.52	22.03	3.91	0.08	0.02	102.48
1995-1996 RUAPEHU												
1995 Ruapehu	Rua95#2	55.61	0.32	1.37	0.09	15.83	0.33	26.44	2.08	0.05	0.05	102.16
	Rua95#7	56.04	0.19	2.35	0.17	11.66	0.24	29.04	2.05	0.05	0.06	101.85

	Rua95#10	55.90	0.31	1.12	0.06	15.93	0.35	25.53	2.22	0.04		0.04	101.48
	Rua95#10												
	_2	55.36	0.32	1.31	0.06	17.34	0.37	25.09	2.08	0.03		0.01	101.98
1996 Ruapehu	Rua96#5	52.68	0.87	3.66	0.10	11.69	0.30	18.85	12.30	0.26		0.04	100.73
	Rua96#12	55.85	0.23	1.39	0.03	15.50	0.33	25.65	2.75	0.10		0.01	101.84
	Rua96#13	54.67	0.37	1.53	0.04	15.92	0.35	24.01	4.24	0.09		0.03	101.25
	Minimum	50.55	0.05	0.47	0.00	0.89	0.00	0.13	1.33	0.00	0.00	0.00	98.40
	Maximum	59.34	0.87	27.98	0.49	23.13	0.65	31.87	20.84	4.48	0.29	0.07	102.69
	Average	53.74	0.29	1.46	0.04	16.33	0.35	23.64	4.31	0.09	0.00	0.02	100.25
	Std. dev.	1.04	0.11	1.65	0.06	3.30	0.08	3.71	5.25	0.27	0.02	0.02	0.68

Appendix C10. Microprobe analyses of average glass compositions, the calculated whole rock compositions, and their standard deviations (std dev 2σ), from intermediate tephra of the Tongariro Volcanic Centre. Mangatawai and Tufa Trig glasses were analysed using a JEOL JXA-8900R electron microprobe equipped with four wavelength-dispersive spectrometers at the Institute of Earth Sciences, Academia Sinica, Taipei, Taiwan. Ngauruhoe 1972-1975 and Ruapehu 1995-1996 glasses were analysed using a JEOL JXA-8800R electron microprobe equipped with four wavelength-dispersive spectrometers at the Graduate School of Science, Hokkaido University, Sapporo, Japan. n*: n for average glass is the number of analyses of glass, whereas n for the calculated whole rock is the number of plagioclase and pyroxene analyses, respectively. Glass compositions were used as starting materials in MELTS modelling runs because of the low microlite content (see Petrography in the Results section). Indeed, we tested this assumption by calculating the whole rock compositions combining the weighed (i.e., content) average of the glass composition analyses and the average of the mineral composition analyses. It resulted in whole rock compositions within the range of the glass compositions. Thus, we consider it faithful to use the glass compositions as starting compositions for crystal content $<24\%$.

Tephra unit, and microlite contents		n*	SiO ₂	TiO ₂	Al ₂ O ₃	FeO	MnO	MgO	CaO	Na ₂ O	K ₂ O	Total	
407-14 Plg: 6% Px: 6%	Average glass	5	58.78	1.02	15.31	8.53	0.14	2.78	6.94	3.01	1.45	97.83	
	Std dev (2σ)		4.78	0.45	5.74	2.81	0.09	0.21	3.40	0.76	0.56	1.43	
	Calculated whole rock	18	14	57.99	0.92	15.38	8.50	0.14	3.95	7.16	2.84	1.29	98.14
	Std dev (2σ)			4.60	0.42	5.44	2.90	0.09	1.53	4.00	0.79	0.52	1.36
407-15 Plg: 7% Px: 3%	Average glass	12	59.20	1.10	14.30	8.75	0.11	2.96	6.52	2.31	1.68	96.93	
	Std dev (2σ)		1.29	0.21	0.89	0.90	0.07	0.61	0.62	0.54	0.24	0.90	
	Calculated whole rock	37	23	58.63	1.00	13.88	8.93	0.13	4.47	6.52	2.18	1.52	97.25
	Std dev (2σ)			1.55	0.20	1.07	1.64	0.07	1.48	2.24	0.60	0.23	0.90
407-16 Plg: 15%	Average glass	5	60.69	1.25	14.22	8.59	0.11	2.46	6.22	2.60	1.89	98.03	
	Std dev (2σ)		0.88	0.25	2.44	1.96	0.05	0.64	0.80	1.04	0.57	1.08	

Px: 3%	Calculated whole rock	15	3	59.15	1.04	16.09	7.68	0.10	2.83	7.29	2.62	1.58	98.39
	Std dev (2 σ)			2.10	0.24	4.12	2.04	0.06	2.18	1.78	1.23	0.52	1.02
407-17	Average glass	3		59.40	1.23	13.77	9.47	0.14	2.66	6.43	2.13	1.89	97.10
Plg: 12%	Std dev (2 σ)			2.90	0.22	1.32	0.60	0.08	0.32	1.32	0.95	0.47	1.11
Px: 9%	Calculated whole rock	12	9	57.96	1.00	13.78	9.49	0.15	5.08	6.80	1.94	1.50	97.70
	Std dev (2 σ)			3.00	0.20	1.64	2.05	0.10	2.75	3.94	1.08	0.42	1.06
407-18	Average glass	6		59.02	1.20	13.94	9.20	0.13	2.78	6.38	2.00	2.13	96.76
Plg: 14%	Std dev (2 σ)			1.22	0.22	1.05	0.68	0.07	0.60	0.56	0.89	1.47	1.06
Px: 5%	Calculated whole rock	40	17	57.60	1.01	15.88	8.25	0.15	3.05	7.41	2.10	1.78	97.24
	Std dev (2 σ)			2.33	0.21	1.77	0.90	0.17	0.95	1.68	1.12	1.34	0.96
407-47	Average glass	4		60.58	1.06	14.06	8.17	0.11	2.74	6.00	2.42	1.83	96.97
Plg: 12%	Std dev (2 σ)			0.69	0.11	0.73	0.43	0.07	0.45	0.32	0.39	0.22	0.48
Px: 5%	Calculated whole rock	37	11	59.36	0.90	15.30	7.63	0.11	3.53	6.75	2.44	1.54	97.56
	Std dev (2 σ)			1.50	0.11	1.12	0.94	0.07	1.39	2.41	0.63	0.20	0.55
407-49	Average glass	5		61.27	1.19	13.87	8.47	0.10	2.43	5.94	2.74	1.91	97.92
Plg: 7%	Std dev (2 σ)			2.35	0.20	1.21	1.02	0.08	1.23	1.40	1.12	0.81	1.27
Px: 4%	Calculated whole rock	22	10	60.47	1.09	14.30	8.22	0.11	2.94	6.63	2.70	1.72	98.18
	Std dev (2 σ)			2.92	0.28	3.36	2.54	0.09	1.80	3.54	1.11	0.80	1.27
407-54	Average glass	8		60.21	1.21	13.58	8.68	0.12	2.75	6.26	2.46	1.77	97.04
Plg: 7%	Std dev (2 σ)			0.83	0.21	0.53	0.44	0.07	0.59	0.38	0.35	0.29	0.97

Px: 5%	Calculated whole rock			59.29	1.09	14.11	8.31	0.12	3.32	7.16	2.42	1.57	97.39
	Std dev (2 σ)			1.07	0.20	0.67	1.34	0.07	2.25	3.59	0.38	0.27	0.95
407-56 Plg: 14% Px: 7%	Average glass	15		61.00	1.18	13.64	8.37	0.11	2.72	6.02	2.39	1.98	97.41
	Std dev (2 σ)			1.43	0.17	0.94	0.59	0.06	0.74	0.59	0.41	0.20	0.79
	Calculated whole rock	25	2	59.29	0.97	14.96	7.66	0.11	3.51	7.45	2.40	1.59	97.93
	Std dev (2 σ)			1.72	0.15	1.20	2.87	0.10	2.99	5.56	0.71	0.18	0.79
407-59 Plg: 10% Px: 3%	Average glass	7		60.06	1.12	14.14	8.36	0.14	2.73	5.99	2.57	2.13	97.24
	Std dev (2 σ)			0.93	0.13	0.78	1.00	0.07	0.33	1.02	0.84	0.96	1.44
	Calculated whole rock	20	12	59.13	0.99	15.27	7.86	0.13	3.14	6.60	2.61	1.87	97.61
	Std dev (2 σ)			1.31	0.13	0.99	1.15	0.07	0.68	1.16	0.84	0.90	1.40
Tufa Trig 8 Plg: 7% Px: 3%	Average glass	6		62.14	0.94	14.79	6.57	0.07	2.36	5.05	2.85	2.25	97.03
	Std dev (2 σ)			1.29	0.16	0.63	0.42	0.10	0.32	0.75	1.14	0.34	1.27
	Calculated whole rock	43	37	61.27	0.86	15.26	6.50	0.08	2.90	5.50	2.86	2.04	97.28
	Std dev (2 σ)			1.45	0.17	3.51	2.00	0.10	3.00	2.32	1.23	0.33	1.22
Tufa Trig 13 Plg: 11% Px: 3%	Average glass	8		61.86	0.96	14.70	6.78	0.09	2.21	4.92	2.57	2.69	96.77
	Std dev (2 σ)			1.00	0.14	0.41	0.65	0.06	0.20	0.16	0.31	0.45	1.07
	Calculated whole rock	29	27	60.68	0.84	15.72	6.38	0.08	2.66	5.79	2.68	2.34	97.18
	Std dev (2 σ)			1.18	0.15	3.07	2.13	0.07	2.78	2.97	0.63	0.42	1.04
Tufa Trig 14 Plg: 11%	Average glass	7		62.32	1.06	14.90	6.79	0.09	2.23	4.88	2.36	2.55	97.18
	Std dev (2 σ)			0.85	0.09	0.56	0.56	0.05	0.34	0.38	1.38	0.29	1.14

Px: 3%	Calculated whole rock	38	29	60.88	0.92	16.13	6.46	0.09	2.68	5.73	2.43	2.22	97.54
	Std dev (2 σ)			1.95	0.09	1.40	0.82	0.05	0.56	1.39	1.46	0.28	1.10
1972 Ngauruhoe Plg: 13% Px: 3%	Average glass	6		61.79	1.38	13.20	9.02	0.14	2.59	5.81	3.44	2.45	99.83
	Std dev (2 σ)			1.26	0.09	1.18	0.76	0.04	1.05	0.19	0.23	0.24	0.94
	Calculated whole rock	3	3	60.71	N/A	14.73	8.26	N/A	2.76	6.64	3.48	N/A	99.83
	Std dev (2 σ)			1.34	N/A	1.20	1.46	N/A	1.90	2.61	0.27	N/A	0.89
1975 Ngauruhoe Plg: 15% Px: 9%	Average glass	3		64.05	1.12	14.03	7.78	0.15	1.79	4.97	3.57	2.45	99.90
	Std dev (2 σ)			5.13	0.04	1.54	1.53	0.03	1.13	1.79	0.23	0.82	0.23
	Calculated whole rock	3	3	61.80	N/A	14.92	7.90	N/A	3.34	5.89	3.37	N/A	100.16
	Std dev (2 σ)			4.55	N/A	1.38	2.16	N/A	2.22	1.79	0.33	N/A	0.35
1995 Ruapehu Plg: 5% Px: 3%	Average glass	3		63.04	0.97	15.35	6.12	0.12	2.59	5.42	3.94	2.54	100.09
	Std dev (2 σ)			1.76	0.11	0.65	0.27	0.04	0.63	0.83	0.12	0.46	0.65
	Calculated whole rock	3	3	62.43	N/A	15.61	6.13	N/A	3.20	5.65	3.86	N/A	100.25
	Std dev (2 σ)			1.77	N/A	0.73	1.05	N/A	0.92	0.82	0.18	N/A	0.71
1996 Ruapehu Plg: 13% Px: 4%	Average glass	3		63.64	1.10	14.77	6.53	0.12	2.10	5.09	3.66	2.78	99.79
	Std dev (2 σ)			0.91	0.16	0.87	0.30	0.04	0.18	0.42	0.49	0.19	0.48
	Calculated whole rock	3	3	62.27	N/A	15.88	6.12	N/A	2.69	5.99	3.65	N/A	100.02
	Std dev (2 σ)			1.10	N/A	1.01	0.98	N/A	1.44	2.10	0.45	N/A	0.73

N/A: no analysis

Appendix C11. Pyroxene major element compositions analysed for the TgVC eruptive sequences studied. Mangatawai and Tufa Trig samples were analysed using a JEOL JXA-8900R electron microprobe equipped with four wavelength-dispersive spectrometers at the Institute of Earth Sciences, Academia Sinica, Taipei, Taiwan. 1972-1975 Ngauruhoe and 1995-1996 Ruapehu samples were analysed using a JEOL JXA-8800R electron microprobe equipped with four wavelength-dispersive spectrometers at the Graduate School of Science, Hokkaido University, Sapporo, Japan. The analyses highlighted in yellow were used for hygrometobarometric calculations and *MELTS* modelling.

Eruptive sequence and tephra	Comment	SiO ₂	TiO ₂	Al ₂ O ₃	FeO	MnO	MgO	CaO	Na ₂ O	K ₂ O	Total	Mg#	Mg#
Mangatawai													
407-14	No14-1	54.36	0.17	1.28	13.24	0.23	28.40	1.69	0.06	0.00	99.53	0.79	79
	No14-2	53.47	0.20	1.41	16.95	0.34	26.04	1.71	0.04	0.00	100.15	0.73	73
	No14-3	53.76	0.31	1.34	17.86	0.37	25.05	1.93	0.02	0.00	100.67	0.71	71
	No14-4	55.24	0.16	1.06	13.84	0.30	28.09	1.92	0.04	0.00	100.74	0.78	78
	No14-25	54.38	0.27	0.67	16.82	0.31	26.01	2.11	0.03	0.00	100.61	0.73	73
	No14-26	53.64	0.27	1.37	15.61	0.28	25.97	2.38	0.02	0.00	99.57	0.75	75
	No14-35	54.03	0.26	1.13	15.75	0.33	25.80	2.56	0.02	0.00	99.94	0.74	74
	No14-36	53.78	0.32	0.93	17.20	0.29	25.33	2.29	0.06	0.00	100.24	0.72	72
	No14-42	53.36	0.21	1.41	16.00	0.33	26.21	1.73	0.01	0.00	99.42	0.74	74
	No14-43	53.33	0.29	1.39	17.87	0.34	24.99	1.82	0.02	0.00	100.04	0.71	71
	No14-44	54.05	0.17	0.83	16.51	0.32	26.52	1.68	0.01	0.00	100.13	0.74	74
	No14-45	53.02	0.24	0.96	17.09	0.33	23.18	4.30	0.07	0.00	99.19	0.71	71

No14-52	51.17	0.39	3.61	8.49	0.15	15.65	19.82	0.33	0.00	99.72	0.77	77
No14-55	54.18	0.27	1.47	16.60	0.42	22.60	3.96	0.06	0.13	99.68	0.71	71
Average	53.70	0.25	1.35	15.70	0.31	24.99	3.56	0.06	0.01	99.97	0.74	74
2 σ	1.83	0.13	1.39	4.94	0.13	6.21	9.50	0.17	0.07	0.97	0.05	5
No15-11	53.41	0.21	0.87	17.53	0.33	23.25	4.14	0.00	0.00	99.77	0.70	70
No15-13	54.36	0.25	0.80	17.49	0.32	25.13	2.29	0.04	0.00	100.66	0.72	72
No15-23	52.94	0.32	1.30	17.09	0.36	25.32	2.21	0.04	0.00	99.62	0.73	73
No15-24	53.84	0.23	1.91	13.44	0.27	27.75	2.50	0.05	0.00	100.19	0.79	79
No15-26	54.86	0.17	1.58	13.24	0.28	28.18	1.70	0.03	0.01	100.19	0.79	79
No15-27	54.78	0.20	1.80	14.18	0.26	27.33	1.72	0.04	0.00	100.36	0.77	77
No15-28	55.19	0.28	1.74	13.93	0.22	27.86	1.71	0.01	0.00	100.97	0.78	78
No15-29	55.77	0.14	0.92	13.23	0.30	28.07	1.83	0.00	0.00	100.27	0.79	79
No15-30	54.62	0.20	1.87	14.30	0.30	27.36	1.81	0.02	0.00	100.52	0.77	77
No15-34	54.57	0.31	1.49	14.43	0.33	26.56	2.55	0.06	0.00	100.37	0.77	77
No15-40	53.15	0.26	2.47	5.16	0.12	17.61	20.69	0.21	0.01	100.00	0.86	86
No15-44	53.60	0.21	1.14	16.18	0.42	22.45	5.58	0.07	0.00	99.65	0.71	71
No15-45	55.04	0.29	2.00	15.82	0.33	22.70	3.11	0.23	0.17	99.73	0.72	72
No15-46	55.37	0.18	1.04	13.37	0.28	27.67	2.19	0.02	0.00	100.13	0.79	79
No15-47	53.93	0.26	1.01	17.40	0.35	24.85	2.28	0.04	0.00	100.11	0.72	72
No15-54	54.78	0.23	0.96	15.11	0.32	26.45	2.21	0.02	0.00	100.10	0.76	76
No15-55	54.59	0.19	1.78	13.57	0.34	27.30	2.46	0.04	0.00	100.40	0.78	78
No15-63	54.74	0.24	0.69	15.84	0.38	25.91	2.33	0.04	0.00	100.21	0.74	74
No15-64	53.70	0.20	1.18	16.42	0.30	25.36	2.35	0.05	0.00	99.57	0.73	73

407-15

	No15-65	53.79	0.31	1.17	17.08	0.34	25.05	2.46	0.02	0.00	100.23	0.72	72
	No15-73	55.04	0.21	1.49	13.41	0.31	27.67	2.21	0.04	0.00	100.45	0.79	79
	No15-74	55.13	0.17	1.66	13.16	0.33	28.31	1.79	0.03	0.00	100.73	0.79	79
	No15-77	53.91	0.28	1.26	17.22	0.41	22.82	5.05	0.09	0.00	101.08	0.70	70
	Average	54.40	0.23	1.40	14.72	0.31	25.69	3.35	0.05	0.01	100.23	0.76	76
	2 σ	1.51	0.10	0.91	5.29	0.13	5.15	7.83	0.11	0.07	0.81	0.08	8
													0
407-16	No16-2	53.56	0.28	0.63	18.22	0.45	21.87	4.56	0.10	0.00	99.67	0.68	68
	No16-7	53.76	0.25	0.78	18.47	0.39	20.99	5.16	0.09	0.00	99.89	0.67	67
	No16-15	54.08	0.18	0.63	18.27	0.40	22.81	4.04	0.03	0.00	100.48	0.69	69
	No16-17	53.63	0.37	1.49	17.57	0.35	23.82	2.59	0.06	0.00	99.93	0.71	71
	No16-29	54.76	0.18	1.71	13.41	0.27	28.08	1.74	0.02	0.00	100.27	0.79	79
	No16-30	55.04	0.15	1.64	13.56	0.29	28.17	1.65	0.02	0.00	100.61	0.79	79
	No16-34	53.78	0.35	1.72	16.87	0.33	24.83	2.52	0.04	0.00	100.51	0.72	72
	No16-35	55.03	0.20	0.98	14.76	0.33	26.73	2.25	0.02	0.00	100.32	0.76	76
	No16-45	55.59	0.15	0.98	13.19	0.26	27.69	2.52	0.06	0.00	100.55	0.79	79
	No16-46	54.75	0.26	1.81	14.51	0.31	26.63	2.03	0.05	0.01	100.56	0.77	77
	No16-51	54.40	0.18	0.80	16.90	0.35	23.07	3.81	0.01	0.01	99.56	0.71	71
	No16-56	54.25	0.21	0.87	17.13	0.47	22.64	4.20	0.07	0.00	99.84	0.70	70
	No16-57	54.54	0.25	0.67	17.46	0.32	23.29	3.76	0.06	0.00	100.36	0.70	70
	No16-74	54.02	0.26	1.05	16.09	0.34	23.87	3.84	0.07	0.00	99.56	0.73	73
	No16-76	53.80	0.35	1.95	17.53	0.35	21.94	4.12	0.16	0.05	100.25	0.69	69
	Average	54.33	0.24	1.18	16.26	0.35	24.43	3.25	0.06	0.00	100.16	0.73	73
	2 σ	1.21	0.14	0.96	3.75	0.12	4.86	2.23	0.08	0.03	0.76	0.08	8

407-17	No17-4	53.68	0.24	1.41	16.31	0.32	25.18	2.62	0.09	0.00	99.86	0.73	73
	No17-9	54.63	0.28	0.65	19.12	0.35	23.61	2.16	0.01	0.00	100.82	0.69	69
	No17-10	54.25	0.19	0.65	18.77	0.40	23.80	2.15	0.03	0.00	100.24	0.69	69
	No17-14	52.33	0.40	2.84	7.92	0.16	16.33	19.39	0.22	0.00	99.71	0.79	79
	No17-17	54.04	0.29	0.91	17.57	0.56	24.42	1.81	0.00	0.00	99.59	0.71	71
	No17-18	54.94	0.20	0.84	15.49	0.31	25.74	2.30	0.03	0.00	99.84	0.75	75
	No17-19	53.46	0.28	1.26	17.71	0.36	23.89	2.39	0.02	0.00	99.38	0.71	71
	No17-26	54.82	0.19	1.62	13.27	0.30	27.98	1.73	0.01	0.00	100.00	0.79	79
	No17-27	53.57	0.43	1.58	15.40	0.38	22.26	6.59	0.10	0.00	100.30	0.72	72
	No17-35	55.24	0.16	0.91	14.84	0.24	27.01	2.16	0.04	0.00	100.68	0.76	76
	No17-60	53.80	0.26	0.75	17.80	0.46	22.61	4.08	0.04	0.00	99.78	0.69	69
	No17-63	54.16	0.22	0.63	17.29	0.32	25.15	2.31	0.03	0.00	100.11	0.72	72
	No17-76	53.17	0.32	1.55	17.64	0.28	23.98	2.95	0.04	0.00	99.98	0.71	71
	No17-87	54.03	0.26	0.92	16.73	0.39	24.73	2.24	0.04	0.00	99.33	0.72	72
	Average	54.01	0.27	1.18	16.13	0.34	24.05	3.92	0.05	0.00	99.97	0.73	73
2 σ	1.54	0.15	1.20	5.70	0.19	5.42	9.25	0.12	0.00	0.87	0.07	7	
407-18	No18-10	51.91	0.42	1.64	17.51	0.36	22.19	4.81	0.09	0.03	99.00	0.69	69
	No18-21	53.71	0.22	0.76	17.32	0.35	23.45	4.08	0.08	0.00	99.99	0.71	71
	No18-30	53.39	0.20	0.69	17.79	0.46	22.40	4.12	0.09	0.00	99.14	0.69	69
	No18-31	52.95	0.30	1.07	17.10	0.51	22.24	5.36	0.06	0.00	99.63	0.70	70
	No18-32	53.18	0.38	1.38	17.89	0.37	24.20	2.28	0.05	0.00	99.80	0.71	71
	No18-33	52.43	0.35	1.34	17.34	0.34	21.84	5.32	0.05	0.00	99.00	0.69	69

No18-34	52.77	0.32	1.25	17.59	0.39	22.59	4.09	0.09	0.00	99.12	0.70	70	
No18-35	53.03	0.22	0.61	18.17	0.42	23.01	3.91	0.05	0.00	99.41	0.69	69	
No18-47	53.49	0.27	0.63	17.42	0.34	25.11	2.23	0.05	0.00	99.53	0.72	72	
No18-58	53.25	0.21	1.33	15.21	0.37	26.47	2.20	0.00	0.00	99.08	0.76	76	
No18-59	53.59	0.24	1.63	15.16	0.38	26.45	2.21	0.04	0.00	99.79	0.76	76	
No18-93	53.50	0.23	0.96	17.07	0.42	25.34	2.15	0.02	0.01	99.70	0.73	73	
No18-95	53.82	0.22	1.71	15.05	0.34	26.71	1.71	0.03	0.00	99.58	0.76	76	
No18-96	53.76	0.21	1.72	14.70	0.39	26.90	1.78	0.03	0.00	99.54	0.77	77	
No18-97	53.81	0.21	1.70	13.18	0.24	27.99	1.79	0.01	0.00	99.05	0.79	79	
No18-103	52.31	0.36	0.76	21.19	0.36	20.27	4.31	0.09	0.00	99.65	0.63	63	
No18-104	52.55	0.31	1.71	15.15	0.45	22.49	6.91	0.12	0.02	99.74	0.73	73	
Average	53.14	0.27	1.23	16.75	0.38	24.10	3.49	0.05	0.00	99.46	0.72	72	
2 σ	1.16	0.14	0.85	3.68	0.12	4.47	3.14	0.07	0.02	0.65	0.08	8	
407-47	No47-15	54.15	0.23	1.02	10.01	0.29	16.51	17.98	0.23	0.00	100.41	0.75	75
	No47-16	54.12	0.20	1.61	16.21	0.38	25.77	1.83	0.02	0.00	100.16	0.74	74
	No47-17	55.12	0.22	1.60	15.38	0.38	26.32	1.76	0.01	0.00	100.86	0.75	75
	No47-18	55.19	0.23	1.55	14.98	0.41	27.35	1.57	0.02	0.00	101.35	0.76	76
	No47-19	55.58	0.22	1.33	15.78	0.41	26.43	1.83	0.05	0.00	101.62	0.75	75
	No47-20	55.17	0.17	1.31	15.47	0.37	26.61	1.70	0.03	0.00	100.86	0.75	75
	No47-21	54.80	0.14	1.78	15.36	0.32	26.21	1.67	0.00	0.00	100.30	0.75	75
	No47-24	56.04	0.24	1.99	14.36	0.32	25.31	1.99	0.14	0.06	100.50	0.76	76
	No47-26	54.59	0.25	1.16	15.78	0.36	23.37	4.53	0.05	0.00	100.11	0.73	73
	No47-47	54.61	0.24	1.13	17.29	0.43	24.95	2.02	0.03	0.00	100.70	0.72	72

	No47-48	54.74	0.23	1.37	16.53	0.32	25.18	1.85	0.05	0.00	100.30	0.73	73
	Average	54.92	0.22	1.44	15.19	0.36	24.91	3.52	0.06	0.01	100.65	0.74	74
	2 σ	1.16	0.07	0.59	3.78	0.09	5.96	9.73	0.13	0.03	0.98	0.03	3
407-49	No49-6	53.74	0.41	1.85	9.65	0.26	16.33	18.37	0.26	0.00	100.95	0.75	75
	No49-7	52.86	0.48	2.48	9.65	0.20	15.69	18.39	0.32	0.00	100.11	0.74	74
	No49-8	52.55	0.47	2.78	10.22	0.21	15.91	17.67	0.27	0.00	100.18	0.73	73
	No49-9	52.82	0.48	2.34	9.30	0.27	15.88	18.67	0.26	0.00	100.06	0.75	75
	No49-10	52.98	0.39	2.37	9.53	0.24	16.23	18.91	0.28	0.00	101.05	0.75	75
	No49-11	53.40	0.34	1.98	9.80	0.28	16.26	18.19	0.28	0.00	100.58	0.75	75
	No49-21	54.68	0.38	1.66	17.07	0.42	22.86	3.32	0.12	0.05	100.60	0.70	70
	No49-30	54.06	0.30	0.80	18.27	0.41	21.47	4.17	0.05	0.02	99.60	0.68	68
	No49-31	53.95	0.28	0.70	18.05	0.47	22.42	4.07	0.05	0.00	99.99	0.69	69
	No49-33	52.70	0.33	1.08	20.10	0.38	20.27	4.50	0.06	0.00	99.45	0.64	64
	Average	53.37	0.38	1.80	13.16	0.31	18.33	12.62	0.20	0.01	100.26	0.72	72
	2 σ	1.41	0.15	1.46	9.09	0.19	6.05	14.85	0.22	0.03	1.06	0.08	8
407-54	No54-1	51.99	0.56	2.11	10.61	0.32	14.66	19.48	0.30	0.00	100.06	0.71	71
	No54-2	52.19	0.62	2.07	12.09	0.37	14.48	18.02	0.33	0.00	100.16	0.68	68
	No54-9	54.37	0.30	1.35	16.13	0.36	25.22	2.33	0.00	0.00	100.07	0.74	74
	No54-12	54.55	0.31	1.34	16.30	0.28	24.79	2.49	0.02	0.00	100.19	0.73	73
	No54-23	52.38	0.43	2.36	10.07	0.26	15.19	18.49	0.28	0.00	99.48	0.73	73
	No54-24	52.11	0.55	2.76	10.50	0.26	15.26	18.24	0.36	0.00	100.07	0.72	72
	No54-51	52.36	0.52	2.38	9.65	0.20	15.59	19.03	0.29	0.00	100.05	0.74	74

	Average	52.85	0.47	2.05	12.19	0.29	17.88	14.01	0.22	0.00	100.01	0.72	72
	2 σ	2.22	0.25	1.07	5.70	0.12	9.76	15.88	0.30	0.00	0.49	0.04	4
407-56	No56-47	53.61	0.40	1.47	17.10	0.45	21.52	5.35	0.08	0.00	100.04	0.69	69
	No56-36	52.47	0.42	2.52	9.57	0.22	15.15	19.63	0.31	0.00	100.28	0.74	74
	Average	53.04	0.41	1.99	13.34	0.33	18.33	12.49	0.19	0.00	100.16	0.71	71
	2 σ	1.62	0.02	1.49	10.65	0.33	9.01	20.18	0.32	0.00	0.35	0.07	7
407-59	No59-5	55.01	0.22	0.68	18.97	0.42	22.83	2.20	0.05	0.00	100.38	0.68	68
	No59-6	53.51	0.21	1.16	20.64	0.47	21.91	2.25	0.00	0.00	100.14	0.65	65
	No59-7	54.30	0.33	1.19	19.89	0.48	22.22	2.20	0.00	0.00	100.62	0.67	67
	No59-8	55.54	0.14	0.91	15.48	0.38	26.43	1.71	0.00	0.00	100.60	0.75	75
	No59-9	55.41	0.20	1.00	16.10	0.34	26.12	1.68	0.03	0.02	100.92	0.74	74
	No59-12	54.54	0.26	1.52	15.76	0.34	26.11	2.00	0.09	0.00	100.71	0.75	75
	No59-13	54.73	0.28	1.64	15.73	0.26	25.80	1.92	0.04	0.01	100.47	0.75	75
	No59-14	54.77	0.28	1.54	16.30	0.30	25.93	1.95	0.03	0.00	101.14	0.74	74
	No59-15	54.91	0.29	1.55	16.03	0.32	25.95	2.08	0.06	0.00	101.27	0.74	74
	No59-16	55.14	0.27	1.55	15.54	0.28	26.11	1.98	0.04	0.00	101.03	0.75	75
	No59-18	55.10	0.19	0.88	15.17	0.28	26.86	1.99	0.03	0.00	100.56	0.76	76
	No59-19	54.44	0.24	1.56	15.42	0.34	25.43	2.78	0.01	0.00	100.33	0.75	75
	No59-43	50.74	0.39	2.45	9.04	0.19	15.63	19.50	0.32	0.00	98.40	0.75	75
	Average	54.47	0.25	1.35	16.16	0.34	24.41	3.40	0.05	0.00	100.50	0.73	73
	2 σ	2.47	0.13	0.92	5.64	0.17	6.25	9.69	0.17	0.01	1.43	0.07	7

Tufa Trig

108-131	No131-6	54.06	0.30	0.84	15.34	0.40	26.42	2.04	0.03	0.00	99.42	0.75	75
Tf8	No131-8	53.82	0.19	1.20	15.54	0.28	26.35	2.03	0.01	0.00	99.46	0.75	75
	No131-24	54.60	0.19	0.91	15.98	0.35	25.83	2.08	0.03	0.00	99.97	0.74	74
	No131-25	54.06	0.28	1.13	15.40	0.44	26.29	2.14	0.00	0.00	99.76	0.75	75
	No131-33	53.11	0.30	1.30	17.74	0.37	24.93	2.26	0.03	0.00	100.03	0.71	71
	No131-34	53.74	0.28	1.14	17.68	0.34	24.59	2.30	0.06	0.00	100.16	0.71	71
	No131-35	53.56	0.36	1.06	17.93	0.32	24.68	2.11	0.04	0.00	100.07	0.71	71
	No131-44	53.84	0.27	1.35	15.07	0.34	26.35	2.48	0.08	0.00	99.78	0.76	76
	No131-45	54.06	0.27	1.01	15.24	0.33	26.65	2.02	0.05	0.00	99.64	0.76	76
	No131-46	53.90	0.18	1.28	17.65	0.36	25.33	1.43	0.00	0.00	100.13	0.72	72
	No131-47	53.62	0.37	1.22	17.63	0.28	25.19	1.94	0.00	0.00	100.27	0.72	72
	No131-48	54.86	0.16	0.68	15.08	0.28	27.09	1.85	0.04	0.00	100.02	0.76	76
	No131-50	54.15	0.26	1.15	15.43	0.31	26.35	1.91	0.02	0.00	99.58	0.75	75
	No131-54	53.36	0.29	0.47	11.07	0.29	15.25	18.79	0.25	0.00	99.77	0.71	71
	No131-55	52.31	0.42	1.07	10.59	0.23	15.71	19.20	0.22	0.00	99.75	0.73	73
	No131-56	51.21	0.72	2.22	10.95	0.24	15.58	18.47	0.26	0.00	99.68	0.72	72
	No131-60	52.59	0.32	1.50	19.39	0.31	23.06	1.89	0.03	0.00	99.10	0.68	68
	No131-62	54.61	0.36	1.31	15.16	0.25	26.56	1.95	0.02	0.00	100.25	0.76	76
	No131-63	54.34	0.35	1.58	15.40	0.33	26.29	2.05	0.16	0.04	100.57	0.75	75
	No131-68	53.29	0.34	1.31	18.32	0.42	24.50	1.94	0.01	0.00	100.17	0.70	70
	No131-69	53.07	0.19	0.93	20.23	0.32	23.47	1.68	0.07	0.00	99.98	0.67	67
	No131-77	52.85	0.35	1.09	19.68	0.38	23.23	1.73	0.06	0.00	99.38	0.68	68
	No131-78	53.44	0.28	1.16	18.32	0.32	24.22	1.97	0.06	0.00	99.77	0.70	70
	No131-81	52.97	0.35	1.75	16.78	0.43	24.66	2.33	0.05	0.00	99.32	0.72	72

	No131-83	53.84	0.34	1.15	18.54	0.33	24.04	1.91	0.01	0.00	100.15	0.70	70
	No131-84	53.94	0.23	0.95	17.88	0.38	24.58	1.94	0.04	0.00	99.96	0.71	71
	No131-85	54.65	0.21	0.75	16.62	0.39	25.39	1.94	0.01	0.00	99.95	0.73	73
	No131-91	53.24	0.32	1.20	19.18	0.30	23.85	1.77	0.06	0.00	99.94	0.69	69
	No131-92	53.21	0.26	1.19	19.96	0.36	23.39	1.66	0.06	0.00	100.09	0.68	68
	No131-93	51.71	0.62	2.01	11.23	0.20	14.61	19.01	0.34	0.00	99.75	0.70	70
	No131-94	52.76	0.31	1.32	20.26	0.41	23.49	1.74	0.04	0.00	100.38	0.67	67
	No131-95	53.02	0.27	1.18	19.75	0.34	23.55	1.80	0.02	0.00	99.95	0.68	68
	No131-96	53.21	0.35	1.17	20.09	0.42	23.80	1.80	0.02	0.00	100.85	0.68	68
	No131-97	52.98	0.27	1.20	19.88	0.32	23.75	1.83	0.04	0.00	100.26	0.68	68
	No131-98	54.49	0.28	0.88	15.88	0.28	26.26	1.85	0.05	0.00	99.98	0.75	75
	No131-99	54.63	0.20	1.05	15.29	0.33	26.73	1.93	0.04	0.00	100.20	0.76	76
	Average	53.53	0.31	1.19	16.73	0.33	23.94	3.83	0.06	0.00	99.93	0.72	72
	2 σ	1.65	0.22	0.67	5.42	0.12	6.65	10.80	0.16	0.01	0.71	0.06	6
108-137	No137-4	51.75	0.25	2.01	7.45	0.18	17.13	19.52	0.32	0.00	99.01	0.80	80
Tf13	No137-5	50.94	0.64	2.42	9.42	0.22	16.36	18.66	0.26	0.00	99.05	0.76	76
	No137-7	51.35	0.60	1.94	10.38	0.23	15.73	18.82	0.20	0.00	99.31	0.73	73
	No137-9	52.56	0.45	1.32	20.80	0.32	22.76	1.92	0.03	0.00	100.18	0.66	66
	No137-10	52.96	0.40	1.31	18.16	0.34	24.27	2.45	0.08	0.00	99.97	0.70	70
	No137-11	53.11	0.29	1.10	18.51	0.39	24.45	2.07	0.02	0.00	99.95	0.70	70
	No137-16	54.35	0.05	1.66	8.32	0.23	31.87	2.05	0.02	0.00	99.04	0.87	87
	No137-22	54.08	0.20	0.88	15.74	0.40	26.42	2.02	0.03	0.00	99.75	0.75	75
	No137-23	53.97	0.17	1.57	14.06	0.22	28.27	1.60	0.00	0.00	99.90	0.78	78

	No137-24	54.02	0.21	1.72	14.70	0.31	27.68	1.66	0.01	0.00	100.37	0.77	77
	No137-25	53.89	0.09	1.56	13.67	0.23	27.84	1.65	0.05	0.00	99.02	0.78	78
	No137-37	52.98	0.32	1.13	19.73	0.38	23.33	1.99	0.04	0.00	99.89	0.68	68
	No137-38	52.23	0.35	1.39	19.80	0.41	23.28	1.75	0.00	0.00	99.21	0.68	68
	No137-39	52.94	0.22	1.35	20.27	0.42	23.39	1.73	0.01	0.00	100.37	0.67	67
	No137-48	52.64	0.30	1.29	19.64	0.34	23.97	1.86	0.02	0.00	100.10	0.69	69
	No137-49	52.53	0.26	1.15	20.35	0.40	23.80	1.81	0.04	0.00	100.34	0.68	68
	No137-50	52.81	0.23	1.17	19.80	0.38	23.60	1.78	0.02	0.00	99.81	0.68	68
	No137-51	52.88	0.23	1.21	20.65	0.36	23.72	1.79	0.01	0.00	100.84	0.67	67
	No137-52	52.87	0.35	1.33	19.90	0.42	23.41	1.87	0.03	0.00	100.22	0.68	68
	No137-55	53.03	0.33	1.08	19.64	0.51	23.53	2.12	0.04	0.00	100.27	0.68	68
	No137-66	54.07	0.17	1.90	6.80	0.17	19.42	17.55	0.19	0.00	100.38	0.84	84
	No137-67	51.41	0.49	4.66	6.35	0.20	16.73	19.95	0.32	0.00	100.44	0.82	82
	No137-70	53.75	0.31	1.00	18.39	0.41	24.57	2.05	0.05	0.00	100.53	0.70	70
	No137-75	52.24	0.28	2.67	7.45	0.16	16.74	20.84	0.27	0.00	100.85	0.80	80
	No137-76	52.61	0.31	2.69	6.87	0.20	16.62	20.73	0.31	0.00	100.51	0.81	81
	No137-77	52.22	0.40	2.68	7.47	0.21	16.35	20.57	0.30	0.00	100.25	0.80	80
	No137-81	54.13	0.20	0.75	18.37	0.33	25.17	1.93	0.03	0.00	100.93	0.71	71
	Average	52.90	0.30	1.66	14.91	0.31	22.61	7.14	0.10	0.00	100.02	0.74	74
	2 σ	1.84	0.27	1.63	10.97	0.20	8.60	16.50	0.24	0.00	1.16	0.12	12
108-138	No138-3	53.89	0.20	0.85	17.54	0.34	25.31	2.07	0.04	0.00	100.25	0.72	72
Tf14	No138-9	54.00	0.27	0.90	17.77	0.33	25.42	2.02	0.05	0.00	100.74	0.72	72
	No138-10	53.87	0.25	0.84	18.20	0.47	24.83	2.16	0.04	0.00	100.64	0.71	71

No138-11	52.82	0.36	2.51	17.26	0.33	24.69	2.53	0.04	0.01	100.58	0.72	72
No138-17	53.74	0.27	0.76	18.56	0.36	24.60	2.02	0.05	0.00	100.36	0.70	70
No138-19	52.76	0.33	1.24	19.90	0.36	23.53	1.82	0.02	0.00	99.98	0.68	68
No138-20	52.42	0.15	2.17	19.25	0.34	24.05	1.66	0.03	0.00	100.24	0.69	69
No138-21	52.70	0.24	1.89	18.53	0.32	24.82	1.45	0.03	0.00	100.11	0.70	70
No138-22	53.07	0.39	1.42	19.62	0.37	23.96	1.79	0.03	0.00	100.72	0.69	69
No138-23	53.43	0.31	0.75	18.36	0.30	24.44	1.94	0.03	0.00	99.55	0.70	70
No138-29	53.31	0.26	0.71	21.27	0.38	22.21	2.04	0.00	0.00	100.19	0.65	65
No138-30	54.51	0.16	1.54	13.09	0.18	28.53	1.52	0.03	0.00	99.73	0.80	80
No138-31	54.15	0.21	1.90	13.35	0.31	28.70	1.53	0.05	0.00	100.24	0.79	79
No138-32	53.57	0.22	1.71	15.64	0.31	27.06	1.51	0.03	0.00	100.05	0.76	76
No138-33	54.06	0.25	1.49	17.18	0.35	25.39	1.80	0.03	0.00	100.56	0.72	72
No138-34	53.51	0.40	1.20	19.92	0.40	23.82	1.79	0.03	0.00	101.08	0.68	68
No138-35	52.93	0.40	1.73	18.85	0.33	24.46	1.94	0.04	0.01	100.75	0.70	70
No138-49	53.51	0.29	1.00	18.55	0.41	24.29	2.14	0.04	0.00	100.26	0.70	70
No138-50	53.81	0.33	1.18	17.26	0.35	25.29	2.06	0.03	0.01	100.37	0.72	72
No138-53	54.43	0.27	0.76	17.40	0.36	25.36	1.90	0.02	0.01	100.50	0.72	72
No138-54	53.35	0.32	1.31	17.53	0.29	25.34	2.07	0.02	0.00	100.23	0.72	72
No138-67	53.48	0.32	0.96	18.87	0.39	24.86	1.94	0.03	0.00	100.86	0.70	70
No138-68	53.43	0.20	0.86	17.35	0.33	25.70	1.88	0.04	0.00	99.85	0.73	73
No138-69	53.25	0.34	1.31	18.35	0.32	25.02	1.93	0.06	0.00	100.58	0.71	71
No138-70	53.45	0.28	1.22	18.28	0.42	24.86	1.81	0.01	0.00	100.34	0.71	71
No138-84	53.57	0.26	0.89	18.85	0.29	24.57	1.94	0.05	0.00	100.45	0.70	70
No138-85	53.31	0.29	0.90	18.46	0.38	24.90	1.89	0.04	0.00	100.18	0.71	71

	No138-87	53.03	0.21	1.08	20.52	0.38	23.90	1.33	0.03	0.00	100.48	0.67	67
	No138-88	52.59	0.27	0.95	19.93	0.41	24.16	1.48	0.00	0.00	99.84	0.68	68
	Average	53.44	0.28	1.24	18.13	0.35	24.97	1.86	0.03	0.00	100.33	0.71	71
	2 σ	1.05	0.13	0.93	3.58	0.11	2.63	0.51	0.03	0.01	0.70	0.06	6
1972-1975													
Ngauruhoe													
1972													
	No72-3_3	55.01	0.24	0.71	17.73	0.47	22.67	4.28	0.08		101.34	0.69	69
	No72-4	53.91	0.24	0.61	22.13	0.52	20.11	4.21	0.09		101.89	0.62	62
	No72-11	52.21	0.85	2.13	14.81	0.32	13.52	17.28	0.22		101.38	0.62	62
	Average	53.71	0.44	1.15	18.22	0.44	18.77	8.59	0.13		101.54	0.65	65
	2 σ	2.82	0.70	1.70	7.37	0.21	9.44	15.05	0.16		0.61	0.09	9
1973													
	No73-3	54.22	0.34	0.71	21.74	0.53	19.87	4.34	0.04		101.82	0.62	62
	No73-6	54.97	0.27	0.63	19.44	0.46	20.96	5.09	0.04		101.94	0.66	66
	No73-15	53.26	0.41	0.81	22.64	0.52	18.79	4.36	0.06		100.90	0.60	60
	Average	54.15	0.34	0.72	21.28	0.50	19.87	4.60	0.05		101.55	0.62	62
	2 σ	1.71	0.14	0.19	3.30	0.07	2.17	0.85	0.03		1.13	0.06	6
1974													
	No74-1	52.70	0.58	2.48	16.35	0.44	18.87	9.04	0.16		100.65	0.67	67
	No74-6	54.29	0.38	1.60	17.21	0.46	21.96	5.65	0.08		101.70	0.69	69
	No74-11_2	53.95	0.39	0.68	23.13	0.56	18.48	4.63	0.07		101.90	0.59	59

	No74-16	55.21	0.31	1.14	19.26	0.52	22.03	3.91	0.08	102.48	0.67	67
	Average	54.04	0.42	1.48	18.99	0.49	20.33	5.81	0.10	101.68	0.66	66
	2 σ	2.07	0.23	1.54	6.04	0.11	3.86	4.53	0.08	1.52	0.09	9
1975												
Ngauruhoe	No75-3	54.28	0.24	0.60	21.99	0.61	20.17	3.71	0.04	101.66	0.62	62
	No75-7	55.52	0.22	0.99	17.12	0.43	25.55	2.07	0.03	101.94	0.73	73
	No75-11_2	53.95	0.24	0.56	22.03	0.65	19.51	4.30	0.06	101.29	0.61	61
	Average	54.58	0.24	0.71	20.38	0.56	21.74	3.36	0.04	101.63	0.66	66
	2 σ	1.66	0.02	0.47	5.64	0.23	6.62	2.31	0.03	0.65	0.13	13
1995-1996												
Ruapehu												
1995 Ruapehu	No95-2	55.61	0.32	1.37	15.83	0.33	26.44	2.08	0.05	102.16	0.75	75
	No95-7	56.04	0.19	2.35	11.66	0.24	29.04	2.05	0.05	101.85	0.82	82
	No95-10_2	55.36	0.32	1.31	17.34	0.37	25.09	2.08	0.03	101.98	0.72	72
	Average	55.67	0.28	1.68	14.94	0.31	26.86	2.07	0.04	101.99	0.76	76
	2 σ	0.68	0.14	1.17	5.89	0.13	4.02	0.04	0.02	0.32	0.10	10
1996 Ruapehu												
	No96-5	52.68	0.87	3.66	11.69	0.30	18.85	12.30	0.26	100.73	0.74	74
	No96-12	55.85	0.23	1.39	15.50	0.33	25.65	2.75	0.10	101.84	0.75	75
	No96-13	54.67	0.37	1.53	15.92	0.35	24.01	4.24	0.09	101.25	0.73	73
	Average	54.40	0.49	2.19	14.37	0.32	22.83	6.43	0.15	101.28	0.74	74
	2 σ	3.21	0.67	2.55	4.66	0.05	7.10	10.28	0.19	1.11	0.02	2

Appendix C12. Plagioclase major element compositions analysed for the TgVC eruptive sequences studied. Mangatawai and Tufa Trig samples were analysed using a JEOL JXA-8900R electron microprobe equipped with four wavelength-dispersive spectrometers at the Institute of Earth Sciences, Academia Sinica, Taipei, Taiwan. 1972-1975 Ngauruhoe and 1995-1996 Ruapehu samples were analysed using a JEOL JXA-8800R electron microprobe equipped with four wavelength-dispersive spectrometers at the Graduate School of Science, Hokkaido University, Sapporo, Japan. The analyses highlighted in yellow were used for hygromobarmetric calculations and *MELTS* modelling.

Eruptive sequence and tephra	Comment	SiO ₂	TiO ₂	Al ₂ O ₃	FeO	MnO	MgO	CaO	Na ₂ O	K ₂ O	Total	X _{Ab}
Mangatawai												
407-14	No14-6	50.93	0.06	30.29	0.608	0.00	0.14	13.72	3.45	0.13	99.34	0.31
	No14-7	48.38	0.00	32.21	0.643	0.03	0.11	15.65	2.29	0.07	99.38	0.21
	No14-8	51.36	0.07	30.09	0.726	0.00	0.13	13.60	3.33	0.15	99.46	0.30
	No14-9	49.94	0.09	30.68	0.711	0.00	0.14	14.62	2.93	0.11	99.21	0.26
	No14-19	53.37	0.01	28.38	0.709	0.04	0.16	12.07	4.11	0.18	99.02	0.38
	No14-22	50.06	0.02	30.79	0.685	0.00	0.12	14.77	2.99	0.10	99.53	0.27
	No14-23	48.53	0.03	32.11	0.864	0.05	0.15	15.83	2.25	0.08	99.88	0.20
	No14-24	51.99	0.02	29.52	0.909	0.00	0.19	13.36	3.59	0.13	99.70	0.32
	No14-27	53.84	0.05	28.15	0.901	0.01	0.23	11.62	4.32	0.22	99.40	0.40
	No14-29	52.21	0.03	28.91	0.892	0.00	0.18	12.70	3.98	0.17	99.08	0.36
	No14-39	52.42	0.04	28.77	0.964	0.00	0.16	12.54	3.95	0.17	99.01	0.36
	No14-40	48.75	0.03	32.02	0.679	0.04	0.14	15.30	2.39	0.08	99.42	0.22
	No14-41	48.32	0.00	32.01	0.626	0.00	0.16	15.47	2.56	0.06	99.21	0.23
	No14-48	50.02	0.02	30.96	0.854	0.00	0.16	14.89	2.79	0.14	99.84	0.25

407-15

No14-49	52.98	0.04	29.14	0.930	0.00	0.18	12.58	4.00	0.19	100.05	0.36
No14-50	50.25	0.10	30.59	0.691	0.00	0.13	14.21	3.17	0.10	99.25	0.29
No14-56	50.65	0.07	30.47	0.805	0.02	0.15	14.44	3.17	0.10	99.89	0.28
No14-57	47.89	0.03	32.31	0.799	0.02	0.13	16.00	2.07	0.09	99.34	0.19
Average	50.66	0.04	30.41	0.778	0.01	0.15	14.08	3.19	0.13	99.45	0.29
2 σ	3.72	0.06	2.75	0.230	0.03	0.06	2.73	1.41	0.09	0.62	
No15-3	47.50	0.04	32.66	0.690	0.00	0.11	16.25	2.08	0.06	99.39	0.19
No15-4	47.41	0.05	32.50	0.802	0.00	0.14	16.31	2.20	0.08	99.49	0.20
No15-5	52.75	0.08	28.83	0.947	0.00	0.17	12.40	4.02	0.21	99.40	0.36
No15-7	53.39	0.10	28.07	0.964	0.00	0.16	12.02	4.08	0.24	99.03	0.37
No15-8	53.27	0.09	28.19	0.844	0.02	0.15	11.83	4.42	0.24	99.04	0.40
No15-10	53.34	0.04	28.63	0.923	0.00	0.16	12.11	4.10	0.20	99.49	0.38
No15-16	50.95	0.05	30.26	0.894	0.00	0.13	13.98	3.09	0.15	99.52	0.28
No15-21	53.42	0.00	28.50	0.953	0.06	0.19	12.14	4.17	0.24	99.67	0.38
No15-25	47.53	0.07	32.54	0.776	0.04	0.15	16.33	2.07	0.09	99.58	0.19
No15-31	51.87	0.05	30.35	0.918	0.02	0.16	13.66	3.42	0.13	100.57	0.31
No15-32	47.60	0.03	33.05	0.772	0.00	0.10	16.56	2.03	0.07	100.20	0.18
No15-33	54.10	0.09	28.58	0.908	0.00	0.22	12.40	4.08	0.21	100.58	0.37
No15-35	54.08	0.02	28.44	0.982	0.00	0.17	12.13	4.25	0.22	100.31	0.38
No15-38	53.07	0.03	29.91	0.800	0.00	0.19	13.21	3.71	0.15	101.07	0.33
No15-39	53.01	0.05	28.77	0.956	0.00	0.17	12.54	4.02	0.19	99.71	0.36
No15-42	51.25	0.07	30.36	0.692	0.00	0.16	14.12	3.20	0.12	99.98	0.29
No15-43	54.14	0.07	28.52	1.008	0.00	0.18	12.07	4.29	0.21	100.51	0.39

No15-51	53.61	0.10	28.61	0.904	0.05	0.20	12.47	4.13	0.25	100.32	0.37	
No15-53	53.89	0.09	27.68	0.835	0.00	0.13	11.70	4.47	0.24	99.05	0.40	
No15-56	49.59	0.09	31.12	0.829	0.02	0.18	14.74	2.76	0.10	99.44	0.25	
No15-57	53.44	0.04	28.54	0.997	0.00	0.21	12.33	3.90	0.20	99.66	0.36	
No15-58	53.64	0.06	28.63	0.810	0.00	0.19	12.37	4.05	0.23	99.98	0.37	
No15-59	49.79	0.03	31.11	0.890	0.03	0.14	14.87	2.89	0.13	99.88	0.26	
No15-60	50.64	0.04	30.22	0.791	0.04	0.19	14.14	3.19	0.12	99.38	0.29	
No15-61	49.99	0.01	31.10	0.710	0.00	0.14	14.67	2.87	0.14	99.62	0.26	
No15-62	48.13	0.01	32.55	0.685	0.04	0.13	16.12	2.04	0.06	99.78	0.19	
No15-68	50.18	0.05	30.83	0.778	0.01	0.15	14.38	3.02	0.13	99.52	0.27	
No15-69	47.84	0.00	32.64	0.756	0.04	0.12	16.66	1.96	0.07	100.08	0.17	
No15-70	48.22	0.00	32.16	0.630	0.00	0.12	15.73	2.17	0.07	99.12	0.20	
No15-71	47.47	0.00	32.82	0.676	0.05	0.13	16.58	1.77	0.06	99.55	0.16	
No15-72	48.73	0.07	32.12	0.612	0.01	0.14	15.95	2.21	0.06	99.90	0.20	
No15-75	48.96	0.00	32.22	0.890	0.00	0.15	15.81	2.32	0.08	100.45	0.21	
No15-76	50.03	0.05	31.03	0.811	0.02	0.13	15.02	2.75	0.11	99.95	0.25	
No15-78	51.57	0.04	30.48	0.999	0.01	0.18	13.88	3.29	0.14	100.60	0.30	
No15-79	48.66	0.04	31.73	1.076	0.00	0.30	16.09	2.00	0.14	100.04	0.18	
No15-83	53.92	0.05	27.90	1.118	0.01	0.29	12.05	4.28	0.27	99.87	0.38	
No15-84	54.23	0.03	28.13	0.859	0.05	0.18	12.15	4.34	0.21	100.19	0.39	
Average	51.11	0.05	30.26	0.851	0.01	0.16	13.99	3.23	0.15	99.84	0.29	
2 σ	4.93	0.06	3.51	0.246	0.04	0.09	3.48	1.81	0.14	0.99		
407-16	No16-1	54.18	0.06	28.10	0.875	0.01	0.13	11.92	4.34	0.24	99.85	0.39

No16-3	53.85	0.04	28.62	0.776	0.03	0.13	11.92	4.14	0.24	99.75	0.38
No16-4	53.35	0.07	28.89	0.969	0.00	0.21	12.64	3.95	0.23	100.30	0.36
No16-6	54.54	0.05	28.59	0.972	0.00	0.13	12.14	4.17	0.23	100.82	0.38
No16-8	54.01	0.06	28.25	0.936	0.00	0.18	12.15	4.21	0.24	100.03	0.38
No16-11	50.53	0.08	30.60	0.830	0.00	0.18	14.39	3.02	0.10	99.73	0.27
No16-12	51.56	0.02	29.98	0.823	0.00	0.20	13.87	3.39	0.15	100.00	0.30
No16-13	46.94	0.04	33.01	0.616	0.06	0.07	17.06	1.67	0.05	99.53	0.15
No16-14	52.38	0.06	29.64	0.704	0.04	0.17	13.52	3.59	0.13	100.22	0.32
No16-16	54.67	0.02	28.14	0.836	0.00	0.14	11.67	4.22	0.22	99.92	0.39
No16-18	53.86	0.08	28.09	0.820	0.00	0.17	11.97	4.24	0.22	99.46	0.39
No16-19	54.23	0.05	28.12	0.923	0.00	0.15	11.89	4.28	0.26	99.89	0.39
No16-20	53.11	0.06	28.74	1.101	0.05	0.20	12.64	4.06	0.22	100.18	0.36
No16-23	52.00	0.05	29.66	0.847	0.00	0.18	13.35	3.53	0.17	99.79	0.32
No16-24	49.95	0.01	30.92	0.802	0.00	0.14	15.28	2.71	0.10	99.91	0.24
No16-25	50.83	0.01	30.23	0.874	0.00	0.17	13.93	3.24	0.13	99.41	0.29
No16-27	53.45	0.03	28.66	0.850	0.02	0.19	12.53	4.07	0.20	99.99	0.37
No16-28	51.19	0.02	30.29	0.870	0.04	0.18	14.37	3.01	0.14	100.12	0.27
No16-31	53.58	0.19	27.15	2.005	0.03	0.70	12.70	3.65	0.31	100.34	0.34
No16-33	52.46	0.04	29.60	0.835	0.01	0.17	13.56	3.57	0.14	100.37	0.32
No16-40	49.84	0.05	31.37	0.828	0.00	0.12	14.84	2.76	0.13	99.93	0.25
No16-41	50.17	0.08	31.22	0.864	0.00	0.14	14.90	2.74	0.13	100.24	0.25
No16-42	53.02	0.07	28.98	1.016	0.04	0.19	12.98	3.87	0.20	100.36	0.35
No16-43	54.41	0.03	28.12	0.945	0.00	0.18	11.93	4.17	0.21	99.98	0.38
No16-44	53.97	0.00	28.18	1.038	0.00	0.17	11.97	4.32	0.21	99.86	0.39

No16-47	54.39	0.04	27.72	0.887	0.02	0.17	11.83	4.37	0.27	99.73	0.39	
No16-48	49.02	0.08	31.86	0.819	0.00	0.15	15.60	2.32	0.07	99.92	0.21	
No16-49	51.25	0.05	30.75	0.909	0.03	0.18	14.54	3.15	0.13	100.98	0.28	
No16-50	54.31	0.07	27.98	0.962	0.00	0.16	11.88	4.47	0.23	100.08	0.40	
No16-52	50.70	0.01	30.24	0.807	0.00	0.18	14.40	3.04	0.12	99.50	0.27	
No16-53	47.77	0.00	32.66	0.618	0.06	0.09	17.01	1.75	0.05	100.01	0.16	
No16-54	47.25	0.00	32.99	0.666	0.00	0.10	17.09	1.74	0.03	99.87	0.16	
No16-64	49.87	0.02	31.17	0.764	0.01	0.16	15.39	2.80	0.11	100.27	0.25	
No16-65	46.64	0.01	33.35	0.561	0.00	0.11	17.34	1.68	0.03	99.73	0.15	
No16-66	47.49	0.01	32.60	0.587	0.01	0.11	16.96	1.89	0.06	99.73	0.17	
No16-67	47.86	0.04	32.68	0.627	0.02	0.11	16.42	1.93	0.06	99.75	0.17	
No16-68	46.35	0.05	33.66	0.665	0.00	0.10	17.52	1.49	0.04	99.88	0.13	
No16-69	51.88	0.07	30.24	0.921	0.00	0.14	13.88	3.41	0.17	100.71	0.30	
No16-70	53.62	0.00	28.35	0.934	0.00	0.16	12.07	4.29	0.26	99.69	0.39	
No16-71	54.12	0.03	28.31	0.947	0.02	0.17	12.11	4.34	0.22	100.26	0.39	
No16-72	51.17	0.15	30.44	0.919	0.04	0.17	14.33	3.19	0.10	100.50	0.29	
No16-73	51.23	0.05	29.88	0.828	0.00	0.16	13.92	3.42	0.13	99.62	0.31	
No16-81	53.76	0.02	28.36	0.783	0.00	0.17	11.97	4.30	0.23	99.59	0.39	
Average	51.64	0.05	29.92	0.864	0.01	0.17	13.82	3.36	0.16	99.99	0.30	
2 σ	5.04	0.08	3.57	0.434	0.04	0.18	3.67	1.83	0.15	0.71	0.17	
407-17	No17-1	51.84	0.05	29.78	0.862	0.00	0.17	13.38	3.61	0.16	99.85	0.33
	No17-5	51.10	0.04	30.82	0.972	0.01	0.12	14.56	3.25	0.11	100.98	0.29
	No17-6	51.47	0.00	30.72	0.959	0.03	0.16	14.38	3.31	0.15	101.18	0.29

No17-7	52.87	0.09	29.51	0.682	0.04	0.08	12.85	3.74	0.15	100.00	0.34
No17-8	51.14	0.05	30.17	0.901	0.04	0.14	14.06	3.30	0.13	99.90	0.30
No17-11	53.00	0.08	28.81	0.933	0.02	0.16	13.09	3.87	0.19	100.17	0.34
No17-12	52.81	0.08	29.15	0.758	0.04	0.11	12.79	3.89	0.15	99.77	0.35
No17-13	50.91	0.03	30.10	0.780	0.00	0.12	13.88	3.29	0.12	99.23	0.30
No17-15	51.67	0.06	29.10	0.901	0.00	0.16	13.46	3.62	0.17	99.13	0.32
No17-16	52.64	0.06	29.03	0.867	0.00	0.17	12.94	3.92	0.15	99.78	0.35
No17-21	46.48	0.04	33.60	0.472	0.03	0.08	17.50	1.40	0.06	99.65	0.13
No17-22	46.69	0.02	33.03	0.650	0.00	0.06	17.46	1.63	0.04	99.58	0.14
No17-23	51.02	0.00	30.26	0.758	0.00	0.16	13.97	3.32	0.10	99.61	0.30
No17-24	51.25	0.01	30.46	0.896	0.11	0.19	14.05	3.10	0.12	100.18	0.28
No17-25	52.15	0.06	29.88	1.009	0.00	0.20	13.55	3.47	0.11	100.42	0.31
No17-28	51.27	0.07	30.30	0.863	0.04	0.17	13.91	3.30	0.10	100.02	0.30
No17-29	46.94	0.00	33.46	0.696	0.00	0.08	17.32	1.51	0.03	100.03	0.14
No17-30	54.22	0.02	28.49	0.977	0.00	0.21	12.03	4.20	0.18	100.34	0.38
No17-31	51.00	0.05	30.90	0.789	0.00	0.13	14.48	3.05	0.11	100.50	0.27
No17-32	53.03	0.04	28.87	0.845	0.00	0.17	12.90	3.91	0.17	99.93	0.35
No17-33	51.08	0.03	30.20	0.803	0.00	0.12	14.40	3.12	0.13	99.89	0.28
No17-34	50.80	0.05	30.10	0.888	0.00	0.15	14.05	3.17	0.12	99.33	0.29
No17-36	50.25	0.02	30.39	0.825	0.00	0.13	14.73	2.97	0.08	99.39	0.27
No17-37	47.95	0.00	32.74	0.596	0.00	0.10	16.45	2.01	0.04	99.89	0.18
No17-38	48.12	0.00	32.75	0.702	0.02	0.09	16.68	1.90	0.07	100.33	0.17
No17-39	52.29	0.01	29.66	0.843	0.00	0.18	13.49	3.64	0.16	100.28	0.32
No17-40	52.47	0.05	28.98	0.707	0.05	0.17	13.08	3.70	0.12	99.33	0.34

No17-41	50.96	0.06	30.22	0.812	0.00	0.09	14.31	3.23	0.14	99.85	0.29
No17-42	51.46	0.07	29.84	0.895	0.06	0.13	13.47	3.62	0.14	99.67	0.32
No17-43	53.39	0.09	28.88	1.038	0.05	0.15	12.55	3.99	0.20	100.34	0.36
No17-44	52.36	0.01	29.27	0.839	0.00	0.20	13.39	3.59	0.14	99.81	0.32
No17-45	52.49	0.08	28.83	0.962	0.06	0.16	13.21	3.86	0.19	99.86	0.34
No17-46	47.89	0.00	32.55	0.857	0.03	0.09	16.77	1.94	0.07	100.20	0.17
No17-57	46.95	0.01	33.01	0.669	0.03	0.09	17.52	1.68	0.06	100.03	0.15
No17-58	47.58	0.01	33.37	0.666	0.02	0.10	17.25	1.66	0.05	100.73	0.15
No17-59	47.06	0.07	33.32	0.616	0.01	0.08	17.03	1.71	0.03	99.93	0.15
No17-61	51.12	0.07	30.27	0.617	0.00	0.16	14.24	3.14	0.10	99.72	0.28
No17-62	53.57	0.06	28.44	0.860	0.00	0.15	12.29	4.20	0.22	99.79	0.38
No17-64	52.27	0.06	28.86	0.995	0.00	0.21	13.19	3.46	0.18	99.23	0.32
No17-65	49.82	0.03	31.23	0.803	0.00	0.17	15.18	2.67	0.10	100.00	0.24
No17-66	50.78	0.07	30.58	0.784	0.00	0.18	14.51	3.05	0.11	100.05	0.27
No17-67	48.66	0.00	32.40	0.638	0.00	0.10	16.08	2.21	0.03	100.12	0.20
No17-68	46.88	0.03	32.93	0.602	0.00	0.10	16.72	1.80	0.04	99.10	0.16
No17-70	46.77	0.08	33.30	0.614	0.00	0.13	16.92	1.74	0.04	99.60	0.16
No17-71	48.60	0.04	32.42	0.609	0.03	0.14	16.04	2.17	0.07	100.11	0.20
No17-72	47.03	0.02	33.40	0.524	0.01	0.10	17.27	1.59	0.07	100.01	0.14
No17-73	47.40	0.03	33.51	0.606	0.00	0.07	17.38	1.57	0.03	100.62	0.14
No17-74	52.48	0.01	28.99	0.923	0.00	0.15	12.82	3.90	0.19	99.47	0.35
No17-75	53.10	0.04	28.92	0.808	0.02	0.22	12.86	3.93	0.16	100.08	0.35
No17-77	52.29	0.00	29.51	0.997	0.00	0.21	13.22	3.70	0.13	100.05	0.33
No17-81	55.75	0.12	26.18	1.944	0.01	1.00	10.60	4.49	0.42	100.54	0.42

407-18

No17-82	53.31	0.05	29.07	0.966	0.03	0.19	12.85	3.94	0.20	100.60	0.35
No17-83	46.79	0.05	33.08	0.673	0.01	0.08	17.34	1.67	0.04	99.73	0.15
No17-84	47.14	0.02	32.98	0.607	0.02	0.11	17.10	1.67	0.07	99.75	0.15
No17-85	47.07	0.00	32.99	0.579	0.01	0.09	17.05	1.71	0.05	99.57	0.15
No17-86	51.02	0.03	30.68	0.861	0.04	0.14	14.10	3.22	0.15	100.23	0.29
No17-1	51.84	0.05	29.78	0.862	0.00	0.17	13.38	3.61	0.16	99.86	0.33
No17-61	51.12	0.07	30.27	0.617	0.00	0.16	14.24	3.14	0.10	99.72	0.28
No17-62	53.57	0.06	28.44	0.860	0.00	0.15	12.29	4.20	0.22	99.79	0.38
No17-77	52.29	0.00	29.51	0.997	0.00	0.21	13.22	3.70	0.13	100.05	0.33
Average	50.62	0.04	30.64	0.811	0.01	0.15	14.53	3.02	0.12	99.95	0.27
2 σ	4.81	0.06	3.56	0.410	0.04	0.24	3.59	1.81	0.13	0.85	0.16
No18-7	53.34	0.08	28.72	0.012	0.11	4.16	12.45	4.16	0.21	99.88	0.37
No18-8	51.01	0.00	30.38	0.000	0.15	3.35	13.87	3.35	0.14	99.61	0.30
No18-9	51.56	0.06	29.49	0.000	0.16	3.58	13.47	3.58	0.18	99.59	0.32
No18-12	51.56	0.06	29.54	0.000	0.14	3.76	13.16	3.76	0.19	99.39	0.34
No18-16	51.23	0.00	29.61	0.000	0.27	3.37	13.67	3.37	0.17	99.20	0.31
No18-17	52.87	0.11	28.80	0.000	0.16	4.15	12.55	4.15	0.21	99.73	0.37
No18-18	51.14	0.08	29.56	0.044	0.19	3.62	13.43	3.62	0.15	99.04	0.32
No18-19	51.46	0.00	29.47	0.000	0.17	3.61	13.63	3.61	0.15	99.27	0.32
No18-23	52.89	0.04	28.79	0.000	0.16	4.21	12.39	4.21	0.21	99.59	0.38
No18-24	52.51	0.05	28.71	0.005	0.17	3.86	12.67	3.86	0.22	99.02	0.35
No18-25	53.67	0.05	28.39	0.000	0.14	4.27	11.77	4.27	0.22	99.33	0.39
No18-37	53.08	0.05	28.45	0.000	0.16	4.31	12.16	4.31	0.25	99.47	0.39

No18-38	51.45	0.09	29.25	0.000	0.21	3.84	13.24	3.84	0.21	99.40	0.34
No18-40	49.87	0.00	30.73	0.012	0.13	3.09	14.20	3.09	0.14	99.09	0.28
No18-41	54.12	0.03	28.27	0.000	0.18	4.29	11.95	4.29	0.25	99.97	0.39
No18-43	51.90	0.03	29.37	0.046	0.18	3.83	13.25	3.83	0.13	99.39	0.34
No18-45	52.01	0.00	28.93	0.020	0.25	3.97	12.81	3.97	0.16	99.02	0.36
No18-52	46.23	0.01	33.94	0.000	0.08	1.56	17.33	1.56	0.02	99.79	0.14
No18-53	51.67	0.09	29.19	0.015	0.18	4.06	13.07	4.06	0.14	99.09	0.36
No18-55	50.29	0.00	30.27	0.000	0.12	3.42	14.01	3.42	0.12	99.04	0.30
No18-61	49.80	0.05	30.95	0.000	0.18	3.01	14.46	3.01	0.10	99.25	0.27
No18-62	46.21	0.02	33.71	0.000	0.10	1.70	17.49	1.70	0.03	100.05	0.15
No18-63	51.07	0.04	29.92	0.012	0.18	3.47	13.61	3.47	0.16	99.32	0.31
No18-65	46.22	0.03	33.13	0.000	0.11	1.50	17.54	1.50	0.05	99.12	0.13
No18-66	46.23	0.03	33.75	0.030	0.11	1.61	17.53	1.61	0.03	99.90	0.14
No18-67	46.64	0.02	33.17	0.077	0.10	1.90	16.78	1.90	0.05	99.20	0.17
No18-68	46.55	0.08	32.85	0.000	0.11	1.98	16.90	1.98	0.05	99.08	0.17
No18-72	45.89	0.00	33.47	0.000	0.11	1.60	17.42	1.60	0.03	99.25	0.14
No18-74	52.01	0.06	29.37	0.000	0.19	3.86	12.63	3.86	0.19	99.29	0.35
No18-78	52.76	0.09	28.49	0.000	0.20	4.25	12.45	4.25	0.25	99.44	0.38
No18-81	47.23	0.05	32.42	0.017	0.10	2.24	16.22	2.24	0.07	99.05	0.20
No18-82	46.27	0.02	33.29	0.000	0.09	1.74	17.18	1.74	0.02	99.24	0.15
No18-83	46.40	0.04	33.14	0.005	0.13	1.83	17.02	1.83	0.04	99.22	0.16
No18-84	46.16	0.04	33.55	0.000	0.12	1.61	17.37	1.61	0.04	99.47	0.14
No18-86	47.09	0.01	33.11	0.005	0.07	1.94	16.68	1.94	0.04	99.53	0.17
No18-87	51.88	0.01	29.15	0.000	0.17	3.85	13.08	3.85	0.16	99.36	0.34

	No18-89	47.10	0.05	32.68	0.041	0.10	1.86	16.74	1.86	0.05	99.26	0.17
	No18-98	52.72	0.07	28.61	0.000	0.20	4.10	12.56	4.10	0.21	99.50	0.37
	No18-100	52.03	0.06	28.87	0.042	0.24	4.09	12.79	4.09	0.15	99.36	0.36
	Average	50.10	0.04	30.60	0.010	0.15	3.14	14.40	3.14	0.13	99.38	0.28
	2 σ	5.51	0.06	3.99	0.036	0.10	2.06	4.05	2.06	0.15	0.56	0.19
407-47	No47-1	51.53	0.03	30.84	0.786	0.02	0.17	14.16	3.11	0.13	100.77	0.28
	No47-2	53.91	0.05	29.18	0.961	0.00	0.20	12.69	3.93	0.23	101.15	0.35
	No47-3	51.27	0.05	30.73	0.808	0.00	0.10	14.30	3.07	0.11	100.45	0.28
	No47-4	54.65	0.04	28.24	0.843	0.00	0.14	11.61	4.34	0.20	100.08	0.40
	No47-5	55.10	0.02	28.26	0.597	0.00	0.15	11.46	4.41	0.20	100.21	0.41
	No47-6	52.18	0.00	30.21	0.654	0.00	0.11	13.68	3.28	0.14	100.25	0.30
	No47-7	49.86	0.00	31.02	0.706	0.00	0.11	15.07	2.44	0.11	99.31	0.23
	No47-8	52.71	0.06	29.22	0.677	0.00	0.10	12.97	3.72	0.16	99.62	0.34
	No47-9	54.88	0.08	28.42	0.619	0.03	0.14	11.53	4.41	0.23	100.32	0.40
	No47-10	53.44	0.03	28.90	0.782	0.00	0.15	12.94	3.85	0.19	100.29	0.35
	No47-11	54.17	0.02	28.30	0.810	0.05	0.16	11.93	4.25	0.20	99.89	0.39
	No47-22	57.25	0.09	26.61	0.798	0.01	0.11	9.77	5.42	0.36	100.42	0.49
	No47-23	56.38	0.00	27.53	0.693	0.00	0.13	10.76	4.99	0.33	100.82	0.45
	No47-25	52.41	0.05	30.12	0.817	0.00	0.12	13.43	3.52	0.15	100.61	0.32
	No47-27	52.91	0.04	29.56	1.023	0.03	0.17	12.88	3.64	0.16	100.41	0.34
	No47-28	52.72	0.00	29.34	0.816	0.00	0.17	13.01	3.75	0.19	99.98	0.34
	No47-29	51.27	0.09	30.63	0.649	0.02	0.08	14.31	2.96	0.09	100.10	0.27
	No47-30	52.49	0.04	29.89	0.686	0.00	0.13	13.45	3.66	0.16	100.51	0.33

No47-31	49.58	0.08	31.73	0.626	0.02	0.13	15.71	2.36	0.08	100.30	0.21	
No47-32	51.56	0.03	30.56	0.750	0.01	0.13	13.78	3.21	0.12	100.13	0.29	
No47-33	52.49	0.05	29.83	0.621	0.00	0.12	13.05	3.46	0.16	99.78	0.32	
No47-34	52.12	0.09	30.41	0.603	0.00	0.08	13.86	3.32	0.16	100.65	0.30	
No47-35	54.96	0.04	28.79	0.671	0.00	0.12	11.88	4.20	0.21	100.87	0.39	
No47-36	55.03	0.06	27.98	0.988	0.00	0.23	11.56	4.43	0.25	100.52	0.40	
No47-38	52.55	0.04	29.81	0.734	0.00	0.15	13.37	3.42	0.14	100.21	0.31	
No47-39	54.37	0.02	28.27	0.664	0.00	0.07	12.11	4.25	0.21	100.01	0.38	
No47-40	51.18	0.03	30.68	0.733	0.03	0.08	14.44	3.07	0.15	100.40	0.28	
No47-41	51.62	0.02	30.25	0.679	0.01	0.11	14.11	3.20	0.12	100.13	0.29	
No47-42	53.28	0.05	29.44	0.646	0.00	0.14	13.00	3.65	0.16	100.36	0.33	
No47-43	53.20	0.06	29.66	0.769	0.07	0.11	12.98	3.81	0.19	100.84	0.34	
No47-44	51.45	0.02	30.70	0.772	0.00	0.13	14.46	3.01	0.11	100.67	0.27	
No47-45	48.46	0.02	32.59	0.706	0.06	0.07	16.64	1.73	0.07	100.34	0.16	
No47-46	48.81	0.06	32.21	0.750	0.00	0.10	16.05	2.06	0.09	100.13	0.19	
No47-49	52.40	0.03	29.92	0.775	0.00	0.14	13.70	3.49	0.15	100.61	0.31	
No47-50	51.87	0.02	30.52	0.792	0.00	0.09	13.77	3.32	0.13	100.51	0.30	
No47-51	52.85	0.05	29.33	0.925	0.00	0.12	13.15	3.65	0.18	100.25	0.33	
No47-52	54.54	0.03	28.23	0.987	0.02	0.14	12.06	4.24	0.19	100.43	0.38	
Average	52.74	0.04	29.67	0.754	0.01	0.13	13.23	3.58	0.17	100.33	0.33	
2 σ	3.86	0.05	2.58	0.225	0.04	0.07	2.87	1.51	0.12	0.72	0.14	
407-49	No49-1	52.67	0.01	29.92	0.787	0.00	0.15	13.49	3.50	0.17	100.69	0.32
	No49-2	52.89	0.04	29.53	0.839	0.00	0.11	13.37	3.63	0.16	100.57	0.33

No49-3	51.33	0.03	30.85	0.743	0.00	0.10	14.48	2.90	0.14	100.57	0.26	
No49-4	56.08	0.06	28.05	1.066	0.07	0.29	11.28	4.45	0.26	101.60	0.41	
No49-14	55.85	0.05	27.79	0.907	0.00	0.18	11.33	4.49	0.26	100.86	0.41	
No49-15	55.75	0.09	28.06	0.884	0.05	0.16	11.62	4.63	0.28	101.51	0.41	
No49-16	60.58	1.11	14.73	7.728	0.16	3.09	6.87	3.68	1.36	99.30	0.44	
No49-17	61.05	1.01	14.79	7.527	0.14	3.00	6.91	3.91	1.27	99.61	0.46	
No49-19	59.34	0.90	14.45	8.429	0.16	3.97	8.51	3.12	1.34	100.21	0.36	
No49-20	61.04	0.97	15.04	8.122	0.14	3.13	6.21	3.83	1.35	99.81	0.47	
No49-22	52.93	0.03	29.41	0.855	0.00	0.10	12.89	3.87	0.18	100.32	0.35	
No49-23	53.99	0.05	29.49	0.794	0.03	0.14	12.58	3.98	0.21	101.25	0.36	
No49-24	54.40	0.09	28.79	0.824	0.00	0.09	12.30	4.29	0.21	101.00	0.38	
No49-25	52.36	0.02	30.42	0.728	0.00	0.15	13.93	3.13	0.16	100.90	0.29	
No49-26	53.39	0.00	29.39	0.691	0.00	0.13	12.99	3.77	0.18	100.53	0.34	
No49-27	54.33	0.05	28.56	0.668	0.00	0.14	12.24	4.25	0.24	100.47	0.38	
No49-28	47.44	0.05	33.12	0.632	0.00	0.07	16.93	1.62	0.02	99.88	0.15	
No49-29	52.85	0.00	29.18	0.728	0.00	0.15	12.75	4.03	0.20	99.91	0.36	
No49-34	51.55	0.09	29.94	0.877	0.00	0.15	13.36	3.57	0.15	99.69	0.32	
No49-35	50.56	0.05	30.34	0.817	0.01	0.10	14.19	3.02	0.13	99.21	0.28	
No49-37	51.99	0.06	29.42	0.870	0.02	0.13	12.88	3.68	0.19	99.25	0.34	
No49-43	51.60	0.09	29.93	0.783	0.00	0.13	13.16	3.54	0.18	99.42	0.32	
Average	54.27	0.22	26.87	2.105	0.04	0.71	12.01	3.68	0.39	100.30	0.35	
2 σ	7.13	0.75	11.91	5.654	0.12	2.52	5.33	1.32	0.91	1.45	0.14	
407-54	No54-3	52.51	0.05	29.77	0.905	0.07	0.13	13.94	3.60	0.16	101.12	0.32

No54-4	51.75	0.02	29.93	0.786	0.00	0.14	13.95	3.39	0.18	100.16	0.30
No54-5	49.36	0.00	31.03	0.715	0.00	0.09	15.20	2.61	0.13	99.15	0.24
No54-6	53.01	0.05	29.18	0.739	0.00	0.13	12.98	3.95	0.18	100.21	0.35
No54-8	51.99	0.03	29.87	1.000	0.00	0.13	13.83	3.47	0.19	100.56	0.31
No54-10	50.89	0.07	29.83	0.912	0.04	0.12	14.08	3.03	0.13	99.09	0.28
No54-14	52.93	0.04	28.80	0.984	0.00	0.14	13.47	3.73	0.18	100.30	0.33
No54-15	52.50	0.06	29.49	0.884	0.00	0.14	13.33	3.66	0.19	100.24	0.33
No54-16	53.50	0.04	28.75	0.701	0.00	0.14	12.73	4.03	0.17	100.06	0.36
No54-17	52.57	0.05	29.08	0.638	0.00	0.14	13.17	3.83	0.16	99.63	0.34
No54-18	52.28	0.00	29.52	0.778	0.00	0.11	13.49	3.56	0.18	99.91	0.32
No54-19	51.70	0.07	29.64	0.674	0.05	0.11	13.96	3.40	0.14	99.76	0.30
No54-20	52.04	0.07	30.06	0.807	0.00	0.13	13.83	3.44	0.13	100.50	0.31
No54-21	50.49	0.03	30.73	0.740	0.00	0.11	14.68	2.98	0.13	99.90	0.27
No54-22	52.68	0.08	29.69	0.845	0.00	0.13	13.54	3.77	0.18	100.91	0.33
No54-28	51.91	0.06	29.80	0.876	0.00	0.12	14.04	3.41	0.18	100.39	0.30
No54-29	52.51	0.08	29.06	0.716	0.00	0.09	13.45	3.62	0.14	99.67	0.32
No54-30	51.87	0.04	29.51	0.720	0.04	0.13	13.88	3.43	0.14	99.76	0.31
No54-31	52.47	0.02	29.08	0.688	0.00	0.12	13.17	3.73	0.18	99.48	0.34
No54-32	51.07	0.04	29.94	0.799	0.02	0.15	14.28	3.21	0.14	99.64	0.29
No54-33	51.85	0.00	29.92	0.800	0.04	0.15	13.78	3.47	0.14	100.19	0.31
No54-34	55.15	0.11	27.00	1.052	0.00	0.22	11.67	4.38	0.30	99.90	0.40
No54-42	52.19	0.06	29.16	0.971	0.00	0.13	13.49	3.67	0.17	99.85	0.33
No54-43	51.60	0.00	30.29	0.721	0.00	0.12	14.28	3.37	0.14	100.52	0.30
No54-44	52.01	0.07	29.24	0.832	0.01	0.11	13.38	3.64	0.19	99.49	0.33

	No54-45	53.21	0.04	29.22	0.854	0.00	0.12	13.10	3.62	0.17	100.34	0.33
	No54-46	53.71	0.03	28.47	0.839	0.01	0.09	12.48	4.08	0.22	99.93	0.37
	No54-47	52.12	0.00	29.40	0.809	0.00	0.14	13.27	3.51	0.17	99.41	0.32
	No54-48	52.07	0.02	29.68	0.834	0.00	0.10	13.77	3.46	0.16	100.09	0.31
	No54-49	52.37	0.03	29.45	0.910	0.01	0.13	13.24	3.64	0.17	99.97	0.33
	Average	52.21	0.04	29.49	0.818	0.01	0.13	13.58	3.56	0.17	100.00	0.32
	2 σ	2.06	0.06	1.44	0.208	0.04	0.05	1.33	0.68	0.07	0.94	0.06
407-56	No56-1	50.81	0.01	29.87	0.793	0.01	0.12	13.95	3.30	0.15	99.01	0.30
	No56-2	51.43	0.03	29.46	0.837	0.01	0.11	14.12	3.41	0.14	99.58	0.30
	No56-3	52.30	0.02	29.02	0.726	0.00	0.12	12.92	3.94	0.18	99.22	0.35
	No56-4	52.60	0.03	28.96	0.808	0.03	0.11	13.45	3.75	0.19	99.92	0.33
	No56-5	52.26	0.07	28.65	0.785	0.00	0.12	13.14	3.85	0.21	99.08	0.34
	No56-6	52.06	0.06	29.58	0.875	0.00	0.12	13.80	3.59	0.19	100.29	0.32
	No56-7	52.30	0.04	29.08	0.792	0.01	0.14	13.07	3.89	0.19	99.52	0.35
	No56-10	54.27	0.03	27.82	0.739	0.07	0.14	12.77	4.02	0.22	100.09	0.36
	No56-12	52.14	0.10	28.50	0.969	0.02	0.18	13.99	3.29	0.18	99.37	0.30
	No56-16	53.45	0.03	27.75	0.897	0.00	0.17	12.96	3.79	0.19	99.23	0.34
	No56-23	55.50	0.07	26.92	0.976	0.06	0.20	11.45	4.47	0.28	99.92	0.41
	No56-24	54.97	0.09	27.30	0.938	0.05	0.18	11.91	4.53	0.26	100.21	0.40
	No56-25	53.07	0.08	28.73	0.782	0.01	0.13	13.46	3.70	0.19	100.15	0.33
	No56-26	53.46	0.06	28.87	0.702	0.00	0.15	13.49	3.68	0.19	100.61	0.33
	No56-27	52.61	0.04	29.04	0.800	0.06	0.12	13.60	3.59	0.15	100.02	0.32
	No56-31	52.20	0.01	29.21	0.820	0.02	0.08	13.81	3.38	0.16	99.68	0.30

407-59

No56-32	50.08	0.03	31.13	0.771	0.02	0.10	15.45	2.65	0.10	100.32	0.24
No56-33	51.70	0.00	29.35	0.715	0.00	0.12	13.73	3.51	0.19	99.33	0.31
No56-37	52.13	0.04	29.62	0.929	0.00	0.13	13.65	3.39	0.14	100.03	0.31
No56-38	51.72	0.09	29.89	0.843	0.02	0.15	13.94	3.22	0.15	100.02	0.29
No56-39	53.15	0.05	28.55	0.798	0.03	0.15	12.68	4.14	0.20	99.79	0.37
No56-41	55.32	0.04	27.37	0.961	0.00	0.17	11.36	4.53	0.28	100.03	0.41
No56-43	51.20	0.00	29.99	0.772	0.00	0.09	14.05	3.25	0.17	99.52	0.29
No56-44	52.33	0.00	29.76	0.853	0.00	0.13	13.46	3.42	0.16	100.12	0.31
Average	52.63	0.04	28.93	0.828	0.02	0.13	13.34	3.68	0.18	99.79	0.33
2 σ	2.70	0.06	1.96	0.162	0.04	0.06	1.78	0.90	0.09	0.87	0.08
No59-3	53.18	0.04	29.53	0.854	0.00	0.12	13.24	3.78	0.21	100.94	0.34
No59-4	55.29	0.09	27.78	0.941	0.00	0.10	11.61	4.76	0.31	100.86	0.42
No59-11	52.17	0.03	30.01	0.708	0.00	0.04	14.29	3.41	0.14	100.79	0.30
No59-17	54.58	0.12	27.35	1.362	0.00	0.34	12.24	4.15	0.30	100.44	0.37
No59-21	50.64	0.04	30.69	0.682	0.00	0.10	14.77	3.01	0.13	100.08	0.27
No59-23	50.92	0.05	30.38	0.817	0.01	0.13	14.42	3.20	0.14	100.11	0.28
No59-24	51.15	0.03	29.85	0.692	0.01	0.12	13.70	3.57	0.15	99.26	0.32
No59-25	50.75	0.02	30.73	0.711	0.01	0.11	14.51	3.20	0.16	100.20	0.28
No59-26	51.40	0.03	29.96	0.824	0.00	0.12	14.02	3.37	0.17	99.89	0.30
No59-27	53.60	0.09	28.68	0.958	0.00	0.17	12.43	4.15	0.22	100.28	0.37
No59-29	53.49	0.06	28.12	0.676	0.03	0.10	12.07	4.39	0.24	99.16	0.39
No59-30	52.24	0.07	29.15	0.719	0.03	0.13	13.02	3.90	0.15	99.43	0.35
No59-31	52.99	0.00	28.77	0.737	0.00	0.10	12.56	4.17	0.19	99.52	0.37

Tufa Trig
108-131
Tf8

No59-33	52.16	0.07	28.92	0.892	0.00	0.12	13.09	3.83	0.18	99.27	0.34
No59-34	52.61	0.08	28.95	0.999	0.00	0.13	12.83	4.01	0.22	99.82	0.36
No59-35	51.13	0.08	29.50	0.907	0.04	0.09	13.60	3.59	0.19	99.13	0.32
No59-38	49.82	0.02	30.89	0.845	0.00	0.09	15.06	2.81	0.14	99.71	0.25
No59-41	54.06	0.08	28.26	0.839	0.00	0.14	12.09	4.30	0.23	100.04	0.39
No59-42	53.66	0.07	28.28	0.853	0.03	0.16	12.43	4.12	0.20	99.81	0.37
No59-44	50.25	0.08	30.40	0.828	0.05	0.10	14.30	3.33	0.14	99.46	0.29
Average	52.30	0.06	29.31	0.842	0.01	0.13	13.31	3.75	0.19	99.91	0.33
2 σ	3.06	0.06	2.09	0.312	0.03	0.12	2.06	1.02	0.10	1.12	0.09
No131-2	53.80	0.00	27.79	0.848	0.02	0.17	11.97	4.39	0.28	99.26	0.39
No131-4	54.32	0.04	27.77	0.906	0.01	0.17	11.69	4.51	0.28	99.72	0.40
No131-11	54.18	0.08	27.60	0.737	0.03	0.12	11.38	4.68	0.29	99.12	0.42
No131-12	53.82	0.05	27.65	0.857	0.02	0.16	11.66	4.62	0.29	99.13	0.41
No131-13	50.34	0.04	30.80	0.570	0.01	0.11	14.42	3.09	0.15	99.53	0.28
No131-14	49.77	0.00	31.22	0.681	0.03	0.09	14.78	2.91	0.14	99.63	0.26
No131-16	53.40	0.04	28.56	0.782	0.00	0.14	12.39	4.12	0.20	99.63	0.37
No131-17	53.39	0.06	28.12	0.855	0.04	0.12	12.00	4.42	0.25	99.25	0.39
No131-18	54.18	0.05	27.61	0.859	0.00	0.14	11.33	4.67	0.26	99.09	0.42
No131-19	53.32	0.04	28.86	0.730	0.00	0.16	12.23	4.10	0.20	99.65	0.37
No131-22	54.08	0.05	28.24	0.776	0.00	0.14	11.75	4.51	0.28	99.83	0.40
No131-23	55.05	0.09	27.17	0.824	0.04	0.15	10.75	4.93	0.35	99.35	0.44
No131-27	54.36	0.07	27.73	0.870	0.00	0.17	11.52	4.60	0.28	99.63	0.41
No131-28	53.78	0.10	27.78	0.832	0.00	0.14	11.61	4.53	0.26	99.04	0.41

No131-37	54.26	0.12	27.66	0.920	0.05	0.13	11.09	4.76	0.35	99.34	0.43
No131-38	54.60	0.04	27.56	0.840	0.00	0.14	11.11	4.70	0.30	99.29	0.43
No131-39	53.09	0.00	28.61	0.820	0.04	0.11	12.38	4.04	0.21	99.30	0.37
No131-40	57.31	0.38	23.44	3.054	0.04	0.83	9.54	3.62	0.91	99.14	0.38
No131-41	53.49	0.05	28.43	0.649	0.00	0.08	11.90	4.27	0.25	99.14	0.39
No131-42	51.45	0.06	29.79	0.675	0.00	0.08	13.25	3.75	0.18	99.22	0.34
No131-43	52.71	0.06	28.96	0.631	0.04	0.12	12.32	4.21	0.25	99.30	0.38
No131-57	53.46	0.08	28.76	0.817	0.00	0.16	12.12	4.04	0.23	99.66	0.37
No131-58	55.90	0.08	26.89	0.668	0.00	0.08	10.42	5.17	0.38	99.59	0.46
No131-64	51.94	0.01	29.76	0.663	0.00	0.12	13.05	3.50	0.20	99.24	0.32
No131-65	53.63	0.06	28.44	0.749	0.00	0.12	11.61	4.29	0.28	99.17	0.39
No131-66	53.54	0.04	28.31	0.764	0.00	0.15	11.97	4.38	0.24	99.44	0.39
No131-67	54.36	0.09	27.50	0.905	0.03	0.13	11.26	4.75	0.31	99.33	0.43
No131-71	54.54	0.04	28.17	0.715	0.06	0.13	11.30	4.62	0.28	99.85	0.42
No131-72	53.13	0.05	28.62	0.740	0.00	0.14	12.31	4.26	0.22	99.47	0.38
No131-73	53.74	0.03	28.16	0.792	0.00	0.11	11.85	4.46	0.28	99.42	0.40
No131-75	53.04	0.01	28.60	0.849	0.01	0.12	12.27	4.32	0.21	99.44	0.38
No131-79	52.31	0.03	29.16	0.594	0.00	0.12	12.98	3.76	0.21	99.15	0.34
No131-80	52.40	0.08	29.11	0.607	0.00	0.13	12.94	3.71	0.23	99.22	0.34
No131-86	55.00	0.10	27.84	1.018	0.00	0.14	10.75	4.58	0.30	99.74	0.43
No131-87	53.43	0.06	28.70	0.859	0.00	0.14	11.69	4.16	0.23	99.26	0.39
No131-88	54.51	0.07	27.72	0.815	0.03	0.15	11.40	4.59	0.26	99.53	0.42
No131-89	52.56	0.03	29.32	0.847	0.00	0.11	13.01	3.84	0.18	99.89	0.34
No131-90	51.91	0.05	29.87	0.703	0.00	0.11	13.50	3.76	0.21	100.10	0.33

	No131-100	52.99	0.06	28.66	0.821	0.02	0.13	12.48	4.11	0.25	99.52	0.37
	No131-101	53.88	0.07	28.04	0.848	0.04	0.13	11.51	4.51	0.22	99.24	0.41
	No131-104	54.76	0.05	27.13	0.971	0.00	0.16	11.05	4.82	0.29	99.22	0.43
	Average	53.55	0.06	28.29	0.841	0.01	0.15	11.96	4.27	0.27	99.42	0.39
	2 σ	2.69	0.11	2.42	0.738	0.04	0.22	1.99	0.96	0.23	0.51	0.08
108-137	No137-8	55.12	0.08	27.62	0.971	0.00	0.12	11.12	4.87	0.38	100.27	0.43
Tf13	No137-20	53.01	0.05	28.46	0.811	0.03	0.10	12.12	4.43	0.24	99.25	0.39
	No137-21	53.30	0.06	28.73	0.786	0.00	0.11	11.97	4.36	0.27	99.58	0.39
	No137-27	53.00	0.04	28.96	0.748	0.01	0.13	12.47	4.09	0.29	99.72	0.37
	No137-28	53.54	0.06	28.57	0.642	0.00	0.09	12.06	4.29	0.34	99.60	0.38
	No137-30	55.63	0.05	27.08	0.590	0.02	0.10	10.38	5.28	0.35	99.48	0.47
	No137-31	53.04	0.05	28.92	0.559	0.00	0.04	12.62	4.19	0.25	99.66	0.37
	No137-32	53.77	0.07	28.71	0.697	0.00	0.07	11.79	4.37	0.29	99.75	0.39
	No137-33	54.62	0.10	27.79	0.581	0.00	0.06	11.20	4.81	0.34	99.48	0.43
	No137-34	54.64	0.08	27.75	0.633	0.00	0.06	11.07	4.84	0.37	99.44	0.43
	No137-35	53.68	0.08	28.37	0.634	0.00	0.06	11.68	4.40	0.28	99.19	0.40
	No137-36	53.29	0.10	28.37	0.687	0.00	0.11	12.14	4.40	0.27	99.36	0.39
	No137-41	52.88	0.10	29.03	0.721	0.00	0.12	12.92	3.99	0.25	100.01	0.35
	No137-45	53.12	0.07	28.05	0.832	0.00	0.15	12.56	4.13	0.28	99.20	0.37
	No137-54	55.75	0.04	26.58	0.664	0.00	0.08	10.53	5.14	0.38	99.15	0.46
	No137-57	53.95	0.03	27.59	0.728	0.00	0.12	11.94	4.57	0.27	99.22	0.40

No137-59	53.85	0.06	27.77	0.779	0.00	0.13	11.84	4.43	0.30	99.18	0.40	
No137-61	53.80	0.05	27.87	0.786	0.00	0.07	11.98	4.39	0.25	99.19	0.39	
No137-62	53.49	0.04	28.24	0.674	0.00	0.10	12.22	4.44	0.31	99.51	0.39	
No137-64	52.67	0.05	29.07	0.740	0.01	0.09	12.76	4.05	0.28	99.72	0.36	
No137-65	52.67	0.07	29.20	0.681	0.02	0.09	12.72	4.03	0.29	99.77	0.36	
No137-68	53.14	0.05	28.90	0.943	0.00	0.08	12.31	4.20	0.25	99.87	0.38	
No137-69	53.37	0.10	27.83	0.981	0.01	0.18	12.03	4.19	0.32	99.02	0.38	
No137-82	53.09	0.09	28.67	0.757	0.00	0.13	12.42	4.22	0.27	99.65	0.37	
No137-83	54.22	0.02	27.66	0.753	0.02	0.09	11.58	4.64	0.30	99.29	0.41	
No137-84	51.90	0.03	29.79	0.674	0.00	0.13	13.26	3.79	0.14	99.71	0.34	
No137-85	54.25	0.07	28.16	0.579	0.00	0.08	11.47	4.71	0.29	99.64	0.42	
No137-86	53.07	0.03	29.58	0.655	0.00	0.13	13.11	3.94	0.20	100.71	0.35	
Average	53.64	0.06	28.33	0.725	0.00	0.10	12.01	4.40	0.29	99.56	0.39	
2 σ	1.79	0.05	1.48	0.223	0.02	0.06	1.43	0.71	0.10	0.74	0.06	
108-138	No138-2	53.86	0.12	27.74	0.949	0.03	0.12	11.83	4.52	0.30	99.48	0.40
Tf14	No138-6	53.52	0.06	28.40	0.758	0.09	0.12	12.20	4.42	0.29	99.85	0.39
	No138-7	54.62	0.10	27.59	0.774	0.01	0.12	11.32	4.72	0.28	99.58	0.42
	No138-8	54.19	0.11	28.11	0.840	0.01	0.12	11.77	4.60	0.30	100.05	0.41
	No138-12	53.69	0.09	27.78	0.896	0.00	0.17	11.39	4.67	0.33	99.01	0.42
	No138-24	53.73	0.06	28.62	0.746	0.00	0.11	11.93	4.33	0.27	99.79	0.39
	No138-25	51.62	0.04	30.11	0.640	0.00	0.11	13.46	3.52	0.20	99.70	0.32
	No138-26	49.24	0.01	31.25	0.584	0.02	0.11	15.29	2.74	0.14	99.37	0.24
	No138-27	49.94	0.04	31.13	0.634	0.01	0.06	14.86	3.04	0.12	99.83	0.27

No138-28	50.85	0.00	30.73	0.662	0.00	0.09	14.06	3.40	0.17	99.95	0.30
No138-48	52.86	0.06	28.80	0.812	0.00	0.11	12.15	4.09	0.24	99.12	0.37
No138-51	54.52	0.07	27.37	0.838	0.00	0.12	11.13	4.80	0.31	99.15	0.43
No138-55	47.01	0.01	32.86	0.588	0.00	0.08	16.69	1.99	0.09	99.31	0.18
No138-56	48.03	0.03	32.25	0.612	0.00	0.06	16.16	2.31	0.08	99.53	0.20
No138-57	48.73	0.04	31.77	0.548	0.00	0.09	15.56	2.65	0.11	99.50	0.23
No138-58	48.25	0.06	32.78	0.563	0.00	0.08	15.91	2.26	0.08	99.99	0.20
No138-59	51.20	0.02	30.53	0.712	0.01	0.10	14.34	3.38	0.19	100.52	0.30
No138-61	47.57	0.03	32.33	0.577	0.01	0.09	16.22	2.13	0.07	99.03	0.19
No138-62	53.74	0.02	28.05	0.852	0.00	0.12	11.63	4.35	0.28	99.05	0.40
No138-63	55.19	0.03	27.44	1.046	0.00	0.12	10.95	5.01	0.34	100.11	0.44
No138-64	53.22	0.02	28.23	0.789	0.00	0.11	12.03	4.29	0.30	99.01	0.39
No138-65	54.60	0.04	27.71	0.911	0.01	0.09	11.08	4.95	0.35	99.73	0.44
No138-71	52.44	0.03	29.64	0.876	0.02	0.08	12.93	4.03	0.22	100.26	0.36
No138-72	53.22	0.07	28.64	0.872	0.05	0.12	12.12	4.41	0.25	99.77	0.39
No138-73	52.60	0.06	29.49	0.761	0.02	0.07	12.85	3.94	0.23	100.05	0.35
No138-74	53.35	0.00	29.09	0.693	0.02	0.10	12.25	4.17	0.22	99.90	0.38
No138-75	54.73	0.05	27.61	0.658	0.04	0.08	10.85	4.93	0.32	99.30	0.44
No138-79	51.35	0.01	30.04	0.601	0.00	0.11	13.50	3.51	0.16	99.30	0.32
No138-80	47.71	0.05	33.03	0.643	0.02	0.10	16.45	1.99	0.07	100.05	0.18
No138-81	46.83	0.00	33.04	0.585	0.01	0.08	16.91	1.84	0.07	99.38	0.16
No138-82	51.09	0.01	30.08	0.619	0.00	0.11	13.59	3.61	0.14	99.24	0.32
No138-83	51.07	0.02	30.51	0.696	0.00	0.13	13.99	3.41	0.17	99.99	0.30
No138-89	51.69	0.06	30.12	0.805	0.00	0.09	13.65	3.56	0.19	100.16	0.32

	No138-90	46.71	0.00	33.06	0.545	0.00	0.09	16.75	1.79	0.06	99.03	0.16
	No138-91	47.69	0.05	32.94	0.578	0.00	0.06	16.62	2.00	0.04	99.98	0.18
	No138-104	53.47	0.10	28.21	0.723	0.00	0.12	11.68	4.54	0.27	99.11	0.41
	No138-105	54.66	0.05	27.66	0.675	0.02	0.10	11.01	4.91	0.37	99.49	0.44
	No138-106	54.28	0.00	28.19	0.770	0.04	0.10	11.43	4.69	0.31	99.82	0.42
	Average	51.66	0.03	30.08	0.711	0.01	0.10	13.60	3.55	0.20	99.61	0.32
	2 σ	5.36	0.05	4.05	0.256	0.03	0.04	4.26	2.21	0.20	0.88	0.20
1972-1975												
Ngauruhoe												
1972 Ngauruhoe	No72-2	54.63		28.29	1.139		0.17	11.69	4.27	0.39	100.57	0.39
	No72-6_2	55.59		27.10	0.947		0.18	11.45	4.71	0.39	100.37	0.42
	No72-10	55.83		27.76	1.074		0.21	11.55	4.58	0.44	101.45	0.41
	Average	55.35		27.72	1.053		0.19	11.56	4.52	0.41	100.80	0.40
	2 σ	1.27		1.19	0.195		0.05	0.23	0.46	0.05	1.14	0.03
1973 Ngauruhoe	Ng73#1	53.92		29.15	1.030		0.11	13.39	3.76	0.23	101.60	0.33
	Ng73#2_2	57.57		26.80	0.944		0.13	10.84	5.19	0.46	101.93	0.45
	Ng73#9_2	54.13		28.97	1.034		0.14	12.39	4.47	0.35	101.48	0.39
	Ng73#14	56.44		28.12	1.006		0.12	11.34	4.94	0.43	102.40	0.43
	Average	56.05		27.96	0.995		0.13	11.53	4.87	0.41	101.94	0.42
	2 σ	3.51		2.19	0.092		0.02	1.58	0.73	0.11	0.91	0.07

1974 Ngauruhoe	No74-2	57.57	25.01	2.037	0.37	10.84	4.26	0.60	100.68	0.40
	No74-9	55.70	28.21	1.103	0.16	11.95	4.64	0.28	102.05	0.41
	No74-13	55.99	25.57	2.122	0.60	10.56	4.28	0.60	99.73	0.41
	No74-18	52.60	30.16	1.046	0.15	13.87	3.67	0.21	101.70	0.32
	Average	55.46	27.24	1.577	0.32	11.81	4.21	0.42	101.04	0.38
	2 σ	4.15	4.79	1.163	0.42	3.00	0.80	0.41	2.10	0.08
1975 Ngauruhoe	No75-1_2	54.50	27.76	1.036	0.11	12.44	4.25	0.26	100.34	0.38
	No75-9	54.00	28.40	1.024	0.14	12.58	4.12	0.27	100.53	0.37
	No75-12_2	55.67	27.72	0.955	0.10	11.34	4.76	0.34	100.89	0.42
	Average	54.72	27.96	1.005	0.11	12.12	4.38	0.29	100.59	0.39
	2 σ	1.72	0.77	0.087	0.04	1.35	0.67	0.09	0.55	0.06
1995 Ruapehu	No95-4	53.96	29.54	0.757	0.15	12.64	4.25	0.26	101.56	0.37
	No95-5	56.21	28.65	0.888	0.15	11.91	4.77	0.38	102.95	0.41
	No95-11	55.69	28.12	0.957	0.18	11.83	4.77	0.39	101.92	0.41
	Average	55.29	28.77	0.867	0.16	12.13	4.60	0.34	102.14	0.40
	2 σ	2.35	1.44	0.203	0.03	0.89	0.60	0.14	1.44	0.05
1996 Ruapehu	No96-4	56.15	26.62	1.156	0.50	11.34	4.66	0.42	100.85	0.42
	No96-10	56.31	27.58	0.926	0.25	11.71	4.79	0.40	101.96	0.42
	No96-15	55.41	27.28	0.882	0.16	11.86	4.61	0.33	100.53	0.40
	Average	55.96	27.16	0.988	0.30	11.64	4.68	0.38	101.11	0.41
	2 σ	0.96	0.99	0.294	0.36	0.53	0.19	0.09	1.51	0.01

Appendix C13. Glass major element compositions analysed for the TgVC eruptive sequences studied. Mangatawai and Tufa Trig samples were analysed using a JEOL JXA-8900R electron microprobe equipped with four wavelength-dispersive spectrometers at the Institute of Earth Sciences, Academia Sinica, Taipei, Taiwan. 1972-1975 Ngauruhoe and 1995-1996 Ruapehu samples were analysed using a JEOL JXA-8800R electron microprobe equipped with four wavelength-dispersive spectrometers at the Graduate School of Science, Hokkaido University, Sapporo, Japan. The analyses highlighted in **yellow** were used for hygrothermobarometric calculations and *MELTS* modelling.

Eruptive sequence and tephra	Comment	SiO ₂	TiO ₂	Al ₂ O ₃	FeO	MnO	MgO	CaO	Na ₂ O	K ₂ O	Total
Mangatawai											
407-14	No14-10	59.91	1.13	13.94	9.38	0.14	2.84	6.25	3.38	1.54	98.50
	No14-11	59.90	1.15	14.19	8.84	0.09	2.74	6.24	3.25	1.58	97.97
	No14-12	60.72	1.04	13.97	9.38	0.13	2.74	5.73	3.19	1.46	98.36
	No14-21	54.71	0.63	20.44	6.06	0.14	2.65	9.93	2.74	0.98	98.28
	No14-51	58.68	1.17	13.99	9.02	0.22	2.92	6.54	2.48	1.71	96.73
	Average	58.78	1.02	15.31	8.53	0.14	2.78	6.94	3.01	1.45	97.97
	2 σ	4.78	0.45	5.74	2.81	0.09	0.21	3.40	0.76	0.56	1.43
407-15	No15-2	59.97	1.13	14.36	8.23	0.10	2.61	6.54	3.04	1.77	97.75
	No15-9	60.05	1.30	13.60	9.57	0.11	2.48	6.03	2.06	1.88	97.07
	No15-12	60.02	1.24	13.43	9.64	0.10	2.44	5.84	1.97	1.90	96.58
	No15-14	58.55	1.07	14.49	8.79	0.12	3.21	6.71	2.38	1.59	96.91
	No15-15	58.39	0.99	14.78	8.49	0.08	3.16	6.71	2.12	1.60	96.33
	No15-17	58.60	0.96	14.67	8.78	0.17	3.26	6.68	2.43	1.54	97.07

	No15-22	58.65	1.08	14.48	8.72	0.11	3.17	6.75	2.34	1.60	96.90
	No15-41	59.06	1.04	14.28	8.74	0.18	3.08	6.59	2.19	1.63	96.79
	No15-52	59.67	1.20	13.83	8.85	0.13	2.74	6.21	2.22	1.78	96.61
	No15-80	59.77	1.11	14.49	8.31	0.12	3.10	6.73	2.34	1.69	97.64
	No15-81	59.05	1.07	14.54	8.54	0.11	3.23	6.67	2.38	1.62	97.20
	No15-82	58.68	0.98	14.71	8.31	0.06	3.05	6.74	2.22	1.60	96.36
	Average	59.20	1.10	14.30	8.75	0.11	2.96	6.52	2.31	1.68	96.93
	2 σ	1.29	0.21	0.89	0.90	0.07	0.61	0.62	0.54	0.24	0.90
407-16	No16-9	60.42	1.22	13.99	8.89	0.14	2.51	6.33	2.47	1.80	97.76
	No16-10	60.47	1.41	13.41	9.40	0.13	2.46	6.26	2.13	1.88	97.55
	No16-21	61.44	1.34	13.23	9.22	0.11	2.36	5.81	2.53	2.00	98.04
	No16-36	60.73	1.08	16.28	6.94	0.07	2.03	6.81	3.49	1.50	98.94
	No16-75	60.40	1.22	14.19	8.49	0.10	2.92	5.89	2.37	2.28	97.86
		60.69	1.25	14.22	8.59	0.11	2.46	6.22	2.60	1.89	98.03
		0.88	0.25	2.44	1.96	0.05	0.64	0.80	1.04	0.57	1.08
407-17	No17-2	59.13	1.11	13.87	9.52	0.09	2.78	6.50	2.20	1.73	96.93
	No17-47	60.97	1.32	13.06	9.15	0.16	2.48	5.74	1.63	2.16	96.66
	No17-80	58.11	1.25	14.37	9.74	0.16	2.71	7.05	2.57	1.77	97.72
	Average	59.40	1.23	13.77	9.47	0.14	2.66	6.43	2.13	1.89	97.10
	2 σ	2.90	0.22	1.32	0.60	0.08	0.32	1.32	0.95	0.47	1.11

407-18	No18-15	58.87	1.15	14.17	9.54	0.13	2.91	6.81	1.96	1.46	96.99
	No18-22	58.19	1.08	14.43	9.02	0.14	3.31	6.55	1.46	3.55	97.73
	No18-42	59.66	1.40	13.52	8.81	0.07	2.52	6.14	2.52	2.03	96.67
	No18-44	59.03	1.21	14.02	9.24	0.17	2.49	6.15	2.32	1.84	96.47
	No18-48	58.60	1.14	14.37	8.92	0.15	2.76	6.47	2.25	1.77	96.43
	No18-51	59.77	1.25	13.10	9.65	0.12	2.69	6.13	1.48	2.12	96.30
	Average	59.02	1.20	13.94	9.20	0.13	2.78	6.38	2.00	2.13	96.76
	2 σ	1.22	0.22	1.05	0.68	0.07	0.60	0.56	0.89	1.47	1.06
407-47	No47-12	60.59	1.03	14.17	8.07	0.07	2.81	6.04	2.61	1.89	97.27
	No47-13	60.46	1.11	14.25	7.94	0.14	2.83	6.18	2.18	1.73	96.81
	No47-14	60.23	1.00	14.29	8.23	0.08	2.91	6.01	2.53	1.76	97.05
	No47-37	61.05	1.11	13.51	8.45	0.14	2.41	5.79	2.35	1.96	96.75
	Average	60.58	1.06	14.06	8.17	0.11	2.74	6.00	2.42	1.83	96.97
	2 σ	0.69	0.11	0.73	0.43	0.07	0.45	0.32	0.39	0.22	0.48
407-49	No49-5	63.17	1.34	13.00	9.27	0.10	1.40	5.01	2.64	2.43	98.36
	No49-12	61.03	1.21	13.80	8.53	0.16	2.45	5.94	2.40	1.92	97.43
	No49-13	61.36	1.12	13.94	8.42	0.06	2.70	5.97	2.36	1.94	97.85
	No49-18	60.00	1.09	14.70	7.87	0.09	3.03	6.97	3.72	1.30	98.75
	No49-32	60.81	1.19	13.93	8.29	0.13	2.58	5.79	2.57	1.94	97.23
	Average	61.27	1.19	13.87	8.47	0.10	2.43	5.94	2.74	1.91	97.92
	2 σ	2.35	0.20	1.21	1.02	0.08	1.23	1.40	1.12	0.81	1.27

407-54	No54-13	61.04	1.39	13.46	8.73	0.11	2.04	5.93	2.65	2.05	97.40
	No54-25	59.89	1.19	13.32	8.70	0.12	2.89	6.11	2.27	1.77	96.26
	No54-26	60.06	1.21	13.40	8.83	0.09	2.74	6.13	2.40	1.79	96.65
	No54-27	60.40	1.26	13.40	8.90	0.18	2.78	6.38	2.29	1.76	97.35
	No54-38	60.11	1.08	14.15	8.17	0.08	2.82	6.49	2.78	1.56	97.23
	No54-39	59.65	1.08	13.73	8.68	0.09	2.93	6.35	2.41	1.63	96.53
	No54-40	60.25	1.22	13.61	8.72	0.15	2.95	6.43	2.48	1.77	97.58
	No54-41	60.31	1.27	13.54	8.73	0.15	2.82	6.29	2.39	1.81	97.30
	Average	60.21	1.21	13.58	8.68	0.12	2.75	6.26	2.46	1.77	97.04
	2 σ	0.83	0.21	0.53	0.44	0.07	0.59	0.38	0.35	0.29	0.97
407-56	No56-15	60.73	1.11	13.67	8.31	0.08	2.90	6.19	2.43	1.99	97.41
	No56-18	60.83	1.12	13.66	8.13	0.14	2.66	6.20	2.39	1.96	97.10
	No56-19	59.71	1.10	13.09	8.79	0.15	3.69	6.36	2.34	1.80	97.02
	No56-20	62.15	1.24	13.50	7.90	0.15	2.38	5.82	2.45	2.01	97.58
	No56-21	61.71	1.14	13.75	8.21	0.10	2.51	6.05	2.61	1.91	97.99
	No56-22	61.12	1.21	13.86	8.12	0.10	2.63	5.99	2.58	2.00	97.62
	No56-28	61.30	1.13	14.02	8.15	0.10	2.62	6.11	2.42	1.96	97.80
	No56-29	60.70	1.15	13.72	8.59	0.07	2.67	6.12	2.50	1.99	97.50
	No56-30	60.41	1.16	14.09	8.23	0.10	2.74	6.34	2.41	1.87	97.33
	No56-34	60.40	1.12	14.10	8.49	0.10	2.70	6.17	2.53	1.91	97.51
	No56-35	60.45	1.12	14.23	8.53	0.13	2.74	6.38	2.55	1.91	98.02
	No56-40	62.31	1.32	12.99	8.50	0.11	2.09	5.45	1.79	2.17	96.73
	No56-42	60.97	1.16	14.11	8.14	0.09	2.72	5.52	2.43	2.16	97.30

	No56-45	60.52	1.32	12.70	9.03	0.11	3.25	5.62	2.14	2.02	96.70
	No56-46	61.68	1.33	13.10	8.46	0.17	2.46	5.94	2.29	2.04	97.48
	Average	61.00	1.18	13.64	8.37	0.11	2.72	6.02	2.39	1.98	97.41
	2 σ	1.43	0.17	0.94	0.59	0.06	0.74	0.59	0.41	0.20	0.79
407-59	No59-1	60.31	1.07	14.14	8.37	0.12	2.66	6.17	2.44	1.96	97.25
	No59-2	60.12	1.02	14.27	8.10	0.20	2.66	6.19	2.38	1.84	96.78
	No59-20	60.43	1.13	14.17	8.80	0.15	2.45	6.29	2.87	1.84	98.12
	No59-22	59.78	1.17	13.57	9.20	0.11	2.82	6.31	3.13	1.93	98.01
	No59-28	59.15	1.11	14.86	7.97	0.10	2.84	6.44	2.94	1.79	97.19
	No59-36	60.14	1.13	13.98	7.73	0.14	2.71	5.10	1.98	3.09	96.00
	No59-37	60.48	1.23	14.01	8.33	0.17	2.97	5.42	2.24	2.48	97.33
	Average	60.06	1.12	14.14	8.36	0.14	2.73	5.99	2.57	2.13	97.24
	2 σ	0.93	0.13	0.78	1.00	0.07	0.33	1.02	0.84	0.96	1.44
Tufa Trig	No131-3	61.36	1.07	15.03	6.39	0.14	2.60	5.53	2.43	2.12	96.68
108-131	No131-5	61.73	0.91	14.69	6.56	0.01	2.34	5.24	2.43	2.32	96.22
Tf8	No131-26	63.19	1.00	14.25	6.31	0.11	2.25	4.46	3.79	2.10	97.46
	No131-49	62.51	0.86	15.09	6.58	0.10	2.15	5.25	3.32	2.11	97.96
	No131-51	62.17	0.91	14.71	6.90	0.03	2.36	5.02	2.58	2.54	97.22
	No131-82	61.86	0.89	14.98	6.70	0.05	2.47	4.83	2.55	2.30	96.64

	Average	62.14	0.94	14.79	6.57	0.07	2.36	5.05	2.85	2.25	97.03
	2 σ	1.29	0.16	0.63	0.42	0.10	0.32	0.75	1.14	0.34	1.27
108-137	No137-12	62.04	1.10	14.82	7.05	0.11	2.23	4.96	2.64	2.61	97.54
Tf13	No137-14	60.76	0.91	14.70	7.45	0.09	2.41	5.04	2.66	2.52	96.54
	No137-26	62.17	0.99	14.22	6.76	0.11	2.12	4.77	2.70	3.05	96.89
	No137-29	62.12	0.92	14.75	6.46	0.11	2.28	4.92	2.78	3.05	97.40
	No137-71	62.35	0.97	14.71	6.72	0.04	2.09	4.97	2.52	2.60	96.97
	No137-72	61.78	0.85	14.82	6.63	0.08	2.23	4.94	2.33	2.56	96.21
	No137-73	61.64	0.95	14.72	6.65	0.04	2.14	4.88	2.46	2.55	96.02
	No137-74	62.06	0.98	14.88	6.49	0.11	2.21	4.88	2.44	2.57	96.63
	Average	61.86	0.96	14.70	6.78	0.09	2.21	4.92	2.57	2.69	96.77
	2 σ	1.00	0.14	0.41	0.65	0.06	0.20	0.16	0.31	0.45	1.07
108-138	No138-1	62.04	1.09	14.56	6.87	0.06	2.20	4.81	2.68	2.56	96.87
Tf14	No138-4	62.85	1.03	14.73	6.75	0.10	2.13	4.93	2.35	2.51	97.37
	No138-47	62.94	0.99	15.19	6.25	0.06	2.06	4.56	3.77	2.48	98.28

	No138-100	62.35	1.04	15.01	6.73	0.13	2.20	5.17	1.85	2.64	97.13
	No138-101	62.21	1.04	15.19	6.79	0.11	2.23	4.79	1.97	2.65	96.98
	No138-102	61.95	1.08	15.07	7.05	0.09	2.22	4.95	2.06	2.74	97.22
	No138-103	61.89	1.12	14.56	7.11	0.09	2.60	4.96	1.82	2.29	96.44
	Average	62.32	1.06	14.90	6.79	0.09	2.23	4.88	2.36	2.55	97.18
	2 σ	0.85	0.09	0.56	0.56	0.05	0.34	0.38	1.38	0.29	1.14
1972-1975											
Ngauruhoe											
1972 Ngauruhoe	No72-1	60.93	1.40	13.34	8.85	0.13	2.38	5.86	3.62	2.57	99.09
	No72-7	61.09	1.36	12.09	9.76	0.17	3.66	5.82	3.31	2.29	99.55
	No72-8	62.35	1.45	13.20	8.96	0.16	2.37	5.64	3.34	2.54	100.02
	No72-9	62.15	1.35	13.27	8.95	0.12	2.27	5.77	3.41	2.55	99.84
	No72-12	61.88	1.41	13.86	8.65	0.13	2.38	5.92	3.46	2.33	100.01
	No72-13	62.34	1.33	13.46	8.94	0.14	2.49	5.84	3.52	2.41	100.47
	Average	61.79	1.38	13.20	9.02	0.14	2.59	5.81	3.44	2.45	99.83
	2 σ	1.26	0.09	1.18	0.76	0.04	1.05	0.19	0.23	0.24	0.94
1973 Ngauruhoe	No73-4	63.70	1.46	13.27	8.90	0.16	2.21	5.93	3.84	2.22	101.67
	No73-8	62.77	1.36	14.35	8.43	0.13	1.81	5.55	3.28	2.47	100.16
	No73-10	63.22	1.48	13.54	9.14	0.13	1.90	5.28	3.31	2.67	100.67
	No73-11	64.19	1.57	13.18	8.91	0.17	1.68	4.89	3.24	3.16	100.97

	No73-16	64.71	1.56	13.23	8.80	0.13	1.68	5.07	3.59	2.95	101.71
	Average	63.72	1.49	13.51	8.83	0.14	1.86	5.34	3.45	2.69	101.04
	2 σ	1.54	0.17	0.98	0.52	0.04	0.43	0.82	0.51	0.75	1.33
1974 Ngauruhoe	No74-3	64.16	1.44	14.14	8.64	0.15	1.58	5.45	3.79	1.65	101.00
	No74-8	64.77	1.50	13.50	8.73	0.15	1.57	4.81	3.39	3.01	101.43
	No74-12	63.91	1.45	13.48	8.62	0.14	1.65	5.18	3.17	2.81	100.40
	No74-14	63.81	1.42	12.83	9.62	0.16	2.56	4.95	3.30	2.49	101.15
	No74-19	64.29	1.50	13.19	9.24	0.18	1.54	4.83	3.63	2.69	101.10
	Average	64.19	1.46	13.43	8.97	0.15	1.78	5.05	3.46	2.53	101.01
	2 σ	0.76	0.07	0.96	0.89	0.03	0.88	0.54	0.50	1.05	0.76
1975 Ngauruhoe	No75-2	61.25	1.14	14.77	8.65	0.16	2.42	5.95	3.47	2.01	99.81
	No75-10	64.64	1.11	14.08	7.43	0.14	1.64	4.76	3.55	2.52	99.86
	No75-13	66.27	1.11	13.23	7.25	0.14	1.32	4.20	3.69	2.83	100.03
	Average	64.05	1.12	14.03	7.78	0.15	1.79	4.97	3.57	2.45	99.90
	2 σ	5.13	0.04	1.54	1.53	0.03	1.13	1.79	0.23	0.82	0.23
1995-1996 Ruapehu											
1995 Ruapehu	No95-1	63.76	1.03	15.04	6.19	0.11	2.35	5.11	3.93	2.64	100.14
	No95-8	62.06	0.91	15.69	5.97	0.10	2.95	5.89	3.90	2.27	99.74
	No95-9	63.29	0.96	15.33	6.21	0.14	2.49	5.26	4.01	2.71	100.39
	Average	63.04	0.97	15.35	6.12	0.12	2.59	5.42	3.94	2.54	100.09
	2 σ	1.76	0.11	0.65	0.27	0.04	0.63	0.83	0.12	0.46	0.65

1996 Ruapehu	No96-6	64.11	1.19	14.28	6.70	0.10	2.01	4.85	3.39	2.89	99.52
	No96-9	63.59	1.07	14.91	6.46	0.13	2.19	5.18	3.73	2.72	99.98
	No96-16	63.21	1.03	15.12	6.43	0.13	2.11	5.23	3.87	2.74	99.87
	Average	63.64	1.10	14.77	6.53	0.12	2.10	5.09	3.66	2.78	99.79
	2 σ	0.91	0.16	0.87	0.30	0.04	0.18	0.42	0.49	0.19	0.48

Appendix D: Statements of Contribution

Appendix D1. Statement of Contribution for Chapter 4 which was accepted and published in *Microscopy and Microanalysis* in December 2018.

Lormand C., Georg F., Zellmer G.F., Németh K., Kilgour G., Mead S., Palmer A.S., Sakamoto N., Yurimoto H., Moebis A. (2018) Weka Trainable Segmentation plugin in ImageJ: a semi-automatic tool applied to Crystal Size Distributions of microlites in volcanic rocks. *Microscopy and Microanalysis*, **24**: 667–675.

DOI: <https://doi.org/10.1017/S1431927618015428>

DRC 16



STATEMENT OF CONTRIBUTION DOCTORATE WITH PUBLICATIONS/MANUSCRIPTS

We, the candidate and the candidate's Primary Supervisor, certify that all co-authors have consented to their work being included in the thesis and they have accepted the candidate's contribution as indicated below in the *Statement of Originality*.

Name of candidate:	Charline Lormand	
Name/title of Primary Supervisor:	Georg Florian Zellmer	
Name of Research Output and full reference:		
<small>Lormand, C., Zellmer, G.F., Németh, K., Kilgus, G., Mead, S., Palmer, A. S., Sakamoto, N., Yurimoto, H., Moebs, A. (2019) Weka Trainable Segmentation plugin in ImageJ: a semi-automatic tool applied to crystal size distributions of microclasts in volcanic rock</small>		
In which Chapter is the Manuscript /Published work:	Chapter 4	
Please indicate:		
<ul style="list-style-type: none"> The percentage of the manuscript/Published Work that was contributed by the candidate: 	85%	
and		
<ul style="list-style-type: none"> Describe the contribution that the candidate has made to the Manuscript/Published Work: 	The candidate sampled and prepared two of the samples for imaging purposes. The candidate collected images of the samples using Scanning Electron Microscopes. The candidate processed the data, wrote and edited the manuscript	
For manuscripts intended for publication please indicate target journal:		
Microscopy and Microanalysis		
Candidate's Signature:	Charline Lormand	<small>Digitally signed by Charline Lormand Date: 2019.12.05 11:12:47 +13'00'</small>
Date:	05 December 2019	
Primary Supervisor's Signature:	Georg F. Zellmer	<small>Digitally signed by Georg F. Zellmer Date: 2019.12.05 14:25:16 +13'00'</small>
Date:	05 December 2019	

(This form should appear at the end of each thesis chapter/section/appendix submitted as a manuscript/ publication or collected as an appendix at the end of the thesis)

GRS Version 4– January 2019

Appendix D2. Statement of Contribution for Chapter 5 which will be submitted for publication in *Frontiers in Earth Science*, under the title of “*Intermittent ascent of aphyric andesitic melts revealed by cryptic micro-antecryst textures*”.

DRC 16



STATEMENT OF CONTRIBUTION DOCTORATE WITH PUBLICATIONS/MANUSCRIPTS

We, the candidate and the candidate's Primary Supervisor, certify that all co-authors have consented to their work being included in the thesis and they have accepted the candidate's contribution as indicated below in the *Statement of Originality*.

Name of candidate:	Charline Lormand	
Name/title of Primary Supervisor:	Georg Zellmer	
Name of Research Output and full reference:		
Lormand, C. Zellmer, O. F. Sakamoto, N. Kilgour, O. Palmer, A. Németh, K. Usuki, T. Itzuka, Y. Moëlis A. Yurimoto, H. (to be submitted) Intermittent ascent of aphyric andesitic melts revealed by cryptic micro-antecryst textures		
In which Chapter is the Manuscript /Published work:	Chapter 5	
Please indicate:		
<ul style="list-style-type: none"> The percentage of the manuscript/Published Work that was contributed by the candidate: 	80%	
and		
<ul style="list-style-type: none"> Describe the contribution that the candidate has made to the Manuscript/Published Work: 	The candidate sampled and prepared 9 out of 22 samples for analytical purposes. The candidate collected images of the samples using Scanning Electron Microscopes and the 1270 Secondary Ion Mass Spectrometer in Japan. The	
For manuscripts intended for publication please indicate target journal:		
Frontiers in Earth Science		
Candidate's Signature:	Charline Lormand	Digitally signed by Charline Lormand Date: 2020.04.16 12:17:33 +12'00'
Date:	16 April 2020	
Primary Supervisor's Signature:	Georg F. Zellmer	Digitally signed by Georg F. Zellmer Date: 2020.04.16 12:46:32 +12'00'
Date:	16 April 2020	

(This form should appear at the end of each thesis chapter/section/appendix submitted as a manuscript/ publication or collected as an appendix at the end of the thesis)

GRS Version 4– January 2019

Appendix D3. Statement of Contribution for Chapter 6 which has been submitted and reviewed for publication in Journal of Petrology, was deemed acceptable pending revisions, and the revised script has been resubmitted under the title of “*Slow ascent of unusually hot intermediate magmas triggering Strombolian to sub-Plinian eruptions*”.

DRC 16



STATEMENT OF CONTRIBUTION DOCTORATE WITH PUBLICATIONS/MANUSCRIPTS

We, the candidate and the candidate's Primary Supervisor, certify that all co-authors have consented to their work being included in the thesis and they have accepted the candidate's contribution as indicated below in the *Statement of Originality*.

Name of candidate:	Charline Lormand	
Name/title of Primary Supervisor:	Georg Florian Zellmer	
Name of Research Output and full reference:		
<small>Lormand, C., Zellmer, G. F., Rigour, G., Nénéth, K., Pakser, A., Salamoto, Y., Kuriki, T., Iizuka, Y., Moebis, A. (in review in Journal of Petrology) Slow ascent of unusually hot intermediate magmas triggering Strombolian to sub-Plinian eruptions.</small>		
In which Chapter is the Manuscript /Published work:	Chapter 6	
Please indicate:		
• The percentage of the manuscript/Published Work that was contributed by the candidate:	80%	
and		
• Describe the contribution that the candidate has made to the Manuscript/Published Work:	The candidate sampled and prepared 9 out of 22 samples for analytical purposes. The candidate collected images of the samples using Scanning Electron Microscopes. The candidate processed the data, wrote and edited the manuscript	
For manuscripts intended for publication please indicate target journal:		
Journal of Petrology		
Candidate's Signature:	Charline Lormand	<small>Digitally signed by Charline Lormand Date: 2019.12.05 11:29:27 +13'00'</small>
Date:	05 December 2019	
Primary Supervisor's Signature:	Georg F. Zellmer	<small>Digitally signed by Georg F. Zellmer Date: 2019.12.05 14:24:28 +13'00'</small>
Date:	05 December 2019	

(This form should appear at the end of each thesis chapter/section/appendix submitted as a manuscript/ publication or collected as an appendix at the end of the thesis)

GRS Version 4– January 2019



17 March 2020

Symbolic climb to Mount Ruapehu's summit four days after my PhD oral examination to contemplate Crater Lake (Te Wai ā-moe)'s response to another heating cycle.

What a view!